Studies in Computational Intelligence 581

Ahmad Taher Azar
Sundarapandian Vaidyanathan *Editors*

Chaos Modeling and Control Systems Design

Springer

Studies in Computational Intelligence

Volume 581

Series editor

Janusz Kacprzyk, Polish Academy of Sciences, Warsaw, Poland
e-mail: kacprzyk@ibspan.waw.pl

About this Series

The series "Studies in Computational Intelligence" (SCI) publishes new developments and advances in the various areas of computational intelligence—quickly and with a high quality. The intent is to cover the theory, applications, and design methods of computational intelligence, as embedded in the fields of engineering, computer science, physics and life sciences, as well as the methodologies behind them. The series contains monographs, lecture notes and edited volumes in computational intelligence spanning the areas of neural networks, connectionist systems, genetic algorithms, evolutionary computation, artificial intelligence, cellular automata, self-organizing systems, soft computing, fuzzy systems, and hybrid intelligent systems. Of particular value to both the contributors and the readership are the short publication time frame and the world-wide distribution, which enable both wide and rapid dissemination of research output.

More information about this series at http://www.springer.com/series/7092

Ahmad Taher Azar
Sundarapandian Vaidyanathan
Editors

Chaos Modeling and Control Systems Design

Springer

Editors
Ahmad Taher Azar
Faculty of Computers and Information
Benha University
Benha
Egypt

Sundarapandian Vaidyanathan
Research and Development Centre
Vel Tech University
Chennai
India

ISSN 1860-949X ISSN 1860-9503 (electronic)
Studies in Computational Intelligence
ISBN 978-3-319-13131-3 ISBN 978-3-319-13132-0 (eBook)
DOI 10.1007/978-3-319-13132-0

Library of Congress Control Number: 2014957150

Springer Cham Heidelberg New York Dordrecht London

Printed on acid-free paper

Springer International Publishing AG Switzerland is part of Springer Science+Business Media (www.springer.com)

Preface

About the Subject

Modeling, analysis, and control of dynamical systems have interested scientists and engineers for a long time. With the invention of digital computers, modeling and control have taken great importance with numerous applications in various fields. The basic steps involved in a control process are: (1) model the system mathematically (with some assumptions), (2) analyze the mathematical model and study its properties, (3) design a feedback control mechanism to meet the performance requirements, and (4) implement the control system and test its performance.

Mathematical modeling, analysis, and design of control systems are important research areas. The modern trend in engineering systems deals with complex systems having multiple-inputs and multiple-outputs and modern control theory with state space modeling is used to deal with such complex systems. Some classical examples of control systems are Watt governor, speed control system, temperature control system, DC motor, etc.

Nonlinear control systems have some exotic properties like chaos and fractals, and special control strategies are devised for control and synchronization of chaotic systems such as active control, adaptive control, sliding mode control, back stepping control, etc.

About the Book

The new Springer book, *Chaos Modeling and Control Systems Design,* consists of 15 contributed chapters by subject experts who are specialized in the various topics addressed in this book. The special chapters have been brought out in this book after a rigorous review process in the broad areas of Control Systems, Power Electronics, Computer Science, Information Technology, modeling, and engineering applications. Special importance was given to chapters offering practical

solutions and novel methods for the recent research problems in the main areas of this book, viz., Control Systems, Modeling, Computer Science, IT, and engineering applications.

This book discusses trends and applications of chaos modeling and control systems design in science and engineering.

Objectives of the Book

The objective of this book takes a modest attempt to cover the framework of chaos modeling and control systems design in a single volume. The book is not only a valuable title on the publishing market, but is also a successful synthesis of computational intelligence techniques in world literature. Several multidisciplinary applications in Control, Engineering, and Information Technology are discussed inside this book where control engineering methods have excellent potentials for use.

Organization of the Book

This well-structured book consists of 15 full chapters. They are organized into two parts.

Part I Chaos Modeling and Applications
Part II Control Systems and Applications

Book Features

- The book chapters deal with recent research problems in the areas of chaos theory, control systems, computer science, information technology, and engineering.
- The chapters contain a good literature survey with a long list of references.
- The chapters are well written with a good exposition of the research problem, methodology, and block diagrams.
- The chapters are lucidly illustrated with numerical examples and simulations.
- The chapters discuss details of engineering applications and future research areas.

Audience

The book is primarily meant for researchers from academia and industry working in the research areas—Chaos Theory, Control Engineering, Computer Science, and Information Technology. The book can also be used at the graduate or advanced undergraduate level as a textbook or major reference for courses such as control systems, process control and instrumentation, mathematical modeling, computational science, numerical simulation, applied artificial intelligence, fuzzy logic control, and many others.

Acknowledgments

As the editors, we hope that the chapters in this well-structured book will stimulate further research in chaos and control systems and utilize them in real-world applications. We would like to thank all the reviewers for their diligence in reviewing the chapters.

We hope sincerely that this book, covering so many different topics, will be useful for all readers.

We would like to thank all the reviewers for their diligence in reviewing the chapters.

Special thanks go to Springer, especially the book Editorial team.

Egypt Ahmad Taher Azar
India Sundarapandian Vaidyanathan

Contents

Part I Chaos Modeling and Applications

Analysis and Control of a 4-D Novel Hyperchaotic System 3
Sundarapandian Vaidyanathan and Ahmad Taher Azar

Analysis, Control and Synchronization of a Nine-Term 3-D Novel Chaotic System 19
Sundarapandian Vaidyanathan and Ahmad Taher Azar

Backstepping Controller Design for the Global Chaos Synchronization of Sprott's Jerk Systems 39
Sundarapandian Vaidyanathan, Babatunde A. Idowu and Ahmad Taher Azar

Multi-scroll Chaotic Oscillator Based on a First-Order Delay Differential Equation 59
Viet-Thanh Pham, Christos K. Volos and Sundarapandian Vaidyanathan

Projective Synchronization Scheme Based on Fuzzy Controller for Uncertain Multivariable Chaotic Systems 73
A. Boulkroune, A. Bouzeriba and S. Hamel

Part II Control Systems and Applications

Deadbeat Control for Multivariable Discrete Time Systems with Time Varying Delays 97
Ahmad Taher Azar and Fernando E. Serrano

Control of Smart Grid Residential Buildings with Demand Response 133
Sergi Rotger-Griful and Rune Hylsberg Jacobsen

Application of Some Modern Techniques in Load Frequency Control in Power Systems 163
Naglaa Kamel Bahgaat, Mohammed Ibrahim El-Sayed Ahmed, Mohamed A. Moustafa Hassan and Fahmy M. Bendary

Investigating Metaheuristics Applications for Capacitated Location Allocation Problem on Logistics Networks 213
Yonglin Ren and Anjali Awasthi

Classification of Heart Disorders Based on Tunable-Q Wavelet Transform of Cardiac Sound Signals 239
Shivnarayan Patidar and Ram Bilas Pachori

Reliability-Constrained Optimal Distribution System Reconfiguration 265
Salem Elsaiah, Mohammed Benidris and Joydeep Mitra

Machine Learning Aided Efficient Tools for Risk Evaluation and Operational Planning of Multiple Contingencies 291
Venkat Krishnan

Goal Directed Synthesis of Serial Manipulators Based on Task Descriptions 319
Sarosh Patel, Tarek Sobh and Ausif Mahmood

Intelligent Tracking Control System for Fast Image Scanning of Atomic Force Microscopes 351
Sajal K. Das, Hemanshu R. Pota and Ian R. Petersen

Fault Diagnosis Algorithms by Combining Structural Graphs and PCA Approaches for Chemical Processes 393
Rafika El Harabi, Rahma Smaili and Mohamed Naceur Abdelkrim

Part I
Chaos Modeling and Applications

Analysis and Control of a 4-D Novel Hyperchaotic System

Sundarapandian Vaidyanathan and Ahmad Taher Azar

Abstract Hyperchaotic systems are defined as chaotic systems with more than one positive Lyapunov exponent. Combined with one null Lyapunov exponent along the flow and one negative Lyapunov exponent to ensure boundedness of the solution, the minimal dimension for a continuous hyperchaotic system is four. The hyperchaotic systems are known to have important applications in secure communications and cryptosystems. First, this work describes an eleven-term 4-D novel hyperchaotic system with four quadratic nonlinearities. The qualitative properties of the novel hyperchaotic system are described in detail. The Lyapunov exponents of the system are obtained as $L_1 = 0.7781, L_2 = 0.2299, L_3 = 0$ and $L_4 = -12.5062$. The maximal Lyapunov exponent of the system (MLE) is $L_1 = 0.7781$. The Lyapunov dimension of the novel hyperchaotic system is obtained as $D_L = 3.0806$. Next, the work describes an adaptive controller design for the global chaos control of the novel hyperchaotic system. The main result for the adaptive controller design has been proved using Lyapunov stability theory. MATLAB simulations are described in detail for all the main results derived in this work for the eleven-term 4-D novel hyperchaotic system with four quadratic nonlinearities.

Keywords Chaos · Chaotic system · Hyperchaos · Hyperchaotic system · Adaptive control

S. Vaidyanathan (✉)
Research and Development Centre, Vel Tech University, Avadi, Chennai 600062, Tamil Nadu, India
e-mail: sundarvtu@gmail.com

A.T. Azar
Faculty of Computers and Information, Benha University, Benha, Egypt
e-mail: ahmad_t_azar@ieee.org

A.T. Azar and S. Vaidyanathan (eds.), *Chaos Modeling and Control Systems Design*, Studies in Computational Intelligence 581, DOI 10.1007/978-3-319-13132-0_1

1 Introduction

A chaotic system is a nonlinear dynamical system having a positive Lyapunov exponent. Since the discovery chaos in a 3-D weather model [29], there has been an active research on the modelling and analysis of new chaotic systems in the last 4 decades.

Some well-known paradigms of 3-D chaotic systems in the literature are [1, 3, 5, 6, 23, 28, 30, 39, 44, 49, 50, 56–58, 70, 72].

Chaotic systems have several important applications in science and engineering such as oscillators [18, 41], lasers [24, 66], chemical reactions [10, 34], cryptosystems [38, 51], secure communications [9, 32, 68], biology [7, 20], ecology [11, 46], robotics [31, 33, 59], cardiology [36, 62], neural networks [15, 17, 27], finance [13, 45], etc.

A hyperchaotic system is a chaotic system having more than one positive Lyapunov exponent. For continuous-time dynamical systems, the minimal dimension for a hyperchaotic system is four. The first hyperchaotic system was found by Rössler [40]. This was followed by the discovery of many hyperchaotic systems such as hyperchaotic Lorenz system [16], hyperchaotic Lü system [4], hyperchaotic Chen system [26], hyperchaotic Wang system [60], etc.

Hyperchaotic systems have attractive features like high security, high capacity and high efficiency and they find miscellaneous applications in several research areas like neural networks [14, 25, 37], oscillators [12, 73], circuits [2, 8, 35, 67], secure communications [21, 63], encryption [69], synchronization [22, 43, 53, 64, 65, 71], etc.

The problem of control of a chaotic system is to find a state feedback control law to stabilize a chaotic system around its unstable equilibrium [42, 61]. Some popular methods for chaos control are active control [48, 54], adaptive control [47, 52], sliding mode control [55], etc.

This research work is organized as follows. Section 2 introduces the eleven-term 4-D novel hyperchaotic system with four quadratic nonlinearities. In this section, the phase portraits of the novel chaotic system are also displayed using MATLAB. Section 3 details the qualitative properties of the 4-D novel hyperchaotic system. Section 4 describes new results for the adaptive controller design for stabilizing the 4-D novel hyperchaotic system with unknown parameters. MATLAB simulations are shown to validate and illustrate all the main adaptive control results for the hyperchaos control of the 4-D novel hyperchaotic system. Section 5 contains a summary of the main results derived in this research work.

2 An Eleven-Term 4-D Novel Hyperchaotic System

This section describes the equations and phase portraits of the eleven-term 4-D novel hyperchaotic system with four quadratic nonlinearities.

The novel hyperchaotic system is described by the 4-D dynamics

$$\begin{aligned}\dot{x}_1 &= a(x_2 - x_1) + x_4\\ \dot{x}_2 &= -x_1x_3 + bx_1 - x_2\\ \dot{x}_3 &= x_1x_2 - cx_3\\ \dot{x}_4 &= dx_4 + 0.5x_2^2 - x_1x_3\end{aligned} \tag{1}$$

where x_1, x_2, x_3, x_4 are the states and a, b, c, d are constant, positive, parameters.

The system (1) depicts a strange hyperchaotic attractor when the constant parameter values are taken as

$$a = 10, \quad b = 28, \quad c = 2.7, \quad d = 2.2 \tag{2}$$

For simulations, the initial values of the novel chaotic system (1) are taken as

$$x_1(0) = 1.2, \quad x_2(0) = 0.8, \quad x_3(0) = 1.2, \quad x_4(0) = 2.4 \tag{3}$$

Figure 1 describes the 3-D projection of the strange hyperchaotic attractor of the novel hyperchaotic system (1) in (x_1, x_2, x_3)-space. From the phase portrait given in Fig. 1, it is clear the strange attractor obtained is a two-scroll hyperchaotic attractor.

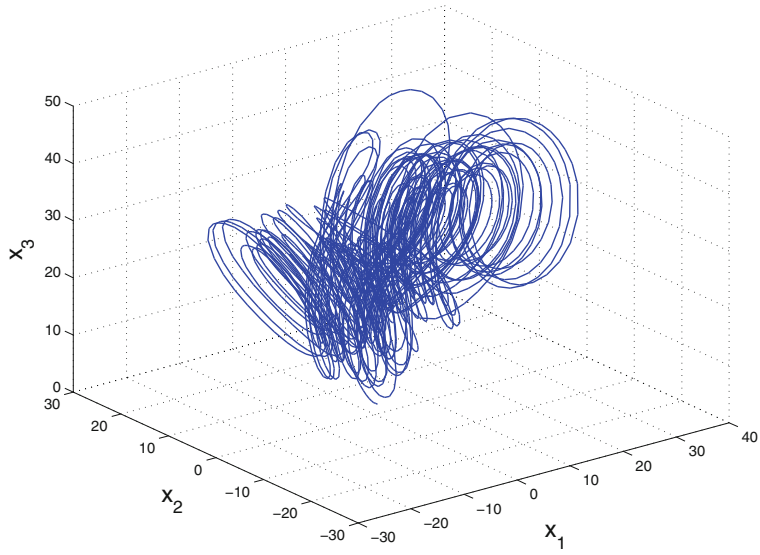

Fig. 1 Strange attractor of the novel hyperchaotic system in (x_1, x_2, x_3)-space

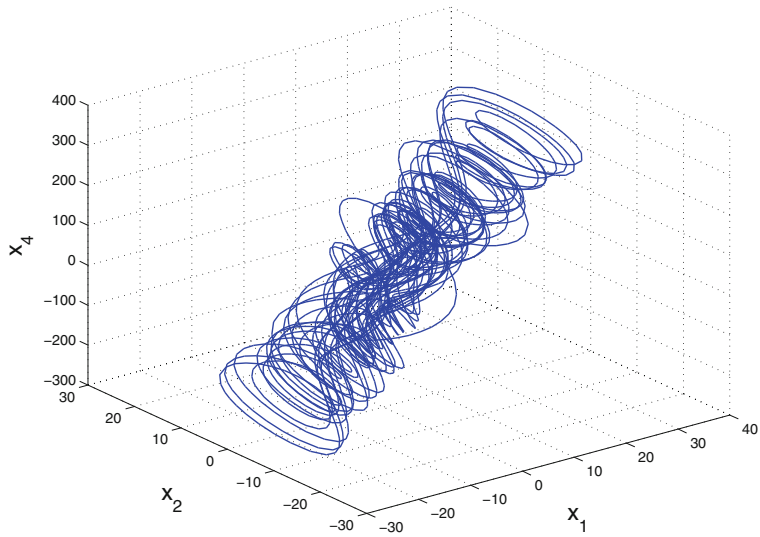

Fig. 2 Strange attractor of the novel hyperchaotic system in (x_1, x_2, x_4)-space

Figure 2 describes the 3-D projection of the strange hyperchaotic attractor of the novel hyperchaotic system (1) in (x_1, x_2, x_4)-space. From the phase portrait given in Fig. 2, it is clear the strange attractor obtained is a two-scroll hyperchaotic attractor.

Figure 3 describes the 3-D projection of the strange hyperchaotic attractor of the novel hyperchaotic system (1) in (x_1, x_3, x_4)-space. From the phase portrait given in Fig. 3, it is clear the strange attractor obtained is a two-scroll hyperchaotic attractor.

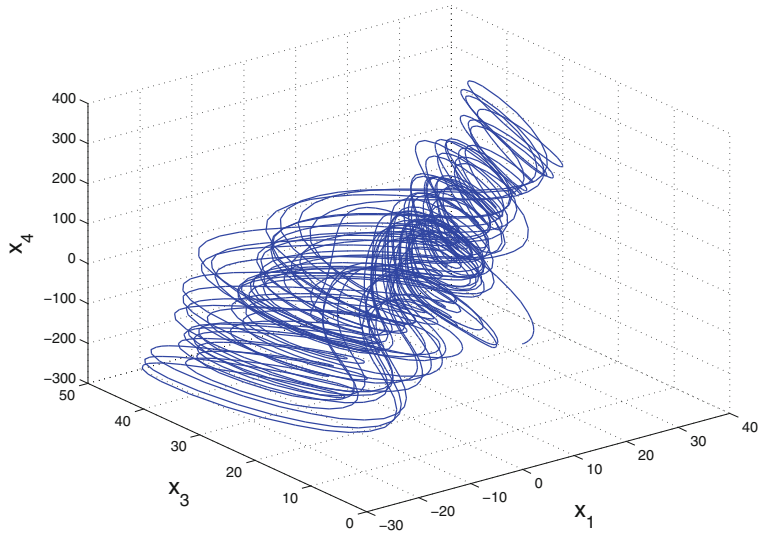

Fig. 3 Strange attractor of the novel hyperchaotic system in (x_1, x_3, x_4)-space

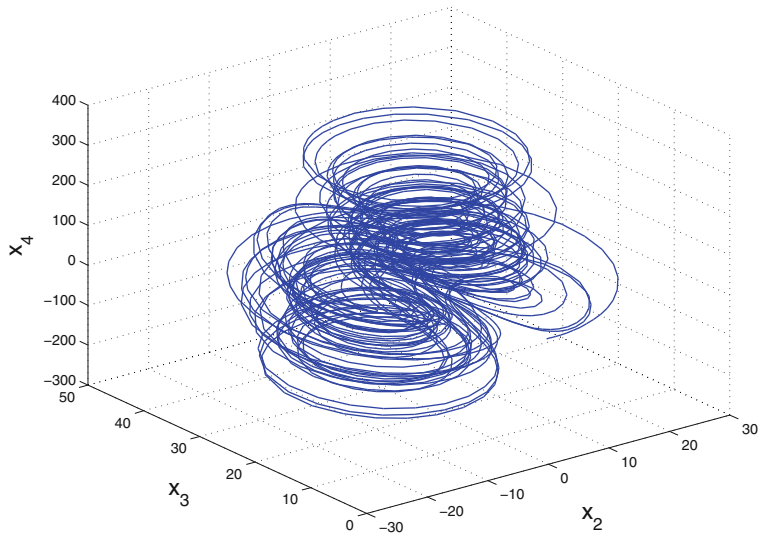

Fig. 4 Strange attractor of the novel hyperchaotic system in (x_2, x_3, x_4)-space

Figure 4 describes the 3-D projection of the strange hyperchaotic attractor of the novel hyperchaotic system (1) in (x_2, x_3, x_4)-space. From the phase portrait given in Fig. 4, it is clear the strange attractor obtained is a two-scroll hyperchaotic attractor.

3 Analysis of the Novel Hyperchaotic System

This section gives the qualitative properties of the nine-term novel 4-D hyperchaotic system proposed in this research work.

3.1 Dissipativity

We write the system (1) in vector notation as

$$\dot{x} = f(x) = \begin{bmatrix} f_1(x) \\ f_2(x) \\ f_3(x) \\ f_4(x) \end{bmatrix}, \tag{4}$$

where

$$\begin{aligned} f_1(x) &= a(x_2 - x_1) + x_4 \\ f_2(x) &= -x_1x_3 + bx_1 - x_2 \\ f_3(x) &= x_1x_2 - cx_3 \\ f_4(x) &= 0.5x_2^2 - x_1x_3 + dx_4 \end{aligned} \tag{5}$$

We take the parameter values as

$$a = 10, \quad b = 28, \quad c = 2.7, \quad d = 2.2 \tag{6}$$

The divergence of the vector field f on $\mathbb{R}^4$ is obtained as

$$div\, f = \frac{\partial f_1(x)}{\partial x_1} + \frac{\partial f_2(x)}{\partial x_2} + \frac{\partial f_3(x)}{\partial x_3} + \frac{\partial f_4(x)}{\partial x_4} = -(a + 1 + c - d) = -\mu \tag{7}$$

where

$$\mu = a + 1 + c - d = 10 + 1 + 2.7 - 2.2 = 11.5 > 0 \tag{8}$$

Let Ω be any region in $\mathbb{R}^4$ with a smooth boundary. Let $\Omega(t) = \Phi_t(\Omega)$, where Φ_t is the flow of the vector field f.

Let $V(t)$ denote the hyper-volume of $\Omega(t)$.

By Liouville's theorem, it follows that

$$\frac{dV(t)}{dt} = \int\limits_{\Omega(t)} (div\, f) dx_1 dx_2 dx_3 dx_4 \tag{9}$$

Substituting the value of $divf$ in (9) leads to

$$\frac{dV(t)}{dt} = -\mu \int\limits_{\Omega(t)} dx_1 dx_2 dx_3 dx_4 = -\mu V(t) \tag{10}$$

Integrating the linear differential Eq. (10), $V(t)$ is obtained as

$$V(t) = V(0) \exp(-\mu t), \quad \text{where} \quad \mu = 11.5 > 0. \tag{11}$$

From Eq. (11), it follows that the volume $V(t)$ shrinks to zero exponentially as $t \to \infty$. Thus, the novel hyperchaotic system (1) is dissipative. Hence, any asymptotic motion of the system (1) settles onto a set of measure zero, *i.e.* a strange hyperchaotic attractor.

3.2 Invariance

It is easily seen that the x_3-axis is invariant for the flow of the novel hyperchaotic system (1). Hence, all orbits of the system (1) starting from the x_3 axis stay in the x_3 axis for all values of time.

3.3 Equilibria

The equilibrium points of the novel hyperchaotic system (1) are obtained by solving the nonlinear equations

$$\begin{aligned} f_1(x) &= a(x_2 - x_1) + x_4 = 0 \\ f_2(x) &= -x_1x_3 + bx_1 - x_2 = 0 \\ f_3(x) &= x_1x_2 - cx_3 = 0 \\ f_4(x) &= 0.5x_2^2 - x_1x_3 + dx_4 = 0 \end{aligned} \tag{12}$$

We take the parameter values as in the hyperchaotic case, viz.

$$a = 10, \quad b = 28, \quad c = 2.7, \quad d = 2.2 \tag{13}$$

It is clear that the novel system (1) has a unique equilibrium point at $x = 0$. The Jacobian matrix of the novel hyperchaotic system (1) at $x = 0$ is obtained as

$$J = \begin{bmatrix} -a & a & 0 & 1 \\ b & -1 & 0 & 0 \\ 0 & 0 & -c & 0 \\ 0 & 0 & 0 & d \end{bmatrix} = \begin{bmatrix} -10 & 10 & 0 & 1 \\ 28 & -1 & 0 & 0 \\ 0 & 0 & -2.7 & 0 \\ 0 & 0 & 0 & 1.2 \end{bmatrix} \tag{14}$$

The matrix J has the eigenvalues

$$\lambda_1 = -22.8277, \quad \lambda_2 = -2.7, \quad \lambda_3 = 11.8277, \quad \lambda_4 = 2.2 \tag{15}$$

This shows that the equilibrium point E_0 is a saddle-point, which is unstable.

3.4 Lyapunov Exponents and Lyapunov Dimension

We take the initial values of the novel hyperchaotic system as

$$x_1(0) = 1.2, \quad x_2(0) = 0.8, \quad x_3(0) = 1.2, \quad x_4(0) = 2.4 \tag{16}$$

We take the parameter values as in the hyperchaotic case, viz.

$$a = 10, \quad b = 28, \quad c = 2.7, \quad d = 2.2 \tag{17}$$

Then the Lyapunov exponents of the novel 4-D system (1) are numerically obtained as

$$L_1 = 0.7781, \quad L_2 = 0.2299, \quad L_3 = 0 \quad and \quad L_4 = -12.5062 \tag{18}$$

Since L_1 and L_2 are both positive, it is clear that (1) is hyperchaotic.
Since $L_1 + L_2 + L_3 + L_4 = -11.4982 < 0$, the system (1) is dissipative.
Also, the Lyapunov dimension of the system (1) is obtained as

$$D_L = 3 + \frac{L_1 + L_2 + L_3}{|L_4|} = 3.0806 \tag{19}$$

Figure 5 depicts the dynamics of the Lyapunov exponents of the novel chaotic system (1). From Fig. 5, it is seen that the maximal Lyapunov exponent (MLE) of the novel hyperchaotic system (1) is $L_1 = 0.7781$.

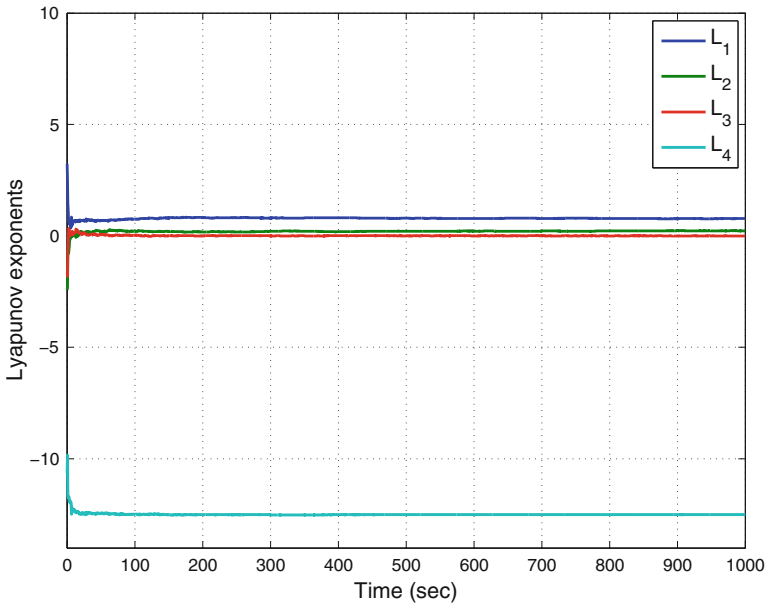

Fig. 5 Dynamics of the Lyapunov exponents of the novel hyperchaotic system

4 Adaptive Control of the Novel Hyperchaotic System

This section derives new results for the adaptive controller to stabilize the unstable novel hyperchaotic system with unknown parameters for all initial conditions in $\mathbb{R}^4$.

The controlled novel 4-D hyperchaotic system is given by

$$\begin{aligned}\dot{x}_1 &= a(x_2 - x_1) + x_4 + u_1\\ \dot{x}_2 &= -x_1x_3 + bx_1 - x_2 + u_2\\ \dot{x}_3 &= x_1x_2 - cx_3 + u_3\\ \dot{x}_4 &= dx_4 + 0.5x_2^2 - x_1x_3 + u_4\end{aligned} \tag{20}$$

where x_1, x_2, x_3, x_4 are state variables, a, b, c, d are constant, unknown, parameters of the system and u_1, u_2, u_3, u_4 are adaptive controls to be designed.

An adaptive control law is taken as

$$\begin{aligned}u_1 &= -A(t)(x_2 - x_1) - x_4 - k_1x_1\\ u_2 &= x_1x_3 - B(t)x_1 + x_2 - k_2x_2\\ u_3 &= -x_1x_2 + C(t)x_3 - k_3x_3\\ u_4 &= -D(t)x_4 - 0.5x_2^2 + x_1x_3 - k_4x_4\end{aligned} \tag{21}$$

where $A(t), B(t), C(t), D(t)$ are estimates for the unknown parameters a, b, c, d, respectively, and k_1, k_2, k_3, k_4 are positive gain constants.

The closed-loop control system is obtained by substituting (21) into (20) as

$$\begin{aligned}\dot{x}_1 &= (a - A(t))(x_2 - x_1) - k_1x_1\\ \dot{x}_2 &= (b - B(t))x_1 - k_2x_2\\ \dot{x}_3 &= -(c - C(t))x_3 - k_3x_3\\ \dot{x}_4 &= (d - D(t))x_4 - k_4x_4\end{aligned} \tag{22}$$

To simplify (22), we define the parameter estimation error as

$$\begin{aligned}e_a(t) &= a - A(t)\\ e_b(t) &= b - B(t)\\ e_c(t) &= c - C(t)\\ e_d(t) &= d - D(t)\end{aligned} \tag{23}$$

Using (23), the closed-loop system (22) can be simplified as

$$\begin{aligned}\dot{x}_1 &= e_a(x_2 - x_1) - k_1 x_1\\ \dot{x}_2 &= e_b x_1 - k_2 x_2\\ \dot{x}_3 &= -e_c x_3 - k_3 x_3\\ \dot{x}_4 &= e_d x_4 - k_4 x_4\end{aligned} \tag{24}$$

Differentiating the parameter estimation error (23) with respect to t, we get

$$\begin{aligned}\dot{e}_a &= -\dot{A}\\ \dot{e}_b &= -\dot{B}\\ \dot{e}_c &= -\dot{C}\\ \dot{e}_d &= -\dot{D}\end{aligned} \tag{25}$$

Next, we find an update law for parameter estimates using Lyapunov stability theory.

Consider the quadratic Lyapunov function defined by

$$V(x_1, x_2, x_3, x_4, e_a, e_b, e_c, e_d) = \frac{1}{2}\left(x_1^2 + x_2^2 + x_3^2 + x_4^2 + e_a^2 + e_b^2 + e_c^2 + e_d^2\right), \tag{26}$$

which is positive definite on $\mathbb{R}^8$.

Differentiating V along the trajectories of (24) and (25), we get

$$\begin{aligned}\dot{V} = -k_1 x_1^2 - k_2 x_2^2 - k_3 x_3^2 - k_4 x_4^2 + e_a\left[x_1(x_2 - x_1) - \dot{A}\right]\\ e_b\left(x_1 x_2 - \dot{B}\right) + e_c\left(-x_3^2 - \dot{C}\right) + e_d\left(-x_4^2 - \dot{D}\right)\end{aligned} \tag{27}$$

In view of Eq. (27), an update law for the parameter estimates is taken as

$$\begin{aligned}\dot{A} &= x_1(x_2 - x_1)\\ \dot{B} &= x_1 x_2\\ \dot{C} &= -x_3^2\\ \dot{D} &= -x_4^2\end{aligned} \tag{28}$$

Theorem *The novel hyperchaotic system* (20) *with unknown system parameters is globally and exponentially stabilized for all initial conditions* $x(0) \in \mathbb{R}^4$ *by the adaptive control law* (21) *and the parameter update law* (28)*, where* $k_i, (i = 1, 2, 3, 4)$ *are positive constants.*

Proof The result is proved using Lyapunov stability theory [19]. We consider the quadratic Lyapunov function V defined by (26), which is positive definite on $\mathbb{R}^8$.

Substitution of the parameter update law (28) into (27) yields

$$\dot{V} = -k_1 x_1^2 - k_2 x_2^2 - k_3 x_3^2 - k_4 x_4^2, \tag{29}$$

which is a negative semi-definite function on $\mathbb{R}^8$.

Therefore, it can be concluded that the state vector $x(t)$ and the parameter estimation error are globally bounded, i.e.

$$[x_1(t)x_2(t)x_3(t)x_4(t)e_a(t)e_b(t)e_c(t)e_d(t)]^T \in L_\infty. \tag{30}$$

Define

$$k = \min\{k_1, k_2, k_3, k_4\} \tag{31}$$

Then it follows from (29) that

$$\dot{V} \leq -k\|x\|^2 \quad or \quad k\|x\|^2 \leq -\dot{V} \tag{32}$$

Integrating the inequality (32) from 0 to t, we get

$$k\int_0^t \|x(\tau)\|^2 d\tau \leq -\int_0^t \dot{V}(\tau)\, d\tau = V(0) - V(t) \tag{33}$$

From (33), it follows that $x(t) \in L_2$.

Using (24), it can be deduced that $\dot{x}(t) \in L_\infty$.

Hence, using Barbalat's lemma, we can conclude that $x(t) \to 0$ exponentially as $t \to \infty$ for all initial conditions $x(0) \in \mathbb{R}^4$.

This completes the proof. □

For numerical simulations, the parameter values of the novel system (20) are taken as in the chaotic case, *viz.*

$$a = 10, \quad b = 28, \quad c = 2.7, \quad d = 2.2 \tag{34}$$

The gain constants are taken as

$$k_1 = 5, \quad k_2 = 5, \quad k_3 = 5, \quad k_4 = 5 \tag{35}$$

The initial values of the parameter estimates are taken as

$$A(0) = 18, \quad B(0) = 27, \quad C(0) = 18, \quad D(0) = 22 \tag{36}$$

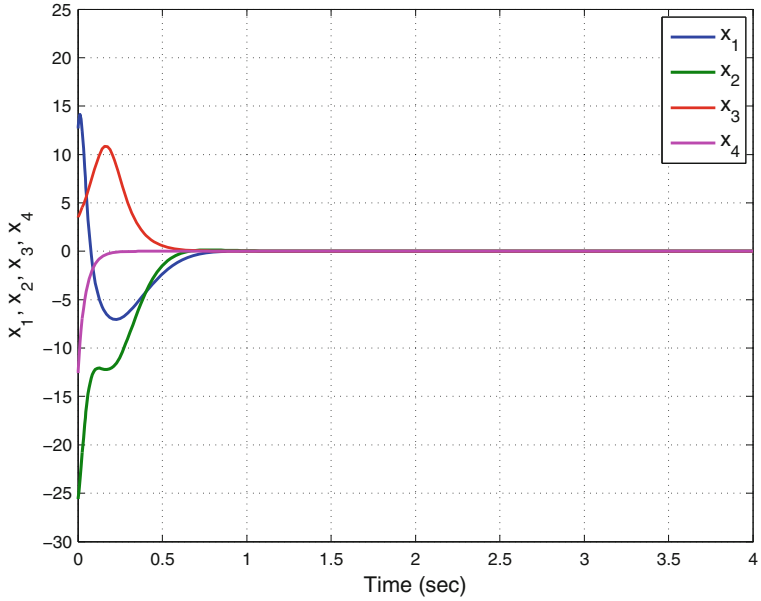

Fig. 6 Time-history of the states $x_1(t), x_2(t), x_3(t), x_4(t)$

The initial values of the novel system (20) are taken as

$$x_1(0) = 12.7, \quad x_2(0) = -25.6, \quad x_3(0) = 3.5, \quad x_4(0) = -12.6 \tag{37}$$

Figure 6 shows the time-history of the controlled states $x_1(t), x_2(t), x_3(t), x_4(t)$.

From Fig. 6, it is seen that the states $x_1(t), x_2(t), x_3(t)$ and $x_4(t)$ are stabilized in 2 s (MATLAB). This shows the efficiency of the adaptive controller defined by (21).

5 Conclusions

In this research work, an eleven-term 4-D novel hyperchaotic system with four quadratic nonlinearities has been proposed and its qualitative properties have been derived. The Lyapunov exponents of the eleven-term novel hyperchaotic system have been obtained as $L_1 = 0.7781, L_2 = 0.2299, L_3 = 0$ and $L_4 = -12.5062$. Since the sum of the Lyapunov exponents is negative, the novel hyperchaotic system is dissipative. The Lyapunov dimension of the novel hyperchaotic system has been obtained a $D_L = 3.0806$. The novel hyperchaotic system has an unstable equilibrium point at the origin. Next, an adaptive controller has been derived for globally stabilizing the novel hyperchaotic system with unknown system parameters. The adaptive control result was proved using Lyapunov stability theory.

MATLAB simulations were shown to demonstrate and validate all the main results derived in this work for the eleven-term 4-D novel hyperchaotic system. As future research directions, new control techniques like sliding mode control or back-stepping control may be considered for stabilizing the novel hyperchaotic system for all initial conditions.

References

1. Arneodo, A., Coullet, P., Tresser, C.: Possible new strange attractors with spiral structure. Common. Math. Phys. **79**(4), 573–576 (1981)
2. Banerjee, T., Biswas, D., Sarkar, B.C.: Design of chaotic and hyperchaotic time-delayed electronic circuit. Bonfring Int. J. Power Syst. Integr Circuits **2**(4), 13–17 (2012)
3. Cai, G., Tan, Z.: Chaos synchronization of a new chaotic system via nonlinear control. J. Uncertain Syst. **1**(3), 235–240 (2007)
4. Chen, A., Lu, J., Lü, J., Yu, S.: Generating hyperchaotic Lü attractor via state feedback control. Physica A: Stat. Mech. Appl. **364**(C), 103–110 (2006)
5. Chen, G., Ueta, T.: Yet another chaotic attractor. Int. J. Bifurc. Chaos **9**(7), 1465–1466 (1999)
6. Chen, H.K., Lee, C.I.: Anti-control of chaos in rigid body motion. Chaos, Solitons Fractals **21** (4), 957–965 (2004)
7. Das, S., Goswami, D., Chatterjee, S., Mukherjee, S.: Stability and chaos analysis of a novel swarm dynamics with applications to multi-agent systems. Eng. Appl. Artif. Intell. **30**, 189–198 (2014)
8. Elwakil, A.S., Kennedy, M.P.: Inductorless hyperchaos generator. Microelectron. J. **30**(8), 739–743 (1999)
9. Feki, M.: An adaptive chaos synchronization scheme applied to secure communication. Chaos, Solitons Fractals **18**(1), 141–148 (2003)
10. Gaspard, P.: Microscopic chaos and chemical reactions. Physica A **263**(1–4), 315–328 (1999)
11. Gibson, W.T., Wilson, W.G.: Individual-based chaos: Extensions of the discrete logistic model. J. Theoreti. Biol. **339**, 84–92 (2013)
12. Grygiel, K., Szlachetka, P.: Chaos and hyperchaos in coupled Kerr oscillators. Opt. Commun. **177**(1–6), 425–431 (2000)
13. Guégan, D.: Chaos in economics and finance. Annu. Rev. Control **33**(1), 89–93 (2009)
14. Huang, Y., Yang, X.S.: Hyperchaos and bifurcation in a new class of four-dimensional Hopfield neural networks. Neurocomputing **69**(13–15), 1787–1795 (2006)
15. Huang, X., Zhao, Z., Wang, Z., Li, Y.: Chaos and hyperchaos in fractional-order cellular neural networks. Neurocomputing **94**, 13–21 (2012)
16. Jia, Q.: Hyperchaos generated from the Lorenz chaotic system and its control. Phys. Lett. A **366**(3), 217–222 (2007)
17. Kaslik, E., Sivasundaram, S.: Nonlinear dynamics and chaos in fractional-order neural networks. Neural Netw. **32**, 245–256 (2012)
18. Kengne, J., Chedjou, J.C., Kenne, G., Kyamakya, K.: Dynamical properties and chaos synchronization of improved Colpitts oscillators. Commun. Nonlinear Sci. Numer. Simul. **17** (7), 2914–2923 (2012)
19. Khalil, H.K.: Nonlinear Systems. Prentice Hall, New Jersey (2001)
20. Kyriazis, M.: Applications of chaos theory to the molecular biology of aging. Exp. Gerontol. **26**(6), 569–572 (1991)
21. Li, C., Liao, X., Wong, K.: Lag synchronization of hyperchaos with application to secure communications. Chaos, Solitons Fractals **23**(1), 183–193 (2005)
22. Li, C.-L., Xiong, J.-B., Li, W.: A new hyperchaotic system and its generalized synchronization. Optik—Int. J. Light Electron Opt. **125**(1), 575–579 (2014)

23. Li, D.: A three-scroll chaotic attractor. Phys. Lett. A **372**(4), 387–393 (2008)
24. Li, N., Pan, W., Yan, L., Luo, B., Zou, X.: Enhanced chaos synchronization and communication in cascade-coupled semiconductor ring lasers. Commun. Nonlinear Sci. Numer. Simul. **19**(6), 1874–1883 (2014)
25. Li, Q., Yang, X.S., Yang, F.: Hyperchaos in Hopfield-type neural networks. Neurocomputing **67**(1–4), 275–280 (2004)
26. Li, X.: Modified projective synchronization of a new hyperchaotic system via nonlinear control. Commun. Theor. Phys. **52**(2), 274–278 (2009)
27. Lian, S., Chen, X.: Traceable content protection based on chaos and neural networks. Appl. Soft Comput. **11**(7), 4293–4301 (2011)
28. Liu, C., Liu, T., Liu, L., Liu, K.: A new chaotic attractor. Chaos, Solitions Fractals **22**(5), 1031–1038 (2004)
29. Lorenz, E.N.: Deterministic periodic flow. J. Atmos. Sci. **20**(2), 130–141 (1963)
30. Lü, J., Chen, G.: A new chaotic attractor coined. Int. J. Bifurc. Chaos **12**(3), 659–661 (2002)
31. Mondal, S., Mahanta, C.: Adaptive second order terminal sliding mode controller for robotic manipulators. J. Franklin Inst. **351**(4), 2356–2377 (2014)
32. Murali, K., Lakshmanan, M.: Secure communication using a compound signal from generalized chaotic systems. Phys. Lett. A **241**(6), 303–310 (1998)
33. Nehmzow, U., Walker, K.: Quantitative description of robotenvironment interaction using chaos theory. Robot. Auton. Syst. **53**(3–4), 177–193 (2005)
34. Petrov, V., Gaspar, V., Masere, J., Showalter, K.: Controlling chaos in Belousov-Zhabotinsky reaction. Nature **361**, 240–243 (1993)
35. Qi, G., van Wyk, M.A., van Wyk, B.J., Chen, G.: A new hyperchaotic system and its circuit implementation. Chaos, Solitons Fractals **40**(5), 2544–2549 (2009)
36. Qu, Z.: Chaos in the genesis and maintenance of cardiac arrhythmias. Prog. Biophys. Mol. Biol. **105**(3), 247–257 (2011)
37. Rech, P.C.: Chaos and hyperchaos in a Hopfield neural network. Neurocomputing **74**(17), 3361–3364 (2011)
38. Rhouma, R., Belghith, S.: Cryptoanalysis of a chaos based cryptosystem on DSP. Commun. Nonlinear Sci. Numer. Simul. **16**(2), 876–884 (2011)
39. Rössler, O.E.: An equation for continuous chaos. Phys. Lett. **57A**(5), 397–398 (1976)
40. Rössler, O.E.: An equation for hyperchaos. Phys. Lett. A **71**(2–3), 155–157 (1979)
41. Sharma, A., Patidar, V., Purohit, G., Sud, K.K.: Effects on the bifurcation and chaos in forced Duffing oscillator due to nonlinear damping. Commun. Nonlinear Sci. Numer. Simul. **17**(6), 2254–2269 (2012)
42. Shi, J., Zhao, F., Shen, X., Wang, X.: Chaotic operation and chaos control of travelling wave ultrasonic motor. Ultrasonics **53**(6), 1112–1123 (2013)
43. Smaoui, N., Karouma, A., Zribi, M.: Secure communications based on the synchronization of the hyperchaotic Chen and the unified chaotic systems. Commun. Nonlinear Sci. Numer. Simul. **16**(8), 3279–3293 (2011)
44. Sprott, J.C.: Some simple chaotic flows. Phys. Rev. E **50**(2), 647–650 (1994)
45. Sprott, J.C.: Competition with evolution in ecology and finance. Phys. Lett. A **325**(5–6), 329–333 (2004)
46. Suérez, I.: Mastering chaos in ecology. Ecol. Model. **117**(2–3), 305–314 (1999)
47. Sundarapandian, V.: Adaptive control and synchronization of uncertain Liu-Chen-Liu system. Int. J. Comput. Inf. Syst. **3**(2), 1–6 (2011)
48. Sundarapandian, V.: Output regulation of the Tigan system. Int. J. Comput. Sci. Eng. **3**(5), 2127–2135 (2011)
49. Sundarapandian, V., Pehlivan, I.: Analysis, control, synchronization, and circuit design of a novel chaotic system. Math. Comput. Model. **55**(7–8), 1904–1915 (2012)
50. Tigan, G., Opris, D.: Analysis of a 3D chaotic system. Chaos, Solitons Fractals **36**, 1315–1319 (2008)
51. Usama, M., Khan, M.K., Alghatbar, K., Lee, C.: Chaos-based secure satellite imagery cryptosystem. Comput. Math. Appl. **60**(2), 326–337 (2010)

52. Vaidyanathan, S.: Adaptive control and synchronization of the Shaw chaotic system. Int. J. Found. Comput. Sci. Technol. **1**(1), 1–11 (2011)
53. Vaidyanathan, S.: Adaptive control and synchronization of uncertain Liu-Liu-Liu-Su chaotic system. Int. J. Control Theory Appl. **4**(2), 99–109 (2011)
54. Vaidyanathan, S.: Output regulation of the Sprott-G chaotic system by state feedback control. Int. J. Instrum.Control Syst. **1**(1), 20–30 (2011)
55. Vaidyanathan, S.: Sliding mode control based global chaos control of Liu-Liu-Liu-Su chaotic system. Int. J. Control Theory Appl. **5**(1), 15–20 (2012)
56. Vaidyanathan, S.: A new six-term 3-D chaotic system with an exponential nonlinearity. Far East J. Math. Sci. **79**(1), 135–143 (2013)
57. Vaidyanathan, S.: Analysis and adaptive synchronization of two novel chaotic systems with hyperbolic sinusoidal and cosinusoidal nonlinearity and unknown parameters. J. Eng. Sci. Technol. Rev. **6**(4), 53–65 (2013)
58. Vaidyanathan, S.: A new eight-term 3-D polynomial chaotic system with three quadratic nonlinearities. Far East J. Math. Sci. **84**(2), 219–226 (2014)
59. Volos, C.K., Kyprianidis, I.M., Stouboulos, I.N.: Experimental investigation on coverage performance of a chaotic autonomousmobile robot. Robot. Auton. Syst. **61**(12), 1314–1322 (2013)
60. Wang, J., Chen, Z.: A novel hyperchaotic system and its complex dynamics. Int. J. Bifurc. Chaos **18**(11), 3309–3324 (2008)
61. Wang, J., Zhang, T., Che, Y.: Chaos control and synchronization of two neurons exposed to ELF external electric field. Chaos, Solitons Fractals **34**(3), 839–850 (2007)
62. Witte, C.L., Witte, M.H.: Chaos and predicting varix hemorrhage. Med. Hypotheses **36**(4), 312–317 (1991)
63. Wu, X., Wang, H., Lu, H.: Modified generalized projective synchronization of a new fractional-order hyperchaotic system and its application to secure communication. Nonlinear Anal. Real World Appl. **13**(3), 1441–1450 (2012)
64. Yassen, M.T.: On hyperchaos synchronization of a hyperchaotic Lü system. Nonlinear Anal. Theory, Methods Appl. **68**(11), 3592–3600 (2008)
65. Yassen, M.T.: Synchronization hyperchaos of hyperchaotic systems. Chaos, Solitons Fractals **37**(2), 465–475 (2008)
66. Yuan, G., Zhang, X., Wang, Z.: Generation and synchronization of feedback-induced chaos in semiconductor ring lasers by injection-locking. Optik—Int. J. Light Electron Opt. **125**(8), 1950–1953 (2014)
67. Yujun, N., Xingyuan, W., Mingjun, W., Huaguang, Z.: A new hyperchaotic system and its circuit implementation. Commun. Nonlinear Sci. Numer. Simul. **15**(11), 3518–3524 (2010)
68. Zaher, A.A., Abu-Rezq, A.: On the design of chaos-based secure communication systems. Commun. Nonlinear Syst. Numer. Simul. **16**(9), 3721–3727 (2011)
69. Zhang, Q., Guo, L., Wei, X.: A novel image fusion encryption algorithm based on DNA sequence operation and hyper-chaotic system. Optik—Int. J. Light Electron Opt. **124**(18), 3596–3600 (2013)
70. Zhou, W., Xu, Y., Lu, H., Pan, L.: On dynamics analysis of a new chaotic attractor. Phys. Lett. A **372**(36), 5773–5777 (2008)
71. Zhu, C.: Adaptive synchronization of two novel different hyperchaotic systems with partly uncertain parameters. Appl. Math. Comput. **215**(2), 557–561 (2009)
72. Zhu, C., Liu, Y., Guo, Y.: Theoretic and numerical study of a new chaotic system. Intell. Inf. Manag. **2**, 104–109 (2010)
73. Zou, Y.L., Zhu, J., Chen, G., Luo, X.S.: Synchronization of hyperchaotic oscillators via single unidirectional chaotic coupling. Chaos, Solitons Fractals **25**(5), 1245–1253 (2005)

Analysis, Control and Synchronization of a Nine-Term 3-D Novel Chaotic System

Sundarapandian Vaidyanathan and Ahmad Taher Azar

Abstract This research work describes a nine-term 3-D novel chaotic system with four quadratic nonlinearities. First, this work describes the dynamic analysis of the novel chaotic system and qualitative properties of the novel chaotic system are derived. The Lyapunov exponents of the nine-term novel chaotic system are obtained as $L_1 = 9.45456$, $L_2 = 0$ and $L_3 = -30.50532$. Since the maximal Lyapunov exponent (MLE) of the novel chaotic system is $L_1 = 9.45456$, which is a high value, the novel chaotic system exhibits strong chaotic properties. Next, this work describes the adaptive control of the novel chaotic system with unknown system parameters. Also, this work describes the adaptive synchronization of the identical novel chaotic systems with unknown system parameters. The adaptive control and synchronization results are proved using Lyapunov stability theory. MATLAB simulations are given to demonstrate and validate all the main results derived in this work for the nine-term 3-D novel chaotic system.

Keywords Chaos · Chaotic system · Chaos control · Chaos synchronization

1 Introduction

Chaotic systems are nonlinear dynamical systems which are sensitive to initial conditions, topologically mixing and with dense periodic orbits. Sensitivity to initial conditions of chaotic systems is popularly known as the *butterfly effect* [1].

S. Vaidyanathan (✉)
Research and Development Centre, Vel Tech University, Avadi, Chennai 600062, Tamil Nadu, India
e-mail: sundarvtu@gmail.com

A.T. Azar
Faculty of Computers and Information, Benha University, Banha, Egypt
e-mail: ahmad_t_azar@ieee.org

A.T. Azar and S. Vaidyanathan (eds.), *Chaos Modeling and Control Systems Design*, Studies in Computational Intelligence 581, DOI 10.1007/978-3-319-13132-0_2

The Lyapunov exponent is a measure of the divergence of phase points that are initially very close and can be used to quantify chaotic systems. A positive maximal Lyapunov exponent and phase space compactness are usually taken as defining conditions for a chaotic system.

In 1963, Lorenz modelled a 3-D chaotic system to study convection in the atmosphere and experimentally verified that a very small difference in the initial conditions resulted in very large changes in his deterministic weather model [28].

In the last four decades, there is a great deal of interest in the chaos literature in modelling and analysis of new chaotic systems. Some well-known paradigms of 3-D chaotic systems in the literature are [2, 3, 5, 6, 21, 26, 29, 40, 48, 54, 56, 65–67, 79, 80].

Chaotic systems have several important applications in science and engineering such as oscillators [18, 46], lasers [22, 75], chemical reactions [11, 35], cryptosystems [39, 59], secure communications [9, 31, 76], biology [8, 20], ecology [12, 50], robotics [30, 32, 69], cardiology [36, 72], neural networks [15, 17, 24], finance [13, 49], etc.

The problem of control of a chaotic system is to find a state feedback control law to stabilize a chaotic system around its unstable equilibrium [47, 71].

Some popular methods for chaos control are active control [53, 61], adaptive control [52, 60], sliding mode control [62], etc.

Major works on synchronization of chaotic systems deal with the complete synchronization [38, 55, 68] which has the goal of using the output of the master system to control the slave system so that the output of the slave system tracks the output of the master system asymptotically.

Pecora and Carroll pioneered the research on synchronization of chaotic systems with their seminal papers in 1990s [4, 34]. The active control method [27, 37, 51, 58, 64, 70] is commonly used when the system parameters are available for measurement and the adaptive control method [14, 25, 41–43, 73] is commonly used when some or all the system parameters are not available for measurement and estimates for unknown parameters of the systems.

Other popular methods for chaos synchronization are the sampled-data feedback method [10, 23, 74, 77], time-delay feedback method [7, 16, 44, 45], backstepping method [33, 57, 63, 78], etc.

This research work is organized as follows. Section 2 introduces the nine-term 3-D novel chaotic system with four quadratic nonlinearities. In this section, the phase portraits of the novel chaotic system are also displayed using MATLAB. Section 3 details the qualitative properties of the 3-D novel chaotic system. The Lyapunov exponents of the novel chaotic system are obtained as $L_1 = 9.45456, L_2 = 0$ and $L_3 = -30.50532$. The Lyapunov dimension of the novel chaotic system is obtained as $D_L = 2.30993$. As the maximal Lyapunov exponent (MLE) of the novel chaotic system is $L_1 = 9.45456$, which is a high value, it is noted that the 3-D novel chaotic system exhibits strong chaotic properties. Section 4 describes new results for the adaptive controller design for stabilizing the 3-D novel chaotic system with unknown parameters. Section 5 describes new results for the design of adaptive synchronization of the identical 3-D novel chaotic systems with

unknown parameters. MATLAB simulations are shown to validate and illustrate all the main adaptive results derived for the control and synchronization of the 3-D novel chaotic system. Section 6 contains a summary of the main results derived in this research work.

2 A Nine-Term 3-D Novel Chaotic System

This section describes the equations and phase portraits of a nine-term 3-D novel chaotic system. It is shown that the nine-term novel chaotic system exhibits an attractor, which may be named as *umbrella attractor*.

The novel chaotic system is described by the 3-D dynamics

$$\begin{aligned} \dot{x}_1 &= a(x_2 - x_1) + 30x_2x_3, \\ \dot{x}_2 &= bx_1 + cx_2 - x_1x_3, \\ \dot{x}_3 &= 0.5x_1x_3 - dx_3 + x_1^2, \end{aligned} \tag{1}$$

where x_1, x_2, x_3 are the states and a, b, c, d are constant, positive, parameters.

The system (1) is a nine-term polynomial chaotic system with four quadratic nonlinearities.

The system (1) depicts a strange chaotic attractor when the constant parameter values are taken as

$$a = 25, \quad b = 33, \quad c = 11, \quad d = 6 \tag{2}$$

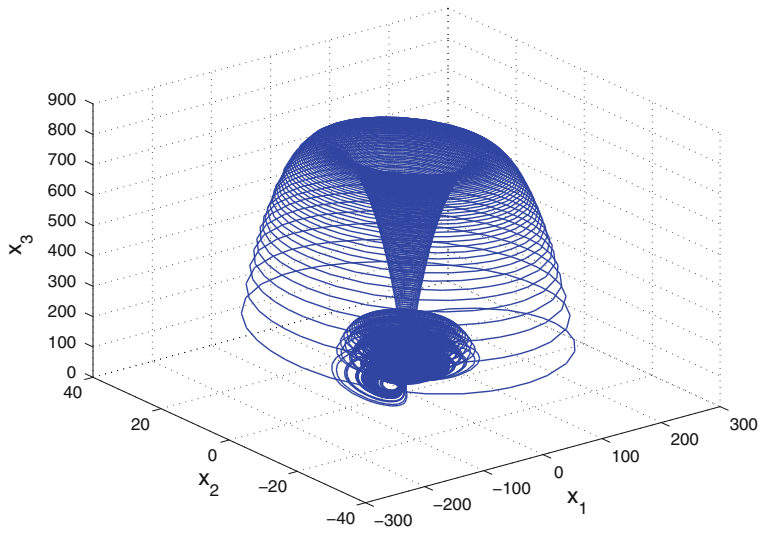

Fig. 1 Strange attractor of the novel chaotic system in $\mathbb{R}^3$

For simulations, the initial values of the novel chaotic system (1) are taken as

$$x_1(0) = 1.2, \quad x_2(0) = 0.6, \quad x_3(0) = 1.8 \tag{3}$$

Figure 1 describes the strange chaotic attractor of the novel chaotic system (1) in 3-D view. It is easily seen that the strange chaotic attractor is strongly chaotic and it has the shape of an "umbrella". In view of this observation, the strange chaotic attractor obtained for the novel chaotic system (1) may be also called as an "umbrella attractor".

3 Analysis of the Novel Chaotic System

This section gives the qualitative properties of the nine-term novel 3-D chaotic system proposed in this research work.

3.1 Dissipativity

We write the system (1) in vector notation as

$$\dot{x} = f(x) = \begin{bmatrix} f_1(x) \\ f_2(x) \\ f_3(x) \end{bmatrix}, \tag{4}$$

where

$$\begin{aligned} f_1(x) &= a(x_2 - x_1) + 30x_2x_3 \\ f_2(x) &= bx_1 + cx_2 - x_1x_3 \\ f_3(x) &= 0.5x_1x_3 - dx_3 + x_1^2 \end{aligned} \tag{5}$$

We take the parameter values as

$$a = 8, \quad b = 55, \quad c = 4, \quad d = 5 \tag{6}$$

The divergence of the vector field f on $\mathbb{R}^3$ is obtained as

$$\mathrm{div} f = \frac{\partial f_1(x)}{\partial x_1} + \frac{\partial f_2(x)}{\partial x_2} + \frac{\partial f_3(x)}{\partial x_3} = c - (a + d) = -\mu \tag{7}$$

where

$$\mu = a + d - c = 25 + 6 - 11 = 20 > 0 \tag{8}$$

Let $\boldsymbol{\Omega}$ be any region in $\mathbb{R}^3$ with a smooth boundary. Let $\boldsymbol{\Omega}(t) = \boldsymbol{\Phi}_t(\boldsymbol{\Omega})$, where $\boldsymbol{\Phi}_t$ is the flow of the vector field f.

Let $V(t)$ denote the volume of $\boldsymbol{\Omega}(t)$.

By Liouville's theorem, it follows that

$$\frac{dV(t)}{dt} = \int\limits_{\Omega(t)} (\mathrm{div} f) dx_1 dx_2 dx_3 \tag{9}$$

Substituting the value of $\mathrm{div} f$ in (9) leads to

$$\frac{dV(t)}{dt} = -\mu \int\limits_{\boldsymbol{\Omega}(t)} dx_1 dx_2 dx_3 = -\mu V(t) \tag{10}$$

Integrating the linear differential Eq. (10), $V(t)$ is obtained as

$$V(t) = V(0) exp(-\mu t), \quad \text{where} \quad \mu = 20 > 0. \tag{11}$$

From Eq. (11), it follows that the volume $V(t)$ shrinks to zero exponentially as $t \to \infty$.

Thus, the novel chaotic system (1) is dissipative. Hence, any asymptotic motion of the system (1) settles onto a set of measure zero, i.e. a strange attractor.

3.2 Invariance

It is easily seen that the x_3-axis is invariant for the flow of the novel chaotic system (1). Hence, all orbits of the system (1) starting from the x_3 axis stay in the x_3 axis for all values of time.

3.3 Equilibria

The equilibrium points of the novel chaotic system (1) are obtained by solving the nonlinear equations

$$\begin{aligned} f_1(x) &= a(x_2 - x_1) + 30 x_2 x_3 = 0 \\ f_2(x) &= b x_1 + c x_2 - x_1 x_3 = 0 \\ f_3(x) &= 0.5 x_1 x_3 - d x_3 + x_1^2 = 0 \end{aligned} \tag{12}$$

We take the parameter values as in the chaotic case, viz.

$$a = 25, \quad b = 33, \quad c = 11, \quad d = 6 \tag{13}$$

Solving the nonlinear system of Eq. (12) with the parameter values (13), we obtain three equilibrium points of the novel chaotic system (1) as

$$E_0 = \begin{bmatrix} 0 \\ 0 \\ 0 \end{bmatrix}, \quad E_1 = \begin{bmatrix} 8.0776 \\ 0.1974 \\ 33.2688 \end{bmatrix} \quad \text{and} \quad E_3 = \begin{bmatrix} -24.7120 \\ -0.6039 \\ 33.2688 \end{bmatrix}. \tag{14}$$

The Jacobian matrix of the novel chaotic system (1) at $(x_1^{\star}, x_2^{\star}, x_3^{\star})$ is obtained as

$$J(x^{\star}) = \begin{bmatrix} -25 & 25 + 30x_3^{\star} & 30x_2^{\star} \\ 33 - x_3^{\star} & 11 & -x_1^{\star} \\ 0.5x_3^{\star} + 2x_1^{\star} & 0 & 0.5x_1^{\star} - 6 \end{bmatrix} \tag{15}$$

The Jacobian matrix at E_0 is obtained as

$$J_0 = J(E_0) = \begin{bmatrix} -25 & 25 & 0 \\ 33 & 11 & 0 \\ 0 & 0 & -6 \end{bmatrix} \tag{16}$$

The matrix J_0 has the eigenvalues

$$\lambda_1 = -6, \quad \lambda_2 = -40.8969, \quad \lambda_3 = 26.8969 \tag{17}$$

This shows that the equilibrium point E_0 is a saddle-point, which is unstable. The Jacobian matrix at E_1 is obtained as

$$J_1 = J(E_1) = \begin{bmatrix} -25.00 & 1023.06 & 5.92 \\ -0.27 & 11.00 & -8.08 \\ 32.79 & 0 & -1.96 \end{bmatrix} \tag{18}$$

The matrix J_1 has the eigenvalues

$$\lambda_1 = -71.5851, \quad \lambda_{2,3} = 27.8120 \pm 55.1509i \tag{19}$$

This shows that the equilibrium point E_1 is a saddle-focus, which is unstable. The Jacobian matrix at E_2 is obtained as

$$J_2 = J(E_2) = \begin{bmatrix} -25.00 & 1023.06 & -18.12 \\ -0.27 & 11.00 & 24.71 \\ -32.79 & 0 & -18.36 \end{bmatrix} \tag{20}$$

The matrix J_2 has the eigenvalues

$$\lambda_1 = -107.62, \quad \lambda_{2,3} = 37.63 \pm 79.67i \tag{21}$$

This shows that the equilibrium point E_2 is a saddle-focus, which is unstable.

Hence, E_0, E_1, E_2 are all unstable equilibrium points of the 3-D novel chaotic system (1), where E_0 is a saddle point and E_1, E_2 are saddle-focus points.

3.4 Lyapunov Exponents and Lyapunov Dimension

We take the initial values of the novel chaotic system (1) as in (3) and the parameter values of the novel chaotic system (1) as (2).

Then the Lyapunov exponents of the novel chaotic system (1) are numerically obtained as

$$L_1 = 9.45456, \quad L_2 = 0, \quad L_3 = -30.50532 \tag{22}$$

Since $L_1 + L_2 + L_3 = -21.05076 < 0$, the system (1) is dissipative.

Also, the Lyapunov dimension of the system (1) is obtained as

$$D_L = 2 + \frac{L_1 + L_2}{|L_3|} = 2.1095 \tag{23}$$

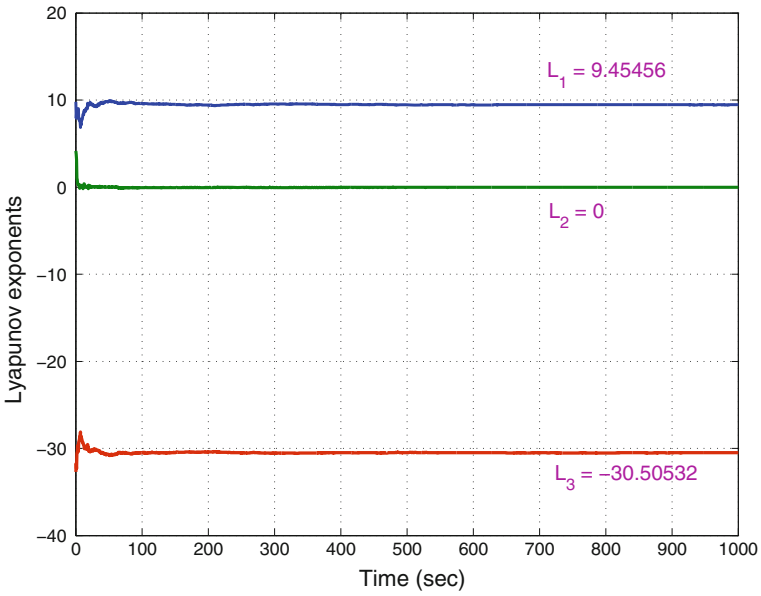

Fig. 2 Dynamics of the Lyapunov exponents of the novel chaotic system

Figure 2 depicts the dynamics of the Lyapunov exponents of the novel chaotic system (1). From this figure, it is seen that the maximal Lyapunov exponent of the novel chaotic system (1) is $L_1 = 9.45456$, which is a large value. Thus, the novel chaotic system (1) exhibits strong chaotic properties.

4 Adaptive Control of the Novel Chaotic System

This section derives new results for the adaptive controller to stabilize the unstable novel chaotic system with unknown parameters for all initial conditions.

The controlled novel 3-D chaotic system is given by

$$\begin{aligned} \dot{x}_1 &= a(x_2 - x_1) + 30x_2x_3 + u_1 \\ \dot{x}_2 &= bx_1 + cx_2 - x_1x_3 + u_2 \\ \dot{x}_3 &= 0.5x_1x_3 - dx_3 + x_1^2 + u_3 \end{aligned} \tag{24}$$

where x_1, x_2, x_3 are state variables, a, b, c, d are constant, unknown, parameters of the system and u_1, u_2, u_3 are adaptive controls to be designed.

An adaptive control law is taken as

$$\begin{aligned} u_1 &= -A(t)(x_2 - x_1) - 30x_2x_3 - k_1x_1 \\ u_2 &= -B(t)x_1 - C(t)x_2 + x_1x_3 - k_2x_2 \\ u_3 &= -0.5x_1x_3 + D(t)x_3 - x_1^2 - k_3x_3 \end{aligned} \tag{25}$$

where $A(t), B(t), C(t), D(t)$ are estimates for the unknown parameters a, b, c, d, respectively, and k_1, k_2, k_3 are positive gain constants.

The closed-loop control system is obtained by substituting (25) into (24) as

$$\begin{aligned} \dot{x}_1 &= (a - A(t))(x_2 - x_1) - k_1x_1 \\ \dot{x}_2 &= (b - B(t))x_1 + (c - C(t))x_2 - k_2x_2 \\ \dot{x}_3 &= -(d - D(t))x_3 - k_3x_3 \end{aligned} \tag{26}$$

To simplify (26), we define the parameter estimation error as

$$\begin{aligned} e_a(t) &= a - A(t) \\ e_b(t) &= b - B(t) \\ e_c(t) &= c - C(t) \\ e_d(t) &= d - D(t) \end{aligned} \tag{27}$$

Using (27), the closed-loop system (26) can be simplified as

$$\begin{aligned}\dot{x}_1 &= e_a(x_2 - x_1) - k_1 x_1\\ \dot{x}_2 &= e_b x_1 + e_c x_2 - k_2 x_2\\ \dot{x}_3 &= -e_d x_3 - k_3 x_3\end{aligned} \tag{28}$$

Differentiating the parameter estimation error (27) with respect to t, we get

$$\begin{aligned}\dot{e}_a &= -\dot{A}\\ \dot{e}_b &= -\dot{B}\\ \dot{e}_c &= -\dot{C}\\ \dot{e}_d &= -\dot{D}\end{aligned} \tag{29}$$

Next, we find an update law for parameter estimates using Lyapunov stability theory.

Consider the quadratic Lyapunov function defined by

$$V(x_1, x_2, x_3, e_a, e_b, e_c, e_d) = \frac{1}{2}\left(x_1^2 + x_2^2 + x_3^2 + e_a^2 + e_b^2 + e_c^2 + e_d^2\right), \tag{30}$$

which is positive definite on $\mathbb{R}^7$.

Differentiating V along the trajectories of (28) and (29), we get

$$\begin{aligned}\dot{V} = &-k_1 x_1^2 - k_2 x_2^2 - k_3 x_3^2 + e_a\left[x_1(x_2 - x_1) - \dot{A}\right] + e_b\left(x_1 x_2 - \dot{B}\right)\\ &+ e_c\left(x_2^2 - \dot{C}\right) + e_d\left(-x_3^2 - \dot{D}\right)\end{aligned} \tag{31}$$

In view of Eq. (31), an update law for the parameter estimates is taken as

$$\begin{aligned}\dot{A} &= x_1(x_2 - x_1)\\ \dot{B} &= x_1 x_2\\ \dot{C} &= x_2^2\\ \dot{D} &= -x_3^2\end{aligned} \tag{32}$$

Theorem 1 *The novel chaotic system* (24) *with unknown system parameters is globally and exponentially stabilized for all initial conditions* $x(0) \in \mathbb{R}^3$ *by the adaptive control law* (25) *and the parameter update law* (32)*, where* $k_i, (i = 1, 2, 3)$ *are positive constants.*

Proof The result is proved using Lyapunov stability theory [19]. We consider the quadratic Lyapunov function V defined by (30), which is positive definite on $\mathbb{R}^7$.

Substitution of the parameter update law (32) into (31) yields

$$\dot{V} = -k_1 x_1^2 - k_2 x_2^2 - k_3 x_3^2, \tag{33}$$

which is a negative semi-definite function on $\mathbb{R}^7$.

Therefore, it can be concluded that the state vector $x(t)$ and the parameter estimation error are globally bounded, i.e.

$$[x_1(t) \quad x_2(t) \quad x_3(t) \quad e_a(t) \quad e_b(t) \quad e_c(t) \quad e_d(t)]^T \in L_\infty. \tag{34}$$

Define

$$k = \min\{k_1, k_2, k_3\} \tag{35}$$

Then it follows from (33) that

$$\dot{V} \leq -k\|x\|^2 \quad \text{or} \quad k\|x\|^2 \leq -\dot{V} \tag{36}$$

Integrating the inequality (36) from 0 to t, we get

$$k\int_0^t \|x(\tau)\|^2 d\tau \leq -\int_0^t \dot{V}(\tau)d\tau = V(0) - V(t) \tag{37}$$

From (37), it follows that $x(t) \in L_2$.

Using (28), it can be deduced that $\dot{x}(t) \in L_\infty$.

Hence, using Barbalat's lemma, we can conclude that $x(t) \to 0$ exponentially as $t \to \infty$ for all initial conditions $x(0) \in \mathbb{R}^3$.

This completes the proof. □

For numerical simulations, the parameter values of the novel system (24) are taken as in the chaotic case, viz.

$$a = 25, \quad b = 33, \quad c = 11, \quad d = 6 \tag{38}$$

The gain constants are taken as

$$k_1 = 5, \quad k_2 = 5, \quad k_3 = 5 \tag{39}$$

The initial values of the parameter estimates are taken as

$$A(0) = 7, \quad B(0) = 12, \quad C(0) = 25, \quad D(0) = 15 \tag{40}$$

The initial values of the novel system (24) are taken as

$$x_1(0) = 12.5, \quad x_2(0) = -5.6, \quad x_3(0) = 9.4 \tag{41}$$

Figure 3 shows the time-history of the controlled states $x_1(t), x_2(t), x_3(t)$.

From Fig. 3, it is seen that the states $x_1(t), x_2(t)$ and $x_3(t)$ are stabilized in 2 s (MATLAB). This shows the efficiency of the adaptive controller defined by (25).

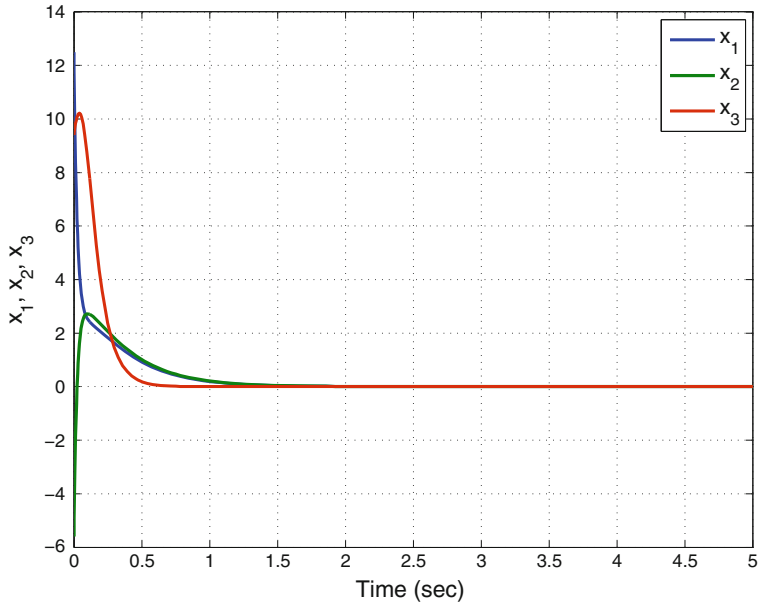

Fig. 3 Time-history of the states $x_1(t), x_2(t), x_3(t)$

5 Adaptive Synchronization of the Identical Novel Chaotic Systems

This section derives new results for the adaptive synchronization of the identical novel chaotic systems with unknown parameters.

The master system is given by the novel chaotic system

$$\begin{aligned} \dot{x}_1 &= a(x_2 - x_1) + 30x_2x_3 \\ \dot{x}_2 &= bx_1 + cx_2 - x_1x_3 \\ \dot{x}_3 &= 0.5x_1x_3 - dx_3 + x_1^2 \end{aligned} \tag{42}$$

where x_1, x_2, x_3 are state variables and a, b, c, d are constant, unknown, parameters of the system.

The slave system is given by the controlled novel chaotic system

$$\begin{aligned} \dot{y}_1 &= a(y_2 - y_1) + 30y_2y_3 + u_1 \\ \dot{y}_2 &= by_1 + cy_2 - y_1y_3 + u_2 \\ \dot{y}_3 &= 0.5y_1y_3 - dy_3 + y_1^2 + u_3 \end{aligned} \tag{43}$$

where y_1, y_2, y_3 are state variables and a, b, c, d are constant, unknown, parameters of the system.

The synchronization error is defined as

$$\begin{aligned} e_1 &= y_1 - x_1 \\ e_2 &= y_2 - x_2 \\ e_3 &= y_3 - x_3 \end{aligned} \tag{44}$$

The error dynamics is easily obtained as

$$\begin{aligned} \dot{e}_1 &= a(e_2 - e_1) + 30(y_2y_3 - x_2x_3) + u_1 \\ \dot{e}_2 &= be_1 + ce_2 - y_1y_3 + x_1x_3 + u_2 \\ \dot{e}_3 &= -de_3 + 0.5(y_1y_3 - x_1x_3) + y_1^2 - x_1^2 + u_3 \end{aligned} \tag{45}$$

An adaptive control law is taken as

$$\begin{aligned} u_1 &= -A(t)(e_2 - e_1) - 30(y_2y_3 - x_2x_3) - k_1e_1 \\ u_2 &= -B(t)e_1 - C(t)e_2 + y_1y_3 - x_1x_3 - k_2e_2 \\ u_3 &= D(t)e_3 - 0.5(y_1y_3 - x_1x_3) - y_1^2 + x_1^2 - k_3e_3 \end{aligned} \tag{46}$$

where $A(t), B(t), C(t), D(t)$ are estimates for the unknown parameters a, b, c, d, respectively, and k_1, k_2, k_3 are positive gain constants.

The closed-loop control system is obtained by substituting (46) into (45) as

$$\begin{aligned} \dot{e}_1 &= (a - A(t))(e_2 - e_1) - k_1e_1 \\ \dot{e}_2 &= (b - B(t))e_1 + (c - C(t))e_2 - k_2e_2 \\ \dot{e}_3 &= -(d - D(t))e_3 - k_3e_3 \end{aligned} \tag{47}$$

To simplify (26), we define the parameter estimation error as

$$\begin{aligned} e_a(t) &= a - A(t) \\ e_b(t) &= b - B(t) \\ e_c(t) &= c - C(t) \\ e_d(t) &= d - D(t) \end{aligned} \tag{48}$$

Using (48), the closed-loop system (47) can be simplified as

$$\begin{aligned} \dot{e}_1 &= e_a(e_2 - e_1) - k_1e_1 \\ \dot{e}_2 &= e_be_1 + e_ce_2 - k_2e_2 \\ \dot{e}_3 &= -e_de_3 - k_3e_3 \end{aligned} \tag{49}$$

Differentiating the parameter estimation error (48) with respect to t, we get

$$\begin{aligned}\dot{e}_a &= -\dot{A}\\ \dot{e}_b &= -\dot{B}\\ \dot{e}_c &= -\dot{C}\\ \dot{e}_d &= -\dot{D}\end{aligned} \tag{50}$$

Next, we find an update law for parameter estimates using Lyapunov stability theory.

Consider the quadratic Lyapunov function defined by

$$V(e_1, e_2, e_3, e_a, e_b, e_c, e_d) = \frac{1}{2}\left(e_1^2 + e_2^2 + e_3^2 + e_a^2 + e_b^2 + e_c^2 + e_d^2\right), \tag{51}$$

which is positive definite on $\mathbb{R}^7$.

Differentiating V along the trajectories of (49) and (50), we get

$$\begin{aligned}\dot{V} = &-k_1 e_1^2 - k_2 e_2^2 - k_3 e_3^2 + e_a\left[e_1(e_2 - e_1) - \dot{A}\right] + e_b\left(e_1 e_2 - \dot{B}\right)\\ &+ e_c\left(e_2^2 - \dot{C}\right) + e_d\left(-e_3^2 - \dot{D}\right)\end{aligned} \tag{52}$$

In view of Eq. (31), an update law for the parameter estimates is taken as

$$\begin{aligned}\dot{A} &= e_1(e_2 - e_1)\\ \dot{B} &= e_1 e_2\\ \dot{C} &= e_2^2\\ \dot{D} &= -e_3^2\end{aligned} \tag{53}$$

Theorem 2 *The identical novel chaotic systems* (42) *and* (43) *with unknown system parameters are globally and exponentially synchronized for all initial conditions* $x(0), y(0) \in \mathbb{R}^3$ *by the adaptive control law* (46) *and the parameter update law* (53)*, where* $k_i, (i = 1, 2, 3)$ *are positive constants.*

Proof The result is proved using Lyapunov stability theory [19].

We consider the quadratic Lyapunov function V defined by (51), which is positive definite on $\mathbb{R}^7$.

Substitution of the parameter update law (53) into (52) yields

$$\dot{V} = -k_1 e_1^2 - k_2 e_2^2 - k_3 e_3^2, \tag{54}$$

which is a negative semi-definite function on $\mathbb{R}^7$.

Therefore, it can be concluded that the synchronization error vector $e(t)$ and the parameter estimation error are globally bounded, i.e.

$$[e_1(t)\, e_2(t)\, e_3(t)\, e_a(t)\, e_b(t)\, e_c(t)\, e_d(t)]^T \in L_\infty. \tag{55}$$

Define

$$k = \min\{k_1, k_2, k_3\} \tag{56}$$

Then it follows from (54) that

$$\dot{V} \leq -k\|e\|^2 \quad \text{or} \quad k\|e\|^2 \leq -\dot{V} \tag{57}$$

Integrating the inequality (36) from 0 to t, we get

$$k\int_0^t \|e(\tau)\|^2 d\tau \leq -\int_0^t \dot{V}(\tau)d\tau = V(0) - V(t) \tag{58}$$

From (58), it follows that $e(t) \in L_2$.

Using (49), it can be deduced that $\dot{e}(t) \in L_\infty$.

Hence, using Barbalat's lemma, we can conclude that $e(t) \to 0$ exponentially as $t \to \infty$ for all initial conditions $e(0) \in \mathbb{R}^3$.

This completes the proof. □

For numerical simulations, the parameter values of the novel systems (42) and (43) are taken as in the chaotic case, viz.

$$a = 25, \quad b = 33, \quad c = 11, \quad d = 6 \tag{59}$$

The gain constants are taken as $k_i = 5$ for $i = 1, 2, 3$.

The initial values of the parameter estimates are taken as

$$A(0) = 16, \quad B(0) = 8, \quad C(0) = 4, \quad D(0) = 7 \tag{60}$$

The initial values of the master system (42) are taken as

$$x_1(0) = 6.8, \quad x_2(0) = 3.7, \quad x_3(0) = -9.1 \tag{61}$$

The initial values of the slave system (43) are taken as

$$y_1(0) = 3.4, \quad y_2(0) = -12.5, \quad y_3(0) = 1.8 \tag{62}$$

Figures 4, 5 and 6 show the complete synchronization of the identical chaotic systems (42) and (43).

Figure 4 shows that the states $x_1(t)$ and $y_1(t)$ are synchronized in 2 s (MATLAB). Figure 5 shows that the states $x_2(t)$ and $y_2(t)$ are synchronized in 2 s (MATLAB). Figure 6 shows that the states $x_3(t)$ and $y_3(t)$ are synchronized in 2 s (MATLAB).

Figure 7 shows the time-history of the synchronization errors $e_1(t), e_2(t), e_3(t)$. From Fig. 7, it is seen that the errors $e_1(t), e_2(t)$ and $e_3(t)$ are stabilized in 2 s (MATLAB).

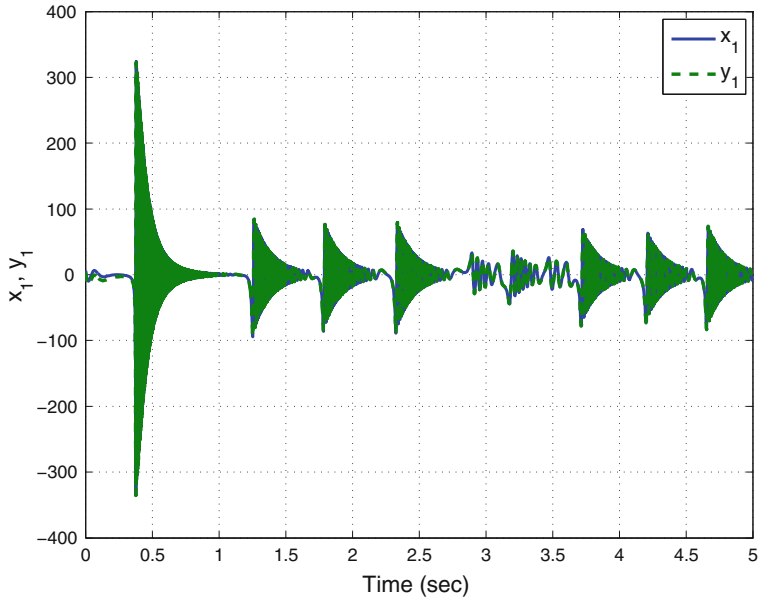

Fig. 4 Synchronization of the states x_1 and y_1

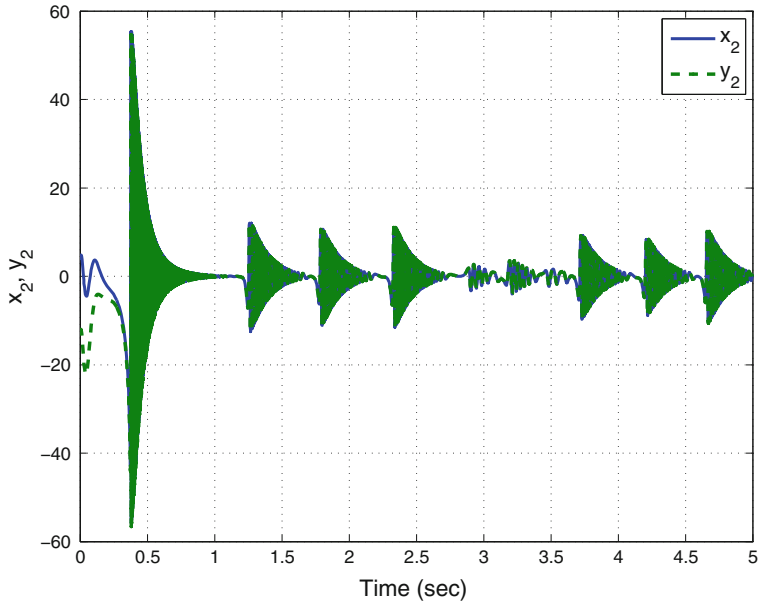

Fig. 5 Synchronization of the states x_2 and y_2

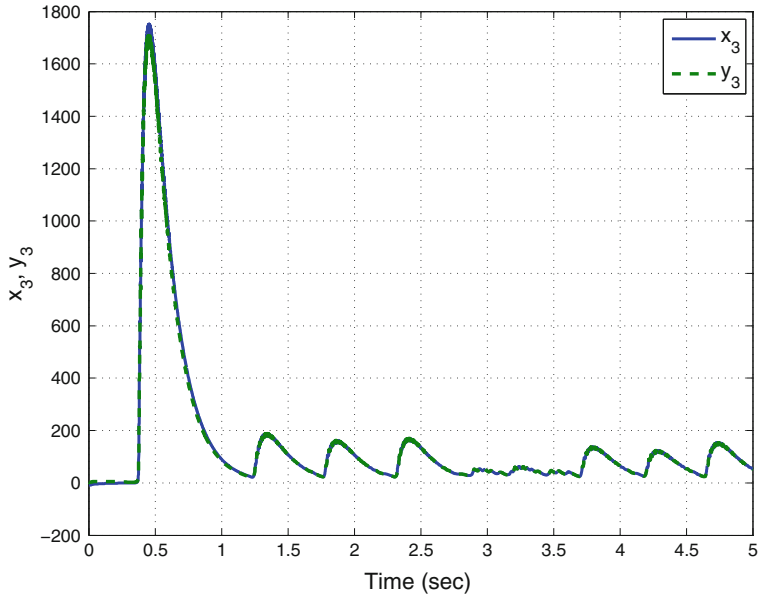

Fig. 6 Synchronization of the states x_3 and y_3

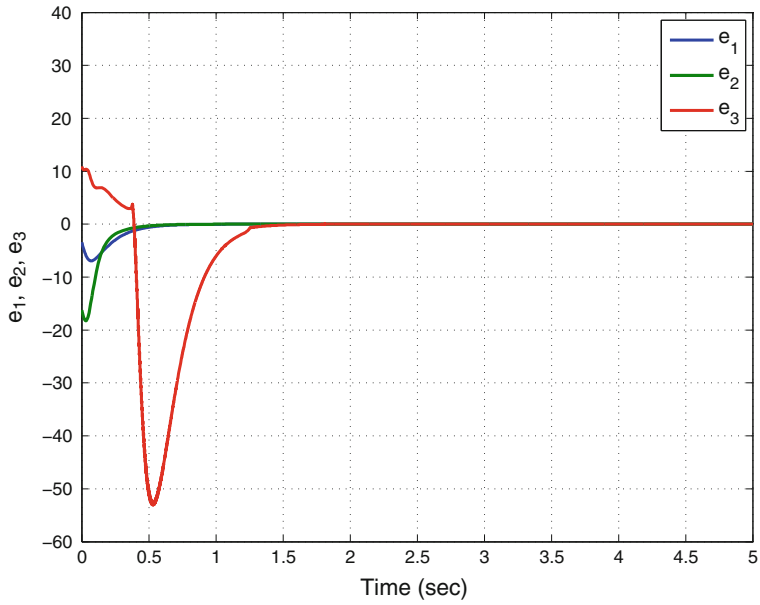

Fig. 7 Time-history of the synchronization errors e_1, e_2, e_3

6 Conclusions

In this research work, a nine-term 3-D novel chaotic system with four quadratic nonlinearities has been proposed and its qualitative properties have been derived. The Lyapunov exponents of the nine-term novel chaotic system have been obtained as $L_1 = 9.45456, L_2 = 0$ and $L_3 = -30.50532$. Since the maximal Lyapunov exponent (MLE) of the novel chaotic system is $L_1 = 9.45456$, which is a high value, the novel chaotic system exhibits strong chaotic properties. The novel chaotic system has three unstable equilibrium points. Next, an adaptive controller has been derived for globally stabilizing the novel chaotic system with unknown system parameters. Furthermore, an adaptive synchronizer has been derived for completely and globally synchronizing the identical novel chaotic systems with unknown system parameters. The adaptive control and synchronization results were proved using Lyapunov stability theory. MATLAB simulations were shown to demonstrate and validate all the main results derived in this work for the nine-term 3-D novel chaotic system. As future research directions, new control techniques like sliding mode control or backstepping control may be considered for stabilizing the novel chaotic system with three unstable equilibrium points or synchronizing the identical novel chaotic systems for all initial conditions.

References

1. Alligood, K.T., Sauer, T., Yorke, J.A.: Chaos: An Introduction to Dynamical Systems. Springer, New York (1997)
2. Arneodo, A., Coullet, P., Tresser, C.: Possible new strange attractors with spiral structure. Common. Math. Phys. **79**(4), 573–576 (1981)
3. Cai, G., Tan, Z.: Chaos synchronization of a new chaotic system via nonlinear control. J. Uncertain Syst. **1**(3), 235–240 (2007)
4. Carroll, T.L., Pecora, L.M.: Synchronizing chaotic circuits. IEEE Trans. Circ. Syst. **38**(4), 453–456 (1991)
5. Chen, G., Ueta, T.: Yet another chaotic attractor. Int. J. Bifurcat. Chaos **9**(7), 1465–1466 (1999)
6. Chen, H.K., Lee, C.I.: Anti-control of chaos in rigid body motion. Chaos Solitons Fractals **21** (4), 957–965 (2004)
7. Chen, W.-H., Wei, D., Lu, X.: Global exponential synchronization of nonlinear time-delay Lure systems via delayed impulsive control. Commun. Nonlinear Sci. Numer. Simul. **19**(9), 3298–3312 (2014)
8. Das, S., Goswami, D., Chatterjee, S., Mukherjee, S.: Stability and chaos analysis of a novel swarm dynamics with applications to multi-agent systems. Eng. Appl. Artif. Intell. **30**, 189–198 (2014)
9. Feki, M.: An adaptive chaos synchronization scheme applied to secure communication. Chaos Solitons Fractals **18**(1), 141–148 (2003)
10. Gan, Q., Liang, Y.: Synchronization of chaotic neural networks with time delay in the leakage term and parametric uncertainties based on sampled-data control. J. Franklin Inst. **349**(6), 1955–1971 (2012)
11. Gaspard, P.: Microscopic chaos and chemical reactions. Phys. A **263**(1–4), 315–328 (1999)

12. Gibson, W.T., Wilson, W.G.: Individual-based chaos: Extensions of the discrete logistic model. J. Theor. Biol. **339**, 84–92 (2013)
13. Guégan, D.: Chaos in economics and finance. Annu. Rev. Control **33**(1), 89–93 (2009)
14. Huang, J.: Adaptive synchronization between different hyperchaotic systems with fully uncertain parameters. Phys. Lett. A **372**(27–28), 4799–4804 (2008)
15. Huang, X., Zhao, Z., Wang, Z., Li, Y.: Chaos and hyperchaos in fractional-order cellular neural networks. Neurocomputing **94**, 13–21 (2012)
16. Jiang, G.-P., Zheng, W.X., Chen, G.: Global chaos synchronization with channel time-delay. Chaos Solitons Fractals **20**(2), 267–275 (2004)
17. Kaslik, E., Sivasundaram, S.: Nonlinear dynamics and chaos in fractional-order neural networks. Neural Netw. **32**, 245–256 (2012)
18. Kengne, J., Chedjou, J.C., Kenne, G., Kyamakya, K.: Dynamical properties and chaos synchronization of improved Colpitts oscillators. Commun. Nonlinear Sci. Numer. Simul. **17** (7), 2914–2923 (2012)
19. Khalil, H.K.: Nonlinear Systems. Prentice Hall, Englewood Cliffs (2001)
20. Kyriazis, M.: Applications of chaos theory to the molecular biology of aging. Exp. Gerontol. **26**(6), 569–572 (1991)
21. Li, D.: A three-scroll chaotic attractor. Phys. Lett. A **372**(4), 387–393 (2008)
22. Li, N., Pan, W., Yan, L., Luo, B., Zou, X.: Enhanced chaos synchronization and communication in cascade-coupled semiconductor ring lasers. Commun. Nonlinear Sci. Numer. Simul. **19**(6), 1874–1883 (2014)
23. Li, N., Zhang, Y., Nie, Z.: Synchronization for general complex dynamical networks with sampled-data. Neurocomputing **74**(5), 805–811 (2011)
24. Lian, S., Chen, X.: Traceable content protection based on chaos and neural networks. Appl. Soft Comput. **11**(7), 4293–4301 (2011)
25. Lin, W.: Adaptive chaos control and synchronization in only locally Lipschitz systems. Phys. Lett. A **372**(18), 3195–3200 (2008)
26. Liu, C., Liu, T., Liu, L., Liu, K.: A new chaotic attractor. Chaos Solitions Fractals **22**(5), 1031–1038 (2004)
27. Liu, L., Zhang, C., Guo, Z.A.: Synchronization between two different chaotic systems with nonlinear feedback control. Chin. Phys. **16**(6), 1603–1607 (2007)
28. Lorenz, E.N.: Deterministic periodic flow. J. Atmos. Sci. **20**(2), 130–141 (1963)
29. Lü, J., Chen, G.: A new chaotic attractor coined. Int. J. Bifurcat. Chaos **12**(3), 659–661 (2002)
30. Mondal, S., Mahanta, C.: Adaptive second order terminal sliding mode controller for robotic manipulators. J. Franklin Inst. **351**(4), 2356–2377 (2014)
31. Murali, K., Lakshmanan, M.: Secure communication using a compound signal from generalized chaotic systems. Phys. Lett. A **241**(6), 303–310 (1998)
32. Nehmzow, U., Walker, K.: Quantitative description of robot—environment interaction using chaos theory. Robot. Auton. Syst. **53**(3–4), 177–193 (2005)
33. Njah, A.N., Ojo, K.S., Adebayo, G.A., Obawole, A.O.: Generalized control and synchronization of chaos in RCL-shunted Josephson junction using backstepping design. Phys. C **470**(13–14), 558–564 (2010)
34. Pecora, L.M., Carroll, T.L.: Synchronization in chaotic systems. Phys. Rev. Lett. **64**(8), 821–824 (1990)
35. Petrov, V., Gaspar, V., Masere, J., Showalter, K.: Controlling chaos in Belousov-Zhabotinsky reaction. Nature **361**, 240–243 (1993)
36. Qu, Z.: Chaos in the genesis and maintenance of cardiac arrhythmias. Prog. Biophys. Mol. Biol. **105**(3), 247–257 (2011)
37. Rafikov, M., Balthazar, J.M.: On control and synchronization in chaotic and hyperchaotic systems via linear feedback control. Commun. Nonlinear Sci. Numer. Simul. **13**(7), 1246–1255 (2007)
38. Rasappan, S., Vaidyanathan, S.: Global chaos synchronization of WINDMI and Coullet chaotic systems by backstepping control. Far East J. Math. Sci. **67**(2), 265–287 (2012)

39. Rhouma, R., Belghith, S.: Cryptoanalysis of a chaos based cryptosystem on DSP. Commun. Nonlinear Sci. Numer. Simul. **16**(2), 876–884 (2011)
40. Rössler, O.E.: An equation for continuous chaos. Phys. Lett. **57A**(5), 397–398 (1976)
41. Sarasu, P., Sundarapandian, V.: Adaptive controller design for the generalized projective synchronization of 4-scroll systems. Int. J. Syst. Signal Control Eng. Appl. **5**(2), 21–30 (2012)
42. Sarasu, P., Sundarapandian, V.: Generalized projective synchronization of two-scroll systems via adaptive control. Int. J. Soft Comput. **7**(4), 146–156 (2012)
43. Sarasu, P., Sundarapandian, V.: Generalized projective synchronization of two-scroll systems via adaptive control. Eur. J. Sci. Res. **72**(4), 504–522 (2012)
44. Shahverdiev, E.M., Bayramov, P.A., Shore, K.A.: Cascaded and adaptive chaos synchronization in multiple time-delay laser systems. Chaos Solitons Fractals **42**(1), 180–186 (2009)
45. Shahverdiev, E.M., Shore, K.A.: Impact of modulated multiple optical feedback time delays on laser diode chaos synchronization. Opt. Commun. **282**(17), 3568–3572 (2009)
46. Sharma, A., Patidar, V., Purohit, G., Sud, K.K.: Effects on the bifurcation and chaos in forced Duffing oscillator due to nonlinear damping. Commun. Nonlinear Sci. Numer. Simul. **17**(6), 2254–2269 (2012)
47. Shi, J., Zhao, F., Shen, X., Wang, X.: Chaotic operation and chaos control of travelling wave ultrasonic motor. Ultrasonics **53**(6), 1112–1123 (2013)
48. Sprott, J.C.: Some simple chaotic flows. Phys. Rev. E **50**(2), 647–650 (1994)
49. Sprott, J.C.: Competition with evolution in ecology and finance. Phys. Lett. A **325**(5–6), 329–333 (2004)
50. Suérez, I.: Mastering chaos in ecology. Ecol. Model. **117**(2–3), 305–314 (1999)
51. Sundarapandian, V.: Output regulation of the Lorenz attractor. Far East J. Math. Sci. **42**(2), 289–299 (2010)
52. Sundarapandian, V.: Adaptive control and synchronization of uncertain Liu-Chen-Liu system. Int. J. Comput. Inf. Syst. **3**(2), 1–6 (2011)
53. Sundarapandian, V.: Output regulation of the Tigan system. Int. J. Comput. Sci. Eng. **3**(5), 2127–2135 (2011)
54. Sundarapandian, V., Pehlivan, I.: Analysis, control, synchronization, and circuit design of a novel chaotic system. Math. Comput. Model. **55**(7–8), 1904–1915 (2012)
55. Suresh, R., Sundarapandian, V.: Global chaos synchronization of a family of *n*-scroll hyperchaotic Chua circuits using backstepping control with recursive feedback. Far East J. Math. Sci. **73**(1), 73–95 (2013)
56. Tigan, G., Opris, D.: Analysis of a 3D chaotic system. Chaos Solitons Fractals **36**, 1315–1319 (2008)
57. Tu, J., He, H., Xiong, P.: Adaptive backstepping synchronization between chaotic systems with unknown Lipschitz constant. Appl. Math. Comput. **236**, 10–18 (2014)
58. Ucar, A., Lonngren, K.E., Bai, E.W.: Chaos synchronization in RCL-shunted Josephson junction via active control. Chaos Solitons Fractals **31**(1), 105–111 (2007)
59. Usama, M., Khan, M.K., Alghatbar, K., Lee, C.: Chaos-based secure satellite imagery cryptosystem. Comput. Math Appl. **60**(2), 326–337 (2010)
60. Vaidyanathan, S.: Adaptive control and synchronization of the Shaw chaotic system. Int. J. Found. Comput. Sci. Technol. **1**(1), 1–11 (2011)
61. Vaidyanathan, S.: Output regulation of the Sprott-G chaotic system by state feedback control. Int. J. Instrum. Control Syst. **1**(1), 20–30 (2011)
62. Vaidyanathan, S.: Sliding mode control based global chaos control of Liu-Liu-Liu-Su chaotic system. Int. J. Control Theor. Appl. **5**(1), 15–20 (2012)
63. Vaidyanathan, S.: Adaptive backstepping controller and synchronizer design for Arneodo chaotic system with unknown parameters. Int. J. Comput. Sci. Inf. Technol. **4**(6), 145–159 (2012)
64. Vaidyanathan, S.: Output regulation of the Liu chaotic system. Appl. Mech. Mater. **110–116**, 3982–3989 (2012)

65. Vaidyanathan, S.: A new six-term 3-D chaotic system with an exponential nonlinearity. Far East J. Math. Sci. **79**(1), 135–143 (2013)
66. Vaidyanathan, S.: Analysis and adaptive synchronization of two novel chaotic systems with hyperbolic sinusoidal and cosinusoidal nonlinearity and unknown parameters. J. Eng. Sci. Technol. Rev. **6**(4), 53–65 (2013)
67. Vaidyanathan, S.: A new eight-term 3-D polynomial chaotic system with three quadratic nonlinearities. Far East J. Math. Sci. **84**(2), 219–226 (2014)
68. Vaidyanathan, S., Rajagopal, K.: Global chaos synchronization of four-scroll chaotic systems by active nonlinear control. Int. J. Control Theor. Appl. **4**(1), 73–83 (2011)
69. Volos, C.K., Kyprianidis, I.M., Stouboulos, I.N.: Experimental investigation on coverage performance of a chaotic autonomous mobile robot. Robot. Auton. Syst. **61**(12), 1314–1322 (2013)
70. Wang, F., Liu, C.: A new criterion for chaos and hyperchaos synchronization using linear feedback control. Phys. Lett. A **360**(2), 274–278 (2006)
71. Wang, J., Zhang, T., Che, Y.: Chaos control and synchronization of two neurons exposed to ELF external electric field. Chaos Solitons Fractals **34**(3), 839–850 (2007)
72. Witte, C.L., Witte, M.H.: Chaos and predicting varix hemorrhage. Med. Hypotheses **36**(4), 312–317 (1991)
73. Wu, X., Guan, Z.-H., Wu, Z.: Adaptive synchronization between two different hyperchaotic systems. Nonlinear Anal. Theor. Meth. Appl. **68**(5), 1346–1351 (2008)
74. Xiao, X., Zhou, L., Zhang, Z.: Synchronization of chaotic Lure systems with quantized sampled-data controller. Commun. Nonlinear Sci. Numer. Simul. **19**(6), 2039–2047 (2014)
75. Yuan, G., Zhang, X., Wang, Z.: Generation and synchronization of feedback-induced chaos in semiconductor ring lasers by injection-locking. Optik Int. J. Light Electron Opt. **125**(8), 1950–1953 (2014)
76. Zaher, A.A., Abu-Rezq, A.: On the design of chaos-based secure communication systems. Commun. Nonlinear Syst. Numer. Simul. **16**(9), 3721–3727 (2011)
77. Zhang, H., Zhou, J.: Synchronization of sampled-data coupled harmonic oscillators with control inputs missing. Syst. Control Lett. **61**(12), 1277–1285 (2012)
78. Zhang, J., Li, C., Zhang, H., Yu, J.: Chaos synchronization using single variable feedback based on backstepping method. Chaos Solitons Fractals **21**(5), 1183–1193 (2004)
79. Zhou, W., Xu, Y., Lu, H., Pan, L.: On dynamics analysis of a new chaotic attractor. Phys. Lett. A **372**(36), 5773–5777 (2008)
80. Zhu, C., Liu, Y., Guo, Y.: Theoretic and numerical study of a new chaotic system. Intell. Inf. Manage. **2**, 104–109 (2010)

Backstepping Controller Design for the Global Chaos Synchronization of Sprott's Jerk Systems

Sundarapandian Vaidyanathan, Babatunde A. Idowu and Ahmad Taher Azar

Abstract This research work investigates the global chaos synchronization of Sprott's jerk chaotic system using backstepping control method. Sprott's jerk system (1997) is algebraically the simplest dissipative chaotic system consisting of five terms and a quadratic nonlinearity. Sprott's chaotic system involves only five terms and one quadratic nonlinearity, while Rössler's chaotic system (1976) involves seven terms and one quadratic nonlinearity. This work first details the properties of the Sprott's jerk chaotic system. The phase portraits of the Sprott's jerk system are described. The Lyapunov exponents of the Sprott's jerk system are obtained as $L_1 = 0.0525$, $L_2 = 0$ and $L_3 = -2.0727$. The Lyapunov dimension of the Sprott's jerk system is obtained as $D_L = 2.0253$. Next, an active backstepping controller is designed for the global chaos synchronization of identical Sprott's jerk systems with known parameters. The backstepping control method is a recursive procedure that links the choice of a Lyapunov function with the design of a controller and guarantees global asymptotic stability of strict-feedback chaotic systems. Finally, an adaptive backstepping controller is designed for the global chaos synchronization of identical Sprott's jerk systems with unknown parameters. MATLAB simulations are provided to validate and demonstrate the effectiveness of the proposed active and adaptive chaos synchronization schemes for the Sprott's jerk systems.

Keywords Chaos · Backstepping control · Sprott's jerk system · Active control · Adaptive control

S. Vaidyanathan (✉)
Research and Development Centre, Vel Tech University,
Avadi, Chennai 600062, Tamil Nadu, India
e-mail: sundarvtu@gmail.com

B.A. Idowu
Department of Physics, Lagos State University, Lagos, Nigeria
e-mail: babaidowu@yahoo.com

A.T. Azar
Faculty of Computers and Information, Benha University, Banha, Egypt
e-mail: ahmad_t_azar@ieee.org

A.T. Azar and S. Vaidyanathan (eds.), *Chaos Modeling and Control Systems Design*,
Studies in Computational Intelligence 581, DOI 10.1007/978-3-319-13132-0_3

1 Introduction

Chaos is a nonlinear behavior which is a strange random aggregate of responses to internal and external stimuli in dynamical systems. Chaos occurs, when the dynamical system is highly sensitive towards initial conditions. That is, chaotic systems starting off from very similar initial states can develop into radically divergent trajectories. Such sensitive dependence of chaotic systems is popularly known as the *butterfly effect* [1].

Mathematically, chaotic systems are classified as nonlinear dynamical systems which are sensitive to initial conditions, topologically mixing and with dense periodic orbits. The Lyapunov exponent is a measure of the divergence of phase points that are initially very close and can be used to quantify chaotic systems. A positive maximal Lyapunov exponent and phase space compactness are usually taken as defining conditions for a chaotic system.

Since the discovery of a 3-D chaotic system in 1963 by Lorenz to study convection in the atmosphere [27], there is a great deal of interest in the chaos literature in modelling and analysis of new chaotic systems. Some well-known paradigms of 3-D chaotic systems in the literature are [2, 3, 5, 6, 21, 25, 28, 38, 45, 50, 52, 58–60, 71, 72].

Recently, there is a great interest in finding elegant chaos, especially algebraically simple chaotic flows [45]. In 1997, Sprott discovered algebraically the simplest dissipative chaotic system consisting of only five terms and one quadratic nonlinearity [46]. Sprott's system (1997) has two terms fewer than the famous Rössler chaotic system [38], which consists of seven terms and one quadratic nonlinearity.

Sprott's simplest dissipative chaotic system (1997) is a simple jerk system consisting of five terms and one quadratic nonlinearity [46]. In this work, the phase portraits of the Sprott's jerk system are described. The Lyapunov exponents of the Sprott's jerk system are obtained as $L1 = 0.0525$; $L2 = 0$ and $L3 = -2.0727$. The Lyapunov dimension of the Sprott's jerk system is obtained as $DL = 2.0253$. Since the maximal Lyapunov exponent (MLE) of the Sprott's jerk system is $L1 = 0.0525$, which is a small number, it follows that the Sprott's system exhibits mild chaos only.

Chaotic systems have several important applications in science and engineering. Some important applications can be mentioned as oscillators [18, 44], lasers [22, 67], chemical reactions [11, 33], cryptosystems [37, 55], secure communications [9, 29, 68], biology [8, 20], ecology [12, 48], robotics [30, 62], cardiology [34, 64], neural networks [15, 17], finance [13, 47], etc.

Synchronization of chaotic systems is a phenomenon that occurs when two or more chaotic systems are coupled or when a chaotic system drives another chaotic system [36, 51, 61].

Because of the butterfly effect which causes exponential divergence of the trajectories of two identical chaotic systems started with nearly the same initial conditions, the synchronization of chaotic systems is a challenging research problem in the chaos literature.

Major works on synchronization of chaotic systems deal with the complete synchronization (CS) which has the goal of using the output of the master system to control the slave system so that the output of the slave system tracks the output of the master system asymptotically.

Pecora and Carroll pioneered the research on synchronization of chaotic systems with their seminal papers in 1990s [4, 32]. The active control method [26, 35, 49, 54, 57, 63] is commonly used when the system parameters are available for measurement and the adaptive control method [14, 24, 39–41, 65] is commonly used when some or all the system parameters are not available for measurement and estimates for unknown parameters of the systems.

Other important methods for chaos synchronization are the sampled-data feedback method [10, 23, 66, 69], time-delay feedback method [7, 16, 42, 43], backstepping method [31, 53, 56, 70], etc.

The backstepping control method is a recursive procedure that links the choice of a Lyapunov function with the design of a controller and guarantees global asymptotic stability of strict-feedback chaotic systems. The backstepping method is based on the mathematical model of the examined system, introducing new variables into it in a form depending on the state variables, controlling parameters and stabilizing functions. The use of backstepping method creates an additional nonlinearity and eliminates undesirable nonlinearities from the system.

This research work is organized as follows. Section 2 describes the Sprott's jerk system (1997). In this section, the phase portraits of the Sprott's chaotic system are also displayed using MATLAB. The Lyapunov exponents of the Sprott's system are also obtained in this system and the Lyapunov dimension of the Sprott's system is obtained using MATLAB. The dynamics of the Lyapunov exponents is plotted using MATLAB. Section 3 describes new results for the active backstepping controller design for the global chaos synchronization of identical Sprott's systems with known parameters. Section 4 describes new results for the adaptive backstepping controller design for the global chaos synchronization of identical Sprott's systems with unknown parameters. MATLAB simulations are shown to validate and illustrate all the main synchronization results derived for the Sprott's chaotic systems. Section 5 contains a summary of the main results derived in this research work.

2 Sprott's 3-D Jerk Chaotic System

This section describes the equations and phase portraits of the Sprott's jerk chaotic system (1997), which is algebraically the simplest dissipative chaotic system.

The Sprott chaotic system is described by the 3-D dynamics

$$\begin{aligned} \dot{x}_1 &= x_2, \\ \dot{x}_2 &= x_3, \\ \dot{x}_3 &= -ax_1 + x_2^2 - bx_3 \end{aligned} \tag{1}$$

where x_1, x_2, x_3 are the states and a, b are constant, positive, parameters.

The system (1) is a five-term polynomial chaotic system with just one quadratic nonlinearity.

The system (1) depicts a strange chaotic attractor when the constant parameter values are taken as

$$a = 1, \quad b = 2.02 \tag{2}$$

For simulations, the initial values of the Sprott chaotic system (1) are taken as

$$x_1(0) = 4.0, \quad x_2(0) = 2.0, \quad x_3(0) = 0.5. \tag{3}$$

Figure 1 describes the strange chaotic attractor of the Sprott chaotic system (1) in 3-D view. The phase portrait of the Sprott chaotic system also indicates that the Sprott attractor is mildly chaotic. This will be also made clear the Lyapunov exponents of the Sprott attractor are calculated.

The Lyapunov exponents of the Sprott chaotic system (1) are numerically obtained as

$$L_1 = 0.0525, \quad L_2 = 0, \quad L_3 = -2.0727 \tag{4}$$

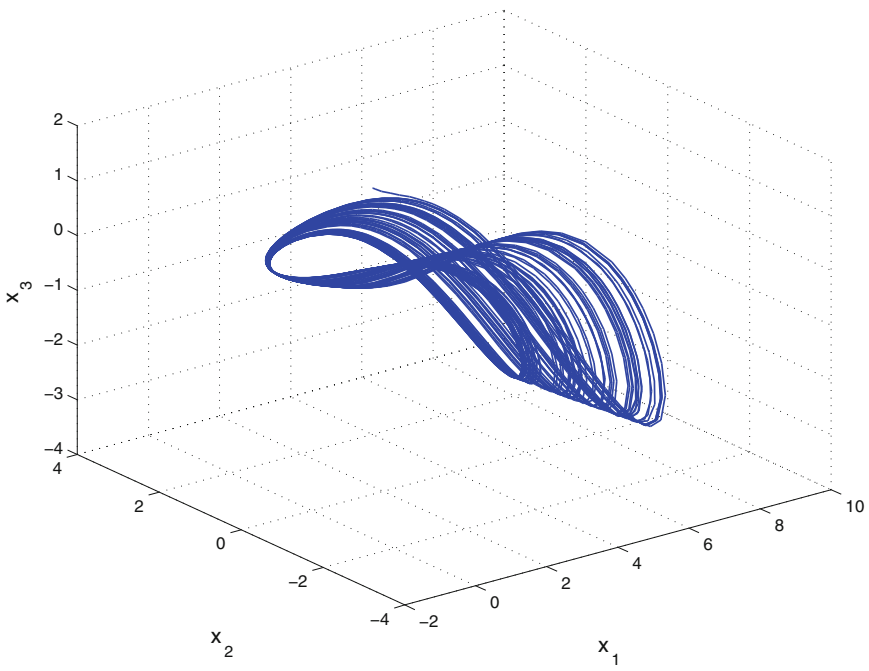

Fig. 1 Strange attractor of the Sprott chaotic system (1997) in $\mathbb{R}^3$

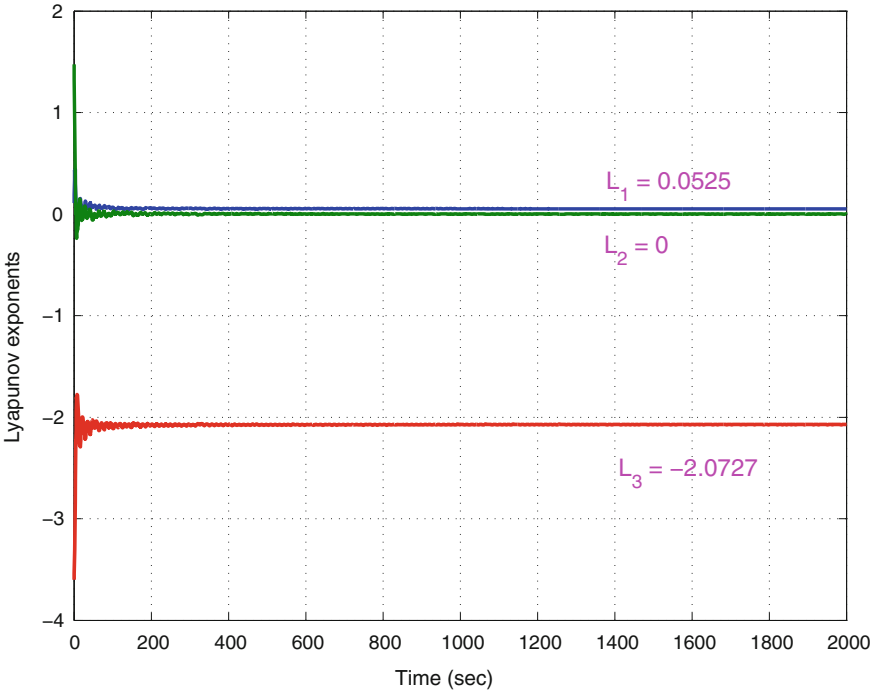

Fig. 2 Dynamics of the Lyapunov exponents of the Sprott chaotic system (1997)

Since $L_1 + L_2 + L_3 = -2.0202 < 0$, the system (1) is dissipative. Also, the Lyapunov dimension of the system (1) is obtained as

$$D_L = 2 + \frac{L_1 + L_2}{|L_3|} = 2.0523 \tag{5}$$

Figure 2 depicts the dynamics of the Lyapunov exponents of the novel chaotic system (1). From this figure, it is seen that the maximal Lyapunov exponent of the novel chaotic system (1) is $L_1 = 0.0525$, which is a very small value. Thus, the Sprott chaotic system (1) exhibits only mild chaotic properties.

3 Active Backstepping Design for the Synchronization of Identical Sprott Jerk Chaotic Systems

This section derives new results for the active backstepping design for the global chaos synchronization of the identical Sprott jerk systems with known parameters. The main result of this section is proved using Lyapunov stability theory.

The master system is described by the Sprott chaotic system

$$\begin{aligned}\dot{x}_1 &= x_2\\ \dot{x}_2 &= x_3\\ \dot{x}_3 &= -ax_1 + x_2^2 - bx_3\end{aligned} \tag{6}$$

where x_1, x_2, x_3 are state variables and a, b are positive, constant, parameters.

The slave system is described by the controlled Sprott chaotic system

$$\begin{aligned}\dot{y}_1 &= y_2\\ \dot{y}_2 &= y_3\\ \dot{y}_3 &= -ay_1 + y_2^2 - by_3 + u\end{aligned} \tag{7}$$

where y_1, y_2, y_3 are state variables and $u(t)$ is the active backstepping controller to be designed.

The synchronization error between the master system (6) and the slave system (7) is defined as

$$\begin{aligned}e_1(t) &= y_1(t) - x_1(t)\\ e_2(t) &= y_2(t) - x_2(t)\\ e_3(t) &= y_3(t) - x_3(t)\end{aligned} \tag{8}$$

The error dynamics is obtained as

$$\begin{aligned}\dot{e}_1 &= e_2\\ \dot{e}_2 &= e_3\\ \dot{e}_3 &= -ae_1 + y_2^2 - x_2^2 - be_3 + u\end{aligned} \tag{9}$$

Next, we shall prove the main result of this section.

Theorem 1 *The identical Sprott jerk chaotic systems (6) and (7) are globally and exponentially synchronized for all initial conditions* $x(0), y(0) \in \mathbb{R}^3$ *by the active controller*

$$u(t) = (a-3)e_1 - 5e_2 + (b-3)e_3 - y_2^2 + x_2^2 \tag{10}$$

where the parameters a and b are known.

Proof We prove this main result by using Lyapunov stability theory Khalil. First, we define a Lyapunov function candidate

$$V_1(z_1) = \frac{1}{2}z_1^2 \tag{11}$$

where

$$z_1 = e_1 \tag{12}$$

Differentiating V_1 along the dynamics (9), we get

$$\dot{V}_1 = z_1\dot{z}_1 = e_1e_2 = -z_1^2 + z_1(e_1 + e_2) \tag{13}$$

Next, we define

$$z_2 = e_1 + e_2 \tag{14}$$

Then the Eq. (13) can be simplified as

$$\dot{V}_1 = -z_1^2 + z_1z_2 \tag{15}$$

Secondly, we choose the Lyapunov function candidate as

$$V_2(z_1, z_2) = V_1(z_1) + \frac{1}{2}z_2^2 = \frac{1}{2}(z_1^2 + z_2^2) \tag{16}$$

Differentiating V_2 along the dynamics (9), we get

$$\dot{V}_2 = \dot{V}_1 + z_2\dot{z}_2 = -z_1^2 - z_2^2 + z_2(2e_1 + 2e_2 + e_3) \tag{17}$$

Next, we define

$$z_3 = 2e_1 + 2e_2 + e_3 \tag{18}$$

Then the Eq. (17) can be simplified as

$$\dot{V}_2 = -z_1^2 - z_2^2 + z_2z_3 \tag{19}$$

Finally, we choose the Lyapunov function candidate as

$$V(z_1, z_2, z_3) = V_2(z_1, z_2) + \frac{1}{2}z_3^2 = \frac{1}{2}(z_1^2 + z_2^2 + z_3^2) \tag{20}$$

By definition, V is a quadratic, positive-definite function on $\mathbb{R}^3$.
Differentiating V along the dynamics (9), we get

$$\dot{V} = -z_1^2 - z_2^2 - z_3^2 + z_3\left[(3-a)e_1 + 5e_2 + (3-b)e_2 + y_2^2 - x_2^2 + u\right] \tag{21}$$

Substituting the active controller (10) into (21), we obtain

$$\dot{V} = -z_1^2 - z_2^2 - z_3^2 \tag{22}$$

which is a quadratic, negative-definite function on $\mathbb{R}^3$.

Thus, by Lyapunov stability theory [19], $z_i(t) \to 0 \ \ (i = 1, 2, 3)$ as $t \to \infty$ exponentially for all initial conditions $z(0) \in \mathbb{R}^3$.

Hence, it is immediate that $e_i(t) \to 0$ ($i = 1, 2, 3$) as $t \to \infty$ exponentially for all initial conditions $e(0) \in \mathbb{R}^3$.

Hence, the identical Sprott jerk chaotic systems (6) and (7) are globally and exponentially synchronized for all initial conditions $x(0), y(0) \in \mathbb{R}^3$.

This completes the proof. □

For numerical simulations, the fourth-order classical Runge-Kutta method with initial step $h = 10^{-8}$ has been used to solve the two systems of differential Eqs. (6) and (7) with the active backstepping controller defined by (10).

The parameter values are taken as in the chaotic case, i.e.

$$a = 1, \quad b = 2.02 \tag{23}$$

The initial values of the master system are taken as

$$x_1(0) = 2.7, \quad x_2(0) = -3.8, \quad x_3(0) = 0.9 \tag{24}$$

The initial values of the slave system are taken as

$$y_1(0) = -1.5, \quad y_2(0) = 3.1, \quad y_3(0) = 1.7 \tag{25}$$

Figure 3 shows the complete synchronization of the states $x_1(t)$ and $y_1(t)$. From Fig. 3, it is seen that the states $x_1(t)$ and $y_1(t)$ are synchronized in 7 S. This shows the efficiency of the active backstepping controller defined by (10).

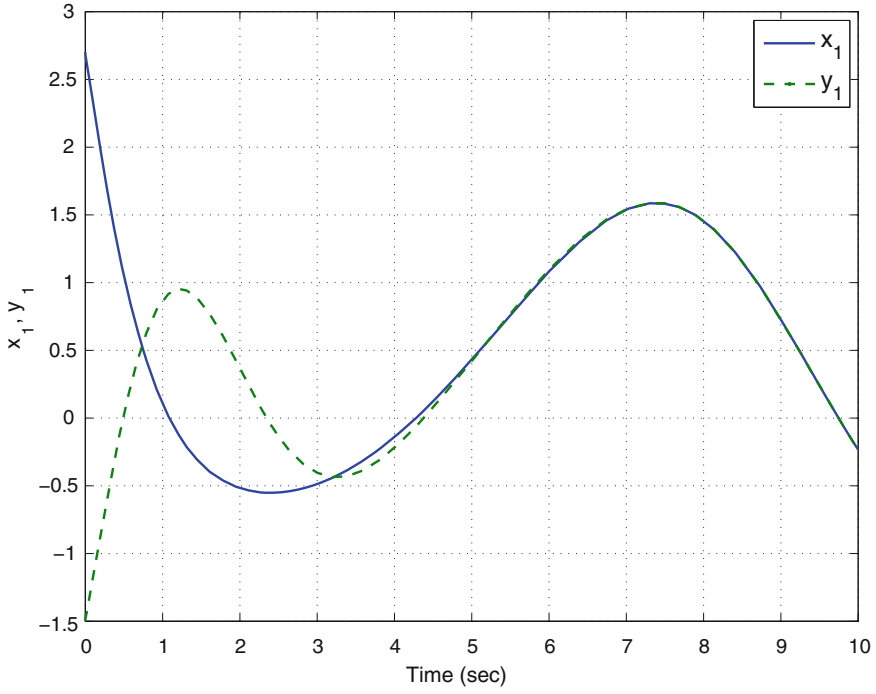

Fig. 3 Synchronization of the states $x_1(t)$ and $y_1(t)$

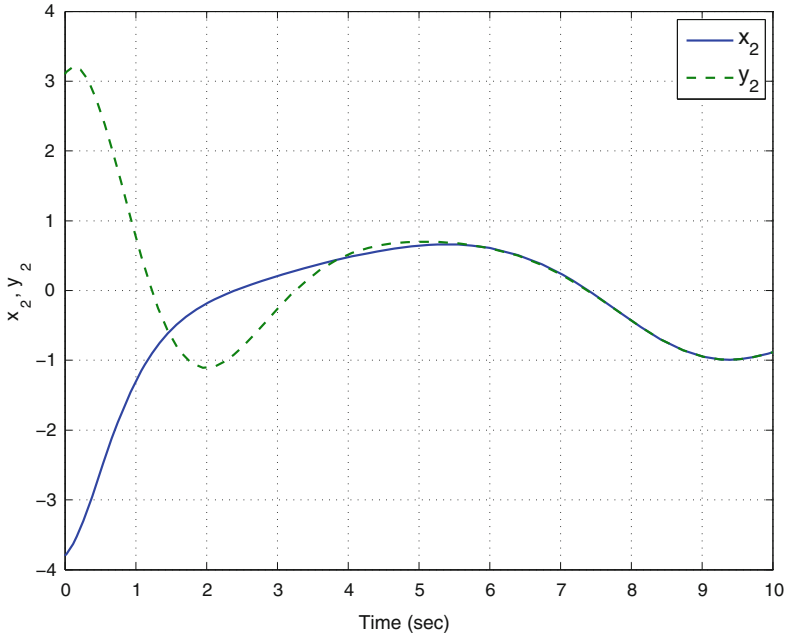

Fig. 4 Synchronization of the states $x_2(t)$ and $y_2(t)$

Figure 4 shows the complete synchronization of the states $x_2(t)$ and $y_2(t)$. From Fig. 4, it is seen that the states $x_2(t)$ and $y_2(t)$ are synchronized in 7 s. This shows the efficiency of the active backstepping controller defined by (10).

Figure 5 shows the complete synchronization of the states $x_3(t)$ and $y_3(t)$. From Fig. 5, it is seen that the states $x_3(t)$ and $y_3(t)$ are synchronized in 7 s. This shows the efficiency of the active backstepping controller defined by (10).

Figure 6 shows the time-history of the synchronization errors $e_1(t)$, $e_2(t)$, $e_3(t)$. From Fig. 6, it is seen that the errors $e_1(t)$, $e_2(t)$, $e_3(t)$ exponentially converge to zero in 7 s. This shows the efficiency of the active backstepping controller defined by (10).

4 Adaptive Backstepping Design for the Synchronization of Identical Sprott Jerk Chaotic Systems

This section derives new results for the adaptive backstepping design for the global chaos synchronization of the identical Sprott jerk systems with unknown parameters. The main result of this section is proved using Lyapunov stability theory.

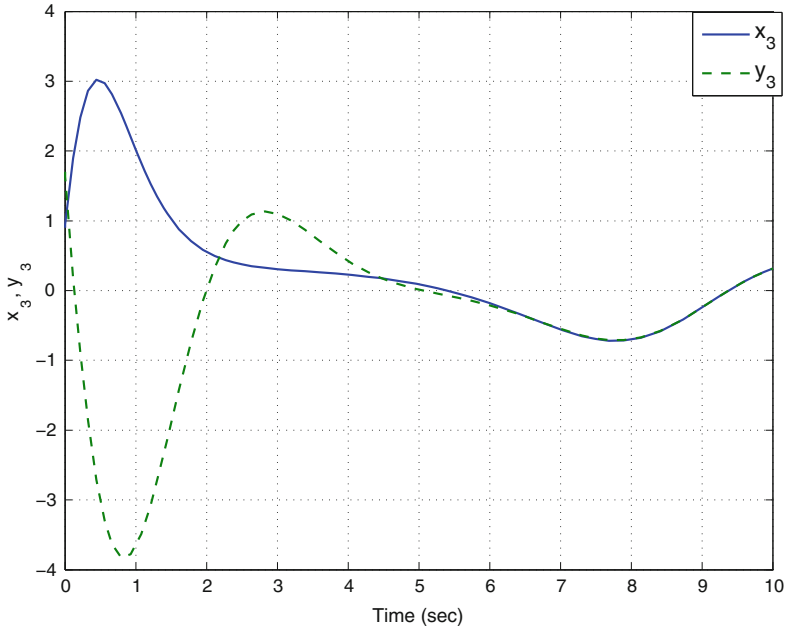

Fig. 5 Synchronization of the states $x_3(t)$ and $y_3(t)$

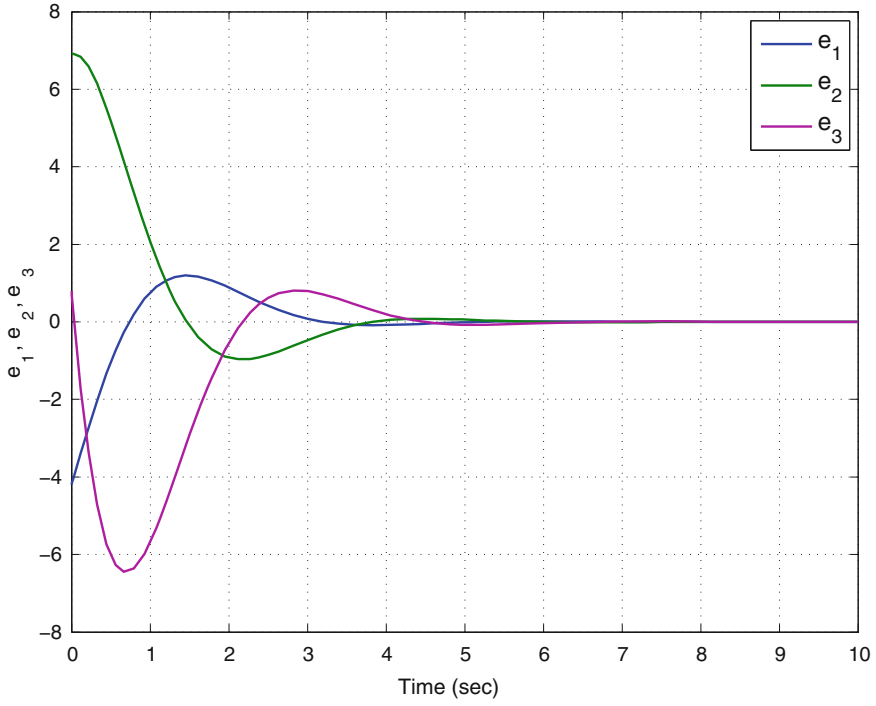

Fig. 6 Time history of the synchronization errors $e_1(t)$, $e_2(t)$, $e_3(t)$

The master system is described by the Sprott chaotic system

$$\begin{aligned}\dot{x}_1 &= x_2\\ \dot{x}_2 &= x_3\\ \dot{x}_3 &= -ax_1 + x_2^2 - bx_3\end{aligned} \tag{26}$$

where x_1, x_2, x_3 are state variables and a, b are unknown parameters.

The slave system is described by the controlled Sprott chaotic system

$$\begin{aligned}\dot{y}_1 &= y_2\\ \dot{y}_2 &= y_3\\ \dot{y}_3 &= -ay_1 + y_2^2 - by_3 + u\end{aligned} \tag{27}$$

where y_1, y_2, y_3 are state variables and $u(t)$ is the adaptive backstepping controller to be designed.

The synchronization error between the master system (26) and the slave system (27) is defined as

$$\begin{aligned}e_1(t) &= y_1(t) - x_1(t)\\ e_2(t) &= y_2(t) - x_2(t)\\ e_3(t) &= y_3(t) - x_3(t)\end{aligned} \tag{28}$$

The error dynamics is obtained as

$$\begin{aligned}\dot{e}_1 &= e_2\\ \dot{e}_2 &= e_3\\ \dot{e}_3 &= -ae_1 + y_2^2 - x_2^2 - be_3 + u\end{aligned} \tag{29}$$

The design problem is to find $u(t)$ so that the error converges to zero asymptotically, i.e. $e_i(t) \to 0$ as $t \to \infty$ for $i = 1, 2, 3$.

Inspired by the control law defined by (10) in the active control case, we may consider the adaptive control law

$$u(t) = (\hat{a}(t) - 3)e_1 - 5e_2 + (\hat{b}(t) - 3)e_3 - y_2^2 + x_2^2 \tag{30}$$

where $\hat{a}(t)$ and $\hat{b}(t)$ are estimates of the unknown parameters a and b, respectively.

We define the parameter estimation errors as

$$\begin{aligned}e_a(t) &= a - \hat{a}(t)\\ e_b(t) &= b - \hat{b}(t)\end{aligned} \tag{31}$$

We note that

$$\begin{aligned} \dot{e}_a(t) &= -\dot{\hat{a}}(t) \\ \dot{e}_b(t) &= -\dot{\hat{b}}(t) \end{aligned} \tag{32}$$

Next, we shall prove the main result of this section.

Theorem 2 *The identical Sprott jerk chaotic systems (26) and (27) with unknown system parameters are globally and exponentially synchronized for all initial conditions* $x(0), y(0) \in \mathbb{R}^3$ *and* $\hat{a}(0), \hat{b}(0) \in \mathbb{R}$ *by the adaptive controller law*

$$u(t) = (\hat{a}(t) - 3)e_1 - 5e_2 + (\hat{b}(t) - 3)e_3 - y_2^2 + x_2^2 \tag{33}$$

where the parameter update law is given by

$$\begin{aligned} \dot{\hat{a}}(t) &= -(2e_1 + 2e_2 + e_3)e_1 \\ \dot{\hat{b}}(t) &= -(2e_1 + 2e_2 + e_3)e_2 \end{aligned} \tag{34}$$

Proof We prove this main result by using Lyapunov stability theory Khalil. First, we define a Lyapunov function candidate

$$V_1(z_1) = \frac{1}{2} z_1^2 \tag{35}$$

where

$$z_1 = e_1 \tag{36}$$

Differentiating V_1 along the dynamics (29), we get

$$\dot{V}_1 = z_1 \dot{z}_1 = e_1 e_2 = -z_1^2 + z_1(e_1 + e_2) \tag{37}$$

Next, we define

$$z_2 = e_1 + e_2 \tag{38}$$

Then the Eq. (37) can be simplified as

$$\dot{V}_1 = -z_1^2 + z_1 z_2 \tag{39}$$

Secondly, we choose the Lyapunov function candidate as

$$V_2(z_1, z_2) = V_1(z_1) + \frac{1}{2} z_2^2 = \frac{1}{2} (z_1^2 + z_2^2) \tag{40}$$

Differentiating V_2 along the dynamics (29), we get

$$\dot{V}_2 = \dot{V}_1 + z_2\dot{z}_2 = -z_1^2 - z_2^2 + z_2(2e_1 + 2e_2 + e_3) \tag{41}$$

Next, we define

$$z_3 = 2e_1 + 2e_2 + e_3 \tag{42}$$

Then the Eq. (41) can be simplified as

$$\dot{V}_2 = -z_1^2 - z_2^2 + z_2 z_3 \tag{43}$$

Finally, we choose the Lyapunov function candidate as

$$V(z_1, z_2, z_3, e_a, e_b) = V_2(z_1, z_2) + \frac{1}{2}z_3^2 + \frac{1}{2}e_a^2 + \frac{1}{2}e_b^2 \tag{44}$$

That is, V is defined as

$$V(z_1, z_2, z_3, e_a, e_b) = \frac{1}{2}\left(z_1^2 + z_2^2 + z_3^2 + e_a^2 + e_b^2\right) \tag{45}$$

By definition, V is a quadratic, positive-definite function on $\mathbb{R}^5$.
Differentiating V along the dynamics (29) and (32), we get

$$\begin{aligned}\dot{V} = &-z_1^2 - z_2^2 - z_3^2 + z_3\left[(3-a)e_1 + 5e_2 + (3-b)e_2 + y_2^2 - x_2^2 + u\right] \\ &- e_a\hat{a}(t) - e_b\hat{b}(t)\end{aligned} \tag{46}$$

Substituting the adaptive controller (33) into (46), we obtain

$$\dot{V} = -z_1^2 - z_2^2 - z_3^2 + e_a(-z_3e_1 - \dot{\hat{a}}) + e_b(-z_3e_2 - \dot{\hat{b}}) \tag{47}$$

Substituting the parameter update law (32) into (47), we obtain

$$\dot{V} = -z_1^2 - z_2^2 - z_3^2 \tag{48}$$

which is a negative semi-definite function on $\mathbb{R}^5$.
If we define

$$z(t) = \begin{bmatrix} z_1(t) \\ z_2(t) \\ z_3(t) \end{bmatrix}, \tag{49}$$

then it can be concluded from (48) that the vector $z(t)$ and the parameter estimation error are globally bounded, i.e.

$$[\, z_1(t) \quad z_2(t) \quad z_3(t) \quad e_a(t) \quad e_b(t) \,]^T \in L_\infty. \tag{50}$$

From (48), it follows that

$$\dot{V} \leq -\|z\|^2 \quad \text{or} \quad \|z\|^2 \leq -\dot{V} \tag{51}$$

Integrating the inequality (51) from 0 to t, we get

$$\int_0^t \|z(\tau)\|^2 d\tau \leq -\int_0^t \dot{V}(\tau)\, d\tau = V(0) - V(t) \tag{52}$$

From (52), it follows that $z(t) \in L_2$.

From (29), it can be deduced that $\dot{z}(t) \in L_\infty$.

Hence, using Barbalat's lemma (19), it can be concluded that $z(t) \to 0$ exponentially as $t \to \infty$ for all initial conditions $z(0) \in \mathbb{R}^3$.

Hence, the identical Sprott jerk chaotic systems (26) and (27) with unknown system parameters are globally and exponentially synchronized for all initial conditions $x(0), y(0) \in \mathbb{R}^3$ and $\hat{a}(0), \hat{b}(0) \in \mathbb{R}$.

This completes the proof. □

For numerical simulations, the fourth-order classical Runge-Kutta method with initial step $h = 10^{-8}$ has been used to solve the two systems of differential Eqs. (26) and (27) with the adaptive backstepping controller defined by (33) and the parameter update law (32).

The parameter values are taken as in the chaotic case, i.e.

$$a = 1, \quad b = 2.02 \tag{53}$$

The parameter estimates are taken as

$$\hat{a}(0) = 4.7, \quad \hat{b} = 2.3 \tag{54}$$

The initial values of the master system are taken as

$$x_1(0) = 1.0, \quad x_2(0) = 0.7, \quad x_3(0) = 0.4 \tag{55}$$

The initial values of the slave system are taken as

$$y_1(0) = 0.3, \quad y_2(0) = 0.1, \quad y_3(0) = 0.2 \tag{56}$$

Figure 7 shows the complete synchronization of the states $x_1(t)$ and $y_1(t)$. From Fig. 7, it is seen that the states $x_1(t)$ and $y_1(t)$ are synchronized in 10 s. This shows the efficiency of the active backstepping controller defined by (33).

Figure 8 shows the complete synchronization of the states $x_2(t)$ and $y_2(t)$. From Fig. 8, it is seen that the states $x_2(t)$ and $y_2(t)$ are synchronized in 10 s. This shows the efficiency of the active backstepping controller defined by (33).

Figure 9 shows the complete synchronization of the states $x_3(t)$ and $y_3(t)$. From Fig. 9, it is seen that the states $x_3(t)$ and $y_3(t)$ are synchronized in 10 s. This shows the efficiency of the active backstepping controller defined by (33).

Figure 10 shows the time-history of the synchronization errors $e_1(t)$, $e_2(t)$, $e_3(t)$. From Fig. 10, it is seen that the errors $e_1(t)$, $e_2(t)$, $e_3(t)$ exponentially converge to zero in 10 s. This shows the efficiency of the active backstepping controller defined by (33).

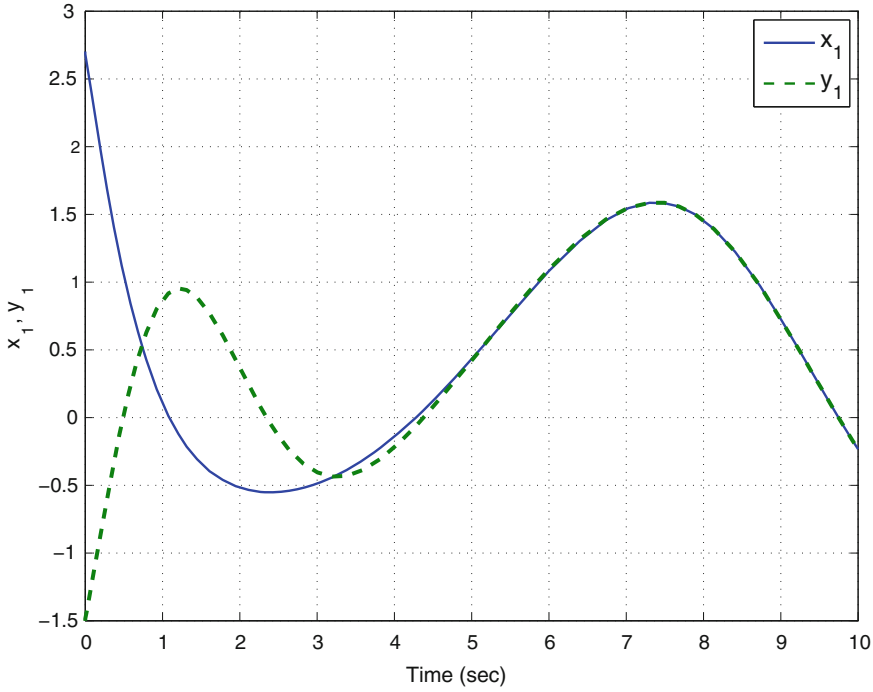

Fig. 7 Synchronization of the states $x_1(t)$ and $y_1(t)$

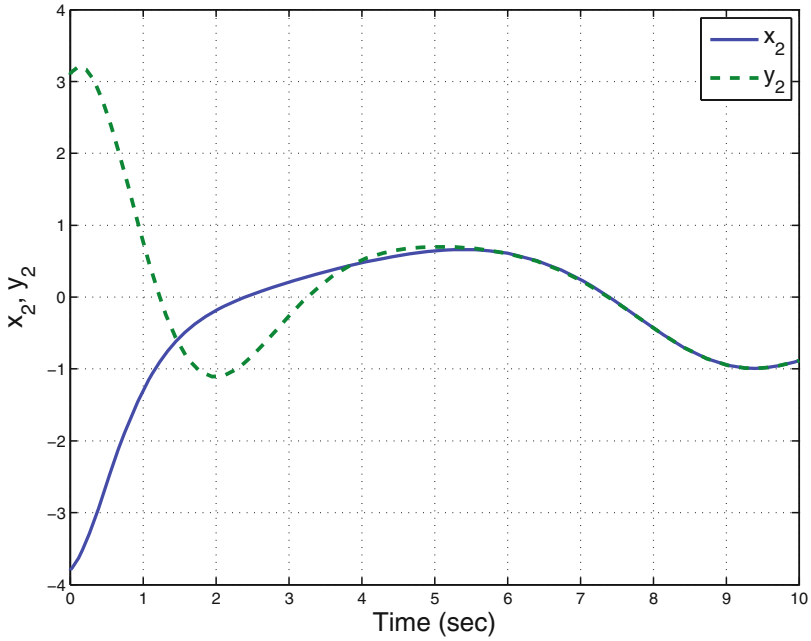

Fig. 8 Synchronization of the states $x_2(t)$ and $y_2(t)$

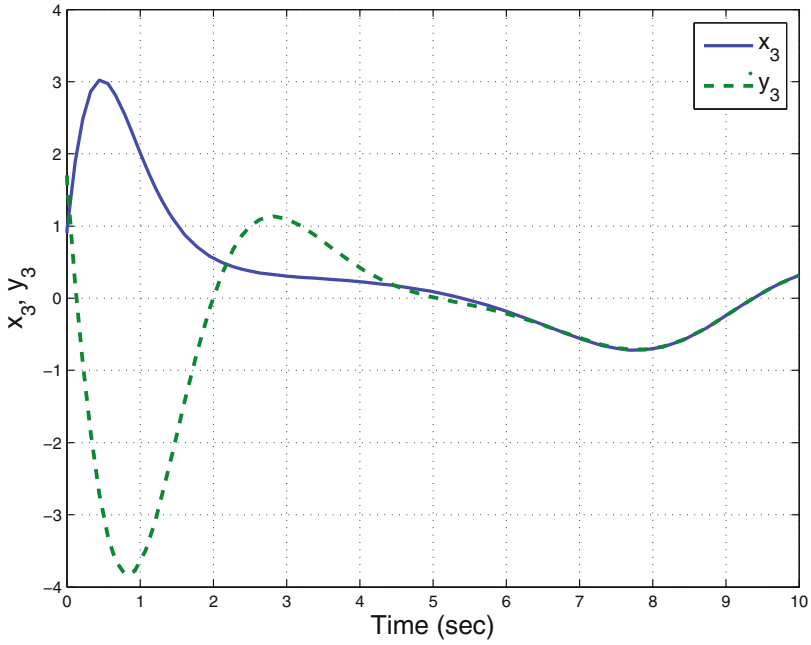

Fig. 9 Synchronization of the states $x_3(t)$ and $y_3(t)$

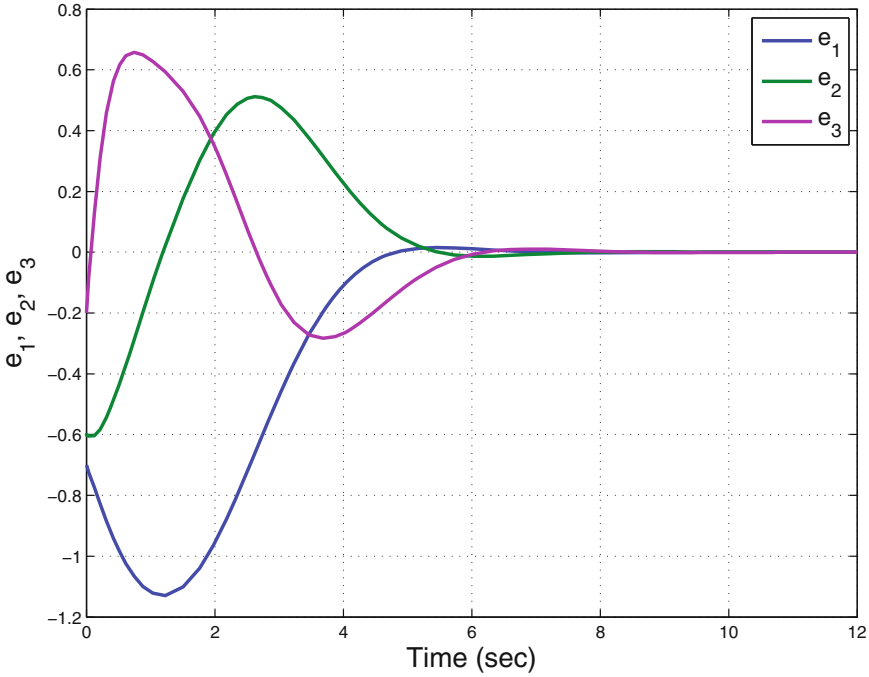

Fig. 10 Time history of the synchronization errors $e_1(t)$, $e_2(t)$, $e_3(t)$

5 Conclusions

In this research work, active and adaptive backstepping controllers were derived the global chaos synchronization of Sprott's jerk chaotic system and the main results were proved using Lyapunov stability theory. This paper investigated synchronization properties for the Sprott's jerk system (1997), which is algebraically the simplest dissipative chaotic system consisting of five terms and a quadratic nonlinearity. Sprott's chaotic system involves only five terms and one quadratic nonlinearity, while Rössler's chaotic system (1976) involves seven terms and one quadratic nonlinearity. This work first detailed the properties of the Sprott's jerk chaotic system. The phase portraits of the Sprott's jerk system were described. The Lyapunov exponents of the Sprott's jerk system were obtained as $L_1 = 0.0525$, $L_2 = 0$ and $L_3 = -2.0727$. The Lyapunov dimension of the Sprott's jerk system was obtained as $D_L = 2.0253$. An active backstepping controller was derived for the global chaos synchronization of identical Sprott's jerk systems with known parameters. The backstepping control method is a recursive procedure that links the choice of a Lyapunov function with the design of a controller and guarantees global asymptotic stability of strict-feedback chaotic systems. Finally, an adaptive backstepping controller was derived for the

global chaos synchronization of identical Sprott's jerk systems with unknown parameters. MATLAB simulations are provided in detail to illustrate all the main results presented in this work.

References

1. Alligood, K. T., Sauer, T., and Yorke, J. A:. Chaos: An Introduction to Dynamical Systems. Springer, Berlin. (1997)
2. Arneodo, A., Coullet, P., Tresser, C.: Possible new strange attractors with spiral structure. Common. Math. Phys. **79**(4), 573–576 (1981)
3. Cai, G., Tan, Z.: Chaos synchronization of a new chaotic system via nonlinear control. J. Uncertain Syst. **1**(3), 235–240 (2007)
4. Carroll, T.L., Pecora, L.M.: Synchronizing chaotic circuits. IEEE Trans. Circ. Syst. **38**(4), 453–456 (1991)
5. Chen, G., Ueta, T.: Yet another chaotic attractor. Int. J. Bifurcat. Chaos **9**(7), 1465–1466 (1999)
6. Chen, H.K., Lee, C.I.: Anti-control of chaos in rigid body motion. Chaos Solitons Fractals **21** (4), 957–965 (2004)
7. Chen, W.-H., Wei, D., Lu, X.: Global exponential synchronization of nonlinear time-delay Lure systems via delayed impulsive control. Commun. Nonlinear Sci. Numer. Simul. **19**(9), 3298–3312 (2014)
8. Das, S., Goswami, D., Chatterjee, S., Mukherjee, S.: Stability and chaos analysis of a novel swarm dynamics with applications to multi-agent systems. Eng. Appl. Artif. Intell. **30**, 189–198 (2014)
9. Feki, M.: An adaptive chaos synchronization scheme applied to secure communication. Chaos Solitons Fractals **18**(1), 141–148 (2003)
10. Gan, Q., Liang, Y.: Synchronization of chaotic neural networks with time delay in the leakage term and parametric uncertainties based on sampled-data control. J. Franklin Inst. **349**(6), 1955–1971 (2012)
11. Gaspard, P.: Microscopic chaos and chemical reactions. Phys. A **263**(1–4), 315–328 (1999)
12. Gibson, W.T., Wilson, W.G.: Individual-based chaos: Extensions of the discrete logistic model. J. Theor. Biol. **339**, 84–92 (2013)
13. Guégan, D.: Chaos in economics and finance. Ann. Rev. Control **33**(1), 89–93 (2009)
14. Huang, J.: Adaptive synchronization between different hyperchaotic systems with fully uncertain parameters. Phys. Lett. A **372**(27–28), 4799–4804 (2008)
15. Huang, X., Zhao, Z., Wang, Z., Li, Y.: Chaos and hyperchaos in fractional-order cellular neural networks. Neurocomputing **94**, 13–21 (2012)
16. Jiang, G.-P., Zheng, W.X., Chen, G.: Global chaos synchronization with channel time-delay. Chaos Solitons Fractals **20**(2), 267–275 (2004)
17. Kaslik, E., Sivasundaram, S.: Nonlinear dynamics and chaos in fractional-order neural networks. Neural Networks **32**, 245–256 (2012)
18. Kengne, J., Chedjou, J.C., Kenne, G., Kyamakya, K.: Dynamical properties and chaos synchronization of improved Colpitts oscillators. Commun. Nonlinear Sci. Numer. Simul. **17** (7), 2914–2923 (2012)
19. Khalil, H. K.:. Nonlinear Systems. Prentice Hall, Englewood Cliffs (2001)
20. Kyriazis, M.: Applications of chaos theory to the molecular biology of aging. Exp. Gerontol. **26**(6), 569–572 (1991)
21. Li, D.: A three-scroll chaotic attractor. Phys. Lett. A **372**(4), 387–393 (2008)

22. Li, N., Pan, W., Yan, L., Luo, B., Zou, X.: Enhanced chaos synchronization and communication in cascade-coupled semiconductor ring lasers. Commun. Nonlinear Sci. Numer. Simul. **19**(6), 1874–1883 (2014)
23. Li, N., Zhang, Y., Nie, Z.: Synchronization for general complex dynamical networks with sampled-data. Neurocomputing **74**(5), 805–811 (2011)
24. Lin, W.: Adaptive chaos control and synchronization in only locally Lipschitz systems. Phys. Lett. A **372**(18), 3195–3200 (2008)
25. Liu, C., Liu, T., Liu, L., Liu, K.: A new chaotic attractor. Chaos Solitions and Fractals **22**(5), 1031–1038 (2004)
26. Liu, L., Zhang, C., Guo, Z.A.: Synchronization between two different chaotic systems with nonlinear feedback control. Chin. Phys. **16**(6), 1603–1607 (2007)
27. Lorenz, E.N.: Deterministic periodic flow. J. Atmos. Sci. **20**(2), 130–141 (1963)
28. Lü, J., Chen, G.: A new chaotic attractor coined. Int. J. Bifurcat. Chaos **12**(3), 659–661 (2002)
29. Murali, K., Lakshmanan, M.: Secure communication using a compound signal from generalized chaotic systems. Phys. Lett. A **241**(6), 303–310 (1998)
30. Nehmzow, U., Walker, K.: Quantitative description of robot environment interaction using chaos theory. Robot. Autono. Syst. **53**(3–4), 177–193 (2005)
31. Njah, A.N., Ojo, K.S., Adebayo, G.A., Obawole, A.O.: Generalized control and synchronization of chaos in RCL-shunted Josephson junction using backstepping design. Phys. C **470**(13–14), 558–564 (2010)
32. Pecora, L.M., Carroll, T.L.: Synchronization in chaotic systems. Phys. Rev. Lett. **64**(8), 821–824 (1990)
33. Petrov, V., Gaspar, V., Masere, J., Showalter, K.: Controlling chaos in Belousov-Zhabotinsky reaction. Nature **361**, 240–243 (1993)
34. Qu, Z.: Chaos in the genesis and maintenance of cardiac arrhythmias. Prog. Biophys. Mol. Biol. **105**(3), 247–257 (2011)
35. Rafikov, M., Balthazar, J.M.: On control and synchronization in chaotic and hyperchaotic systems via linear feedback control. Commun. Nonlinear Sci. Numer. Simul. **13**(7), 1246–1255 (2007)
36. Rasappan, S., Vaidyanathan, S.: Global chaos synchronization of WINDMI and Coullet chaotic systems by backstepping control. Far East J. Math. Sci. **67**(2), 265–287 (2012)
37. Rhouma, R., Belghith, S.: Cryptoanalysis of a chaos based cryptosystem on DSP. Commun. Nonlinear Sci. Numer. Simul. **16**(2), 876–884 (2011)
38. Rössler, O.E.: An equation for continuous chaos. Phys. Lett. **57A**(5), 397–398 (1976)
39. Sarasu, P., Sundarapandian, V.: Adaptive controller design for the generalized projective synchronization of 4-scroll systems. Int. J. Syst. Sig. Control Eng. Appl. **5**(2), 21–30 (2012)
40. Sarasu, P., Sundarapandian, V.: Generalized projective synchronization of two-scroll systems via adaptive control. Int. J. Soft Comput. **7**(4), 146–156 (2012)
41. Sarasu, P., Sundarapandian, V.: Generalized projective synchronization of two-scroll systems via adaptive control. Eur. J. Sci. Res. **72**(4), 504–522 (2012)
42. Shahverdiev, E.M., Bayramov, P.A., Shore, K.A.: Cascaded and adaptive chaos synchronization in multiple time-delay laser systems. Chaos Solitons Fractals **42**(1), 180–186 (2009)
43. Shahverdiev, E.M., Shore, K.A.: Impact of modulated multiple optical feedback time delays on laser diode chaos synchronization. Opt. Commun. **282**(17), 3568–3572 (2009)
44. Sharma, A., Patidar, V., Purohit, G., Sud, K.K.: Effects on the bifurcation and chaos in forced Duffing oscillator due to nonlinear damping. Commun. Nonlinear Sci. Numer. Simul. **17**(6), 2254–2269 (2012)
45. Sprott, J.C.: Some simple chaotic flows. Phys. Rev. E **50**(2), 647–650 (1994)
46. Sprott, J.C.: Simplest dissipative chaotic flow. Phys. Lett. A **228**(4–5), 271–274 (1997)
47. Sprott, J.C.: Competition with evolution in ecology and finance. Phys. Lett. A **325**(5–6), 329–333 (2004)
48. Suérez, I.: Mastering chaos in ecology. Ecol. Model. **117**(2–3), 305–314 (1999)

49. Sundarapandian, V.: Output regulation of the Lorenz attractor. Far East J. Math. Sci. **42**(2), 289–299 (2010)
50. Sundarapandian, V., Pehlivan, I.: Analysis, control, synchronization, and circuit design of a novel chaotic system. Math. Comput. Model. **55**(7–8), 1904–1915 (2012)
51. Suresh, R., Sundarapandian, V.: Global chaos synchronizatoin of a family of *n*-scroll hyperchaotic Chua circuits using backstepping control with recursive feedback. Far East J. Math. Sci. **73**(1), 73–95 (2013)
52. Tigan, G., Opris, D.: Analysis of a 3D chaotic system. Chaos Solitons Fractals **36**, 1315–1319 (2008)
53. Tu, J., He, H., Xiong, P.: Adaptive backstepping synchronization between chaotic systems with unknown Lipschitz constant. Appl. Math. Comput. **236**, 10–18 (2014)
54. Ucar, A., Lonngren, K.E., Bai, E.W.: Chaos synchronization in RCL-shunted Josephson junction via active control. Chaos, Solitons Fractals **31**(1), 105–111 (2007)
55. Usama, M., Khan, M.K., Alghatbar, K., Lee, C.: Chaos-based secure satellite imagery cryptosystem. Comput. Math Appl. **60**(2), 326–337 (2010)
56. Vaidyanathan, S.: Adaptive backstepping controller and synchronizer design for Arneodo chaotic system with unknown parameters. Int. J. Comp. Sci. Inf. Technol. **4**(6), 145–159 (2012)
57. Vaidyanathan, S.: Output regulation of the Liu chaotic system. Appl. Mech. Mater. **110–116**, 3982–3989 (2012)
58. Vaidyanathan, S.: A new six-term 3-D chaotic system with an exponential nonlinearity. Far East J. Math. Sci. **79**(1), 135–143 (2013)
59. Vaidyanathan, S.: Analysis and adaptive synchronization of two novel chaotic systems with hyperbolic sinusoidal and cosinusoidal nonlinearity and unknown parameters. J. Eng. Sci. Technol. Rev. **6**(4), 53–65 (2013)
60. Vaidyanathan, S.: A new eight-term 3-D polynomial chaotic system with three quadratic nonlinearities. Far East J. Math. Sci. **84**(2), 219–226 (2014)
61. Vaidyanathan, S., Rajagopal, K.: Global chaos synchronization of four-scroll chaotic systems by active nonlinear control. Int. J. Control Theor. Appl. **4**(1), 73–83 (2011)
62. Volos, C.K., Kyprianidis, I.M., Stouboulos, I.N.: Experimental investigation on coverage performance of a chaotic autonomous mobile robot. Robot. Auton. Syst. **61**(12), 1314–1322 (2013)
63. Wang, F., Liu, C.: A new criterion for chaos and hyperchaos synchronization using linear feedback control. Phys. Lett. A **360**(2), 274–278 (2006)
64. Witte, C.L., Witte, M.H.: Chaos and predicting varix hemorrhage. Med. Hypotheses **36**(4), 312–317 (1991)
65. Wu, X., Guan, Z.-H., Wu, Z.: Adaptive synchronization between two different hyperchaotic systems. Nonlinear Anal. Theor. Methods Appl. **68**(5), 1346–1351 (2008)
66. Xiao, X., Zhou, L., Zhang, Z.: Synchronization of chaotic Lure systems with quantized sampled-data controller. Commun. Nonlinear Sci. Numer. Simul. **19**(6), 2039–2047 (2014)
67. Yuan, G., Zhang, X., Wang, Z.: Generation and synchronization of feedback-induced chaos in semiconductor ring lasers by injection-locking. Optik—Int. J. Light Electron Opt. **125**(8), 1950–1953 (2014)
68. Zaher, A.A., Abu-Rezq, A.: On the design of chaos-based secure communication systems. Commun. Nonlinear Syst. Numer. Simul. **16**(9), 3721–3727 (2011)
69. Zhang, H., Zhou, J.: Synchronization of sampled-data coupled harmonic oscillators with control inputs missing. Syst. Control Lett. **61**(12), 1277–1285 (2012)
70. Zhang, J., Li, C., Zhang, H., Yu, J.: Chaos synchronization using single variable feedback based on backstepping method. Chaos Solitons Fractals **21**(5), 1183–1193 (2004)
71. Zhou, W., Xu, Y., Lu, H., Pan, L.: On dynamics analysis of a new chaotic attractor. Phys. Lett. A **372**(36), 5773–5777 (2008)
72. Zhu, C., Liu, Y., Guo, Y.: Theoretic and numerical study of a new chaotic system. Intell. Inf. Manage. **2**, 104–109 (2010)

Multi-scroll Chaotic Oscillator Based on a First-Order Delay Differential Equation

Viet-Thanh Pham, Christos K. Volos and Sundarapandian Vaidyanathan

Abstract After the discovery of the well-known chaotic Lorenz's system, the study of chaos has received considerable attention due to its promising applications in a variety of fields, ranging from physics, economics, biology to engineering. Moreover, chaotic systems with multiple scrolls can exhibit more rich dynamics than the general chaotic ones with few attractors. This expansion of dynamics leads to multi-scroll chaotic oscillators showing better performance in several chaotic-based applications, such as secure communication, encrypting fingerprint image, controlling motion directions of autonomous mobile robots, or generating pseudo random numbers etc. As a result, investigating new chaotic oscillators with multiple scrolls has been become an attractive research direction of both theoretical and practical interest recently. Although numerous approaches for constructing multi-scroll attractors from conventional three-dimension chaotic systems have been reported intensively, there are few publications regarding the multi-scroll attractors from infinite dimensional time-delay systems. This work presents a new multi-scroll chaotic oscillator and its circuital design. This chaotic system is described by a first-order delay differential equation with piecewise linear function. It is shown through simulations that the proposed system can exhibit odd number of scrolls of chaotic attractors such as three-, five-, seven-, and nine-scroll attractors. In addition, the detailed implementation of the proposed multi-scroll oscillator using the electronic simulation package Multisim is also presented to show the feasibility of the oscillator. The Multisim results of the chaotic oscillator are well agree with the numerical simulation results. It is noting that the new multi-scroll chaotic circuit

V.-T. Pham (✉)
School of Electronics and Telecommunications, Hanoi University of Science and Technology, Hanoi, Vietnam
e-mail: pvt3010@gmail.com

C.K. Volos
Physics Department, Aristotle University of Thessaloniki, Thessaloniki, Greece
e-mail: chvolos@gmail.com

S. Vaidyanathan
Research and Development Centre, Vel Tech University, Chennai, Tamil Nadu, India
e-mail: sundar@veltechuniv.edu.in

A.T. Azar and S. Vaidyanathan (eds.), *Chaos Modeling and Control Systems Design*, Studies in Computational Intelligence 581, DOI 10.1007/978-3-319-13132-0_4

has been designed with simple common components, like resistors, capacitors, and operational amplifiers.

Keywords Chaos · Multi-scroll attractor · Time delay · Oscillator · Circuit · Multisim

1 Introduction

Chaotic systems have been studied for recent decades after the discovery of the first classical chaotic attractor in 1963 [1]. Despite the fact that there is not an universal definition of chaos, three remarkable characteristics of a chaotic system are: dynamical instability, topological mixing and dense periodic orbits [2]. Dynamical instability is known as the "butterfly effect", which means that a small change in initial conditions of a system can create significant differences. In other word, this vital characteristic makes the system highly sensitive to initial conditions [1, 3]. Topologically mixing is refers as stretching and folding of the phase space, which means that the chaotic trajectory at the phase space will evolve in time so that each given area of this trajectory will eventually cover part of any particular region. Dense periodic orbits means that the trajectory can come arbitrarily close every possible asymptotic state. Therefore, chaotic systems have been widely applied in various practical fields [4, 5].

Interestingly, systems with multi-scroll attractors have become potential candidates for using in chaos-based applications because of their complex dynamics compared with conventional chaotic systems with few attractors. For example, fingerprint images were encrypted via a two-dimensional chaotic sequence achieved from multi-scroll chaotic attractors [6]. The entropy of a random number generator was improved by increasing the number of scrolls in generalized Jerk circuit [7]. In addition, encrypted audio and image information were transmitted when considering the synchronization of Chua's circuits with multi-scroll attractor [8]. A parameter determination method for double-scroll chaotic systems was also applied to chaotic cryptanalysis [9]. As a result, there are numerous researches on generating multi-scroll chaotic attractor (see [10] and references cited there in).

The presence of time delay has been observed in various dynamical systems [11, 12]. In order to describe exactly their special features, delay differential equations (DDEs) have used because delay differential equations differ from ordinary differential equations in that the evolution of dependent variables at a certain time depend on their values at previous times. Infinite dimensional dynamics of time-delay systems could make complex phenomena [13, 14] which do not exist in original systems. As a result, chaotic oscillator can be constructed by using a time-delay system. In particular, the oscillators described by first-order DDEs can exhibit chaos [15]. These oscillators have attracted considerable attention due to

their simplicities and feasibilities. It is worth noting that, multi-scroll attractors could be obtained from time-delay chaotic systems [16].

In this work a novel multi-scroll oscillator, which is modelled by a first-order delay differential equation, is proposed. This work is organized as follows. After presenting the related works in Sect. 2, the mathematical model of the new proposed oscillator is introduced in Sect. 3. Then, the circuital realization of a three-scroll oscillator is described and illustrated in Sect. 4. In Sect. 5, the obtained results are represented. Discussions relating to the implementation and the potential applications of the new time-delayed oscillator are given in Sect. 6. Finally, some conclusion remarks are drawn in the last Section.

2 Related Works

Chua's circuit, an invention of L.O. Chua [17], is one of the most well-known nonlinear electronic circuits This simple electronic circuit satisfies three criteria to exhibit chaotic behavior due to the fact that Chua's circuit includes three energy storage elements (two capacitors and an inductor), a locally active resistor and a nonlinear element (Chua's diode with a piecewise-linear characteristic). Despite of its simple structure, Chua's circuit can display complex dynamics. Therefore, Chua's circuit is considered as a platform for the study of nonlinear phenomena, like chaos [18].

It is interesting that Chua's circuit can display the classical double scroll. Based on this known circuit, Suykens and Vandewalle investigated a new family of n-double scroll attractors by modifying the characteristic of the nonlinear resistor with additional break points [19]. The major breakthrough of Suykens and Vandewalle has promoted a considerable number of studies on nonlinear systems with multi-scroll attractors. Diverse noticeable design approaches to generate multi-scroll attractors have been reported in the literature, i.e. quasi-linear function approach, nonlinear modulating function approach, step function approach, hysteresis series approach, saturated function series approach, or step series switching approach etc. [10, 20–24]. Recently, generating the multi-scroll attractors from infinite dimensional time-delay systems have been a focal topic of interest because even one delay differential equation is enough to generate multi-scroll chaos [7, 16, 25, 26].

While a large number of studies [27–30] focused mainly on time-delay oscillators with mono- and double-scroll attractors, there are a few reported oscillators can display multi-scroll attractors [7, 16]. In fact, designed multi-scroll oscillators have built mainly based on suitable nonlinear functions. Some typical nonlinear functions are summarized as follows.

A simple time-delay systems was introduced by Sprott [31] with a sinusoidal nonlinearity

$$F(x) = \sin(x). \tag{1}$$

This system displayed 6-scroll chaotic attractor. Here, the sine function can be implemented by using a trigonometric function integrated circuit AD639. Wang [26] considered the activation function took a reflection symmetric piecewise linear function of the form

$$F(x) = Ax + 0.5(A - B)[(|x + m| - |x - m|) - (|x + n| - |x - n|)], \quad (2)$$

with $A = 4.3$, $B = -5.8$, $m = 1.1$ and $n = 3.3$. By adjusting the value of only a single parameter, four-scroll attractor was obtained. This nonlinear function could be built conveniently by operational amplifiers and constant voltage sources. A piecewise linear function with a threshold controller [25] was applied in the following form

$$F(x) = AF^* - Bx, \quad (3)$$

where

$$F^* = \begin{cases} -x^* & x < -x^* \\ x & -x^* \le x \le x^* \\ x^* & x > x^*, \end{cases} \quad (4)$$

where $A = 5.2$, $B = 3.5$, and $x^* = 0.7$ is the controllable threshold value. The nonlinearity was implemented by using only two diodes and few operational amplifiers. By adding more number of threshold values, two double-scroll attractors could be produced. In addition, Yalcin [7] proposed a nonlinearity based on a hard limited function

$$F(x) = \sum_{i=1}^{M_x} g_{(-2i+1)/2}(x) + \sum_{i=1}^{N_x} g_{(-2i+1)/2}(x), \quad (5)$$

where

$$g_\theta(\zeta) = \begin{cases} 1 & \zeta \ge \theta,\ \theta > 0 \\ 0 & \zeta < \theta,\ \theta > 0 \\ 0 & \zeta \ge \theta,\ \theta < 0 \\ -1 & \zeta < \theta,\ \theta < 0. \end{cases} \quad (6)$$

The system exhibited n-scroll chaotic attractor for suitable values of M_x and N_x. For example, three-, four-, five-, and six-scroll attractors obtained when $\{M_x = 1, N_x = 1\}$, $\{M_x = 1, N_x = 2\}$, $\{M_x = 0, N_x = 4\}$, and $\{M_x = 1, N_x = 4\}$, respectively. Nonlinear block comprised voltage comparators whose total number depending on the number of scrolls. Moreover, Kilinc [16] represented a oscillator employed the nonlinearity as a function of hysteresis series

$$F(x) = \sum_{i=1}^{N}(h(x-2i)-i) + \sum_{j=0}^{M}(h(x+2j)+j), \tag{7}$$

where $h(x)$ is the basic hysteresis function

$$h(x) = \begin{cases} -1 & x < 0.5 \\ 1, & x > -0.5 \end{cases} \tag{8}$$

Similar to the previous system (5), by choosing the appropriate values of M and N, $N + M + 2$ scrolls could be generated. For instance, the three-, four-, and five-scroll attractors could be observed when $\{N = 0, M = 1\}$, $\{N = 0, M = 2\}$, and $\{N = 0, M = 3\}$, respectively. Hysteresis comparators were realized employing positive feedback around the classical operational amplifiers. In order to generate N-double scroll delayed chaotic attractors Wang [32] studied a piecewise-linear activation function of the form

$$F_{2N}(x) = m_N x + \frac{1}{2}\sum_{i=1}^{N}(m_{i-1} - m_i)(|x + c_i| - |x - c_i|), \tag{9}$$

where N represents number of double scroll. Here m_i and c_i are the parameters which present the slopes and values in the abscissa corresponding inflexion of the piecewise-linear activation function, respectively [32]. For example, a four-double scroll chaotic attractor could be obtained when $N = 4$, $m_0 = m_2 = m_4 = 6.5$, $m_1 = m_3 = 8.5$, $c_1 = 0.8$, $c_2 = 2.4$, $c_3 = 4$, and $c_4 = 5.6$. The piecewise-linear activation function (9) could be easily implemented by a combination of operational amplifiers, resistors, and dc voltage sources. It is easy to see that novel time-delayed systems could be proposed by discovering appropriate nonlinear functions.

3 Mathematical Model of New Multi-Scroll Oscillators

The first-order DDE describing the proposed oscillator can be written in the following form

$$\frac{dx}{dt} = -ax(t) - bF_{2N+1}(x_\tau), \tag{10}$$

where a and b are positive parameters, x is a dynamical variable, $x_\tau = x(t - \tau)$ with τ is a constant time delay. $F_{2N+1}(x_\tau)$ is a piecewise linear function, which is given as

$$F_{2N+1}(x_\tau) = x_\tau - \sum_{k=1}^{N}[sgn(x_\tau + (2k-1)) + sgn(x_\tau - (2k-1))], \tag{11}$$

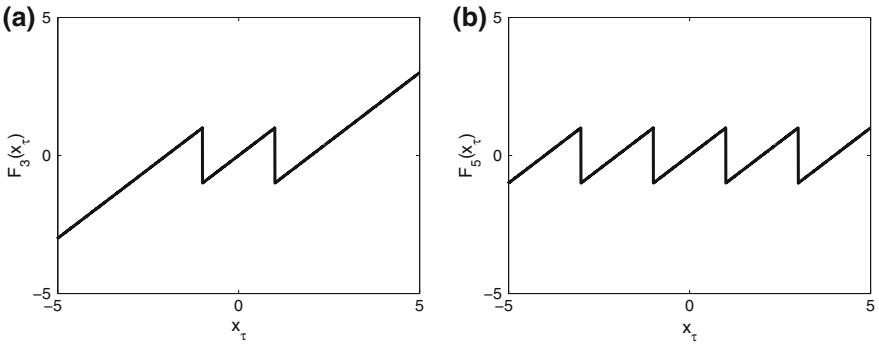

Fig. 1 The piecewise linear function $F_{2N+1}(x_\tau)$: **a** $F_3(x_\tau)$ when $N = 1$, **b** $F_5(x_\tau)$ when $N = 2$

where N and k are positive integers, while the signum function $sgn(.)$ is defined by

$$sgn(x_\tau) = \begin{cases} -1 & x_\tau < 0 \\ 0 & x_\tau = 0 \\ 1 & x_\tau > 0. \end{cases} \tag{12}$$

In this work the parameters of system (10) are determined as: $a = 0.1$, $b = 15$ and $\tau = 0.15$. The piecewise linear function $F_{2N+1}(x_\tau)$ has the saw-tooth shape. Moreover the break points can vary when increasing the value of N, i.e. the piecewise linear functions corresponding to $N = 1$ and $N = 2$ are drawn in Fig. 1. According to the mentioned effect methodology [10], multi-scroll attractors can be generated by adding some additional break points into the piecewise linear functions.In the other word, multi-scroll attractor can be created by changing the value of N. The number of scrolls generated from the system (10) is equal to $2N + 1$. Figure 2 shows the attractors obtained from the system (10) with different values of N. Obviously, the proposed chaotic oscillator can generate odd number of scrolls of chaotic attractors such as three-, five-, seven, and nine-scroll attractors.

4 Circuitry Design of Multi-Scroll Chaotic Oscillator

The simple physical approach for investigating dynamics of a chaotic system is design the electronic circuit which emulates the system [33, 34]. There are some obvious advantages of this approach. Firstly this approach avoids the uncertainties arise from systematic and statistical errors in numerical simulations [35], for example the discretization and round-off errors in the numerical procedures or finite-time approximation of a quantity that is properly described by an infinite-time integral. Secondly signals generated from chaotic electronic oscillators can be displayed on the oscilloscope and observed quickly, comparing to the long

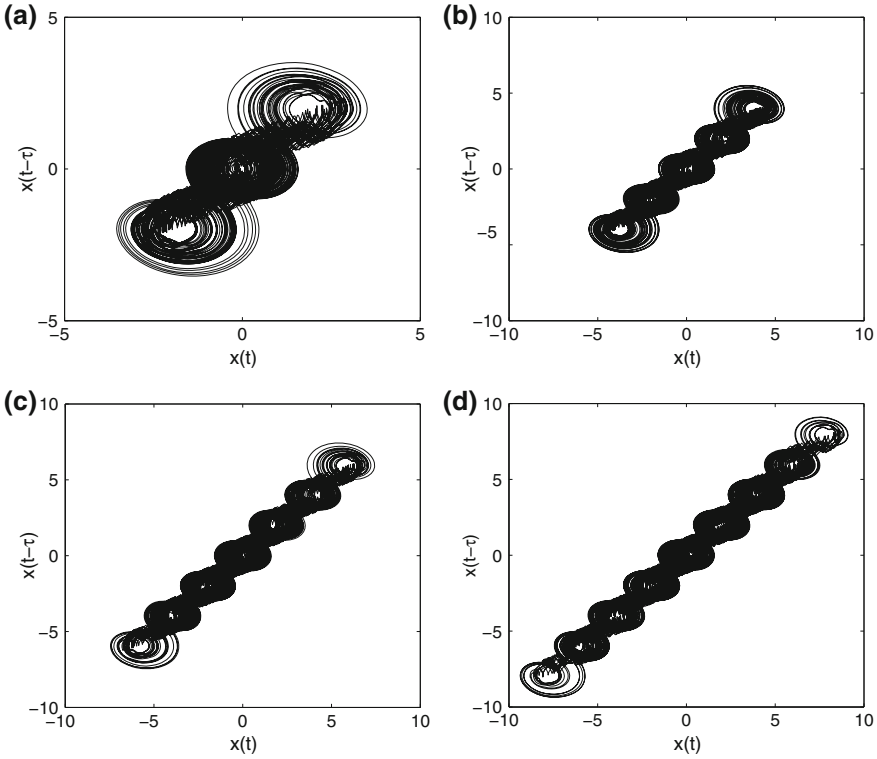

Fig. 2 Multi-scroll attractors obtained from the new chaotic oscillator (10) when changing the value of N: **a** three-scroll attractor ($N = 1$), **b** five-scroll attractor ($N = 2$), **c** seven-scroll attractor ($N = 3$), and **d** nine-scroll attractor ($N = 4$)

computer-based simulation time. In fact, the experimental bifurcation diagram can be also obtained conveniently by changing the value of circuital components. As a result, a wide range of dynamical behavior of the circuit can be compared with the numerical simulations of the corresponding theoretical model. Moreover circuital realization of chaotic system plays an important role in practical applications, i.e. secure communications [36, 37], random generator [38, 39], image encryption [40] or path planning for autonomous robots [18, 37].

Hence, in this Section, the proposed multi-scroll chaotic oscillator will be realized by using a general circuital diagram as illustrated in Fig. 3. There are three main blocks: the integrator (which includes the two resistors R_1, R_2, a capacitor C_0 and an operational amplifier U_1), the piecewise linear block and the time-delay block. In the design and simulation, a lossless transmission line is utilized as a time-delay block [41]. In practice the time-delay block can be implemented by either a network of T-type LCL filters [15, 42] or a series of Bessel filters in cascade [43].

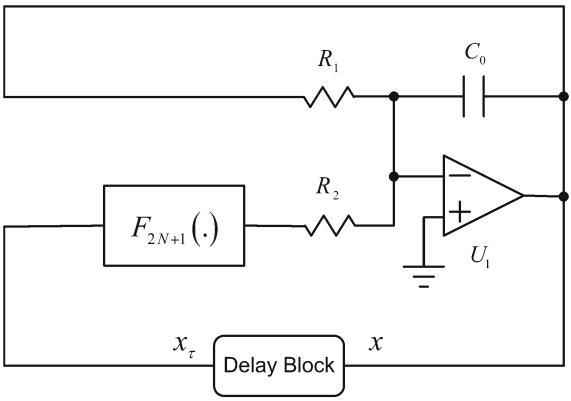

Fig. 3 Circuit diagram of the multi-scroll oscillator. The values of components are chosen as R_1 = 150 kΩ, R_2 = 1 kΩ, C_0 = 0.2 μF

Here the power supplies are ±15 V. From the Sect. 3, it is obvious that the state variables of the multi-scroll chaotic system (10) are in a range between −10 and +10 V. So it does not require rescale the state variables.

The state variable x of the mathematical model (10) is the voltage across the capacitor C_0. The circuit equation has the following form

$$\frac{dV_{C_0}(t)}{dt} = -\frac{1}{R_1 C_0} V_{C_0}(t) - \frac{1}{R_2 C_0} F_{2N+1}\left(V_{C_0}\left(t - T_{delay}\right)\right), \tag{13}$$

where $R_1 = R_0/a$ and $R_2 = R_0/b$ with R_0 = 15 kΩ.

The value of the time-delay implemented in delay block is T_{delay} = 450 μs, so the dimensionless delay τ is calculated as

$$\tau = \frac{T_{delay}}{R_0 C_0} = 0.15. \tag{14}$$

For the sake of simplicity, only the implementation of the piecewise function $F_3(x_\tau)$ is introduced in this Section as an example (see Fig. 3). However the realization of other functions $F_{2N+1}(x_\tau)$, i.e. $F_5(x_\tau)$ can be implemented in the same way. It is worth noting that we only use common electronics components to realize the function $F_3(x_\tau)$. Hence, the nonlinearity block can be realized in an easy and compact way. Selected components are summarized in Table 1.

Table 1 Values of selected circuital components in Figs. 2 and 3

Circuit's components	Selected values
R	10 kΩ
R_1	150 kΩ
R_2	1 kΩ
R_3	10 kΩ
R_4, R_5	142.5 kΩ
R_6, R_7, R_8, R_9	150 kΩ
C_0	0.2 μF

5 Obtained Results

The designed circuit is implemented by using Multisim. It is an electronic schematic capture and simulation program of National Instruments (NI). Multisim provides an advanced, industry-standard SPICE simulation environment and is used widely in the world. The whole circuit is realized by only simple off-the-shelf circuital components like resistors, a capacitor and operational amplifiers. In this work, operational amplifiers TL084 have been used. The simulation of the circuit of Fig. 4, which realizes the function in Multisim reveals the piecewise linear nature of this function (Fig. 5a). It is clear that the circuit can produce three-scroll chaotic attractor (Fig. 5b). Figure 5 also shows a good qualitative agreement between the numerical simulation in Sect. 3 and the Multisim results of the designed circuit.

Furthermore, in order to illustrate the feasibility, practicality and flexibility of the introduced model (10), obtained phase portraits with Multisim of another circuit with piecewise linear function $F_5(x_\tau)$ are also presented in Fig. 6, which are consistent with the numerical results in Figs. 1b and 2b. The results in Figs. 5 and 6 confirm that different multi-scroll attractors can be generated when changing the piecewise linear function (11).

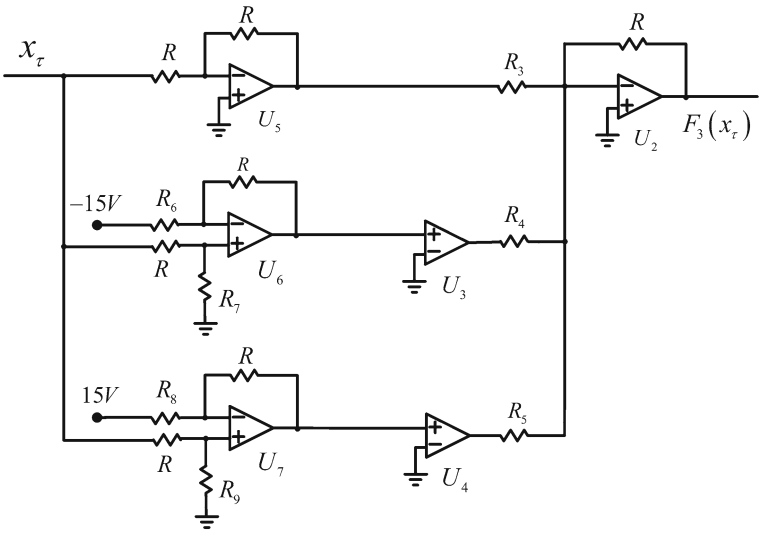

Fig. 4 Circuit diagram of piecewise linear function $F_3(x_\tau)$. The circuit parameters are set as $R_3 = R = 10$ kΩ, $R_4 = R_5 = 142.5$ kΩ and $R_6 = R_7 = R_8 = R_9 = 150$ kΩ

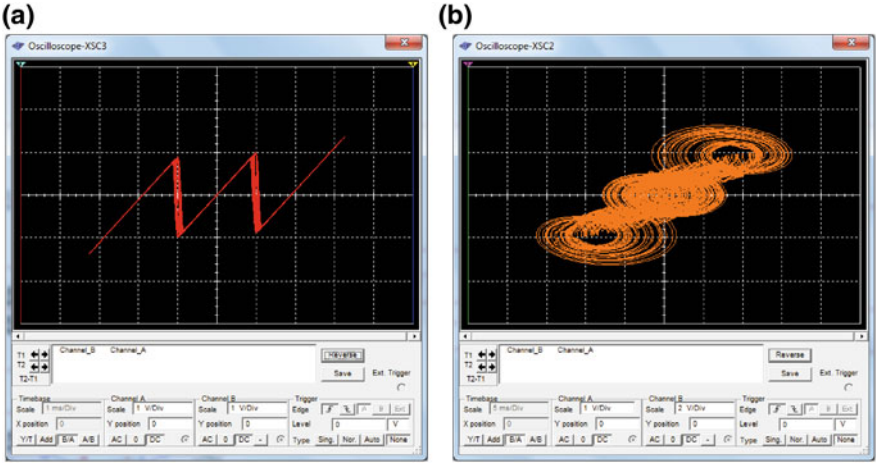

Fig. 5 Simulation results with Multisim of the circuit in Fig. 3 with piecewise linear function $F_3(x_\tau)$: **a** measured characteristic curve of the piecewise linear function $F_3(x_\tau)$, **b** three-scroll attractor presented in $x(t) - x(t - \tau)$ plane

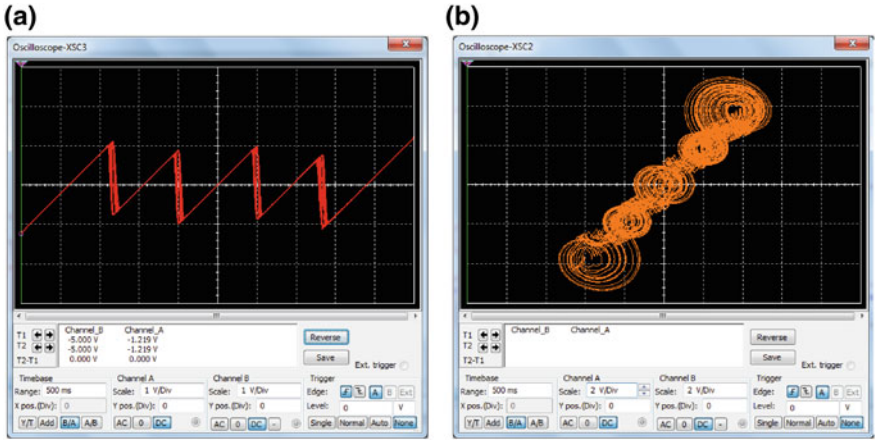

Fig. 6 Simulation results with Multisim of the designed circuit with piecewise linear function $F_5(x_\tau)$ (for the sake of simplicity, detailed design of this function is not reported in this work): **a** measured characteristic curve of the piecewise linear function $F_5(x_\tau)$, **b** five-scroll attractor displayed in $x(t) - x(t - \tau)$ plane

6 Discussion

Dynamical systems with the presence of time delays have been observed in diverse fields such as engineering [11, 13], neutral system [44], physics [14] or biology [45, 46] and so on. The presence of time delay is unavoidable because of the limit

calculation speed, memory effects, finite transmission velocity etc. Hence time-delay systems have been described more accurately practical models, for example a single vehicle induced by traffic light and speedup [47], broadband bandpass electro-optic oscillator [48], road traffic [49], or food web systems [50].

On one hand, delay can be utilized to stabilize nonlinear systems. Time-delay feedback control [51] is a highly effective control method which has applied in different systems [13, 14, 52]. The most advantage of this method is that it does not require the prior knowledge about the model. Different to the conventional feedback control, the feedback signal is proportional to the difference of output signal and its delayed version. Time-delay feedback control can stabilize the chaotic behavior to one of unstable fixed points or unstable periodic orbits embedded within chaotic attractor. There are two control parameters: the feedback gain and the feedback time delay. It is worth noticing that the feedback time-delay is often different from the intrinsic delay of time-delay system. Two parameters have been selected by trial-and-error procedures or Lyapunov stability analysis approaches. In particular, for stabilizing of the unstable periodic orbit, the controller time delay has to be chosen as an integer multiple of the period of the desired unstable periodic orbit.

On the other hand, delay could lead to complex behaviors which do not exist in original systems. For example, the systems described by first order delay differential equations (DDE) can exhibit complex phenomena, like chaos [15]. Such systems have attracted more attention because of their complex chaotic attractors as well as their feasibilities, reliability and practicality. For these reasons, there are many efforts to design chaotic time-delay systems, which can generate multiple scrolls. Although some such systems can be found in the literature [7, 16], their nonlinear functions are often extremely complicated to realize in electronic circuits. Therefore two advanced features of the proposed system (10) can be taken into account: the simplicity and the application potentiality. In the former feature, the implementation of the whole system uses only common off-the-shelf circuital components. In other words, the complexity of the implementation stage is reduced significantly. In addition, different numbers of scroll attractors can be obtained easily by changing the nonlinear function (11). Moreover, from the view point of on-chip realization, the proposed system is a suitable candidate for a integrated circuit chaotic generator. Because of its richness of dynamics, the introduced multi-scroll chaotic oscillator is more appropriate to chaos-based applications, especially chaos-based secure communication [53, 54]. Obviously, the new oscillator (10) contains higher dimensional chaotic behavior of delay differential equation and the ability to create multi-scroll chaotic attractors. Hence, if it is involved in chaos-based secure communication architecture, the eavesdropper cannot reconstruct the chaotic attractor and retrieve the hidden message [55–57].

7 Conclusion

In this work, a mathematical model of a multi-scroll oscillator has proposed. Although the new oscillator is described by only a DDE, it can exhibit complex behaviors. By changing the piecewise linear function of the oscillator, three-, five-, seven-, and nine-scroll attractors have been observed. The proposed oscillator has also implemented with analog electronic circuit using common electronic components. The Multisim results of the circuit agree well with the numerical calculations. Because the new oscillator generates complex multi-scroll chaotic attractor, it can be used for secure communication applications or a random bit generator. However, when being applied in secure communications, synchronization property of the new oscillator should be considered carefully in future works. Furthermore, another future direction of research is how to obtain even numbers of scrolls from this oscillator.

Acknowledgments This research is funded by Vietnam National Foundation for Science and Technology Development (NAFOSTED) under grant number 102.99-2013.06.

References

1. Lorenz, E.N.: Deterministic non-periodic flow. J. Atmos. Sci. **20**, 130–141 (1963)
2. Hasselblatt, B., Katok, A.: A First Course in Dynamics: With a Panorama of Recent Developments. Cambridge University Press, Cambridge (2003)
3. Strogatz, S.H.: Nonlinear Dynamics and Chaos: with Applications to Physics, Biology, Chemistry, and Engineering. Perseus Books, Massachusetts (1994)
4. Boccaletti, S., Kurths, J., Osipov, G., Valladares, D.L., Zhou, C.S.: The synchronization of chaotic systems. Phys. Rep. **366**, 1–101 (2002)
5. Chen, G.R.: Controlling Chaos and Bifurcations in Engineering Systems. CRC Press, Boca Raton (1999)
6. Han, F., Hu, J., Yu, X., Wang, Y.: Fingerprint images encryption via multi-scroll chaotic attractors. Appl. Math. Comput. **185**, 931–939 (2007)
7. Yalcin, M.E.: Increasing the entropy of a random number generator using n-scroll chaotic attractors. Int. J. Bifurcat. Chaos **17**, 4471–4479 (2007)
8. Gamez-Guzman, L., Cruz-Hernandez, C., Lopez-Gutierrez, R., Garcia-Guerrero, E.E.: Synchronization of chua's circuits with multi-scroll attractors: application to communication. Commun. Nonlinear Sci. Numer. Simul. **14**, 2765–2775 (2009)
9. Orue, A.B., Alvarez, G., Pastor, G., Romera, M., Montoya, F., Li, S.: A new parameter determination method for some double-scroll chaotic systems and its applications to chaotic cryptanalysis. Commun. Nonlinear Sci. Numer. Simul. **15**, 3471–3483 (2010)
10. Lu, J.H., Chen, G.R.: Generating multiscroll chaotic attractors: theories, methods and applications. Int. J. Bifurcat. Chaos **16**, 775–858 (2006)
11. Ikeda, K., Daido, H., Akimoto, O.: Optical turbulence: chaotic behavior of transmitted light from a ring cavity. Phys. Rev. Lett. **45**, 709–712 (1980)
12. Mackey, M.C., Glass, L.: Oscillation and chaos in physiological control system. Science **197**, 287–289 (1977)
13. Ikeda, K., Matsumoto, K.: High-dimensional chaotic behaviour in system with time-delayed feedback. Physica D **29**, 223–235 (1987)

14. Xia, Y., Fu, M., Shi, P.: Analysis and synthesis of dynamical systems with time-delays. Springer, New York (2009)
15. Lu, H., He, Z.: Chaotic behavior in first-order autonomous continuous-time systems with delay. IEEE Trans. Circuits Syst. I: Fundam. Theory Appl. **43**, 700–702 (1996)
16. Kilinc, S., Yalcin, M., Ozoguz, S.: Multiscroll chaotic attractors from a hysteresis based time-delay differential equation. Int. J. Bifurcat. Chaos **20**, 3275–3281 (2010)
17. Matsumoto, T.: A chaotic attractor from Chua's circuit. IEEE Trans. Circuit Syst. I **31**, 1055–1058 (1984)
18. Fortuna, L., Frasca, M., Xibilia, M.G.: Chua's circuit implementation: Yesterday, today and tomorrow. World Scientific, Singapore (2009)
19. Suykens, J.A.K., Vandewalle, J.: Generation of n-double scrolls (n = 1, 2, 3, 3, …). IEEE Trans. Circuit Syst. I **31**, 1055–1058 (1984)
20. Carbajal-Gomez, V.H., Tlelo-Cuautle, E., Fernandez, F.V.: Optimizing the positive Lyapunov exponent in multi-scroll chaotic oscillators with differential evolution algorithm. Appl. Math. Comput. **219**, 8163–8168 (2013)
21. Dadras, S., Momeni, H.R.: A novel three-dimensional autonomous chaotic system generating two, three and four-scroll attractors. Phys. Lett. A **373**, 3637–3642 (2009)
22. Liu, C., Yi, J., Xi, X., An, L., Fu, Y.: Research on the multi-scroll chaos generation based on Jerk mode. Procedia Eng. **29**, 957–961 (2012)
23. Luo, X.H., Lui, H.Q., Dai, X.G.: A family of multi-scroll chaotic attractors and its circuit design. Acta. Phys. Sin. **57**, 7511–7516 (2008)
24. Yalcin, M.E., Suykens, J.A.K., Vandewalle, J.: Cellular Neural Networks, Multi-Scroll Chaos and Synchronization. World Scientific, Singapore (2005)
25. Srinivasan, K., Mohamed, I.R., Murali, K., Lakshmanan, M., Sinha, S.: Design of time delayed chaotic circuit with threshold controller. Int. J. Bifurcat. Chaos **20**, 2185–2191 (2010)
26. Wang, L., Yang, X.: Generation of multi-scroll delayed chaotic oscillator. Electron. Lett. **42**, 1439–1441 (2006)
27. Duan, S., Wang, L.: A novel delayed chaotic neural model and its circuitry implementation. Comput. Math. Appl. **57**, 1736–1742 (2009)
28. Horbelt, W., Timmer, J., Voss, H.U.: Parameter estimation in nonlinear delayed feedback systems from noisy data. Phys. Lett. A **299**, 513–521 (2002)
29. Le, L.B., Konishi, K., Hara, N.: Design and experimental verification of multiple delay feedback control for time-delay nonlinear oscillator. Nonlinear Dyn. **67**, 1407–1418 (2012)
30. Tamasevicius, A., Pyragine, T., Meskauskas, M.: Two scroll attractor in a delay dynamical system. Int. J. Bifurcat. Chaos **17**, 3455–3460 (2007)
31. Sprott, J.C.: A simple chaotic delay differential equation. Phys. Lett. A **366**, 397–402 (2007)
32. Wang, L., Duan, S., Yang, X. (2008). Generation and circuitry implementation of N-double scroll delayed chaotic attractors . In: Proceedings of the International Workshop on Nonlinear Dynamics and Synchronization
33. Bouali, S., Buscarino, A., Fortuna, L., Frasca, M., Gambuzza, L.V. (2012). Emulating complex business cycles by using an electronic analogue. Nonlinear Anal. Real World Appl. **13,** 2459–2465
34. Sprott, J.C.: Simple chaotic systems and circuits. Am. J. Phys. **68**, 758–763 (2013)
35. Sprott, J.C.: A proposed standard for the publication of new chaotic systems. Int. J. Bifurcat. Chaos **21**, 2391–2394 (2011)
36. Cuomo, K.M., Oppenheim, A.V.: Circuit implementation of synchronized chaos with applications to communications. Phys. Rev. Lett. **71**, 65–68 (1993)
37. Volos, C.K., Kyprianidis, I.M., Stouboulos, I.N.: Various synchronization phenomena in bidirectionally coupled double scroll circuits. Commun. Nonlinear Sci. Numer. Simul. **71**, 3356–3366 (2011)
38. Barakat, M., Mansingka, A., Radwan, A.G., Salama, K.N.: Generalized hardware post processing technique for chaos-based pseudorandom number generators. ETRI J. **35**, 448–458 (2013)

39. Yalcin, M.E., Suykens, J.A.K., Vandewalle, J.: True random bit generation from a double-scroll attractor. IEEE Trans. Circuits Syst. I, Regular Papers **51**, 1395–1404 (2004)
40. Volos, C.K., Kyprianidis, I.M., Stouboulos, I.N.: Image encryption process based on chaotic synchronization phenomena. Sig. Process. **93**, 1328–1340 (2013)
41. Hoang, T.-M., Nguyen, T., Nguyen, V., Chedjou, J., and Kyamakya, K. (2009). Design and simulation of circuit for synchronization of multidelay feeback systems. In: Proceedings of the International Symposium on Theoretical Engineering
42. Namajunas, A., Pyragas, K., Tamasevicius, A.: An electronic analog of the Mackey-Glass system. Phys. Lett. A **201**, 42–46 (1995)
43. Buscarino, A., Fortuna, L., Frasca, M., Sciuto, G.: Design of time-delay chaotic electronic circuits. IEEE Trans. Circuits Syst. I Regular Papers **58**, 1888–1896 (2011)
44. Liao, X., Guo, S., Li, C.: Stability and bifurcation analysis in tri-neuron model with time delay. Nonlinear Dyn. **49**, 319–345 (2007)
45. Pei, L., Wang, Q., Shi, H.: Bifurcation dynamics of the modified physiological model of artificial pancreas with insulin secretion delay. Nonlinear Dyn. **63**, 417–427 (2011)
46. Yongzhen, P., Shuping, L., Changguo, L.: Effect of delay on a predator-prey model with parasitic infection. Nonlinear Dyn. **63**, 311–321 (2011)
47. Nagatani, T.: Chaos and dynamical transition of a single vehicle induced by traffic light and speedup. Phys. A **348**, 561–571 (2005)
48. Peil, M., Jacquot, M., Chembo, Y., Larger, L., Erneux, T.: Routes to chaos and multiple time scale dynamics in broadband bandpass nonlinear delay electro-optic oscillators. Phys. Rev. E **79**, 026208 (2009)
49. Safonov, L.A., Tomer, E., Strygin, V., Ashkenazy, Y., Havlin, S.: Multifractal chaotic attractors in a system of delay-differential equations modeling road traffic. Chaos **12**, 1006–1014 (2002)
50. Wang, X., Yu, H., Zhong, S., Agarwal, R.: Analysis of mathematics and dynamics in a food web system with impulsive perturbations and distributed time delay. Appl. Math. Model. **34**, 3850–3863 (2010)
51. Pyragas, K.: Continuous control of chaos by self-controlling feedback. Phys. Lett. A **170**, 421–428 (1992)
52. Sun, C., Lin, Y., Han, M.: Stability and Hopf bifurcation for an epidemic disease model with delay. Chaos, Solitons Fractals **30**, 204–216 (2006)
53. Ponomarenko, V., Prokhorov, M., Karavaev, A., Kulminskiy, D.: An experimental digital communication scheme based on chaotic time-delay system. Nonlinear Dyn. **74**, 1013–1020 (2013)
54. Tang, Y., Wang, Z., Fang, J.A.: Image encryption using chaotic coupled map lattices with time-varying delays. Commun. Nonlin. Sci. Numer. Simul. **15**, 2456–2468 (2010)
55. Kwon, O., Park, J., Lee, S.: Secure communication based on chaotic synchronization via interval time varying delay feedback control. Nonlinear Dyn. **63**, 239–252 (2011)
56. Ponomarenko, V., Karavaev, A., Glukhovskaya, E., Prokhorov, M.: Hidden data transmission based on time delayed feedback system with switched delay time. Tech. Phys. Lett. **38**, 51–54 (2012)
57. Prokhorov, M.D., Ponomarenko, V.I.: Encryption and decryption of information in chaotic communication systems governed by delay-differential equations. Chaos, Solitons Fractals **63**, 871–877 (2008)

Projective Synchronization Scheme Based on Fuzzy Controller for Uncertain Multivariable Chaotic Systems

A. Boulkroune, A. Bouzeriba and S. Hamel

Abstract In this chapter, a projective synchronization problem of master–slave chaotic systems is investigated. More specifically, a fuzzy adaptive controller is designed to achieve a projective synchronization of uncertain multivariable chaotic systems. The adaptive fuzzy systems are used to approximate the unknown nonlinear functions. A decomposition property of the control gain matrix is used in the controller design and the stability analysis. A Lyapunov approach is employed to derive the parameter adaptation laws and prove the boundedness of all signals of the closed-loop system as well as the exponential convergence of the synchronization errors to an adjustable region. Numerical simulations are performed to verify the effectiveness of the proposed synchronization system.

Keywords Projective synchronization · Fuzzy adaptive control · Multivariable chaotic systems

1 Introduction

Chaotic systems are commonly used in system engineering because of their attractive features, such as: a noise-like waveform, a broadband spectrum, an extreme sensitivity to initial conditions as well as parameter variations and an unpredictable behavior [6, 7, 10, 17]. Of particular interest, a remarkable research activity has been devoted to the chaos synchronization since the pioneer contributions [17, 33]. The rationale behind this particular interest is the potential applications of chaos synchronization in information processing, secure communications, chemical reactions, power convertors, laser systems, pattern recognition,

A. Boulkroune (✉) · A. Bouzeriba · S. Hamel
LAJ Laboratory, University of Jijel, BP. 98, Ouled-Aissa, 18000 Jijel, Algeria
e-mail: boulkroune2002@yahoo.fr

S. Hamel
e-mail: bouzeriba.amel@yahoo.fr

A.T. Azar and S. Vaidyanathan (eds.), *Chaos Modeling and Control Systems Design*,
Studies in Computational Intelligence 581, DOI 10.1007/978-3-319-13132-0_5

ecological systems and biological systems, and so on [17]. The primary configuration of chaos synchronization consists of two chaotic systems: a drive system (a master system) and a response system (slave system). Note that the master and slave systems can be identical (with different initial conditions) or quite different. The drive system drives the response system via coupling signals so that the drive system and the response system synchronize each other's behavior. Several types of synchronization have been already used in the available applications, namely the complete synchronization [14, 16, 42], the phase synchronization [34, 39], the lag synchronization [15], the generalized synchronization [30, 31], the generalized projective synchronization [26–28], and so on.

Many control methods have also been applied for achieving an appropriate synchronization of a particular class of chaotic master-slave systems (i.e. chaotic master-slave systems with a simple input) such as: sliding mode control [22, 32, 45, 51], backstepping control [44], adaptive control [25, 40, 41, 49], active control [5] and (non-adaptive) fuzzy control [20, 21, 23]. However, all these works suffer from the following limitations: (1) These synchronization schemes are presented for a typical or special class of chaotic systems. Note that the extension of these fundamental results to multivariable uncertain chaotic systems is not a trivial task. (2) These works have not addressed the problem of dynamic disturbances. Note that, in the presence of the latter, these synchronization systems may fail. (3) The model of the master-slave systems are assumed to be partially known or known. To solve the problem of uncertainties, the adaptive fuzzy control systems have been incorporated in the synchronization schemes [19, 24, 29, 36–38, 46, 47].

Fuzzy adaptive controller is defined as an fuzzy logic system equipped with an adaptation mechanism. Moreover, it is constructed from a collect of fuzzy IF-THEN rules using fuzzy logic principles, and the adaptation mechanism associated can adjust online the free parameters of the fuzzy systems. Like the conventional adaptive control, the adaptive fuzzy control can be conceptually classed into 3 categories: direct adaptive control, indirect adaptive control and hybrid (direct and indirect) adaptive control. In the direct adaptive fuzzy control schemes, the fuzzy systems can directly approximate the so-called unknown optimal controller. Hence, linguistic fuzzy control rules can be directly incorporated into the controller. But, in the indirect adaptive fuzzy control schemes, the fuzzy systems are employed to approximate online the model of the plant. Thereafter, fuzzy IF-THEN rules describing the plant can be directly incorporated into the indirect adaptive fuzzy controller. Based on the universal approximation feature [43], adaptive fuzzy control systems [19, 24, 29, 36–38, 46, 47] have been developed for a particular class of chaotic uncertain systems. The stability of the underlying control systems has been investigated using a Lyapunov approach. The robustness issues with respect to the fuzzy approximation error and the unavoidable disturbances have been enhanced by appropriately modifying these available adaptive fuzzy controllers. The corner stone of such a modification consists in a robust compensator, which is conceived using a sliding mode control design [19, 29, 36, 37], an $H\infty$ based robust control design [24, 46] and a variable structure control design [38, 47]. The key modeling assumptions in these above fuzzy adaptive control schemes are:

(1) The systems considered are characterized by inputs appearing linearly in the system equation, that is, the systems considered are affine-in-control. (2) These chaotic systems are not assumed to be subject to dynamic disturbances depending on the system states. To overcome these problems, an adaptive fuzzy backstepping controller for a simple class of multivariable non-affine chaotic systems has been recently developed in [48]. However, the fundamental results of this paper have not been derived rigorously in mathematics, because the virtual control input is not derivable. Hence, the contribution of this paper is questionable.

In this chapter, we aim at addressing the projective synchronization problem of a class of multivariable nonaffine chaotic systems subject to dynamic disturbances using a suitable fuzzy adaptive control approach. The latter is designed to perform a practical projective synchronization of the master-slave systems. The main difficulties are how to deal with unknown nonlinear functions, nonaffine multivariable control, and the combined effect of the unknown non-linear dynamic disturbances, fuzzy approximation errors together with the higher-order terms (HOT) issued from the use of the Taylor series expansion (the principle difficulty lies in the fact that these HOT depend explicitly on control inputs). In this chapter, these difficulties can be, respectively, solved by fuzzy approximation, the Taylor series expansion and robust dynamic compensation. A Lyapunov approach is adopted to carry out the parameter adaptation design, the convergence and the stability analysis involved in the proposed synchronization system. Compared to works in [19, 24, 29, 36–38, 46–48], the main contributions of this chapter lie in the following:

1. A practical projective synchronization scheme based on fuzzy adaptive controller is proposed for uncertain perturbed multivariable non-affine chaotic systems.
2. A dynamic robust adaptive control term is designed to compensate for the combined effect of the fuzzy approximation error, the dynamic disturbances together with the higher order terms (HOT) issued from the use of the Taylor series expansion.
3. The model of these non-affine chaotic systems is assumed to be completely unknown, except its relative degree.

2 Problem Statement, Preliminaries and Fuzzy Logic Systems

2.1 Problem Statement and Preliminaries

As mentioned in the introduction, the main motivation of this paper consists in investigating a projective synchronization system of master-slave chaotic multivariable systems. The practical projective synchronization between the master and slave systems can be achieved by designing an adequate fuzzy adaptive control system, as shown in Fig. 1.

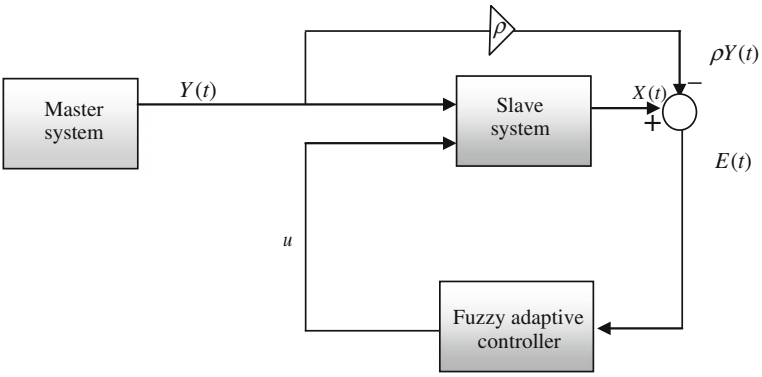

Fig. 1 The proposed synchronization scheme

Consider the following class of uncertain chaotic master systems:

$$Y^{(r)} = H_1(Y) \tag{1}$$

with $Y^{(r)} = \left[y_1^{(r_1)}, \ldots, y_p^{(r_p)}\right] \in R^p$, and $Y = [Y_1^T, \ldots, Y_p^T]^T \in R^r$ is the overall state vector of the master system which is assumed to be measureable, where $Y_i = [y_i, \ldots, y_i^{(r_i-1)}]^T \in R^{r_i}$, $\forall i = 1, \ldots, p$ and $r = r_1 + \cdots + r_p$. And $H_1(Y) = [h_{11}(Y), \ldots, h_{1p}(Y)] \in R^p$ is a vector of smooth unknown nonlinear functions.

The uncertain chaotic MIMO slave system affected by matched unknown perturbations can be given as:

$$X^{(r)} = H_2(X, u) + P(t, X) \tag{2}$$

where $X^{(r)} = \left[x_1^{(r_1)}, \ldots, x_p^{(r_p)}\right] \in R^p$, and $X = [X_1^T, \ldots, X_p^T]^T \in R^r$, with $X_i = [x_i, \ldots, x_i^{(r_i-1)}]^T \in R^{r_i}$ for $i = 1, \ldots, p$, is the overall state vector of the slave system which is assumed to be available for measurement. $r = r_1 + \cdots + r_p$ is the total relative degree, $H_2(X, u) = [h_{21}(X, u), \ldots, h_{2p}(X, u)] \in R^p$ is a vector of smooth unknown nonlinear functions. $u = [u_1, \ldots, u_P]^T \in R^p$ is the control input vector and $P(t, X) = [P_1(t, X), \ldots, P_p(t, X)] \in R^p$ denotes the unknown external disturbance vector.

Assumption 1 The matrix $G(X) = \partial H_2(X, u)/\partial u$ is with non-zero leading principal minors and their signs are assumed to be known.

Remark 1 Assumption 1 ensures that the matrix $G(X)$ is always regular. This assumption can be seen as a controllability condition and is not restrictive as it is satisfied by many physical systems: e.g. robotic systems and chaotic systems.

Remark 2 The systems (1) and (2) represent a relatively large class of uncertain MIMO chaotic systems: e.g. gyro systems, unified chaotic systems and the centrifugal flywheel governor. They are of higher practical significance.

Our objective consists in designing continuous adaptive control laws u_i (for all $i = 1,\ldots,p$) which achieve a practical projective synchronization between the master system (1) and the slave system (2), while all the signals in the derived closed-loop system remain bounded despite uncertainties and dynamic external disturbances. To quantify this objective, the synchronization errors are defined as follows:

$$\begin{aligned} e_1 &= x_1 - \rho y_1 \\ &\vdots \\ e_P &= x_P - \rho y_P \end{aligned} \tag{3}$$

where ρ is a nonzero constant, and is a scaling factor defining a proportional relation between the synchronized systems. Hence, complete synchronizations and anti-synchronizations are the special cases of projective synchronization when the scaling factor $\rho = +1$ and $\rho = -1$, respectively.

Let us define also the filtered tracking error as

$$S = [S_1, \ldots, S_p]^T \tag{4}$$

with

$$S_i = [\frac{d}{dt} + \lambda_i]^{r_i - 1} e_{i,} \quad \text{for } \lambda_i > 0, \ \forall\, i = 1, \ldots, p. \tag{5}$$

Remark 3 It has been shown in [50] that the definition (5) has the following important features:

1. $S_i = 0$ defines a time-varying hyperplan in R^{r_i} on which the synchronization error converges to zero asymptotically.
2. if $e_i(0) = 0$ and $|S_i(t)| < C_i, \forall t \geq 0$ with constant $C_i > 0$, then $e_i(t) \in \Omega_{ci}, \forall t \geq 0$ with:

$$\Omega_{ci} = \left\{ e_i \middle| |e_{ij}| \leq 2^{r_i - 1} \lambda_i^{j - r_i} C_i, \quad j = 1, 2, \ldots, r_i \right\}, \quad \text{with } \lambda_i > 0 \tag{6}$$

where $e_{ij} = e_i^{(j-1)}$, $j = 1, 2, \ldots, r_i$.

3. if $e_i(0) \neq 0$ and $|S_i(t)| < C_i$, then $e_i(t)$ converges to Ω_{ci}, with a time-constant $(r_i - 1)/\lambda_i$.

The dynamics of S_i are described by:

$$\dot{S}_i = [0\ \lambda_i^{r_i-1}\ (r_i-1)\lambda_i^{r_i-2} \ldots (r_i-1)\lambda_i]E_i + e_i^{(r_i)} = C_{ri}^T E_i + e_i^{(r_i)}, \quad \text{for } i = 1, \ldots, p \tag{7}$$

where $C_{ri}^T = [0\ \lambda_i^{r_i-1}\ (r_i-1)\lambda_i^{r_i-2} \ldots\ (r_i-1)\lambda_i]$ and $E_i = [e_i\, \dot{e}_i \ldots e_i^{(r_i-2)}\, e_i^{(r_i-1)}]^T$.

Now, let's note $C_r^T = diag\left[C_{r1}^T, C_{r2}^T, \ldots, C_{rp}^T\right]_{(p\times r)}, E = \left[E_1^T E_2^T \ldots E_p^T\right]_{(r\times 1)}^T$.

Thus, we can write the dynamics of S as follows:

$$\dot{S} = C_r^T E - \rho H_1(Y) + H_2(X,u) + P(t,X) \tag{8}$$

Now, to facilitate control system design, we transform the non-affine system (8) into an affine system in control by performing a Taylor series expansion around an unknown optimal control $u = u^*(X)$ as follows:

$$H_2(X,u) = F(X) + G(X)u + HOT(X,u) \tag{9}$$

with

$$F(X) = \left[F_1(X), \ldots, F_p(X)\right]^T = H_2(X,u^*(X)) - [\partial H_2(X,u)/\partial u]_{u=u^*(X)} u^*(X),$$
$$G(X) = \left[g_{ij}(X)\right] = [\partial H_2(X,u)/\partial u]_{u=u^*(X)}$$

where $HOT(X,u)$ is the higher order terms (HOT) of the expansion, and $u = u^*(X)$ is an unknown smooth function minimizing the HOT.

The following important lemma will be exploited in the controller design and stability analysis [9, 12, 13, 18]:

Lemma 1 *Any real matrix $G(X) \in R^{p\times p}$ with non-zero leading principal minors can be decomposed as follows:*

$$G(X) = G_s(X)DT(X) \tag{10}$$

where $G_s(X) \in R^{p\times p}$ is a symmetric positive-definite matrix, $D \in R^{p\times p}$ is a diagonal matrix with +1 or −1 on the diagonal, and $T(X) \in R^{p\times p}$ is a unity upper triangular matrix. The diagonal elements of D are nothing else than the ratios of the signs of the leading principal minors of $G(X)$.

2.2 Dynamics of the Filtered Synchronization Errors

Using the matrix decomposition (10) and the expression (9), the dynamics (8) can be rewritten as follows:

$$\dot{S} = C_r^T E - \rho H_1(Y) + F(X) + G_s(X)DT(X)u + \Lambda(t, X, u) \tag{11}$$

where $\Lambda(t, X, u) = P(t, X) + HOT(X, u)$.

Assumption 2 The matrix $G(X)$ is of class C^1 and satisfies the following property:

$$\frac{\partial g_{ij}(X)}{\partial x_i^{(r_i-1)}} = 0, \quad \forall\, i = 1, \ldots, p \text{ and } j = 1, \ldots p$$

Remark 4 The required property on the partial derivatives of the control gain matrix ensures that the time derivative of $G_s^{-1}(X)$ depends only on the state vector X, i.e. it ensures that $\frac{dG_s^{-1}(X)}{dt}$ does not depend on the system inputs [12, 13].

Equation (11) can be rewritten as

$$G_1(X)\dot{S} = G_1(X)\left[C_r^T E - \rho H_1(Y) + F(X)\right] + DT(X)u + G_1(X)\Lambda(t, X, u) \tag{12}$$

where $G_1(X) = G_s^{-1}(X)$.

We can write (12) as follows:

$$\begin{aligned} G_2(X)\left[D^{-1}\dot{S}\right] = {} & D^{-1}G_1(X)\left[C_r^T E - \rho H_1(Y) + F(X)\right] + T(X)u \\ & + D^{-1}G_1(X)\Lambda(t, X, u) \end{aligned} \tag{13}$$

where $G_2(X) = D^{-1}G_1(X)D$.

Due to special form of D and $G_1(X)$, the matrix $G_2(X)$ preserve the nice properties of the original matrix $G_1(X)$ or $G_s(X)$. Indeed, one can easily show that $G_2(X)$ is also positive-definite and symmetric. This property is of fundamental interest when investigating the control system and the stability.

We denote

$$F_1(X, Y) = D^{-1}G_1(X)[C_r^T E - \rho H_1(Y) + F(X)], \tag{14}$$

And by posing $\bar{S} = \left[\bar{S}_1, \ldots, \bar{S}_p\right]^T = D^{-1}S$ and $R(t, X, u) = D^{-1}G_1(X)\Lambda(t, X, u)$, Eq. (13) becomes

$$\begin{aligned} \frac{1}{2}\dot{G}_2(X)\bar{S} + G_2(X)\dot{\bar{S}} &= \frac{1}{2}\dot{G}_2(X)\bar{S} + F_1(X, Y) + \left(-I_p + T(X)\right)u + u + R(t, X, u) \\ &= \alpha(z) + u + R(t, X, u) \end{aligned} \tag{15}$$

with

$$\alpha(z) = [\alpha_1(z_1), \ldots, \alpha_p(z_p)]^T = \frac{1}{2}\dot{G}_2(X)\bar{S} + F_1(X, Y) + (-I_p + T(X))u \tag{16}$$

where $z = [z_1^T, z_2^T, \ldots, z_p^T]^T$. By examining the expressions of $\alpha(z)$, the vectors z_i can be determined as follows:

$$\begin{aligned} z_1 &= \left[X^T, u_2, \ldots, u_p\right]^T \\ z_2 &= \left[X^T, u_3, \ldots, u_p\right]^T \\ &\vdots \\ z_{P-1} &= \left[X^T, u_p\right]^T \\ z_P &= X \end{aligned} \tag{17}$$

It is clear from the property of the matrix of $-I_p + T(X)$, that z_1 depends on control inputs $u_2, \ldots, u_p$, z_2 depends on $u_3, \ldots, u_p$, and so on. In fact, the structure of the nonlinearities $\alpha(z)$ is known under the name "upper triangular control structure". Recall that this useful structure allows for algebraic loop free sequential synthesis of control signals u_i, $\forall i = 1, 2, \ldots, p$.

Define the operating compact sets as follows:

$$\begin{aligned} &\Omega_{z_i} = \left\{[X^T, u_{i+1}, \ldots, u_p]^T \backslash X \in \Omega_X \subset R^r, Y \in \Omega_Y\right\}, \quad i = 1, \ldots, p-1, \\ &\Omega_{z_p} = \{X \backslash X \in \Omega_X \subset R^r\}. \end{aligned} \tag{18}$$

Remark 5 Since the nonlinear functions $\alpha(z)$ and $R(t, X, u)$ are unknown nonlinear functions, moreover $R(t, X, u)$ depends explicitly on the input u, the design of a control system to practically stabilize the dynamics (15) is not easy. Thereafter, to overcome such problems, we will use

- an adaptive fuzzy system to approximate the unknown nonlinear functions $\alpha(z)$,
- a dynamic adaptive robust control to dynamically compensate for the effect of the uncertain nonlinearity $R(t, X, u)$.

2.3 Description of the Fuzzy Logic System

The basic configuration of a fuzzy logic system consists of a fuzzifier, some fuzzy IF–THEN rules, a fuzzy inference engine and a defuzzifier, as shown in Fig. 2. The fuzzy inference engine uses the fuzzy IF–THEN rules to perform a mapping from

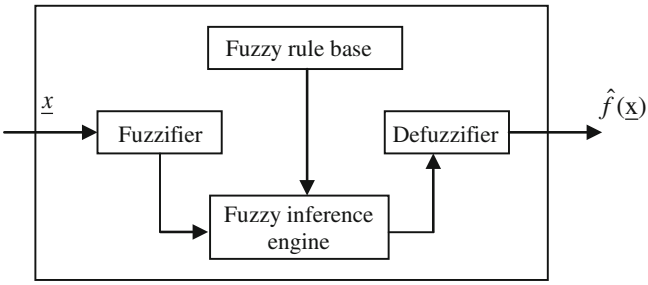

Fig. 2 Basic configuration of a fuzzy logic system

an input vector $\underline{x}^T = [x_1, x_2, \ldots, x_n] \in R^n$ to an output $\hat{f} \in R$. The ith fuzzy rule is written as

$$R^{(i)}: \textit{if } x_1 \textit{ is } A_1^i \textit{ and } \ldots \textit{and } x_n \textit{ is } A_n^i \textit{ then } \hat{f} \textit{ is } f^i \tag{19}$$

where $A_1^i, A_2^i, \ldots$ and A_n^i are fuzzy sets and f^i is the fuzzy singleton for the output in the ith rule. By using the singleton fuzzifier, product inference, and center-average defuzzifier, the output of the fuzzy system can be expressed as follows:

$$\hat{f}(\underline{x}) = \frac{\sum_{i=1}^{m} f^i (\prod_{j=1}^{n} \mu_{A_j^i}(x_j))}{\sum_{i=1}^{m} (\prod_{j=1}^{n} \mu_{A_j^i}(x_j))} = \theta^T \psi(\underline{x}) \tag{20}$$

where $\mu_{A_j^i}(x_j)$ is the degree of membership of x_j to A_j^i, m is the number of fuzzy rules, $\theta^T = [f^1, f^2, \ldots, f^m]$ is the adjustable parameter vector (composed of consequent parameters), and $\psi^T = [\psi^1 \psi^2 \ldots \psi^m]$ with

$$\psi^i(\underline{x}) = \frac{(\Pi_{j=1}^{n} \mu_{A_j^i}(x_j))}{\sum_{i=1}^{m} (\prod_{j=1}^{n} \mu_{A_j^i}(x_j))} \tag{21}$$

being the fuzzy basis function (FBF). Throughout the paper, it is assumed that the FBFs are selected so that there is always at least one active rule [43], i.e. $\sum_{i=1}^{m} (\prod_{j=1}^{n} \mu_{A_j^i}(x_j)) > 0$.

Note that the fuzzy system (20) is widely applied in modeling and control of nonlinear systems because it has been proven by Wang [43] that this fuzzy system can approximate an arbitrary nonlinear smooth function $f(\underline{x})$ defined on a compact operating space to a given accuracy. Of particular importance, it is assumed that the FBFs, $\psi(\underline{x})$, are properly specified beforehand by designer. But, the consequent parameters θ are determined by appropriate adaptation algorithms (which will be designed later).

3 Design of Fuzzy Adaptive Controller

In the sequel, we need the following mild assumption to facilitate the design of the controller and the stability analysis:

Assumption 3 There exists an unknown continuous positive function $\bar{\alpha}_i(z_i)$ such that:

$$\left|\alpha_i(z_i)\right| \leq \bar{\alpha}_i(z_i), \quad \forall z_i \in \Omega_{z_i} \text{ for } i = 1, \ldots, p \tag{22}$$

The unknown nonlinear function $\bar{\alpha}_i(z_i)$ can be approximated, on the compact set Ω_{z_i}, by the linearly parameterized fuzzy systems (20) as follows:

$$\hat{\bar{\alpha}}_i(z_i, \theta_i) = \theta_i^T \psi_i(z_i), \text{ with } \quad i = 1, \ldots, p \tag{23}$$

where $\psi_i(z_i)$ is the FBF vector, which is fixed a priori by the designer, and θ_i is the adjustable parameter vector of the fuzzy system.

Let us define

$$\theta_i^* = \arg\min_{\theta_i} \left[\sup_{z_i \in \Omega_{z_i}} \left| \bar{\alpha}_i(z_i) - \hat{\bar{\alpha}}_i(z_i, \theta_i) \right| \right] \tag{24}$$

as the optimal value of θ_i which is mainly introduced for analysis purposes as its value is not needed when implementing the controller.

Define

$$\tilde{\theta}_i = \theta_i - \theta_i^*, \quad \text{and } \varepsilon_i(z_i) = \bar{\alpha}_i(z_i) - \hat{\bar{\alpha}}_i(z_i, \theta_i^*) = \bar{\alpha}_i(z_i) - \theta_i^{*T} \psi_i(z_i) \tag{25}$$

as the parameter estimation error and the fuzzy approximation error, respectively.

As in the fuzzy control literature [2–4, 8, 11, 43], one assumes that the used fuzzy systems do not violate the universal approximation property on the compact set Ω_{z_i}, which is assumed large enough so that the input vector of those fuzzy systems remains in Ω_{z_i} under the closed-loop control system. It is hence reasonable to assume that the fuzzy approximation error is bounded for all $z_i \in \Omega_{z_i}$, i.e. $|\varepsilon_i(z_i)| \leq \bar{\varepsilon}_i$, $\forall z_i \in \Omega_{z_i}$, where $\bar{\varepsilon}_i$ is an unknown constant.

Now, let us denote

$$\begin{aligned} \hat{\bar{\alpha}}(z, \theta) &= [\hat{\bar{\alpha}}_1(z_1, \theta_1), \ldots, \hat{\bar{\alpha}}_p(z_p, \theta_p)]^T = [\theta_1^T \psi_1(z_1), \ldots, \theta_p^T \psi_p(z_p)]^T, \\ \varepsilon(z) &= [\varepsilon_1(z_1), \ldots, \varepsilon_p(z_p)]^T, \\ \bar{\varepsilon} &= [\bar{\varepsilon}_1, \ldots, \bar{\varepsilon}_p]^T. \end{aligned}$$

From the above analysis, we have

$$\begin{aligned}\hat{\bar{\alpha}}(z,\theta)-\bar{\alpha}(z) &= \hat{\bar{\alpha}}(z,\theta)-\hat{\bar{\alpha}}(z,\theta^*)+\hat{\bar{\alpha}}(z,\theta^*)-\bar{\alpha}(z),\\ &= \hat{\bar{\alpha}}(z,\theta)-\hat{\bar{\alpha}}(z,\theta^*)-\varepsilon(z),\\ &= \tilde{\theta}^T\psi(z)-\varepsilon(z)\end{aligned} \tag{26}$$

where $\tilde{\theta}^T\psi(z)=[\tilde{\theta}_1^T\psi_1(z_1),\ldots,\tilde{\theta}_p^T\psi_p(z_p)]^T$ and $\tilde{\theta}_i=\theta_i-\theta_i^*$, for $i=1,\ldots,p$.

For the master-slave system (1)–(2), we can consider the following fuzzy adaptive controller:

$$u=-M_t\theta^T\psi(z)-K\bar{S}-u_r \tag{27}$$

with

$$M_t=Diag[\mathrm{Tan}h\left(\bar{S}_1\theta_1^T\psi_1(z_1)/\varepsilon_{t0}\right),\ldots,\mathrm{Tan}h\left(\bar{S}_p\theta_p^T\psi_p\left(z_p\right)/\varepsilon_{t0}\right)] \tag{28}$$

where $\theta^T\psi(z)=[\theta_1^T\psi_1(z_1),\ldots,\theta_p^T\psi_p\left(z_p\right)]^T$, $K=Diag[k_1,\ldots,k_p]$, where $k_i>0$ for $i=1,\ldots,p$, are free positive design constants. $\varepsilon_{t0}>0$ is a small design constant, and θ_i is the online estimate of θ_i^*. $u_r=[u_{r1},\ldots,u_{rp}]^T$ is an adaptive control term added in order to dynamically compensate for the effect of the uncertain term $R(t,X,u)$. It will be designed later.

The system (15) can be rewritten as follows:

$$\frac{d}{dt}\left[\frac{1}{2}\bar{S}^TG_2(X)\bar{S}\right]=\bar{S}^T\alpha(z)+\bar{S}^Tu+\bar{S}^TR(t,X,u) \tag{29}$$

Using the expression (26) and control law (27), (29) becomes:

$$\begin{aligned}\frac{d}{dt}\left[\frac{1}{2}\bar{S}^TG_2(X)\bar{S}\right] &\le \left|\bar{S}^T\right|\theta^{*T}\psi(z)+\left|\bar{S}^T\right||\varepsilon(z)|-\bar{S}^TK\bar{S}-\bar{S}^Tu_r\\ &\quad+\left|\bar{S}^T\right||R(t,X,u)|-\sum_{i=1}^{p}\bar{S}_i\theta_i^T\psi_i(z_i)\mathrm{Tan}h\left(\bar{S}_i\theta_i^T\psi_i(z_i)/\varepsilon_{t0}\right).\\ &\le -\left|\bar{S}^T\right|\tilde{\theta}^T\psi(z)+\sum_{i=1}^{p}|\bar{S}_i|\theta_i^T\psi_i(z_i)-\bar{S}^TK\bar{S}-\bar{S}^Tu_r\\ &\quad+\left|\bar{S}^T\right|R_1(t,X,u)-\sum_{i=1}^{p}\bar{S}_i\theta_i^T\psi_i(z_i)\mathrm{Tan}h\left(\bar{S}_i\theta_i^T\psi_i(z_i)/\varepsilon_{t0}\right)\end{aligned} \tag{30}$$

with $\theta^{*T}\psi(z) = [\theta_1^{*T}\psi_1(z_1), \ldots, \theta_p^{*T}\psi_p(z_p)]^T$ and

$$R_1(t, X, u) = |\varepsilon(z)| + |R(t, X, u)| \tag{31}$$

Assumption 4 We assume that:

$$|R_1(t, X, u)| \leq \kappa^* \bar{R}(t, X, u) \tag{32}$$

with $\bar{R}(t, X, u) = 1 + \|X\| + \|u\|$, where $\kappa^* = [\kappa_1^*, \ldots, \kappa_p^*]^T$ is an unknown constant vector.

Using Assumption (4), we get

$$\begin{aligned}\frac{d}{dt}\left[\frac{1}{2}\bar{S}^T G_2(X)\bar{S}\right] \leq & \sum_{i=1}^{p}\left|\bar{S}_i\theta_i^T\psi_i(z_i)\right| \\ & - \sum_{i=1}^{p}\bar{S}_i\theta_i^T\psi_i(z_i)\mathrm{Tan}h\left(\bar{S}_i\theta_i^T\psi_i(z_i)/\varepsilon_{t0}\right) - \sum_{i=1}^{p}\tilde{\theta}_i^T\psi_i(z_i)|\bar{S}_i| \\ & - \sum_{i=1}^{p}k_i\bar{S}_i^2 - \sum_{i=1}^{p}\bar{S}_i u_{r_i} + \bar{R}(t, X, u)\sum_{i=1}^{p}\kappa_i^*|\bar{S}_i|\end{aligned} \tag{33}$$

Because $\dot{\theta}_i$ is designed such as $\theta_i(t) > 0, \forall t > 0$, thus $\left|\bar{S}_i\theta_i^T\psi_i(z_i)\right| = |\bar{S}_i|\theta_i^T\psi_i(z_i)$. Using the following nice property with regard to function tan$h$ [35]:

$$0 \leq |s| - s\ \mathrm{Tan}h(s/\varepsilon_0) \leq \bar{\varepsilon}_0 = 0.2785\ \varepsilon_0, \tag{34}$$

we can obtain the following inequality

$$\begin{aligned}\frac{d}{dt}\left[\frac{1}{2}\bar{S}^T G_2(X)\bar{S}\right] \leq & -\sum_{i=1}^{p}|\bar{S}_i|\tilde{\theta}_i^T\psi_i(z_i) + p\bar{\varepsilon}_{t0} - \sum_{i=1}^{p}k_i\bar{S}_i^2 - \sum_{i=1}^{p}\bar{S}_i u_{r_i} \\ & + \bar{R}(t, X, u)\sum_{i=1}^{p}\kappa_i^*|\bar{S}_i|\end{aligned} \tag{35}$$

The dynamic robust control term u_{r_i} is given by:

$$\dot{u}_{r_i} = -\gamma_{r_i}u_{r_i} + \gamma_{r_i}\left[\bar{S}_i - \frac{sign(u_{r_i})}{|u_{r_i}| + \delta_i^2}\bar{R}(t, X, u)\kappa_i|\bar{S}_i|\right], \quad for\ i = 1, \ldots, p \tag{36}$$

with

$$\dot{\delta}_i = -\gamma_{\delta_i} \frac{\delta_i}{|u_{r_i}| + \delta_i^2} \bar{R}(t, X, u) \kappa_i |\bar{S}_i| - \gamma_{\delta_i} \sigma_{\delta_i} \delta_i, \ \delta_i(0) > 0, \quad for \ i = 1, \ldots, p \quad (37)$$

where κ_i is the estimate of κ_i^* and γ_{r_i}, γ_{δ_i} and σ_{δ_i} are strictly positive design parameters.

Adaptation laws associated to the proposed controller (27) are given by:

$$\dot{\theta}_i = -\sigma_{\theta_i} \gamma_{\theta_i} \theta_i + \gamma_{\theta_i} |\bar{S}_i| \psi_i(z_i), \quad \text{with } \theta_{ij}(0) > 0 \quad (38)$$

$$\dot{\kappa}_i = -\gamma_{\kappa_i} \sigma_{\kappa_i} \kappa_i + \gamma_{k_i} \bar{R}(t, X, u) |\bar{S}_i|, \quad \text{with } \kappa_i(0) > 0 \quad (39)$$

where $\gamma_{\theta i}, \gamma_{\kappa i}$, $\sigma_{\theta i}$ and σ_{κ_i} are strictly positive design parameters.

Remark 6 Owing to special structure of the nonlinearities $\alpha(z)$ [defined by Eqs. (16) and (17)] and dynamical feature of the control robust compensator u_r [given by Eqs. (36) and (37)], the proposed adaptive controller is free of the algebraic loop.

Our main result is summarized by the following theorem.

Theorem 1 *Consider the master-slave system* (1) *and* (2) *with Assumptions 1–4. Then, the control law defined by* (27) *and* (36)–(39) *can guarantee the following properties:*

- *All the variables in* the closed-loop system *are semi-globally uniformly ultimately bounded (SUUB).*
- *The filtered synchronization errors S_i exponentially converge to an adjustable domain defined as:*

$$\Omega_{S_i} = \left\{ S_i | \, |S_i| \leq \left(\frac{2}{\sigma_{g2}} \frac{\pi}{\mu} \right)^{1/2} \right\} \quad (40)$$

where π, μ and σ_{g2} will be defined later.

Proof of Theorem 1 Let us consider the following Lyapunov function candidate:

$$V = \frac{1}{2} \bar{S}^T G_2(X) \bar{S} + \sum_{i=1}^{p} \frac{1}{2\gamma_{\theta_i}} \tilde{\theta}_i^T \tilde{\theta}_i + \sum_{i=1}^{p} \frac{1}{2\gamma_{\kappa_i}} \tilde{\kappa}_i^2 + \sum_{i=1}^{p} \frac{1}{2\gamma_{\delta_i}} \delta_i^2 + \sum_{i=1}^{p} \frac{1}{2\gamma_{r_i}} u_{r_i}^2 \quad (41)$$

with $\tilde{\kappa}_i = \kappa_i - \kappa_i^*$, for $i = 1, \ldots, p$.

The time derivative of V can be given by

$$\dot{V} = \bar{S}^T G_2(X)\dot{\bar{S}} + \frac{1}{2}\bar{S}^T \dot{G}_2(X)\bar{S} + \sum_{i=1}^{p}\frac{1}{\gamma_{\theta_i}}\tilde{\theta}_i^T\dot{\theta}_i + \sum_{i=1}^{p}\frac{1}{\gamma_{\kappa_i}}\tilde{\kappa}_i\dot{\kappa}_i + \sum_{i=1}^{p}\frac{1}{\gamma_{\delta_i}}\delta_i\dot{\delta}_i + \sum_{i=1}^{p}\frac{1}{\gamma_{r_i}}u_{r_i}\dot{u}_{r_i} \tag{42}$$

Using (35)–(39), (42) can be written as follows

$$\dot{V} \leq -\sum_{i=1}^{P} k_i\bar{S}_i^2 - \sum_{i=1}^{p}\sigma_{\theta_i}\tilde{\theta}_i^T\theta_i - \sum_{i=1}^{p}\sigma_{\kappa_i}\tilde{\kappa}_i\kappa_i - \sum_{i=1}^{p}u_{r_i}^2 - \sum_{i=1}^{p}\sigma_{\delta_i}\delta_i^2 + p\bar{\varepsilon}_{t0} \tag{43}$$

We can easily verify that

$$-\sigma_{\theta_i}\tilde{\theta}_i^T\theta_i \leq -\frac{\sigma_{\theta_i}}{2}\|\tilde{\theta}_i\|^2 + \frac{\sigma_{\theta_i}}{2}\left\|\theta_i^*\right\|^2 \tag{44}$$

$$-\sigma_{\kappa_i}\tilde{\kappa}_i\kappa_i \leq -\frac{\sigma_{\kappa_i}}{2}|\tilde{\kappa}_i|^2 + \frac{\sigma_{\kappa_i}}{2}\left|\kappa_i^*\right|^2 \tag{45}$$

Using the previous inequalities, (43) becomes

$$\dot{V} \leq -\sum_{i=1}^{p} k_i\bar{S}_i^2 - \sum_{i=1}^{p}u_{r_i}^2 - \sum_{i=1}^{p}\sigma_{\delta_i}\delta_i^2 - \sum_{i=1}^{p}\frac{\sigma_{\theta_i}}{2}\|\tilde{\theta}_i\|^2 - \sum_{i=1}^{p}\frac{\sigma_{\kappa_i}}{2}|\tilde{\kappa}_i|^2 + \sum_{i=1}^{p}\frac{\sigma_{\theta_i}}{2}\left\|\theta_i^*\right\|^2 + \sum_{i=1}^{p}\frac{\sigma_{\kappa_i}}{2}\left|\kappa_i^*\right|^2 + p\bar{\varepsilon}_{t0} \tag{46}$$

Taking into account the nice property of $G_s(X)$, there exists a positive scalar σ_{gs} such that $G_s(X) \geq \sigma_{gs}I_p$ and henceforth

$$\bar{S}^T G_2(x)\bar{S} = S^T G_1(x)S \leq \frac{1}{\sigma_{gs}}\|\bar{S}\|^2 \tag{47}$$

And using (46) and (47) yields

$$\dot{V} \leq -\mu V + \pi \tag{48}$$

where $\pi = \sum_{i=1}^{p}\frac{\sigma_{\theta_i}}{2}\|\theta_i^*\|^2 + \sum_{i=1}^{p}\frac{\sigma_{\kappa_i}}{2}\left|\kappa_i^*\right|^2 + p\bar{\varepsilon}_{t0}$, and

$$\mu = \min\left\{\min_i\left\{2\sigma_{gs}k_i\right\}, \min_i\left\{2\gamma_{r_i}\right\}, \min_i\left\{2\gamma_{\delta_i}\sigma_{\delta_i}\right\}, \min_i\left\{\gamma_{\theta_i}\sigma_{\theta_i}\right\}, \min_i\left\{\gamma_{\kappa_i}\sigma_{\kappa_i}\right\}\right\}$$

Multiplying (48) by $e^{\mu t}$ yields

$$\frac{d}{dt}(Ve^{\mu t}) \leq \pi e^{\mu t} \tag{49}$$

And integrating (49) over [0,t], one has

$$0 \leq V(t) \leq \frac{\pi}{\mu} + \left(V(0) - \frac{\pi}{\mu}\right)e^{-\mu t} \tag{50}$$

Therefore, all signals in the closed-loop control system (i.e. $S_i, u_{r_i}, \delta_i, \tilde{\theta}_i, \theta_i, E_i, X_i, \kappa_i$ and $\tilde{\kappa}_i$) are SUUB. And hence the input u_i is bounded. Since $G_2(x)$ is symmetric and positive definite, i.e. *there exists an unknown positive constant* σ_{g2} *such that:* $G_2(x) \geq \sigma_{g2} I_p$, it follows from (50) and (41) that

$$|\bar{S}_i| = |S_i| \leq \left(\frac{2}{\sigma_{g2}}\left(\frac{\pi}{\mu} + \left(V(0) - \frac{\pi}{\mu}\right)e^{-\mu t}\right)\right)^{1/2} \tag{51}$$

Then, the solution of S_i exponentially converges to a bounded adjustable domain defined as follows $\Omega_{S_i} = \left\{S_i \middle| |S_i| \leq \left(\frac{2}{\sigma_{g2}}\frac{\pi}{\mu}\right)^{1/2}\right\}$. This ends the proof of the theorem. □

Remark 7 According to the definition of μ and π, it can be seen that the size of μ depends on the controller design parameters $\gamma_{\theta_i}, \gamma_{\kappa_i}, \sigma_{\theta_i}, \sigma_{\kappa_i}, \gamma_{r_i}, \gamma_{\delta_i}, \sigma_{\delta_i}$ and k_{1i} (which must be chosen strictly positive) and the size of π depends on the design parameters $\varepsilon_{t0}, \sigma_{\theta_i}$ and σ_{κ_i}. It is clear that if we increase the parameters ($\gamma_{\theta_i}, \gamma_{\kappa_i}, \gamma_{r_i}, \gamma_{\delta_i}$ and k_{1i}) and decrease ($\varepsilon_{t0}, \sigma_{\theta_i}$ and σ_{κ_i}), it will help to reduce the term $\left(2\pi/\sigma_{g2}\mu\right)^{1/2}$. This implies that the filtered synchronization errors S_i and the synchronization error E_i can be made arbitrary small by appropriately choosing those design parameters.

4 Simulation Results

In this section, we will verify the effectiveness of the proposed scheme for the synchronization of two non-autonomous centrifugal flywheel governors (CFG). It has been shown that the CFG system exhibits very rich and complex dynamics such as chaos. For more details about the dynamics of this systems, one can refer to [1].

The master system:

$$\begin{cases} \dot{y}_1 = y_2 \\ \dot{y}_2 = \left(E_m + n_m^2 y_3^2\right) \sin y_1 \cos y_1 - \left(E_m + g_m/l_m\right) \sin y_1 - b_m y_2 \\ \dot{y}_3 = \dfrac{(\alpha_m \cos y_1 - F_m)}{I_m} - a_m \sin \omega_m t \end{cases} \tag{52}$$

The slave system:

$$\begin{cases} \dot{x}_1 = x_2 \\ \dot{x}_1 = (E_s + n_s^2 x_3^2) \sin x_1 \cos x_1 - (E_s + g_s/l_s) \sin x_1 - b_s x_2 + 0.01 u_1^3 + u_1 + P_1(t, X) \\ \dot{x}_1 = \dfrac{(\alpha_s \cos x_1 - F_s)}{I_s} - a_s \sin \omega_s t + 0.1 \sin(u_2) + u_2 + P_2(t, X) \end{cases} \tag{53}$$

where $X = [x_1, x_2, x_3]^T$ is the state vector of this slave system. The parameters of the master system are selected as follows: $n_m = 4$, $l_m = 0.5, a_m = 0.4$, $\omega_m = 2$, $E_m = 0.5, b_m = 0.3, I_m = 0.5, \alpha_m = 0.432$, $F_m = 0.35$ and $g_m = 9.8$. But, those of the slave system are chosen as: $n_s = 3$, $l_s = 1.5, a_s = 0.8$, $\omega_s = 1$, $E_s = 0.3, b_s = 0.4, I_s = 1.2, \alpha_s = 0.611$, $F_s = 0.3$and $g_s = 9.8$.

The external dynamic disturbances are selected as follows: $P_1(t, X) = -0.2 \sin(5x_2) + 0.25 \cos(2t)$, and $P_2(t, X) = -0.35 \sin(6x_3) + 0.25 \cos(3t)$. Our objective consists in allowing the slave states x_1, x_2, and x_3 to respectively track the corresponding master states y_1, y_2 and y_3.

The initial conditions of the master and slave systems are randomly selected as: $Y(0) = [0.3, 0.2, 0.1]^T$ and $X(0) = [0.01, 0.02, 0.03]^T$. The first fuzzy system $\theta_1^T \psi_1(z_1)$ has the vector $[X^T, u_2]^T$ as input, but the second fuzzy system $\theta_2^T \psi_2(z_2)$ has the state vector X^T as input. The fuzzy membership functions are defined for each variable x_j, for j = 1,2,3 as follows:

$$\mu_{A_j^1}(x_j) = \frac{1}{1 + \exp\left(3(x_j + 0.25)\right)},$$

$$\mu_{A_j^2}(x_j) = \exp\left(-\frac{1}{2}\left(\frac{x_j^2}{0.6}\right)\right)$$

$$\mu_{A_j^3}(x_j) = \frac{1}{1 + \exp\left(-3(x_j - 0.25)\right)}$$

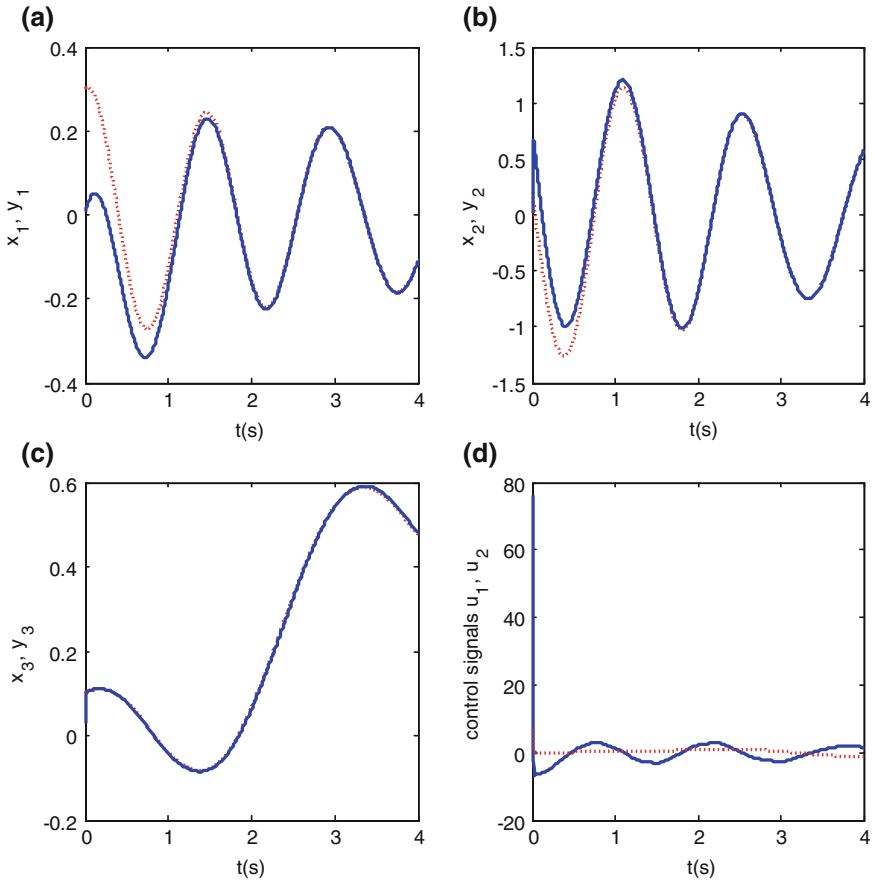

Fig. 3 Complete synchronization: **a** x_1 (*solid line*) and y_1 (*dotted line*). **b** x_2 (*solid line*) and y_2 (*dotted line*). **c** x_3 (*solid line*) and y_3 (*dotted line*). **d** u_1 (*solid line*) and u_2 (*dotted line*)

But for the input variable u_2, they are defined as follows:

$$\mu_{A^1}(u_2) = \frac{1}{1+\exp(u_2+4)},$$
$$\mu_{A^2}(u_2) = \exp\left(-\frac{1}{2}\left(\frac{u_2^2}{0.6}\right)\right)$$
$$\mu_{A^3}(u_2) = \frac{1}{1+\exp(-(u_2-4))}$$

The design parameters are chosen as follows: $\lambda_1 = \lambda_2 = 2, k_1 = k_2 = 5, \varepsilon_{t0} = 1$, $\gamma_{\theta_1} = \gamma_{\theta_2} = 300$, $\sigma_{\theta_1} = \sigma_{\theta_2} = 10^{-3}$, $\gamma_{r_1} = \gamma_{r_2} = 500$, $\sigma_{\delta_1} = \sigma_{\delta_2} = 10^{-7}$, $\gamma_{\delta_1} = \gamma_{\delta_2} = 10^{-5}$, $\gamma_{\kappa_1} = \gamma_{\kappa_2} = 500$, $\sigma_{\kappa_1} = \sigma_{\kappa_2} = 2 \times 10^{-3}$.

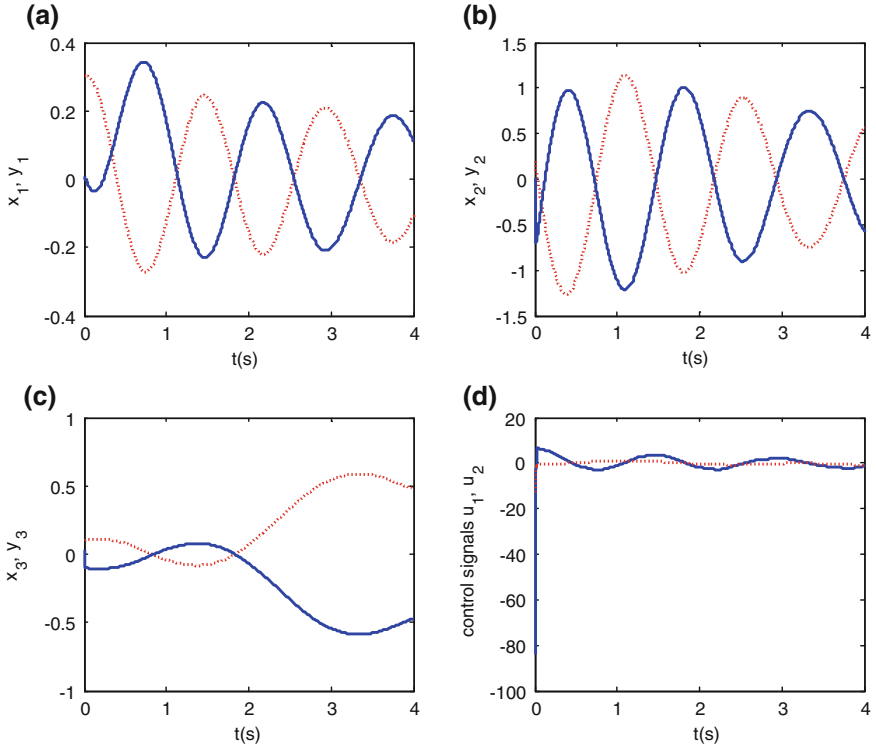

Fig. 4 Anti-phase synchronization: **a** x_1 (*solid line*) and y_1 (*dotted line*). **b** x_2 (*solid line*) and y_2 (*dotted line*). **c** x_3 (*solid line*) and y_3 (*dotted line*). **d** u_1 (*solid line*) and u_2 (*dotted line*)

The initial conditions of the adaptive laws are selected as follows: $u_{r_1}(0) = u_{r_2}(0) = 0, \delta_1(0) = \delta_2(0) = 1.5, \kappa_1(0) = \kappa_2(0) = 10$, and $\theta_{1j}(0) = \theta_{2j}(0) = 0.01$.

Figure 3a–c and d respectively show the simulation results of a complete synchronization (i.e. with a scaling factor $\rho = 1$) and the corresponding control signals. From these figures, it is obvious to see that the drive system practically synchronizes with the response system and the control signals are bounded and smooth. Figure 4a–c and d respectively illustrate the simulation results of an anti-phase synchronization (i.e. with a scaling factor $\rho = -1$) and the associated control signals. From these figures, we can see that all signals are bounded and the control signal is smooth and admissible.

In summary, we can conclude that all simulation results verify our theoretical findings and demonstrate the effectiveness of the proposed synchronization scheme.

5 Conclusion

In this chapter, we have presented a practical projective synchronization system for a class of uncertain multivariable chaotic systems. The projective synchronization has been achieved by a fuzzy adaptive controller. A decomposition property of the control gain matrix has been exploited in the design of this control system. Of fundamental interest, a suitable Lyapunov based analysis has been carried out to conclude the stability as well as the synchronization error convergence. Simulation results have been given to emphasize the effectiveness of the proposed synchronization system.

References

1. Aghababa, M.P.: Design of an adaptive finite-time controller for synchronization of two identical/different non-autonomous chaotic flywheel governor systems. Chin. Phys. B **21**, 030502 (2012)
2. Azar, A.T.: Adaptive Neuro-Fuzzy Systems. In: Azar, A.T. (ed.) Fuzzy Systems. IN- TECH, Vienna, Austria (2010)
3. Azar, A.T.: Fuzzy Systems. IN-TECH, Vienna, Austria (2010)
4. Azar, A.T.: Overview of type-2 fuzzy logic systems. Int. J. Fuzzy Syst. Appl. **2**, 1–28 (2012)
5. Botmart, T., Niamsup, P.: Adaptive control and synchronization of the perturbed Chua's circuit system. Math. Comput. Simul. **75**, 37–55 (2007)
6. Boulkroune, A., Chekireb, H., Tadjine, M., Bouatmane, S.: Observer-based adaptive feedback controller of a class of chaotic systems. Int. J. Bifurcat. Chaos **16**, 189–196 (2006)
7. Boulkroune, A., Chekireb, H., Tadjine, M., Bouatmane, S.: An adaptive feedback controller with observer for linearizable Chaotic systems. Control Intell. Syst. **35**, 1–8 (2007)
8. Boulkroune, A., Tadjine, M., M'saad, M., Farza, M.: How to design a fuzzy adaptive control based on observers for uncertain affine nonlinear systems. Fuzzy Sets Syst. **159**, 926–948 (2008)
9. Boulkroune, A., M'saad, M., Chekireb, H.: Design of a fuzzy adaptive controller for MIMO nonlinear time-delay systems with unknown actuator nonlinearities and unknown control direction. Inf. Sci. **180**, 5041–5059 (2010)
10. Boulkroune, A., M'saad, M.: A fuzzy adaptive variable-structure control scheme for uncertain chaotic MIMO systems with sector nonlinearities and dead-zones. Expert Syst. Appl. **38**, 4744–14750 (2011)
11. Boulkroune, A., M'saad, M.: On the design of observer-based fuzzy adaptive controller for nonlinear systems with unknown control gain sign. Fuzzy Sets Syst. **201**, 71–85 (2012)
12. Boulkroune, A., M'saad, M., Farza, M.: Adaptive fuzzy tracking control for a class of MIMO nonaffine uncertain systems. Neurocomputing **93**, 48–55 (2012)
13. Boulkroune, A., M'saad, M., Farza, M.: Fuzzy approximation-based indirect adaptive controller for multi-input multi-output non-affine systems with unknown control direction. IET Control Theor. Appl. **17**, 2619–2629 (2012)
14. Bowonga, S., Kakmenib, M., Koinac, R.: Chaos synchronization and duration time of a class of uncertain systems. Math. Comput. Simul. **71**, 212–228 (2006)
15. Cailian, C., Gang, F., Xinping, G.: An adaptive lag-synchronization method for time-delay chaotic systems. In: Proceedings of the American Control Conference, pp. 4277–4282 (2005)
16. Carroll, T.L., Heagy, J.F., Pecora, L.M.: Transforming signals with chaotic synchronization. Phys. Rev. E **54**, 4676–4680 (1996)

17. Chen, G., Dong, X.: From Chaos to Order: Methodologies, Perspectives and Applications. World-Scientific, Singapore (1998)
18. Chen, J., Behal, A., Dawson, D.M.: Adaptive output feedback control for a class of MIMO nonlinear systems. In Proceedings of the American Control Conference, Minneapolis, MN, pp. 5300–5305 (2006)
19. Chen, C., Chen, H.: Robust adaptive neural-fuzzy-network control for the synchronization of uncertain chaotic systems. Nonlinear Anal. Real World Appl. **10**, 1466–1479 (2009)
20. Chen, D., Zhang, R., Sprott, J.C., Ma, X.: Synchronization between integer-order chaotic systems and a class of fractional-order chaotic system based on fuzzy sliding mode control. Nonlinear Dyn. **70**, 1549–1561 (2012)
21. Chen, D., Zhao, W., Sprott, J.C., Ma, X.: Application of Takagi–Sugeno fuzzy model to a class of chaotic synchronization and anti-synchronization. Nonlinear Dyn. **73**, 1495–1505 (2013)
22. Dadras, S., Momeni, H.R.: Adaptive sliding mode control of chaotic dynamical systems with application to synchronization. Math. Comput. Simul. **80**, 2245–2257 (2010)
23. Farivar, F., Shoorehdeli, M.A.: Fault tolerant synchronization of chaotic heavy symmetric gyroscope systems versus external disturbances via Lyapunov rule-based fuzzy control. ISA Trans. **51**, 50–64 (2012)
24. Hwang, E., Hyun, C., Kim, E., Park, M.: Fuzzy model based adaptive synchronization of uncertain chaotic systems: robust tracking control approach. Phys. Lett. A **373**, 1935–1939 (2009)
25. Jia, Q.: Adaptive control and synchronization of a New Hyperchaotic system with unknown parameters. Phys. Lett. A **362**, 424–429 (2007)
26. Jianping, Y., Changpin, L.: Generalized projective synchronization of a unified chaotic system. Chaos, Solitons Fractals **26**, 1119–1124 (2005)
27. Li, Z., Xu, D.: A secure communication scheme using projective Chaos Synchronization. Chaos, Solitons & Fractals **22**, 477–484 (2004)
28. Li, G.: Projective synchronization of chaotic system using Backstepping control. Chaos, Solitons & Fractals **29**, 490–598 (2006)
29. Lin, T.-C., Lee, T.-Y., Balas, V.E.: Adaptive fuzzy sliding mode control for synchronization of uncertain fractional order chaotic systems. Chaos, Solitons & Fractals **44**, 791–801 (2011)
30. Morgul, O., Solak, E.: Observer-based synchronization of chaotic systems. Phys. Rev. E **54**, 4803–4811 (1996)
31. Morgul, O., Solak, E.: On the synchronization of chaotic systems by using state observers. Int. J. Bifurcat. Chaos **7**, 1307–1322 (1997)
32. Noroozi, N., Roopaei, M., Karimaghaee, P., Safavi, A.: Simple adaptive variable structure control for unknown chaotic systems. Commun. Nonlinear Sci. Numer. Simul. **15**, 707–727 (2010)
33. Pecora, L.M., Carroll, T.L.: Synchronization in chaotic systems. Phys. Rev. Lett. **64**, 821–824 (1990)
34. Pikovsky, A.S., Rosenblum, M.G., Osipov, G.V., Kurths, J.: Phase synchronization of chaotic oscillators by external driving. Physica D **104**, 219–238 (1997)
35. Polycarpou, M.M., Ioannou, P.A.: A robust adaptive nonlinear control design. Automatica **32**, 423–427 (1996)
36. Poursamad, A., Davaie-Markazi, A.H.: Robust adaptive fuzzy control of unknown chaotic systems. Appl. Soft Comput. **9**, 970–976 (2009)
37. Roopaei, M., Jahromi, M.Z.: Synchronization of two different chaotic systems using novel adaptive fuzzy sliding mode control. Chaos **18**, 033133 (2008)
38. Roopaei, M.,·Jahromi, M.Z., Ranjbar-Sahraei, B., Lin T.-C.: Synchronization of two different chaotic systems using novel adaptive interval type-2 fuzzy sliding mode control. Nonlinear Dyn. **66**, 667–680 (2011)
39. Rosenblum, M.G., Pikovsky, A.S., Kurths, J.: Phase synchronization of chaotic oscillators. Phys. Rev. Lett. **76**, 1804–1807 (1996)

40. Salarieh, H., Alasty, A.: Adaptive control of chaotic systems with stochastic time varying unknown parameters. Chaos, Solitons & Fractals **38**, 168–177 (2008)
41. Shi, X.R., Wang, Z.L.: Adaptive added-order anti-synchronization of chaotic systems with fully unknown parameters. Appl. Math. Comput. **215**, 1711–1717 (2009)
42. Sun, J., Zhang, Y.: impulsive control and synchronization of chua's oscillators. Math. Comput. Simul. **66**, 499–508 (2004)
43. Wang, L.X.: Adaptive fuzzy systems and control: design and stability analysis. Prentice-Hall, Englewood Cliffs, NJ (1994)
44. Wang, J., Gao, J., Ma, X.: Synchronization control of cross-strict feedback hyperchaotic system based on cross active backstepping design. Phys. Lett. A **369**, 452–457 (2007)
45. Wang, H., Han, Z., Xie, Q., Zhang, W.: Sliding mode control for chaotic systems based on LMI. Commun. Nonlinear Sci. Numer. Simul. **14**, 1410–1417 (2009)
46. Wang, J., Chen, L., Deng, B.: Synchronization of Ghostbusters neuron in external electrical stimulation via H∞ variable universe fuzzy adaptive control. Chaos, Solitons & Fractals **39**, 2076–2085 (2009)
47. Wang, Y., Fan, Y., Wang, Q., Zhang, Y.: Adaptive fuzzy synchronization for a class of chaotic systems with unknown nonlinearities and disturbances. Nonlinear Dyn. **69**, 1167–1176 (2012)
48. Wen, J., Jiang, C.-S.: Adaptive fuzzy control for a class of chaotic systems with nonaffine inputs. Commun. Nonlinear Sci. Numer. Simul. **16**, 475–492 (2011)
49. Yau, H.T., Yan, J.J.: Chaos synchronization of different chaotic systems subjected to input nonlinearity. Appl. Math. Comput. **197**, 775–788 (2008)
50. Zhang, T., Zhang, S.S., Hang, C.C.: Stable adaptive control for a class of nonlinear systems using a modified Lyapunov function. IEEE Trans. Autom. Control **45**, 129–132 (2000)
51. Zribi, M., Smaoui, N., Salim, H.: Synchronization of the unified chaotic systems using a sliding mode controller. Chaos, Solitons & Fractals **42**, 3197–3209 (2009)

Part II
Control Systems and Applications

Deadbeat Control for Multivariable Discrete Time Systems with Time Varying Delays

Ahmad Taher Azar and Fernando E. Serrano

Abstract In this chapter a novel approach for the deadbeat control of multivariable discrete time systems is proposed. Deadbeat control is a well known technique that has been implemented during the last decades in SISO and MIMO discrete time systems due to the ripple free characteristics and the designer selection of the output response. Deadbeat control consist in establishing the minimum number of steps in which the desired output response must be reached, this objective is achieved by placing the appropriate number of closed loop poles at the origin and cancelling the transmission zeros of the system. On the other side, constant time delays in the state or the input of the system is a phenomena found in many continuous and discrete time systems, produced by delays in the communication channels or other kind of sources, yielding unwanted effects on the systems like performance deterioration, or instability on the system. Even when the analysis and design of appropriate controllers with constant time delays in the state or the input has been studied by several researchers applying several control techniques such as state and output feedback, in this chapter the development of a deadbeat control for discrete time systems with constant delays is explained as a preamble of the main topic of this chapter related to the deadbeat control of discrete time systems with time varying delays. This first approach is derived by implementing a state feedback controller, and in opposition of the implementation of traditional techniques such as optimal control where a stable gain is obtained by solving the required Riccati equations, the deadbeat controller is obtained by selecting the appropriate gain matrix solving the necessary LMI's placing the required number of poles at the origin and eliminating the finite transmission zeros of the system in order to obtain the required deadbeat characteristics in

A.T. Azar (✉)
Faculty of Computers and Information, Scientific Research Group in Egypt (SRGE), Benha University, Banha, Egypt
e-mail: ahmad_t_azar@ieee.org
URL: http://www.egyptscience.net

F.E. Serrano
Department of Electrical Engineering, Florida International University, 10555 West Flagler St, Miami, FL 33174, USA
e-mail: fserr002@fiu.edu

A.T. Azar and S. Vaidyanathan (eds.), *Chaos Modeling and Control Systems Design*, Studies in Computational Intelligence 581, DOI 10.1007/978-3-319-13132-0_6

which the desired system response is reached in minimun time steps. After this overview, deadbeat controllers are designed considering the time varying delays, following a similar approach such as the constant time delay counterpart. In order to obtain an appropriate deadbeat controller, a state feedback controller gain is obtained by solving the required LMI's, placing the required poles in order to obtain the desired response cancelling the finite transmission zeros. The theoretical background is tested by several illustrative examples and finally the discussion and conclusions of this work are shown in the end of this chapter.

Keywords Deadbeat control · Time delay systems · Discrete time systems · MIMO systems

1 Introduction

In this chapter the derivation and design of deadbeat controllers for multivariable discrete time system is proposed in order to overcome with this problem when time varying delays are found in the states or the input of the system. Deadbeat control is an efficient control technique that has been implemented for decades in single input single output systems SISO and later the design of this controller has been transferred to multi input multi output MIMO systems. Deadbeat control consist in deriving a controller that makes the system variables to reach the steady state value in a minimum number of time steps, this objective is met by placing the right number of poles at the origin and cancelling the finite transmission zeros.

It can be found in literature that deadbeat control can be implemented in SISO systems. one common problem found when this kind of controllers are implemented is ripple, this phenomena occurs when some deviations take place in the error signal at different time steps [11] in order to solve this problem different deadbeat control strategies has been developed by several researcher for example selecting an equivalent deadbeat continuous time system that is equivalent to the discrete time counterpart for both output and input signal [11]. Another well known strategy for the deadbeat control of SISO system is implemented by optimal pole placement design where, as it is known, the proper selection of the closed loop poles of the system is achieved by selecting an appropriate deadbeat compensator [7]. Another approach for deadbeat compensation is shown in the stabilization of SISO system by output feedback in which the derivation of a suitable controller gain is done by implementing an appropriate control algorithm [6].

For the multi input multi output MIMO systems similar approaches to SISO systems has been derived in order to obtain the appropriate deadbeat control, some MIMO deadbeat control strategies are found in literature in which the implementation of state feedback or output feedback controllers are designed in order to set all the system parameters such as poles and transmission zeros in the right position obtaining ripple free deadbeat controllers for SISO discrete time systems

as explained in [19] where the effects of ripple are eliminating by avoiding the cancellation of the plant poles by the controller zeros.

In the case of multivariable discrete time system several deadbeat control strategies has been proposed in order to solve this problem either by output feedback or state feedback. Some of this strategies consist in deriving a suitable control law by placing the required poles at the origin and cancelling the transmission zeros. In the case of output feedback deadbeat controller several strategies but with different perspective are found in literature, for example, the derivation of a deadbeat control algorithm by the minimization of a quadratic cost function with cheap control, which means that there is no cost on the input where the main purpose is to drive the output of the system to the final value in a minimum number of time steps [16]. Another deadbeat output feedback control approach is shown in [20] where a similar deadbeat controller design as explained before where an optimal control approach is developed by the minimization of a cost function with no cost on the input (cheap control) and introducing a weighting matrix in the states in order to find a suitable control algorithm to stabilize the system in a minimum number of time steps. In [10] the deadbeat control problem is solved by the implementation of periodic output feedback then two deadbeat control problems are formulated in order to overcome with this problem. Even when output feedback is a common alternative for the solution of deadbeat control problems, a similar approach is found in literature for the solution of this problem implementing state feedback, this is obviously the main approach applicated by the control system community. Most of these works are based on optimal control by minimizing a cost functional as shown in [4, 5] and as explained in [14] the state feedback deadbeat controller is obtained by the solution of the Riccati equations. Another approach is explained in [9] where a minimal energy deadbeat control approach is implemented in order to stabilizes the system.

Even when deadbeat controllers has been implemented in SISO and MIMO systems with no time delay, in this chapter we consider this problem which is an important consideration to take into account because of delay is found in many physical systems, and this phenomena yields many unwanted effects that deteriorate the system response and they are a potential source of instability. In this chapter the deadbeat controller design of multivariable discrete time system with time varying delays in the states and the input of the system are explained in order to design suitable deadbeat controllers that overcome the effects yielded by time delays. Time varying delays are a more feasible representation of the real effects produced by this phenomena due to the variable characteristic of delays in physical systems. However in this chapter the design of deadbeat controller for multivariable discrete time systems with constant time delays are explained first as a preamble of the design of deadbeat controllers for multivariable time varying delay systems. This work is divided in the following sections; In Sect. 2 a short explanation of previous work related to the deadbeat control of discrete time multivariable system is shown, as a preamble of the main topic of this chapter about the design of deadbeat controllers for discrete time MIMO systems with time varying delays. In Sect. 3 the design of state feedback deadbeat controllers for discrete time MIMO systems with constant

time delay is developed and explained as a preamble of the main topic of this chapter. In Sect. 4 the design and derivations of state feedback deadbeat controllers for discrete time MIMO systems with time varying delays in the states is shown. In Sect. 5 then the analysis and design of state feedback deadbeat controllers for discrete time MIMO systems with time varying delays in the input is shown to stabilizes this kind of systems. Finally, in Sects. 6 and 7 the respective discussion and conclusions of this work are shown to analyze the results evinced in this chapter.

2 Previous Work

As explained in the previous section, there are different kinds of deadbeat control strategy for SISO and MIMO system, but previous works found in literature for time delay deadbeat control basically are very limited and has not been considered by the control systems community. Even when time delays are considered a source of performance deterioration and instability, this problem has not been treated before and the analysis, design and development of a suitable deadbeat controller for multivariable discrete time systems is necessary due to this physical phenomena produced by communication delays and other sources. Time varying delays are very common in many physical systems, and they can deteriorate the system performance and yield instability, the main problem arises because of this kind of phenomena are more complex than the constant time delay case, so an appropriate mathematical model must be derived taking in count the stability characteristics of the system designing a suitable control strategy, that in this case, a deadbeat controller for MIMO discrete time systems with time varying delays must be designed.

As explained in the previous section, deadbeat control consists in designing an appropriate controller which leads the system variables to reach the steady state values in a minimum number of time steps. This strategy is implemented in the SISO and MIMO cases producing the expected results. In the case of SISO systems, some effective control strategies has been developed in the past that yield the desired system response. In [6] the problem of deadbeat control is solved for the SISO discrete time case, implementing an output feedback controller that is a simple and efficient approach to overcome with this problem. It must be considered that there is a vast amount of control strategies found in literature that deals with this control problem, for example, the implementation of linear quadratic regulators and optimization theory. Apart from this deadbeat control approach for SISO systems, another approach is proposed by [7] where a pole placement algorithm is designed to obtain a suitable deadbeat controller, the incorporation of one closed loop problem which incorporates interpolation constraints with the help of linear programming is proposed by these authors. In [11] a discrete time deadbeat controller for SISO systems is designed based in a continuous time deadbeat controller, considering the possibility of designing a ripple-free deadbeat controller; in this approach the main idea is to prove that a continuous time deadbeat controller is equivalent to the discrete time SISO counterpart, dealing with this control problem.

Another ripple—free deadbeat controller for SISO systems is implemented as shown in [19, 21] where this kind of controllers can be designed if and only if the systems poles and zeros are disjoint.

In the case of multivariable deadbeat controllers for discrete time systems the control strategies are based on output and state feedback, where these two approaches are usually solved by the minimization of an optimal control functional and then the gain matrices are obtained by the solution of the required Riccati equations. In [16], the deadbeat control problem is solved by minimizing an optimal control functional with cheap control (no constraints in the inputs) and the poles of the systems are placed in the origin. In [20] this problem is solved by output feedback in which a change of basis on the original discrete time system is implemented in order to place a specified number of poles at the origin and cancelling the finite transmission zeros. In [10], the solution of the deadbeat controller problem is solved by a periodic output feedback at the beginning of the period and then two deadbeat controller strategies are proposed to overcome this problem.

In the case of deadbeat control for multivariable discrete time systems with state feedback there are several works found in literature such as [3–5] where the deadbeat controller design is considered after a change of basis in order to stabilizes the system in a minimum number of time steps. Even when the works related to the deadbeat control of MIMO system with time delays found in literature are limited, previous works related to the stabilization of time delay systems is found by overcoming this problem solving the required LMI's. The control system design problem can be implemented by static output feedback or state feedback. In the case of constant time delays the derivation of a feasible controller is found in [18] where a simple and systematic method for systems with time delays are explained when this phenomena is found in the input of the system. In the case when time varying delays are present in the inputs or the states, some approaches are found such as the state or output feedback, in [8] where an output feedback controller synthesis is implemented by solving the required LMI's to find a suitable gain matrix. Another interesting approach can be found in [24] where the stabilization of discrete time fuzzy system is done by obtaining first an stability condition and then the required LMI's are obtained by implementing a Lyapunov-Krasovskii functional. Finally in [1, 22] the control of uncertain control systems with time delays and the robust stabilization of time delay system is explained where an LMI approach is implemented to solve a robust controller for time delay systems proposing the necessary Lyapunov-Krasovskii functional.

3 Deadbeat Control for Multivariable Systems with Constant Time Delays

In this section the design and development of a deadbeat controller for multivariable discrete time systems with constant time delays is explained as a preamble of the main topic of this book chapter related to the deadbeat control of multivariable

discrete time systems with time varying delays. Deadbeat control consist in designing a control system that stabilizes the system in a minimum number of time steps, so the main idea envinced in this section is to design an appropriate deadbeat controller that overcomes the time delay effects when this are present in the states. As it is well known time delays are a source of system performance deterioration and instability, so it is necessary to derive a suitable control strategy that deals with this effect in order to obtain a better performance and avoid instabilities on the system. The theoretical background for the design of deadbeat controllers for multivariable discrete time systems with constant time delays in the states, is obtained by designing an state feedback controller in order to place an specified number of poles at the origin and eliminate the transmission zeros of the system, keeping in mind that the system must be stabilized in minimum time steps. In this case some conditions are established in order to yield the robust stabilization of the system by solving the required LMI's [12, 13, 17] where the LMI's conditions are obtained by defining a Lyapunov functional by augmenting the state vector, so by making a change of basis on the system it is possible to design appropriate deadbeat controllers when delays are present in the states.

In this section the derivation of a state feedback controller is shown to proved that is possible to obtain a feasible gain matrix by solving the required LMI's instead of the optimal control approach found in literature [2] so establishing the required Lyapunov function it is possible to obtain the LMI's that are implemented to find the controller gain matrix by solving an optimization problem. The deadbeat controller synthesis is obtained by a Lyapunov approach that is more effective than the solution of a optimal control problem and the main advantage of this approach, is that the controller synthesis can be obtained by a H_∞ approach [15, 23] where a robust controller design can be done by selecting an appropriate gain that improves the disturbance rejection properties and unmodelled dynamics of the system. The derivation of the state feedback deadbeat controller for multivariable discrete time systems with constant time delays, consist in implementing a change of basis of the original system in order to obtain $(n - p)$ eigenvalues of the system at the origin where p are the finite transmission zeros of the system and n is the state dimension.

3.1 Deadbeat Control Design for Multivariable Discrete Time System with Constant Time Delay

The deadbeat controller design for multivariable control systems with constant time delays in the state consist in finding a stable state feedback matrix gain, this gain is found by implementing the required LMI's that results from establishing a Lyapunov functional to analyze and design a stable controller according to the Lyapunov stability theorem. The first step in the design of deadbeat controller for system with constant time delays is to established the minimum time steps in which the system is stabilized, this objective is reached by implementing a change of basis

in order to obtain $(n-p)$ eigenvalues at the origin where n is the state dimension and p is the number of stable transmission zeros of the system. Then the linear matrix inequalities LMI's are found by implementing a Lyapunov functional.

In order to design the deadbeat controller for multivariable discrete time systems, the following discrete time model with state delays must be considered:

$$\begin{aligned} x(k+1) &= Ax(k) + A_d x(k-d) + Bu(k) \\ y(k) &= Cx(k) \end{aligned} \tag{1}$$

where $x(k) \in \Re^n$ is the state vector, d is a nonnegative integer that represent the delays, $u(k) \in \Re^m$ is the input vector and $y(k) \in \Re^l$ is the measured output.

Definition 1 In order to design a stable state feedback deadbeat controller, system (1) must be controllable and observable.

Define the following state feedback control law that is implemented for the deadbeat control of multivariable discrete time systems.

$$u(k) = -K_{\star} x(k) \tag{2}$$

This control law is selected in order to obtain the deadbeat controller of the system, that is, stabilizing the system in a minimum number of time steps. This requirement is met by analyzing the steady state solution of the system where the initial condition of the system is transferred to the final value in a minimum number of time steps. The solution of the system is obtained recursively to obtain the deadbeat response of the system:

$$x(k) = (A - BK_{\star})^k x(0) + \sum_{i=0}^{k-1} A_d (A - BK_{\star})^{k-1-i} x(i-d) \tag{3}$$

where $x(0)$ is the initial condition of the system. Then the control law is defined to stabilizes the system by deadbeat, in order to drive the system to the desired final value.

$$y(k) = C((A - BK_{\star})^{\mu} x(0) + \sum_{i=0}^{k-1} A_d (A - BK_{\star})^{k-1-i} x(i-d)) \tag{4}$$

where μ is the minimum number of steps to reach the final value infinite time. This objective is achieved by selecting the appropriate value of μ in order that the $n-p$ eigenvalues of A be located at the origin and the rest are pick in order to coincide with the system's zeros [20], where n is the state dimension and p is the number of stable transmission zeros of the system.

In order to design the deadbeat controller it is necessary to apply a change of basis for the original systems, considering the following similarity transformation matrix:

$$T = [T_1 : T_2] \tag{5}$$

In order to design the deadbeat controller it is necessary to select $n - p$ linear independent vectors for the basis where n is the state dimension and p is the number of finite transmission zeros of the system. The following similarity transformation is implemented in order to make a change os basis:

$$\begin{aligned} x'(k+1) &= T^{-1}ATx'(k) + T^{-1}A_dTx'(k-d) + T^{-1}Bu(k) \\ y(k) &= CTx'(k) \end{aligned} \tag{6}$$

Then the resulting closed loop system implementing the state feedback control law is:

$$\begin{aligned} x'(k+1) &= (T^{-1}AT - T^{-1}BK_{\star})x'(k) + T^{-1}A_dTx'(k-d) \\ y(k) &= CTx'(k) \end{aligned} \tag{7}$$

and then for model reduction the following equivalent matrices are defined:

$$\begin{aligned} A_p &= T^{-1}AT \\ A_{pd} &= T^{-1}A_dT \\ B_p &= T^{-1}B \\ C_p &= CT \end{aligned} \tag{8}$$

Transforming [7] in:

$$\begin{aligned} x'(k+1) &= (A_p - B_pK_{\star})x'(k) + A_{pd}x'(k-d) \\ y(k) &= C_px'(k) \end{aligned} \tag{9}$$

Selecting C_p such as the system has transmission zeros at infinity.

In order to obtain the gain matrix $K_{\star}$ the following theorem must be considered in order to find this matrix by a LMI approach finding the required matrices to assured the closed loop system stability.

Theorem 1 *The closed loop stability of system* [9] *is assured if there exist positive definite matrices* $Q > 0$ *and* $P > 0$ *found by solving the following linear matrix inequality in order to solve for the gain matrix* $K_{\star}$

$$\begin{bmatrix} \Phi^T P\Phi - P + Q & \Phi PA_{pd} \\ A_{pd}^T P\Phi & A_{pd}^T PA_{pd} - Q \end{bmatrix} < 0 \tag{10}$$

where Φ is defined later.

Proof Consider the following Lyapunov-Krasovskii functional [2, 12, 13]:

$$V(x(k)) = x'^{T}(k)Px'(k) + \sum_{j=k-d}^{k-1} x'^{T}(j)Qx'(j) \tag{11}$$

□

Considering that $\Delta V(k) = V(k+1) - V(k)$, the first derivative of the Lyapunov functional is:

$$\begin{aligned}\Delta V(x(k)) = {} & x'^{T}(k)\Phi^{T}P\Phi x'(k) + x'^{T}(k)\Phi^{T}PA_{pd}x'(k-d) \\ & + x'^{T}(k-d)A_{pd}^{T}P\Phi x'(k) + x'^{T}(k-d)A_{pd}^{T}PA_{pd}x'(k-d) \\ & - x'^{T}(k)Px'(k) + x'^{T}(k)Qx'(k) - x'^{T}(k-d)Qx'(k-d)\end{aligned} \tag{12}$$

where $\Phi = A_p - B_pK_*$Then defining an augmented state vector as shown in (13):

$$\xi = \begin{bmatrix} x'(k) \\ x'(k-d) \end{bmatrix} \tag{13}$$

Then the following representation of $\Delta V(x(k))$ is:

$$\Delta V(x(k)) = \xi^{T}R\xi \tag{14}$$

So by solving the following LMI the resulting matrices P, Q and $K_{\star}$ are found [2]:

$$R = \begin{bmatrix} \Phi^{T}P\Phi - P + Q & \Phi PA_{pd} \\ A_{pd}^{T}P\Phi & A_{pd}^{T}PA_{pd} - Q \end{bmatrix} < 0 \tag{15}$$

After defining the conditions in order to find a stable deadbeat controller gain matrix, a deadbeat controller can be designed in order to meet all the system performance requirements according to the deadbeat specifications. In order to clarify the theoretical background of this section an illustrative example is done to analyze the performance of a numerical example.

3.2 Example 1

Consider the following multivariable discrete time system with constant time delays in the states.

$$\begin{aligned} x(k+1) &= \begin{bmatrix} -9 & 5 \\ 0 & 7 \end{bmatrix}x(k) + \begin{bmatrix} 3 & 9 \\ 3 & 0 \end{bmatrix}x(k-d) + \begin{bmatrix} 1 & 0 \\ 0 & 1 \end{bmatrix}u(k) \\ y(k) &= \begin{bmatrix} 1 & 0 \\ 0 & 1 \end{bmatrix}x(k) \end{aligned} \tag{16}$$

where $d = 1$ s and sampling period $T_s = 10$ s. Then the following matrices are found by solving the respective LMI expressed in (10) at different minimum time steps. For $\mu = 2$ the following transformation matrix is implemented:

$$T = \begin{bmatrix} 2 \times 10^{-5} & 0 \\ 0 & 10^{-8} \end{bmatrix} \tag{17}$$

obtaining

$$\begin{aligned} Q &= \begin{bmatrix} 4.9945 & 0 \\ 0 & 4.9945 \end{bmatrix} \times 10^{8} \\ P &= \begin{bmatrix} 0.4494 & 0.0000 \\ 0.0000 & 0.0002 \end{bmatrix} \times 10^{-4} \\ K_{\star} &= \begin{bmatrix} -0.4995 & 0 \\ 0 & -0.4995 \end{bmatrix} \times 10^{-4} \end{aligned} \tag{18}$$

For $\mu = 1$ the following transformation matrix is implemented:

$$T = \begin{bmatrix} 2 \times 10^{6} & 9 \times 10^{6} \\ 0 & 1 \times 10^{6} \end{bmatrix} \tag{19}$$

Obtaining:

$$\begin{aligned} Q &= \begin{bmatrix} 4.9978 & 0 \\ 0 & 4.9978 \end{bmatrix} \times 10^{8} \\ P &= \begin{bmatrix} 0.0023 & 0.0063 \\ 0.0063 & 0.0147 \end{bmatrix} \\ K_{\star} &= \begin{bmatrix} -0.4998 & 0 \\ 0 & -0.4998 \end{bmatrix} \times 10^{-4} \end{aligned} \tag{20}$$

For $\mu = 0$ The following transformation matrix is implemented:

$$T = \begin{bmatrix} 12 & 25 \\ 14 & 9 \end{bmatrix} \times 10^{6} \tag{21}$$

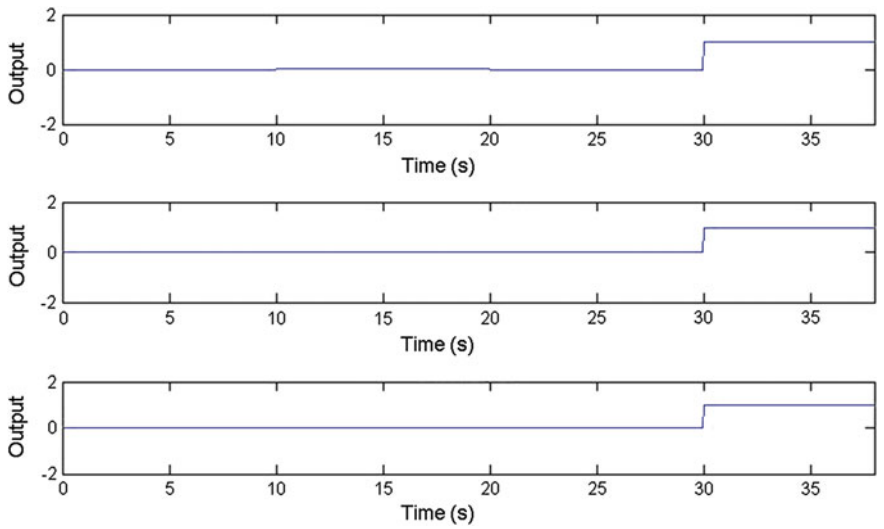

Fig. 1 System response for the variable x_1

Obtaining:

$$Q = \begin{bmatrix} 4.9944 & 0 \\ 0 & 4.9944 \end{bmatrix} \times 10^8$$
$$P = \begin{bmatrix} -0.2868 & -0.0388 \\ -0.0388 & 0.0570 \end{bmatrix} \tag{22}$$
$$K_{\star} = \begin{bmatrix} -0.4994 & 0 \\ 0 & -0.4994 \end{bmatrix} \times 10^{-4}$$

In Fig. 1 the systems response of the variable x_1 is depicted, for the three minimum time steps, $\mu = 0, 1, 2$, given for the design of deadbeat controller where as can be noticed the desired system response is reach with a minimum time according to the selection of the transformation matrix and the parameter μ. So the system objective are reached by a proper selection of the system poles and transmission zeros keeping the stability properties of the system.

In Fig. 2 the system response of the variable x_2 is depicted, showing that this system variable reaches the desired final value after a minimum number of time steps according to the parameter setting μ. The system variable x_2 follows a similar trajectory as the variable x_1, so the system is stabilizes as required by the deadbeat controller design. The variables x_1 and x_2 are required to follow a specified trajectory in a minimum time when a step reference signal change the setpoint to one in $t = 0$ s. As it is corroborated later the system variables reach the desired value from an specified initial conditions $[0, 0]^T$ to the desired final values as specified in (4).

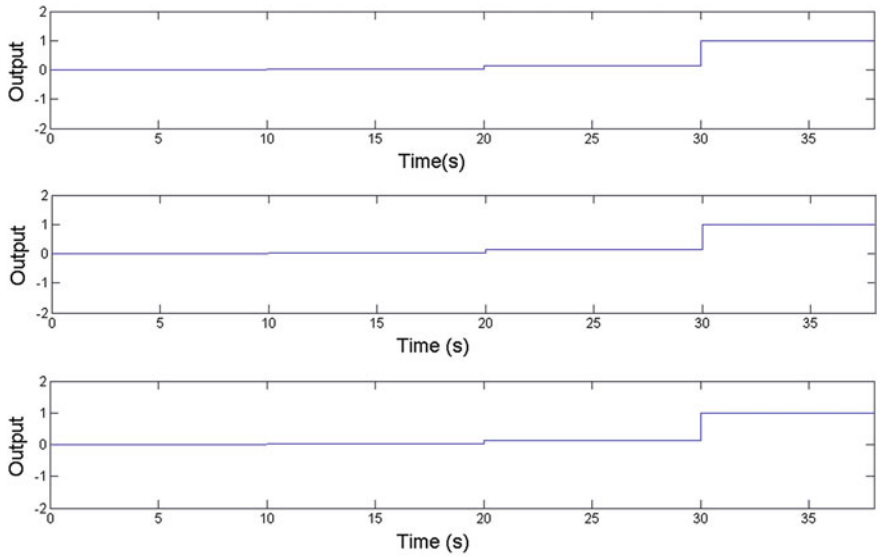

Fig. 2 System response for the variable x_2

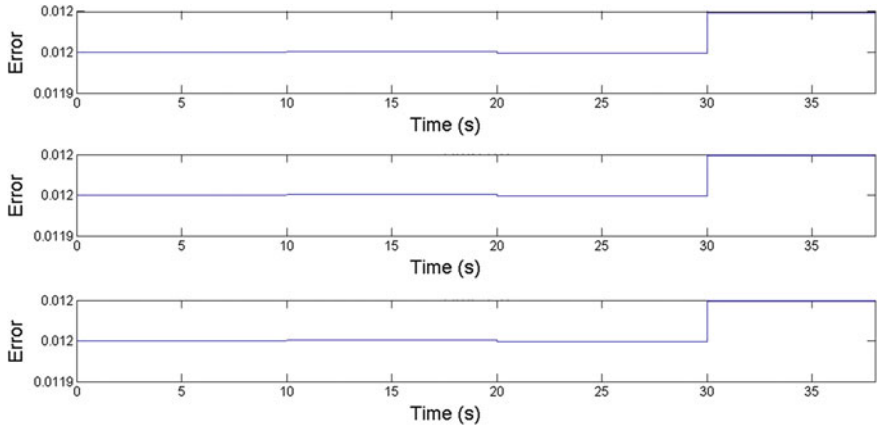

Fig. 3 System error for the variable x_1

In Fig. 3 the system error signal for the variable x_1 is shown where as it is corroborated the signal error is kept into the desired range due to the stabilization of the system variables. The gain matrix K_∞ found by solving the required LMI, minimize the errors between the reference signal and the output signal as long as possible because of the poles are placed in the required position to minimize the error due to a proper selection of the gain matrix.

In Fig. 4 the system error variable for x_2 is shown and as it is corroborated the error signal is kept into a small margin as expected, according to the design

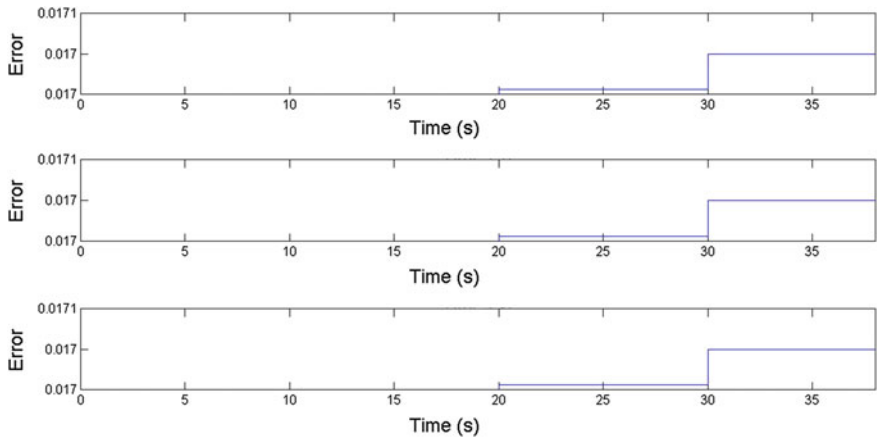

Fig. 4 System error for the variable x_2

procedure. The selection of an appropriate gain matrix $K_{\star}$ drive the system variables to the desired final value so the error margin is as small as possible because of the appropriate pole placement and transmission zeros allocation.

In this section the development and design of deadbeat controllers for multivariable discrete time systems with constant time delays is explained. It is proved that this kind of systems can be stabilized by a state feedback control law according to the stability properties of the system, established by a proper selection of a Lyapunov-Krasovskii functional in order to obtain the stability conditions of the system and establishing the linear matrix inequalities to find positive definite matrices that meet the stability conditions.

The deadbeat controller explained in this section is developed by designing an appropriate state feedback control law which drive the system states to the steady state values in a minimum number of time steps. This objective is accomplished by solving the resulting LMI obtained by a Lyapunov approach, as it is explained in the works of [15, 23] this deadbeat controller design can be done by solving a H_{∞} control problem to improve the closed loop system robustness and makes the system more reliable when external disturbances and unmodelled dynamics are present in the model.

The development of a deadbeat controller for multivariable discrete time systems with constant time delays is done as a preamble for the main topic of this chapter, related to the state feedback controller design of deadbeat controllers for multivariable discrete time systems with time varying delays. The theoretical background for constant time delay systems shown in this section are the basis for the design of deadbeat controller when time varying delays are present in the models. That is the main reason to begin with this topic to show the fundamentals of deadbeat control for time delay systems. Finally, the application of the theoretical background explained in this section is illustrated by a numerical example to analyze the system performance with different time steps parameters.

4 Deadbeat Control for Multivariable Systems with Time Varying Delays in the States

In this section the development and design of deadbeat controllers for multivariable systems with time varying delays in the state is shown. Time varying delays are common in many kinds of systems produced by communication delays and other kind of sources, this effect is the main origin of many unwanted effects such as performance deterioration and instability, therefore, time delay systems has increased the interest on this kind of problems in the control system community. Two kinds of stability conditions have been reported in literature, the delay dependent condition (the condition containing delay information) and delay independent condition (the condition without containing delay information) [25], so this conditions must be considered in order to design an appropriate deadbeat controller for multivariable discrete time system with state delay. Many of the works found in literature about discrete time multivariable systems with state delays, propose a solution for this kind of problems by designing an appropriate Lyapunov-Krasovskii functional in order to assure the stability of the systems even when delays are present in the state of the system [12, 17, 25]. The Lyapunov-Krasovskii functional is selected in order to assure the robust stability of the system of discrete time systems with time varying delays, so this approach is suitable for the state feedback design of deadbeat controllers. Then after designing the right Lyapunov-Krasovskii function, this kind of problems can be solved by a convex optimization problem represented as linear matrix inequalities LMI's in order to obtain the right selection of the controller parameters.

As explained in the previous section, the deadbeat controller design for multivariable discrete time systems is usually solved as an optimal control problem where a cost functional is minimized, implementing a cheap control functional (with no input function), and then finding the required matrices by solving the respective Riccati equation. Even when this approach yields acceptable results, the solution of the stability conditions for this kind of problems is more efficient when the solutions are found by a convex optimization problem defined by the linear matrix inequalities LMI's when time varying delays are found in the states of discrete time systems. The design and development of deadbeat controllers for multivariable discrete time systems with time varying delays is done by following a similar approach as constant time delay systems, as explained in the previous section; first, a change of basis is necessary to place the required poles at the origin and cancel the transmission zeros, selecting the suitable system matrices, in order to obtain a deadbeat controller characteristics. Then, the discrete time model with time varying state delays is considered by designing an appropriate Lyapunov-Krasovskii functional to establish the stability conditions of the model when the system has time delays in its states. Finally, the required matrices are found by solving a convex optimization problem given by the linear matrix inequalities LMI's. In the following subsection the derivation of the deadbeat controller for multivariable discrete time systems with time varying delays in the states is done in order to solve this control system problem. A numerical simulation example is shown in order to illustrate the results obtained in this section.

4.1 Deadbeat Control Design for Multivariable Discrete Time System with Time Varying Delays in the States

The design of deadbeat controllers for multivariable discrete time systems with time varying delays follows a similar procedure as in the constant time delay systems case. In order to design a suitable controller is necessary to make a change of basis on the original system, in order to place $(n-p)$ poles at the origin where n is the state dimension and p is the number of finite transmission zeros of the system. This requirement is met by selecting a appropriate basis which includes $(n-p)$ linear independent vectors to form a basis on $\Re^n$. Then by selecting an appropriate Lyapunov-Krasovskii functional in order to establish the stability conditions of the system the gain matrix can be found to be implemented in a state feedback form in order to stabilizes the system in a minimum number of time steps.

In order to design the deadbeat controller for multivariable discrete time systems with time varying state delays, the following system must be considered:

$$\begin{aligned} x(k+1) &= Ax(k) + A_d x(k-\tau(k)) + Bu(k) \\ y(k) &= Cx(k) \end{aligned} \tag{23}$$

where $x(k) \in \Re^n$ is the state vector, $\tau(k)$ is a nonnegative time varying integer that represent the delay, $u(k) \in \Re^m$ is the input vector and $y(k) \in \Re^l$ is the measured output.

The following condition is met by the time varying delay

$$\tau_1 \leq \tau(k) \leq \tau_2 \tag{24}$$

where τ_1 is the lower bound represented by a positive integer and τ_2 is the upper bound represented by a positive integer.

Define the following state feedback control law that is implemented for the deadbeat control of multivariable discrete time systems.

$$u(k) = -K_{\star} x(k) \tag{25}$$

In order to obtain a deadbeat controller it is necessary to make a change of basis by the following transformation matrix

$$T = [T_1 : T_2] \tag{26}$$

where $(n-p)$ linearly independent vectors must be selected in order to make a basis for the original system. Where n is the state dimension and p is the number of finite transmission zeros of the system. Then the original system is transform into:

$$\begin{aligned} x'(k+1) &= T^{-1}ATx'(k) + T^{-1}A_dTx'(k-\tau(k)) + T^{-1}Bu(k) \\ y(k) &= CTx'(k) \end{aligned} \tag{27}$$

Then the closed loop system is given by:

$$\begin{aligned} x'(k+1) &= (T^{-1}AT - T^{-1}BK_{\star})x'(k) + T^{-1}A_dTx'(k-\tau(k)) \\ y(k) &= CTx'(k) \end{aligned} \tag{28}$$

and then for model reduction the following equivalent matrices are defined:

$$\begin{aligned} A_p &= T^{-1}AT \\ A_{pd} &= T^{-1}A_dT \\ B_p &= T^{-1}B \\ C_p &= CT \end{aligned} \tag{29}$$

Transforming (28) in:

$$\begin{aligned} x'(k+1) &= (A_p - B_pK_{\star})x'(k) + A_{pd}x'(k-\tau(k)) \\ y(k) &= C_px'(k) \end{aligned} \tag{30}$$

Selecting C_p as long as the system includes transmission zeros at infinity.

In order to stabilizes the system by deadbeat control the following theorem must be implemented to find the appropriate matrices for the deadbeat state feedback controller for discrete time systems.

Theorem 2 *The closed loop stability of system* [9] *is assured if there exist positive definite matrices* $Q > 0$ *and* $P > 0$ *found by solving the following linear matrix inequality in order to solve for the gain matrix* $K_{\star}$ *that stabilizes the system in a minimum number of time steps k*

$$\begin{bmatrix} \Phi^T P\Phi - P + (\tau_2 - \tau_1 + k - 1)Q & \Phi^T PA_{pd} \\ A_{pd}^T P\Phi & A_{pd}^T PA_{pd} \end{bmatrix} < 0 \tag{31}$$

where Φ is defined later.

Proof Consider the following Lyapunov-Krasovskii functional [8, 12, 17, 25]:

$$V(x'(k)) = V_1(x'(k)) + V_2(x'(k)) + V_3(x'(k)) \tag{32}$$

where

$$\begin{aligned} V_1(x'(k)) &= x'^T(k)Px'(k) \\ V_2(x'(k)) &= \sum_{i=k-\tau(k)}^{k-1} x'^T(i)Qx'(i) \\ V_3(x'(k)) &= \sum_{j=2-\tau_2}^{-\tau_1+k-1} \sum_{l=k+j-1}^{k-1} x'^T(l)Qx'(l) \end{aligned} \tag{33}$$

□

Considering that $\Delta V_i(k) = V_i(k+1) - V_i(k)$ the derivative of each term of the Lyapunov-Krasovskii functional yield [25]:

$$\begin{aligned} \Delta V_1(x'(k)) = {} & x'(k)^T \Phi^T P \Phi x'(k) + x'(k)^T \Phi^T A_{pd} x'(k-\tau(k)) \\ & + x'^T(k-\tau(k)) A_{pd}^T P \Phi x'(k) \\ & + x'^T(k-\tau(k)) A_{pd}^T A_{pd} x'(k-\tau(k)) - x'(k)^T P x'(k) \end{aligned} \tag{34}$$

$$\Delta V_2(x'(k)) = \sum_{i=k+1-\tau(k+1)}^{k} x'^T(i)Qx'(i) - \sum_{i=k-\tau(k)}^{k-1} x'^T(i)Qx'(i) \tag{35}$$

$$\Delta V_3(x'(k)) = (\tau_2 - \tau_1 + k - 2)x'^T(k)Qx'(k) - \sum_{j=2-\tau_2}^{-\tau_1+k-1} x'^T(j+k-1)Qx'(j+k-1) \tag{36}$$

where $\Phi = A_p - B_p K_*$

In order to resolve for $\Delta V_3(x'(k))$ the following change of variable must be applied:

$$\begin{aligned} n &= k + j - 1 \\ j &= n - k + 1 \end{aligned} \tag{37}$$

Obtaining the following result due to:

$$\sum_{n=k+1-\tau_2}^{-\tau_1+k-1} x'^T(n)Qx'(n) = \sum_{n=k+1-\tau_2}^{k-1} x'^T(n)Qx'(n) - \sum_{n=k-\tau_1}^{k-1} x'^T(n)Qx'(n)$$

$$\begin{aligned}\Delta V_3(x'(k)) = (\tau_2 - \tau_1 + k - 2)x'^T(k)Qx'(k) \\ - \sum_{n=k+1-\tau_2}^{k} x'^T(n)Qx'(n) \\ + \sum_{n=-\tau_1+k}^{k-1} x'^T(n)Qx'(n) + x'^T(k)Qx'(k)\end{aligned} \tag{38}$$

Then computing $\Delta V_2(x'(k)) + \Delta V_3(x'(k))$ and due to $\tau(k) \leq \tau_2$

$$\sum_{n=k+1-\tau(k+1)}^{k} x'^T(n)Qx'(n) - \sum_{n=k+1-\tau_2}^{k} x'^T(n)Qx'(n) \leq 0 \tag{39}$$

and due to $\tau_1 \geq 0$

$$\sum_{n=k-\tau_1}^{k-1} x'^T(n)Qx'(n) - \sum_{n=k-\tau(k)}^{k-1} x'^T(n)Qx'(n) \leq 0 \tag{40}$$

Therefore the following upper bound is valid for:

$$\Delta V_2(x'(k)) + \Delta V_3(x'(k)) \leq (\tau_2 - \tau_1 + k - 1)x'^T(k)Qx'(k) \tag{41}$$

Then defining a vector:

$$\Gamma = \begin{bmatrix} x'(k) \\ x'(k - \tau(k)) \end{bmatrix} \tag{42}$$

and a matrix ϕ, then the following limit for $V(x'(k))$ the following inequality is obtained:

$$\Delta V(x'(k)) \leq \Delta V_1(x'(k)) + \Delta V_2(x'(k)) + \Delta V_3(x'(k)) \leq \Gamma^T \phi \Gamma \tag{43}$$

so the following linear matrix inequality is obtained in order to assure the system stability [12]:

$$\begin{bmatrix} \Phi^T P \Phi - P + (\tau_2 - \tau_1 + k - 1)Q & \Phi^T P A_{pd} \\ A_{pd}^T P \Phi & A_{pd}^T P A_{pd} \end{bmatrix} < 0 \tag{44}$$

where k is the minimum time step of the system and P and Q are matrices that assure the stability of the system, these matrices are necessary to find the gain K_*. With these derivations the proof is complete.

With this linear matrix inequality the required matrices are found in order to meet the stability conditions and then the deadbeat controller designed by state

feedback can be implemented in order to stabilize multivariable discrete time systems in a minimum number of time steps.

It is important to notice that the minimum number of time steps is given by the variable k so in order to stabilizes the system in minimum time this variable along with the appropriate number selection of linear independent vectors for the transformation matrix, place the required number of poles at the origin and cancel the finite transmission zeros of the system. As can be noticed, the deadbeat controller design is similar to the constant delay counterpart, but as explained in the previous section, an important fact that must be considered is the appropriate selection of a Lyapunov-Krasovskii functional, because with this functional the stability conditions and the linear matrix inequality to find the gain matrix that stabilizes the system by a state feedback control law.

In the next subsection, an illustrative numerical simulation is done in order evince the performance and advantage of this control strategy and to obtain some conclusions about this section.

4.2 Example 2

Consider the following multivariable discrete time system with constant time delays in the states.

$$\begin{aligned} x(k+1) &= \begin{bmatrix} 100 & 0 \\ 0 & 200 \end{bmatrix} x(k) + \begin{bmatrix} 7 & 5 \\ 0 & 3 \end{bmatrix} x(k-\tau(k)) + \begin{bmatrix} 1 & 0 \\ 0 & 1 \end{bmatrix} u(k) \\ y(k) &= \begin{bmatrix} 1 & 0 \\ 0 & 1 \end{bmatrix} x(k) \end{aligned} \tag{45}$$

with $k = 5$, $\tau_1 = 14$, $\tau_2 = 48$, sampling period T_s = 10 s and the transformation matrix T

$$T = \begin{bmatrix} 1 & 0 \\ 0 & 1 \end{bmatrix} \tag{46}$$

The following matrices are obtained:

$$\begin{aligned} Q &= \begin{bmatrix} 247 & 0 \\ 0 & 447 \end{bmatrix} \\ P &= \begin{bmatrix} 1 & 0 \\ 0 & 1 \end{bmatrix} \\ K_{\star} &= \begin{bmatrix} 247.9960 & 0 \\ 0 & 447.9978 \end{bmatrix} \end{aligned} \tag{47}$$

with $k = 25$, $\tau_1 = 5$, $\tau_2 = 29$ and the transformation matrix T

$$T = \begin{bmatrix} -2 & 5 \\ 0 & 1 \end{bmatrix} \tag{48}$$

The following matrices are obtained:

$$\begin{aligned} Q &= \begin{bmatrix} 272 & 250 \\ 250 & 472 \end{bmatrix} \\ P &= \begin{bmatrix} 1 & 0 \\ 0 & 1 \end{bmatrix} \\ K_{\star} &= \begin{bmatrix} 272.2483 & 248.7569 \\ 248.7569 & 479.2207 \end{bmatrix} \end{aligned} \tag{49}$$

with $k = 10$, $\tau_1 = 1$, $\tau_2 = 79$ and the transformation matrix T

$$T = \begin{bmatrix} -3 & 9 \\ 4 & 12 \end{bmatrix} \tag{50}$$

The following matrices are obtained:

$$\begin{aligned} Q &= \begin{bmatrix} 386.00 & 166.67 \\ 166.67 & 386.00 \end{bmatrix} \\ P &= \begin{bmatrix} 1 & 0 \\ 0 & 1 \end{bmatrix} \\ K_{\star} &= \begin{bmatrix} 386.03 & 166.65 \\ 166.64 & 386.01 \end{bmatrix} \end{aligned} \tag{51}$$

The simulation results are shown below:

In Fig. 5 the system response of the variable x_1 is shown, where as it is expected, the system trajectory for the three cases is driven from the initial value to the final value following a step function trajectory. As it is corroborated later the trajectory path is follow efficiently while the error is minimized.

In Fig. 6 the system response of the variable x_2 is shown, where as it is expected, the system trajectory for the three cases is driven from the initial value to the final value following a step function trajectory. The tracking error is minimized in order to make the variable trajectory to follow the reference path. It can be noticed that the final value is reach in a greater number of time steps than the minimum value required in order to obtain a deadbeat response.

In Fig. 7 the error signal for the variable x_1 is shown, where as it is corroborated the error signal is kept in a small margin in order to make this variable to follow the reference efficiently.

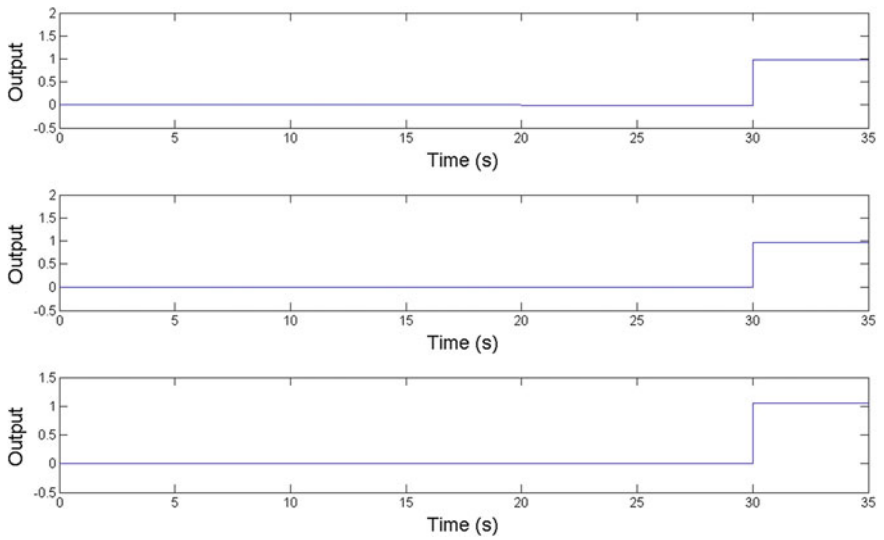

Fig. 5 System response of the variable x_1

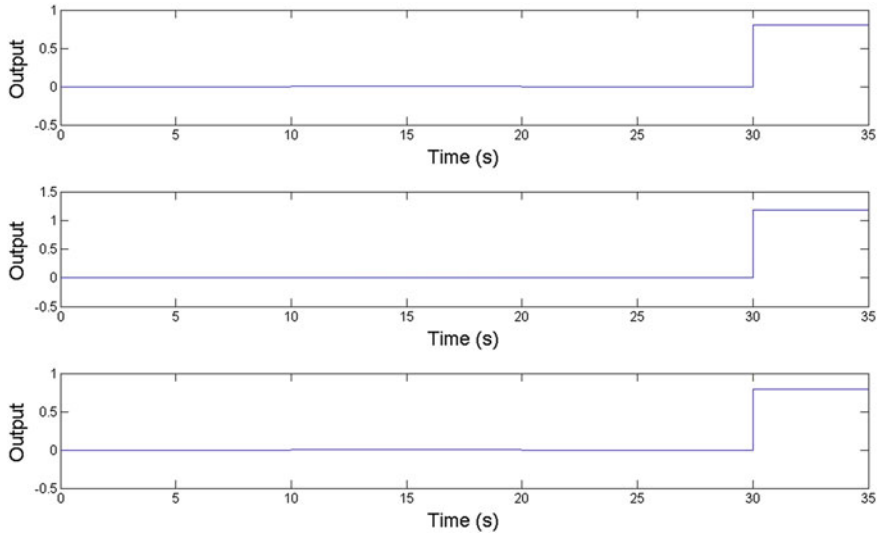

Fig. 6 System response of the variable x_2

In Fig. 8 the error signal for the variable x_2 is shown, where as it is corroborated the error signal is kept in a small margin in order to make this variable to follow the reference efficiently. The error signal depicted in Fig. 8 shows how the deadbeat controller improves the system performance while minimizing the tracking error, this is an important characteristics that must be considered in order to make the

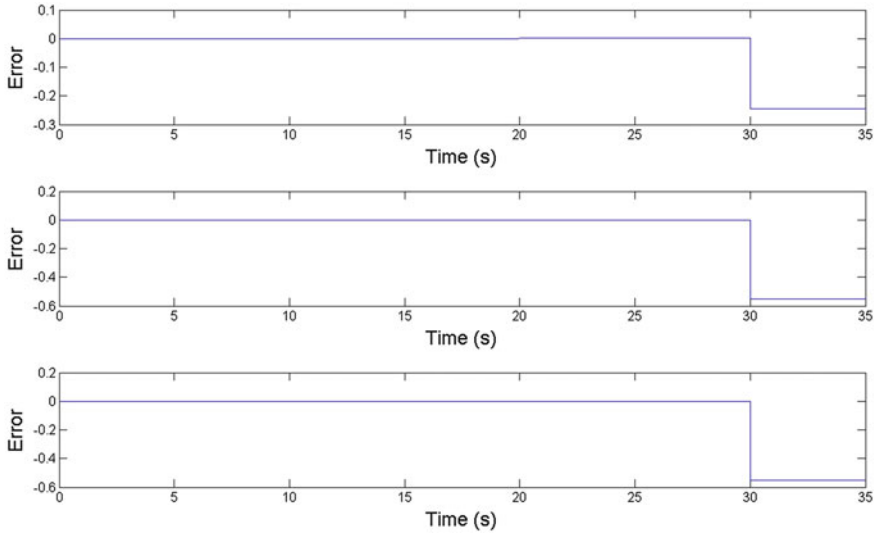

Fig. 7 System error of the variable x_1

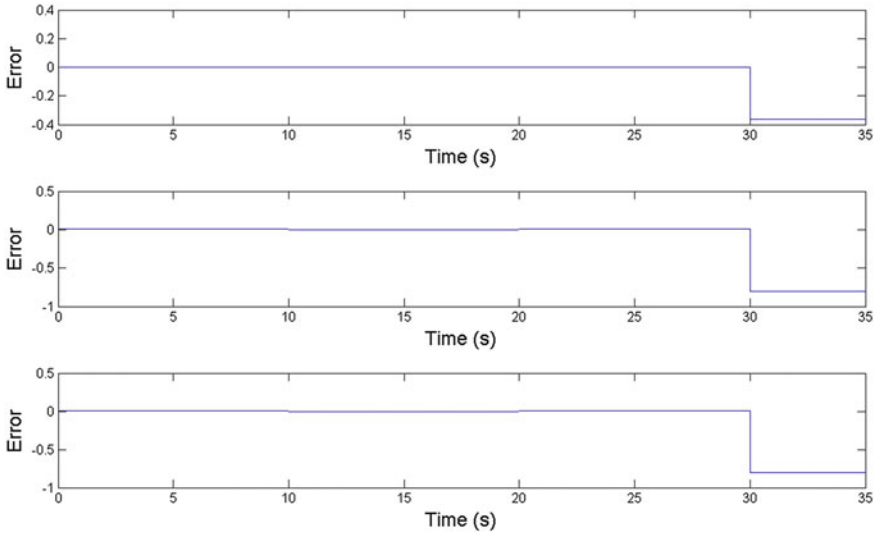

Fig. 8 System error of the variable x_2

system, variables to reach the desired values in a minimum number of time steps reducing the steady state error in the case of multivariable discrete time systems with time varying delays when different values of the system parameters.

In this section the development and design of deadbeat controllers for multivariable discrete time systems with time varying delays is proposed. In order to design an

efficient deadbeat controller for this kind of system, it is important to recognize the system properties in term of the system poles and transmission zeros of the model. A change of basis is required in order to place a specified number of closed loop poles at the origin and cancelling the transmission zeros of the original system.

After a change of basis, considering that dealing with time varying delays is not an easy task, the specification of an appropriate Lyapunov-Krasovskii functional establishes the stability conditions of the system taking in count the time varying characteristics of the time delay model. By the specification of the Lyapunov-Krasovskii functional the resulting linear matrix inequalities LMI's are implemented in order to obtain the required matrices that establish the stability conditions in order to obtain a feasible controller gain for the deadbeat controller represented by a state feedback control law.

In this section an illustrative numerical example is done in order to show the system response of a multivariable discrete time system with time varying delays in the states stabilized by a deadbeat controller. It is proved that the state variables reach the desired value when a step reference signal is applied to the input of the system. The error signal of the system is kept into a small margin as expected by the deadbeat control system specifications, improving the system performance. In the following section, a similar problem is solved but in this case the design of deadbeat controllers for multivariable discrete time systems with time varying delays in the inputs is considered.

5 Deadbeat Control for Multivariable Systems with Time Varying Delays in the Inputs

In this section the development and design of deadbeat controllers for multivariable discrete time systems with time varying delays in the input is explained in order to find a suitable state feedback control that meets the stability condition along by driving the system states to the desired final value in a minimum number of time steps. Similar as the stabilization of discrete time systems with time varying delays on the state, time varying delays in the input are produced by signal transmission lags and other effects yielded by the implemented hardware, this phenomena is a sources of many unwanted effects such as system performance deterioration and even instability. The time varying delay characteristics when this phenomena is found in the state of the system, are very similar when time varying delays are found in the input, so the deadbeat controller synthesis for multivariable discrete time system in the states is very similar to the case explained in the previous section. In order to design suitable deadbeat controllers for multivariable discrete time systems with time varying delays in the inputs, it is necessary to make a change of basis of the original system, in order to place a $(n-p)$ number of poles at the origin, where n is the state dimension and p is the number of finite transmission zeros of the original system. Then by making an appropriate selection of the transformation matrix, in which $(n-p)$ linear independent vectors must be

selected, the original closed loop system is transformed to another coordinate system, and then the deadbeat controller synthesis can be done by finding the required state feedback control gain. Similar as the controller synthesis of discrete systems with time varying delays in the states, instead of solving this problem by an optimal control problem minimizing a cost functional or cheap control (no cost on the input), the approach evinced in this section is based on the proper selection of a Lyapunov-Krasovskii functional in order to establish the necessary stability conditions of the system, in order to find an stable state feedback gain that drives the system to the desired final in a minimum number of time steps to meet the conditions of the deadbeat controller. After selecting an appropriate Lyapunov-Krasovskii functional, a suitable gain matrix can be found by solving a convex optimization problem established by the required linear matrix inequalities.

In the first part of this section, the derivation of deadbeat controllers for multivariable discrete time system with time varying delays in the inputs is developed in order to find a state feedback control gain to obtain a deadbeat response in which the states are driven to the desired final value in a minimum number of time steps, this requirement is met by selecting an appropriate transformation matrix to make a change of basis and the selection of an appropriate Lyapunov-Krasovskii functional. In the second part of this section, a numerical simulation example is done in order to show the deadbeat response of the system states with the required gain matrix found by solving a set of linear matrix inequalities LMI.

5.1 Deadbeat Control Design for Multivariable Discrete Time System with Time Varying Delays in the Inputs

The derivation of a deadbeat controller for multivariable discrete time systems with time varying delays in the inputs, follows a similar procedure as explained in Sect. 4, where a change of basis of the original model must be done, in order to make a change of coordinates; this objective is achieved by selecting an appropriate transformation matrix in order to place $(n-p)$ poles at the origin and cancelling the finite transmission zeros of the closed loop system. Then selecting an appropriate Lyapunov-Krasovskii functional in order to established the required stability conditions of the system and find the appropriate gain matrix that stabilizes the system by solving the resulting linear matrix inequalities.

Consider the following discrete time system with time varying delays in the inputs:

$$\begin{aligned} x(k+1) &= Ax(k) + Bu(k-\tau(k)) \\ y(k) &= Cx(k) \end{aligned} \tag{52}$$

where $x(k) \in \Re^n$ is the state vector, $\tau(k)$ is a nonnegative time varying integer that represent the delay, $u(k) \in \Re^m$ is the input vector and $y(k) \in \Re^l$ is the measured output.

The following condition is met by the time varying delay

$$\tau_1 \leq \tau(k) \leq \tau_2 \tag{53}$$

where τ_1 is the lower bound represented by a positive integer and τ_2 is the upper bound represented by a positive integer. Define the following state feedback control law that is implemented for the deadbeat control of multivariable discrete time systems.

$$u(k - \tau(k)) = -K_{\star} x(k - \tau(k)) \tag{54}$$

In order to obtain a deadbeat controller it is necessary to make a change of basis by the following transformation matrix

$$T = [T_1 : T_2] \tag{55}$$

The first step in order to design a deadbeat controller it is necessary to find the minimum number of time steps to stabilizes the system from the initial condition.

$$x(k) = A^k x(0) - \sum_{i=0}^{k-1} A^{k-1-i} B K_{\star} x(i - \tau(k)) \tag{56}$$

where k is the minimum number of time steps. Then the following change of basis is done in order to place the required poles and transmission zeros by state feedback.

$$\begin{aligned} x'(k+1) &= T^{-1} A T x'(k) - T^{-1} B K_{\star} T x'(k - \tau(k)) \\ y(k) &= C T x'(k) \end{aligned} \tag{57}$$

and then for model reduction the following equivalent matrices are defined:

$$\begin{aligned} A_p &= T^{-1} A T \\ A_{pd} &= T^{-1} B K_{\star} T \\ C_p &= C T \end{aligned} \tag{58}$$

Choosing C_p to cancelled the finite transmission zeros of the system. In order to stabilizes the system by deadbeat control the following theorem must be implemented to find the appropriate matrices for the deadbeat state feedback controller for discrete time systems.

Theorem 3 *The closed loop stability of system* [9] *is assured if there exist positive definite matrices* $Q > 0$ *and* $P > 0$ *found by solving the following linear matrix inequality in order to solve for the gain matrix* $K_{\star}$ *that stabilizes the system in a minimum number of time steps* k

$$\begin{bmatrix} A_p^T P A_p - P + (\tau_2 - \tau_1 + k - 1)Q & A_p^T P A_{pd} \\ A_{pd}^T P A_p & A_{pd}^T P A_{pd} \end{bmatrix} < 0 \tag{59}$$

Proof Consider the following Lyapunov-Krasovskii functional [8, 12, 17, 25]:

$$V(x'(k)) = V_1(x'(k)) + V_2(x'(k)) + V_3(x'(k)) \tag{60}$$

where

$$\begin{aligned} V_1(x'(k)) &= x'^T(k) P x'(k) \\ V_2(x'(k)) &= \sum_{i=k-\tau(k)}^{k-1} x'^T(i) Q x'(i) \\ V_3(x'(k)) &= \sum_{j=2-\tau_2}^{-\tau_1+k-1} \sum_{l=k+j-1}^{k-1} x'^T(l) Q x'(l) \end{aligned} \tag{61}$$

□

Due to $\Delta V_i(k) = V_i(k+1) - V_i(k)$, the derivative of each term of the Lyapunov-Krasovskii functional yield [25]:

$$\begin{aligned} \Delta V_1(x'(k)) = {} & x'^T(k) A_p^T P A_p x'(k) + x'^T(k) A_p^T P A_{pd} x'(k - \tau(k)) \\ & - x'^T(k - \tau(k)) A_{pd}^T P A_p x'(k) + x'^T(k - \tau(k)) A_{pd}^T P A_{pd} x'(k - \tau(k)) \\ & - x'^T(k) P x'(k) \end{aligned} \tag{62}$$

$$\Delta V_2(x'(k)) = \sum_{i=k+1-\tau(k+1)}^{k} x'^T(i) Q x'(i) - \sum_{i=k-\tau(k)}^{k-1} x'^T(i) Q x'(i) \tag{63}$$

$$\Delta V_3(x'(k)) = (\tau_2 - \tau_1 + k - 2) x'^T(k) Q x'(k) - \sum_{j=2-\tau_2}^{-\tau_1+k-1} x'^T(j + k - 1) Q x'(j + k - 1) \tag{64}$$

In order to resolve for $\Delta V_3(x'(k))$ the following change of variable must be applied:

$$\begin{aligned} n &= k + j - 1 \\ j &= n - k + 1 \end{aligned} \tag{65}$$

Obtaining the following result due to:

$$\sum_{n=k+1-\tau_2}^{-\tau_1+k-1} x'^T(n)Qx'(n) = \sum_{n=k+1-\tau_2}^{k-1} x'^T(n)Qx'(n) - \sum_{n=k-\tau_1}^{k-1} x'^T(n)Qx'(n)$$

$$\begin{aligned}\Delta V_3(x'(k)) = {} & (\tau_2 - \tau_1 + k - 2)x'^T(k)Qx'(k) \\ & - \sum_{n=k+1-\tau_2}^{k} x'^T(n)Qx'(n) \\ & + \sum_{n=-\tau_1+k}^{k-1} x'^T(n)Qx'(n) + x'^T(k)Qx'(k)\end{aligned} \tag{66}$$

Then computing $\Delta V_2(x'(k)) + \Delta V_3(x'(k))$ and due to $\tau(k) \leq \tau_2$

$$\sum_{n=k+1-\tau(k+1)}^{k} x'^T(n)Qx'(n) - \sum_{n=k+1-\tau_2}^{k} x'^T(n)Qx'(n) \leq 0 \tag{67}$$

and due to $\tau_1 \geq 0$

$$\sum_{n=k-\tau_1}^{k-1} x'^T(n)Qx'(n) - \sum_{n=k-\tau(k)}^{k-1} x'^T(n)Qx'(n) \leq 0 \tag{68}$$

Therefore the following upper bound is valid for:

$$\Delta V_2(x'(k)) + \Delta V_3(x'(k)) \leq (\tau_2 - \tau_1 + k - 1)x'^T(k)Qx'(k) \tag{69}$$

Then defining a vector:

$$\Gamma = \begin{bmatrix} x'(k) \\ x'(k - \tau(k)) \end{bmatrix} \tag{70}$$

and a matrix ϕ, then the following limit for $V(x'(k))$ the following inequality is obtained:

$$V(x'(k)) \leq V_1(x'(k)) + V_2(x'(k)) + V_3(x'(k)) \leq \Gamma^T \phi \Gamma \tag{71}$$

so the following linear matrix inequality is obtained in order to assure the system stability [12]:

$$\begin{bmatrix} A_p^T P A_p - P + (\tau_2 - \tau_1 + k - 1)Q & A_p^T P A_{pd} \\ A_{pd}^T P A_p & A_{pd}^T P A_{pd} \end{bmatrix} < 0 \tag{72}$$

where k is the minimum time step of the system and P and Q are matrices that assure the stability of the system, these matrices are necessary to find the gain matrix K_*. With these derivations the proof is complete.

With this theorem, the stability of the multivariable discrete time system is assured and the corresponding matrices for the deadbeat controller by state feedback can be found in order to stabilizes the system in a minimum number of time steps. Even when dealing with time varying delays in the inputs is not an easy task it is confirmed that a feasible matrix gain can be found in order to place the required number of closed loop poles at the origin cancelling the finite transmission zeros of the original system.

In the following section an illustrative numerical example is shown in order to visualize the theoretical background explained in this section and analyze the performance of a numerical model when a deadbeat controller is designed for a multivariable discrete time system with time varying delays in the inputs.

5.2 Example 3

Consider the following multivariable discrete time system with constant time delays in the inputs.

$$\begin{aligned} x(k+1) &= \begin{bmatrix} 100 & 0 \\ 0 & 200 \end{bmatrix} x(k) + \begin{bmatrix} 1 & 0 \\ 0 & 1 \end{bmatrix} u(k-\tau(k)) \\ y(k) &= \begin{bmatrix} 1 & 0 \\ 0 & 1 \end{bmatrix} x(k) \end{aligned} \tag{73}$$

with $k = 5$, $\tau_1 = 14$, $\tau_2 = 58$, sampling period T_s = 10 s and the transformation matrix T

$$T = \begin{bmatrix} 1 & 0 \\ 0 & 1 \end{bmatrix} \tag{74}$$

The following matrices are obtained:

$$\begin{aligned} Q &= \begin{bmatrix} 147 & 0 \\ 0 & 247 \end{bmatrix} \\ P &= \begin{bmatrix} 1 & 0 \\ 0 & 1 \end{bmatrix} \\ K_{\star} &= \begin{bmatrix} 148.00 & 0 \\ 0 & 248.00 \end{bmatrix} \end{aligned} \tag{75}$$

with $k = 50$, $\tau_1 = 5$, $\tau_2 = 29$ and the transformation matrix T

$$T = \begin{bmatrix} -2 & 0 \\ 0 & 1 \end{bmatrix} \tag{76}$$

The following matrices are obtained:

$$\begin{aligned} Q &= \begin{bmatrix} 192 & 0 \\ 0 & 292 \end{bmatrix} \\ P &= \begin{bmatrix} 1 & 0 \\ 0 & 1 \end{bmatrix} \\ K_{\star} &= \begin{bmatrix} 193.00 & 0 \\ 0 & 293.00 \end{bmatrix} \end{aligned} \tag{77}$$

with $k = 10$, $\tau_1 = 1$, $\tau_2 = 79$ and the transformation matrix T

$$T = \begin{bmatrix} -3 & 0 \\ 0 & 12 \end{bmatrix} \tag{78}$$

The following matrices are obtained:

$$\begin{aligned} Q &= \begin{bmatrix} 152.00 & 0.00 \\ 0.00 & 252.00 \end{bmatrix} \\ P &= \begin{bmatrix} 1 & 0 \\ 0 & 1 \end{bmatrix} \\ K_{\star} &= \begin{bmatrix} 153.00 & 0 \\ 0.00253.00 & \end{bmatrix} \end{aligned} \tag{79}$$

The simulation results are shown below:

In Fig. 9 the system response of the variable x_1 is shown where as it can be noticed the system response in the three cases depicted in this figure shows how this variable reach the desired final value in a minimum number of time steps. This system variable behaviour is obtained due to an appropriate selection of the gain matrix implemented by a state feedback controller in order to stabilizes the system in a minimum number of time steps according to the deadbeat controller design. As it is corroborated later, the deadbeat controller is designed in order to minimize the system error by an appropriate poles and transmission zeros of the system.

In Fig. 10 the system response of the variable x_2 is shown in order to observe the system performance of this variable in the three cases as explained before. As it can be noticed, the system response depicted in this figure shows how this system variable is stabilized in a minimum number of time steps by the selection and implementation of an appropriate gain matrix in a state feedback form which meet the deadbeat response requirements. This objective is reached by selecting a

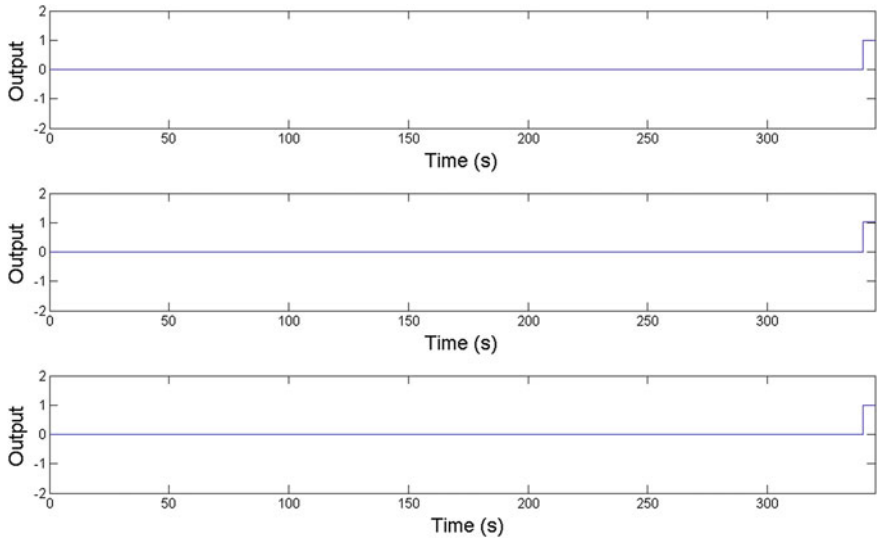

Fig. 9 System response of the variable x_1

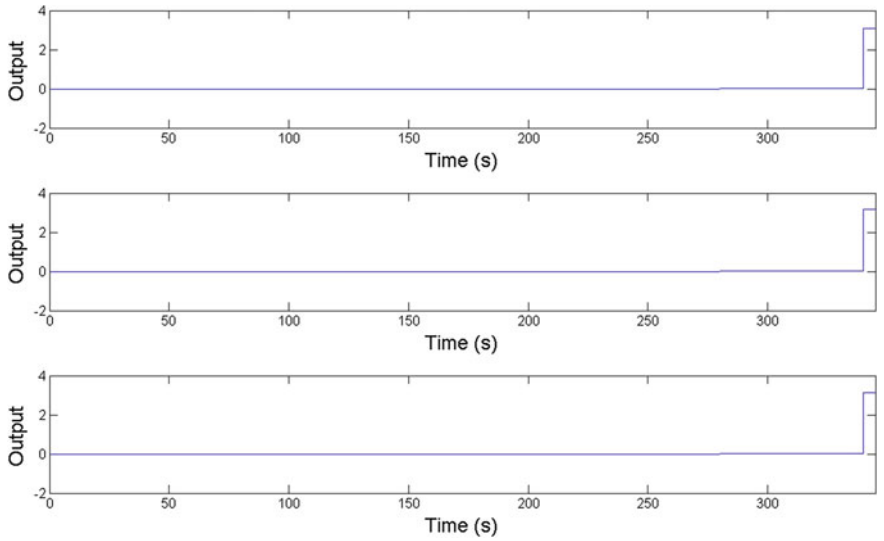

Fig. 10 System response of the variable x_2

suitable controller gain matrix in order to place the poles and the transmission zeros of the system in the right position.

In Fig. 11 the error signal of the variable x_1 is shown. As can be noticed the tracking error of this variable is kept in a small margin as expected due to an appropriate

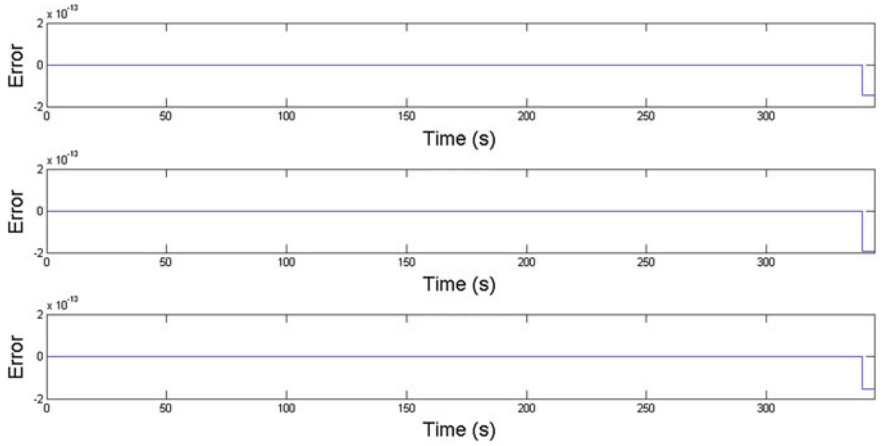

Fig. 11 Error signal of the variable x_1

selection of the gain matrix, obtained by solving the linear matrix inequalities LMI in the three cases. An appropriate selection and placement of the poles and transmission zeros of the closed loop system makes the error signal of this variable as small a possible when a step reference function is applied in the system inputs.

In Fig. 12 the error signal of the variable x_2 is shown and as can be noticed a small tracking error margin is obtained by an appropriate selection of the gain matrix derived from the solution of the linear matrix inequality in the three cases.

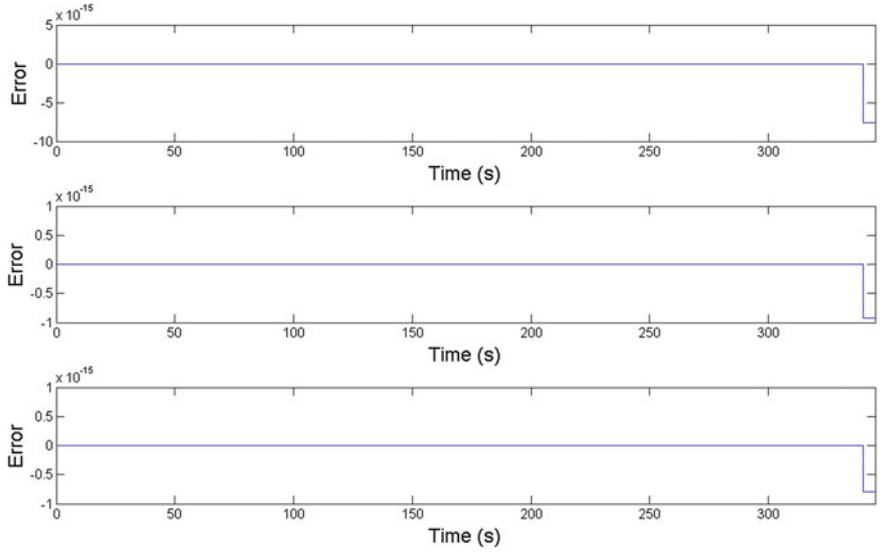

Fig. 12 Error signal of the variable x_2

The deadbeat response of the system is obtained due to an appropriate selection of the transformation matrix in order to make a change of basis and later a suitable gain matrix is obtained by solving the required linear matrix inequalities.

In this section the development of a deadbeat controller for multivariable discrete time system with time varying delays in its inputs is shown in order to design a controller which drives the system from its initial values to the desired final value in a minimum number of time steps. This objective is accomplished by selecting an appropriate transformation matrix in order to make a change of basis or a change of coordinates from the original model to solve this problem by a state feedback controller. Even when dealing with time varying delays in the inputs of the system are difficult to analyze, it is possible to stabilizes this kind of systems by selecting an appropriate Lyapunov-Krasovskii functional in order to analyze the closed loop stability of the system and establish the stability conditions that are represented by linear matrix inequalities LMI's in order to obtain the gain matrix that guarantees the stability of the system by maintaining the required deadbeat response. In this section, it is proved that understanding the deadbeat controller for multivariable time system with time delays in the states is very important in order to consider the time varying delays in the system input case, because a similar approach can be implemented in both cases when delays are found by different sources such as signal transmission lags, damaged hardware, etc.

With the derivation and design of the proposed techniques showed in this chapter the discussion and analysis of the three control strategies shown in this chapter. Later, the conclusions of this work are evinced to expose the advantages, disadvantages and characteristics of the proposed control strategies shown in this paper.

6 Discussion

In this chapter the derivation of deadbeat controllers for multivariable discrete time systems with time varying delays is exposed. It is proven that a system with deadbeat response can be obtained by selecting a state feedback gain matrix that meets the stability requirements in order to stabilizes the system in a minimum number of time steps. From the results obtained in Sect. 3, where a deadbeat controller for multivariable discrete time systems with constant time delays is obtained, it is proved that by selecting an appropriate Lyapunov-Krasovskii functional, the stability conditions of the system are established in order to meet the system performance requirements, even when this is a basic form in which delays are found in physical systems, the main objective for the analysis of discrete time systems with constant time delays is to develop a feasible control strategy that is used later in the design of deadbeat controllers for discrete time systems with time varying delays, considering the complexity of this kind of models when this phenomena is found in the systems. As it is verified, when constant time delays are found in the system, the unwanted effects yielded by time delays, such as performance deterioration or even instability, are cancelled by placing the right number of poles at the origin while cancelling the

finite transmission zeros, for this purpose, a change of basis is necessary in order to find later the required state feedback gain matrices that places the poles and transmission zeros of the model in the right position. The simulation results obtained in this section, evince the deadbeat system response and, as can be checked, the system is stabilized in a minimum number of time steps as established by the appropriate selection of poles and transmission zeros avoiding the unwanted effects yielded by time delays, that in this case, are found in the system states. The main idea of the analysis and design of deadbeat controllers for discrete time systems with constant state delays, is to introduce the basic concepts about how to deal with discrete time systems with time delays, in order to overcome this kind of problems later in the time varying delay case. For the design of deadbeat controllers for multivariable discrete time systems with time varying delays in the states, a similar approach when constant time delays are found in the states is followed, considering the complexity of time varying delays, a required Lyapunov-Krasovskii functional is proposed in order to obtain the stability conditions for this kind of systems to implement a state feedback controller with deadbeat response properties stabilizing the system in a minimum number of time steps. As in the constant time delays in the states case, the first step, a change of basis or a change of coordinates is necessary in order to cancel the finite transmission zeros of the system obtaining the closed loop system state feedback gain matrix that is found by a convex optimization problem, established by solving the linear matrix inequalities LMI's in order to meet all the system stability requirements of the model. In Sect. 4 an illustrative numerical example is shown in order to evaluate the system performance when a deadbeat controller is implemented in a multivariable discrete time system with time varying delays in the states. It is found that the deadbeat system response is accomplished by solving the required linear matrix inequalities finding the state feedback gain matrix that meets the stability conditions. It can be verified that the deadbeat system response is obtained when three different minimum time steps requirements are established in order to compare the system performance in the three cases and to analyze the tracking errors of the model when different time varying delays characteristics in the model are implemented. In Sect. 5, the design of deadbeat controllers for multivariable discrete time systems with time varying delays in the inputs is evinced where a similar approach as the two cases explained before is implemented in order to find a suitable controller that meets the stability requirements while keeping a deadbeat response. The design procedure explained in this section consist in making a change of basis of the original system, similar as the deadbeat approach when time varying delays are found in the states, in order to place the required poles at the origin and cancelling the finite transmission zeros. Then a Lyapunov-Krasovskii functional is proposed in order to establish the stability conditions when time varying delays are found in the inputs. Then this problem is solved by establishing the linear matrix inequalities LMI's which provide the necessary conditions to obtain the state feedback gain matrix that yields a deadbeat response on the system. Similar as the previous cases, an illustrative numerical example is shown to test the proposed control algorithm when time varying delays are found in the inputs. The results of this simulation show that the deadbeat controller stabilize the system in a minimum number of time steps,

as required by the deadbeat controller design, when time varying delays are found in the inputs of the system. The tracking error of the system is minimized by obtaining an appropriate state feedback gain matrix solving the linear matrix inequalities LMI's that establishing the stability conditions of the system. As a concluding remark of the three control strategies proposed in this chapter, it can be verified that effective deadbeat controllers can be designed in order to reach the desired final value given by the reference signal and with any initial condition in a minimum number of time steps, these results are achieved by an appropriate selection of the closed loop poles and transmission zeros which define the conditions in which a deadbeat response of the system can be obtained when time delays are found in the system avoiding or cancelling the unwanted effects yield by this phenomena.

7 Conclusions

In this chapter the derivation of deadbeat controllers for multivariable discrete time systems with time varying delays in the states and the inputs is proposed. In the first part of this chapter the derivation of deadbeat controller for multivariable discrete time systems with constant time delays in the state is analyzed. The deadbeat controller proposed is based in a change of coordinates of the original model in order to place a required number of poles at the origin while cancelling the finite transmission zeros, then considering this change of basis a Lyapunov-Krasovskii functional is proposed in order to establish the stability conditions of the model. The deadbeat controller is obtained by a state feedback control law in order to stabilize the system in a minimum number of time steps while minimizing the tracking error of the system when a step function is used as the reference signal of the closed loop system. In order to find the required state feedback matrix gain, it is necessary to solve the required linear matrix inequalities that guarantees the stability of the system. This linear matrix inequalities LMI's are designed to obtain the required matrices that assures the stability of the system including the state feedback gain matrix that stabilizes the closed loop system in a minimum number of time steps.

Based on the derivation and design of deadbeat controllers for multivariable discrete time systems with constant time delays in the states, a time varying delay version is implemented for the design of deadbeat controllers for multivariable discrete time systems with time varying delays in the states. It is proved that in the constant delays and time varying delay cases it is possible to find stable deadbeat controllers by selecting an appropriate transformation matrix in order to make a change of basis for the original system in order to place the required number of closed loop poles at the origin and cancelling the finite transmission zeros. Then by designing an appropriate Lyapunov-Krasovskii functional, similar as the constant time delay case, the stability conditions are established in order to derive the necessary linear matrix inequalities LMI's implemented to find the controller gain that stabilizes the system in a minimum number of time steps. Similar as the constant time delay case, a state feedback control law is implemented to place the

required poles and transmission zeros in the required position in the complex plane to obtain stable deadbeat controllers that drive the states to the desired final value independently of the initial conditions imposed on the model.

In the third case, the deadbeat controller design for multivariable discrete time systems with time varying delays in the inputs is considered, and following a similar approach as the previous two cases, a change of basis is necessary to place the poles and transmission zeros in the right position in the complex plane by implementing a state feedback control law in order to drive the states of the system to the desired final value independently of the initial conditions of the model. A Lyapunov-Krasovskii functional is implemented to establish the necessary stability conditions of the closed loop system and derive the required linear matrix inequalities LMI's to find the resulting matrices that prove the stability of the system. By solving a convex stabilization problem, the required state feedback matrix is found in order to stabilize the system and obtaining a deadbeat response. This objective is achieved by solving the required linear matrix inequalities in order to drive the system states in a minimum number of time steps, as required by the deadbeat controller design. In order to test the system performance for the three cases explained in this article, a series of numerical simulation examples were performed to exposed the system performance when time delays are found in the system. It was proved that the stabilization of multivariable discrete time systems with time delays by deadbeat controllers is a feasible and efficient control approach when this phenomena are found in this kind of systems. It is proved that many of the unwanted effects yield by time delays, such as performance deterioration and instability, are cancelled by selecting the appropriate deadbeat controller, minimizing the tracking errors of the system while a step input function is used as a reference signal of the model.

References

1. de Souza, C.E., Coutinho, D.: Robust stability and control of uncertain linear discrete-time periodic systems with time-delay. Automatica **50**(2), 431–441 (2014)
2. Debeljkovic, D., Dimitrijevic, N., Popov, D., Stojanovic, S.: On Non-Lyapunov stability of linear discrete time delay systems: LMIs approach. In: Proceedings of the 10th World Congress on Intelligent Control and Automation, IEEE, Beijing, China, 6–8, July 2012
3. Eldem, V., Selbuz, H.: On the general solution of the state deadbeat control problem. IEEE Trans. Autom. Control **39**(5), 1002–1006 (1994)
4. Emami-Naeini, A.: Deadbeat control of linear multivariable generalized state-space systems. In: Proceedings of the 29th Conference on Decision and Control Honolulu, IEEE, Hawaii, (1990)
5. Emami-Naeini, A.: Deadbeat control of linear multivariable generalized state-space systems. IEEE Trans. Autom. Control **37**(5), 648–652 (1992)
6. Genesio, R., Tesi, A.: The output stabilization of SISO bilinear systems. IEEE Trans. Autom. Control **33**(10), 950–952 (1988)
7. Halpern, M.E., Evans, R.J., Hill, R.D.: Optimal pole placement design for SISO discrete-time systems. IEEE Trans. Autom. Control **41**(9), 1322–1326 (1996)

8. He, Y., Wu, M., Liu, G.-P., She, J.-H.: Output feedback stabilization for a discrete-time system with a time-varying delay. IEEE Tras. Autom. Control **53**(10), 2372–2377 (2008)
9. Jordan, D., Korn, J.: Deadbeat algorithms for multivariable process control. IEEE Trans. Autom. Control **25**(3), 486–491 (1980)
10. Kaczorek, T.: Deadbeat control of linear discrete-time systems by periodic output-feedback. IEEE Trans. Autom. Control **31**(12), 1153–1156 (1986)
11. Katoh, H., Funahashi, Y.: Continuous-time deadbeat control for sampled-data systems. IEEE Trans. Autom. Control **41**(10), 1478–1481 (1996)
12. Leite, V. J. S. and Miranda, M. F., 2008. Stabilization of discrete time-varying delay systems: a convex parameter dependent approach. In: 2008 American Control Conference Westin Seattle Hotel, IEEE, Seattle, Washington, USA, 11–13, June 2008
13. Leite, V.J. S., Tarbouriech, S., Peres, P.L. D.: A convex approach for robust state feedback control of discrete-time systems with state delay. In: Proceeding of the 2004 American Control Conference Boston, IEEE, Massachusetts, 30 June, 2 July, 2004
14. Lewis, F.L.: A general riccati equation solution to the deadbeat control problem. IEEE Trans. Autom. Control **27**(1), 186–188 (1982)
15. Man, S., Zhenpu, G., Peng, L.: Delay-dependent robust H infinity control for discrete systems with time-delay and polytopic uncertainty. In: Proceedings of the 29th Chinese Control Conference, IEEE, Beijing, China, 29–31 July, 2010
16. Marrari, M.R., Emani-Naeini, A., Franklin, G.F.: Output deadbeat control of discrete-time multivariable systems. IEEE Trans. Autom. Control **34**(6), 644–648 (1989)
17. Miranda, M.F., Leite, V.J.S., Caldeira, A.F.: Robust stabilization of polytopic discrete-time systems with time-varying delay in the states. In: 49th IEEE Conference on Decision and Control, IEEE, Hilton Atlanta Hotel, Atlanta, GA, USA, 15–17 Dec, 2010
18. Olgac, N., Sipahi, R.: An exact method for the stability analysis of time-delayed linear time-invariant (LTI) systems. IEEE Trans. Autom. Control **47**(5), 793–797 (2002)
19. Sirisena, H.R.: Ripple-free deadbeat control of SISO discrete systems. IEEE Trans. Autom. Control **30**(2), 168–170 (1985)
20. Spurgeon, S.K., Pugh, A.C.: On output deadbeat control of discrete-time multivariable systems. IEEE Trans. Autom. Control **36**(7), 894–896 (1991)
21. Urikura, S., Nagata, A.: Ripple-free deadbeat control for sampled-data systems. IEEE Trans. Autom. Control **32**(6), 474–482 (1987)
22. Wang, Y., Yan, X., Zuo, Z., Zhao, H.: Robust stability and stabilization of discrete time-delay system with time-varying delay and non-linear perturbations. In: 2008 IEEE International Symposium on Intelligent Control Part of 2008 IEEE Multi-conference on Systems and Control, IEEE, San Antonio, Texas, USA, 3–5 Sept, 2008
23. Xiaofu, J., Jinfeng, G.: Delay-dependent robust H infinity control for uncertain discrete singular linear time-delay systems. In: Proceedings of the 30th Chinese Control Conference, IEEE, Yantai, China, 22–24 July, 2011
24. Yoneyama, J.: Robust stability and stabilization for uncertain discrete-time fuzzy systems with time-varying delay. In: Proceedings of the 7th Asian Control Conference, IEEE, Hong Kong, China, 27–29 Aug, 2009
25. Yu, M., Wang, L., Chu, T.: Robust stabilization of discrete-time systems with time-varying delays. In: 2005 American Control Conference, IEEE, Portland, OR, USA, 8–10 June, 2005

Control of Smart Grid Residential Buildings with Demand Response

Sergi Rotger-Griful and Rune Hylsberg Jacobsen

Abstract The higher penetration of renewable energies into the electrical grid and the increasing power demand will transform the current grid model. The traditional production-oriented grid will be replaced by a more dynamic grid, known as the Smart Grid, where consumption will be adapted to the momentary available production. Getting flexibility in the demand side is a multidisciplinary challenge that is gaining the attention of both academia and industry. This chapter describes a residential building that can support the electrical grid providing flexibility (demand response) to a third party (aggregator) and discusses about computational intelligence techniques to be used in this scenario. For that purpose, a virtual power plant of a residential building is used to regulate the energy resources in the building in an optimal way and bring flexibility to the grid by aggregating demand response of households. The virtual power plant receives as inputs sensor data of the building and also external information from the electricity market, the customers, the aggregator and prediction models. The computational intelligence of the virtual power plant processes all these inputs to make decisions about the flexibility to provide to the grid and to control the electricity systems in the building using a model predictive control. The content of the chapter is supported by a description of a pilot study carried out in the city of Aarhus in Denmark, where a prototype of a virtual power plant will monitor and control a building with 159 apartments.

Keywords Smart grid · Demand response · Residential buildings · Virtual power plant · Model predictive control

S. Rotger-Griful (✉) · R.H. Jacobsen
Aarhus University, Finlandsgade 22, 8200 Aarhus, Denmark
e-mail: srgr@eng.au.dk

R.H. Jacobsen
e-mail: rhj@eng.au.dk

A.T. Azar and S. Vaidyanathan (eds.), *Chaos Modeling and Control Systems Design*,
Studies in Computational Intelligence 581, DOI 10.1007/978-3-319-13132-0_7

1 Introduction

In the near future the electrical grid will experience a higher penetration of renewable energies, making it more challenging to balance the electricity generation with the consumption. This future electrical grid is known as the Smart Grid. In the Smart Grid, higher flexibility will be needed from the demand side to adapt their consumption to the intermittent generation of renewable energies in the absence of a feasible solution to store energy. Demand response is lately emerging to be a key tool for providing this flexibility.

The residential domain accounts for an important part of the overall consumption and can provide part of the required flexibility for balancing the electrical grid. The flexibility provided by a single household is modest, however a set of apartments grouped in a residential building present a load aggregation level interesting for the grid. Providing this flexibility to the grid while optimising the local energy resources of the building present a challenging control engineering problem.

The aim of this chapter is to present the challenges to be faced in the integration of a residential building in the Smart Grid, to propose a possible solution and to discuss the computational intelligence techniques applicable in this scenario. The chapter has been divided in the following way. The first part provides a brief introduction to relevant concepts and introduces the control problem in residential buildings. The second part presents the state of the art of demand response. The following section deepens on the monitoring and controlling of energy usage in a residential building. The final sections explain the different models used for optimisation and the customer involvement. Finally, the chapter ends with a description of an on-going pilot study in Denmark and the conclusions.

1.1 Towards the Smart Grid

In March 2007 the European Council set three key targets for the 2020 European Union's climate and energy policy [33]: 20–30 %reduction of greenhouse gases, 20 % electricity produced by renewable energies and 20 % increase in energy efficiency.

Fulfilling these goals will imply an increasing share of sustainable energy, which will mainly come from wind and solar resources. Compared to traditional power plants, these distributed energy resources are not available on demand, thus requiring a smarter way of balancing the electricity generation with the consumption. This future grid is known as the Smart Grid.

There is no precise and comprehensive definition of the Smart Grid but a large amount of definitions that complement to each other [14]. A possible definition follows:

The Smart Grid is the electrical grid of the future that by means of information and communication technology will handle a large amount of distributed energy resources, increasing the efficiency but also the reliability of the global system.

The interest on smart grids is growing. This is reflected on the increasing number of smart grid projects carried out in Europe [15].

The National Institute of Standards and Technologies (NIST) of the United States has been making a big effort on defining smart grid standards and protocols. One important contribution of the NIST is a conceptual model that helps to better understand the different actors involved in the Smart Grid (Fig. 1).

A key actor in the presented model is the *Customer* who in the absence of sufficient and feasible energy storage capacity will need to adapt the consumption to the *Bulk Generation* to support in balancing the grid. Among all the different customers, the residential domain accounts to an important part of the pie, leading to an estimation of 25 % of electricity consumed in residential buildings by 2030 [50]. The *Customer* aims to lower the energy operation while the grid aims to energy operation with a high degree of flexibility. The interplay of these two goals in the residential domain is discussed in this chapter, where a virtual power plant (VPP) is considered for such task.

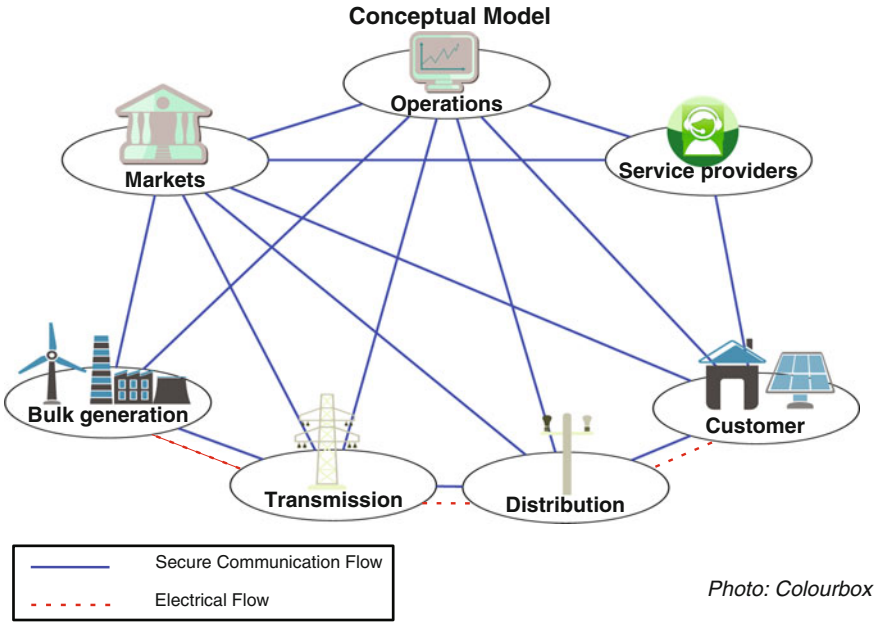

Fig. 1 Actors interaction in the different Smart Grid domains created by the National Institute of Standards and Technologies (NIST) [30]

There are several definitions of a VPP [25], however one that suits the purpose of the chapter is given:

> 'A VPP is a cluster of dispersed generator units, controllable loads and storage systems, aggregated in order to operate as a unique power plant.' [36]

It is very important to highlight that the VPP can aggregate load because the available flexibility in a single house is rather modest.

In the United States, there are about 40 curtailment service providers, that are able to aggregate up to 10,000 MW of flexibility on the demand side [17]. These entities mainly focus on big industries. In Europe, there have been different projects focusing on different aggregation levels: at a building level [2], at a neighbourhood level [27] and at a city level [10]. In this chapter a VPP aggregates load at a building level.

1.2 Control of Smart Grid Residential Buildings

This chapter addresses the challenge of integrating a residential building in the Smart Grid paradigm. A system level description of a smart grid residential building is shown in Fig. 2. The building may have some storage solution and local generation like a photovoltaic. The indoor climate conditions of the building are influenced by the external temperature but also for the presence of the customers (residents) and their actuation on electricity loads such as air conditioning. The electricity market will interact with the building by modifying the electricity prices.

In the scenario describe above, the VPP will take control over the energy resource of the building and optimise their performance based on price signals and outdoor conditions. At the same time, the VPP will provide some flexibility to the electricity market by means of demand response.

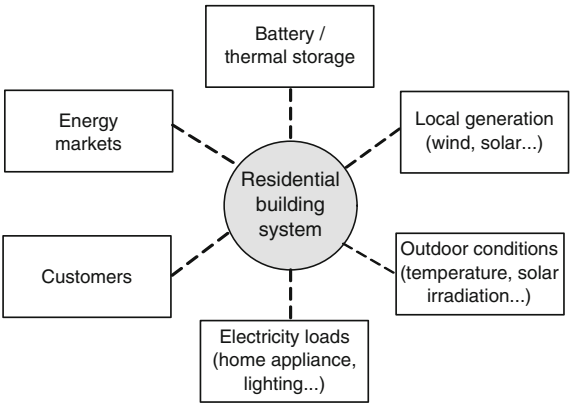

Fig. 2 Smart grid residential building system

Using the conceptual model introduced in Fig. 1, the VPP would be placed in the *Service Provider* domain. By means of sensors the VPP monitors the energy usage of the *Customers*, in this case a residential building. Upon external triggers, such as electricity prices provided by the *Market*, customers preferences, weather conditions etc. the VPP actuates over some electricity resources in the building. These resources can be classified in three areas [37]: Heating, ventilation and air condition systems (HVAC), lighting and plug-loads.

2 State of the Art in Demand Response

This section starts with a definition of demand response followed by an explanation of the benefits of providing it. The section finalises with a description of the different demand response triggers and demand response resources in the residential domain.

2.1 Demand Response Definition

The Department of Energy of the United States defines demand response as:

> 'Changes in electric usage by end-use customers from their normal consumption patterns in response to changes in the price of electricity over time, or to incentive payments designed to induce lower electricity use at times of high wholesale market prices or when system reliability is jeopardized.' [17]

The concept of demand response is easily misunderstood and confused. In some literature they use a similar concept like *active demand*, which means active participation of customers in the electricity market [6].

Demand response should be seen as a tool to provide flexibility on the electricity consumption. This implies that it is not directly an energy efficiency mechanism: energy efficiency measures imply a permanent change (reduction) on the electricity use, like replacing a regular bulb for a LED one, while demand response is a temporal adjustment on electricity consumption [17]. This adjustment does not necessarily imply a reduction of the electricity load but shifting the electricity consumption on time: reduce and increase load under certain circumstances.

Demand response can be expressed in many different ways, some of the most common ones are:

- Load reduction: Implies to reduce the electricity usage. Similar terms are *load shedding* or *peak clipping*.
- Load shifting: Implies to modify the energy consumption to shift the load to a more convenient time period.

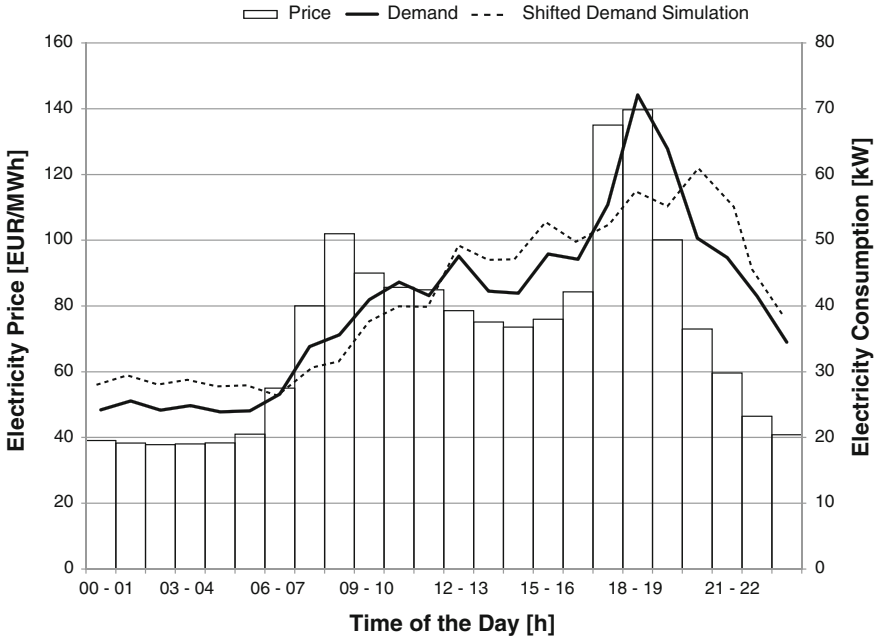

Fig. 3 Load shifting scenario. The electricity consumption data has been extracted from 154 apartments of the test bed building in Denmark. The electricity prices have been extracted from the Nord Pool Spot website (www.nordpoolspot.com). All the data corresponds to a winter day

Figure 3 illustrates a load shifting scenario. Electricity consumption can be moved to periods where prices are lower and reduced when the prices are higher. The overall energy consumption can be the same but the shape of the curve can vary. Some of the characteristics required to provide demand response are:

- Response time: Depending on the purpose, demand response will require a faster or slower response. The order of magnitude of the delivery time can vary from a few seconds to a few hours [19].
- Load shifted: This is the electricity energy consumption to be shifted (kWh).
- Start time and duration: The starting time and the duration when the mentioned load must be shifted.
- Value: Demand response provides flexibility that brings some service to the grid and therefore has value that can be reflected as a monetary remuneration for the customers. In [5], demand response has been considered as a resource in the trading market while in [17] the authors carry out a survey on different demand response programs where the price for demand response varies from 0.1–0.6 $ per kWh.

2.2 Demand Response Benefits

Demand response is an important resource that can provide several benefits for both the customers and the grid operators. There are several papers that discuss the advantages of it but they mainly focus in specific regions such as the European Nordic market [4] and the United Kingdom market [42]. Some of the benefits listed below have been extracted from the mentioned documents.

- Grid benefits:
  - Reduction of generation margin: Reduced peak demand may decrease investments in the total capacity installed[1] [17].
  - Avoid grid collapse/congestion: During contingencies demand response may act as a reserve capacity, offering load reductions to avoid grid congestion or collapse.
  - Valley filling: Demand response can help to fill the valley periods where energy is cheap.
  - Enable the Smart Grid: The flexibility provided by demand response can deal with intermittent energy resources, like wind and solar energy, and therefore can be an enabler for the Smart Grid.
- Customer benefits:
  - Electricity bill reduction: Demand response can provide to customers a reduction on their electricity bill.
  - Social responsibility: By providing demand response the customers have the opportunity of doing something for the greater good, e.g. reducing CO_2 emissions.

Some of the benefits mentioned above present some interest conflicts. From one side the grid aims to global optimisation while the customers aim to local (individual households) optimisation. The mismatch between these two goals is being studied and could be approached by monetary exchanges.

2.3 Demand Response Triggers

In order to identify the conditions that trigger demand response it is first necessary to introduce the different demand response programs. In the literature one can find various classifications of these programs, however they mainly fall into three categories [38]:

[1] The Federal Energy Regulatory Commission (FERC) estimated the contribution from existing United States demand response resources at about 5.8 per cent of 2008 summer peak demand. Moreover, FERC recently estimated nationwide achievable demand response potential at 138,000 MW (14 per cent of peak demand) by 2019.

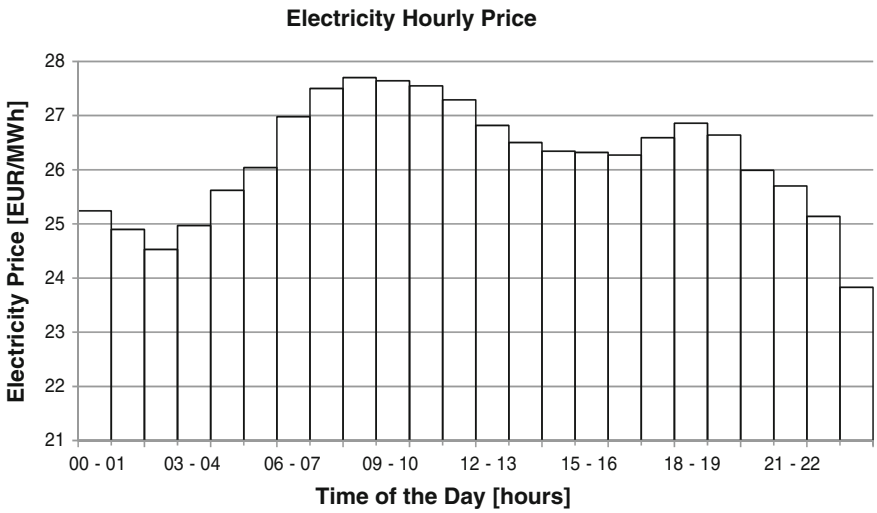

Fig. 4 Hourly electricity price for Denmark on 7 March 2014 extracted from Nord Pool Spot website (www.nordpoolspot.com)

- Price-based programs: These are market-driven programs which change the electricity price upon time slots. The main goal is to motivate customers to change their electricity consumption pattern. The hourly price variation of an electricity market is shown in Fig. 4.
- Incentive or event-based programs: In these programs a set of demand response requests are sent from the utility to the demand response provider. The main reason for this request is to provide reliability (ancillary) services to the grid.
- Demand reduction bids: In these programs customers send demand reduction bids to the utility company or aggregator. These bids would inform about the available demand to be shifted and the requested price.

Three different signals that trigger demand response have been identified from the described programs:

- Electricity price: The electricity price per time unit (EUR/MWh) is a control input for the demand response provider.
- Demand response request: The utility asks the demand response provider (aggregator) some flexibility in exchange of some economic incentives.
- Demand response offer: The demand response provider offers flexibility to the utility which accepts the demand response bid in exchange of an economic incentive.

2.4 Demand Response Resources

Demand response techniques in commercial buildings are addressed in [29] and some of the information can be extrapolated to residential buildings. In residential households demand response resources mainly fall in one of the three categories:

- HVAC systems: Heating, ventilation and air conditioning appliances have a large demand response potential. From one side they consume large amounts of power (order of kW) while the service that they provide, indoor climate conditions, can be stored by the thermal inertia of the building. In warm countries the main contribution would come from air conditioners. In cold countries there is a movement towards integration of heat pumps [12].
- Lighting: These systems are not as suitable for demand response purposes as HVAC systems because their energy consumption is lower and their usage very depends on the customers.
- Plug-loads: These loads differ from the previous ones on being distributed rather than centralised. The usage of appliances inside this category is very dependent on the customer willingness and their electricity power consumption varies from a few W to kW. The term smart appliance falls in this category. In [45] there is a full description on how smart appliances can provide the required flexibility. There is a growing interest in smart appliances, important white goods companies like General Electric and Whirlpool have announced that their future products will have the capability to react upon demand response signals such as electricity price [17].

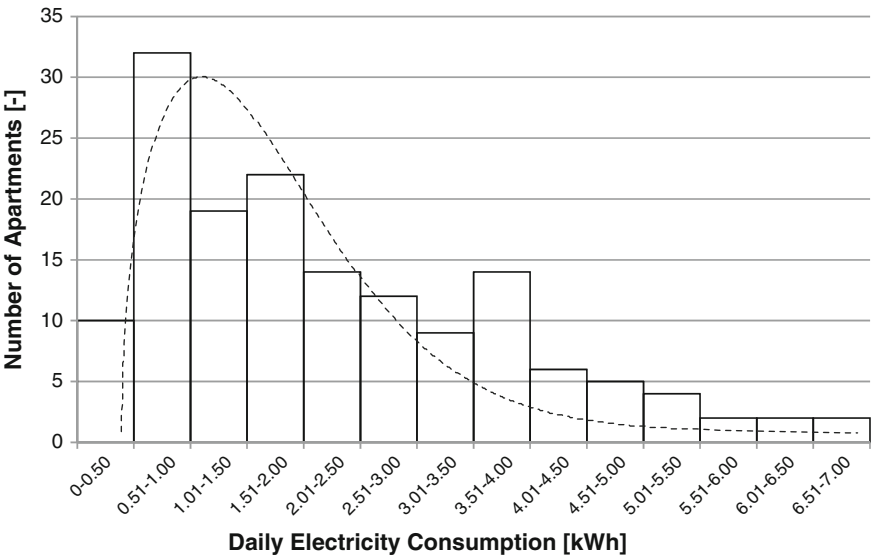

Fig. 5 Histogram of daily electricity consumption for a winter day. The data is extracted from the test bed building. The consumption data can be approximated by a *Log-normal* distribution

The demand response resources in a residential building can also be classified upon their controllability: automatic control (e.g. fridge), semi-automatic control (e.g. a washing machine) and manual control (e.g. coffee machine). This classification is related with the degree of involvement of the customer.

Although each person is different, people tend to have similar habits, like cooking at the same time, going to work at similar hours etc. These patterns are reflected in similar energy consumptions like shown in Fig. 5.

3 Monitoring and Controlling a Residential Building

The previous sections are meant to provide background information to introduce the reader in the key topic of this chapter: monitoring and controlling of a residential building to provide demand response by means of a VPP. First the overall architecture of the system is introduced. Second, the monitoring infrastructure is presented. Finally the control methods driven inside the VPP to provide demand response while optimising the energy usage of the building are described.

3.1 System Overview

The VPP is an entity with a two-fold objective: from one side it monitors and controls the energy usage in the building in an optimal way while from the other side it provides demand response to the electricity grid helping the stability of the latter. To achieve both goals the interaction with the customers and a set of external actors is crucial. The VPP has access to sensor data from inside the building. It receives information about the electricity price in the market and local weather forecast. The computational intelligence of the VPP processes all this information and through controllers it regulates the energy resources in the building.

The VPP is connected to an aggregator and provides demand response to it. The VPP may modify the optimal schedule of energy usage in the building to satisfy the needs of the aggregator receiving in exchange a monetary remuneration.

In the context diagram in Fig. 6 the VPP can be seen together with all the actors that interact with it. To better understand the overall system each actor is described in more detail:

- Aggregator: This actor represents an external system which is in contact with the distribution system operator and interacts with the VPP by exchanging demand response requests and offers.
- Electricity market: This actor represents the market where the electricity price is set. It provides the VPP with updated data of the electricity price profiles as the one shown in Fig. 4.

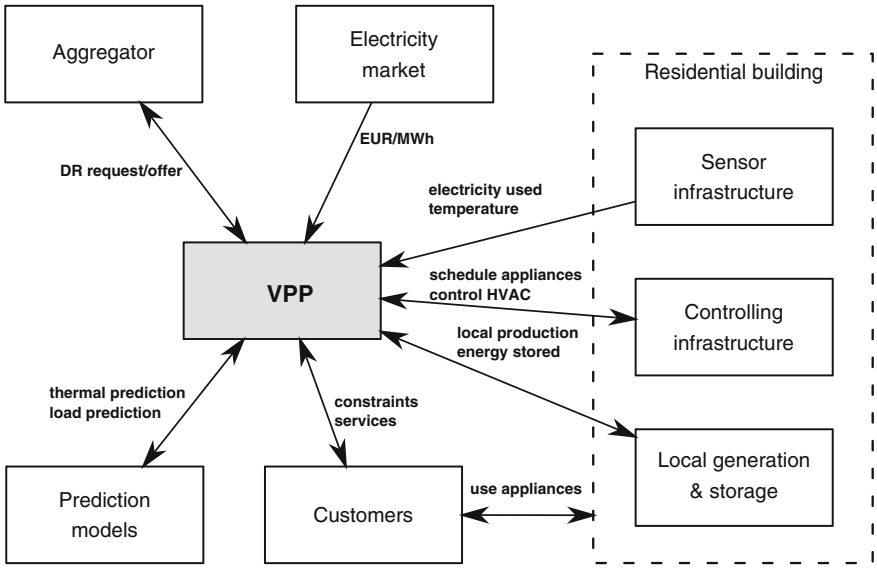

Fig. 6 Context diagram of a VPP of a residential building

- Local generation and storage: This actor represents the local production of electricity and the storage capacity in the building. The VPP decides whether the building should use local generation or stored electricity or buy it to the grid.
- Customers: This actor represents the residents and people who interact with the VPP by setting some constraints in the indoor climate conditions, by getting some services, like energy optimisation, and by responding to some petitions, like load shifting.
- Controlling infrastructure: This actor represents all the electronic equipment that provides the VPP with control over the energy consuming devices in the building.
- Sensor infrastructure: This actor represents an external system that provides the VPP with updated data of the energy usage and other local information send by sensors in the building.
- Predictions models: This actor represents external systems that provide forecast on local weather, load prediction and thermal conditions among others.

3.2 Monitoring Infrastructure

Monitoring of the energy usage is the first necessary step towards the integration of the VPP in a residential building. The monitoring program of the VPP supports the system operation, enables fault detection and control decisions. The information

provided is useful for the residents because they can gain a better insight on their energy habits and they can be provided with energy recommendations for a more sustainable and economic behaviour. These data are also useful for the grid because they can gain understanding on the energy habits of the end-users.

The VPP of a residential building monitors the energy usage in the building and information from external systems. The list below provides the different information that is under observation by the VPP:

- Electricity consumption: The electricity consumed in the different households and common areas in the building is used for customer awareness and to support control tasks.
- Indoor climate conditions: The environmental conditions of the building like the temperature, humidity and CO_2 level are used for regulating the HVAC systems for optimal indoor climate conditions. Additionally, in absence of passive infrared sensors[2] the CO_2 concentration can provide an estimation of human presence.
- Water usage: By monitoring the water consumption the customers can receive some recommendations on their water usage. Additionally, the use of water in an apartment can also be an indicator of whether a person is at home or not.
- Local production and storage: The produced and stored energy is monitored by the VPP to decide whether to buy electricity from the grid or to use the locally produced and/or stored. In addition, the VPP can decide when the electricity price is low to buy electricity and recharge the battery. There are several international standard of performance monitoring of different local production options, like photovoltaic power system, and battery solutions. Some of these standards are presented in [16].
- Electricity price: The electricity price per time unit is used for the VPP to optimise the economic benefits of the customers. From one side by scheduling the operation of several electric consumption devices (HVAC, lighting and plug-loads) and from the other by deciding when to buy energy or when to use the locally produced and/or stored. In a price-based demand response program it can also be used for demand response provision.
- Weather forecast: The outdoor weather conditions are used by the VPP for optimal control of HVAC systems and make use of the thermal storage of the building.

The VPP monitors all the information listed above in near real time. The information from electricity consumption, indoor climate conditions, water usage and local production and storage is provided by a sensor network deployed in the building. The other information is provided by external actors.

Important information that could be extracted from all the observed data is the presence of a person inside an apartment. Knowing if a home is empty would enable the VPP to carry some actions such as switching off devices with standby

[2] Passive infra-red (PIR) sensors are used for motion detection.

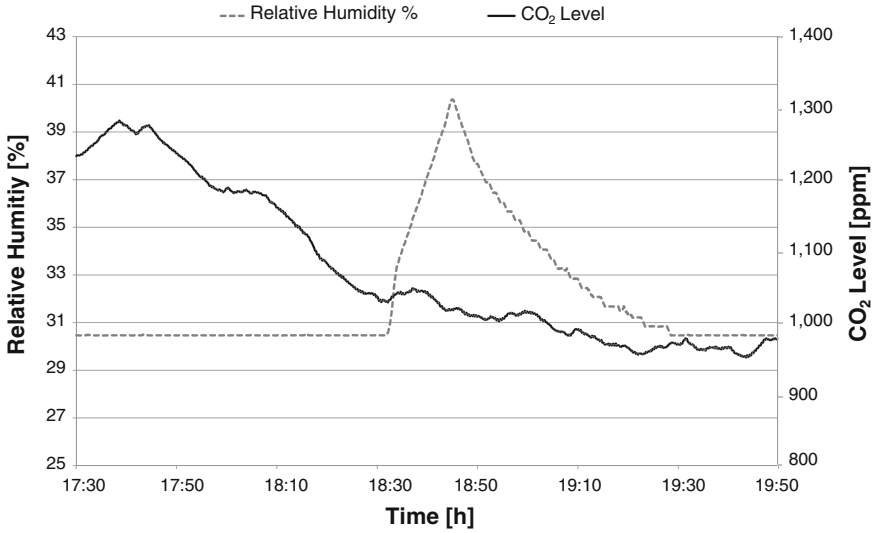

Fig. 7 Monitoring indoor climate conditions. Relative humidity and CO_2 concentration level of an apartment in the test bed building in Denmark with 5 s resolution

mode or modifying the indoor climate conditions. Computational intelligent techniques such neuronal networks and support vector machine regressions could be used to obtain a reliable and computationally fast model to identify the presence of a person in an apartment based on data like CO_2 levels, water usage and electricity consumption. An example of the data that the VPP is monitoring can be seen in Fig. 7, where the indoor climate conditions of an apartment are shown.

With high granularity electricity consumption data it is possible to use pattern recognition models to accurately identify the different electronic devices being used [7]. This can enable the VPP to provide demand response in a fast manner but also to analyse possible malfunctions of electric appliances. In [34] the authors present the profile of several home appliances with a resolution of one second. These data can be used to gain insight on the demand response potential of different white goods but also to develop accurate electricity load models.

3.3 Building Control with Demand Response Support

Building automation systems can reduce electricity costs by shaping the demand profile. It is possible to switch the peak demand by making use of the thermal mass of the building and local electric storage and production. However, this requires planning based on detailed information of current and prediction of future states in weather conditions, building usage and electricity prices among others.

The basic operation of the building is to maintain a high level of comfort for the residents while at the same time keeping operational costs low. This includes minimizing the energy consumption and the carbon dioxide emission related to the building operation. This implies balancing the heat in the building zones to control temperatures and to balance air to control pressures and pollutants e.g., carbon dioxide at appropriate concentration levels. This operation is a complicated task since disturbances such as external temperature, solar irradiation, wind and humidity conditions change over time. In addition, heat gains from electrical equipment, lighting, heat and air losses need to be part of the equation. Finally, the presence and behaviour of the residents must be taken into account.

Logic-based management systems utilizing decision tree rules (e.g., if-then-else statements) are widely used for energy management in literature. In [47], the authors introduce a three-level hierarchical rule-based supervisory control using fuzzy logic to regulate a low energy building. They claim that fuzzy rule based controllers are suitable for systems with high uncertainties like the latter. In [49], the authors propose an operational building automation system to be conceptually decomposed into hierarchical levels such as unit commitment (e.g., the start-up and shut-down of equipment), economic dispatch governed by energy market prices and feedback and control. This leads to a decision hierarchy in which each branch in the tree can be assigned a weight reflecting the incentives governing the decision e.g., economic incentives. The authors propose a proactive optimisation-based energy management framework able to incorporate disturbances forecasts and predictive building models [49]. The goal is to find optimum policies for a set of binaries modelling the on/off behaviour of appliances and a set of continuous control variable that minimise future and expected costs of the building system operation.

Intelligent thermal mass control strategies can then be identified in a simulation environment using an analysis tool such as the one presented in [9]. It is argued that it is only necessary to change the control strategy used for adjusting zone temperature set-points. This puts limitation on how quick a response can be obtained from the control of a heating and cooling system of a building. Earlier studies have also shown that the energy saving potential and 'best' control strategy are very dependent upon the system and particular weather conditions [9].

The main problem of current energy management systems is that their control is reactive, implying that the control decision are made with the current states of disturbances and system variables. This can lead to instability of the system due to a high frequency in start-ups and shut-downs. In [26], the authors analyse the different control inefficiencies in HVAC systems and outline possible approaches to tackle these problems, like model predictive control (MPC). MPC has lately emerged as a suitable solution and has been used in many studies to regulate HVAC systems in buildings [21, 46]. MPC has also been used to regulate lighting, local storage and local production [31, 49]. The main benefit of using MPC is its inherent ability on tackle complex dynamics and system constraints.

The control algorithm that VPP uses to regulate the energy resource of a residential building is based on a MPC. This controller regulates the HVAC system, the lighting system, some plug-loads, the local storage and the local production. The

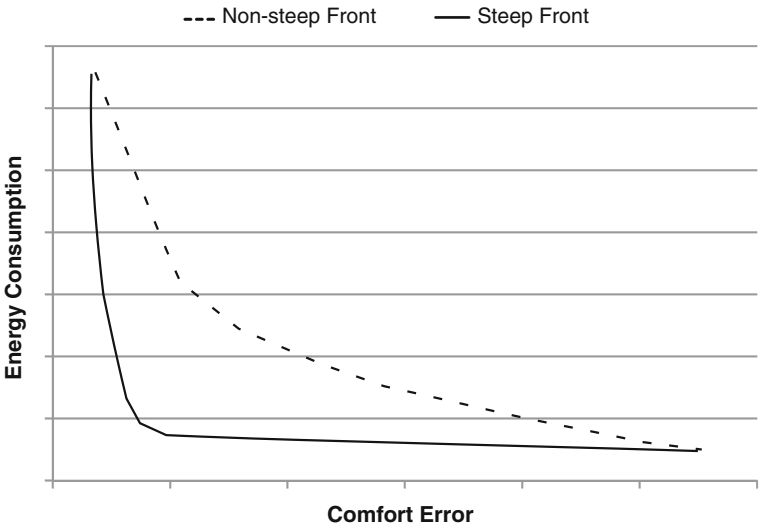

Fig. 8 Steep and non-steep Pareto fronts

control variables are chosen by solving a multi-objective optimisation problem: maximise residents comfort, minimise electricity costs and provide demand response. The latter optimisation parameter can be defined as minimising the difference between the current and the desired electricity consumption with a demand response event. Some studies also include the CO_2 emissions in the optimisation function (e.g. [46]), however CO_2 levels have not been considered in this work.

Multi-objective optimisation functions may have the problem of conflicting goals, also known as Pareto efficiency, meaning that one cannot minimise one parameter without incrementing another. This problem is addressed in [48] where they try to maximise the user comfort and minimise the electricity usage. This situation can be better understood by an illustration of the Pareto front[3] in Fig. 8. If a Pareto front is steep it means that a short error in one optimisation parameter leave to a high divergence in another: a short error in the comfort leads to a higher energy consumption. It is then necessary to use the flexibility in one parameter, e.g. resident's comfort, to increase the overall performance. In [48], the authors solve this problem by a utopia-tracking approach where they minimise the distance to the utopia point rather than calculating the Pareto front. However, this problem can also be miti-gated by introducing soft-constraints in the designed MPC. The main disadvantage of using this kind of constraints is that per each soft-constraint a new optimisation parameter is introduced, increasing the computational time and complexity when solving the equation.

[3] The Pareto front is a curve that represents the optimal performance for a multi-objective optimisation with conflicting goals.

Computational intelligence techniques such as genetic algorithm (GA) and particle swarm optimisation (PSO) have been used to solve multi-objective optimisation problems with conflicting goals. In [32], the authors proved that using PSO in a multi-objective optimisation can solve efficiently well-known problems such as concavity and discontinuity of the Pareto front. In [18], the authors claim that by using a PSO they speed up the search of the Pareto front for a multi-objective optimisation, which may be even more critical for steep fronts due to the need of good resolution in the steeped part of the curve. Apart from PSO techniques, GA can also be used to solve multi-objective optimisations. In [22] the authors use a GA using a specialised fitness function and implementing methods to stimulate solution diversity.

Another problem that the VPP needs to tackle is the fact that some of the variables in the system are binary variables (e.g. on/off actuators). In linear systems with non-continuous variables, the optimisation function cannot be solved by the regular techniques and requires solving a mixed-integer linear problem (MILP). In [41], a similar multi-objective MILP problem to the one solved by the VPP is presented. The authors goal is to minimise the annual energy costs of a building with local generation and storage subject to a set of constraints (e.g. energy balancing) to design an optimal operating schedule and decide on investment of new technologies (e.g. inversion on new photovoltaic). The problem faced by the VPP is slightly different than the latter due to the non-linearities present in building energy systems, leading to solve a mixed-integer non-linear problem (MINLP) instead.

The problem to be solved by the VPP differs from the reviewed above on the need to provide demand response. The demand response is triggered by electricity prices established by the electricity market but also by demand response petitions of the aggregator. The choice of optimisation targets motivates demand response provision. It is important to highlight that the VPP does not trade demand response with the electricity market, this negotiation is handled by the aggregator who sends demand response petitions to the VPP. If that was the case, the VPP should incorporate game theory or agent-based systems [49]. The VPP receives demand response petitions in a similar way as defined in [40]: it receives a starting time of the demand response event, duration and a load to be shifted. Additionally, a monetary value associate to the demand response event could be included [40]. This income would need to be considered in the optimisation function but for simplicity it has been omitted.

The block diagram of the designed MPC that controls the energy usage of a residential building is shown in Fig. 9. The functionality of the systems is the following. By means of sensors the current states of the building (temperature, electricity consumption etc.) are measured and fed into the building model. With the provided measurements, the control signal and the disturbances (e.g. weather conditions) the building model makes a prediction on the system values. These predicted values are fed in the optimisation block together with the cost function and the constraints that must be held to define the control actions. The control signals are sent again to the model until the prediction horizon is reached, when the control signal is sent to the different subsystems inside the real building. The

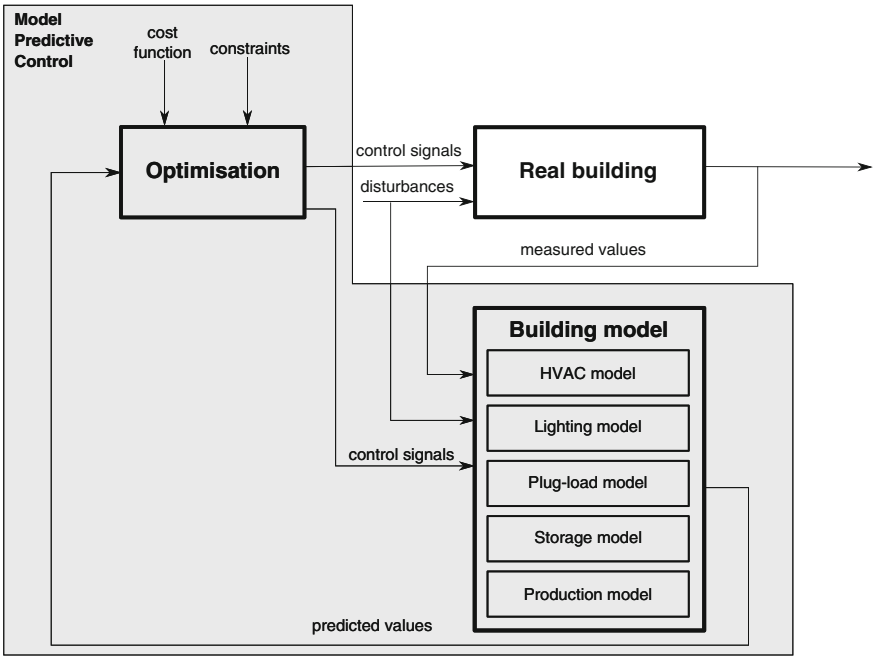

Fig. 9 Block diagram of the model predictive control of a residential building

described process is iterative and the performance of it depends on the prediction horizon, the estimation accuracy, the weight parameters in the optimisation function and the constraints.

Following the typical control nomenclature the system variables at the kth instant are $x(k)$, the control inputs are $u(k)$, the measurements are $y(k)$ and the disturbances are $d(k)$. The system variables can be expressed as:

$$x(k) = [x_{\text{hvac}}(k)\ x_{\text{lighting}}(k)\ x_{\text{plug-load}}(k)\ x_{\text{storage}}(k)\ x_{\text{production}}(k)]^T \quad (1)$$

Examples of these variables could be indoor temperature, indoor light level, home appliance consumption, battery capacity and nominal production. The control inputs can be expressed in a similar way:

$$u(k) = [u_{\text{hvac}}(k)\ u_{\text{lighting}}(k)\ u_{\text{plug-load}}(k)\ u_{\text{storage}}(k)\ u_{\text{production}}(k)]^T \quad (2)$$

Examples of these variables could be turning on/off a fan, a window control, signals to smart plugs, discharging the battery and control parameter to regulate the local production (e.g. pitch angle in a wind turbine). The system disturbances considered are mainly of two kinds: outdoor weather conditions and human behaviour. The former act as a slow dynamic disturbance while the second as a fast disturbance.

The optimisation function to be solved takes into account four different targets: minimise the electricity costs, minimise the residents discomfort, minimise the difference between the electricity consumption and the desirable if providing demand response and minimising the divergence on the soft-constraints. The optimisation function is restricted to hard-constraints, that cannot be violated, and soft-constraints, that can be violated but it is not desirable. An example of a hard-constraint is that the consumed electricity is equal to the sum of local production, battery use and grid electricity. An example of soft-constraint is the comfort level of the residents. The mathematical formulation of the optimisation problem is the following:

$$\min(w_1\Phi_1 + w_2\Phi_2 + w_3\Phi_3 + w_4\Phi_4) \tag{3}$$

$$s.t.\ h_{\text{hard}}(x,u,d) \leq 0 \tag{4}$$

$$h_{\text{soft}}(x,u,d) \leq 0 \tag{5}$$

where w_i is the weight to each of the different targets Φ, h_{hard} and h_{soft} are the hard and soft-constraints respectively. Each optimisation function Φ is reflecting one of the optimisation criteria:

$$\Phi_1(k) = \text{EL Price}(k) \cdot \text{EL Consumption}(k) \tag{6}$$

$$\Phi_2(k) = f(\text{temperature}(k), \text{CO}_2(k), \text{humidity}(k)) \tag{7}$$

$$\Phi_3(k) = \|\text{EL Consumption}(k) - \text{EL Consumption DR}(k)\| \tag{8}$$

$$\Phi_4(k) = \|\varepsilon(k)\| \tag{9}$$

where *EL Consumption* means the electricity provided by the grid and ε are the new variables introduced due to the soft-constraints:

$$x_{\min} - \varepsilon(k) \leq x(k) \leq x_{\max} + \varepsilon(k) \tag{10}$$

The different optimisation criteria Φ have different metrics and need to be normalised. Φ_1 concerns the economic costs, Φ_2 the resident comfort, Φ_3 the demand response and Φ_4 the soft-constraints.

As mentioned before, the optimisation problem defined is a MINLP and it is not easy to solve. Two different ways of solving MINLP problems are proposed in [49]: warm-staring technique and approximation and hierarchical approaches. The warm-starting technique is based on the fact that the solution at the kth instant is closely related to the one at the $(k + 1)$th instant. The second approach aims to obtain an alternative approximation solution based on hierarchic decomposition and linearisation of the problem. Beside the complexity of the problem, another challenge that the VPP needs to tackle is to solve the optimisation problem in an efficient and fast manner to provide the services required. A possible solution in order to simplify

and faster the calculation is the use of the utopia-tracking proposed in [48] or to reformulate and relax the proposed problem as described in [1]. Nevertheless, there is a need of computational intelligence techniques to solve the proposed problem.

4 Prediction Models for Optimisation

The control strategy presented in the previous section is based on a set of models of different nature. When regulating HVAC systems the building's physics are usually modelled, e.g. thermal model of a system [31, 51]. Local weather forecast models are also used in this scenario. When regulating plug-loads and lighting systems the involvement of the user is larger than for HVAC systems. For the latter, there are a set of load forecasting models that are based on the behaviour of the customers rather than the physics of the building. The optimisation function presented before needs a price signal for maximising the profit of the customer. This price can be provided by the electricity market or by a model. All these models mentioned above can be used by the VPP for its operation.

In addition to the prediction capability, the VPP needs models that are able to run in an efficient and fast manner because they are iteratively used by the MPC. This section presents some of these models that could be used by the VPP for its operation. Some of the models presented could be used to construct the building model shown in Fig. 9 while others, e.g. electricity price models, could provide information to be used in the optimisation algorithm. Computational intelligence techniques, such as neuronal network, present interesting advantages that are discussed in the following subsections. Table 1 summarises the benefits that each model described can provide to the VPP.

4.1 Thermal Models

A thermal model of a system, e.g. a residential building, is able to predict the thermal indoor conditions for a given set-up (indoor temperature, outdoor

Table 1 Models used for optimising the energy usage in a building

Model	Benefits for energy optimisation
Thermal	Support control strategy by predicting indoor climate conditions to ensure customer thermal comfort (HVAC model)
Local weather forecast	Providing weather forecast data to be used in thermal and load prediction models (support HVAC and load prediction models)
Load prediction	Provide an estimation of the electricity load to plan but also to assess demand response strategies (lighting and plug-loads models)
Electricity price	Schedule the electricity usage to optimise the monetary benefit (optimisation function)

temperature, humidity etc.). There are different techniques to provide a forecast of the indoor climate conditions of a building.

In [31, 51], the authors present a model based on heat transfer theory to predict the environmental conditions. The predicted values are used to optimally control the indoor climate conditions of the building, i.e. minimising energy consumption and maximising user comfort. In [44], the authors describe a numerical model that is able to predict indoor environment conditions such as air temperature, air velocity and water vapour pressure in the air. The proposed model is based on computational fluid dynamics.[4] The authors claim that their model can be used to predict the thermal comfort accurately.

In [23], the authors describe a model based on dynamic neural network. They used this model for a multi-objective optimisation similar to the one solved by the VPP: maximise energy savings and keep room temperature at an acceptable level. To solve this optimisation problem they used a PSO algorithm. The authors demonstrated the performance of the model in a test bed and claim savings up to 30 % of energy while keeping the temperature at an adequate range.

The methods described above provide an estimation of the indoor climate conditions like temperature and humidity. The firsts introduced models are based on the physics of the system while the last one is based on data mining. The main advantage of using a data-based approach is simplicity: there is no need of explicit knowledge about the underlying physical process being modelled and non-linearities of physic-based models can be removed [46]. Both types of prediction models can be used by the VPP in the HVAC model for an optimal control of the thermal conditions in a building. By means of these models, the VPP can forecast the results of control strategy and assess whether or not the customer thermal comfort would be compromised.

4.2 Local Weather Forecast Models

The building thermal models described in the previous section require some outdoor values, e.g. the local outdoor temperature, to predict the thermal behaviour inside a building. These environmental conditions can be provided by a local weather forecast model.

Weather forecast models can provide different kinds of information. In [8], they present a model named THOR that is able to provide forecast on air pollution on a local level, i.e. street level. In [31], instead of modelling the weather conditions they model the uncertainty of the weather information provided by the national weather service of Switzerland (MeteoSwiss). The authors use the outside temperature, wet-bulb temperature and solar radiation provided by MeteoSwiss to control the indoor

[4] Computational fluid dynamics (CFD) is a branch of fluid mechanics that solve problems related with fluid flows using numerical methods and algorithms.

climate conditions of the system. Additionally, they use the model of the uncertainty on the weather information as a disturbance in their control loop.

Local weather forecast models provide information that can be introduced in a building thermal model (physics-based and data-based). Therefore, the VPP can use these models to get an estimation of the local outdoor environmental variables, e.g. outdoor temperature and air pollution, and use these values as input parameters in a thermal building model.

4.3 Load Prediction Models

Load prediction models are able to predict the electricity consumed in facilities, i.e. a residential building. There are different methodologies to provide a prediction of the energy usage in a building. Some of these techniques are described below.

In [20], the authors present a model based on neuronal networks to predict the energy consumption in buildings. They analyse which input variables are suitable for obtaining good estimation on the electricity usage. They reached the conclusion that weather variables such as solar irradiation and local temperature are important to obtain an accurate result while other like humidity and wind speed are not relevant. The authors claim that they can obtain an accurate 24 h forecast of the electricity load.

In [28], they use a linear regression-based model. This model has as input variables time of the week and outdoor air temperature. The authors used the predicted load to assess the effectiveness of demand response strategies that have already occurred. They used the load prediction model for estimating what would have happened in case a demand response event had not occurred.

Load prediction models can be used by the VPP to get an estimation of the future energy usage in a building, e.g. lighting and plug-loads, and schedule demand response events. Additionally, the VPP can use these models to assess the previous demand response events in a similar way as described in [28].

4.4 Electricity Price Models

These models provide a forecast of the electricity market price and are usually used by power producers. This forecast can also be used by electricity consumers in order to optimise their profits.

There are several models that are able to predict the electricity price given certain input parameters. These models can be classified in two groups: hard-computing and soft-computing models. In the first group there are techniques such as auto-regressive and autoregressive integrated moving average models. In the second group there are techniques such as artificial neuronal networks and fuzzy neuronal

networks. Among all the different models artificial neuronal networks have received the larger attention.

In [3], the authors present a neuronal network model that is able to predict the electricity price for a day-ahead deregulated market. The model uses as input variables the previous electricity price in three time frames: previous hours, previous days and previous weeks. They pre-process these data and introduce it into a feed-forward neuronal network. They have tested their model in two scenarios, one in Spain and the other in the United States, and they have compared their results with 17 other methods. The authors claim that their model is able to produce results with an average accuracy of around 5 per cent within a computational time of 15 ms.

Electricity price models like the one described above provide useful information to the electricity customers because they can adapt their electricity consumption to the price. The VPP can use these models to optimally schedule the load profile in such a way that maximises the profit of the customers.

5 The Involvement of the Customer

The traditional electrical grid considered the electricity consumers as simple load points. However, in the Smart Grid the consumers play a much important role: they consume electricity but they also provide some flexibility or even energy to the grid. It seems that now the traditional consumer is being replace by prosumer, term created by Alvin Toffler in 1980 which stands for the combination of producer and consumer [35]. In this scenario, new services and tools will be deployed to motivate and ease the higher level of engagement of the customers. This section discusses the new role that the customers will play in the Smart Grid.

5.1 Customer Awareness

The first step towards engagement of the customer with the electrical grid is consumption awareness. Most of the customers are agnostic on the electricity they use, they are not conscious about the amount of energy they consume or in which manner they use that energy. Some surveys claim that the customers are willing to get a better understanding of their energy behaviour, both in a device level but also in an aggregate level [39]. There have been many studies on providing feedback to customers about energy consumption in different countries and with different set-ups, regardless of their differences they all claim energy savings of 10 % in average [13].

The feedback programs use different time frames and have different characteristics, however they all can be classified in one of these two categories [13]:

- Indirect feedback: Provide information to the customer after the consumption of energy has occurred.
- Direct feedback: Provide near real time feedback, delayed from a few seconds to a few minutes, on the electricity consumption.

In both cases, the energy information provided to the customer should be easy to understand for the non-technical people and should ensure the privacy of the user. The information collected by the VPP through the monitoring infrastructure can be used to provide customers with feedback on their energy consumption contributing that way to increase the customer awareness.

5.2 Customer Involvement

The next step towards a higher engagement of the customer with the electrical grid is an active participation by shaping their electricity consumption to the needs of the grid. To which extend and how the customer committed is a topic that is being studied thoroughly.

A first challenge in this scenario is to make people understand the need of demand response. Energy efficiency and demand response have been proved to be complicated concepts that require an effort from the customer who would need to be educated [17]. Some surveys show that the customers are not yet willing to learn such new concepts [24].

A first logical step to make the customer adapt their electricity consumption is by providing monetary incentives. The main problem is that there is still the feeling that one should not renounce to some privileges, like taking a long shower or baking rolls in the oven, for energy concerns. These task are seen from the customer as non-negotiable practices [43], and a decrease of cost would not change customers behaviour. The idea of schedule activities to adapt energy consumption is still unacceptable for many.

Taking all constraints that the customers may have three different kind of control strategies have been defined depending on their level of involvement. These three different kinds of interventions have been integrated in the VPP:

- Back stage interventions: In these interventions the customer is not involved but can feel the effects of it. These kind of interventions are the most attractive for the grid because they do not depend on customer behaviour and are therefore more reliable. The designed MPC takes care of these actions.
- Back-front stage interventions: The customer is partially involved on the control strategy. A good example of this intervention can be an optimal control of the indoor climate conditions of a household. The customer sets some constraints on the maximum and minimum temperature that is willing to accept as well

humidity levels and other indoor climate conditions. Then the VPP optimally regulates the HVAC systems to satisfy the needs of the customer. The designed MPC takes care of these actions.

- Front stage interventions: In this kind of interventions the customer is directly involved and is required to actuate. A good example of this intervention would be to ask the customer to put their laundry at a certain time. The designed MPC is not responsible of these actions. A significant divergence between the electricity consumption and the desired consumption profile (with demand response events) will trigger this kind of interventions.

In the on-going pilot study in Denmark the engagement of the customer will be analysed by means of flexibility concepts. A first flexibility concept is based on the thermal comfort. The customers will set some preferences on their indoor climate conditions and the MPC of the VPP will ensure the comfort of the residents. A second flexibility concept is based on providing the user with forecast information on electricity prices, energy recommendations but also show them their consumption through a mobile application. The idea is to influence the customer's behaviour and engage them.

6 A Pilot Study

The proposed concept of the VPP is being under study and development in a Danish research project called *Virtual Power Plant for Smart Grid Ready Buildings and Customers* (VPP4SGR). This on-going project was started in spring 2013 and aims to develop a VPP to monitor and control the energy usage of a residential building while providing demand response to the grid. An active participation of the residents of the building is crucial to provide the required flexibility. This engagement is also being investigated in the project by a group of anthropologists.

The VPP4SGR project uses as a test bed a newly constructed low-energy building with 12 floors and 159 apartments named Grundfos Dormitory Lab placed in the city of Aarhus in Denmark. The building is equipped with district heating, ventilation, heat recovery on waste-water and general consumption. The energy usage in the building is being monitored by more than 3,000 sensors that provide data with a 5 s resolution on indoor climate conditions, electricity usage, district heating and domestic water use per each of the apartments. The Grundfos Dormitory Lab is the house of around 180 students who live either in individual apartments or two-person apartments. Each apartment has a size no larger than 40 m^2 and is equipped with oven, stoves, extraction hood and other devices. The students do not have laundry or dryer in their apartment but there is a common laundry room in the basement.

The consumption profile of the dormitory is shown in Fig. 10. The electricity consumption oscillates around 325 kWh per day. It can be observed that the electricity consumption decreases during the weekends. The observed big drop is

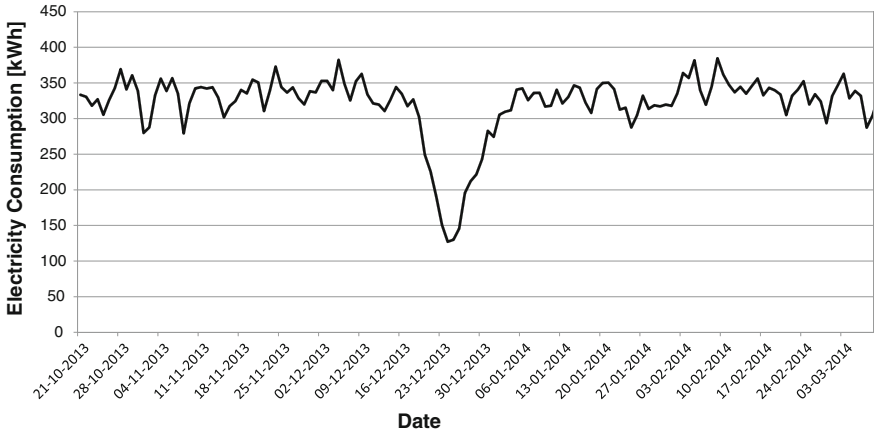

Fig. 10 Electricity consumption of the Grundfos Dormitory Lab from 21 October 2013 to 09 March 2014

due to the Christmas holiday, when most of the students were not in their apartments. A first analysis of the data shows that the daily electricity consumption of all the apartments (excluding laundry room) can be approximated as a *Log-normal* distribution with around 70 % of the apartments consuming between 1 and 2.5 kWh per day. In [11], the authors have analysed a different data set of aggregated electricity consumption in residential households leading also to a *Log-normal* distribution. The low consumption profile of the apartments is caused by the fact that the apartments are small, they are occupied by one or two people and they are not equipped with heavy consuming appliances such washing machine or dishwasher.

All the data collected during the development of this project will be analysed using data mining techniques. To that extend, computational intelligence techniques such as neuronal networks or support vector machine can be used to construct the required models to run the MPC.

The project is expected to provide recommendations on the construction of future buildings and the improvement of the existing ones to be ready for the Smart Grid. Additionally, the project aims to develop models to better understand the energy behaviour of the customers and to gain insight and provide recommendations on means to involve the customers to a larger degree.

7 Conclusions

The upcoming electrical grid, known as the Smart Grid, will need to handle a higher penetration of distributed energy resources thus turning the traditional production-based system towards a demand-based system. This new grid will open a wide

range of opportunities but also challenges. This chapter presents some of the challenges to be faced by a residential building in that scenario and ways to tackle them. This is done by using a VPP that monitors and controls the building's energy resources and provides demand response to the grid.

It is expected that in the near future the present shortcomings to introduce demand response will be solved. This will be achieved by a higher penetration of information and communication technologies together with new control strategies that will enable a more automatic and user-friendly manner to provide demand response. The solution presented in this chapter uses a centralised entity, a VPP, which is responsible of gathering all the required information to rule a residential building.

The VPP takes control over the HVAC systems, the lighting, some plug-loads, the local storage and the local production installed in the building by using a MPC. The designed control strategy aims to optimise the energy resources of the building and provide flexibility to the grid by: minimising the electricity costs, maximising the customer comfort and minimising the difference between the electricity consumption with and without demand response provision. This latter parameter in the optimisation function has not been found in the literature and together with the electricity price minimisation promotes the provision of demand response to the grid.

In order to tackle the conflicting goals identified in the multi-objective optimisation function the proposed MPC uses soft-constraints, thus incrementing the complexity of the optimisation. The optimisation problem has been identified as a MINLP due to the presence of binary variables and non-linearities in the system. The chapter gives an overview of how could this problem be solved and raises the need of computational intelligence techniques to solve this task in a fast and efficient manner.

The proposed MPC uses a set of models during its operation which need to have a short executing time and good accuracy. Among the different techniques that have been presented for the different models, computational intelligence techniques such as neuronal networks and support vector machine present promising results that need to be further investigated.

The on-going research expects to be able to deepen the knowledge on the domain with the presented test bed. Questions like a suitable weight for the different optimisation parameters, the required computational power of the VPP but also suitable models to explain the electricity consumption are expected to be answered during the development of the VPP4SGR project.

The proposed chapter has presented the integration challenges of a residential building in the Smart Grid, it has proposed a solution and has discussed about the computational intelligence techniques to be used in this application domain.

Acknowledgements The work in this document has been funded by the Danish Energy Agency project: Virtual Power Plant for Smart Grid Ready Buildings and Customers (no. 12019).

References

1. Abraham, A., Hassanien, A.E., Siarry, P., Engelbrecht, A.: Foundations of computational intelligence volume 3. In: Studies in Computational Intelligence, vol. 203. Springer, Berlin. (2009). doi:10.1007/978-3-642-01085-9
2. Albano, M., Ferreira, L., Le Guilly, T., Ramiro, M., Faria, J.E., Duenas, L.P., Ferreira, R., Gaylard, E., Cubas, D.J., Roarke, E., Lux, D., Scalari, S., Sorensen, S.M., Gan-golells, M., Pinho, L.M., Skou, A.: The ENCOURAGE ICT architecture for heterogeneous smart grids. In: Eurocon 2013, IEEE, pp. 1383–1390 (2013). doi:10.1109/EUR0C0N.2013.6625159
3. Anbazhagan, S., Kumarappan, N.: Day-ahead deregulated electricity market price forecasting using neural network input featured by DCT. Energy Convers. Manag. **78**, 711–719 (2014). doi:10.1016/j.enconman.2013.11.031
4. Andersen, F.M.l., Jensen, S.G., Larsen, H.V., Meibom, P., Ravn, H., Skytte, K., Togeby, M.: Analyses of demand response in Denmark. Technical report 1565, Risø National Laboratory, Roskilde, Denmark (2006)
5. Arasteh, H, Parsa Moghaddam, M., Sheikh-El-Eslami, M., Abdollahi, A: Integrating commercial demand response resources with unit commitment. Int. J. Electr. Power Energy Syst. **51**:153–161 (2013). doi:10.1016/j.ijepes.2013.02.015
6. Belhomme, R., Cerero, R., Valtorta, G., Eyrolles, P.: The ADDRESS project: developing active demand in smart power systems integrating renewables. In: 2011 IEEE Power and Energy Society General Meeting, IEEE, pp. 1-8 (2011). doi:10.1109/PES.2011.6038975
7. Belley, C., Gaboury, S., Bouchard, B., Bouzouane, A.: An efficient and inexpensive method for activity recognition within a smart home based on load signatures of appliances. Pervasive Mob. Comput. (2013). doi:10.1016/j.pmcj.2013.02.002
8. Brandt, J., H Christensen J, M Frohn L, Berkowicz R, Palmgren F (2000) The DMU-ATMITHOR air pollution forecast system—system description. Technical report 321, National Environmental Research Institute, Roskilde, Denmark
9. Braun, J., Montgomery, K., Chaturvedi, N.: Evaluating the performance of building thermal mass control strategies. HVAC&R Research **7**(4), 403–428 (2001). doi:10.1080/10789669.2001.10391283
10. Buchholz, B., Nestle, D., Kiessling, A.: Individual customers' influence on the operation of virtual power plants. In: 2009 IEEE Power and Energy Society General Meeting, pp. 1–6 (2009). doi:10.1109/PES.2009.5275401
11. Carpaneto, E., Chicco, G.: Probabilistic characterisation of the aggregated residential load patterns. IET Gener. Transm. Distrib. **2**(3), 373 (2008). doi:10.1049/iet-gtd:20070280
12. Danish Energy Agency: The PSO programmes and the energy agreement—Strategy 2010 + for the ForskEL and ForskVE programmes. Technical report, Copenhagen (2009), https://www.energinet.dk/
13. Ehrhardt-Martinez, K., Donnelly, K.A., Laitner, J.A.S., York, D., Talbot, J., Friedrich, K.: Advanced metering initiatives and residential feedback programs : a meta-review for household electricity-saving opportunities. Technical report E105, American Council for an Energy-Efficient Economy, Washington (2010)
14. Fang, X., Misra, S., Xue, G., Yang, D.: Smart grid—the new and improved power grid: a survey. IEEE Commun. Surv. Tutorials **14**(4), 944–980 (2012). doi:10.1109/SURV.2011.101911.00087
15. Giordano, V., Meletiou, A., Covrig, C.F., Mengolini, A., Ardelean, M., Fulli, G., Filiou, C., Sanchez, M. Smart grid projects in Europe : lessons learned and current developments 2012 update. Technical report EUR 25815 EN, Join Research Centre—Institute for Energy and Transport, Petten (2013). doi:10.2790/82707
16. Giusti, A., Garvin, S., Philimis, P.: A system for real-time calculation and monitoring of energy performance and carbon emissions of RET systems and buildings. In: Recent Researches in Environmental and Geological Sciences, pp. 174–179. WSEAS Press (2012)

17. Goldman, C., Reid, M., Levy, R.: Coordination of energy efficiency and demand response. Technical report LBNL-3044E, Ernest Orlando Lawrence Berkeley National Laboratory (2010)
18. Janga Reddy, M., Nagesh Kumar, D.: An efficient multi-objective optimization algorithm based on swarm intelligence for engineering design. Eng. Optim. **39**(1), 49–68 (2007). doi:10.1080/03052150600930493
19. Johal, H., Anaparthi, K., Black, J.: Demand response as a strategy to support grid operation in different time scales. In: 2012 IEEE Energy Conversion Congress and Exposition (ECCE), IEEE, pp. 1461–1467 (2012). doi:10.1109/ECCE.2012.6342642
20. Karatasou, S., Santamouris, M., Geros, V.: Modeling and predicting building's energy use with artificial neural networks: methods and results. Energy Build. **38**(8), 949–958 (2006). doi:10.1016/j.enbuild.2005.11.005
21. Kolokotsa, D., Pouliezos, A., Stavrakakis, G., Lazos, C.: Predictive control techniques for energy and indoor environmental quality management in buildings. Build. Environ. **44**(9), 1850–1863 (2009). doi:10.1016/j.buildenv.2008.12.007
22. Konak, A., Coit, D.W., Smith, A.E.: Multi-objective optimization using genetic algorithms: A tutorial. Reliab. Eng. Syst. Saf. **91**(9), 992–1007 (2006). doi:10.1016/j.ress.2005.11.018
23. Kusiak, A., Xu, G.: Modeling and optimization of HVAC systems using a dynamic neural network. Energy **42**(1), 241–250 (2012). doi:10.1016/j.energy.2012.03.063
24. Lamarche J, Cheney K, Christian S, Roth K (2011) Home energy management products and trends. Technical report, Fraunhofer, Cambridge. http://cse.fraunhofer.org/
25. Law, Y.W., Alpcan, T., Lee, V.C., Lo, A., Marusic, S., Palaniswami, M.: Demand response architectures and load management algorithms for energy-efficient power grids: a survey. In: 2012 Seventh International Conference on Knowledge, Information and Creativity Support Systems, pp. 134–141 (2012). doi:10.1109/KICSS.2012.45
26. Marik, K., Rojicek, J., Stluka, P., Vass, J.: Advanced HVAC control: theory vs. reality. In: 18th IFAC World Congress, pp. 3108–3113 (2011)
27. Marques, A., Serrano, M., Karnouskos, S., Marron, P.J., Sauter, R., Bekiaris, E., Kesi-dou, E., Hoglund, J.: NOBEL—a neighborhood oriented brokerage electricity and monitoring system. In: Hatziargyriou, N., Dimeas, A., Tomtsi, T., Wei-dlich, A. (eds.) Energy-Efficient Computing and Networking, vol. 54, pp. 187–196, Springer, Berlin (2011), doi:10.1007/978-3-642-19322-4_20
28. Mathieu, J.L., Price, P.N., Kiliccote, S., Piette, M.A.: Quantifying changes in building electricity use, with application to demand response. IEEE Trans. Smart Grid **2**(3), 507–518 (2011). doi:10.1109/TSG.2011.2145010
29. Motegi, N., Piette, M.A., Watson, D.S., Kiliccote, S., Xu, P.: Introduction to commercial building control strategies and techniques for demand response. Technical report LBNL-59975, Lawrence Berkeley National Laboratory, Berkeley (2007)
30. Office of the National Coordinator for Smart Grid Interoperability: NIST framework and roadmap for smart grid interoperability standards, release 2.0. Technical report 1108R2 (2012)
31. Oldewurtel, F., Parisio, A., Jones, C.N., Morari, M., Gyalistras, D., Gwerder, M., Stauch, V., Lehmann, B., Wirth, K.: Energy efficient building climate control using stochastic model predictive control and weather predictions. In: American Control Conference (ACC), pp. 5100–5105 (2010)
32. Parsopoulos, K.E., Vrahatis, M.N.: Particle swarm optimization method in multiobjective problems. In: Proceedings of the 2002 ACM Symposium on Applied Computing—SAC '02 3:603 (2002). doi:10.1145/508895.508907
33. Paulou, J., Lonsdale, J., Jamieson, M., Neuweg, I., Trucco, P., Maio, P., Blom, M., Warringa, G.: Financing the energy renovation of buildings with cohesion policy funding. Technical report ENER/C3/2012-415, European Union (2014). doi:10.2833/18766
34. Pipattanasomporn, M., Kuzlu, M., Rahman, S.: Teklu Y (2014) Load profiles of selected major household appliances and their demand response opportunities. IEEE Trans. Smart Grid **5**(2), 742–750 (2013). doi:10.1109/TSG.2268664

35. Ritzer, G., Dean, P., Jurgenson, N.: The coming of age of the prosumer. Am. Behav. Sci. **56** (4), 379–398 (2012). doi:10.1177/0002764211429368
36. Saboori, H., Mohammadi, M., Taghe, R.: Virtual power plant (VPP), definition, concept, components and types. In: 2011 Asia-Pacific Power and Energy Engineering Conference, IEEE, pp. 1–4 (2011). doi:10.1109/APPEEC.2011.5749026
37. Sankur, M., Arnold, D., Auslander, D.: An architecture for integrated commercial building demand response. In: 2013 IEEE Power and Energy Society General Meeting, pp. 1–5 (2013). doi:10.1109/PESMG.2013.6672800
38. Siano, P.: Demand response and smart grids—a survey. Renew. Sustain. Energy Rev. **30**, 461–478 (2014). doi:10.1016/j.rser.2013.10.022
39. Silva, P.G.D., Karnouskos, S., Ilic, D.: A survey towards understanding residential prosumers in smart grid neighbourhoods. In: 2012 3rd IEEE PES Innovative Smart Grid Technologies Europe (ISGT Europe), IEEE, section II, pp. 1–8 (2012). doi:10.1109/ISGTEurope.2012.6465864
40. Smart Energy Demand Coalition: A demand response action plan For Europe—regulatory requirements and market models. Technical report, Brussels (2013). http://sedc-coalition.eu/
41. Stadler, M., Siddiqui, A., Marnay, C., Aki, H., Lai, J.: Optimal Technology Investment and Operation in Zero-Net-Energy Buildings with Demand Response. In: 22nd Annual Western Conference, Advanced Workshop in Regulation and Competition (2009)
42. Strbac, G.: Demand side management: benefits and challenges. Energy Policy **36**(12), 4419–4426 (2008). doi:10.1016/j.enpol.2008.09.030
43. Strengers, Y.: Designing eco-feedback systems for everyday life. In: Proceedings of the 2011 Annual Conference on Human Factors in Computing Systems—CHI '11 p. 2135 (2011). doi:10.1145/1978942.1979252
44. Teodosiu, C., Hohota, R., Rusaouen, G., Woloszyn, M.: Numerical prediction of indoor air humidity and its effect on indoor environment. Build. Environ. **38**(5), 655–664 (2003). doi:10.1016/S0360-1323(02)00211-1
45. Timpe, C.: Smart domestic appliances supporting the system integration of renewable energy. Technical report, Oko-Institut (2009). www.smart-a.org
46. Ward, J.K., Wall, J., West, S., Dear, R.D.: Beyond comfort—managing the impact of HVAC control on the outside world. In: Air Conditioning and the Low Carbon Cooling Challenge, pp. 27–29. London (2008)
47. Yu, Z., Dexter, A.: Hierarchical fuzzy control of low-energy building systems. Sol. Energy **84** (4), 538–548 (2010). doi:10.1016/j.solener.2009.03.014
48. Zavala, V.M., Flores-Tlacuahuac, A.: Stability of multiobjective predictive control: A utopia-tracking approach. Automatica **48**, 2627–2632 (2012). doi:10.1016/j.automatica.2012.06.066
49. Zavala, V.M., Wang, J., Leyffer, S., Constantinescu, E.M., Anitescu, M., Conzelmann, G.: Proactive energy management for next-generation building systems. In: Fourth National Conference of IBPSA-USA, New York (2010)
50. Zervos, A., Kjaer, C., Azau, S., Scola, J., Quesada, J., Bianchin, R.: Pure power wind energy targets for 2020 and 2030 pure power. Technical report, European Wind Energy Association (2009). http://www.ewea.org/
51. Zhou, Z., Zhang, X., Lee, Y.M.: An inventory control and pricing model for smart building load management. In: 5th Innovative Smart Grid Technologies Conference, pp. 1–5. Washington (2014)

Application of Some Modern Techniques in Load Frequency Control in Power Systems

Naglaa Kamel Bahgaat, Mohammed Ibrahim El-Sayed Ahmed, Mohamed A. Moustafa Hassan and Fahmy M. Bendary

Abstract The main objective of Load Frequency Control (LFC) is to regulate the power output of the electric generator within an area in response to changes in system frequency and tie-line loading. Thus the LFC helps in maintaining the scheduled system frequency and tie-line power interchange with the other areas within the prescribed limits. Most LFCs are primarily composed of an integral controller. The integrator gain is set to a level that compromises between fast transient recovery and low overshoot in the dynamic response of the overall system. This type of controller is slow and does not allow the controller designer to take into account possible changes in operating conditions and non-linearities in the generator unit. Moreover, it lacks robustness. This chapter studies LFC in two areas power system using PID controller. In this chapter, PID parameters are tuned using different tuning techniques. The overshoots and settling times with the proposed controllers are better than the outputs of the conventional PID controllers. This chapter uses MATLAB/SIMULINK software. Simulations are done by using the same PID parameters for the two different areas because it gives a better performance for the system frequency response than the case of using two different sets of PID parameters for the two areas. The used methods in this chapter are: (a) Particle

N.K. Bahgaat (✉)
Electrical Communication Department, Faculty of Engineering, Canadian International College (CIC), 6 October City, Giza, Egypt
e-mail: nkahgaat@hotmail.com; n_mohamed2004@yahoo.com

M.I.E.-S. Ahmed
Electrical Power Engineering Department Faculty of Engineering, Al-Azhar University, Cairo, Egypt
e-mail: d_eng2009@yahoo.com

M.A.M. Hassan
Electrical Power Engineering Department Faculty of Engineering, Cairo University, Giza, Egypt
e-mail: mmustafa_98@hotmail.com

F.M. Bendary
Electrical Power Engineering Department Faculty of Engineering, Banha University, Cairo, Egypt
e-mail: fahmybendary10@gmail.com

A.T. Azar and S. Vaidyanathan (eds.), *Chaos Modeling and Control Systems Design*, Studies in Computational Intelligence 581, DOI 10.1007/978-3-319-13132-0_8

Swarm Optimization,(b) Adaptive Weight Particle Swarm Optimization, (c) Adaptive Acceleration Coefficients based PSO (AACPSO) and (d) Adaptive Neuro Fuzzy Inference System (ANFIS). The comparison has been carried out for these different controllers for two areas power system, the study presents advanced techniques for Load Frequency Control. These proposed techniques are based on Artificial Intelligence. It gives promising results.

Keywords Adaptive acceleration coefficients based particle swarm optimization · Adaptive fuzzy · Adaptive weight particle swarm optimization · ANFIS · Load frequency control · Particle swarm optimization technique

1 Introduction

Frequency is an explanation of stability criterion in power systems [17, 18, 27, 35]. To provide the stability, active power balance and steady frequency are required. Frequency depends on active power balance. If any change occurs in active power demand/generation in power systems, frequency cannot be hold in its rated value. So oscillations increase in both power and frequency. Thus, system subjects to a serious instability problem. In electric power generation, system disturbances caused by load fluctuations result in changes to the desired frequency value. Automatic Generation Control (AGC) or Load Frequency Control (LFC) is an important issue in power system operation and control for supplying stable and reliable electric power with good quality [28, 33]. The principle aspect of Automatic Load Frequency Control is to maintain the generator power output and frequency within the prescribed limits.

In order to keep the power system in normal operating state, a number of controllers are used in practice. The PID controller will be used for the stabilization of the frequency in the load frequency control problems [17, 18, 27, 28, 35]. Each control area is responsible for individual load changes and scheduled interchanges with neighboring areas [31]. Area load changes and abnormal conditions leads to mismatches in frequency and tie line power interchanges which are to be maintained in the permissible limits, for the robust operation of the power system. For simplicity, the effects of governor dead band are neglected in the Load Frequency Control studies. To study the realistic analysis of the system performance, the governor dead band effect is to be incorporated. To improve the stability of the power networks, it is necessary to design LFC system that controls the power generation and active power at tie lines.

Many studies have been carried out in the past on this important issue in power systems, which is the load frequency control. As stated in some literature [11, 16, 25], its objective is to minimize the transient deviations in these variables (area frequency and tie-line power interchange) and to ensure their steady state errors to be zeros. In this chapter, different intelligent techniques such that Particle Swarm Optimization

(PSO), Adaptive Weighted Particle Swarm Optimization techniques (AWPSO), Adaptive Acceleration Coefficients based PSO (AACPSO) and Adaptive Neuro Fuzzy Inference System (ANFIS) will be used to determine the parameters of a PID controller according to the system dynamics. Using the same parameters of PID controller for the two different areas because it gives a better performance for the system frequency response than in case of using two different PID parameters for each different area [25]. In the integral controller, if the integral gain is very high, undesirable and unacceptable large overshoots will be occurred. However, adjusting the maximum and minimum values of proportional (K_p), integral (K_i) and integral (K_d) gains respectively, the outputs of the system (voltage, frequency) could be improved. The main objectives of LFC, is to regulate the power output of the electric generator within a prescribed area in response to changes in system frequency, tie line loading so as to maintain the scheduled system frequency and interchange with the other areas within the prescribed limits.

In this simulation study, two area power systems parameters are chosen and load frequency control of this system is made based on PID controller by using Particle Swarm Optimization and Adaptive Weight Particle Swarm Optimization Techniques (PSO) and (AWPSO) to choose best parameters of PID Controller [13, 23, 26] and Also using Adaptive Neuro Fuzzy Inference System (ANFIS) to control LFC in power system [6–8, 24]. This chapter is organized as follow: Section one introduces the chapter. The second section presents literature review of the study. Section three introduces PSO, AWPSO and the Adaptive Acceleration Coefficients based PSO (AACPSO). Section four introduces ANFIS. Section five displays the case study. Section six presents a comparative study between the above methods according to the three types of performance Indices (IAE, ISE and ITAE) and Genetic Algorithm (GA), ordinary PI controller, Ziegler Nichols tuned PID (ZN), Bacteria Foraging Optimization (BFO) tuned PID controller and the results using Particle Swarm Optimization (PSO), Adaptive Weighted Particle Swarm (AWPSO), Adaptive Acceleration Coefficients based PSO (AACPSO), and Adaptive Neuro Fuzzy Inference System (ANFIS) in order to assess the results.

Therefore. Section seven concludes the study. Finally a list of references and Appendix of this chapter are given at the end of the chapter.

2 Literature Review

The PID controller is considered to be a key component of industrial control system. It was first described by Minorsky [4]. During the Second World War a great interest was developed in the classical control theory and particularly the PID control of processes. Its simplicity and general good performance made its operation very widespread in industry. It has been stated that in process control applications more than 95 % of the controllers are PID type. Also, they state that 30 % of the PID loops operate in the manual mode and 25 % of PID loops actually operate under default factory settings. The choice of appropriate PID parameters can be

achieved manually by trial and error, using as guidelines the transient and steady response characteristic of each of the three terms. However, this procedure is very time consuming and requires certain skills [5].

Many investigations have been carried out to design a controller for minimizing the mismatches in frequency and power transfer within the neighboring areas. The controller should provide some degree of strength under various operating conditions. Conventional PD, PI, PID controllers does not provide sufficient control performance with the effect of governor dead band [17, 18, 27, 28, 35]. To tune the controller there are many methods used since 1890s till now, some of the historical methods discussed in the References of the chapter. First method is the manual tuning which used if the system remains online. This tuning method is to first set K_I and K_d values to zero, increase the K_P until the output of the loop oscillates, then K_P should be set to approximately half of that value for a "quarter amplitude decay". Second method is an automatic method called Ziegler–Nichols method which introduced by John G. Ziegler and Nathaniel B. Nichols in the 1940s [28, 35]. It is recognized that the step response of most process control systems has an S-shaped curve called the process reaction curve and can be generated experimentally or from dynamic simulation of the plant. The shape of the curve is characteristic of high order systems, and the plant behavior may be approximated by the following transfer function [34]:

$$\frac{Y(S)}{U(S)} = \frac{K \cdot e^{-t_d \cdot s}}{\tau \cdot S + 1} \tag{1}$$

Which is simply; a first order system plus a transportation lag. The constants in the above equation can be determined from the unit step response of the process. Ziegler and Nichols applied the PID controller to plants without integrator or dominant complex-conjugate poles, whose unit-step response resemble an S shaped curve with no overshoot. This S-shaped curve is called the reaction curve as shown in Fig. 1.

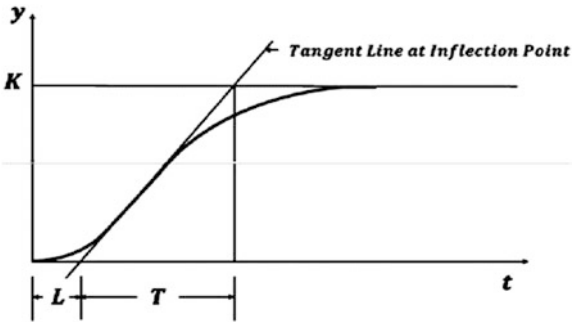

Fig. 1 Reaction curve used by Ziegler and Nichols

The following PID controller parameters were suggested:

$$K_P = 1.2T/L \tag{2}$$

$$K_i = K_P/2L \tag{3}$$

$$K_d = 0.5 \cdot L \cdot K_P \tag{4}$$

Although the method provides a first approximation the response produced is under damped and needs further manual retuning. Some disadvantages of these control techniques for tuning PID controllers are:

a. Excessive number of rules to set the gains.
b. Inadequate dynamics of closed loop responses.
c. Difficulty to deal with nonlinear processes.
d. Mathematical complexity of the control design.

Therefore, it is interesting for academic and industrial communities the aspect of tuning for PID controllers, especially with a reduced number of parameters to be selected and a good performance to be achieved when dealing with complex processes.

Most modern industrial facilities no longer tune loops using the manual calculation methods. Instead, PID tuning and loop optimization software are used to guarantee dependable results [16, 20, 31]. These software packages will gather the data, develop process models, and suggest optimal tuning.

Some software packages can even develop tuning by gathering data from reference changes, such as PSO, AWPSO [23, 24, 26], AACPSO [1] and ANFIS methods ([3, 6–10, 12, 19, 21, 22, 32]). This chapter will discuss the design of the PID controller by using modern method PSO, AWPSO, AACPSO and ANFIS. These methods depend on a computer software program written on MATLAB. These programs had loops and run many times until reach to a solution of the transfer function to have a value of PID parameters which will be described below. These parameters lead to have the smallest value of settling time and over shoot. Therefore, these values of PID parameters (with this used method) are the best values to reach to the best controller parameters.

3 Overview on Practical Swarm Optimization Technique

A Particle Swarm Optimization (PSO) is an optimization algorithm modeled. It's one of Artificial Intelligence (AI) Techniques. It is an intelligent control system combines the techniques. From the fields of AI with those of control engineering to design independent systems that can sense, reason, learn and act in an intelligent method. PSO depends on the simulation of the social behavior of bird and fish school [26]. PSO is developed through the simulation of a bird flocking in two-dimension

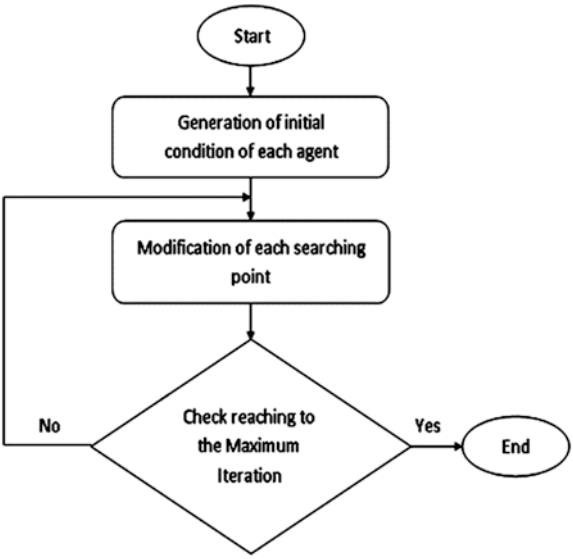

Fig. 2 General flow chart of PSO

space by X-Y axis position where Vx and Vy express the velocity in X direction and Y direction. The flow chart described in Fig. 2, presented the steps of PSO. Modification of the agent position is realized by the position and velocity information [13, 23, 24, 26]. This information is analogy of personal experiences of each agent. Each agent knows its best value so far (Pbest) and its XY position; each agent knows the best value so far in the group (gbest) among Pbests. This information is analogy of knowledge of how the other agents around them have performed. Namely, each agent tries to modify its position using the following information:

Let the particle of the swarm is represented by the N dimensional vector ith

$$X_i = (X_1, X_2, X_3, \ldots X_N) \tag{5}$$

The previous best position of the Nth particles is recorded and represented as follows:

$$\text{Pbest i} = (\text{Pbest 1},\ \text{Pbest 2}, \ldots, \text{Pbest N}) \tag{6}$$

where Pbest is Particle best position (m), N is the total number of iterations.

The best position of the particle among all particles in the swarm is represented by gbest the velocity of the particle is represented as follows:

$$\text{Vi} = (\text{V1},\ \text{V2}, \ldots \text{VN}) \tag{7}$$

where

V_i is the velocity of each i particle.

The modified velocity and position of each particle can be calculated from the current velocity and the distance from particle current position to particle best position P_{best} and to global best position g_{best} as shown in the following equations:

$$V_i(t) = W \cdot V_i(t-1) + C_1 \cdot \text{rand}(0,1) \cdot (P_{best} - X_i(t-1)) + C_2 \cdot \text{rand}(0,1) \cdot (g_{best} - X_i(t-1)) \quad (8)$$

$$X_i(t) = X_i(t-1) + V_i(t) \quad (9)$$

$$i = 1, 2, 3 \ldots N \quad (10)$$

$$j = 1, 2, 3 \ldots D \quad (11)$$

where

$V_i(t)$	Velocity of the particle i at iteration t (m/s)
$X_i(t)$	The Current position of particle i at iteration t (m)
D	The Dimension
C1	The cognitive acceleration coefficient and it is a positive number
C2	Social acceleration coefficient and it is a positive number
rand [0, 1]	A random number obtained from a uniform random distribution function in the interval [0, 1]
gbest	The Global best position (m)
W	The Inertia weight

3.1 Adaptive Weighted Particle Swarm Optimization

Adaptive Weighted Particle Swarm Optimization (AWPSO) technique has been proposed for improving the performance of PSO in multi-objective optimization problems [23, 24]. AWPSO is achieved by two terms [26]: inertia weigh (W) and Acceleration factor (A). The inertia weight function is to balance global exploration and local exploration. It controls previous velocities effect on the new velocity. Larger the inertia weight, larger exploration of search space while smaller the inertia weights, the search will be limited and focused on a small region in the search space. The inertia weight formula is as follows which makes W value changes randomly from W_o to 1 [6–8].

$$W = W_o + \text{rand}\,(0,1)\,(1 - W_o) \quad (12)$$

where

Wo The initial positive constant in the interval chosen from [0, 1]

Particle velocity at ith iteration as follows:

$$V_i(t) = W \cdot V_i(t-1) + AC_1 \cdot \text{rand}(0,1) \cdot (P_{best} - X_i(t-1)) + AC_2 \cdot \text{rand}(0,1) \cdot (g_{best} - X_i(t-1)) \tag{13}$$

Additional term denoted by A called acceleration factor is added in the original velocity equation to improve the swarm search.

The acceleration factor formula is given as follows [26]:

$$A = A_o + \frac{i}{n} \tag{14}$$

where

A_o	Is the initial positive constant in the interval [0.5, 1].
n	is the number of iteration.
C_1 and C_2	Are the constant representing the weighing of the stochastic acceleration terms that pull each particle towards P_{best} and g_{best} positions.

As shown in acceleration factor formula, that the acceleration term will increase as the number of iterations increases. This will enhance the global search ability at the end of the run and help the algorithm to get far from the local optimum region. In this article, the term A_O is set at 0.5. Low values of $C_1$and C_2 allow particles to roam far from the target region before being tugged back. However, high values result in abrupt movement toward, or past, target regions.

3.2 Adaptive Acceleration Coefficients Based PSO

The Time Varying Inertia Weight (TVIW) W in Sect. (3.1) can locate a good solution at a significantly faster rate but its ability to fine tune the optimum solution is weak, due to the lack of diversity at the end of the search. It has been observed by most researchers that in PSO, problem based tuning of parameters is a key factor to find the optimum solution accurately and efficiently [35]. New researches have emerged to improve PSO Algorithms, as Time-Varying Acceleration Coefficients (TVAC), where C_1 and C_2 in [15] change linearly with time, in the way that the cognitive component is reduced while the social component is increased as the search proceeds.

In this section, a new approach called Adaptive Acceleration Coefficients based PSO (AACPSO) to implement the PSO algorithm will be described as illustrated in [1]. A suggestion will be given on how to deal with inertia weight and acceleration factors. The new approach is confident to change acceleration coefficients exponentially (with inertia weight) in the time, with respect to their minimal and

maximal values. The choice of the exponential function is justified by the increasing or decreasing speed of such a function to accelerate the convergence process of the algorithm and to get better search in the exploration s pace. Furthermore, C_1 and C_2 vary adaptively according to the fitness value of G_{best} and P_{best}, [15] becomes:

$$V_i^{(t+1)} = w^{(t)} V_i^{(t)} + C_1^{(t)} r_1 * \left(Pbest_i^{(t)} - X_i^{(t)} \right) + C_2^{(t)} r_2 * \left(Gbest^{(t)} - X_i^{(t)} \right) \quad (15)$$

$$w^{(t)} = w_o * \exp(- \propto_w * t) \quad (16)$$

$$C_1^{(t)} = C_{1o} * \exp\left(- \propto_c * t * k_c^{(t)} \right) \quad (17)$$

$$C_2^{(t)} = C_{2o} * \exp\left(- \propto_c * t * k_c^{(t)} \right) \quad (18)$$

$$\propto_c = \frac{-1}{t_{\max}} \ln\left(\frac{C_{2o}}{C_{1o}} \right) \quad (19)$$

$$k_c^{(t)} = \frac{\left(F_m^{(t)} - Gbest^{(t)} \right)}{F_m^{(t)}} \quad (20)$$

where

$w^{(t)}$	The inertia weight factor
$C_1^{(t)}$	Acceleration coefficient at iteration t
i	Equal 1 or 2
t	The iteration number
ln	The neperian logarithm
α_w	Is determined with respect to initial and final values of ω with the same manner as αc described in [4]
$k_c^{(t)}$	Determined based on the fitness value of Gbest and Pbest at iteration t
ω_o, c_{io}	initial values of inertia weight factor and acceleration coefficients respectively with i = 1 or 2
$F_m^{(t)}$	The mean value of the best positions related to all particles at iteration t

4 Preface to Fuzzy Logic

The word "fuzzy" is defined as unclear, indefinite, fuzzy systems are systems to be precisely defined and fuzzy *control* is a special kind of nonlinear control. The description of the Fuzzy system specified in many references these references

describe the Fuzzification and Defuzzification process and the equations of each case [6, 8, 21, 22, 32]. There are two kinds of explanation for fuzzy systems theory:

a. The real world is too complicated for precise descriptions to be obtained Therefore approximation (or fuzziness) must be introduced in order to obtain a practical, accurate model.
b. As the world moving into the information period, human knowledge becomes increasingly important. A theory is needed to formulate human knowledge in a systematic method and put it into engineering system, together with other information like mathematical models and sensor measurements.

Fuzzy Logic (FL) requires some numerical parameters in order to operate such as what is considered significant error and significant rate-of-change-of-error, but exact values of these numbers are usually not critical unless very responsive performance is required in which case empirical tuning would determine them. Fuzzy logic has many several unique features that make it a particularly good choice for many control problems. In the following there are some of these advantages [33]:

1. It is inherently robust since it does not require precise, noise-free inputs and can be programmed to fail safely if a feedback sensor quits or is destroyed. The output control is a smooth control function despite a wide range of input variations.
2. Since the FL controller processes user-defined rules governing the target control system, it can be modified and tweaked easily to improve or drastically alter system performance. New sensors can easily be incorporated into the system simply by generating appropriate governing rules.
3. FL is not limited to a few feedback inputs and one or two control outputs, nor is it necessary to measure or compute rate-of-change parameters in order for it to be implemented. Any sensor data that provides some indication of a system's actions and reactions is sufficient. This allows the sensors to be inexpensive and imprecise thus keeping the overall system cost and complexity low.
4. Because of the rule-based operation, any reasonable number of inputs can be processed (1–8 or more) and numerous outputs (1–4 or more) generated, although defining the rule base quickly becomes complex if too many inputs and outputs are chosen for a single implementation since rules defining their interrelations must also be defined. It would be better to break the control system into smaller chunks and use several smaller FL controllers distributed on the system, each with more limited responsibilities.
5. Fuzzy Logic can control nonlinear systems that would be difficult or impossible to model mathematically. This opens doors for control systems that would normally be deemed unfeasible for automation.
6. Fuzzy Logic doesn't need any system parameter estimation or identification.
7. Fuzzy Logic can deal with nonlinear systems (there is no need for Linearization).

4.1 Adaptive Neuro Fuzzy Inference System

The acronym ANFIS derives its name from Adaptive Neuro Fuzzy Inference System (ANFIS). In the field of artificial intelligence, Neuro-Fuzzy refers to combinations of artificial neural networks and fuzzy logic.

Neuro-fuzzy was proposed by J. S. R. Jang. Neuro-fuzzy hybridization results in a hybrid intelligent system that synergizes these two techniques by combining the human-like reasoning style of fuzzy systems with the learning and connectionist structure of neural networks.

Neuro-fuzzy hybridization is widely termed as Fuzzy Neural Network (FNN) or Neuro-Fuzzy System (NFS) in the literature. Neuro-fuzzy system (the more popular term is used in imminent) incorporates the human-like reasoning style of fuzzy systems through the use of fuzzy sets and a linguistic model consisting of a set of IF-THEN fuzzy rules.

The main strength of neuro-fuzzy systems is that they are universal approximates with the ability to solicit interpretable IF-THEN rules [7]. The strength of neuro-fuzzy systems involves two contradictory requirements in fuzzy modeling: interpretability versus accuracy. In practice, one of the two properties prevails. The neuro-fuzzy in fuzzy modeling research field is divided into two areas: linguistic fuzzy modeling that is focused on interpretability; and precise fuzzy modeling that is focused on accuracy.

Using a given input and output data set, the toolbox function ANFIS constructs a fuzzy inference system (FIS) whose membership function parameters are tuned (adjusted) using either a back propagation algorithm alone or in combination with a least squares type of method. This adjustment allows the fuzzy systems to learn from the modeling data [14, 29, 30]. Moreover, ANFIS is used in many applications of power system [3, 9, 10, 17–19].

This chapter proposed two inputs-three outputs self tuning of a PID controller. The controller design used the error and change of error as inputs to the self tuning, and the gains (K_P, K_I, K_d) as outputs. The FLC is adding to the conventional PID controller to adjust the parameters of the PID controller on-line according to the change of the signals error and change of the error. The fuzzy logic model presented SIMULINK in MATLAB program is used.

5 Cases Study

Simulations are done by using MATLAB/SIMULINK for the case of two power system areas connected with each other's by tie transmission line as shown in Figs. 4 and 5 [32]. The parameters of area 1 and area 2 are shown in the Appendix. Basically, electric power system components are non-linear; therefore a linearization around a nominal operating point is usually performed to get a linearized system model which is used in the controller design process.

The operating conditions of power systems are continuously changing. Accordingly, the real plant usually differs from the assumed one. Therefore, classical algorithms to design an automatic generation controller using an assumed plant may not ensure the stability of the overall real system [33]. The load frequency controller function is to minimize the transient deviation of the frequency and maintains their values to steady state values and to restore the scheduled interchanges between different areas.

MATLAB programs are used for PSO, AWPSO and AACPSO to make tuning of the PID controller's parameters. These parameters adjusted to have minimum integrated error value with shorted settling time. The objective function is defined as follows [31]:

For Integral of Absolute Error (IAE):

$$IAE = \int_0^\infty |e(t)|dt \tag{21}$$

$$f = IAE_1 + IAE_2 + IAE_{Ptie} \tag{22}$$

Integral of Squared Error (ISE)

$$ISE = \int_0^\infty e^2(t)dt \tag{23}$$

$$f = ISE_1 + ISE_2 + ISE_{Ptie} \tag{24}$$

Integral of Time Weighted Absolute Error (ITAE)

$$ITAE = \int_0^\infty t|e(t)|\mathrm{dt} \tag{25}$$

$$f = ITAE_1 + ITAE_2 + ITAE_{Ptie} \tag{26}$$

where

e	Is the error
f	Is the objective function
$IAE_1, IAE_2, IAE_{Ptie\,1}$	The Integral of Absolute Error of area 1, area 2 and the tie line of the System
$ISE_1, ISE_2, ISE_{Ptie1}$	The Integral of Squared Error of area 1, area 2 and the tie line of the System
$ITAE_1, ITAE_2, ITAE_{Ptie\,1}$	Integral of Time Weighted Absolute Error of area 1, area 2 and the tie line of the System

For the two power system areas, step loading disturbance has been applied for each area, 0.07 p.u load throw has been withdrawn from the first area and 0.05 p.u loading added for the second area. The control objective is to control the frequency

deviation for each area. Figure 4 presents the diagram shows the steps of this study. The study the performance of the PID controller was compared in case of each intelligent technique (PSO, AWPSO, AACPSO and finally using ANFIS algorithms).

The performance index selected by the user in the beginning of the program. Based on this performance index (f) optimization problem can be stated as: Minimize f the nominal system description and parameters are describing in the following.

5.1 Model Description and Parameters

The block diagram of the two areas power system model using PID controller presented at Fig. 3 as presented in [33]. The description for the system parameters is displayed in Table 1 and the parameters values of the system is presented in Table 2.

So the transfer function of governors, turbine, mass and load becomes as given in [33]:

$$G_{h1}(S) = G_{h2}(S) = \frac{1}{0.08s + 1} \tag{27}$$

$$G_{t1}(S) = G_{t2}(S) = \frac{1}{0.3s + 1} \tag{28}$$

$$G_{y1}(S) = G_{y2}(S) = \frac{120}{20s + 1} \tag{29}$$

5.2 Steps of the Study

The flow chart presents in Fig. 4 explains the steps of the study.

To optimize the performance of a PID controlled system, the PID gains K_P, K_i, and K_d of the two-area electric power system shown in Fig. 3 are adjusted to minimize a certain performance index. The performance index is calculated over a time interval; T, normally in the region of $0 < T < ts$ where t_s is the settling time of the system. By using different techniques in conjunction with Eqs: 21–29 the optimal controller parameters under various performance indices were obtained as shown in Tables 1, 2 and 3 show the results of the different methods used based PID controller.

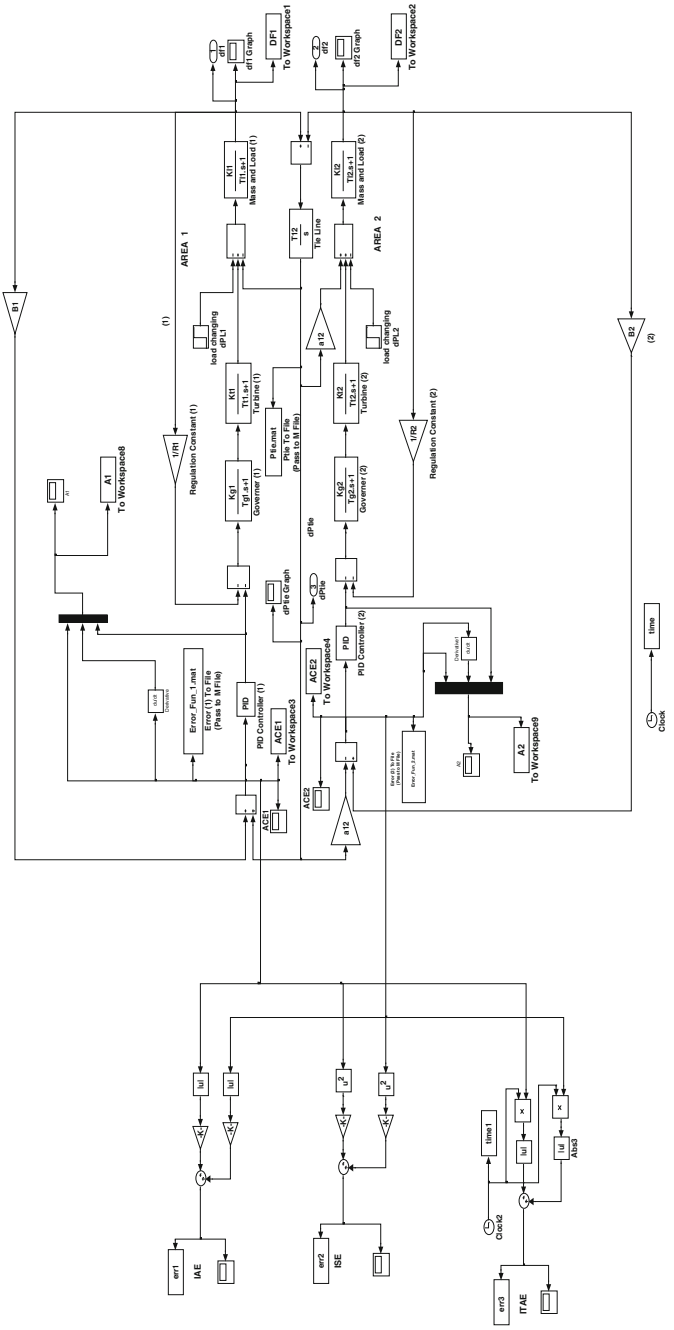

Fig. 3 Two-area power system SIMULINK model using PID controller

Table 1 Parameter description

Parameter	Description
Tg1, Tg2	Time constant for area 1 governor and area 2 governor in (seconds)
Tt1, Tt2	Turbine time delay between switching the valve and output turbine torque (seconds)
Tl1, Tl2	Generator 1 and generator 2 inertia constant
Kl1, Kl2	Power system gain constant (HZ/MW p.u)
R1, R2	Speed regulation constant of the governor (HZ/MW p.u)
B1, B2	Frequency bias p.u. MW/HZ
T12	Tie line synchronizing coefficient with area 2 MW p.u/HZ
a12	Gain
Δf_1 or df_1	Area 1 frequency deviation
Δf_2 or df_2	Area 2 frequency deviation
dPL1, dPL2	Frequency sensitive load change for area 1 and area 2
ΔPtie or dPtie	Net tie line power flow
Vi	Area interface
ACE1	Area 1 control error
ACE2	Area 2 control error

Table 2 Parameters values

System parameters	Value
Tg1, Tg2	0.08 s
Tt1, Tt2	0.3 s
Tl1, Tl2	20 s
Kl1, Kl2	100 HZ/MW p.u
R1, R2	2.4 HZ/MW p.u
B1, B2	0.425 MW p.u/HZ
T12	0.05 MW p.u/HZ
a12	1

5.3 Results in Case of IAE Error

Figures 5 and 6 presents the frequency deviation of area 1 and area 2 without using PID controller.

In the following sections discuss the impact the way the AI techniques used on the Tie Line and area control error ACE of the system.

5.3.1 Tie Line Power

Figure 7 displays the frequency change of the tie line power with using PSO, AWPSO And AAPSO Based PID Controller,

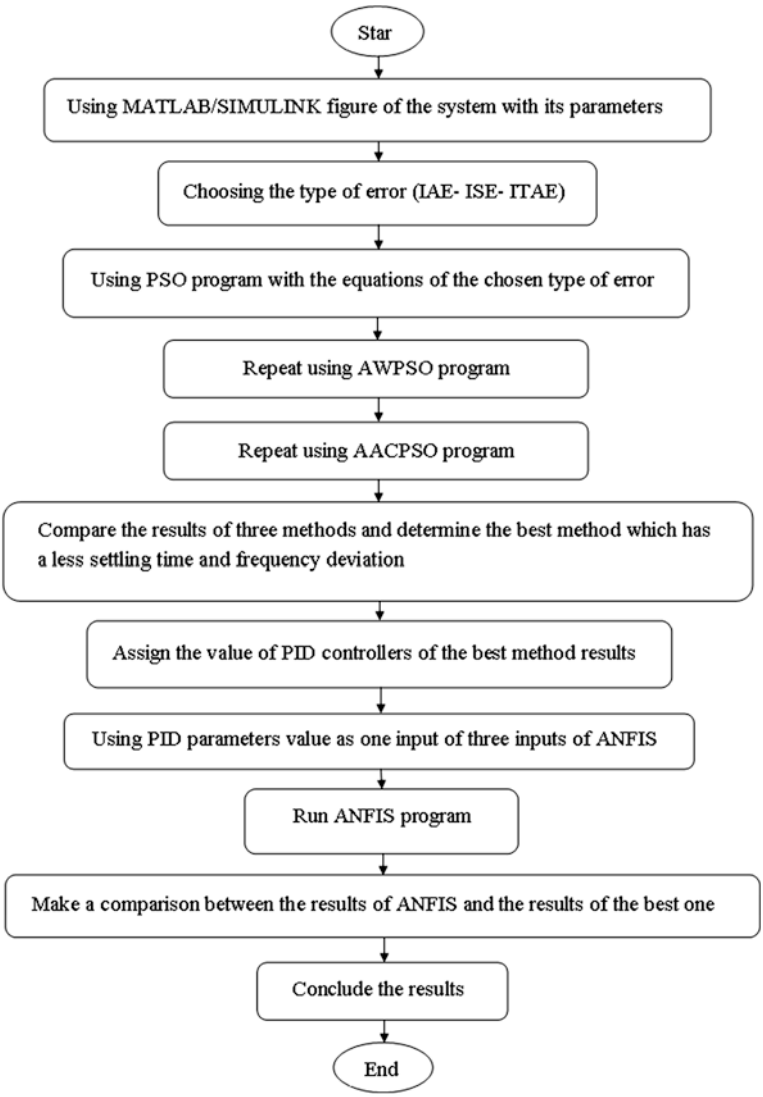

Fig. 4 The steps of the study

The results display in Table 4, Fig. 7 show that:

1. Tables 3 and 4 indicate that on the Tie line power, the value of settling time in case of using AACPSO is the best results and has a smaller value comparing with the other methods used (PSO, AWPSO).
2. The settling time of Tie line in case of using AC is less than its value in case of using AWPSO by about 0.6 s, and less than its value when using PSO by about 4.1 s.
3. Settling time by AWPSO is smaller than using PSO by 0.0359 s.

Table 3 The results of the program using PSO, AWPSO and AACPSO

Items of comparison	PSO	AWPSO	AACPSO
Number of iterations	500	500	500
Error IAE (integrated error)	0.0611	0.0252	0.0149
Settling time _Area 1 (s)	5.4281	1.9323	1.6514
Settling time _Area 2 (s)	7.6946	4.1854	3.569
Settling time _Tie line (s)	7.7624	4.2082	3.6553
Kp1	2.4283	8.1472	9.1995
Ki1	1.5555	7.5774	9.4936
Kd1	1.3753	2.7603	3.2393
Kp2	2.9522	3.4998	4.7149
Ki2	9.2078	1.6218	0.876
Kd2	5.7955	8.6869	2.1397

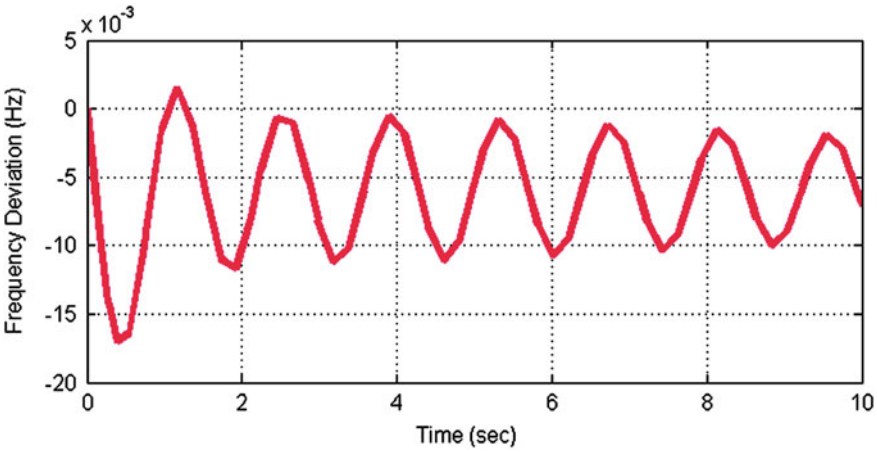

Fig. 5 The frequency deviation of area 1 without controller

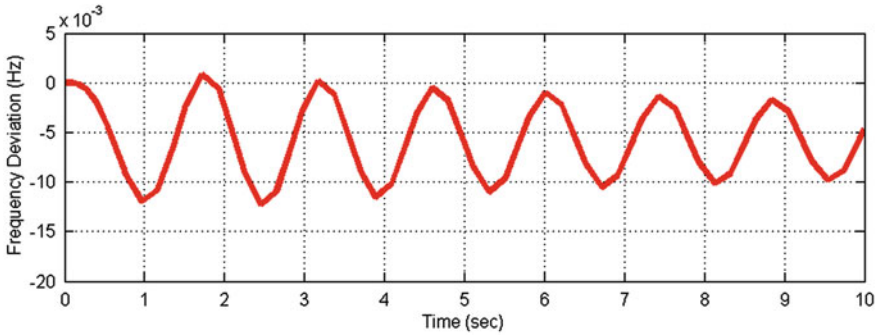

Fig. 6 The frequency deviation of area 2 without controller

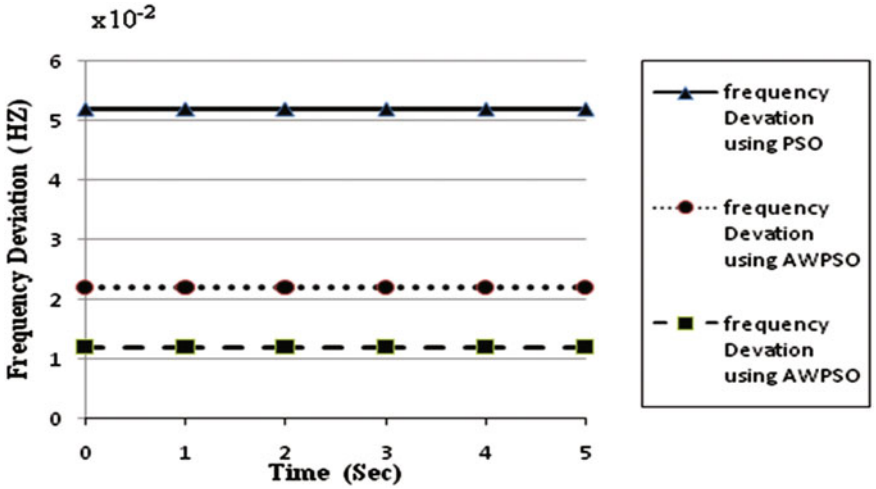

Fig. 7 Tie line power changes using PSO, AWPSO and AAPSO based PID controller in case of using IAE error

Table 4 Tie line behavior at different typed of control

Items of comparison	PSO	AWPSO	AACPSO
Settling time _Tie line (s)	7.7624	4.2082	3.6553
Maximum frequency of tie line power (Hz)	3.00E−07	4.24E−07	1.06E−06
Time at maximum frequency of tie line power (s)	20.502	22.2727	4.8003
Minimum frequency of tie line power (Hz)	−0.0011	−3.66E−04	−3.20E−04
Time at minimum frequency of tie line power (s)	1.0319	0.612	0.5743

4. The maximum frequency of Tie line power in case of using AWPSO is less than its value of the other methods of controller used by a very small value.
5. In general the maximum frequency of Tie line power is construed to be zero.
6. Time at maximum power in case of using AACPSO is less than the other values of PSO and AWPSO. This value is less than the time of maximum power in case of using PSO by about 23.4 % and less than its value in case of using AWPSO by about 21.5 %.
7. The minimum Tie line power in case of using AWPSO and AACPSO are almost equal and less than its value in case of using PSO.
8. Time at minimum power in case of using AACPSO is less than the other values of PSO and AWPSO.

5.3.2 Integral of Absolute Error of Area 1 and Area 2

The first choice of the MATLAB program used in this study is IAE as described above. In the following there are the Figures describe the output of the system after controlling the error on area 1 and area 2. Figure 8 presents the frequency deviation of area 1 with PSO based PID Controller, Fig. 9 presents the frequency deviation of area 1 with AWPSO based PID controller and Fig. 10 illustrates the frequency deviation of area 1 with AACPSO based PID controller.

From the results shown in Table 3 and also the above Figs. 8, 9 and 10 all these show that:

1. The settling time of area 1 to reach to the steady state in case of using AWPSO is less than the value of settling time using PSO by about 3.5 s.

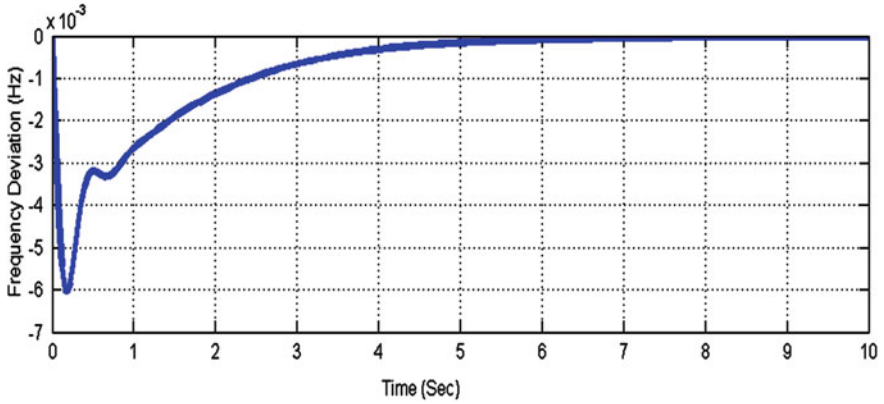

Fig. 8 The frequency deviation of area 1 with PSO based PID controller using IAE performance indices

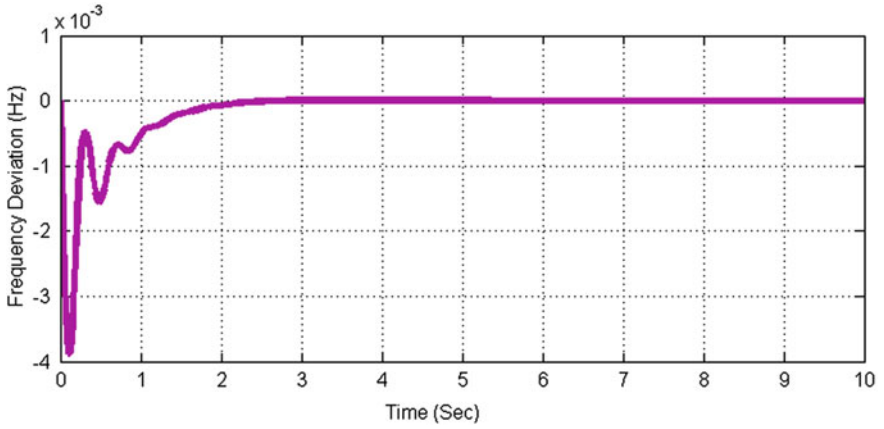

Fig. 9 The frequency deviation of area 1 with AWPSO based PID controller using IAE performance indices

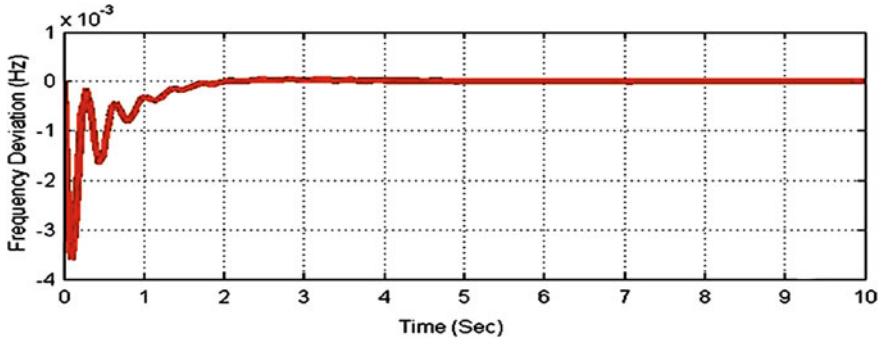

Fig. 10 The frequency deviation of area 1 with AACPSO based PID controller using IAE performance indices

2. The settling time by using AACPSO in the program is less than that value by using AWPSO by about 0.3 s.
3. All these results present that: the best method used to reach the minimum value of settling time in area 1 is AACPSO.

The next Figures present the behavior of area 2 in different cases of Artificial Intelligence techniques.

Figure 11 shows the frequency deviation of area 2 with PSO based PID controller using IAE performance indices; Fig. 12 presents the behavior of the frequency deviation of area 2 in case of using AWPSO, while; Fig. 13 displays The frequency deviation of area 2 with AACPSO based PID controller.

From the results shown in Table 3 and also the Figs. 11, 12 and 13 all these show that:

1. The settling time of area 2 by using AWPAO is less than its value by using PSO by 3.5092 s. While; the settling time becomes smaller if using AACPSO.

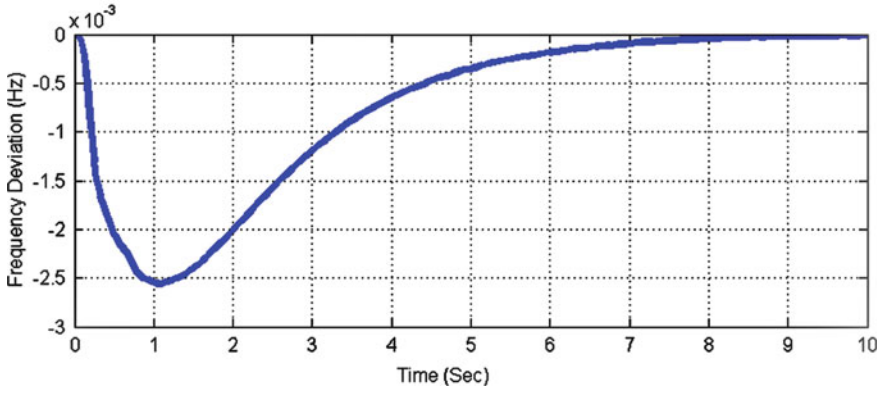

Fig. 11 The frequency deviation of area 2 with PSO based PID controller using IAE performance indices

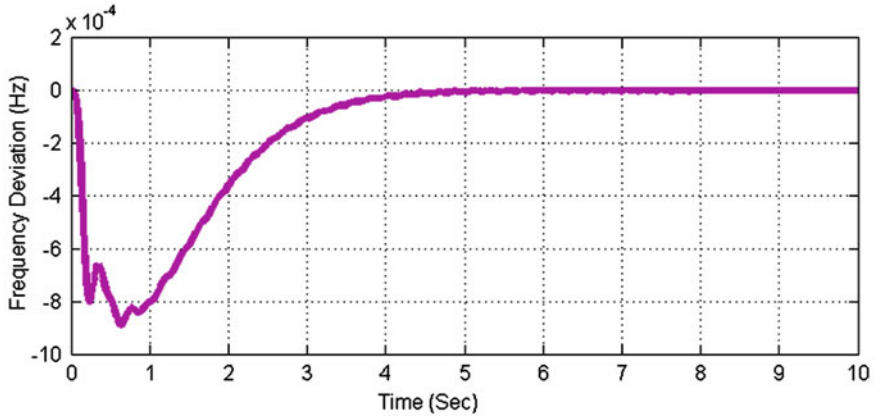

Fig. 12 The frequency deviation of area 2 with AWPSO based PID controller using IAE performance indices

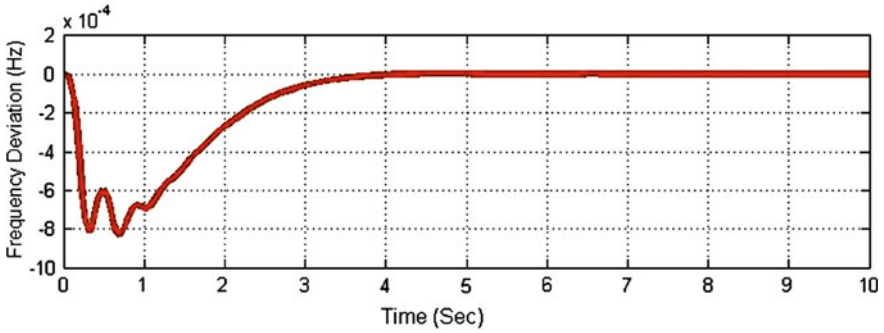

Fig. 13 The frequency deviation of area 2 with AACPSO based PID controller using IAE performance indices

The output results using AACPSO is less than the value using AWPSO by 0.6164 s. And the value of settling time in case of PSO is almost double the value of settling time when using AACPSO.

2. The parameters value of area 1 PID controller (Kp2, Ki2, Kd2) also shown in Table 3.

Figure 14 presents error index (IAE) of area control error ACE of the system with PSO. Figure 15 displays error index (IAE) of ACE of the system with AWPSO. While; Fig. 16 shows error index (IAE) of the system with ACE with AACPSO.

All previous results indicate that the best way using to reduce the IAE error of the two area power systems is AACPSO.

Because of the results of AACPSO which is the best results of all methods to have a minimum value of IAE error at a small value of settling time. So using these values to make a training of ANFIS. Figure 17 shows the two-Area Power Systems SIMULINK Model using ANFIS controller and all necessary changes of the model.

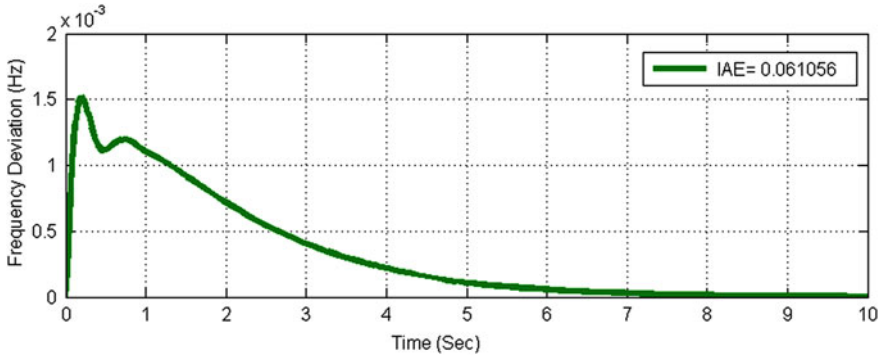

Fig. 14 Error index of ACE with PSO based PID controller in case of using IAE error

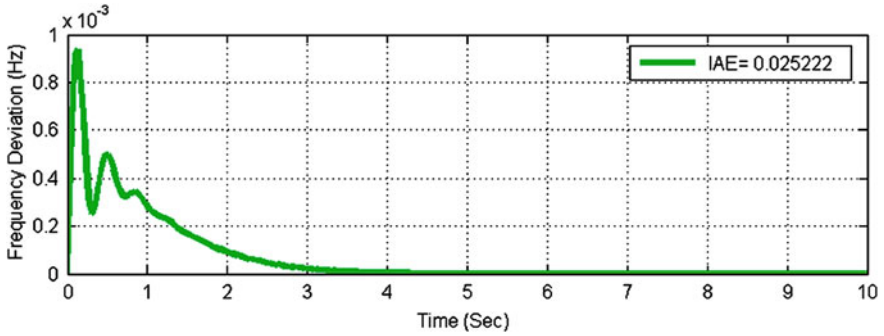

Fig. 15 Error index of ACE with AWPSO based PID controller in case of using IAE error

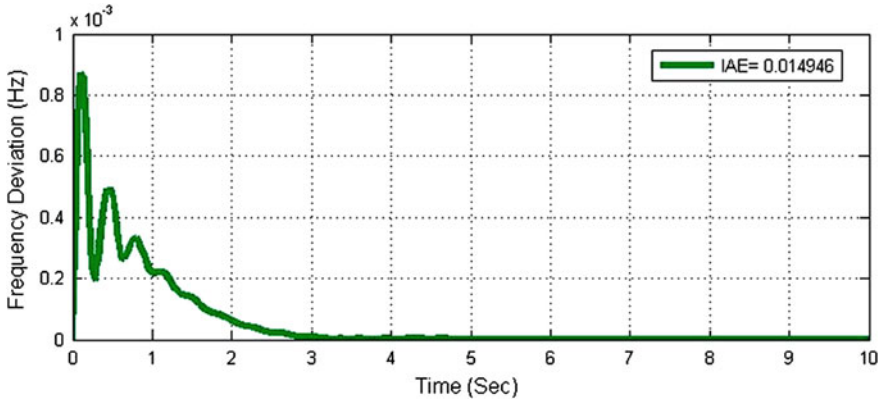

Fig. 16 Error index of ACE with AACPSO based PID controller in case of using IAE error

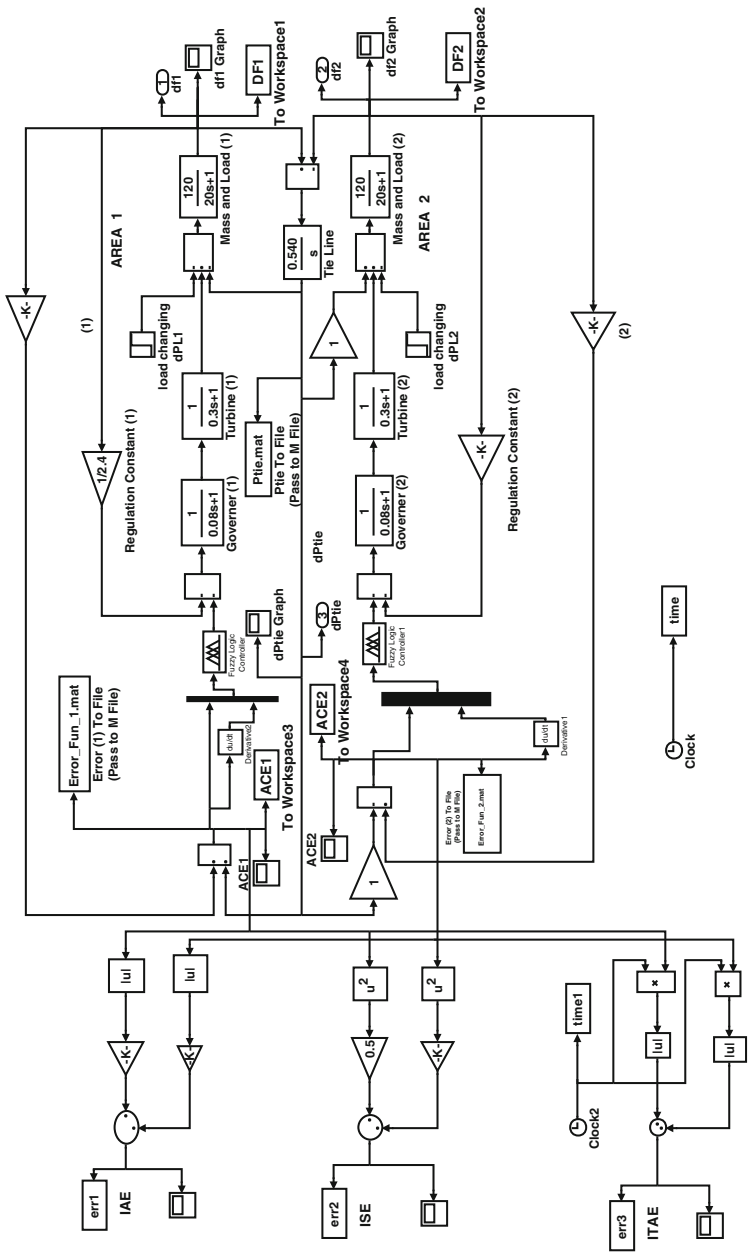

Fig. 17 Two-area power systems SIMULINK model using adaptive fussy controller ANFIS

Table 5 Comparison between PSO, AWPSO, AACPSO and ANFIS

Item of comparison	PSO	AWPSO	AACPSO	ANFIS
Max frequency deviation of area 1 (Hz)	1.09E−06	9.03E−06	4.10E−05	0.0
Minimum frequency deviation of area 1 (Hz)	−0.006	−0.0039	−0.0036	−0.002637
Max frequency deviation of area 2 (Hz)	2.07E−06	2.89E−06	4.14E−06	0.0
Minimum frequency deviation of area 2 (Hz)	−0.0026	−8.91E−04	−8.32E−04	−0.001002

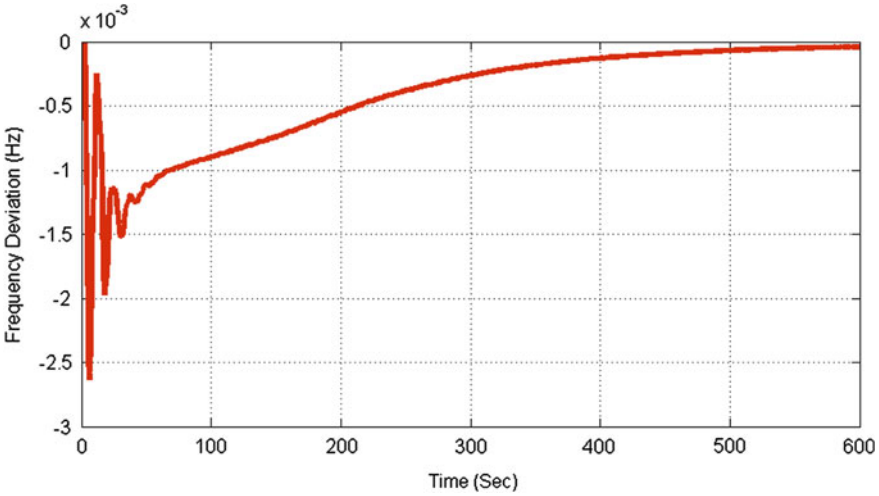

Fig. 18 Frequency deviation of area 1 using ANFIS

By using ANFIS, the results present the performance of the different tuning algorithms for PID controller of the two different areas. Table 5 shows the comparison between the four methods (PSO, AWPSO, AACPSO and ANFIS) used and shows the values of the maximum and minimum values of the frequency deviation of each area. Figures 18 and 19 illustrate the frequency deviation responses of area 1 and area 2 power systems controller tuned by using ANFIS.

The results in Table 5, Figs. 18 and 19 show that:

The maximum frequency deviation value of Area 1 in case of using ANFIS is the smallest value than other methods. PSO comes next after ANFIS method. The minimum Frequency deviation of area 1 using ANFIS is near the value by AACPSO and AWPSO. While; the settling time in case of ANFIS is about 600 s, this value is very big and not accepted because the range of permissible value of settling time is between (0–30 s) as presented in [26].

In area 2 the maximum frequency deviation by using PSO is near the value by using AWPSO and the best method used is ANFIS. However, the minimum

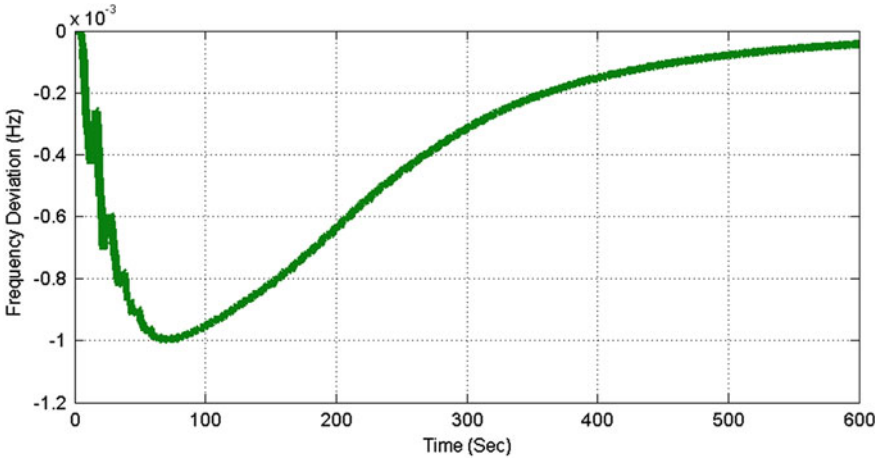

Fig. 19 Frequency deviation of area 2 using ANFIS

frequency deviation using ANFIS is the best and smaller value than other methods. But the settling time is very big value it is about 600 s and off course this value is not acceptable.

Generally, the result shown in Tables 4 and 5 indicate that:

1. The settling time in case of using AACPSO is smaller than its value by using PSO, AWPSO and ANFIS.
2. The maximum frequency deviation in case of using ANFIS is smaller than PSO, AWPSO and AACPSO.
3. The Settling time in case of using ANFIS is not acceptable.
4. Also the disadvantages of ANFIS here in case of IAE Performance Indices which make the using of ANFIS is not acceptable here and take AACPSO as the best method, but ANFIS has many advantages also like it is simple and easy to use compared with the other methods used in this study and it takes less time in the program running.

5.4 Results in Case of Choice ISE Error

Repeating the study with the next type of performance indices which is Integral of Squared Error ISE. Using the same network system presented in Fig. 3, MATLAB program and the parameters display before in Tables 1 and 2.

The study of the performance of the PID controller was compared in case of each intelligent technique (PSO, AWPSO, and AACPSO) and finally the best results of them will use in ANFIS algorithms. Table 6 displays the comparison of the results of the MATLAB program with PSO, AWPSO, and AACPSO. The figures which

Table 6 The results of the program using PSO, AWPSO and AACPSO

Item of comparison	PSO	AWPSO	AACPSO
Number of iterations	500	500	500
Error ISE (integral of absolute error)	4.99E−05	4.78E−05	4.98E−05
Settling time _Area 1 (s)	7.0179	2.2362	1.9323
Settling time _Area 2 (s)	8.4312	4.2489	4.1854
Settling time _Tie line (s)	8.697	4.3416	4.2082
Kp1	5.4209	6.3466	8.1472
Ki1	3.9619	5.7263	7.5774
Kd1	5.1968	2.5784	2.7603
Kp2	0.6806	5.015	3.4998
Ki2	7.64	1.6752	1.6218
Kd2	2.4418	5.6665	8.6869

show the wave form of the frequency deviation of area 1 and area 2 without using PID controller shown above in Figs. 5 and 6.

In the following sections discuss the impact the way the AI techniques used on the Tie Line and area control error ACE of the system.

5.4.1 Tie Line Power

Table 7 presents the comparison between the values of the maximum, minimum frequency deviations and settling time of the Tie line at different types of Artificial Intelligence techniques (PSO, AWPSO and AACPSO).

Figure 20 displays the frequency change of the Tie line power with using PSO, AWPSO and AACPSO based PID controller.

The results display in Tables 7 and Fig. 20 show that:

1. The settling time of Tie line in case of using AACPSO is less than its value in case of using AWPSO by about 0.13 s, and less its value when using PSO by about 4.5 s.

Table 7 Tie line behavior at different typed of control

Items of comparison	PSO	AWPSO	AACPSO
Settling time _Tie line (s)	8.697	4.3416	4.2082
Maximum frequency of tie line power (Hz)	2.59E−05	5.24E−07	4.24E−07
Time at Maximum frequency of tie line power (s)	6.5054	6.5591	22.2727
Minimum frequency of tie line power (Hz)	−4.65E−04	−4.46E−04	−3.66E−04
Time at minimum frequency of tie line power (s)	1.4896	0.7096	0.612

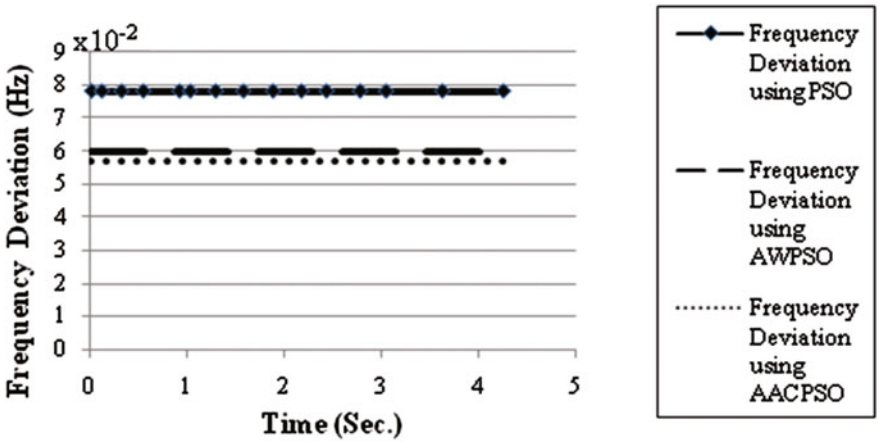

Fig. 20 Tie line power changes using PSO, AWPSO and AAPSO Based PID controller in case of choice ISE error

2. The maximum frequency of Tie line power in case of using AACPSO is less than its value of the other methods of controller used by a very small value.
3. In general the maximum frequency of Tie line power is construed to be zero.
4. Time at maximum frequency deviation of Tie line power in case of using AACPSO is much larger than the other values of PSO and AWPSO. But the value of the time at PSO and AWPSO is almost the same.
5. The minimum frequency deviation of Tie line power in case of using PSO and AWPSO are almost equal. And its value in case of AACPSO is smaller than PSO and AWPSO by a very small value near zero. All the valve of minimum frequency deviation almost is zero.
6. Time at minimum power in case of using AACPSO is less than the other values of PSO and AWPSO. The difference between that time in case of AACPSO and AWPSO is about 0.1 s and its value between AACPSO and PSO is about 0.88 s.

5.4.2 Integral of Squared Error of Area 1 and Area 2

The second choice of the MATLAB program used in this study is ISE as described above. In the following there are the figures describe the output of the system after controlling the error on area 1 and area 2.

From the results shown in Table 6 and also the figures all these show that:

1. The settling time of area 1 in case of using AWPSO is less than the settling time using PSO by 4.78 s to reach to the steady state. While; by using AACPSO the settling time is less than that value by using AWPSO by 0.03 s. So the best method used to reach minimum value of settling time in area 1 is AACPSO.
2. The parameters value of area 1 PID controller (K_{p1}, K_{i1}, K_{d1}) also shown in Table 6.

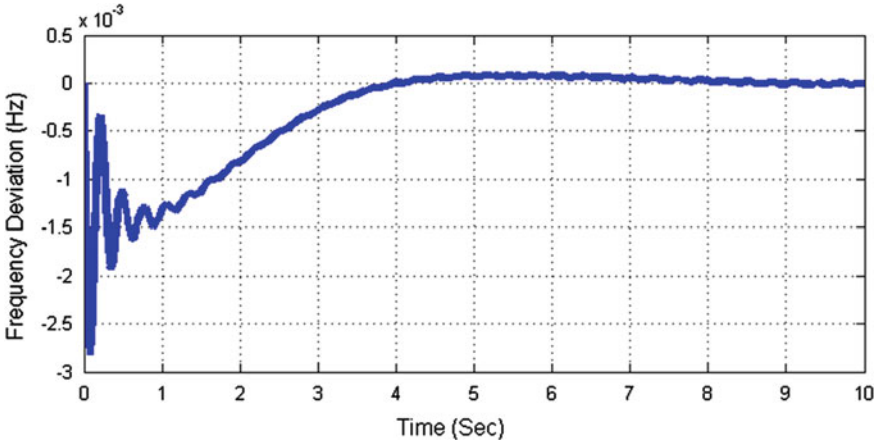

Fig. 21 The frequency deviation of area 1 with PSO based PID controller using ISE performance indices

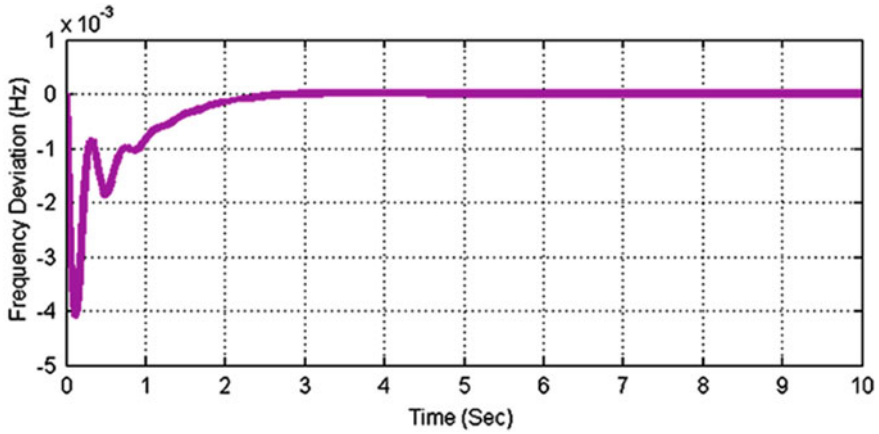

Fig. 22 The frequency deviation of area 1 with AWPSO based PID controller using ISE performance indices

Figure 21 presents the frequency deviation of area 1 with PSO based PID Controller, Fig. 22 presents the frequency deviation of area 1 with AWPSO based PID controller and Fig. 23 illustrates the frequency deviation of area 1 with AACPSO based PID controller.

The figures present the behavior of area 2 in different cases of Artificial Intelligence techniques as follow.

Figure 24 shows the frequency deviation of area 2 with PSO based PID controller using ISE performance indices; Fig. 25 presents the behavior of the frequency deviation of area 2 in case of using AWPSO, while; Fig. 26 displays the frequency deviation of area 2 with AACPSO based PID controller.

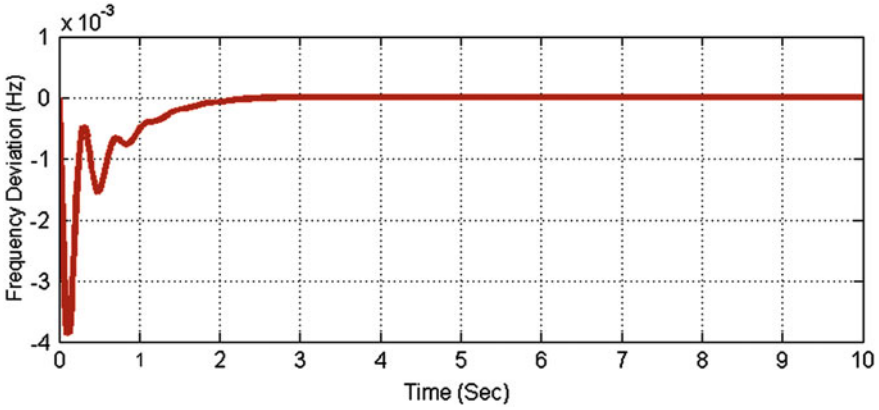

Fig. 23 The frequency deviation of area 1 with AACPSO based PID controller using ISE performance indices

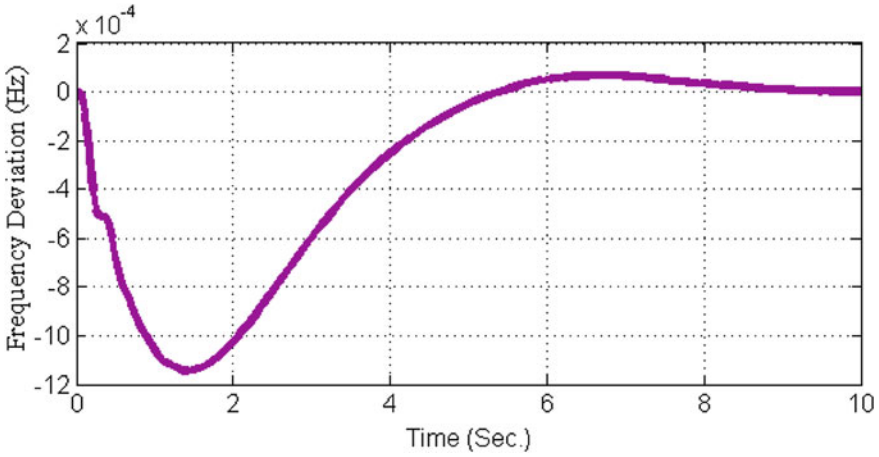

Fig. 24 The frequency deviation of area 2 with PSO based PID controller using ISE performance indices

Figure 27 presents error index (ISE) of area control error ACE of the system with PSO. Figure 28 displays error index (ISE) of ACE of the system with AWPSO. While; Fig. 29 shows error index (ISE) of the system with ACE with AACPSO.

These Figs. 27, 28 and 29 show the change of the frequency deviations of the system with the change of AI techniques (PSO, AWPSO and AACPSO). From all these figures and values shown in Table 6. All previous results indicate that the best way using to reduce the ISE error of the two area power systems is AACPSO.

Because of the results of AACPSO which is the best results of all methods to have a minimum value of ISE error at a small value of settling time. So using these values to make a training of ANFIS. Figure 17 was shown above presents the two-

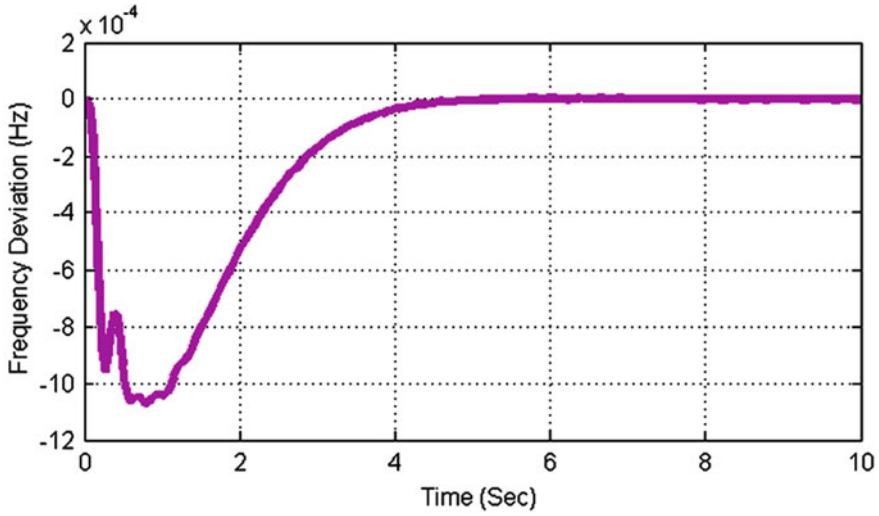

Fig. 25 The frequency deviation of area 2 with AWPSO based PID controller using ISE performance indices

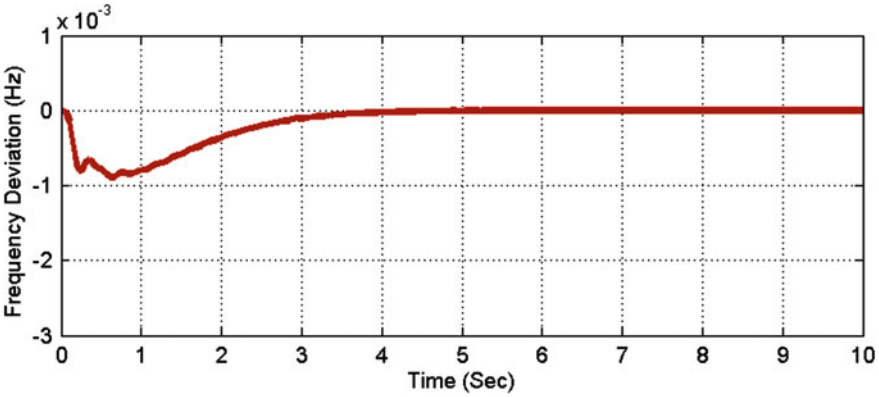

Fig. 26 The frequency deviation of area 2 with AACPSO based PID controller using ISE performance indices

Area Power Systems SIMULINK Model using ANFIS controller and all necessary changes of the model.

By using ANFIS, the results present the performance of the different tuning algorithms for PID controller of the two different areas. Table 8 shows the comparison between the four methods (PSO, AWPSO, AACPSO and ANFIS) used and shows the values of the maximum and minimum values of the frequency deviation of each area.

Figures 30 and 31 illustrate the frequency deviation responses of area 1 and area 2 power systems controller tuned by using ANFIS.

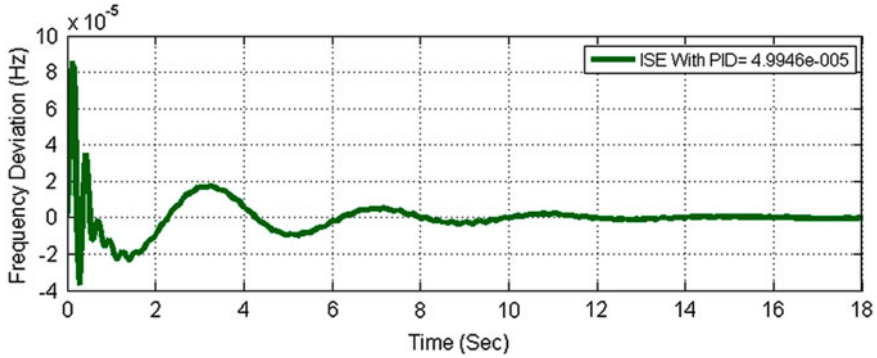

Fig. 27 Error index of ACE with PSO based PID controller in case of choice ISE error

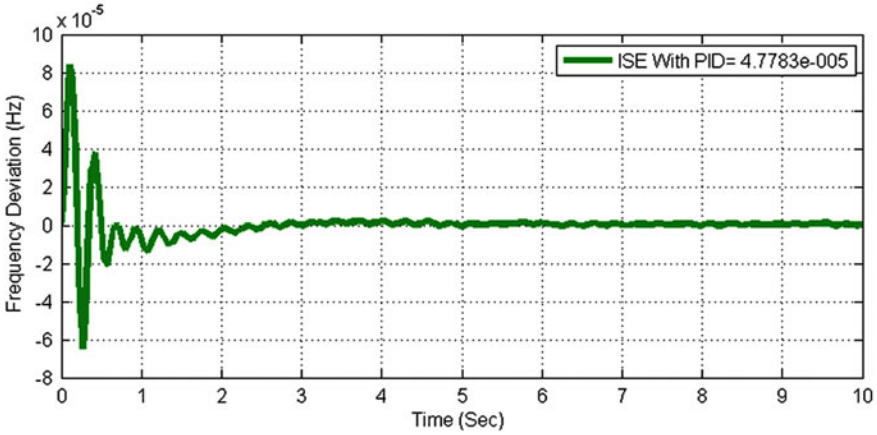

Fig. 28 Error index of ACE with AWPSO based PID controller in case of choice ISE error

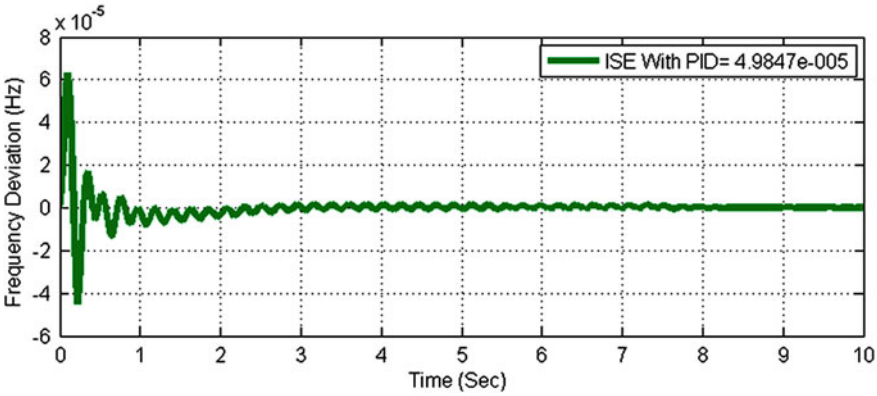

Fig. 29 Error index of ACE with AACPSO based PID controller in case of choice ISE error

Table 8 Comparison between PSO, AWPSO, AACPSO and ANFIS

Item of comparison	PSO	AWPSO	AACPSO	ANFIS
Max frequency deviation of area 1 (Hz)	8.63E−05	1.77E−05	9.03E−06	0.0003608
Minimum frequency deviation of area 1 (Hz)	−0.0028	−0.0041	−0.0039	−0.002098
Max frequency deviation of area 2 (Hz)	6.91E−05	3.83E−06	2.89E−06	0.0
Minimum frequency deviation of area 2 (Hz)	−1.10E−03	−0.0011	−8.91E−04	−0.001035

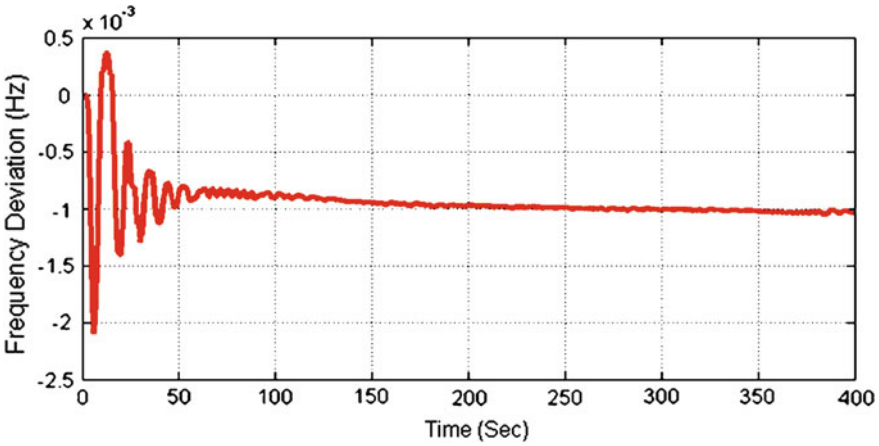

Fig. 30 Frequency deviation of area 1 using ANFIS

The results in Table 8, Figs. 30 and 31 show that:

1. The maximum frequency deviation value of Area 1 in case of using ANFIS is the biggest value than other methods. PSO comes next after ANFIS method.
2. The minimum Frequency deviation of area 1 using ANFIS is near the value by AACPSO.
3. While; the time in case of ANFIS is about 150 s, this value is very big and not accepted because the range of permissible value of settling time is between (0–30 s) as presented in [27].
4. In area 2 the maximum frequency deviation by using AWPSO is near the value by using AACPSO and the best method used is AWPSO. However, the minimum frequency deviation using AWPSO.
5. The maximum frequency deviation by using ANFIS is almost zero. But the settling time is very big value and not acceptable.

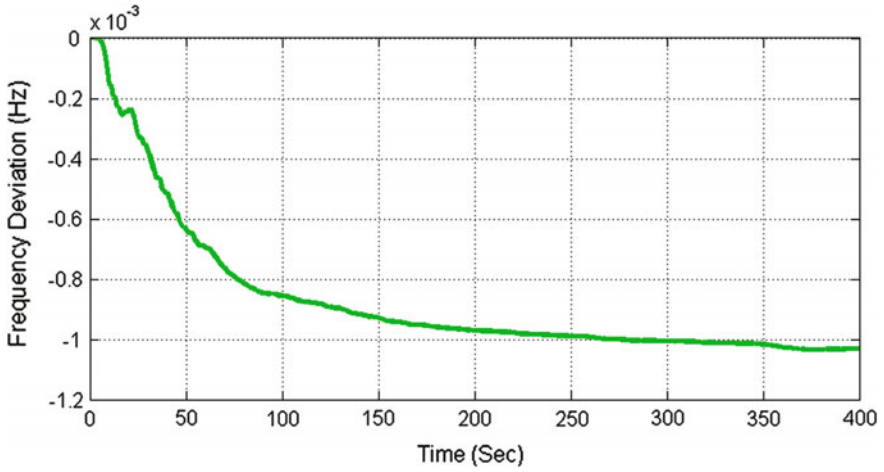

Fig. 31 Frequency deviation of area 2 using ANFIS

Generally, the result shown in Tables 6 and 8 indicate that:

1. The settling time in case of using AACPSO is smaller than its value by using PSO, AWPSO and ANFIS.
2. ANFIS is not acceptable here because of the very large settling time.
3. Also the disadvantages of ANFIS here in case of ISE Performance Indices which make the using of ANFIS is not acceptable here and take AACPSO as the best method, but ANFIS has many advantages also like it is simple and easy to use compared with the other methods used in this study and it takes less time in the program running.

5.5 Results in Case of Choice ITAE Error

Repeating the study with the next type of performance indices which is Integral of Time Weighted Absolute Error (ITAE). Using the same network system presented in Fig. 3, MATLAB program and the parameters display before in Tables 1 and 2.

The study of the performance of the PID controller was compared in case of each intelligent technique (PSO, AWPSO, and AACPSO) and finally the best results of them will use in ANFIS algorithms. Table 9 displays the comparison of the results of the MATLAB program with PSO, AWPSO, and AACPSO. The figures which show the wave form of the frequency deviation of area 1 and area 2 without using PID controller shown above in Figs. 5 and 6.

In the following sections discuss the impact the way the AI techniques used on the Tie Line and area control error ACE of the system.

Table 9 The results of the program using PSO, AWPSO and AACPSO

Item of comparison	PSO	AWPSO	AACPSO
Number of iterations	500	500	500
Error ITAE (integral of time weighted absolute error)	0.0834	0.0608	0.0405
Settling time _Area 1 (s)	3.4403	1.8334	1.7267
Settling time _Area 2 (s)	6.0358	3.3931	2.5288
Settling time _Tie line (s)	5.9679	3.5421	2.5696
Kp1	9.6238	8.8698	3.7517
Ki1	6.1351	9.1419	6.0754
Kd1	4.5189	3.9391	0.8947
Kp2	2.882	3.5254	4.9802
Ki2	8.398	8.0131	1.2982
Kd2	5.5715	3.5553	8.4839

5.5.1 Tie Line Power

Table 10 presents the comparison between the values of the maximum, minimum frequency deviations and settling time of the Tie line at different types of Artificial Intelligence techniques (PSO, AWPSO and AACPSO).

Figure 32 displays the frequency change of the Tie line power with using PSO, AWPSO and AACPSO based PID controller.

The results display in Tables 9 and 10, Fig. 32 show that:

1. On the Tie line power, the value of settling time in case of using AACPSO is the best results and has a smaller value comparing with the other methods used (PSO, AWPSO).
2. The settling time of Tie line in case of using AACPSO is less than its value in case of using AWPSO by about 0.97 s, and less than its value when using PSO by about 3.4 s.
3. Settling time by AWPSO is smaller than using PSO by 2.4 s.
4. The maximum frequency of Tie line power in case of using AWPSO is less than its value of the other methods of controller used by a very small value.
5. The maximum frequency of Tie line power in both AACPSO and PSO is almost equal.

Table 10 Tie line behavior at different typed of control

Items of comparison	PSO	AWPSO	AACPSO
Settling time _Tie line (s)	5.9679	3.5421	2.5696
Maximum frequency of tie line power (Hz)	4.01E−07	5.59E−06	4.98E−07
Time at Maximum frequency of tie line power (s)	23.5062	4.6552	4.0135
Minimum frequency of tie line power (Hz)	−3.22E−04	−3.15E−04	−9.13E−04
Time at minimum frequency of tie line power (s)	0.7932	0.5915	0.442

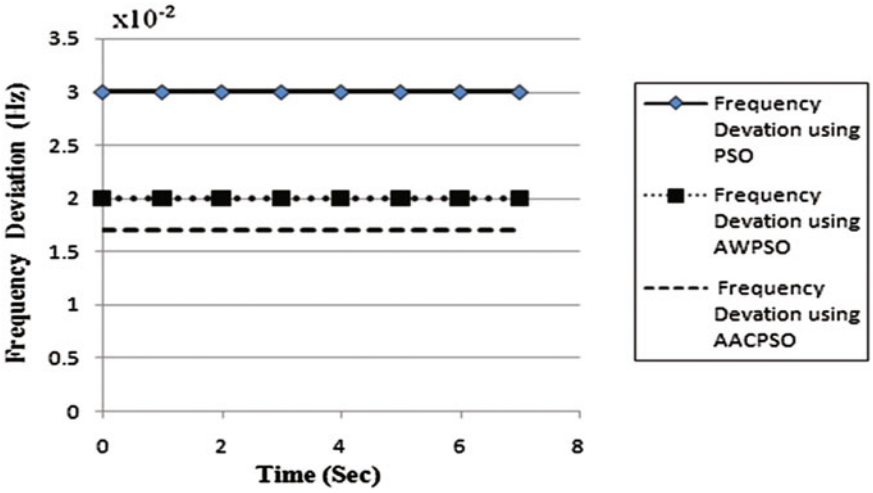

Fig. 32 Tie line power changes using PSO, AWPSO and AAPSO based PID controller in case of choice ITAE error

6. In general the maximum frequency of Tie line power is construed to be zero.
7. Time at maximum power in case of using AACPSO is less than the other values of PSO and AWPSO. This value is less than the time of maximum power in case of using PSO by about 19.5 s and less than its value in case of using AWPSO by about 0.64 s.
8. The minimum Tie line power in case of using PSO and AWPSO are almost equal.
9. The minimum Tie line power in case of using AACPSO is less than its value in case of using PSO and AWPSO.
10. Time at minimum power in case of using AACPSO is less than the other values of PSO and AWPSO.

5.5.2 Integral of Time Weighted Absolute Error of Area 1 and Area 2

The third choice of the MATLAB program used in this study is ITAE as described above. In the following there are the figures describe the output of the system after controlling the error on area 1 and area 2.

Figure 33 presents the frequency deviation of area 1 with PSO based PID Controller, Fig. 34 displays the frequency deviation of area 1 with AWPSO based PID controller and Fig. 35 illustrates the frequency deviation of area 1 with AACPSO based PID controller.

From the results shown in Table 9 and also the Figs. 33, 34 and 35 all these show that:

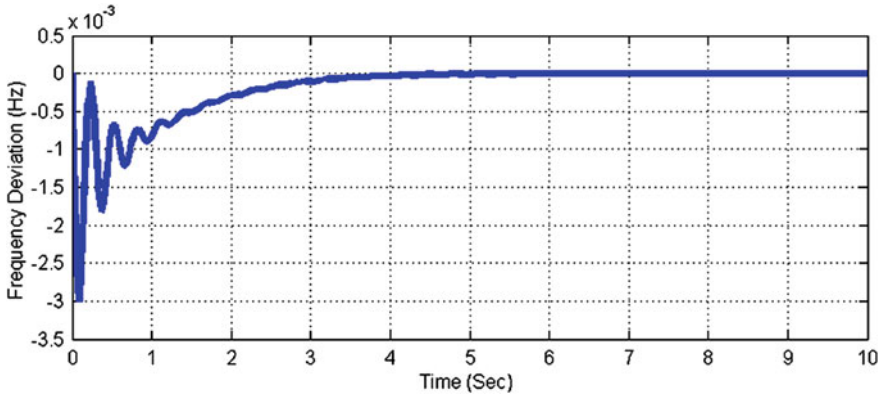

Fig. 33 The frequency deviation of area 1 with PSO based PID controller using ITAE performance indices

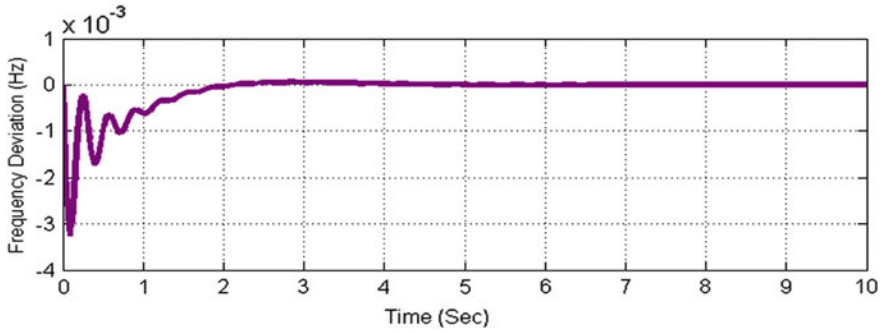

Fig. 34 The frequency deviation of area 1 with AWPSO based PID controller using ITAE performance indices

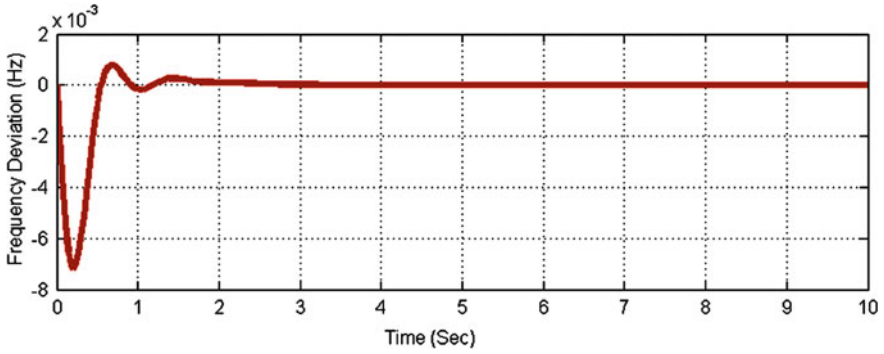

Fig. 35 The frequency deviation of area 1 with AACPSO based PID controller using ITAE performance indices

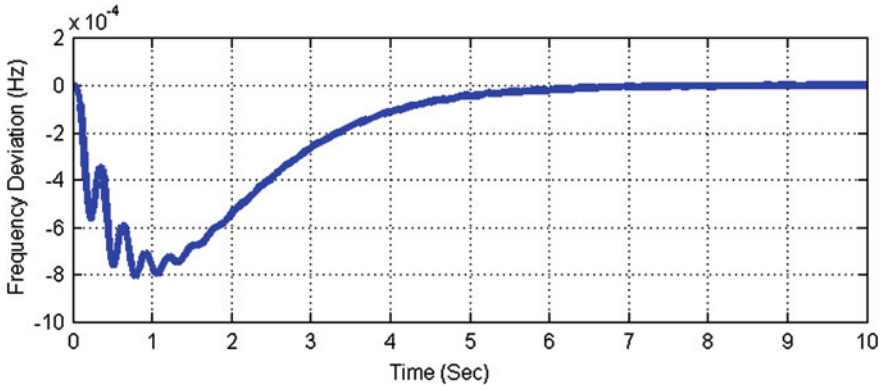

Fig. 36 The frequency deviation of area 2 with PSO based PID controller using ITAE performance indices

1. The ITAE value in case of using AACPSO is less than these values by using PSO and AWPSO. The value of ITAE by using AACPSO is less than PSO by about 0.04 and less than that value by using AWPSO by about 0.02.
2. The settling time of area 1 to reach to the steady state in case of using AACPSO is less than the value of settling time using PSO by about 1.7 s.
3. The settling time by using AACPSO in the program is less than that value by using AWPSO by about 0.1 s.
4. All these results present that: the best method used to reach the minimum ITAE error value at less value of settling time in area 1 is AACPSO.

The next Figures present the behavior of area 2 in different cases of Artificial Intelligence techniques.

Figure 36 shows the frequency deviation of area 2 with PSO based PID controller using ITAE performance indices; Fig. 37 presents the behavior of the frequency deviation of area 2 in case of using AWPSO, while; Fig. 38 displays the frequency deviation of area 2 with AACPSO based PID controller.

From the results shown in Table 9 and also the Figs. 36, 37 and 38 all these show that:

1. The settling time of area 2 by using AWPSO is less than its value by using PSO by 2.64 s. While; the settling time becomes smaller if using AACPSO. The output results using AACPSO is less than the value using AWPSO by 0.86 s. And the value of settling time in case of PSO is almost double the value of settling time when using AWPSO.
2. The parameters value of area 1 PID controller (K_{p2}, K_{i2}, K_{d2}) also presented in Table 9.

The following Figs. 39 and 40 present the shape and values of Integral of Time Weighted Absolute Error ITAE of the system with the using of the different types of control used.

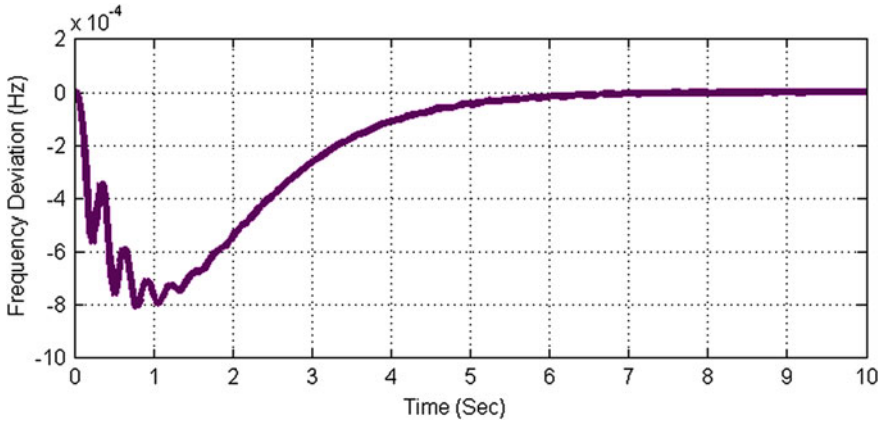

Fig. 37 The frequency deviation of area 2 with AWPSO based PID controller using ITAE performance indices

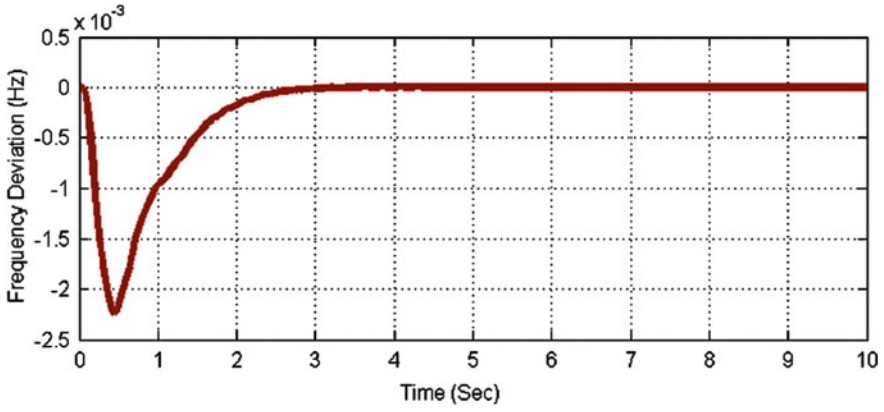

Fig. 38 The frequency deviation of area 2 with AACPSO based PID controller using ITAE performance indices

Figure 39 presents error index (ITAE) of area control error ACE of the system with PSO. Figure 40 displays error index (ITAE) of ACE of the system with AWPSO. While; Fig. 41 presents error index (ITAE) of the system with AACPSO.

All previous results indicate that the best way using to reduce the ITAE error of the two area power systems is AACPSO.

Because of the results of AACPSO which is the best results of all methods to have a minimum value of ITAE error at a small value of settling time. So using these values to make a training of ANFIS. Figure 17 illustrated the two-Area Power Systems SIMULINK Model using ANFIS controller and all necessary changes of the model.

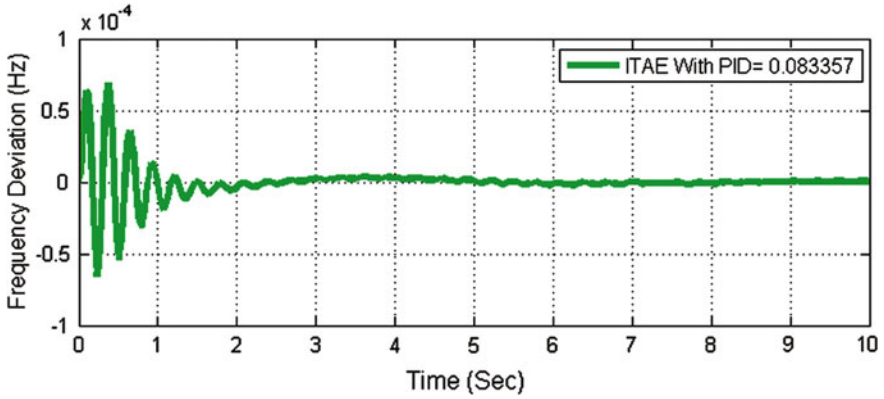

Fig. 39 Error index of ACE with PSO based PID controller in case of choice ITAE error

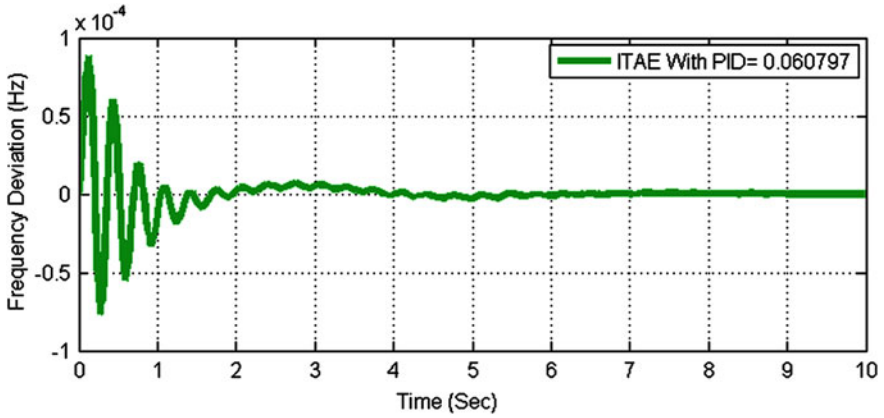

Fig. 40 Error index of ACE with AWPSO based PID controller in case of choice ITAE error

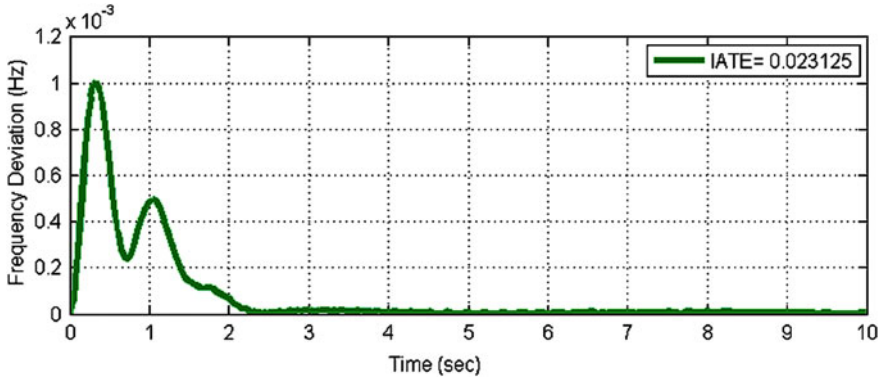

Fig. 41 Error index of ACE with AACPSO based PID controller in case of choice ITAE error

Table 11 Comparison between PSO, AWPSO, AACPSO and ANFIS

Item of comparison	PSO	AWPSO	AACPSO	ANFIS
Max frequency deviation of area 1 (Hz)	4.71E−06	6.45E−05	7.91E−04	2.223E−005
Minimum frequency deviation of area 1 (Hz)	−0.003	−0.0033	−0.0072	−0.002818
Max frequency deviation of area 2 (Hz)	1.77E−06	1.08E−05	4.95E−06	2.857E−006
Minimum frequency deviation of area 2 (Hz)	−8.10E−04	−8.19E−04	−0.0022	−0.0007645

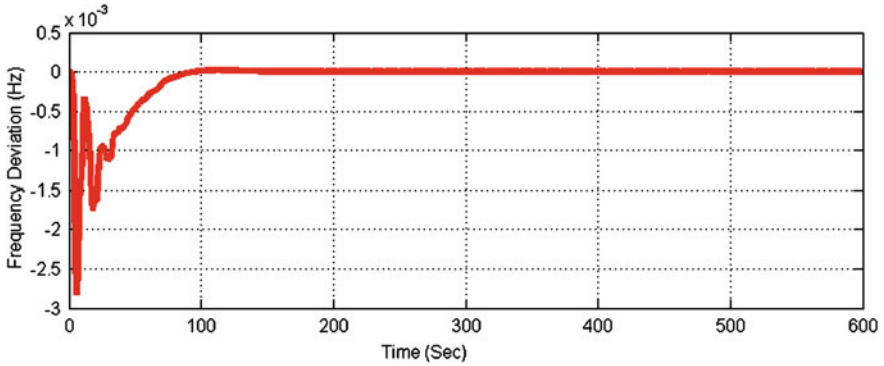

Fig. 42 Frequency deviation of area 1 using ANFIS

By using ANFIS, the results present the performance of the different tuning algorithms for PID controller of the two different areas.

Table 11 shows the comparison between the four methods (PSO, AWPSO, AACPSO and ANFIS) used and shows the values of the maximum and minimum values of the frequency deviation of each area. Figures 42 and 43 illustrate the frequency deviation responses of area 1 and area 2 power systems controller tuned by using ANFIS.

The results in Table 11, Figs. 42 and 43 show that:

1. The maximum frequency deviation value of Area 1 in case of using PSO is the smallest value than other methods. AWPSO comes next after PSO method.
2. The minimum Frequency deviation of area 1 using PSO and AWPSO is almost equal. The value of the minimum Frequency deviation by AACPSO is the smallest value.
3. The settling time in case of ANFIS is about 100 s; this value is very big and not accepted because the range of permissible value of settling time is between (0–30 s) as explained in Rania [27].
4. In area 2 the maximum frequency deviation by using AWPSO is the smallest one. After that PSO comes next.

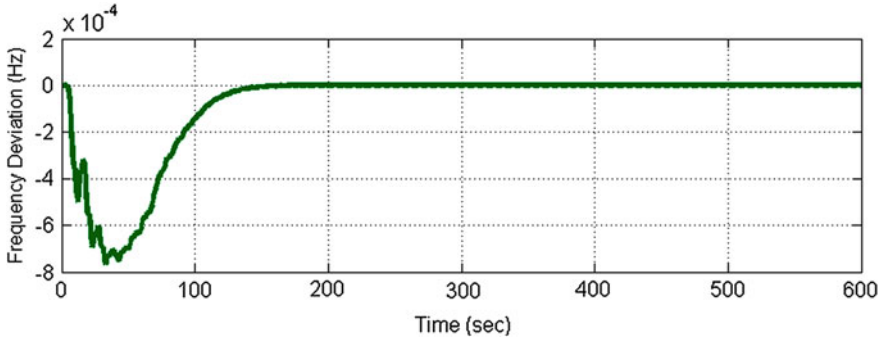

Fig. 43 Frequency deviation of area 2 using ANFIS

5. The difference value between the maximum frequency deviations of area 2 is very small.
6. The minimum frequency deviation in area 2 using ANFIS is the best and smaller value than other methods. But the settling time is very big value it is about 150 s and off course this value is not acceptable.

Generally, the result shown in Tables 9 and 11 indicate that:

1. The settling time in case of using AACPSO is smaller than its value by using PSO, AWPSO and ANFIS.
2. The maximum frequency deviation in case of using ANFIS is smaller than PSO, AWPSO and AACPSO.
3. The Settling time in case of using ANFIS is not acceptable.
4. Also the disadvantages of ANFIS here in case of ITAE Performance Indices which make the using of ANFIS is not acceptable here and take AACPSO as the best method, but ANFIS has many advantages also like it is simple and easy to use compared with the other methods used in this study and it takes less time in the program running.

6 Comparative Study

A comparison study has been carried out with Genetic Algorithm, ordinary PI controller, Ziegler Nichols tuned PID, Bacteria Foraging Optimization (BFO) tuned PID controller as described in [2, 3, 33]. And the results display above for all cases using Particle Swarm Optimization (PSO), Adaptive Weighted Particle Swarm (AWPSO), Adaptive Acceleration Coefficients based PSO (AACPSO), and Adaptive Neuro Fuzzy Inference System (ANFIS) according to the three types of performance Indices (IAE, ISE and ITAE) in order to assess the results.

Table 12 Comparison between different controllers in the first area

Controller	Overshoot (Hz)	Settling Time (s)
Genetic-PID	0.0037	3.6389
BFO based PID	0.0168	4.0415
Ziegler-Nichols PID	0.0149	6.3522
Conventional PI	0.0222	35.0893
AACPSO with IAE	4.10E−05	1.6514
AACPSO with ISE	9.03E−06	1.9323
AACPSO with ITAE	7.91E−04	1.7267

6.1 The First Area

Table 12 displays the Comparison between Adaptive Acceleration Coefficients based PSO (AACPSO), Genetic based PID, BFO based PID, Ziegler-Nicholas Tuned PID and Conventional PI Controller in terms of the frequency deviation in First Area of the power system.

From these results display in Table 12:

1. The settling time of AACPSO with the three types of performance Indices (IAE, ISE and ITAE) was near each other.
2. The result of the settling time by using AACPSO with IAE is the best one from all methods used.
3. The Overshoot value of AACPSO with ISE is small than its value by using other methods of performance Indices.
4. The results by using Conventional PI are the worst one. The value of the settling time is very big and not accepted.

This comparison illustrates that the AACPSO method has the best results of settling time and over shoot frequency deviation for the First Area in all cases studied of performance Indices (IAE, ISE, and ITAE) comparing with the other methods of controller (Genetic based PID, BFO based PID, Ziegler-Nicholas Tuned PID, Conventional PI Controller).

6.2 The Second Area

Table 13 displays the Comparison between Adaptive Acceleration Coefficients based PSO (AACPSO), Genetic based PID, BFO based PID, Ziegler-Nicholas Tuned PID and Conventional PI Controller in terms of the frequency deviation in the Second Area of the system.

From these results:

1. The result of the settling time by using AACPSO with ITAE is the best one from all methods used, so this method is the best one.

Table 13 Comparison between different controllers in the second area

Controller	Overshoot (Hz)	Settling time (s)
Genetic-PID	0.0014	5.208
BFO based PID	0.0123	3.433
Ziegler-Nichols PID	0.0099	8.3539
Conventional PI	0.0178	38.2914
AACPSO with IAE	4.14E−06	3.569
AACPSO with ISE	2.89E−06	4.1854
AACPSO with ITAE	4.95E−06	2.5288

2. The settling time of AACPSO with IAE was near its value by using BFO based PID, but the Overshoot value of AACPSO with IAE is small than its value by using BFO.
3. The overshoot value by using AACPSO with ISE is the best one, but the settling time in this method was bigger than its value by using BFO and AACPSO with IAE and ITAE.
4. The results by using Conventional PI are the worst one. The value of the settling time is very big and not accepted.

6.3 Tie Line Power

Table 14 presents the Comparison between Genetic based PID, BFO based PID, Ziegler-Nicholas Tuned PID and Conventional PI Controller in terms of the Tie Line Power Deviation.

From these results:

1. The result of the settling time by using AACPSO with ITAE is the best one from all methods used.
2. The Overshoot value of AACPSO with ISE is small than its value by using other methods of performance Indices.
3. The overshoot value by using AACPSO in near each other with different methods of performance Indices (IAE, ISE, and ITAE).
4. The results by using Conventional PI are the worst one. The value of the settling time is very big and not accepted.

Table 14 Comparison between different controllers in the tie line

Controller	Overshoot (Hz)	Settling time (s)
Genetic-PID	0.0014	5.208
BFO based PID	0.0123	3.433
Ziegler-Nichols PID	0.0099	8.3539
Conventional PI	0.0178	38.2914
AACPSO with IAE	1.06E−06	3.6553
AACPSO with ISE	4.24E−07	4.2082
AACPSO with ITAE	4.98E−07	2.5696

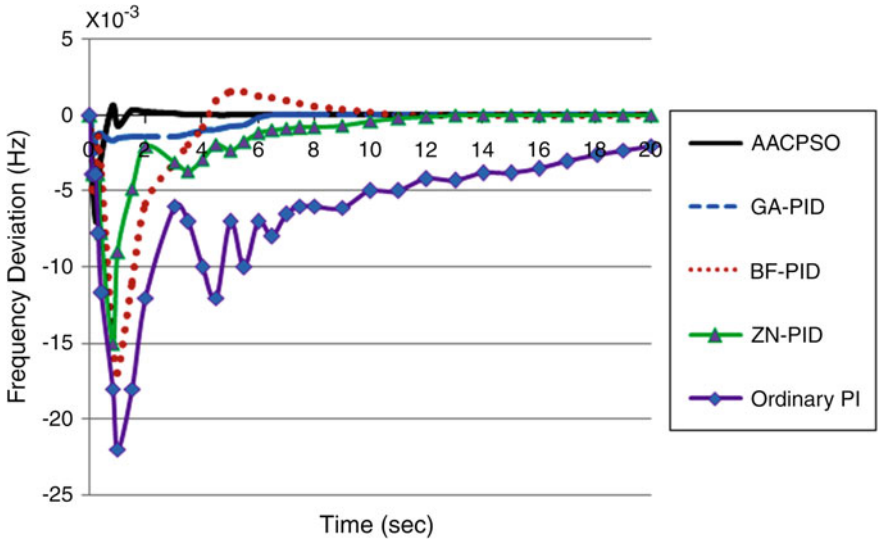

Fig. 44 First area frequency response with AACPAO tuned PID compared to GA-tuned PID, conventional PI, ZN- PID, and BFO-PID

This comparison show that the AACPSO methods have the best results of settling time and over shoot frequency deviation for the Tie line power in all cases studied of performance Indices (IAE, ISE, and ITAE) comparing with the other methods of controller (Genetic based PID, BFO based PID, Ziegler-Nicholas Tuned PID, Conventional PI Controller).

From the results presented in Tables 11, 12 and 13 AACPSO results for first and second area with ITAE performance indices are chosen to compare with Genetic Algorithm, ordinary PI controller, Ziegler Nichols tuned PID and Bacteria Foraging Optimization (BFO) tuned PID controller [2, 3, 33].

Figure 44 presents the time response of the first area using AACPSO tuned PID compared with the Genetic based PID controller with the conventional PI controller, conventionally tuned PID controller (Ziegler Nichols method) and Bacteria Foraging Optimization based PID controller; system was simulated with step change of 0.01 p.u.

Figure 45 presents the time response of the second area using AACPSO tuned PID compared with the Genetic based PID controller with the conventional PI controller, conventionally tuned PID controller (Ziegler Nichols method) and Bacteria Foraging Optimization based PID controller; system was simulated with step change of 0.01 p.u.

Figure 46 displays the time response of the Tie line power using AACPSO tuned PID compared with the Genetic based PID controller with the conventional PI controller, conventionally tuned PID controller (Ziegler Nichols method) and Bacteria Foraging Optimization based PID controller.

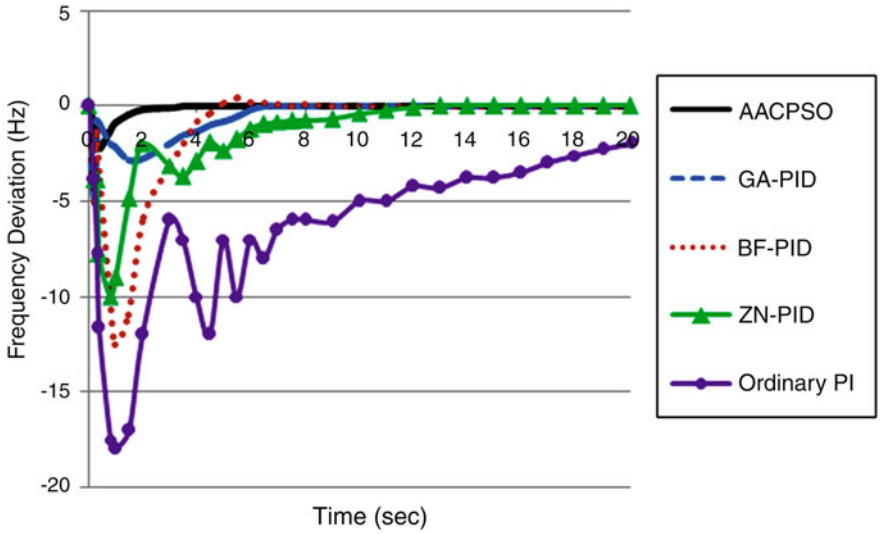

Fig. 45 Second area frequency response with AACPAO tuned PID compared to GA-tuned PID, conventional PI, ZN- PID, and BFO-PID

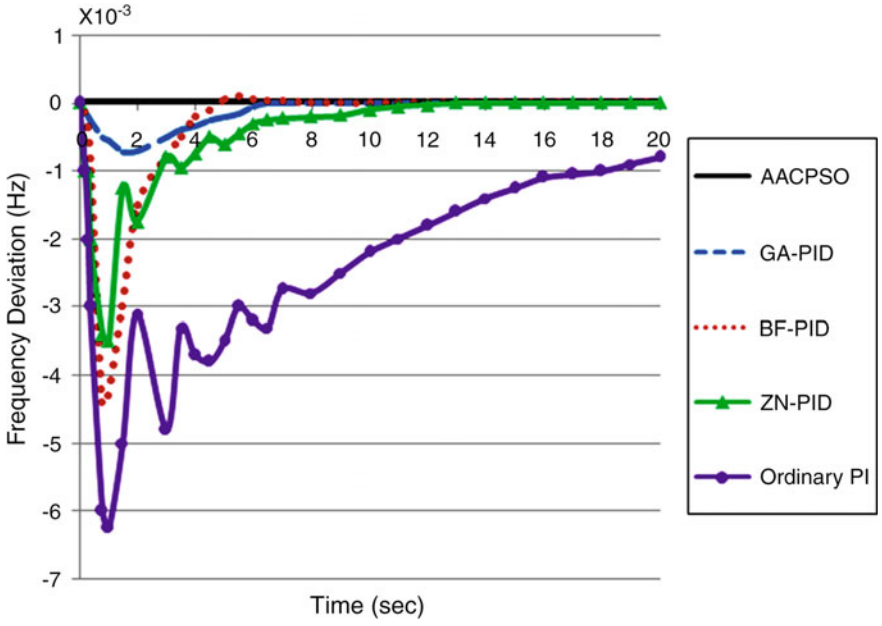

Fig. 46 Tie line power frequency response with AACPAO tuned PID compared to GA-tuned PID, conventional PI, ZN- PID and BFO-PID

7 Conclusion

The simulation of the proposed controllers explained in this chapter, indicate that:

1. Adaptive Acceleration Coefficients based PSO (AACPSO) is the best method which gives the best values of settling time and overshoot frequency deviation comparing with Particle Swarm (PSO) and Adaptive Weighted Particle Swarm (AWPSO).
2. ANFIS was not acceptable here because of the very huge value of settling time when ANFIS used, ANFIS has many advantages also like it is sample and easy to use compared with the other methods used in this study and it takes less time in the program running. ANFIS method is better than using of other methods in some applications especially in case of complicated systems which need to solve the problems in very small time.
3. A comparative study has been carried out for AACPSO which is the best method used to tune the PID controller compared with PSO, AWPSO and ANFIS as presented before, *with* ordinary PI controller; Ziegler Nichols tuned PID, Bacteria Foraging Optimization (BFO) and Genetic tuned PID according to the three types of performance Indices (IAE, ISE and ITAE).
4. This comparative study indicate that the best type of the controller to have the small value of settling time and overshoot frequency deviation was made by PID controller tuning by AACPSO.

Appendix

Transmission line 1 parameters	
$K_g1 = 1$	
Kt1 = 1	
Tg1 = 0.08	
Tt1 = 20	
R1 = 2.4	
T11 = 20	
Kl1 = 120	
a12 = 1	
Transmission line 2 parameters	
$K_g2 = 1$	
Kt2 = 1	
Tg2 = 0.08	
Tt2 = 0.33	
R2 = 2.4	

(continued)

(continued)

Transmission line 1 parameters	
T12 = 20	
Kl2 = 120	
N = 25	Number of swarm beings
d = 6	Two dimensional problem
n = 500	Number of iterations
W0 = 0.15	Percentage of old velocity
A0 = 0.5	Acceleration factor constant between [0 1]
C_1 = 2.05	Percentage towards personal optimum
C_2 = 2.05	Percentage towards
x0range = [0 10]	Range of uniform initial distribution of positions
vstddev = 1	Std. deviation of initial velocities
C_{11} = 2	Percentage towards personal optimum used in ACC
C_{22} = 2.05	Percentage towards used in ACC

References

1. Ahmed, S., Tarek, B. and Djemai, N.: Economic dispatch resolution using adaptive acceleration coefficients based PSO considering generator constraints. International Conference on Control, Decision and Information Technologies', (CoDIT'13) 2013
2. Abd-Elazim, S. M., Ali, E.S.: Optimal PID tuning for load frequency control using bacteria foraging optimization algorithm. International Middle East Power Systems Conference (MEPCON'10), pp. 410–415. Cairo University, Cairo, Egypt (2010)
3. Ali, M.M.I., Hassan, M.A.M.: Speed sensorless field–oriented control of a six-phase saturated model of induction motors drive with online stator resistance estimation using ANFIS. Int. J. Model. Ident. Control **17**(4), 334–347 (2012)
4. Amjady, N., Nasiri-Rad, H.: Nonconvex economic dispatch with AC constraints by a new real coded genetic algorithm. IEEE Trans. Power Syst. **24**(3), 1489–1502 (2009)
5. Ang, K.H., Chong, G.C.Y., Li, Y.P.I.D.: Control system analysis, design, and technology. IEEE Trans. Control Syst. Technol. **13**(4), 559–576 (2005)
6. Azar, A.T.: Fuzzy Systems. IN-TECH. Vienna, Austria, ISBN 978-953-7619-92-3 (2010)
7. Azar, A.T.: Adaptive neuro-fuzzy systems. In: Azar, A.T. (ed.), Fuzzy Systems. IN-TECH, Vienna, Austria, ISBN 978-953-7619-92-3 (2010)
8. Azar, A.T.: Overview of Type-2 fuzzy logic systems. Int. J. Fuzzy Syst. Appl. **2**(4), 1–28 (2012)
9. Aziz, A., Hassan, M.A., El-Zahab, E.A.: An artificial intelligence based approach for high impedance faults analysis in distribution networks. Int. J. Syst. Dyn. Appl. **1**(2), 44–59 (2012)
10. Aziz, M.A., Hassan, M.M., Zahab, E.A.: High-impedance faults analysis in distribution networks using an adaptive Neuro fuzzy inference system. Electr. Power Compon. Syst. **40** (11), 1300–1318 (2012)
11. Bevrani, H.: Robust power system frequency control. Springer Science and Business Media LLC, Brisbane (2009)
12. Chaudhari, O.K., Khot, P.G., Deshmukh, K.C., Bawne, N.G.: Anfis based model in decision making to optimize the profit in farm cultivation. Int. J. Eng. Sci. **4**(2), 442–448 (2012)

13. Gaing, Z.L.: A particle swarm optimization approach for optimum design of PID controller in AVR system. IEEE Trans. Energy Convers. **19**(2), 384–391 (2004)
14. Ghomsheh, V.S., Shoorehdeli, M.A., Teshnehlab M.: Training ANFIS structure with modified PSO algorithm in control and automation. In: Mediterranean Conference on IEEE MED'07, pp. 1–6 (2007)
15. Hamid, A., Abdul-Rahman, T.K.: Short term load forecasting using an artificial neural network trained by artificial immune system learning algorithm in computer modeling and simulation (UKSim). In: 12th International Conference on IEEE, pp. 408–413 (2010)
16. Ismail, A.: Improving UAE power systems control performance by using combined LFC and AVR. In: 7th UAE University Research Conference, Eng pp. 50–60 (2006)
17. Ismail, M.M., Hassan, M.A.: Using positive and negative sequence components of currents and voltages for high impedance fault analysis via ANFIS. Int. J. Syst. Dyn. Appl. **1**(4), 132–157 (2012)
18. Ismail, M.M., Hassan, M.M.: Load frequency control adaptation using artificial intelligent techniques for one and two different areas power system. Int. J. Control Autom. Syst. **1**(1), 12–23 (2012)
19. Kamel, T.S., Hassan, M.A.M., El–Morshedy, A.: Advanced distance protection technique based on multiple classified ANFIS considering different loading conditions for long transmission lines in EPS. Int J Model Ident. Control **16**(2), pp. 108–121 (2012)
20. Kumar, D.V.: 'Intelligent controllers for automatic generation control', in TENCON' 98. IEEE Region, 10th International Conference on Global Connectivity in Energy, Computer, Communication and Control, vol. 2, pp. 557–574 (1998)
21. Loganathan, C., Girija, K.V.: Hybrid learning for adaptive neuro fuzzy inference system. Int. J. Eng. Sci. **2**(11), 6–13 (2013)
22. Lutfy, O.F., Noor, S.B.M., Marhaban, M.H.: A simplified adaptive neuro-fuzzy inference system (ANFIS) controller trained by genetic algorithm to control nonlinear multi-input multi-output systems. Sci. Res. Essays **6**(31), 6475–6486 (2011)
23. Naik, R.S., ChandraSekhar, K., Vaisakh, K.: Adaptive PSO based optimal fuzzy controller design for AGC equipped with SMES and SPSS. J. Theor. Appl. Inf. Technol. **7**(1), 008–017 (2005)
24. Panigrahi, B.K., Pandi, V.R., Das, S.: Adaptive particle swarm optimization approach for static and dynamic economic load dispatch. Energy Convers. Manag. **49**(6), 1407–1415 (2008)
25. RamaSudha, K., Vakula, V.S., Shanthi, R.V.: PSO based design of robust controller for two area load frequency control with nonlinearities. Int. J. Eng. Sci. **2**(5), 1311–1324 (2010)
26. Rania, H. M.: Development of advanced controllers using adaptive weighted PSO algorithm with applications. M.Sc. thesis, Faculty of Engineering, Cairo University, Cairo (2012)
27. Salami, A., Jadid, S., Ramezani, N.: The effect of load frequency controller on load pickup during restoration. In: IEEE International Power and Energy Conference, PECon'06, pp. 225–228 (2006)
28. Skogestad, S.: Simple analytic rules for model reduction and PID controller tuning. J. Proc. Control **13**(4), 291–309 (2003)
29. Song, Y.H., Johns, A.T.: Applications of fuzzy logic in power systems. I. General introduction to fuzzy logic. Power Eng. J. **11**(5), 219–222 (1997)
30. Song, Y.H., Johns, A.T.: Application of fuzzy logic in power systems. II. Comparison and integration with expert systems, neural networks and genetic algorithms. Power Eng. J. **12**(4), 185–190 (1998)
31. Tammam, M.A., Aboelela, M.A.S., Moustafa, M.A., Seif, A.E.A.: Load frequency controller design for interconnected electric power system. In: 55th Annual Power Industry Division Symposium POWID, Austin (2012a)
32. Tammam, M.A., Aboelela, M.A.S., Moustafa, M.A., Seif, A.E.A.: Fuzzy like PID controller tuning by multi-objective genetic algorithm for load frequency control in nonlinear electric power systems. Int. J. Adv. Eng. Technol. **5**(1), 572–583 (2012)

33. Tammam, M.A.: Multi objective genetic algorithm controllers tuning for load frequency control in Electric power systems. M.Sc. thesis, Faculty of Engineering at Cairo University, Cairo (2011)
34. Vlachogiannis, J.G., Lee, K.Y.: Economic load dispatch—a comparative study on heuristic optimization techniques with an improved coordinated aggregation based PSO. IEEE Trans. Power Syst. **24**(2), 991–1001 (2009)
35. Wang, Y., Zhou, R., Wen, C.: Robust load-frequency controller design for power systems. In: IEE Proceedings C, Generation, Transmission and Distribution, IET Digital Library, vol. 140 (1) pp. 11–16 (1993)

Investigating Metaheuristics Applications for Capacitated Location Allocation Problem on Logistics Networks

Yonglin Ren and Anjali Awasthi

Abstract Logistics is vital to sustaining many industrial, commercial, and administrative activities. It is often composed of the logistics service providers and the customers being serviced. The goal of service providers is to maximize revenues by servicing customers efficiently within their preferred timelines. To achieve this goal, they are often involved in activities of location-allocation planning, that is, which logistics facilities be opened, where they should be opened, and how customer allocations should be performed to ensure timely service to customers at least delivery costs to logistics operators. Location-allocation problem is NP-hard. In literature, metaheuristics have been shown to perform better than exact programming approaches to tackle larger NP-hard problems. We present four metaheuristics based solution approaches namely Genetic algorithms (GA), Simulated annealing (SA), Tabu search (TS), and Ant colony optimization (ACO) to address the capacitated location allocation problem on logistics networks. The problem is studied under two cases. In the first case, opening costs of the facilities and only one criterion (distance) is used. In the second case, opening costs of the facilities and multiple criteria (distance, travel cost, travel time) are used. The proposed approaches are tested under various problem instances to verify and validate the model results.

Keywords Metaheuristics · Capacitated location-allocation · Logistics

Y. Ren · A. Awasthi (✉)
CIISE, Concordia University, Montreal, Canada
e-mail: awasthi@ciise.concordia.ca

Y. Ren
e-mail: jacquesmontreal@yahoo.ca

A.T. Azar and S. Vaidyanathan (eds.), *Chaos Modeling and Control Systems Design*,
Studies in Computational Intelligence 581, DOI 10.1007/978-3-319-13132-0_9

1 Introduction

Location planning of logistics depots and customer allocation are important decisions in supply chain network design [12, 29, 35]. A carefully planned network design positively impacts the economics of business organizations and their competitiveness in national and international markets. Improper planning can lead to poor service quality towards customers, long delivery times, and high investment and maintenance costs for the logistics operators, which is detrimental to their business operations and profitability.

The problem treated in this paper is motivated by distribution network design in urban areas under congestion. The decisions concerned are location planning of logistics depots and allocation of clients to the opened logistics depots. In urban environment, opening of logistics depots and clients allocation is affected by a number of factors such as presence of congestion, land and labor cost, proximity to clients, presence of municipal regulations such as time restrictions, access restrictions etc. Therefore, the problem of how many logistics depots to be opened, where to locate them, and how to cluster customers and allocate them to logistics depots etc. is multiobjective and dynamic in nature and not a static or one-time decision as considered in several studies available in literature in this direction. In practice, the LA decision involves consideration of multiple factors such as distance, travel cost, travel time etc [5, 6, 39].

Solutions to location allocation problem have been mainly investigated under two main cases [34, 40]. In the first case, the location planning of logistics depots is performed first and customer allocations are done. In the second case, the customer zones are formed first and then logistical facilities or logistics depots are located at center of zones to ensure better coverage and service for customers.

Distributing goods to customers from several logistics depots produces the problem of optimizing the delivery process. Managers or Logistics operators face the problem of reducing delivery costs, that is, how to ensure efficient delivery processes considering multiple factors such as travel cost, travel time, and travel distance, and how to integrate them altogether in optimizing overall costs for delivery of goods to customers. It is obvious that these problems are multiobjective in nature and therefore compromise solutions have to be found.

Most of the solutions to location and allocation problems have been approached in similar ways as those used for combinatorial optimization problems. If the number of logistics depots and customers are small, the optimal solutions can be found using exact programming approaches. However, if the scale of problem is large, then exact approaches are not enough to provide satisfactory solutions in reasonable amount of time. Therefore, new types of solution approaches need to be developed to resolve large sized location-allocation problems [1, 7, 9, 10, 11, 23, 24, 30].

Location-allocation problem is NP-hard problem [5]. In literature, metaheuristics have been shown to perform better than exact programming approaches to tackle larger NP-hard problems [38]. In this paper, we will address the multiobjective

capacitated location allocation problem and develop solution approaches based on four metaheuristics namely Genetic algorithms (GA), Simulated Annealing (SA), Tabu Search (TS) and Ant Colony Optimization (ACO). The rest of the paper is organized as follows. In Sect. 2, we present the problem definition. The solution approach is provided in detail in Sect. 3. Section 4 presents a numerical application of the four metaheuristics. The model results are verified and validated on Sect. 5. Finally, we provide the conclusions and future works in Sect. 6.

2 Problem Definition

Distribution of goods to customers from logistics depots produces the problem of how to construct the network of logistics depots and customers, and to optimize the delivery process. That is, how to cluster customers and service them through logistics depots considering least distance, cost, time etc. The distinction between the location allocation problem treated in this paper and the traditional location allocation problem lies in its multiobjective and dynamic nature. The multiple objectives considered are travel time, travel distance, travel cost etc. and developed based on practical constraints such as presence of congestion, timing and access restrictions imposed by municipal administrations in urban areas etc. The dynamic aspect means the location allocation results are not fixed forever but vary with change in municipal access or timing regulations, congestion, or land, material and labor costs on logistics networks.

In our problem, each customer should be serviced by a logistics center. It is possible that a logistics depot gets no customer allocations, in that case it will be closed down. Multiple criteria (factors) such as facility opening costs, travel cost, travel distance, and travel time to customers are considered in deciding the opening of logistics depots and customer allocations. The solution for location allocation problem should therefore be 19 developed considering these factors, customer demands and capacity constraints of logistics depots. Figure 1 shows a logistics network comprising of logistics facilities (*depots*) and the customers.

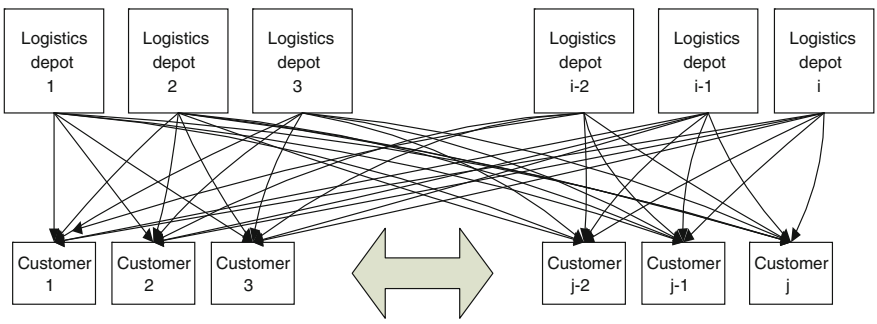

Fig. 1 Network of logistics depots and customers

Let us denote the logistics centers by i, ($i = 1, 2, \ldots, m$) and customers by j ($j = 1, 2, \ldots, n$). The maximum number of depots is denoted by m and the maximum number of customers is denoted by n. The cost of opening a facility i is denoted by ci and its capacity by b_i. The demand for customer j is given by d_j. The distance between depot i and customer j is given by d_{ij}, travel cost by c_{ij}, and travel time by t_{ij}. The binary variable y_i is 1 if facility i is opened, otherwise it is set equal to 0. Similarly, binary variable x_{ij} is equal to 1 is customer j is allocated to depot i and is set equal to 0 in the contrary case. The quantity of goods transported between i and j (*if they are connected*) is given by q_{ij}. The goal is to minimize the total costs, that is, opening costs of facilities and delivery costs of goods to customers from logistics depots. The delivery cost for customers is a weighted function of travel distance (d_{ij}), travel cost (c_{ij}) and travel time (t_{ij}) where the weights of travel distance, travel cost and travel time are represented by w_1, w_2 and w_3 respectively. Since, the facility opening costs, travel distance, travel time, travel costs etc. are in different units, they are normalized before being used in the objective function. Let us denote the normalized values of c_i, d_{ij}, c_{ij} and t_{ij} by c'_i, d'_{ij}, t'_{ij}, c'_{ij} which are computed as follows:

$$c'_i = c_i / \sum c_i$$
$$d'_{ij} = d_{ij} / \sum d_{ij}$$
$$t'_{ij} = t_{ij} / \sum t_{ij}$$
$$c'_{ij} = c_{ij} / \sum c_{ij}$$

Using the normalized values c'_i, d'_{ij}, t'_{ij}, c'_{ij}, the mathematical formulation of the problem is presented as follows:

Objective:

Minimize

$$\sum_{j=1}^{n} y_i \cdot c'_i + \sum_{i=1}^{m} \sum_{j=1}^{n} x_{ij} \cdot (w_1 \cdot d'_{ij} + w_2 \cdot t'_{ij} + (1 - w_1 - w_2) \cdot c'_{ij}) \tag{1}$$

s.t

$$\sum_{i=1}^{m} x_{ij} = 1, \quad \forall j \in 1, 2, \ldots, n \tag{2}$$

$$\sum_{i=1}^{m} q_{ij} x_{ij} = d_j, \quad \forall j \in 1, 2, \ldots, n \tag{3}$$

$$\begin{aligned}
&\sum_{j=1}^{n} q_{ij} x_{ij} \leq b_i y_i, \quad \forall i \in 1, 2, \ldots, m \\
&x_{ij} \in \{0, 1\} \\
&y_i \in \{0, 1\} \\
&q_{ij} \geq 0
\end{aligned} \tag{4}$$

It can be seen from Eq. (1) that the objective function comprises of multiple factors such as facility opening costs (c'_i), travel distance (d''_{ij}), travel cost (c'_{ij}) and travel time (t'_{ij}). If $w_1 = 1$ and $w_2 = 0$, then $w_3 = 0$ and the above objective function reduces to a single factor optimization problem based on minimizing the travel distance only. The objective function (1) now reduces to (5) which is given as follows:

$$\text{Minimize} \quad \sum_{j=1}^{n} y_i \cdot c'_i + \sum_{i=1}^{m} \sum_{j=1}^{n} x_{ij} \cdot d'_{ij} \tag{5}$$

The constraints in single factor optimization model remain the same as in multifactor optimization model. Equation (2) ensures that each client is served by exactly one facility. Equation (3) shows the demand satisfaction constraint of the customers. Equation (4) shows the capacity restriction constraints for the logistics depots. The facility location selection variable x_{ij} and the customer allocation variable to logistics facilities y_i are binary. The quantity allocations q_{ij} are non-negative real numbers.

3 Solution Approach

The location and allocation problem treated in this paper is multi-objective in nature. According to Konak et al. [21] and [33], there are two general approaches to solve multiple-objective optimization problems.

1. Combining individual objective functions into a single composite function or move all but one objective to the constraint set. In the former case, determination of a single objective is possible with methods such as utility theory, weighted sum etc., but the problem lies in the proper selection of the weights which is tricky process as small perturbations in the weights can sometimes lead to quite different solutions. In the latter case, the problem is to move objectives to the constraint set where a constraining value must be established which can again be rather arbitrary.
2. The second approach consists of determining Pareto optimal solutions where a Pareto optimal set is defined as a set of solutions that are non-dominated with

respect to each other. Each Pareto solution dominates other in terms of one objective function value and there is always a certain amount of sacrifice in this objective value when trying to achieve a certain amount of gain in the other objective(s).

3. In our paper, since all the functions are minimization type and the weights of the objective functions can be obtained using multicriteria decision making approaches such as AHP, we have used the weighted sum method [28] for treating the multiobjective problem is used over the Pareto optimal solution. Before applying the weighted sum method, we normalize all the factors used in the model to bring them to a common unit to avoid discrepancies of scale. If s_{ij} represents an element of matrix $S_{m \times n}$where $i = 1, 2, \ldots, m$ and $j = 1, \ldots, n$, then the normalized values a_{ij} can be obtained using any of the following four methods:

$$aij = s_{ij} / \sum (s_{ij}) \tag{6}$$

$$aij = s_{ij} / \max (s_{ij}) \tag{7}$$

$$aij = (s_{ij} - \min s_{ij}) / \max (s_{ij} - \min s_{ij}) \tag{8}$$

$$a_{ij} = s_{ij} / \sqrt{\sum (s_{ij})^2} \tag{9}$$

3.1 Genetic Algorithms

Genetic algorithm is a kind of stochastic search and optimization technique based on principles from evolution theory [18]. Genetic algorithms form part of the larger class of 'Evolutionary algorithms' which generate offsprings for better solution by using techniques inspired from genetic evolution such as crossover, inheritance, selection, mutation etc. Goldberg [15] defines genetic algorithm as a search heuristic that mimics the process of natural evolution. This heuristic is routinely used to generate useful solutions, search and optimize better solution from neighborhood of solution space. Genetic selection for crossover and mutation is important and should be carefully done because it affects the computational speed and quality of final results of the genetic algorithms. Gong et al. [16] propose a Hybrid evolutionary method for capacitated 528 location-allocation problem. Jaramillo et al. [20] use genetic algorithms for solving location problem. Zhou et al. [41] propose A genetic algorithm approach to the bi-criteria allocation of customers to warehouses.

The high level pseudocode for implementing GA is presented as follows:

1. Set iteration counter $t = 0$.
2. Generate the initial population, $P(t)$, randomly.
3. Evaluate fitness of the population $P(t)$ using the objective function.
4. While (number if iterations $t \leq$ Maximum value) or (improvement in objective function value $\leq 10^{-5}$) do

4.1. Set $t = t + 1$
4.2. Select two solutions P1 and P2 from the population using the ranking method.
4.3. Apply genetic operators to P1 and P2

4.3.1. If crossover, then combine P1 and P2 using single point crossover to generate offspring O1.
4.3.2. If O1 is identical to any of its parents, then apply mutation operator to the parent with the best fitness.

4.3.2.1. If mutation, then apply mutation operator to the parent with the best fitness to form a offspring O1.

4.3.3. Evaluate the fitness of the new child set using the objective function
4.3.4. If fitness of chromosome is improved or objective value is reduced (in case of minimization) then utilize the incremental replacement method to create P(t) and update population size.

5. Stop. Print final results.

The advantages of Genetic algorithms are that it supports multi-objective optimization, can be applied to new problems with exploratory type of solutions, always improves solutions over time, and can be easily parallelized or distributed. The limitations are that they require careful selection of chromosomes, cross-over and mutation operators to generate better results over time. If they are not carefully planned, there is risk of getting trapped into local optima and the algorithm may involve high computational times for generating final results.

3.2 Simulated Annealing

Simulated annealing is a generalization of the Monte Carlo method for examining the equations of state and frozen states of *n*-body systems [27]. The concept is based on the manner in which liquids freeze or metals recrystallize in the process of annealing. In an annealing process a melt, initially at high temperature and disordered, is slowly cooled so that the system at any time is approximately in thermodynamic equilibrium. Al-Khedhairi [3] applied simulated annealing for solving p-median problem. Murray and Church [28] use simulated annealing for location planning models. Mark et al. [25] created land allocation zones for forest management using a simulated annealing approach.

The high level pseudocode for simulated annealing is presented as follows:

1. Set initial solution $s = s0$, initial temperature $T = T_{max}$, maximum number of iterations = L, iteration counter $n = 0$, temperature change counter $t = 0$.
2. Initialize temperature decreasing rate R and minimal acceptable temperature T_{min}.

3. While ($T \geq T_{min}$)

   3.1 While (number of iterations $n \leq$ Maximum value L) or (improvement in objective function value $\Delta E \leq 10^{-5}$) do

      3.1.1 Generate a neighboring solution s'.
      3.1.2 Calculate $\Delta E = f(s') - f(s)$.
      3.1.3 If $\Delta E \leq 0$ then

         3.1.3.1 Set $s = s'$
         Else

         3.1.3.2 Select a random number R from U(0, 1). If $R < e^{-\frac{\Delta E}{T}}$ accept $s = s'$ else update s with next best neighboring solution s'' with $\Delta E \leq 0$.

      3.1.4 Set $n = n + 1$;

   3.2 Set $t = t + 1$ and $T = R - (R \times t/L)$;

4. Stop. Print final results.

Simulated Annealing is a simple, effective, and flexible approach, which could be easily understood and applied in many fields without relative inner structure. It can deal with arbitrary systems and cost functions and statistically guarantees finding an optimal solution. It is relatively easy to code even for complex problems and generally gives a "good" solution.

3.3 Tabu Search

Glover [13] proposed the tabu search or tabu algorithm for optimizing problems by tracking and guiding. It begins by setting up a set of feasible solutions, choosing certain solutions in the feasible neighborhood subject to constraints of tabu list for searching the objective solution, and finally generating the solution. Tabu search enhances the performance of a local search method by using memory structures: once a potential solution has been determined, it is marked as "taboo" (tabu) so that the algorithm does not visit that possibility repeatedly.

The high level pseudocode for the proposed tabu search is presented as follows:

1. Generate initial solution s0.
2. Initialize the tabu list, medium-term and long-term memories
3. Set sbest = s0.
4. While (number if iterations ≤ Maximum value) or (improvement in objective function value $\leq 10^{-5}$) do

   4.1 Generate admissible solutions (s)
   4.2 Select best solution s′ from the list of admissible solutions (s)

4.3 Update tabu list, aspiration conditions, medium and long term memories;

4.3.1 If intensification criterion holds, then intensification;
4.3.2 If diversification criterion holds, then diversification;

4.4 If (f(s′) < f(sbest) and (s′ is non-tabu)) or (f(s′) < f(sbest) and (s′ is tabu and aspiration criteria holds) then

Set sbest = s′.
Else
Pick the best move s″ that is non-tabu and set sbest = s″.

4.5 Stop.

The advantage of Tabu Search is that it searches over all the solutions space to find the optimized solution. Due to the presence of Tabu list, only limited solutions in neighborhood are searched which saves lot of computation time and also avoids low quality solutions.

3.4 Ant Colony Optimization

Dorigo [9] developed the ant colony approach. The ant colony optimization (ACO) is a probabilistic technique for solving computational problems which can be reduced to finding good paths through neighborhoods. Alaya et al. [2] apply ant colony optimization for multi-objective optimization problems. Silva, et al. [36] perform rescheduling and optimization of logistic processes using GA and ACO. Kwang and Weng [22] apply multiple ant-colony optimization for network routing. Qin [31] performed Logistics distribution center allocation based on ant colony optimization.

The high level pseudocode for the proposed ACO is presented as follows:

1. Set iteration counter *iter*: = 0.
2. Initialize values of ACO parameters, such as α, β, q_0, etc.
3. While (*iter* ≤ *iter_max) or* (improvement in objective function value $\leq 10^{-5}$)

3.1 Set the value of the initial pheromone trail τ_0, and initial pheromone intensity $\tau_{ij} = \tau_0$ for the path from nodes i to j and $\Delta\tau_{ij} = 0$
3.2 Construct the tabu lists of all ants, which contain all the unvisited nodes for each ant and the tabu list for the best path found by the ant colonies.
3.3 Randomly place the m ants on the n nodes.
3.4 For k: = 1 to m do

3.4.1 Generate a random number q.
3.4.2 If $q \leq q_0$, choose the node j to move to according to the state transition rule defined by Eq. (5).
3.4.3 If $q > q_0$, choose node j to move to with the highest probability p_{ij}^k given by Eq. (6).

3.4.4 Delete the chosen node j from the tabu list S_k of ant k.
3.4.5 Continue moving until the ant k finishes the whole tour.
3.4.6 Update the pheromone trail locally with Eq. (7).

3.5 Evaluate all the feasible tours constructed with respect to objective function value and satisfaction of demand and capacity constraints
3.6 Select the tour with the minimum cost.
3.7 Perform the global update for pheromone trails using Eqs. (8) and (9).
3.8 Re-construct all tabu lists. *iter:* = *iter* + 1.

4. Stop the ACO search process and output the best tour.

4 Numerical Application

We present the numerical examples for application of the four metaheuristics on location and allocation problem under two cases:

(a) single factor (objective function)

$$\sum_{j=1}^{n} c_i y_i + \sum_{i=1}^{m} \sum_{j=1}^{n} d_{ij} x_{ij},$$

(b) multi-factor (objective function)

$$\sum_{j=1}^{n} c_i y_i + \sum_{i=1}^{m} \sum_{j=1}^{n} (w_1 \cdot d_{ij} / \sum d_{ij} + w_2 \cdot t_{ij} / \sum t_{ij} + (1 - w_1 - w_2) \cdot c_{ij} / \sum c_{ij}) x_{ij}).$$

The normalization method used is $a_{ij} = s_{ij}/\sum(sij)$ where s_{ij} represents an element of matrix $S_{m \times n}$ where $i = 1, 2, \ldots, m$ and $j = 1, \ldots, n$, and the normalized values is given by a_{ij}. Four metaheuristics namely GA, SA, TS, and ACO are applied and tested for solving the location allocation problem.

4.1 Location and Allocation Using Single Factor

4.1.1 Input Data

Let us consider a logistics network comprising of 7 depots (D1, D2 … D7) and 21 customers (C1, C2 … C21). The demand, distance, and capacity data for location allocation problem using single factor "distance" in presented in Table 1. The distance matrix is presented at the center of the Table 1. The customer demands are presented

Table 1 Input distance, capacity and demand data for single factor

Customers	Depots							Demand
	D1	D2	D3	D4	D5	D6	D7	
C1	3.4	3.74	4.2	3.2	3.3	4.8	2.1	120
C2	3.10	3.28	3.3	2.7	4.0	3.1	5.8	200
C3	3.8	3.4	3.2	2.9	3.0	2.4	4.8	80
C4	3.5	3.6	3.5	4.9	3.6	2.5	4.9	110
C5	3.7	3.0	3.2	4.6	2.0	3.2	4.6	130
C6	3.6	3.7	3.6	4.7	3.7	3.8	4.7	90
C7	2.88	2.97	7.3	3.31	3.5	3.6	4.5	140
C8	2.5	2.9	3.0	2.83	2.7	3.0	3.2	170
C9	2.6	2.7	4.82	3.2	3.6	3.7	10.8	90
C10	5.8	2.8	3.2	5.3	4.74	4.2	6.1	115
C11	3.1	2.9	6.7	3.0	3.28	3.3	4.4	100
C12	2.4	2.7	2.9	5.0	3.24	6.5	2.0	125
C13	3.5	3.30	3.5	3.6	9.04	2.8	4.5	85
C14	4.2	2.96	2.7	1.0	3.03	3.0	2.3	180
C15	3.1	3.2	2.6	2.74	2.82	3.7	4.1	130
C16	3.2	4.3	2.8	2.88	3.2	3.3	2.8	95
C17	2.7	5.0	3.1	2.92	5.7	6.0	3.1	175
C18	5.9	3.0	2.4	2.47	2.9	3.0	2.4	150
C19	3.5	1.6	3.5	1.30	3.5	3.6	7.5	190
C20	2.7	3.0	5.2	2.96	2.7	3.0	1.2	95
C21	2.6	3.7	4.8	3.28	3.6	6.7	3.8	160
Capacity	800	800	1,100	1,000	700	1,100	900	

in the last column and depot capacities are present in the last row of Table 1. Table 2 presents the opening costs for the logistics depots.

The goal is to minimize the facility opening costs and the allocation costs for customers under the demand and capacity constraints of customers and the logistics depots. The objective function used is $\sum_{j=1}^{n} c_i y_i + \sum_{i=1}^{m} \sum_{j=1}^{n} d_{ij} x_{ij}$. Since the cost and distance data are in different units, they will be normalized before application of metaheuristics GA, SA, TS, and ACO. The formula used for normalization is $a_{ij} = s_{ij} / \sum Sij$ where s_{ij} represents the original data value in matrix$_{ij}$ and a_{ij} represents the normalized value.

In ACO, the values used are α = 0.0051, β = 1.23, R = 0.00017. In SA, they are $e = 0.1^{30}$, T = 2. For TS, t = 3 and for GA, pm = 0.1, pc = 0.7.

Table 2 Opening costs for logistics depots

Depots	D1	D2	D3	D4	D5	D6	D7
Opening costs	14	21	17	15	25	13	22

4.1.2 Application of Proposed Metaheuristics

Table 3 presents a relative comparison of the final results obtained from the four metaheuristics for the single factor. It can be seen that ACO results propose opening of only 5 logistics depots followed by GA (6 depots), whereas all the depots are open in SA and TS which also justifies their least total objective function value shown in Table 4.

Table 4 presents a relative comparison of the computation time and objective function values for the final results obtained from the four metaheuristics for the single factor. It can be seen that ACO performs the fastest in terms of computation time used for generating the results and gives least value for the total objective function equal to 0.7704.

4.2 Location and Allocation Using Multifactors

4.2.1 Input Data

Let us consider the input data for location allocation problem using multiple factors "distance", "time" and "cost" for a logistics network comprising of 7 logistics depots (D1, D2 … D7) and 21 customers (C1, C2 … C21). The distance matrix,

Table 3 Comparison of location allocation results for single factor problem

	Initial solution	GA	SA	TS	ACO
D1	C1, C2, C3	C8, C17, C21	C21	C9, C15, C17	C6, C9, C21
D2	C4, C5, C6	C7, C19	C10, C19	C7, C10	C5, C10, C11, C15, C19
D3	C7, C8, C9	C2	C4	C5	–
D4	C10, C11, C12	C14, C15	C9, C14, C17	C18, C19	C2, C7, C14, C16, C18
D5	C13, C14, C15	C9, C11	C5, C15	C8, C21	–
D6	C16, C17, C18	C3, C4, C10	C2, C3, C6, C7, C8, C13	C2, C3, C4	C3, C4, C13
D7	C19, C20, C21	C1, C5, C6, C12, C13, C16, C18, C20	C1, C11, C12, C16, C18, C 20	C1, C6, C11, C12, C13, C14, C16, C20	C1, C8, C12, C17, C20

Table 4 Comparison of performance results for single factor location allocation problem

	GA	SA	TS	ACO
Number of Iterations	10,000,000	10,000,000	10,000,000	10,000,000
Objective function value (distance normalized)	0.1079	0.1050	0.1550	0.1011
Objective function value (cost normalized)	0.8898	1.0000	1.0000	0.6693
Objective function value (cost plus distance normalized)	0.9977	1.1050	1.1550	0.7704
Computation time (seconds)	4,696.801189	4,965.391465	5,093.268974	4,296.178412

customer demands, and depot capacities are same as presented in Table 1. The time matrix is presented in Table 5 and the cost matrix in Table 6. The depot opening costs are same as in Table 2.

Table 5 Time matrix

Customers	Depots						
	D1	D2	D3	D4	D5	D6	D7
C1	1.0	4.83	3.00	2.7	5.0	3.0	2.1
C2	3.0	2.88	2.86	3.3	4.9	4.1	5.8
C3	4.6	3.76	3.74	4.2	6.1	3.6	4.8
C4	3.4	3.10	3.28	3.3	4.4	2.6	4.9
C5	4.0	3.38	3.24	4.2	6.0	3.4	4.6
C6	13.3	3.4	3.1	3.04	3.63	8.5	4.0
C7	3.1	3.3	3.8	3.31	3.28	3.9	1.8
C8	7.2	3.3	2.8	2.88	2.97	3.3	9.4
C9	2.7	3.0	7.1	2.92	3.0	2.8	2.7
C10	2.9	4.0	8.4	2.47	2.65	2.9	3.5
C11	1.5	2.6	3.5	6.30	3.38	3.7	5.2
C12	2.7	3.0	3.0	2.6	3.1	3.2	2.6
C13	3.6	9.7	5.8	3.28	3.2	4.3	6.8
C14	3.0	3.2	8.6	3.18	2.7	3.0	8.1
C15	3.1	3.2	3.4	3.1	3.04	3.13	3.5
C16	3.2	13.3	1.3	13.8	13.31	3.28	3.2
C17	6.7	13.0	0.3	6.8	2.88	2.97	7.3
C18	2.92	3.05	23.0	3.1	2.92	3.05	2.8
C19	8.47	2.65	3.0	12.4	12.47	2.65	2.9
C20	3.30	3.38	3.6	3.5	3.30	3.38	3.7
C21	9.96	8.14	3.0	3.2	2.96	23.1	3.2

Table 6 Cost matrix

Customers	Depots						
	D1	D2	D3	D4	D5	D6	D7
C1	2.9	3.2	3.5	3.14	3.15	3.0	2.1
C2	3.9	4.0	4.3	3.62	3.60	4.1	5.8
C3	3.5	3.6	3.5	3.14	3.12	3.6	4.8
C4	3.5	3.6	3.6	3.19	3.17	3.6	4.9
C5	3.3	3.4	3.0	2.99	3.07	3.4	4.6
C6	3.3	3.4	3.1	3.04	3.13	3.5	4.7
C7	3.1	3.3	3.8	3.31	3.28	3.2	1.8
C8	2.5	2.9	3.0	2.83	3.00	2.7	3.0
C9	3.2	3.3	3.0	2.88	2.86	3.3	4.1
C10	4.0	4.1	4.6	3.76	3.74	4.2	6.1
C11	3.1	3.3	3.4	3.10	3.28	3.3	4.4
C12	3.1	3.4	4.0	3.38	3.24	3.2	2.0
C13	2.8	3.0	3.2	2.95	3.04	2.8	2.5
C14	3.0	3.2	3.6	3.18	3.03	3.0	2.3
C15	3.1	3.2	2.6	2.74	2.82	3.2	4.1
C16	3.2	3.3	2.8	2.88	2.97	3.3	4.4
C17	2.7	3.0	3.1	2.92	3.05	2.8	2.7
C18	2.9	3.0	2.4	2.47	2.65	2.9	3.5
C19	3.5	3.6	3.5	3.30	3.38	3.7	5.2
C20	2.7	3.0	3.2	2.96	3.14	3.0	3.5
C21	3.6	3.7	3.8	3.28	3.27	3.7	5.1

The goal is to minimize the facility opening costs and the allocation costs for customers under multifactors and the demand and capacity constraints of customers and the logistics depots. The objective function used for the multifactor location allocation problem is given by:

$$\sum_{j=1}^{n} c_i y_i + \sum_{i=1}^{m}\sum_{j=1}^{n} (w_1 \cdot d_{ij}/\sum d_{ij} + w_2 \cdot t_{ij}/\sum t_{ij} + (1 - w_1 - w_2) \cdot c_{ij}/\sum c_{ij}) x_{ij}$$

Since the cost, travel time and distance data are in different units, they will be normalized before application of metaheuristics GA, SA, TS, and ACO. The formula used for normalization is $a_{ij} = s_{ij}/\sum s_{ij}$ where s_{ij} represents the original data value in $\mathrm{matrix}_{\mathrm{ij}}$ and a_{ij} represents the normalized value. Using $w1 = 0.2$, $w2 = 0.3$, and $w3 = 1 - w1 - w2$, the total objective function values obtained are presented in Table 7.

Table 7 Normalized data for multifactor cost, time and distance

	D1	D2	D3	D4	D5	D6	D7
C1	0.0052	0.0068	0.0068	0.0058	0.0066	0.0067	0.0039
C2	0.0066	0.0068	0.0071	0.0062	0.0074	0.0071	0.0109
C3	0.0071	0.0067	0.0065	0.0061	0.0067	0.0061	0.0090
C4	0.0066	0.0066	0.0066	0.0070	0.0066	0.0059	0.0092
C5	0.0066	0.0062	0.0058	0.0069	0.0060	0.0063	0.0086
C6	0.0094	0.0066	0.0061	0.0066	0.0064	0.0082	0.0086
C7	0.0057	0.0060	0.0091	0.0062	0.0063	0.0065	0.0049
C8	0.0061	0.0056	0.0056	0.0053	0.0055	0.0054	0.0077
C9	0.0055	0.0058	0.0079	0.0056	0.0058	0.0063	0.0111
C10	0.0082	0.0069	0.0090	0.0075	0.0073	0.0075	0.0107
C11	0.0054	0.0058	0.0083	0.0067	0.0062	0.0063	0.0085
C12	0.0053	0.0059	0.0066	0.0070	0.0060	0.0079	0.0039
C13	0.0059	0.0078	0.0070	0.0060	0.0091	0.0057	0.0071
C14	0.0063	0.0059	0.0078	0.0048	0.0056	0.0056	0.0061
C15	0.0058	0.0060	0.0051	0.0053	0.0054	0.0063	0.0075
C16	0.0060	0.0098	0.0048	0.0087	0.0088	0.0062	0.0070
C17	0.0063	0.0098	0.0050	0.0066	0.0072	0.0071	0.0067
C18	0.0071	0.0057	0.0107	0.0048	0.0052	0.0056	0.0058
C19	0.0081	0.0054	0.0064	0.0078	0.0091	0.0066	0.0104
C20	0.0053	0.0058	0.0073	0.0057	0.0057	0.0058	0.0053
C21	0.0081	0.0083	0.0075	0.0061	0.0062	0.0144	0.0083

4.2.2 Application of Metaheuristics

Table 8 presents a relative comparison of the final results obtained from the four metaheuristics for the multifactor location allocation problem. It can be seen that only 6 depots are opened in ACO and TS making them least costly solutions (Table 9) for location allocation as compared to GA and SA.

Table 9 presents a relative comparison of the computation time and objective function values for multifactor location allocation problem. It can be seen that TS performs the best followed by ACO in terms of objective function value. The metaheuristic SA is the fastest in terms of computation time followed by GA.

5 Model Verification and Validation

5.1 Model Verification

To verify the model results, we tested our model under three difference scenarios for the same numerical example presented in Sect. 5.1 (multifactor case).

Table 8 Comparison of model results for multifactor location allocation problem

Depots	Initial solution	GA	SA	TS	ACO
D1	C1, C2, C3	C2, C8, C11	C4, C9, C17	C1, C7, C20	C11
D2	C4, C5, C6	C10, C15	C15, C19	C3, C9, C10, C11, C12, C19	C2, C8, C19
D3	C7, C8, C9	C5	C2	C4, C6, C15, C16, C17, C21	C5, C6, C13, C16, C17
D4	C10, C11, C12	C3, C14	C14, C21	C8, C14, C18	–
D5	C13, C14, C15	C4, C21	C8, C11	C5	C9, C10, C15, C20, C21
D6	C16, C17, C18	C9, C17, C19	C3, C5, C10	C2, C13	C3, C4, C14, C18
D7	C19, C20, C21	C1, C6, C7, C2, C13, C16, C18 C20	C1, C6, C7, C12, C13, C16, C1, C20	–	C1, C7, C12

Table 9 Comparison of model performance for multifactor

	GA	SA	TS	ACO
Iteration times	10,000,000	10,000,000	10,000,000	10,500,000
Objective multifactor value	0.1271	0.1259	0.1215	0.1181
Objective normalized cost	1.0000	1.0000	0.8268	0.8819
Objective normalized cost plus multifactor value	1.1271	1.1259	0.9483	1.0000
Computation time	4,844.64 s	3,142.55 s	6,702.69 s	10,867.25 s

- *Scenario* 1: In the scenario 1, the opening cost is same for all the 7 logistics facilities and is equal to $100,000. Demand and capacity constraints are not considered.
- *Scenario* 2: In the scenario 2, we ignore the facility opening costs by setting them equal to 0, in other words all facilities are considered open and customers are allocated to them using different metaheuristic approaches. Demand and capacity constraints are not considered.
- *Scenario* 3: In the scenario 3, the opening costs for facilities are different. Demand and capacity constraints are considered.

The demand data for customers, opening costs of logistics facilities and their capacities and average transit time between the logistics facilities and the customers is presented in Tables 10, 11, 12 and 13.

Table 10 Customer Demand data

Customers	Depots						
	D1	D2	D3	D4	D5	D6	D7
Wallingford (C1)	104,795	102,450	93,708	95,787	95,414	106,554	113,644
Ankeny (C2)	33,370	35,380	39,670	39,887	40,267	113,644	253,360
Posen (C3)	101,682	106,509	115,836	117,401	118,249	104,356	82,507
W.Chicago (C4)	99,334	104,161	113,488	114,988	115,901	102,008	80,159
Indianapolis (C5)	94,008	98,196	110,421	107,535	104,309	96,611	75,274
Louisville (C6)	147,009	153,570	170,860	165,540	160,131	149,225	116,064
Boston (C7)	134,765	1,311,487	119,613	122,454	124,202	137,169	329,263
Baltimore (C8)	396,064	382,395	345,242	176,126	165,874	190,847	162,106
Westland (C9)	175,591	183,075	197,843	199,866	201,282	179,738	151,417
Blaine (C10)	55,259	58,877	65,821	66,995	67,631	57,264	40,833
Charlotte (C11)	126,005	128,567	126,005	126,213	117,697	123,028	97,758
Auburn (C12)	52,472	51,189	46,318	47,543	50,589	53,435	63,643
Kenvil (C13)	376,864	374,128	344,212	351,326	340,564	388,174	367,397
Menands (C14)	25,422	249,092	229,615	234,783	248,297	261,547	276,387
Columbus (C15)	103,026	107,812	119,972	116,538	113,610	106,235	85,180
W.Chester (C16)	98,128	102,294	114,455	111,077	107,812	100,774	79,662
Philadelphia (C17)	136,459	132,669	121,044	246,385	234,508	271,781	122,560
Pittsburgh (C18)	126,983	131,658	138,986	285,553	269,759	259,651	106,198
Nashville (C19)	77,868	80,993	88,301	852,203	82,203	76,961	57,305
Richmond (C20)	148,193	146,717	131,820	134,912	126,340	142,361	119,524
Milwaukee (C21)	75,505	78,587	85,880	87,319	87,832	76,892	60,096
Total	291,8303	2,939,805	2,919,111	3,033,453	2,972,370	3,019,095	2,612,318

Table 11 Opening costs of facilities

S. No.	Depots	Opening costs	Capacity
1	D1 (Baltimore)	3,215,569	2,000,000
2	D2 (Williamsport)	3,327,844	2,000,000
3	D3 (Wheeling)	3,000,000	2,000,000
4	D4 (Pittsburgh)	3,197,605	2,000,000
5	D5 (Erie)	3,094,311	2,000,000
6	D6 (Harrisburg)	3,251,497	2,000,000
7	D7 (Boston)	1,500,000	2,000,000

Table 12 Average transit time (in minutes) between the depot i and customer j

	D1	D2	D3	D4	D5	D6	D7
Wallingford (C1)	269	323	474	440	485	251	127
Ankeny (C2)	955	885	734	733	722	916	1154
Posen (C3)	652	582	440	429	419	613	927
W.Chicago (C4)	699	629	487	476	466	660	974
Indianapolis (C5)	548	478	291	344	395	515	877
Louisville (C6)	565	495	318	371	427	541	904
Boston (C7)	389	444	595	560	524	372	0
Baltimore (C8)	0	76	263	232	347	78	386
Westland (C9)	495	425	284	273	262	456	770
Blaine (C10)	1,050	980	839	827	817	1,011	1,121
Charlotte (C11)	426	376	419	428	554	451	808
Auburn (C12)	434	489	640	606	561	417	81
Kenvil (C13)	188	215	367	332	368	144	247
Menands (C14)	322	356	507	462	358	285	172
Columbus (C15)	384	314	127	180	227	350	713
W. Chester (C16)	194	248	399	365	415	177	195
Philadelphia (C17)	100	174	324	290	392	104	298
Pittsburgh (C18)	230	160	61	0	127	191	554
Nashville (C19)	658	597	475	528	584	671	1,034
Richmond (C20)	149	169	347	325	440	227	531
Milwaukee (C21)	749	679	537	529	516	710	1,024

Table 13 Scenarios for verification

	D1	D2	D3	D4	D5	D6	D7
Scenario 1	100,000	100,000	100,000	100,000	100,000	100,000	100,000
Scenario 2	0	0	0	0	0	0	0
Scenario 3	100,000	70,000	20,000	40,000	80,000	120,000	60,000

The data used for the three scenarios are shown in Table 13.

The unit shipping cost between the logistics facilities/depots and customers is shown in Table 14.

The scenarios were run for 100,000 iterations. The results for the three scenarios are presented in Tables 15, 16 and 17 respectively. It can be seen from the results of Table 15 that Ant Colony provides the least cost objective function value for the

Table 14 Unit shipping cost (in dollars) and demand (in units of products)

	D1	D2	D3	D4	D5	D6	D7
Wallingford (C1)	2.9	3.2	3.5	3.14	3.15	3	2.1
Ankeny (C2)	3.9	4	4.3	3.62	3.6	4.1	5.8
Posen (C3)	3.5	3.6	3.5	3.14	3.12	3.6	4.8
W. Chicago (C4)	3.5	3.6	3.6	3.19	3.17	3.6	4.9
Indianapolis (C5)	3.3	3.4	3	2.99	3.07	3.4	4.6
Louisville (C6)	3.3	3.4	3.1	3.04	3.13	3.5	4.7
Boston (C7)	3.1	3.3	3.8	3.31	3.28	3.2	1.8
Baltimore (C8)	2.5	2.9	3	2.83	3	2.7	3
Westland (C9)	3.2	3.3	3	2.88	2.86	3.3	4.1
Blaine (C10)	4	4.1	4.6	3.76	3.74	4.2	6.1
Charlotte (C11)	3.1	3.3	3.4	3.1	3.28	3.3	4.4
Auburn (C12)	3.1	3.4	4	3.38	3.24	3.2	2
Kenvil (C13)	2.8	3	3.2	2.95	3.04	2.8	2.5
Menands (C14)	3	3.2	3.6	3.18	3.03	3	2.3
Columbus (C15)	3.1	3.2	2.6	2.74	2.82	3.2	4.1
W. Chester (C16)	3.2	3.3	2.8	2.88	2.97	3.3	4.4
Philadelphia (C17)	2.7	3	3.1	2.92	3.05	2.8	2.7
Pittsburgh (C18)	2.9	3	2.4	2.47	2.65	2.9	3.5
Nashville (C19)	3.5	3.6	3.5	3.3	3.38	3.7	5.2
Richmond (C20)	2.7	3	3.2	2.96	3.14	3	3.5
Milwaukee (C21)	3.6	3.7	3.8	3.28	3.27	3.7	5.1

Table 15 Objective function value

Scenario	Initial solution	GA	SA	TS	ACO
1	1.1541	1.105	1.1084	0.96	0.9454
2	0.1631	0.0999	0.1025	0.1073	0.0879
3	1.1542	1.1135	1.1141	0.9602	0.9264

Table 16 Computation time (in seconds)

Scenario	GA	SA	TS	ACO
1	378.22	203.37	1,779.21	528.91
2	351.49	208.57	1,431.79	1,083.93
3	492.528	505.389	1,251.28	1,145.89

three scenarios. Besides, the results of the four meta-heuristics for scenario 1 and 2 follow identical pattern since they consider equal facility opening costs or zero costs and therefore do not contribute towards the total objective function value. This verifies the correctness of our model results with respect to the objective function.

Table 16 presents the computation time for the four metaheuristics. It can be seen that SA takes the least computation time in first two scenarios. Besides, the results of the four meta-heuristics for scenario 1 and 2 follow identical pattern in terms of computation times since they consider equal facility opening costs or zero costs and therefore do not contribute towards the total objective function value. The GA algorithm performs fastest in scenario 3. This verifies the correctness of our model results with respect to the computation time.

The location-allocation results for scenario 1, 2 and 3 can be seen in Table 17 respectively. It can be seen in Table 17 that only 6 logistics facilities(depots) are open when applying Tabu Search and Ant Colony Optimization which also confirms their least cost objective function values (Row 1, Table 15).

From the results of scenario 2 (Table 18), it can be seen that only 6 logistics facilities(depots) are open when applying Ant Colony Optimization which also confirms its least cost objective function value (Row 2, Table 15).

Table 19 presents the results of scenario 3. It can be seen that all 7 logistics facilities(depots) are open when applying the four metaheuristics with GA generating fastest results while TS takes longest time (Table 14). However, the solution generated by TS is the best followed by ACO in terms of minimizing costs (Table 15).

Table 17 Location allocation results for scenario 1 (in seconds)

Depots	Initial solution	Final solution			
		GA	SA	TS	ACO
D1	C3C17	C13C16	C1C2C8C17	C20	C8C11 C16C20
D2	C4C8	C5C8	C3C4C5C6 C11C14	–	–
D3	C5C10	C11C19	C15C18C19	C5C17	C5C6C9 C15C19
D4	C2C7	C18C21	C9	C9	C2C21C18
D5	C1C6C9 C11C13C15	C2C3C4 C6C9C10	C10	C2C3C4C6 C10C15 C19 C21	C3C4C10
D6	C12C14	C1C12C14 C15C17C20	C13C16 C20C21	C11C13C18	C13C14C17
D7	C16C18C19 C20C21	C7	C7C12	C1C7C8C12 C14C16	C1C7C12

Table 18 Location allocation results for scenario 2 (in seconds)

Depots	Initial solution	Final solution			
		GA	SA	TS	ACO
D1	C2C9C19	C8C13C20	C18C20	C8C16C20	C8C11C17 C20
D2	C4C8	C2C3	C4C11C13	C7C11C19	–
D3	C6C18	C4C19	C3C5C15C19	C6	C5C6C15
D4	C12C14C20	C11C18C21	C9C10	C4C15C21	C9C10 C18C21
D5	C11C13C16	C9C10C15	C21	C2C3C9 C14C18	C2C3 C4C19
D6	C1C5C7C10	C5C6C16C17	C2C6C8C16	C1C5C10 C13C17	C13
D7	C3C15C17C21	C1C7C12C14	C1C7C12 C14C17	C12	C1C7C12 C14C16

Table 19 Location allocation results for scenario 3 (in seconds)

Depots	Initial solution	Final solution			
		GA	SA	TS	ACO
D1	C3C6C16	C8C19C20	C4C5C8	C13C15C17	C8C16 C17C20
D2	C7C11	C2C3	C2C20	C5C11C16 C18C19 C20C21	
D3	C17	C6	C6		C5C15
D4	C8C14	C15C21	C15C19	C4C10	C4C6C10 C18C19
D5	C5C21	C4C9	C5	C3C6C9	C2C3C9C21
D6	C18C19C20	C10C11C18	C11C17C18	C2C8	C11C13
D7	C1C2C4C9C10 C12C13C15	C1C5C7C12 C13C14 C16C17	C1C7C9C10 C12C13C14 C16C21	C1C7 C12C14	C1C7 C12C14

5.2 Model Validation

To perform validation of model results, we took the numerical case study presented in [42] which is described as follows:

Let us denote V as a set of nodes representing m customers, U as a set of nodes representing r warehouses, and E as a set of edges representing a connection between customers and warehouses. On each edge (i, j) there are two objective coefficients c_{ij} denoting unit shipping cost and t_{ij} denoting transit time between warehouse j and its customer i. At each customer node i, customer demand is denoted as v_i, and at each warehouse j, its capacity is denoted as q_j. Using the above

notations, the bi-criteria multiple warehouse allocation problem is formulated as follows:

$$Minimize\, f(x) = w_1 \cdot f_1(x) + w_2 \cdot f_2(x)$$

where

w_1 and w_2 are constants representing weights for $f_1(\boldsymbol{x})$ and $f_2(\boldsymbol{x})$, respectively.

$$f_1(x) = \sum_{i-1}^{m} \sum_{j=1}^{r} v_i c_{ij} x_{ij}\ (Minimize\ shipping\ costs)$$

$$f_2(x) = \sum_{i-1}^{m} \sum_{j=1}^{r} t_{ij} x_{ij}\ (Minimize\ total\ transit\ time\ between\ warehouses\ an\ customers\ allocated\ to\ them)$$

Subject to

$$\sum_{j=1}^{r} x_{ij} = 1, i = 1, 2, \ldots, m\ \ (Each\ customer\ is\ allocated\ to\ only\ one\ warehouse)$$

$$\sum_{i=1}^{m} v_i x_{ij} \leq q_j, j = 1, 2, .., r\ \ (Total\ demand\ of\ customers\ does\ not\ exceed\ the\ capacity\ of\ warehouses\ serving\ them)$$

$$x_{ij} = \begin{cases} 1 & If\ customer\ i\ is\ allocated\ to\ warehouse\ j,\ i = 1, 2, \ldots, m; j = 1, 2, \ldots, r \\ 0 & otherwise \end{cases}$$

The shipping cost data and transit time data is same as in Tables 12 and 14. The demand of customers and capacity of warehouses is obtained from Tables 10 and 11 respectively. The four metaheuristics and Zhou et al. [42] were compared under 7 problem scenarios where each scenario allocates different weight values to the shipping cost and transit time functions. Table 20 presents the details of these scenarios.

In their approach, Zhou et al. [42] propose 7 Pareto optimal solutions. It can be seen in Table 21 that our four metaheuristics perform better than the results of Zhou

Table 20 Weights scenario description

Scenario	Weight w1	Weight w2
1	0.1	0.9
2	0.25	0.75
3	0.4	0.6
4	0.55	0.45
5	0.7	0.3
6	0.85	0.15
7	0.95	0.05

Table 21 Transit time results (in seconds)

Scenario	Initial solution	GA	SA	TS	ACO	Zhou et al. [42]
1 (w1 = 0.1, w2 = 0.9)	175.29	110.41	104.71	103.20	97.95	128.49
2 (w1 = 0.25, w2 = 0.75)	175.29	103.77	104.71	101.90	101.21	126.13
3 (w1 = 0.4, w2 = 0.6)	175.29	101.21	102.02	110.17	97.22	125.97
4 (w1 = 0.55, w2 = 0.45)	175.29	105.50	103.98	109.22	101.17	125.65
5 (w1 = 0.7, w2 = 0.3)	175.29	106.10	100.85	115.36	98.46	123.62
6 (w1 = 0.85, w2 = 0.15)	175.29	102.06	98.64	105.85	98.99	123.30
7 (w1 = 0.95, w2 = 0.05)	175.29	99.60	98.67	96.47	102.16	121.09

Table 22 Shipping cost results

Scenario	Initial solution	GA	SA	TS	ACO	Zhou et al. [42]
1 (w1 = 0.1, w2 = 0.9)	8,783,300	7,162,000	6,836,400	7,038,000	6,884,000	7,924,037
2 (w1 = 0.25, w2 = 0.75)	8,783,300	7,240,200	6,863,400	6,962,100	6,870,500	7,930,047
3 (w1 = 0.4, w2 = 0.6)	8,783,300	6,870,500	6,844,100	7,048,100	6,898,700	7,931,645
4 (w1 = 0.55, w2 = 0.45)	8,783,300	7,209,200	6,836,400	7,129,100	6,868,200	7,943,386
5 (w1 = 0.7, w2 = 0.3)	8,783,300	7,054,500	6,863,000	7,073,900	6,890,800	7,952,062
6 (w1 = 0.85, w2 = 0.15)	8,783,300	6,862,900	6,894,800	7,268,600	6,904,500	7,963,803
7 (w1 = 0.95, w2 = 0.05)	8,783,300	6,877,500	6,876,500	6,910,900	6,949,900	7,977,486

et al. [42] in terms of transit time (objective function f1) for all the 7 Pareto optimal solutions with ACO performing best in 5/7 scenarios.

From the results of Table 22, we can say that that our four meta-heuristics perform better than the results of Zhou et al. [42] in terms of shipping cost (objective function f2) for all the 7 Pareto optimal solutions with SA performing best in 6/7 scenarios.

The comparison of our results with Zhou et al. [42] for all the 7 Pareto optimal solutions in Tables 21 and 22 show better performance of the proposed metaheuristics in terms of transit time and shipping costs under the seven weight scenarios listed in Table 20. This validates the results of our study.

6 Conclusions and Future Works

In this paper, we address the problem of multifacility capacitated location allocation problem on logistics networks. This problem can be categorized into two subproblems firstly, the location problem, that is which logistics facilities should be opened and where and secondly, the allocation problem, that is how to perform customer allocations to logistics depots to ensure timely service for customers. The

problem is studied under two cases. In the first case, opening costs of the facilities and only one criterion (distance) is used. In the second case, opening costs of the facilities and multiple criteria (distance, travel cost, travel time) are used. It is evident that the problem is multi-objective in nature due to the presence of different criteria such as travel cost, travel time, travel distance etc. Weighted sum method is used to generate single solutions for the multi-objective location allocation problem treated in the paper.

Four metaheuristics namely Genetic algorithms (GA), Simulated annealing (SA), Tabu search (TS), and Ant colony optimization (ACO) are proposed to address the problem. Since, the problems involve multiple criteria (factors), normalization is performed before aggregating them into the objective function. The models are tested under various problem instances and results compared with some existing models to ensure validity of results. From our computational experiments, it emerged that no metaheuristic performs best under all circumstances; it depends upon the nature of the problem, its size and the level of details involved. However, in majority of the test cases considered in our study, Ant colonyoptimization (ACO) showed better performance over others.

To extend the research work performed in this paper, we propose the following future works:

- Testing of proposed metaheuristics on real problem instances.
- More rigorous model verification and validation on large network sizes.
- Develop hybrid approaches based on the proposed metaheuristics and other approaches available in the literature. For example, screening of facility locations using multicriteria decision making approaches such as AHP and then allocation using heuristics, metaheuristics or exact approaches.
- Combining routing with location-allocation problem.
- Integration of barriers in location planning of logistics facilities.

References

1. Abdinnour-Helm, S.: A hybrid heuristic for the uncapacitated hub location problem. Eur. J. Oper. Res. **106**(2–3), 489–499 (1998)
2. Alaya, I., Solnon, C., Ghedira, K.: Ant colony optimization for multi-objective optimization problems. Proc. 19th IEEE Int. Conf. Tools Artif. Intell. **01**, 450–457 (2007)
3. Al-khedhairi, A.: Simulated annealing metaheuristic for solving P-median problem. Int. J. Contemp. Math. Sci. **3**(28), 1357–1365 (2008)
4. Arora, S., Raghavan, P., Rao, S.: Approximation schemes for Euclidean *k*-medians and related problems. In: Proceedings of the 30th Annual ACM Symposium on Theory of Computing, pp. 106–113 (1998)
5. Azarmand, Z., Neishabouri, E.: Location allocation problem, facility location. Contrib. Manage. Sci. 93–109 (2009)
6. Cooper, L.: Location-allocation problems. Oper. Res., **11**(3), 331–34 (1963)
7. Cooper, L.: Heuristic methods for location-allocation problems. SIAM Rev. **6**(1), 37–53 (1964)

8. Cortinhal, M.J., Eugenia, M.: Genetic algorithms for the single source capacitated location problem. Metaheuristics: Comput. Decis. Making, pp. 187–216. Kluwer Academic Publishers, Berlin (2003)
9. Dorigo, M.: Optimization, learning and natural algorithms. PhD thesis, Politecnico di Milano, Italy (1992)
10. Dorigo, M., Stützle, T.: Ant colony optimization. MIT Press, Cambridge (2004)
11. Drezner, Z.: The planar two-center and two-median problems. Transp. Sci. **18**, 351–361 (1984)
12. Drezner, Z., Hamacher, H. (eds.) Facility location: applications and theory. Springer, Berlin (2002). ISBN 3-540-42172-6
13. Glover, F.: Tabu search, part I. ORSA J. Comput. **1**(3), 190–206 (1989)
14. Glover, F, Kochenberger, G.A.: Handbook of metaheuristics, international series in operations research and management science, 57. pp. 321–353. Kluwer Academic Publishers, Dordrecht (2002)
15. Goldberg, D.E.: Genetic algorithms in search, optimization and machine learning. Kluwer Academic Publishers, Boston (1989)
16. Gong, D., Gen, M., Yamazaki, G., Xu, W.: Hybrid evolutionary method for capacitated location-allocation problem. Comput. Ind. Eng. **33**(3–4), 577–580 (1997)
17. Ho, W., Lee, C.M.L., Ho, G.T.S.: Optimization of the facility location-allocation problem in a customer-driven supply chain. Oper. Manage. Res. **1**, 69–79 (2008)
18. Holland, J.H.: Adaptation in Natural and Artificial Systems. University of Michigan Press, Michigan (1975)
19. Hua, X., Zheng, J., Hu, W.: Ant colony optimization algorithm for computing resource allocation based on cloud computing environment. J. East Chin. Normal Univ. (2010)
20. Jaramillo, J.H., Bhadury, J., Batta, R.: On the use of genetic algorithms to solve location problems. Comput. Oper. Res. **29**, 761–779 (2002)
21. Konak, A., Coit, D.W., Smith, A.E.: Multi-objective optimization using genetic algorithms. Reliabil. Eng. Syst. Saf. **91**(9), 992–1007 (2006)
22. Kwang, M.S., Weng, H.S.: Multiple ant-colony optimization for network routing. In: Proceedings of the First International Symposium on Cyber Worlds. pp. 277–281. Hosei University, Tokyo (2002)
23. Lin, J.-H., Vitter, J.S.: Approximation algorithms for geometric median problems. Inf. Process. Lett. **44**, 245–249 (1992)
24. Lozano, S., Guerrero, F., Onieva, L., Larraneta, J.: Kononen, maps for solving a class of location-allocation problems. Eur. J. Oper. Res. **108**, 106–117 (1998)
25. Mark, B., John, N., Fred, L.B.: Creating land allocation zones for forest management: a simulated annealing approach. Can. J. For. Res. **34**, 1669–1682 (2004)
26. Marler, T., Arora, J.S.: Multi-objective optimization: concepts and methods for engineering. VDM Verlag, Saarbrucken (2009)
27. Metropolis, N., Rosenbluth, A., Rosenbluth, M., Teller, A., Teller, E.: Equation of state calculations by fast computing machines. J. Chem. Phys. **21**(6), 1087–1092 (1953)
28. Murray, A.T., Church, R.L.: Applying simulated annealing to location-planning models. J. Heuristics **2**, 31–53 (1996)
29. Ninlawan C.: Location decision in distribution centers. Department of Industrial Engineering, 2548, 237 (2008)
30. Ostresh, L.M.: SPA: A shortest path algorithm. In: Rushton, G. (ed.) Computer Programs for Location-allocation Problems. Department of Geography, The University of Iowa, Iowa City (1973)
31. Qin, G.: Logistics distribution center allocation based on ant colony optimization. Syst. Eng. Theor. Pract. **4**, 120–124 (2006)
32. Satani, N., Uchida, A., Deguchi, A., Ohgai, A., Sato, S., Hagishima, S.: Commercial facility location model using multiple regression analysis. Comput. Environ. Urban Syst. **22**(3), 219–240 (1998)

33. Sawaragi, Y., Nakayama, H., Tanino, T.: Theory of Multiobjective Optimization. Academic Press Inc, Florida (1985). ISBN 0126203709, (176, Mathematics in Science and Engineering, Orlando)
34. Scaparra, M.P., Scutell`a, M.G.: Facilities, locations, customers: Building blocks of location models: A survey, Technical report TR-01–18, Computer Science Department, University of Pisa, Italy (2001)
35. Scutella, M.G.: The maximum cut congestion problem. In: Gouveia e Mourao (eds.) Proceedings of INOC 2005, Book 3, pp. 670–673. Lisbon (2005)
36. Silva, C.A., Sousa, J.M.C., Runkler, T.A.: Rescheduling and optimization of logistic processes using GA and ACO. Eng. Appl. Artif. Intell. **21**(3), 343–352 (2008)
37. Silva, M.R., Cunha, C.B.: New simple and efficient heuristics for the uncapacitated single allocation hub location problem. Comput. Oper. Res. **36**(12), 3152–3165 (2009)
38. Talbi, E-G.: Metaheuristics: from Design to Implementation. Wiley, New York, 624 p. (2009) ISBN: 978-0-470-27858-1
39. Villegas, J.G, Palacios, F., Medaglia, A.L.: Solution methods for the bi-objective (cost-coverage) unconstrained facility location problem with an illustrative example. Ann. Oper. Res., 109–141. doi:10.1007/s10479-006-0061-4,2006
40. Vos, B., Akkermans, H.: Capturing the dynamics of facility allocation. Int. J. Oper. Prod. Manage. **16**(11), 57–70 (1996)
41. Zhou, G., Min, H., Gen, M.: The balanced allocation of customers to multiple distribution centers in the supply chain network: a genetic algorithm approach. Comput. Ind. Eng. Arch. **43** (1–2), 251–261 (2002)
42. Zhou, G., Min, H., Gen, M.: A genetic algorithm approach to the bi-criteria allocation of customers to warehouses. Int. J. Prod. Econ. **86**, 35–45 (2003)

Classification of Heart Disorders Based on Tunable-Q Wavelet Transform of Cardiac Sound Signals

Shivnarayan Patidar and Ram Bilas Pachori

Abstract The mechanical action of the heart generates sounds which can provide diagnostic information about the functioning of the cardiovascular system. Cardiac auscultation is an important means to diagnose heart disorders by listening to the heart sounds using conventional stethoscope. The traditional cardiac auscultation techniques require sophisticated interpretive skills in diagnosis and it requires long time to expertise. The heart sounds often last for a short period of time and pathological splitting of the heart sound is difficult to discern using traditional auscultation because human ears lack desired sensitivity towards heart sounds and murmurs. Therefore, the automatic heart sound analysis using advanced signal processing techniques based on digital acquisition of these sounds can play an important role. The heart sounds can be captured and processed in the form of cardiac sound signals by placing an electronic stethoscope at the appropriate location on the subject's chest. The cardiac sound signals can be used to extract valuable diagnostic features for detection and identification of the heart valve and other disorders. In this book chapter, a new method for segmentation and classification of cardiac sound signals using tunable-Q wavelet transform (TQWT) has been proposed. The proposed method uses constrained TQWT based segmentation of cardiac sound signals into heart beat cycles. The features obtained from heart beat cycles of separately reconstructed heart sounds and murmur can better represent the various types of cardiac sound signals than that of containing both. Even the parameters evolved during constrained TQWT based separation of heart sounds and murmur can serve as valuable diagnostic features. Therefore, various entropy measures namely time-domain based Shannon entropy, frequency-domain based spectral entropy, and non-linear method based approximate entropy and Lempel-Ziv complexity have been computed for each segmented heart beat cycles. Two features have been created by the parameters that have been optimized while constrained TQWT namely the redundancy and the number of levels of decomposition. These ten features form the

S. Patidar · R.B. Pachori (✉)
Indian Institute of Technology Indore, Indore 452017, India
e-mail: pachori@iiti.ac.in

S. Patidar
e-mail: shivnarayan.patidar@iiti.ac.in

A.T. Azar and S. Vaidyanathan (eds.), *Chaos Modeling and Control Systems Design*,
Studies in Computational Intelligence 581, DOI 10.1007/978-3-319-13132-0_10

final feature set for subsequent classification of cardiac sound signals using artificial neural network (ANN) based technique. In this study, the following classes of cardiac sound signals have been used: normal, aortic stenosis, aortic regurgitation, splitting of S2, mitral regurgitation and mitral stenosis. The performance of the proposed method has been validated with publicly available datasets. The proposed method has provided significant performance in segmentation and classification of cardiac sound signals.

Keywords Cardiac sound signals · Heart sound analysis · Tunable-Q wavelet transform · Heart disorders

1 Introduction

Since the invention of stethoscope in 1816 by René Laennec, a French physician, auscultation has been used as a non-invasive primary diagnostic tool for heart and respiratory disorders [25]. Traditional cardiac auscultation using conventional stethoscope requires sophisticated skills and long time to expertise. Indeed, there is lack of effective educational support to develop the auscultatory skills of the apprentice/primary care clinicians in the primary screen examination [41]. Moreover, the human ear is far more sensitive to the speech having frequencies in the range 1,000–2,000 Hz than to higher and lower frequencies. It lacks desired sensitivity towards heart sounds and murmurs [18, 19, 38]. In addition, the heart sounds often last for a short period of time and interpretation of pathological splitting of the heart sound is difficult to make any decision on presence of heart disorders [54]. Therefore, the automatic heart sound analysis using advanced signal processing techniques based on digital acquisition of these sounds has a lot of potential in cardiac health care. Figure 1 shows the schematic of the cardiac sound acquisition and analysis system which can be used for automatic analysis of heart valve and other heart disorders. In order to record the cardiac sound signals, the chestpiece has to be placed on to the four standard auscultatory locations on the chest. The chestpiece and sensor together convert the acoustic waveforms into electrical signals. These electrical signals can be processed for listening and

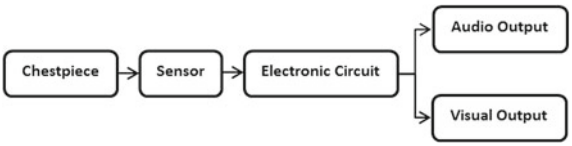

Fig. 1 The schematic of the cardiac sound acquisition and analysis system for heart valve and other heart disorders

transmission to another computer to perform automatic analysis using software based on advanced signal processing techniques. The cardiac sound signals are recorded in a quiet environment to reduce interference from the ambient noise.

1.1 Cardiac Sound Signals

The cardiac sound signals carry a lot of information about the structure and functioning of cardiovascular system [57]. Automatic analysis of cardiac sound signals can be used in medical check-ups for diagnosis of valvular heart diseases, congenital heart diseases such as septal defects, heart rate analysis and in biometric authentication. Therefore, cardiac sound signal based computer aided diagnosis can be a promising and cost effective technology for prompt, noninvasive, convenient and efficient detection and identification of heart valve and other heart disorders. In recent years, with the development of many advanced signal processing techniques, a huge potential exists for development of efficient, informative and accurate state of the art computer aided diagnostic tool for heart valve and other heart disorders [14, 73, 77].

The cardiac sound signals may consist of two types of components, the heart sounds and the murmur. The heart sounds and murmur are low frequency and high frequency components respectively. However, the intensity, frequency content and timings of the heart sounds and murmur vary with involved type of heart valves and other disorder, type of defect, degree of defect, heart rate and blood velocity. The heart beat cycles of normal cardiac sound signals are mostly composed of two types of sound: S1 and S2 heart sounds which are referred as primary heart sounds. The S1 and S2 heart sounds exhibit predominant frequencies in the range 20–150 Hz [6]. The presences of other sounds that may be indicative of cardiac pathology are murmurs, two feeble S3 and S4 heart sounds and other irregularities due to different pathologies of the cardiovascular system. The average murmurs have frequencies in the range 100–600 Hz [10]. The predominant frequencies of S3 and S4 heart sounds lie in the range 20–70 Hz [6]. These heart sounds have comparatively lower amplitude to that of primary heart sounds. The presence of S3 heart sound could be a sign of heart disorder. Generally, S4 heart sound is always considered to be associated with cardiac abnormality.

The ambient noise, respiratory sounds, bowel sounds and other undesired noises such as rubbing of stethoscope on the subject's chest surface, voices etc. needs to be dealt properly in carrying out accurate analysis of cardiac sound signals [42]. The respiratory artifacts occupy frequencies less than 100 Hz to over 300 Hz [50].

1.2 Detection and Identification of Heart Disorders

The detection and identification of heart disorders using cardiac sound signals generally comprise an important primary task of segmentation of cardiac sound signals into heart beat cycles [24, 53]. After segmentation, the heart beat cycles

undergo next stages of feature extraction and classification. However, in reality, due to the non-stationary nature of cardiac sound signals it is difficult to achieve the desired performance at each of these stages [30, 80].

1.2.1 Segmentation of Cardiac Sound Signals

In fact, all the cardiac events such as contraction and relaxation of cardiac muscles, opening and closing of valves etc. take place during a heart beat cycle of cardiac sound signal and thus it can provide the information about the functioning of heart valves and hemodynamics. Therefore, segmentation of cardiac sound signals into heart beat cycles is required for diagnosis. In other words, segmentation of cardiac sound signals into intervals associated with different stages of the cardiac cycle is important to correlate cardiac sound signals to underlying mechanical activities. In case of the accurate segmentation in the resting stage, the heart beat may fall in the range 50–130 beats per minute [6].

Manual and reference signal based segmentation
Earlier, segmentation of cardiac sound signals was carried out manually using expert annotation. The involved annotation procedure, to obtain the cardiac timing information, may use combined audio and visual interpretation of heart sounds and other reference signals. Various annotation approaches have been developed to assist the segmentation [58].

The popular segmentation methods based on reference signal like electrocardiogram (ECG) and/or carotid pulse have been proposed for segmentation as follows. The T wave of ECG has been used to precisely identify the S2 reducing the probability of error in detection of artifacts as S2 heart sounds in [71]. The localization of R wave in ECG to estimate the systole duration using multi-layer perceptron based on subjects heart rate, gender and age has been proposed in [8]. The relative information about the QRS complex in ECG signal and heart sounds in cardiac sound signals have been used to detect S1 and S2 heart sounds in [68]. Segmentation based on the time-domain and frequency-domain characteristics of the components of the heart beat cycles have been proposed in [21, 33, 40]. Instantaneous energy of the ECG signal has been used to segment the cardiac sound signals in [71]. These methods provide high performance but the involved procedure requires attaching and removing ECG electrodes which may cause discomfort to the patients. Moreover, in case of massive medical check-up camps, it may cause to long time in carry out diagnosis even for a medical expert. In addition, in cases of infants/children, it is not easy to attach the leads because of the limited body size and the non cooperation of the baby. Moreover, in children suffering from hypertrophic ventricles, axis deviation of heart leads to an abnormality in ECG signal which complicates the segmentation of cardiac sound signals [27, 69]. Therefore, recent segmentation algorithms rely solely on cardiac sound signals for assuring convenient diagnosis [66].

Automatic segmentation

The automatic segmentation of cardiac sound signals is a formidable task involving constraints such as inconsistent lengths of the heart beat cycles, variation of the number of heart sound components inside individual heart beat cycles, the unpredictable existence of murmurs and the presence of various types of noises like lung sounds, rubbing of stethoscope on the chest, etc. [30]. In order to perform successful segmentation, many methods have been proposed for automatic segmentation of cardiac sound signals. The segmentation without any reference signal can be performed using envelope based approaches such as envelogram [35], energy and simplicity [75], high frequency signature [31], cardiac sound characteristic waveform (CSCW) [12, 28, 52], Viola integral [69, 78] etc. Most of these methods rely on the principle that the duration of systole is relatively constant and shorter than that of diastole as suggested in [46]. These methods can be briefly described as follows.

The envelogram based segmentation method uses envelope of cardiac sound signals. This method is basically based on extraction of envelope using the Shannon energy for the morphological based transformation of the cardiac sound signals. This transformation enhances the heart sounds relatively more with respect to murmurs in the obtained envelope. However, the performance of this method gets affected in presence of noise and murmurs having higher amplitude. The frequency-domain based segmentation algorithm has been proposed which involves tracking the spectrum of the cardiac sound signals [27, 31, 75]. One of these methods involves energy and simplicity based segmentation with wavelet decomposition coefficients. The segmentation algorithm employing high frequency signatures has been provided in [31]. With the help of these frequency-domain methods, certain frequency components are firstly extracted according to the time-domain characteristics, and the timings of heart beat cycles are determined by using the time-domain search method at a given threshold value. However, the choice of the threshold and the removal of the unexpected noise poise difficult problems in these type of methods. Moreover, some murmurs having high frequency signatures may affect the results. The segmentation based on the extraction of CSCW is provided in [28]. Due to inherent limitations this method is incapable of significantly removing murmurs in turn affecting the efficacy of segmentation. Moreover, it requires evaluation of the segmentation performance for more clinical cases. Information regarding the popular envelope based segmentation methods along with their relative comparison has been presented in [12]. The CSCW based envelope has been found to provide significant performance in comparison to the conventional Shannon envelope and Hilbert envelope in segmentation of cardiac sound signals. In order to achieve successful automatic segmentation of cardiac sound signals in presence of murmurs, an envelope based method for segmentation of cardiac sound signals by removing murmurs using constrained TQWT has been proposed in [52]. The method for detecting boundaries of primary heart sounds for available heart beat cycles has been used in [3]. The moment-based algorithm has been presented to be simpler and faster than conventional WT based method [78]. However, the algorithm assumes cardiac sound signals to be approximate periodic signals and it is not easy to vary the value of the

used scale parameter in different clinical cases. A automatic method for cardiac sound moment segmentation using Viola integral based envelopes and detection of peak location of S1/S2 heart sounds using short-time modified Hilbert transform have been proposed for analysis of cardiac sound signals in [69]. Detection of the S3 and S4 heart sounds using Hilbert-Huang transform has been proposed in [74].

The high order statistics based methods involve statistics such as Shannon energy [26], variance fractal dimension [1], recurrence time statistics [64]. It has been found that all of these methods provide better performance in the presence of respiratory noises. However, the performance degrades in the presence of murmurs and these methods take higher computational time.

The radial basis functions (RBF) neural network based method has been proposed to extract the envelope of the cardiac sound signals in [43]. As this method operates directly on the cardiac sound signals without adequate pre-processing, the method shows a good performance for low level of noise but the performance decreases in the presence of high level of noise. The S-transform based heart sound analysis has been performed in [37]. As an extension to this work, a method for heart sounds localization named S-transform and radial basis function (SRBF) neural network has been proposed in [44]. This method extracts the envelope of the cardiac sound signals by computing the features extracted using the S-transform matrix of the cardiac sound signals and the radial basis function (RBF) neural network. This SRBF method has shown to have better results in comparison to some other existing methods as described in [23, 43, 44]. A robust module for cardiac sound signals segmentation has been developed in [45]. This method involves three main parts: (a) heart sounds localization based on the S-transform and Shannon energy, (b) boundaries detection and (c) classification of S1 and S2 heart sounds. The method is based on an optimization of the energy concentration in the time-frequency domain obtained by the S-transform. The singular value decomposition based features have been used to distinguish between S1 and S2 heart sounds.

Detection of the S1 and S2 heart sounds using probabilistic models based on hidden Markov model (HMM) have been found to provide promising results [20]. The matching pursuit based segmentation uses Gabor atoms to represent heart sounds as described in [48]. The ergodic HMM for classification of a cardiac sound signals into four components: S1 heart sound, systolic phase, S2 heart sound, diastolic phase has been proposed in [15]. In several HMM based methods there is no user input requirement and the training process is required for system development [14, 63, 76].

The adaptive singular spectrum analysis to detect murmur or primary heart sounds has been proposed in [62]. A method for detecting the S3 heart sound using wavelet transform (WT) simplicity filter has been developed in [32]. Detection and boundary identification of S1, S2, S3 and S4 heart sounds in cardiac sound sounds using an expert frequency-energy based metric has been proposed in [47].

The other form of cardiac sound signal based segmentation can be achieved by using instantaneous cycle frequency, autocorrelation and p-spectrum based method [6, 10, 30, 53]. In [6], automatic segmentation of cardiac sound signals into heart beat cycles using autocorrelation approach has been implemented with a low cost

digital signal processor. Moreover, this method uses threshold based criteria to detect whether a cardiac sound signal belongs to any heart valve disease or not. The performance of the autocorrelation and instantaneous cycle frequency based segmentation depends largely on variability of heart rate as these methods assume the cardiac sound signals to be stationary.

1.2.2 Methods for Analysis and Classification of Heart Disorders

The basic objectives for cardiac sound signals that have been generally pursued using signal processing techniques are (a) the analysis of the heart sounds, (b) the identification of their components which may or may not based on models, (c) their synthesis and (d) compression/decompression for data archiving and tetemedicine applications. In this subsection, time-domain, frequency-domain, time-frequency/scale domain and nonlinear methods have been described for analysis of heart disorders using cardiac sound signals.

The time intervals between heart sounds and the presence of murmurs in these intervals have been used for detecting heart disorders in [12, 28]. The clustering based diagnosis of heart valve disorders using CSCW have been proposed in [12]. In order to represent murmurs, different spectral characteristics of murmurs in cardiac sound signals have been proposed as described in [10, 13, 33]. For efficient detection and identification of heart valve disorders, various methods based on the short-time Fourier transform (STFT), WT, wavelet packet decomposition, HMM, empirical mode decomposition, cluster analysis, adaptive singular spectrum analysis, S-transform, autoregressive spectral analysis and TQWT have been presented for classifying the cardiac sound signals [4, 11, 13, 47, 51, 56, 58, 62, 68, 72, 73, 80].

The artificial neural network (ANN) and support vector machine (SVM) are commonly used for analysis and classification of heart disorders. ANN have simple structure to implement and have better discriminative training characteristics and ability to approximate the functions. Successful ANN based classification of cardiac sound signals has been achieved in [9]. The seven level WT based decomposition and Coifman fourth order wavelet kernel with ANN have been used for classification of five cardiac sound signals in [59]. ANN based classification of cardiac sound signals using wavelet features has been performed for twelve categories of heart disorders in [5]. In [17], Kohonen's self-organizing map network and an incremental self-organizing map have been examined comparatively for classification of cardiac sound signals. The Daubechies-2 wavelet based features have been used to classify cardiac sound signals in [7, 22, 49].

SVM is an effective binary classifier which can be easily used for solving multiclass classification problem. In SVM, basically, the separation between the considered two classes is achieved by finding the hyperplane that has the largest distance to the nearest training data point of any class. SVM can be efficiently used to solve a non-linear classification problem using the kernel functions in turn mapping the input feature space into high-dimensional feature space. The automatic

segmentation and SVM based classification of cardiac sound signals using STFT and discrete cosine transform based features have been proposed in [30]. The p-spectrum based automatic segmentation and SVM based classification of cardiac sound signals using features that are based on continuous wavelet transform and discrete cosine transform have been proposed in [53]. Based up on the Fishers discriminant ratio, these methods adaptively selects the significant features for improved classification performance. Feature determination for classification of cardiac sound signals based on divergence analysis has been proposed in [16]. Estimation of murmurs in cardiac sound signals by two morphological characteristics in frequency domain using SVM with quadratic programming in feature space has been proposed in [13]. The cardiac sound signals have been successfully categorized using a SVM classifier as normal or disease-related and then the corresponding murmurs in the unhealthy cases were classified as systolic or diastolic as described in [39]. This method has also evaluated the performance of back-propagation neural networks, k-nearest-neighbour and naïve Bayes classifiers for the same diagnostic problems and has found lower performance of these classifiers than the SVM classifiers.

To simplify and parameterize the classification curves based on their shapes, elliptical classification boundary curves have been created using least square method for SVM based classification for diagnosis of ventricular septal defects [70]. In this method, moving windowed Hilbert transform based new method has been used for segmentation of cardiac sound signals into heart beat cycles. Then from each heart beat cycle, Viola integral based envelope of cardiac sound signals has been extracted to obtain the time-domain diagnostic features. In frequency-domain, the envelope has been obtained using moving average method for extracting frequency-domain diagnostic features.

In this chapter, a new method for classification of cardiac sound signals containing murmurs using TQWT has been presented. The heart sounds and murmurs are separately reconstructed by suitably constraining TQWT using genetic algorithm. The proposed method uses separated heart sounds obtained using constrained TQWT for segmentation of cardiac sound signals into heart beat cycles. The features obtained from heart beat cycles of separately reconstructed heart sounds and murmur can better represent the various types of cardiac sound signals than that of containing both. Even the parameters evolved during constrained TQWT bases separation of heart sounds and murmur can serve as valuable diagnostic features. Therefore, entropy based measures namely time-domain based Shannon entropy, frequency-domain based spectral entropy, and non-linear method based approximate entropy and Lempel-Ziv complexity have been computed for each segmented heart beat cycles. Two features have been created by the parameters that has been optimized while constrained TQWT namely the redundancy and the number of levels of decomposition. These ten features constitute the final feature set for classification of cardiac sound signals using ANN based classification tree. The cardiac sound signals corresponding to following clinical cases have been used: normal, aortic stenosis, aortic regurgitation, splitting of S2, mitral regurgitation and

mitral stenosis. The performance of the proposed method has been validated with publicly available datasets. The proposed method has provided significant performance in segmentation and classification of cardiac sound signals.

2 Tunable-Q Wavelet Transform (TQWT)

Multirate signal processing techniques are often applied for the analysis of non-stationary signals in the field of biomedical signal and image processing. The dyadic wavelet transform use dyadic scaling of sampling rates which lead to sub-bands having center frequencies separated by octaves. It has a low Q-factor which is suitable for non-oscillatory signals. In case of oscillatory signals, the wavelet transform should provide relatively high value of Q-factor. However, in most of the wavelet transforms, except the continuous wavelet transform, it is not easy to tune the Q-factor of the wavelet according to the behaviour of the signal under study. Recently, TQWT has been proposed to be a powerful transform for analysis of oscillatory signals in [65]. This transform is quite flexible to use for desired analysis by adjusting its input parameters. The main input parameters of TQWT are Q-factor denoted as Q, total over-sampling rate or redundancy denoted as r and number of levels of decomposition denoted as j. The parameter Q controls the number of oscillations of the wavelet and the parameter r controls the undesired excessive ringing in order to localize the wavelet in time without affecting its shape. The filters of TQWT are nonrational transfer functions which can be easily specified in frequency domain for efficient implementation.

The *jth* level TQWT based decomposition can be implemented by iteratively applying two channel filter banks to the low-pass sub-band signals as shown in Fig. 2. At each stage of TQWT based decomposition, the input signal $s[n]$ with sampling rate f_s is decomposed into low-pass sub-band signal $c^1[n]$ and high-pass sub-band signal $d^1[n]$ having sampling frequencies αf_s and βf_s respectively as illustrated in Fig. 3a. For signal length N, $j + 1$ sub-band signals are obtained with j-levels of decomposition. The cell array containing these sub-band signals can be defined as [65]:

$$C = \{d_1, d_2, d_3, \ldots, d_j, d_{j+1}\}, \tag{1}$$

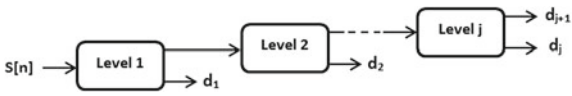

Fig. 2 The *jth* level TQWT based decomposition performed by iteratively applying two channel filter banks to the low-pass sub-band signals

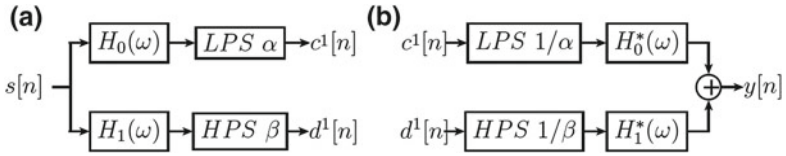

Fig. 3 The single level TQWT based **a** decomposition filter bank and **b** reconstruction filter bank

where, d_{j+1} is the lowest frequency sub-band signal and from d_1 to d_j are the other high-pass sub-band signals. The number of samples in each of these sub-band signals can be obtained using the values of α and β as follows:

$$C_l = [\beta f_s N, \alpha\beta f_s N, \alpha^2\beta f_s N, \ldots, \alpha^{j-1}\beta f_s N, \alpha^j f_s N], \tag{2}$$

The generation of low-pass sub-band $c^1[n]$ uses low-pass filter $H_o(\omega)$ followed by low-pass scaling which is denoted as *LPS* α and similarly the generation of high-pass sub-band $d^1[n]$ uses $H_1(\omega)$ and *HPS* β. Further details about scaling operations can be obtained from [65]. However, in order to prevent over redundancy and to achieve perfect reconstruction with TQWT, the scaling parameters should satisfy the following conditions: $0<\alpha<1; 0<\beta\leq 1$ and $\alpha+\beta>1$ respectively.

The equivalent system for *jth* level TQWT based decomposition of input signal $s[n]$ to generate the low-pass sub-band signal $c^j[n]$ and the high-pass sub-band signal $d^j[n]$ is shown in Fig. 4. The equivalent frequency response for low-pass and high pass sub-band signals generated after j level is given by $H_o^{(j)}(\omega)$ and $H_1^{(j)}(\omega)$ respectively which are defined as [65]:

$$H_o^{(j)}(\omega) := \begin{cases} \prod_{m=0}^{j-1} H_o(\omega/\alpha^m), |\omega| \leq \alpha^j\pi \\ 0, \alpha^j\pi < |\omega| \leq \pi, \end{cases} \tag{3}$$

$$H_1^{(j)}(\omega) := \begin{cases} H_1(\omega/\alpha^{j-1}) \prod_{m=0}^{j-2} H_o(\omega/\alpha^m), \\ \text{for} (1-\beta)\alpha^{j-1} \leq |\omega| \leq \alpha^{j-1}\pi \\ 0, \text{for other} \, \omega \in [-\pi, \pi]. \end{cases} \tag{4}$$

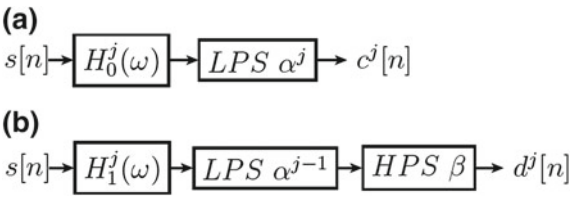

Fig. 4 The equivalent system for *jth* level TQWT based decomposition of input signal $s[n]$ to generate **a** the low-pass sub-band signal $c^j[n]$ and **b** the high-pass sub-band signal $d^j[n]$ [65]

The original signal can be reconstructed using the reconstruction filter bank as depicted in Fig. 3b. The relationship between TQWT input parameters: redundancy and Q-factor, and filter bank parameters α and β can be expressed as follows [65]:

$$r = \frac{\beta}{1-\alpha}, \quad Q = \frac{2-\beta}{\beta}. \tag{5}$$

3 Methodology

The different stages of the proposed TQWT based methodology for segmentation and classification of cardiac sound signals have been shown in Fig. 5. The main subsections of the proposed method includes: datasets, pre-processing, constrained TQWT based separation of heart sounds and murmur, segmentation, feature extraction and ANN based classification. The details of each of these subsections are described as follows.

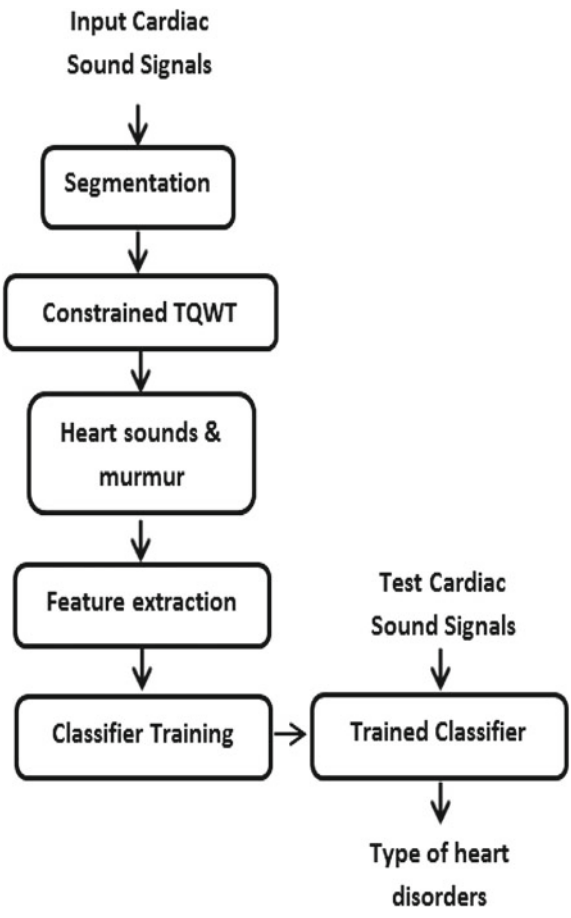

Fig. 5 Block diagram of proposed TQWT based methodology for classification of cardiac sound signals

3.1 Datasets

The cardiac sound signals used for this study have been obtained from the various databases available with the Texas Heart Institute, Michigan University and Washington University. As for dataset used from the Texas Heart Institute, it is available in the form of the heart sounds pod cast series (2011). This series has been produced by the Robert J. Hall Heart Sounds Laboratory at St. Luke's Episcopal Hospital. This dataset contains 50 abnormal cardiac sound signals acquired from variety of subjects with relevant chest positions and different patient maneuver. The sampling frequency of most of the data is 44.100 kHz except for few cases. The number of quantization bits of the data is 16. Some of the recordings in the dataset were corrupted by the human voice, rubbing sound due to stethoscope and other lung sounds. Also, the duration of the heart beat cycles are inconsistent. For more information regarding these dataset, please visit the following websites: www.texasheartinstitute.org, www.med.umich.edu and www.washington.edu.

3.2 Pre-processing

In order to maintain the audio quality for better auscultation, the cardiac sound signals are generally recorded at sampling frequency which is far greater than as decided by Nyquist-Shannon sampling theorem. However, for computer aided analysis, down-sampling or decimation can reduce the overall time of execution and the space complexity of the algorithm. In fact, advanced signal processing techniques can be developed for decimated signals with comparatively lower sampling frequency but still obeying the Nyquist-Shannon sampling theorem. And these techniques can obtain similar performance as that of original signal having higher sampling frequency.

In the proposed methodology, the decimation has been carried out before constrained TQWT based separation of heart sounds and murmur. The input signal is decimated by a factor of 32 from sampling frequency of 44.100 kHz to sampling frequency of 1,378.125 Hz [30, 53]. This process may not significantly affect the heart sounds containing low frequency components. Even the diagnostic murmurs containing high frequency components may not be get affected significantly because the average murmurs have frequency range between 100 and 600 Hz [10]. After the decimation, amplitude normalization can be performed to consider the variations in the recordings due to changes in pressure applied on the chest surface and the amplifier setting.

3.3 Constrained TQWT Based Separation of Heart Sounds and Murmur

The amplitude distribution of primary heart sounds in cardiac sound signals is super-Gaussian. Whereas, the amplitude distribution of murmurs is nearly Gaussian or sub-Gaussian. The amplitude distribution of primary heart sounds have sharper peak and often skewed toward left with relatively larger value of the kurtosis as compared to murmur [62]. This statistical knowledge about the amplitude distributions of primary heart sounds and murmurs can be used to constrain the output of the TQWT for separately reconstructing the desired heart sounds and murmur as follows. The working of constrained TQWT with two adaptive parameters r and j, and a fixed value of Q can be envisaged as working of TQWT with feedback mechanism involving optimizer or optimization method. The difference between the unconstrained and the constrained TQWT is that the later constrains the output of TQWT to be of certain desired statistical characteristics known in advanced by optimally tuning the chosen input parameters during decomposition.

In order to separate the heart sounds, the input parameters of TQWT based decomposition have been adaptively selected such that heart sounds having maximum kurtosis are obtained in the reconstructed signal. The heart sounds are low frequency component therefore the low-pass sub-band at last output stage of TQWT based decomposition has been used for signal reconstruction. It should be noted that while reconstruction with low-pass sub-band, other heart sounds also appear along with reconstructed primary heart sounds. For separation of murmur, only the high-pass sub-bands of each output stage of TQWT based decomposition have been considered during reconstruction. In order to constrain the output of the TQWT, the input parameters of TQWT can be adapted by using any suitable optimization method. As the genetic algorithms are more versatile in global optimization [79], therefore, in this study, genetic algorithm has been used as an optimization method. The kurtosis of the high-pass sub-band signal at the output stage of TQWT based decomposition has been minimized as an objective function.

In [52], the setting and validation of constrained TQWT based separation of heart sounds and murmur have been performed with a training set having five heart beat cycles of each clinical case in the dataset. During this procedure, the possible bounds of the parameters to be optimized have been obtained such that adaptive selection of these parameters results into adequate separation of heart sounds and murmurs. It is noteworthy that expert opinion from a cardiologist has been used through out the setting and validation procedure. From this experimental analysis, it has been found that Q close to unity provides better separation of heart sounds and murmur. It could be due to the fact that the wavelet at lower Q better matches with heart sounds. Moreover, the murmurs exhibit relatively higher oscillations as compared to heart sounds. The low value of Q can adequately enhance and localize heart sounds from overlapping murmur for murmur-free reconstruction of heart sounds. However, these results have been accompanied usually with high value of r.

3.4 Segmentation

The main stages of the methodology for TQWT based segmentation of the cardiac sound signals into heart beat cycles include: decimation and amplitude normalization, constrained TQWT based decomposition and reconstruction, low energy component removal, CSCW extraction, peak detection and boundary estimation. Some of these stages have already been covered in earlier Sects. 3.2 and 3.3. The details of all other remaining stages of the TQWT based segmentation method are described as follows:

3.4.1 Low Energy Component Removal

At this stage, signal processing involves the removal of low energy components from the reconstructed cardiac signal $x_r[n]$. The presence of these components may affect the performance of the next stage of peak detection for extracting the heart beat cycles. The extent of removal of these low amplitude components in the noise attenuated signal $x[n]$ can be determined by analyzing the histogram $h(i)$ and cumulative histogram $c(i)$ which can be obtained as follows [30]:

$$h(i) = \sum_{n} d(x_r[n], i); d(k_1, k_2) = \begin{cases} 1, & k_1 = k_2 \\ 0, & k_1 \neq k_2 \end{cases}, \; 0 \leq i \leq A, \tag{6}$$

$$c(i) = \sum_{x_r=0}^{i} h(x_r), \; 0 \leq i \leq A, \tag{7}$$

where A denotes the maximum amplitude of the signal $x_r[n]$. The threshold for removing low energy components can be determined by using the parameter λ which is obtained by $c(j) = c(A) \times \lambda$. In this chapter, λ is set to 0.93, which has been found to be effective for removing the low energy components. The noise attenuated cardiac sound signal can be obtained as:

$$x[n] = \begin{cases} x_r[n], & |x_r[n]| \geq j \\ 0, & \text{otherwise.} \end{cases} \tag{8}$$

3.4.2 Extraction of CSCW

An analytical model based on single degree-of-freedom (SDOF) system which is shown in Fig. 6 can be used for extracting CSCW of the cardiac sound signals [12, 28]. The model assumes the presence of the mass, spring, and the damper to represent the phenomena. The relationship between the input signal $X(t) = |x_{norm}(t)|$ and the output response $Y(t)$ of this system can be expressed as:

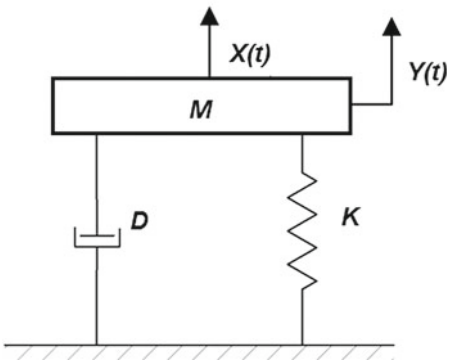

Fig. 6 An analytical modeling of extraction of CSCW using cardiac sound signals [12, 28]

$$M\ddot{Y}(t) + D\dot{Y}(t) + KY(t) = X(t), \tag{9}$$

where M, K, and D represent the mass, the spring coefficient, and the damping coefficient respectively. The above equation can also be expressed as:

$$\ddot{Y}(t) + 2\omega\zeta\dot{Y}(t) + \omega^2 Y(t) = \bar{X}(t), \tag{10}$$

where $\bar{X}(t) = \pm|X(t)/M|$, resonant angular frequency is $\omega = \sqrt{K/M}$ rad/s and the damping parameter is $\zeta = D/2\sqrt{MK} \times 100\ \%$. The default values of ω and ς used in this chapter have been set to 62.832 rad/s and 70.7 % respectively. In order to compensate for time delay between input signal $X(t)$ and above obtained waveform $Y(t)$ the cross correlation $XC[i]$ is used which is calculated as follows [12]:

$$XC[i] = \frac{\sum_{n=0}^{N-1}(X[n] - \mu_X)(Y[n-i] - \mu_Y)}{\sqrt{\sum_{n=0}^{N-1}(X[n] - \mu_X)^2}\sqrt{\sum_{n=0}^{N-1}(Y[n-i] - \mu_Y)^2}}, \tag{11}$$

where delay $i = 1, 2, \ldots, N$. N is the number of samples, and μ_X and μ_Y are the average values of $X[n]$ and $Y[n]$ respectively. Finally, the CSCW which is represented as $W[n]$ can be obtained by using peak location (XC_p) of the cross correlation curve with the following formula:

$$W[n] = Y\left[n + \left|XC_p - \frac{N}{2}\right|\right]. \tag{12}$$

3.4.3 Peak Detection and Boundary Estimation

The peak detection method includes the picking up of the required peaks of primary heart sounds and rejecting the extra peaks as described in [3, 35]. In order to separate the peaks of primary heart sounds from the background proper threshold can be applied either manually or automatically by fuzzy c-means clustering as suggested in [12, 28, 35]. Data clustering techniques are intended to know whether the individuals of a population fall into different clusters. By using appropriate features these methods search for any clustering in the data. The commonly used methods for data clustering are K-means clustering, fuzzy c-means clustering, mountain clustering and subtractive clustering. Even, the clustering of primary heart sounds has been well described in [2]. The peak identification method facilitates the recognition of S1 and S2 heart sounds based on the general fact that the diastolic interval is greater than the systolic interval. Moreover, the systolic interval is relatively constant as compared with diastolic interval. A segmented heart beat cycle begins and ends with either S1 heart sound or S2 heart sound of the two consecutive heart beat cycles. Therefore, after the identification of peaks of primary heart sounds, the approximate boundaries of either S1 heart sound or S2 heart sound can be used to extract the timing information of the heart beat cycles as described in [3, 27]. Finally, the heart beat cycles can be derived by mapping this timing information of CSCW to the original cardiac sound signals.

3.5 Feature Extraction

Feature extraction plays a vital role in detection and identification of heart valve and other disorders by deriving useful information accurately from the raw cardiac sound signals thereby reducing the dimensionality. In comparison to the use of original signal, the extracted lower dimensional feature set can reduce time and space complexity. From the experimental analysis in [52], it has been observed that the values of constrained TQWT based input parameters vary with nature and severity of murmurs in different clinical cases. Therefore, the feature set that has been created by the parameters that have been optimized while constrained TQWT can be used to achieve better representation of various types of cardiac sound signals. Two features have been created by the parameters that has been optimized while constrained TQWT namely the redundancy and the number of levels of decomposition. Moreover, time-domain, frequency-domain and non-linear method based entropy measures can reveal the information about the changes in heart sounds and presence of type of murmurs that take place under various pathological conditions. The time-domain based Shannon entropy, frequency-domain based spectral entropy, and non-linear method based approximate entropy and Lempel-Ziv complexity have been computed for separated heart sounds and murmurs corresponding to each segmented heart beat cycle. These ten features provide the

final feature set for classification of cardiac sound signals using ANN based classification. The entropy based features can be briefly described as follows:

Shannon entropy
Shannon had introduced Shannon entropy as a modern concept of measuring information for data communication. It can be used to characterize the degree of disorder in a system. Shannon entropy is based on the notion of probability and it can measures the uncertainty in a signal [67]. Basically, it measures the spread of data in its probability distribution. Data having broad and flat probability distribution exhibit high entropy. On the other hand, data with a narrow, peaked, probability distribution exhibit low entropy [29]. The normalized form of Shannon entropy which is denoted by *ShEn* is defined as:

$$ShEn = -\frac{\sum_n p_n \log p_n}{\log m} \tag{13}$$

where, n is the range of signal amplitude, p_n is the probability of the signal having amplitude a_n. In this study, the probability density function of the separated heart sounds and murmur have been estimated over the discrete values of a_n by using histogram. For the signal having N samples, the amplitude range of signal can be linearly divided into m bins such that the ratio m/N remains constant. Here, the ratio m/N has been kept at 0.01.

Approximate entropy
The approximate entropy (*ApEn*) is a non-linear statistical property which is used to measure the complexity of the system [55]. The *ApEn* can be defined as follows:

$$ApEn(m, w, N) = \frac{1}{N-m+1}\sum_{i=1}^{N-m+1} \ln S_w^m(i) - \frac{1}{N-m}\sum_{i=1}^{N-m} \ln S_w^{m+1}(i) \tag{14}$$

where, $S_w^m(i) = \frac{N_m(i)}{N-m+1}$. And m is the embedding dimension, N is the number of samples of the sequence, $N_m(i)$ is the number of matching vectors within the tolerance window w. In this study, *ApEn* has been computed for sequences corresponding to the separated heart sounds and murmur. The values of m and w have been set as 2 and 0.1 times the standard deviation respectively.

Lempel-Ziv complexity
Lempel-Ziv complexity is a kind of embedding entropy that directly depends on the finite sequences or time series. It is a non-parametric measure of complexity of finite sequences. It reflects the presence of number of distinct sub-sequences (patterns) and the rate of their occurrence along the sequence. The Lempel-Ziv complexity analysis is based on transforming the time-series into a finite symbol string. In this study, sequences of separated heart sounds and murmurs are transformed into binary sequences by assigning ones and zeros based on median as threshold. For more detail information, the algorithm to evaluate the Lempel-Ziv complexity can be found in [34].

Spectral entropy
The spectral entropy is computed by using the amplitude components of the power spectrum of the signal as the probabilities. In this work, the spectral entropies have been computed using the power spectrum of separated heart sounds and murmur. It can describe the irregularity or complexity in the spectrum of separated heart sounds and murmur. In literature, a variety of methods have been presented to obtain the spectral information, out of which the Fourier transform (FT) is the most common method for computing the power spectral density. The power spectral density function represents the distribution of power with frequency as the independent variable. The normalized form of Spectral entropy which can be denoted by *SpEn* is defined as [61]:

$$SpEn = -\frac{\sum_{j=f_L}^{f_H} P_j \log P_j}{\log N_f} \tag{15}$$

where, P_j is the power density of the signal in the defined frequency band $[f_L, f_H]$ and N_f is the number of frequencies within this band. In this work the frequency band has been specified as [100, 600] Hz.

3.6 ANN Based Classification

The artificial neural network (ANN) is based on heuristic mathematical modelling inspired by the interconnected processing layer of neurons in the brain [36, 60]. ANNs have been widely used for pattern recognition, function approximation and optimization problems. Generally, ANNs have been found to be robust, immune to noise, able to generalize and capable of solving non-linear problems. In this work, a multi-layer perception feed-forward ANN has been used for multi-class classification of cardiac sound signals. Five ANN models (ANN_1 to ANN_5) with different layers have been employed to facilitate the decision tree based classification among the considered classes of cardiac sound signals as shown in Fig. 7. At each stage of this decision tree, the configuration of ANN model with three layers has been chosen empirically to obtain higher classification performance. Each ANN model consists of following three layers: one input layer with 5 neurons, one hidden layer with 5 neurons and one output layer with one neuron. The target values for the ANNs have been kept as 0 and 1 which represent two classes of cardiac sound signals at each stage of decision tree. The input and hidden layer transfer functions of the ANNs are hyperbolic tangent sigmoid transfer function and output transfer function is linear transfer function. In order to train the network, the weights and bias values have been updated with Bayesian regularization back propagation algorithm such that mismatch between the target and the actual output from the network for any given input data can be minimized. The regularization within

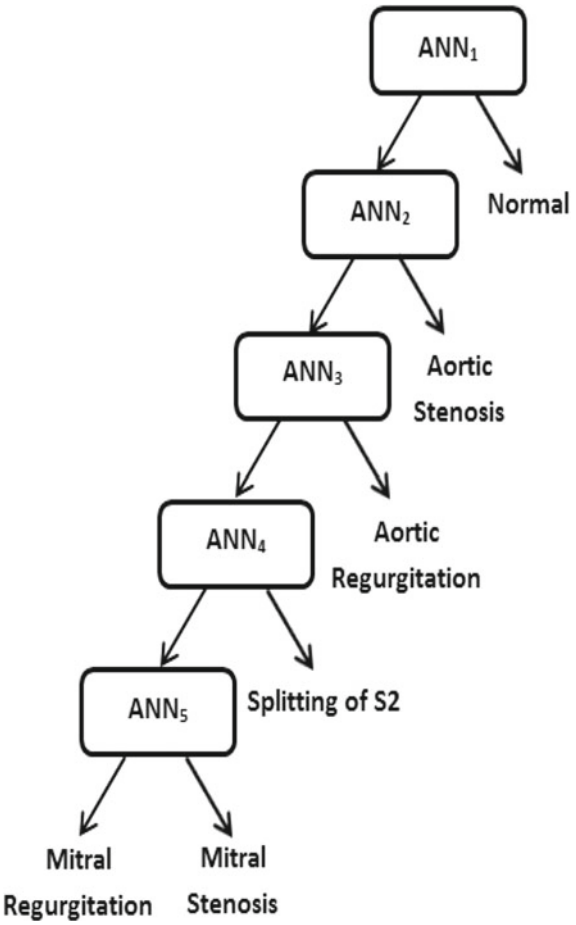

Fig. 7 Design of multi-class classifier based on five ANN models

Levenberg-Marquardt optimization is fast for training moderate-sized feed-forward ANN that have several hundred weights. Therefore, this algorithm has been chosen to train the ANNs.

3.6.1 Performance Evaluation Parameters

The classification performance of the ANN based decision tree for classification of cardiac sound signals can be evaluated by computing the sensitivity, specificity, and accuracy for each ANN. Sensitivity measures the proportion of actual positives which have been correctly identified as such. For example, the percentage of diseased people who have been correctly identified as having the disease. Specificity measures the proportion of negatives which have been correctly identified as such. For example, the percentage of healthy people who have been correctly identified as not having the disease. A perfect classifier would exhibit 100 % sensitivity by

detecting all diseased people as having diseased. Moreover, it would show 100 % specificity by not claiming anyone from the healthy group as diseased. The sensitivity (*Sen*), specificity (*Spe*), and accuracy (*Acc*) can be defined as:

$$Sen = \frac{TP}{TP + FN} \times 100 \tag{16}$$

$$Spe = \frac{TN}{TN + FP} \times 100 \tag{17}$$

$$Acc = \frac{TP + TN}{TP + TN + FP + FN} \times 100 \tag{18}$$

where *TP* and *TN* represents the total number of correctly detected true positive patterns and true negative patterns, respectively. The *FP* and *FN* represent the total number of erroneously positive patterns and erroneously negative patterns, respectively.

4 Experimental Results and Discussion

The proposed method has been implemented using Matlab. The functions of the TQWT toolbox and genetic algorithm and direct search toolbox of Matlab have been used for implementing the proposed method. The Matlab software for TQWT toolbox is available at http://eeweb.poly.edu/iselesni/TQWT/. A data containing recordings of normal, aortic stenosis, aortic regurgitation, splitting of S2 heart sound, mitral stenosis and mitral regurgitation have been used for evaluating the performance of the proposed segmentation and classification of cardiac sound signals. Figure 8 shows the example of classes of signals under study. The cardiac sound signals have been segmented into heart beat cycles by using constrained TQWT based method. Figure 9 shows an example of segmentation of cardiac sound signal into heart beat cycles using constrained TQWT based approach for aortic regurgitation signal. In Fig. 9, a–e represent the original signal, the decimated signal, reconstructed heart sounds, the noise attenuated signal and the CSCW based envelope respectively. Overall 82 cardiac sound signals with 2,283 heart beat cycles have been used in this work. There are 37, 4, 6, 8, 12 and 15 cardiac sound signals of normal, aortic stenosis, aortic regurgitation, splitting of S2 heart sound, mitral stenosis and mitral regurgitation respectively. The corresponding heart beat cycles are 855, 157, 201, 296, 245 and 489 respectively. The segmentation procedure has successfully segmented 2,123 heart beat cycles out of 2,283 heart beat cycles, yielding segmentation rate of 92.99 %. However, all the segmented beats have been used in the next stages of the methodology. The reference actual number of heart beat cycles present in the dataset are manually annotated by an experienced cardiologist. The annotation procedure is carried out by combined audio and visual interpretation of dataset.

After segmentation, the separation of heart sounds and murmur has been achieved using again the constrained TQWT based approach. It is noteworthy that, in order to

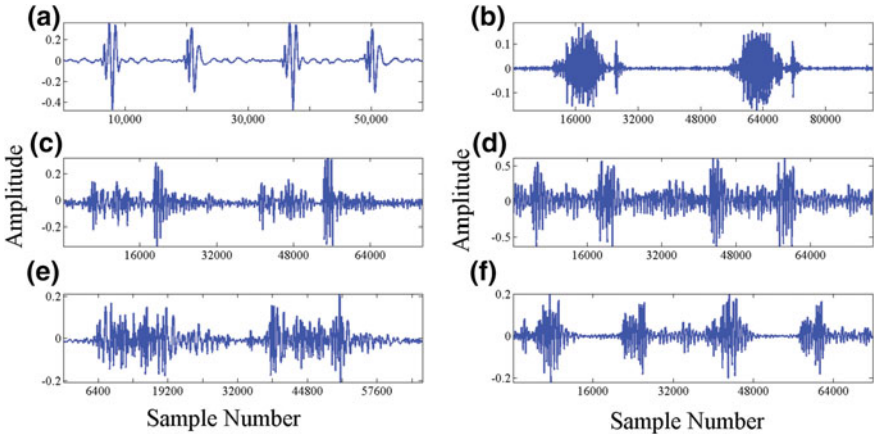

Fig. 8 Example of cardiac sound signals corresponding to **a** normal, **b** aortic stenosis, **c** aortic regurgitation, **d** splitting of S2, **e** mitral regurgitation and **f** mitral stenosis

reduce time of execution of constrained TQWT, the decimation has been carried out before constrained TQWT based separation of heart sounds and murmur by a factor of 32. The decimation considers the Nyquist-Shannon sampling theorem that provides highest expected frequency without affecting the murmurs. The decimation re-samples the heart beat cycles from sampling frequency of 44.100 kHz to that of 1,378.125 Hz .

After separation of heart sounds and murmur, the features have been extracted for ANN based based classification. The entropy measures namely time-domain based Shannon entropy, frequency-domain based spectral entropy, and non-linear method based approximate entropy and Lempel-Ziv complexity have been computed for separated heart sounds and murmur in each segmented heart beat cycles as features. Two features have been created by the parameters that has been optimized while constrained TQWT namely the redundancy and the number of levels of decomposition. These ten features have been used as a final feature set for classification of cardiac sound signals using ANN based technique. Five ANN models have been deployed for decision tree based detection and identification of heart disorders. Ten cross-validation approach has been used to evaluate each ANN model. The classification performance of the ANN based decision tree for classification of cardiac sound signals has been evaluated by computing the sensitivity (*Sen*), specificity (*Spe*), and accuracy (*Acc*) for each ANN model. The statistics of ANN based classification performance has been shown in Table 1. From the experimental results, it has been found that the ANN based classifier has provided promising classification accuracy of 93.40 % with the entropy and constrained TQWT based features. The experimental analysis of the proposed methodology shows that features based on time-frequency properties of constrained TQWT and entropy are quite effective to represent the behavior of cardiac sound signals giving higher classification performance. The entropy based features have been found suitable for analysis of non-stationary signals like cardiac sound signals.

Table 1 The results of cardiac sound signal classification using training and validation set

ANN models	*Sen* (%)	*Spe* (%)	*Acc* (%)	Classes
ANN_1	95.59	95.44	95.46	Normal and abnormal
ANN_2	92.67	98.69	97.92	Aortic stenosis and aortic regurgitation, splitting of S2 heart sound, mitral stenosis, mitral regurgitation
ANN_3	87.49	97.83	96.03	Aortic regurgitation and splitting of S2 heart sound, mitral stenosis, mitral regurgitation
ANN_4	93.23	80.96	80.70	Splitting of S2 heart sound, mitral stenosis, mitral regurgitation
ANN_5	96.14	97.51	96.93	Mitral stenosis and mitral regurgitation
Average	93.02	94.08	93.40	

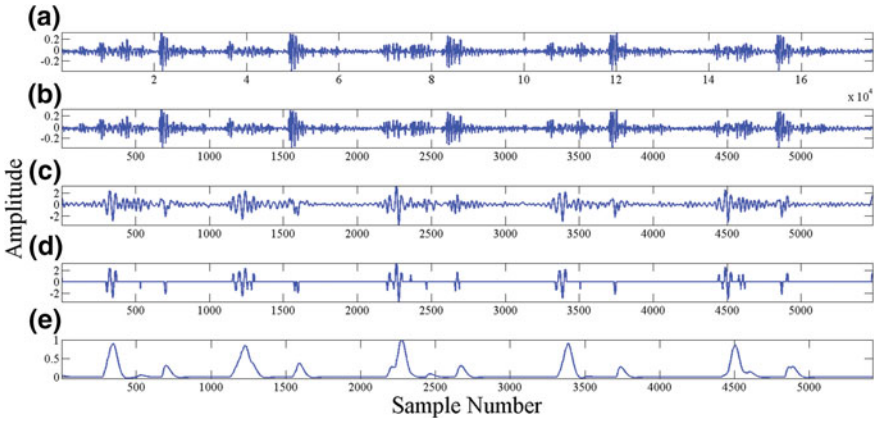

Fig. 9 An example of segmentation of cardiac sound signal into heart beat cycles using constrained TQWT based approach: **a** original aortic regurgitation signal, **b** the decimated signal, **c** reconstructed heart sounds, **d** the noise attenuated signal, **e** CSCW based envelope showing peaks of primary heart sounds which can be used to derive the heart beat cycles

5 Conclusion

The TQWT has been found to be useful and powerful transform for processing and analysis of cardiac sound signals. In this book chapter, a new method for classification of cardiac sound signals using TQWT has been presented. The constrained TQWT based segmentation of cardiac sound signals into heart beat cycles has been performed successfully. The features that are obtained from heart beat cycles of separately reconstructed heart sounds and murmur have been found useful to represent the various types of cardiac sound signals than that of containing both. The parameters evolved during constrained TQWT based separation of heart sounds and murmur and the entropy based measures have been used as valuable diagnostic features. In all, ten features have been used for subsequent classification of cardiac

sound signals using ANN based classification. The five ANN models have been used to classify: normal, aortic stenosis, aortic regurgitation, splitting of S2, mitral regurgitation and mitral stenosis. The performance of the proposed method has been validated with publicly available datasets. The proposed framework reveals the capability of constrained TQWT in adequately separating the heart sounds and the overlapping murmurs. The proposed method has provided significant performance in segmentation and classification of cardiac sound signals. The constrained TQWT and entropy based features have been found effective for classification of cardiac sound signals. The scope of the future work is to validate the proposed method with clinical cases that have not been considered in this study. Moreover, the proposed framework can be extended for detection and identification of cardiac devices especially the artificial heart valves in routine emergency check-ups at hospitals.

Acknowledgments The authors would like to thank Dr. Niranjan Garg, Cardiologist, Department of Cardiology, RD Gardi Medical College, Ujjain, India for his valuable clinical suggestions and discussions to improve the manuscript.

References

1. Amit, G., Lessick, J.,Gavriely, N.,, Intrator, N.: Acoustic indices of cardiac functionality. In: International Coriference on Bio-inspired Systems and Signal Processing (BIOSIGNALS), pp. 77–83. Setubal, Portugal (2008)
2. Amit, G., Gavriely, N., Intrator, N.: Cluster analysis and classification of heart sounds. Biomed. Sig. Process Cont. **4**(1), 26–36 (2009)
3. Ari, S., Saha, G.: On a robust algorithm for heart sound segmentation. J. Mech. Med. Biol. **7**, 129–150 (2007)
4. Ari, S., Saha, G.: Classification of heart sounds using empirical mode decomposition based features. Int. J. Med. Eng. Inform. **1**(1), 91–108 (2008)
5. Ari, S., Saha, G.: In search of an optimization technique for artificial neural network to classify abnormal heart sounds. Appl. Soft. Comput. **9**(1), 330–340 (2009)
6. Ari, S., Sensharma, K., Saha, G.: DSP implementation of heart valve disorder detection system from a phonocardiogram signal. J. Med. Eng. Technol. **32**(2), 122–132 (2008)
7. Ari, S., Hembram, K., Saha, G.: Detection of cardiac abnormality from PCG signal using LMS based least square SVM cassifier. Expert Syst. Appl. **37**, 8019–8026 (2010)
8. Barschdorff, D., Femmer, U., and Trowitzsch, E.: Automatic phonocardiogram signal analysis in infants based on wavelet transforms and artificial neural networks. In: Computers in Cardiology, pp. 753–756. Vienna, Austria (1995)
9. Cathers, I.: Neural network assisted cardiac auscultation. Art. Intell. Med. **7**, 53–66 (1995)
10. Chauhan, S., Wang, P., Lim, C.S., Anantharaman, V.: A computer-aided MFCC-based HMM system for automatic auscultation. Comput. Biol. Med. **38**(2), 221–233 (2008)
11. Choi, S.: Detection of valvular heart disorders using wavelet packet decomposition and support vector machine. Expert Syst. Appl. **35**(4), 1679–1687 (2008)
12. Choi, S., Jiang, Z.: Comparison of envelope extraction algorithms for cardiac sound signal segmentation. Expert Syst. Appl. **34**(2), 1056–1069 (2008)
13. Choi, S., Jiang, Z.: Cardiac sound murmurs classification with autoregressive spectral analysis and multi-support vector machine technique. Comput. Biol. Med. **40**(1), 8–20 (2010)
14. Chung, Y.J. (2008). Using Kullback-Leibler distance in determining the classes for the heart sound signal classification. In: Intelligent Data Engineering and Automated Learning, pp. 49–56. Springer Heidelberg Berlin (2008)

15. Chung, Y.J.: Classification of continuous heart sound signals using the ergodic hidden Markov model. In: Pattern Recognition and Image Analysis, pp. 563–570. Springer Heidelberg Berlin (2007)
16. Dokur, Z., Ölmez, T.: Feature determination for heart sounds based on divergence analysis. Digit. Signal Proc. **19**(3), 521–531 (2009)
17. Dokur, Z., Ölmez, T.: Heart sound classification using wavelet transform and incremental self-organizing map. Digit. Signal Proc. **18**(6), 951–959 (2008)
18. Durand, L.G., Pibarot, P.: Digital signal processing of the phonocardiogram: review of the most recent advancements. Crit. Rev. Biomed. Eng. **23**, 163–219 (1995)
19. Feigen, L.P.: Physical characteristics of sound and hearing. Am. J. Cardiol. **28**, 130–133 (1971)
20. Gamero, L.G., Watrous, R.: Detection of the first and second heart sound using probabilistic models. In: Proceedings of the 25th Annual International Conference of the IEEE Engineering in Medicine and Biology Society, pp. 2877–2880 (2003)
21. Groch, M.W., Domnanovich, J.R., Erwin, W.D.: A new heart-sounds gating device for medical imaging. IEEE Trans. Biomed. Eng. **39**(3), 307–310 (1992)
22. Gupta, C.N., Palaniappan, R., Swaminathan, S., Krishnan, S.M.: Neural network classification of homomorphic segmented heart sounds. Appl. Soft Comput. **7**(1), 286–297 (2007)
23. Hadi, H.M., Mashor, M.Y., Suboh, M.Z., and Mohamed, M.S.: Classification of heart sound based on S-transform and neural networks. In: Proceedings of International Conference on Information Sciences Signal Processing and their Applications, pp. 189–192. Kuala Lumpur, Malaysia (2010)
24. Haghighi-Mood, A., Torry, J.N.: A sub-band energy tracking algorithm for heart sound segmentation. In: Computers in Cardiology, pp. 501–504 (1995)
25. Hanna, I.R., Silverman, M.E.: A history of cardiac auscultation and some of its contributors. Am. J. Cardiol. **90**, 259–267 (2002)
26. Huiying, L., Sakari, L., liro, H.: A heart sound segmentation algorithm using wavelet decomposition and reconstruction. In: Proceedings of 19th International Conference of the IEEE Engineering in Medicine and Biology Society, pp. 1630–1633. Chicago, IL (1997)
27. Iwata, A., Ishii, A.N., Suzumura, N., Ikegaya, K.: Algorithm for detecting the first and the second heart sounds by spectral tracking. Med. Biol. Eng. Comput. **18**, 19–26 (1980)
28. Jiang, Z., Choi, S.: A cardiac sound characteristic waveform method for in-home heart disorder monitoring with electric stethoscope. Expert Syst. Appl. **31**(2), 286–298 (2006)
29. Kannathal, N., Choo, M.L., Acharya, U.R., Sadasivan, P.K.: Entropies for detection of epilepsy in EEG. Comput. Methods Programs Biomed. **80,** 187–194 (2005)
30. Kao, W.C., Wei, C.C.: Automatic phonocardiograph signal analysis for detecting heart valve disorders. Expert Syst. Appl. **38**(6), 6458–6468 (2011)
31. Kumar, D., Carvalho, P., Antunes, M., Henriques, J., Eugenio, L., Schmidt, R., Habetha, J.: Detection of S1 and S2 heart sounds by high frequency signatures. In: Procedings of 28th IEEE Engineering in Medicine and Biology Society Annual International Conference, pp. 1410–1416. New York , USA (2006)
32. Kumar, D., Carvalho, P., Antunes, M., Henriques, J., SaeMelo, A., Schmidt, R., and Habetha, J.: Third heart sound detection using wavelet transform-simplicity filter. In: Proceedings of Annual International Conference of the IEEE Engineering in Medicine and Biology Society, pp. 1277–1281. Lyon, France (2007)
33. Lehner, R.J., Rangayyan, R.M.: A three-channel microcomputer system for segmentation and characterization of the phonocardiogram. IEEE Trans. Biomed. Eng. **34**(6), 485–489 (1987)
34. Lempel, A., Ziv, J.: On the complexity of finite sequences. IEEE Trans. Inf. Theory **22**(1), 75–81 (1976)
35. Liang, H., Lukkarinen, S., Hartimo, I.: Heart sound segmentation algorithm based on heart sound envelogram. In: Computers in Cardiology, pp. 105–108 (1997)
36. Lippmann, R.P.: An introduction to computing with neural nets. IEEE ASSP Mag. **4**(2), 4–22 (1987)
37. Livanos, G., Ranganathan, N., Jiang, J.: Heart sound analysis using the S-transform. In: Computers in Cardiology, pp. 587–590 (2000)

38. Lukkarinen, S., Noponen, A.L., Sikio, K., Angerla, A.: A new phonocardiographic recording system. In: Computers in Cardiology, pp. 117–120 (1997)
39. Maglogiannis, I., Loukis, E., Zafiropoulos, E., Stasis, A.: Support vectors machine-based identification of heart valve diseases using heart sounds. Comput. Methods Programs Biomed. **95**, 47–61 (2009)
40. Malarvili, M.B., Kamarulafizam, I., Hussain, S., and Helmi, D.: Heart sound segmentation algorithm based on instantaneous energy of electrocardiogram. In: Computers in Cardiology, pp. 327–330 (2003)
41. Mangione, S., Nieman, L.Z.: Cardiac auscultatory skills of internal medicine and family practice trainees. J. Am. Med. Assoc. **278**, 717–722 (1997)
42. Messer, S.R., Agzarian, J., Abbott, D.: Optimal wavelet denoising for phonocardiograms. J. Microelectron. **32**, 931–941 (2001)
43. Moukadem, A., Dieterlen, A., Hueber, N., Brandt, C.: Comparative study of heart sounds localization. In: Proceedings of SPIE N8068-27, Bioelectronics, Biomedical, and Bioinspired Systems (2011).
44. Moukadem, A., Dieterlen, A., Hueber, N., and Brandt, C.: Localization of heart sounds based on S-transform and radial basis function neural network. In: IFMBE Proceedings of 15th Nordic-Baltic Conference on Biomedical Engineering and Medical Physics, pp. 168–171 (2011)
45. Moukadem, A., Dieterlen, A., Hueber, N., Brandt, C.: A robust heart sounds segmentation module based on S-transform. Biomed. Signal Process. Control **8**(3), 273–281 (2013)
46. Myint, W.W., Dillard, B.: An electronic stethoscope with diagnosis capability. In: Proc.of the 33rd IEEE Southeastern Symposium on System Theory, pp. 133–137. Athens, OH (2001)
47. Naseri, H., Homaeinezhad, M.R.: Detection and boundary identification of phonocardiogram sounds using an expert frequency-energy based metric. Ann. Biomed. Eng. **41**(2), 279–292 (2013)
48. Nieblas, C.I., Alonso, M.A., Conte, R., Villarreal. S.: High performance heart sound segmentation algorithm based on matching pursuit. In: IEEE Digital Signal Processing and Signal Processing Education Meeting (DSP/SPE), pp. 96–100. Napa, CA (2013)
49. Ölmez, T., Dokur, Z.: Classification of heart sounds using an artificial neural network. Pattern Recogn. Lett. **24**, 617–629 (2003)
50. Pasterkamp, H., Kraman, S.S., Wodicka, G.R.: Respiratory sounds: advances beyond the stethoscope. Am. J. Respir. Crit. Care Med., 974–987 (1997)
51. Patidar, S., Pachori, R.B.: Constrained tunable-Q wavelet transform based analysis of cardiac sound signals. AASRI Procedia **4**, 57–63 (2013)
52. Patidar, S., Pachori, R.B.: Segmentation of cardiac sound signals by removing murmurs using constrained tunable-Q wavelet transform. Biomed. Signal Process. Control **8**(6), 559–567 (2013)
53. Patidar, S., Pachori, R.B.: A continuous wavelet transform based method for detecting heart valve disorders using phonocardiograph signals. In: International Conference on Convergence and Hybrid Information Technology, pp. 513–520. Daejeon, Korea (2012)
54. Pease A.: If the heart could speak. Pictures Future, pp. 60–61 (2001)
55. Pincus, S.M.: Approximate entropy as a measure of system complexity. Proc. Nat. Acad. Sci., 2297–2301 (1991)
56. Rajan, S., Doraiswami, R., Stevenson, R., and Watrous, R.: Wavelet based bank of correlators approach for phonocardiogram signal classification. In: Proceedings of the IEEE-SP International Symposium on Time-Frequency and Time-Scale Analysis, pp. 77–80. Pittsburgh, PA (1998)
57. Rangayyan, R.M., Lehner, R.J.: Phonocardiogram signal analysis: a review. Crit. Rev. Biomed. Eng. **15**(3), 211–236 (1986)
58. Reed, T., Reed, N., and Fritzson, P.: Analysis of heart sounds for symptom detection and machine-aided diagnosis. In: 2nd Conference Modeling and Simulation in Biology, Medicine, and Biomedical Engineering, pp. 1–6. Delft, The Netherlands (2001)
59. Reed, T.R., Reed, N.E., Fritzson, P.: Heart sound analysis for symptom detection and computer-aided diagnosis. Simul. Model. Pract. Theory **12**, 129–146 (2004)

60. Rumelhart, D.E., McClelland, J.L.: Parallel distributed processing: Explorations in the Microstructure of Cognition: Foundations. MIT Press, Cambridge, MA (1986)
61. Sabeti, M., Katebi, S., Boostani, R.: Entropy and complexity measures for EEG signal classification of schizophrenic and control participants. Artif. Intell. Med. **47**, 263–274 (2009)
62. Sanei, S., Ghodsi, M., Hassani, H.: An adaptive singular spectrum analysis approach to murmur detection from heart sounds. Med. Eng. Phys. **33**(3), 362–367 (2011)
63. Schmidt, S.E., Holst-Hansen, C., Graff, C., Toft, E., Struijk, J.J.: Segmentation of heart sound recordings by a duration-dependent hidden Markov model. Physiol. Meas. **31**(4), 513–529 (2010)
64. Sejdic, E., Jiang, J.: Comparative study of three time-frequency representations with applications to a novel correlation method. In: Proceedings of IEEE International Conference on Acoustics, Speech, and Signal Processing (ICASSP), pp. 633–636 (2004)
65. Selesnick, I.W.: Wavelet transform with tunable Q-factor. IEEE Trans. Signal Process. **59**(8), 3560–3575 (2011)
66. Sepehri, A.A., Gharehbaghi, A., Dutoit, T., Kocharian, A., Kiani, A.: A novel method for pediatric heart sound segmentation without using the ECG. Comput. Methods Programs Biomed. **99**, 43–48 (2010)
67. Shannon, C.E., Weaver, W.: The mathematical theory of communication. University of Illinois Press, Champaign (1963)
68. Shino, H., Yoshida, H., Yana, K., Harada, K. Sudoh, J., Harasewa, E.: Detection and classification of systolic murmur for phonocardiogram screening. In: Proceedings of 18th International Conference of the IEEE Engineering in Medical and Biology Society, pp. 123–124 (1996)
69. Sun, S., Jiang, Z., Wang, H., Fang, Y.: Automatic moment segmentation and peak detection analysis of heart sound pattern via short-time modified Hilbert transform. Comput. Methods Programs Biomed. **114** (3), 219-230 (2014)
70. Sun, S., Wang, H., Jiang, Z., Fang, Y., Tao, T.: Segmentation-based heart sound feature extraction combined with classifier models for a VSD diagnosis system. Expert Syst. Appl. **41** (4), 1769–1780 (2014)
71. Syed, Z., Leeds, D., Curtis, D., Nesta, F., Levine, R.A., Guttag, J.: A framework for the analysis of acoustical cardiac signals. IEEE Trans. Biomed. Eng. **54**(4), 651–662 (2007)
72. Tang, H., Li, T., Qiu, T., Park, Y.: Segmentation of heart sounds based on dynamic clustering. Biomed. Signal Process. Control **7**(5), 509–516 (2012)
73. Thompson, W.R., Hayek, C.S., Tuchinda, C., Telford, J.K., Lombardo, J.S.: Automated cardiac auscultation for detection of pathologic heart murmurs, Pediatr. Cardiol, 373–379 (2001)
74. Tseng, Y.L., Ko, P.Y., Jaw, F.S.: Detection of the third and fourth heart sounds using Hilbert-Huang transform. BioMed. Eng. OnLine **11**(8), 1–13 (2012)
75. Vepa, J., Tolay, P., Jain, A.: Segmentation of heart sounds using simplicity features and timing information. In: IEEE International Conference on Acoustics, Speech and Signal Processing, pp. 469–472 (2008)
76. Wang, P., Lim, C.S., Chauhan, S., Foo, J.Y.A., Anantharaman, V.: Phonocardiographic signal analysis method using a modified hidden Markov model. Ann. Biomed. Eng. **35**(3), 367–374 (2007)
77. Watrous, R.L.: Computer-Aided auscultation of the heart: From anatomy and physiology to diagnostic decision support. In: Proceedings of the 28th Annual International Conference of the IEEE Engineering in Medicine and Biology Society, pp. 140–143. New York, USA (2006)
78. Yan, Z., Jiang, Z., Miyamoto, A., Wei, Y.: The moment segmentation analysis of heart sound pattern. Comput. Methods Programs Biomed. **98**, 140–150 (2010)
79. Yuan, J., He, Z., Zi, Y.: Gear fault detection using customized multiwavelet lifting schemes. Mech. Syst. Signal Process. **24**(5), 1509–1528 (2010)
80. Yuenyong, S., Nishihara, A., Kongprawechnon, W., Tungpimolrut, K.: A framework for automatic heart sound analysis without segmentation. BioMed. Eng. Online **10**, 01-23 (2011)

Reliability-Constrained Optimal Distribution System Reconfiguration

Salem Elsaiah, Mohammed Benidris and Joydeep Mitra

Abstract This work describes a method for reliability improvement of power distribution system via feeder reconfiguration. The work presented here is developed based on a linearized network model in the form of DC power flow and linear programming model in which current carrying capacities of distribution feeders and real power constraints have been considered. The optimal open/close status of the sectionalizing and tie-switches are identified using an intelligent binary particle swarm optimization based search method. The probabilistic reliability assessment is conducted using a method based on higher probability order approximation. Several case studies are carried out on a 33 bus radial distribution system and also on 118 buses large-scale distribution system, which are extensively used as examples in solving the distribution system reconfiguration problem. Further, the effect of embedded generation on distribution system reconfiguration has been considered in one case scenario. The test results show that the amount of annual unnerved energy and customer's interruptions can be significantly reduced using the proposed method. Further, the reliability assessment method and the search method proposed in this work have both shown to be computationally efficient and very suitable for reliability-constrained feeder reconfiguration problems.

Keywords Distribution system reconfiguration · Reliability assessment · Particle swarm optimization

S. Elsaiah (✉) · M. Benidris · J. Mitra
Electrical and Computer Engineering Department, Michigan State University, East Lansing, MI, USA
e-mail: elsaiahs@msu.edu

M. Benidris
e-mail: benidris@msu.edu

J. Mitra
e-mail: mitraj@msu.edu

A.T. Azar and S. Vaidyanathan (eds.), *Chaos Modeling and Control Systems Design*, Studies in Computational Intelligence 581, DOI 10.1007/978-3-319-13132-0_11

1 Introduction

The vast majority of power distribution systems are characterized by radial topological structure and poor voltage regulation. The radial topology is necessary in order to facilitate the control and coordination of the protective devices used at the distribution system level. However, with that radial structure, the failure of any single component between the load point and the source node would cause service interruptions and may result in disconnecting several load points. Distribution system reconfiguration can be used to minimize the duration and frequency of service interruptions; and thereby improving the reliability of the system and the quality of service. Distribution system reconfiguration aims at changing the topological structure of the distribution network by altering the open/close status of sectionalizing and tie-switches to achieve certain objectives. The common objective function used in distribution system reconfiguration is distribution system loss reduction and load balancing [2, 8, 9, 16, 21, 22].

In recent years, there has been an increasing interest in improving distribution system reliability using distribution system reconfiguration. The expected energy not supplied (EENS), expected demand not supplied (EDNS), and the expected outage cost (ECOST) are some examples of the reliability measures used in the literature. In Bin et al. [25] reliability worth enhancement based distribution system reconfiguration is proposed. Further, analytical and heuristic methods have been proposed for reliability worth enhancement. A reliability cost-worth model of the distribution system is built up and from which the ECOST and the EENS are obtained. In Bin et al. [25], the interrupted energy assessment rate (IEAR), which is proposed by Goel and Billinton [12] has also been used in Bin et al. [25] to relate the interruption cost and the expected energy not supplied for every feasible configuration.

A distribution system reconfiguration for reliability worth analysis based on simulated annealing is proposed in Skoonpong and Sirisumrannukul [23]. The work reported in Skoonpong and Sirisumrannukul [23] used the same reliability indices and the same customer damage function as in Bin et al. [25]. However, several conclusions about the final system configuration are drawn as the ECOST and the EENS were both considered as objectives in the optimization problem. Reliability improvement of power distribution systems using distributed generation has also been proposed in the literature [18, 24].

Swarm intelligence optimization methods or meta-heuristic methods have been widely used in distribution system reconfiguration for reliability enhancement. Amongst these methods, particle swarm optimization (PSO) based methods are recognized as viable tools in solving the distribution system reconfiguration problem for reliability improvement. The advantages of using particle swarm optimization in handling the distribution system reconfiguration problem are manifold. For instance, the status of sectionalizing and tie-switches in the distribution system can be easily represented as binary numbers of (0, 1). Moreover, particle swarm optimization based methods have considerably fast convergence

characteristics and, generally speaking, have few parameters to tune up compared to some other meta-heuristic approaches. Further, particle swarm optimization has two main parameters, which are the personal best and the global best. Every particle in the swarm remembers its own personal best and at the same time its global best. Consequently, PSO based methods have more memory capability than some other swarm intelligence based methods.

Chakrabarti et al. presented a reliability based distribution system reconfiguration method in Chakrabarti et al. [6]. The objective in this study was to minimize the loss of load expectation (LOLE) and the loss of energy expectation (LOEE). Monte Carlo simulation and particle swarm optimization have also been used as searching tools. Amanulla el al. [1] proposed a reconfiguration method for large systems based on minimal cut set method. The problem of optimal switch placement in power distribution systems has been carried out using trinary PSO in Moradi and Firuzabad [19]. The use of ant colony optimization for placement of sectionalizing switches in power distribution systems has also been proposed in Falaghi et al. [11].

It is worth mentioning here that Brown [5] has reported that distribution systems contribute for up to 90 % of overall consumer's reliability problems. This can not only be attributed to the radial topological structure of distribution systems, but also to the fact that most of nowadays distribution systems are being stressed and operated at heavily loading conditions due to the rapid increase in electricity demand and some other economical and environmental constraints. Statistics have shown also that the vast majority of consumers' outages and service interruptions have taken place at distribution system level [3, 5]. These verities combined with the complexities of today's distribution systems have motivated us to revamp the service of consumers by considering the reliability while reconfiguring the distribution network.

This work proposes a method for distribution system reconfiguration with an objective of reliability improvement. The work presented here is developed based on a linearized network model in the form of DC power flow model and linear programming formulation in which current carrying capacities of distribution feeders and real power constraints have been considered. The linearized network model used in this work is appropriate to use for reliability studies as it is very fast and reliable. The optimal open/close status of the sectionalizing and tie-switches are identified using an intelligent binary particle swarm optimization based search method (BPSO). The probabilistic reliability assessment is conducted using a method based on high probability order approximation. Numerous case studies are demonstrated on a small 33 bus radial distribution system and 118 buses large-scale distribution system, which have both been used as benchmark systems while solving the optimal distribution feeder reconfiguration problem. Distributed generators are constantly used in several of nowadays distribution systems. The effect of distribution generation units on the entire distribution system reliability is considered in one case study.

2 Review of Mathematical Programming Based Methods

Nonlinear optimization methods and linear optimization methods can be used for distribution system operation and planning studies. Each category has its own advantages and disadvantages. The common optimization methods applied to power distribution systems are discussed in Sect. 2.1.

2.1 Nonlinear Optimization Methods

Power systems are inherently nonlinear systems. Consequently, nonlinear optimization techniques can be used to handle power system operation and planning problems. Examples of the nonlinear optimization methods, which are widely used in the literature include, nonlinear programming, quadratic programming, and mixed-integer programming.

In nonlinear programming based optimization, both the objective function and the constraints are nonlinear. In order to handle a nonlinear programming problem, we usually start by choosing a search direction, which is obtained by finding the reduced gradient or the first derivative of the objective function. A key advantage of using nonlinear programming techniques in distribution system operation and planning studies is partly attributed to their ability to achieve higher accuracy. However, the main disadvantage of nonlinear programming based methods is that slow convergence rate may occur, which makes these methods computationally expensive, especially for applications in which repetitive solutions are required such as reliability assessment of power system, for instance. In addition, for a specific type of engineering applications the objective function can be non-differentiable. This in turn could limit the use of the nonlinear programming based methods in handling certain objective functions.

Quadratic programming can in fact be considered as a special case of nonlinear programming based technique. That is, in quadratic programming the objective function is a quadratic while the constraints are linear. A common objective function used in power system operation and planning is to minimize the total generation cost or total emission, which is inherently a quadratic function. The quadratic programming handles this problem efficiently, however, at the same time, the computational burden is considerably large. More prominently, the standard simple form of the quadratic programming is not quite often used because convergence is not always guaranteed.

Nonlinear optimization problems can also be formulated as a mixed-integer programming using certain integer control variables. Handling optimization problems using mixed-integer programming based techniques are extremely computational demanding, especially for large-scale systems.

2.2 Linear Optimization Methods

Linear methods are used to transform nonlinear optimization problems to linear problems. In this context, linear programming (LP) is probably the most popular technique, which has been widely used to handle engineering applications that require repetitive, prompt, and multiple solutions. Unlike nonlinear programming based methods, both the objective function and constraints are linear functions in the LP model. The advantages of using LP based methods in distribution system operation and planning include [27]:

1. Reliability of the optimization and flexibility of the solution.
2. Rapid convergence characteristics and fast execution time.
3. Nonlinear convex curves can be handled using piecewise linear models.
4. Equality and inequality constraints can be equally handled in the basic LP routine.

Now, suppose we have m constraints with n variables, the matrix of the coefficients of the constraints would be of the form [27].

$$A = \begin{pmatrix} a_{11} & a_{11} & \ldots & a_{1n} \\ a_{11} & a_{11} & \ldots & a_{2n} \\ \vdots & \vdots & \vdots & \\ a_{m1} & a_{m1} & \ldots & a_{mn} \end{pmatrix} \tag{1}$$

The right hand side vector b of the constraints consists of m constants,

$$b = (b_1, b_2, \ldots, b_m)^T \tag{2}$$

The row vector of the objective function c consists of n coefficients

$$c = (c_1, c_2, \ldots, c_n)^T \tag{3}$$

The standard *maximum* linear programming problem can be formulated as follows,

$$\max(Z) = \sum_{j=1}^{n} c_j x_j \tag{4}$$

Subject to the following constraints,

$$\begin{cases} \sum\limits_{j=1}^{n} a_{ij} x_j \leq b_i \\ x_j \geq 0 \end{cases} \tag{5}$$

If the slack variables of Eq. (5) are imported, the standard linear programming will have the following form,

$$\max Z = CX \tag{6}$$

With the equality constraints,

$$\begin{cases} AX = b \\ X \geq 0 \end{cases} \tag{7}$$

The dual of this standard *maximum* problem is the standard *minimum* problem, that is,

$$\text{Min}(W) = \sum_{i=1}^{m} b_i y_i \tag{8}$$

Subject to the following constraints,

$$\begin{cases} \sum_{j=1}^{n} a_{ij} y_j \geq c_j \\ y_i \geq 0 \end{cases} \tag{9}$$

The *optimal* and *feasible* solution of Eq. (5), for instance, can be expressed as,

$$X_b = B^{-1} b \tag{10}$$

where B is the optimal basis at the optimal and feasible solution and X_b is the basic variable subvector.

3 Review of Network Models

The structure of distribution systems has been recently changed due to certain environmental, economical, and political reasons. This change has come through the emergence of several real-time engineering applications in both operational and planning stages. Examples of these applications include sizing and placement of distributed generators, economic power dispatch of active distribution systems, feeder reconfiguration for service restoration and reliability enhancement, and so forth. It is very well known that these applications require a power flow study at the first step of the solution. Nevertheless, and not surprisingly, the vast majority of these applications require repetitive and prompt power flow solutions. Performing nonlinear power flow, on one hand, gives high calculation precision but requires a quite extensive computational burden and storage requirements. On the other hand,

and more prominently, the largest part of the aforementioned applications is essentially nonlinear complex combinatorial constrained optimization problems. The formulation of the nonlinear problem, however, tends to be a tedious task and computationally cumbersome in terms of execution time, storage requirements, and programming. These verities combined with the large number of nodes, branches, and switches of distribution system will incontestably increase the complexity of the optimization problem.

The vast majority of power system optimization problems are essentially optimal power flow problems with different objectives. The total load curtailment minimization problem, for instance, is an important objective function that is used for reliability evaluation of power systems. We would like to elaborate here on this objective function, which is concerned with reliability improvement of distribution system. For every task of reliability evaluation, a power flow study is constantly performed. Toward this end, three power flow models have generally been used for reliability evaluation of power systems. These models are the nonlinear power flow model, the capacity flow model, and the DC power flow model. Experience with the nonlinear power flow model has shown, however, that when this model is incorporated in the reliability assessment framework, the task of reliability evaluation becomes extremely complex and oftentimes computationally intractable. Also, the required data and storage both become high. On the other hand, the capacity flow model only uses the capacity constraints of the tie-lines, and thereby; generally speaking, it is not applicable for every reliability study. In view of these reasons, in many cases, it has been found to be more appropriate to utilize the DCPF model.

The DC power flow method, which was devised more than 35 years ago, has been widely utilized in reliability assessment of power and distribution systems [17, 20]. It is denoted as DC power flow (DCPF), in analogy to a DC circuit fed by a DC voltage source. In fact, this model is a linearized version of the nonlinear power flow model; however it ignores most of the aspects of the nonlinear power flow model. The DCPF model is non-iterative, linear, and absolutely convergent, but with less accuracy than the nonlinear power flow model. The DCPF model assumes flat voltage profiles at all buses and lossless transmission lines. It is usually used whenever fast power flow solutions are required as in optimal economic power dispatch, contingency analysis, and reliability and security assessment. The DCPF model is unquestionably a powerful computational tool and was approximately involved in numerous power system operational and planning studies because of its simplicity of formulation and implementation.

It is worth to point out here that the use of the DCPF model in certain reliability evaluation studies of distribution systems has been based on the assumption that adequate information about reactive power flow are unavailable in advance. Such an assumption is justified for several planning studies because reactive power is usually supplied in a form of capacitor banks, which can be treated as a separate optimization problem.

4 Problem Statement

Distribution systems are equipped with sectionalizing and tie-switches. The crucial purpose of the tie-switches is to transfer loads from one feeder to another during abnormal and emergency conditions. The problem being presented in this work can be stated as follows: Given the distribution network with $N_T \in N_{TN}$ tie-switches, where N_{TN} is the number of tie-switches in the distribution system, and $N_S \in N_{SN}$ sectionalizing switches, where N_{SN} is the number of sectionalizing switches in the distribution system. The solution of the optimal distribution system reconfiguration problem (Ω) aims at finding the best combination of the tie-switches and sectionalizing switches $\Omega \in (N_{TN} \cup N_{SN})$ that minimizes the expected power not supplied, and thereby, maximizes the overall reliability of the distribution system.

5 Development of Models and Methods

In this section, the state space of the problem is defined. Probabilistic reliability models for various distribution system components are reviewed. In addition, a reliability evaluation method based on higher probability order is introduced and discussed.

5.1 The State Space of the Problem

The state space in this work represents the set of all possible combinations of generators, distribution feeders, sectionalizing switches, tie-switches, buses, circuit breakers, and distribution transformers. Consequently, the dimension of the state space can be stated as the set of all the aforementioned components. As was mentioned earlier, distribution systems are reconfigured radially for best control of their protective relays and instruments. Therefore, the substation bus is assumed to be perfectly reliable due to the radial topological structure of the realistic power distribution systems. Modeling of these components is addressed in the subsequent section.

5.2 Distribution System Modeling

For distribution system reliability studies, probabilistic modeling techniques are utilized to represent various system components. The availability of any component i in the system can be represented as [3].

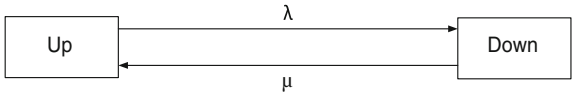

Fig. 1 Two-state Markovian model

$$P_i = \frac{1/\lambda_i}{1/\lambda_i + 1/\mu_i} \tag{11}$$

where λ_i is the failure rate of component i and μ_i is the repair rate of component i, respectively.

In the work presented here, it is assumed that each component in the system can only reside in an up-state or down-state. Therefore, the two-state Markovian model shown in Fig. 1 is used to model various system components [3, 5]. For distribution feeders, a discrete probability density function is constructed for every distribution line. If a distribution feeder is tripped off for certain system state, the line is removed from the bus admittance matrix and its capacity is set equal to zero.

5.3 Reliability Indices

Reliability of distribution system can be defined as the ability of the distribution system to satisfy its consumers load demand under certain operating conditions. This work uses the expected power not supplied (EPNS), which is alternatively known as the expected demand not supplied (EDNS) is used to evaluate distribution system reliability. The loss of load probability (LOLP) is used to calculate the total load curtailment (C). These indices are defined as,

Expected Energy Not Supplied (*EPNS*): The expected number of megawatt per year that the system cannot supply to consumers. Alternatively, it is also known as the expected demand not supplied (EDNS).

Loss of Load probability (*LOLP*): The probability that the system will not be able to supply the load demand under certain operating scenarios.

5.4 Reliability Evaluation

Enumeration all events to compute the exact values of probabilities can sometimes be unnecessary and impractical. In practice, probabilities of occurrence of various events are approximated up to certain level. This work uses a reliability assessment method based on higher probability order approximation [4, 7]. This concept is well represented in Chen and McCalley [7] and is discussed here for the sake of completion.

Suppose we have three events, which are represented as E_1, E_2, and E_3 with individual probabilities of P_1, P_2, and P_3, respectively. The compound probability of the event $(E_1 \cap E_2) \cup E_3$, for instance, can be expressed as,

$$(E_1 \cap E_2) \cup E_3 = P_3 + P_1 \times P_2 - P_1 \times P_2 \times P_3 \tag{12}$$

As can be seen from (12) this compound probability consists of first-order probability, second-order probability, and third-order probability. It is worth pointing out here that the probability of failure of most power system components is quite small. Having said that, the effect of higher-order contingencies could possibly be limited using certain probability or frequency criterion. For instance, in (2) if the individual probabilities P_1, P_2, and P_3 are quite small, then the event $(E_1 \cap E_2) \cup E_3$ can be approximated with $(P_3 + P_1 \times P_2)$ or with (P_3) [7]. The reliability evaluation method followed in this work is developed based on the high probability order approximation so that the effect of any contingency level with a frequency of occurrence less than 10^{-10} has been neglected. This would in turn enhance the computational speed, without significant effect on the degree of accuracy of the estimated indices. We have shown through simulations that this method is tremendously appropriate to use for reliability evaluation studies as it is flexible and computationally efficient.

6 Reliability Evaluation Using Linearized Network Model and Linear Programming

This section formulates the optimal distribution system reconfiguration problem. It first presents the objective function and constraints. Then, it introduces a method to impose the radial topological structure of the distribution system. It also presents a method to calculate the reliability index, which is used in this work.

6.1 Objective Function

A linear Programming formulation, which is similar to similar to that given by Mitra and Singh [17], is used here to minimize total load curtailments. The equality constraints are the power flow injections at each bus, which are represented by the power balance equations. The inequality constraints include the capacity limits of generating units and power carrying capacities of distribution feeders.

The objective function used in this work can be posed as [17],

$$Loss\ of\ Load = min \sum_{i=1}^{N_B} C_i \tag{13}$$

Subject to,

$$\begin{aligned} &\hat{B}\theta + G + C = D \\ &G \leq G^{\max} \\ &C \leq D \\ &b\hat{A}\theta \leq F_f^{\max} \\ &-b\hat{A}\theta \leq F_r^{\max} \\ &G \geq 0 \\ &C \geq 0 \\ &\theta\ is\ unrestricted \end{aligned} \tag{14}$$

Where,

N_B	Number of buses
N_F	Number of distribution feeders
$\hat{B} = (N_B \times N_B)$	Augmented-node susceptance matrix
$b = (N_F \times N_F)$	Distribution feeders susceptance matrix
$\hat{A} = (N_F \times N_B)$	Element-node incidence matrix
$\theta = N_B$	Vector of node voltage angles
$C = N_B$	Vector of bus load curtailments
$D = N_B$	Vector of bus demand
$G^{max} = N_B$	Vector of available generation
$F_f^{max} = N_F$	Vector of forward flow capacities of lines
$F_r^{max} = N_F$	Vector of reverse flow capacities of lines
$G = N_B$	Vector of dispatched generation at buses

In (13) all generation availability and network constrains have been taken into considerations. In addition, in order to get a feasible solution for this standard minimization problem given in (13), it was assumed that one of the bus angles in (14) is considered to be equal to zero.

6.2 Imposing of the Radial Topology Constraint

Distribution systems are reconfigured radially to facilitate the control and coordination of their protective devices. The radial topological structure of the distribution system is taken as a necessary condition during the realization of the presented work. Therefore, this spanning tree structure shall be retained at all times and for all

possible configurations. For this purpose, another constraint, which is developed based on graph theory [10, 13] is introduced into the distribution system reconfiguration problem. Using graph theory and the element-node incidence matrix, this constraint can be imposed as,

$$\det(A) = \begin{cases} \pm 1, \textit{ Radial Toplogy} \\ 0, \textit{ Weakly} - \textit{Meshed} \end{cases} \tag{15}$$

Therefore, for any optimal network configuration that results in presenting at least one loop in the system this configuration is considered to be infeasible and is removed from the search space.

To better understand the spanning tree algorithm developed herein, let us consider the graph shown in Fig. 2 [10, 13]. This graph consists of 4 vertices and 5 edges. The incidence matrix described this graph has one column of each vertex and one row for each edge of the graph. Let us draw our attention to the loop forms by the vertices 1, 2, and 3 and the edges 1, 2, and 3. The matrix describes these vertices and edges can be represented as,

$$A = \begin{bmatrix} -1 & 1 & 0 & 0 \\ 0 & -1 & 1 & 0 \\ -1 & 0 & 1 & 0 \end{bmatrix} \tag{16}$$

The determinant of the incidence matrix given in (16) is obviously equal to zero. This is evident from (16) as the summation of the first two rows yields to the third row. This, in other words, indicates that the matrix described by (16) is linearly dependent. The number of loops in the graph shown below in Fig. 2 is in this case equal to 2.

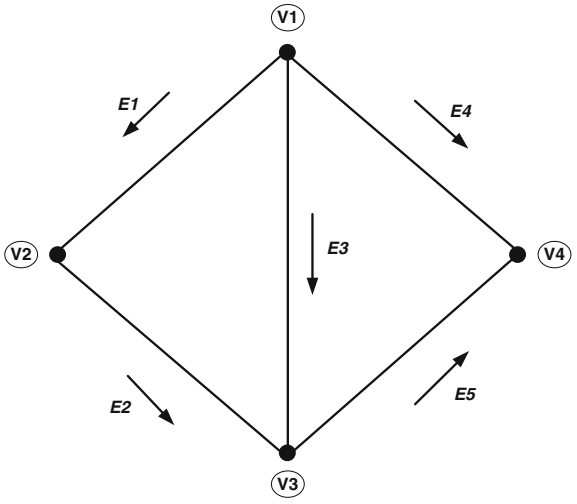

Fig. 2 A graph with $n = 4$ vertices and $m = 5$ edges

6.3 Calculation of the EPNS Reliability Index

The reliability index utilized in this paper is the expected power not supplied EPNS. It is evident that (14) is augmented by a fictitious generator that is equivalent to the required curtailment since the problem aims at minimizing the total load curtailment. In this work, the EPNS is estimated as,

$$EPNS = \sum_{x=1}^{N_c} LOL(x) \times Prob(x)$$

where $LOL(x)$ is the loss of load of state x, which is equivalent to load curtailment of state x, $Prob(x)$ is the probability of state x, and Nc is the number of contingencies.

7 Formulation of the Distribution System Reconfiguration Problem

7.1 Particle Swarm Optimization

Particle swarm optimization is a population-based optimization technique inspired by the social behavior of flocks of birds or schools of fish, which is described in detail in Kennedy and Eberhart [14, 15]. In p Particle swarm optimization, the positions and velocities of the particles are initialized with a population of random feasible solutions and search for optima by updating generations. The advantages of using particle swarm optimization technique in distribution system reconfiguration studies include the following:

1. Particle swarm based optimization only needs few parameters to tune up, unlike some other swarm intelligence such as genetic algorithms, for instance.
2. Distribution systems are equipped with two kinds of switches. These switches are sectionalizing switches and tie-switches. The sectionalizing switches are normally closed and used to connect various distribution feeders segments. On the other hand, the tie-switches are normally opened and used to transfer loads during abnormal and emergency conditions. These switches can be better represented by digital numbers 0 and 1, which are easy to implement using binary particle swarm optimization.
3. More prominently, as will be seen later, the PSO has two main parameters, which are the personal or individual best and the group best. Every particle in the swarm remembers its own personal best and at the same time its global best. Consequently, PSO based methods have more memory capability than some other swarm intelligence based methods such as genetic algorithms, for example.

4. Particle swarm optimization can handle nonlinear and non-differentiable functions efficiently and effectively.
5. Particle swarm optimization could lead to optimal or semi-optimal global solution for wide range of practical problems.

In PSO, the movement of the particles, which represents the potential solutions, is governed by the individual best and the group best. Using these components, a vector that determines the direction and magnitude of each particle in the swarm can therefore be represented as,

$$v_i = v_{i-1} + k_1 \times rand(0,1) \times \left(P_{pbesti} - x_i\right) + k_2 \times rand(0,1) \times \left(P_{gbest} - x_i\right) \tag{17}$$

where, $rand(0,\ 1)$ is a uniformly distributed random number between (0, 1), P_{pbesti} is the particle best position from the probability of a state prospective particle i has ever encountered, P_{gbest} is the group of particles best position from the probability of a state prospective the group has ever encountered. Further, k_1 and are k_2 are acceleration factors. The values of these acceleration factors are given in Table 1. The change in particles positions can be defined by a sigmoid limiting transformation function and a uniformly distributed random number in (0, 1) as following,

$$\mathrm{x_{id}} = \begin{cases} 1, & rand(0,\ 1) < S(v_{id}) \\ 0, & otherwise \end{cases} \tag{18}$$

where $\mathrm{x_{id}}$ is the dth component of particle i, and $S(v_{id})$ is the sigmoid function of the dth's component of particle i, which can be expressed as,

$$S(v_{id}) = \frac{1}{1 + e^{(-v_{id})}} \tag{19}$$

Changes of probabilities are limited by the maximum velocity, which limits the ultimate probability of a bit in particle i to have 0 or 1. Choosing very large or very small values for the maximum velocity can limit the chance of exploring new vectors. Therefore, a careful selection of $v_{\max}$ should be performed. In this work, for a flat start, we have chosen the maximum velocity to be 2.2, which makes $S(v_{id})$ varies between 90 and 10 %.

Table 1 Reliability data

Component name	Failure rate (failure/year)	Repair rate (h)
Transformer	0.05882	144
Bus	0.0045	24
Circuit breaker	0.1	20
Distribution feeder	0.13	5
Sectionalizing Switches	0.2	5

7.2 Binary Particle Swarm Optimization Based an Intelligent Search Method

The main steps of the reliability evaluation and finding the optimal configuration using the BPSO based method are summarized as follows,

1. Initialize the positions and velocities of the particles, respectively. Particles positions are initialized using uniformly distributed random numbers; switches that are in the closed state are represented by 1's and switches that are in the open state are represented by 0's.
2. The length of a particle string equals the number of system switches. One of the particles is chosen to represent the original configuration of the system, that is, all tie-switches are in open states.
3. Check if there are identical particles. If so, discard the identical ones and save the rest of the particles in a temporary array vector by converting the binary numbers to decimal numbers.
4. Check if there are particles already exist in the database, if so, set load curtailments of the existing particles to the system peak load to decrease the chance of visiting these configurations again. Then, save the rest in the database and go to the next step.
5. Check the radiality condition for each particle, if the radiality condition is met, go to next step, otherwise set load curtailments of the particles that represent invalid configuration to the system peak load to decrease the chance of visiting these configurations again.
6. Set system parameters and update the status of the system components (sectionalizing, tie-switches, transformers, distribution feeders, circuit breakers, etc.), for every particle.
7. Perform reliability evaluation for each particle by solving the linear programming optimization problem for every system state to calculate the expected load curtailments for each particle.
8. Determine and update personal best and global best configuration based on minimum load curtailments.
9. Check for convergence. If the stopping criterion is met, stop; otherwise go to next step. The stopping criteria followed here is that after little iteration, if no new better configurations were discovered, terminate the algorithm.
10. Update particles velocities and update particles positions using and go to step 3.

The flowchart depicted in Fig. 3 shows the detailed solution procedures.

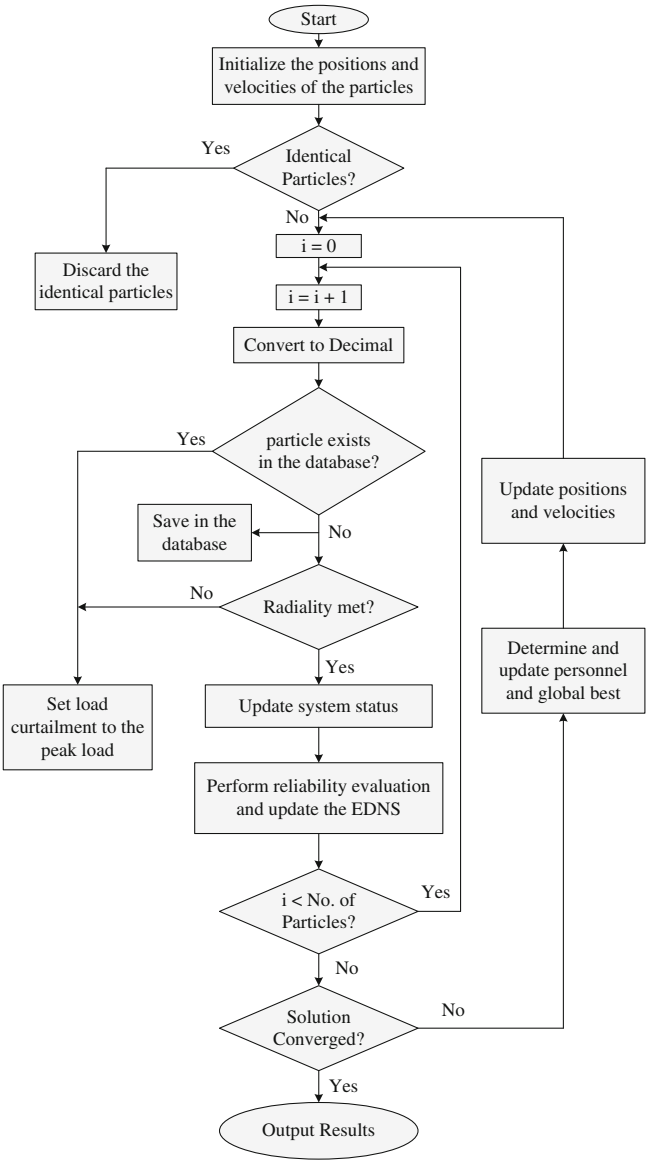

Fig. 3 Flowchart of the proposed method

8 Demonstration and Discussion

This section provides numerous case studies to validate the effectiveness of the proposed method of optimal distribution system reconfiguration for reliability improvement. In addition, this section presents and thoroughly discusses the results.

8.1 The 33 Bus Radial Distribution System Test Case

The first distribution system used in this work is a modified 33 bus radial distribution system. The 33 bus distribution system is a 12.66 kV system, which is widely used as an example in solving the distribution system reconfiguration problem [2]. The single-line diagram of the 33 bus system is depicted in Fig. 4. The total real and reactive power loads on the system are 3,715 KW and 2,300 KVAR,

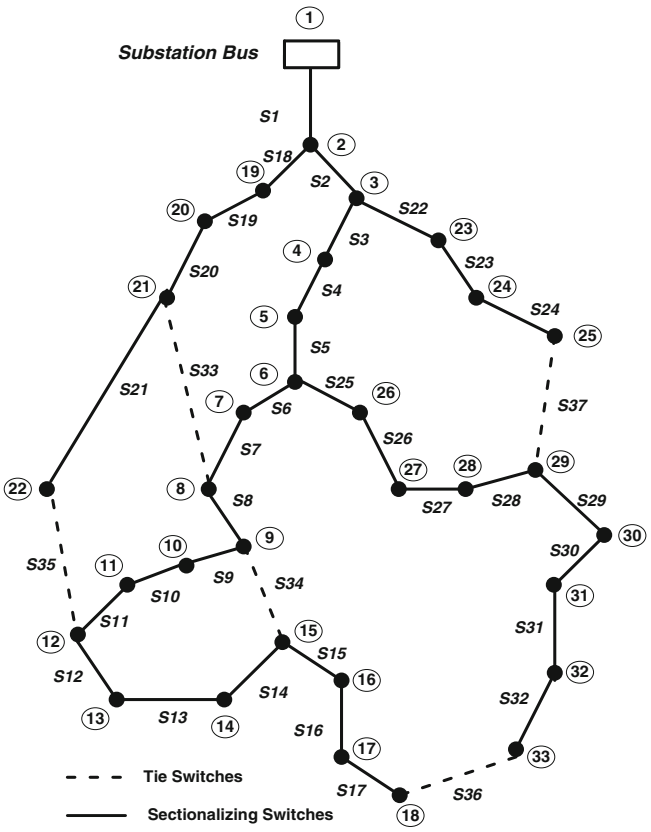

Fig. 4 33 bus distribution system

Table 2 Parameters of the proposed BPSO search method

Parameter	Value
Number of particles	50
Acceleration constant k_1	2
Acceleration constant k_2	2
Maximum number of iterations	1,500

Table 3 Reliability results of the 33 bus system-case study I

Loading conditions	Network status	Opened switches	EPNS (kW/Year)
Peak load	Initial topology	S33, S34, S35, S36, S37	10.01
	Final topology	S6, S10, S13, S27, S32	8.49

respectively. Load data and line data of the 33 bus radial distribution system are given in the appendix. The base values are chosen to be 12.66 kV and 100 KVA. As shown in Fig. 4, this system consists of 33 buses, 32 branches, 3 laterals, and 5 tie lines. In addition, the 33 bus system has a distribution transformer, which is connected to the substation bus. For the initial configuration, the normally opened switches (tie-lines) are {S33, S34, S35, S36, S37}, which are represented by dotted lines. The normally closed switches are denoted as S1–S32 and are represented by solid lines.

The reliability data used in this work are acquired from Amanulla et al. [1], and are given in Table 1. The reliability index used in this paper is the EPNS. The parameters of the BPSO algorithm are given in Table 2. Several case studies have been conducted on the 33 bus distribution system shown in Fig. 4. We have also considered one case scenario for the 33 bus system in the presence of distributed generation units. The results of the different case scenario are presented in Table 3 through Table 5.

8.1.1 Case Study I

In this case study the failure rates of all distribution system components such as transformer; circuit breaker, etc. are considered. Further, it is assumed that every distribution line has a sectionalizing switch. The optimal set of the sectionalizing and tie-switches that yield minimum load curtailment were {S6, S10, S13, S27, S32}.

The number of searched configuration for this case study was 4,857. However the number of the feasible configurations was 110. For comparison purposes, the proposed method of distribution system reconfiguration is first applied on the initial configuration shown in Fig. 4. The results of this case study are summarized below in Table 3.

As can be seen from Table 2 the EPNS is reduced from 10.08 kW/year, for the initial configuration to 8.49 kW/year, after reconfiguration. This is about 15.6 % reduction in the expected power not supplied.

Table 4 Reliability results of the 33 bus system-case study III

Loading conditions	Network status	Opened switches	EPNS (kW/Year)
40 % Increase in peak load	Initial topology	S33, S34, S35, S36, S37	15.14
	Final topology	S7, S11, S14, S17, S27	12.94

8.1.2 Case Study II

This case study is similar to case study I except that the failure rates of sectionalizing switches and distribution feeders are also increased by 20 %. The loading conditions have also been increased by 40 %, to show the effect of the failure rates of system components on its reliability.

The optimal set of the sectionalizing and tie-switches that yield minimum load curtailment were {S7, S11, S14, S17, S27}. The number of searched configuration for this case study was 4,904. The number of the feasible configurations for this particular case was 122. The results of this case study are summarized below in Table 4.

As can be seen from Table 3, the EPNS is reduced from 15.14 kW/year for the initial configuration to 12.94 kW/year after reconfiguration. This is almost 14.53 % reduction in the expected power not supplied.

8.1.3 Case Study III

This case study discusses the inclusion of distribution generation on the reliability of the distribution network. In fact, some of today's distribution systems have certain amount of embedded generation or distributed generation. The advantages of distributed generation include total loss reduction, voltage profile improvement, peak load shaving, and reliability and security enhancement. In this case study, we assume that certain amount of power is injected to the system via distributed generation units in order to improve its overall reliability. The distributed generators used here are modeled as constant PQ nodes with negative injections. This assumption concurs with the IEEE standard 1547–2003 (IEEE standard for Interconnecting Distributed Resources with Electric Power Systems 2003) for interconnecting distributed resources with electric power systems, which emphasizes that distributed generators are not recommended to regulate bus voltages, and thereby they should be modeled as PQ nodes not PV nodes. Further, distributed generators operated at unity power factor have been assumed in this work.

In order to accommodate the penetration of the wind turbine generators in the optimization problem, the right-hand side of (14), which represents the power balance equation, is modified to include the real power injections of the distributed generation units.

Table 5 Reliability results of the 33 bus system-case of distribution generation units

Loading conditions	Network status	Opened switches	EPNS (kW/Year)
Peak load	Initial topology	S33, S34, S35, S36, S37	9.86
	Final topology	S6, S10, S13, S26, S36	7.71

It is important to highlight here that we only consider the penetration level of the distributed generation units in this work. The problem of determining the optimal locations and sizes of distributed generation units that minimizes the total load curtailment is not pertinent to the work being presented here. Further, in this case study, we have assumed a penetration level of 10 %, which is equivalent to approximately 370 kW. Therefore, two distributed generation units, each one is rated at 185 kW, are placed at bus 8 and bus 24 of the 33 bus system, respectively.

The optimal set of the sectionalizing and tie-switches that yield minimum load curtailment for this case study were {S6, S10, S13, S26, S36}. The number of searched configuration for this case study was 4,776. The number of the feasible configurations was 111. For comparison purposes, we have placed the same distributed generation units on the initial configuration shown in Fig. 4. The results of this case study are summarized in Table 5.

As can be seen from Table 5, the EPNS is reduced from 9.86 kW/year for the initial configuration to 7.71 kW/year after reconfiguration. This is about 21.8 % reduction in the expected power not supplied. It is interesting to mention here that the present of the distributed generation units has assisted in decreasing the total amount of the curtailed power as can be seen from Table 5.

8.2 The 118 Buses Large-Scale Distribution System Test Case

The proposed framework has been applied to a more complicated and realistic distribution system to validate its feasibility in such conditions. The system under consideration is an 11 kV, 118 buses large-scale radial distribution system [26]. This system consists of 117 branches and has 15 tie-lines. The results of one case scenario performed on this system are presented. The failure rates of distribution feeders are considered in this case. For the initial configuration, the EPNS has been calculated using the proposed method and was found 313 kW/year. The EPNS has been reduced to 211 kW/year after the network has been reconfigured.

9 Discussion and Concluding Remarks

A was discussed earlier, it has been reported in the literature that distribution systems contribute for up to 90 % of overall consumer's reliability problems [5]. Statistics have shown also that the vast majority of consumers' outages and service interruptions have taken place at distribution system level [3, 5]. In addition, most of

nowadays distribution systems are being stressed and operated at heavily loading conditions due to the rapid increase in electricity demand and some other economical and environmental constraints. These verities combined with the complexities of nowadays distribution systems have motivated us to revamp the service of consumers by considering the reliability while reconfiguring the distribution network.

Distribution systems are equipped with two types of switches; sectionalizing and tie-switches. The sectionalizing switches are normally closed and are used to connect various distribution line segments. The tie-switches, on the other hand, are normally opened and can be used to transfer loads from one feeder to another during abnormal and emergency conditions. Feeder reconfiguration is among the several operational tasks, which are performed frequently on distribution systems. Basically, it denotes to the process of changing the topological structure of the distribution network by altering the open/close status of sectionalizing and tie-switches to achieve certain objectives. Of these objectives reliability and security enhancement are of most concern.

This work has proposed a method for reliability maximization of distribution systems through feeder reconfiguration. This method is developed based on a linearized network model in which the current carrying capacities of distribution feeders and real power limits have been accounted for. From practical perspective, distribution systems are reconfigured radially for best control and coordination of their protective devices. We have therefore developed an algorithm based on the graph theory of trees and forests to preserve the radial topology constraints. Since the time and computational effort spent in evaluating reliability indices are of great concern in both planning and operational stages, this paper uses a probabilistic reliability assessment method based on event tree analysis with higher-order contingency approximation. Consequently, the computational burden has been reduced when compared to some other approaches such as Monte Carlo simulation, for instance, which sometimes tends to be computationally demanding even for planning studies.

In addition, we have proposed an intelligent binary particle swarm optimization based search method to seek the possible combinations of sectionalizing and tie-switches that improve system's reliability. We have demonstrated the effectiveness of the proposed method on a 33-bus radial distribution system, which is extensively used as an example in solving the distribution system reconfiguration problem. We have considered the effect of embedded generation in one case scenario. The test results have shown that amount of annual unnerved energy and customer's interruptions can be significantly decreased when reliability constraints are taken into consideration while reconfiguring the distribution network.

This work proposes a method for distribution system reconfiguration with an objective of reliability improvement. The main features of the work presented in this chapter include:

1. The work presented here is developed based on a linearized network model in the form of DC power flow model and linear programming formulation in which current carrying capacities of distribution feeders and real power constraints have been considered.

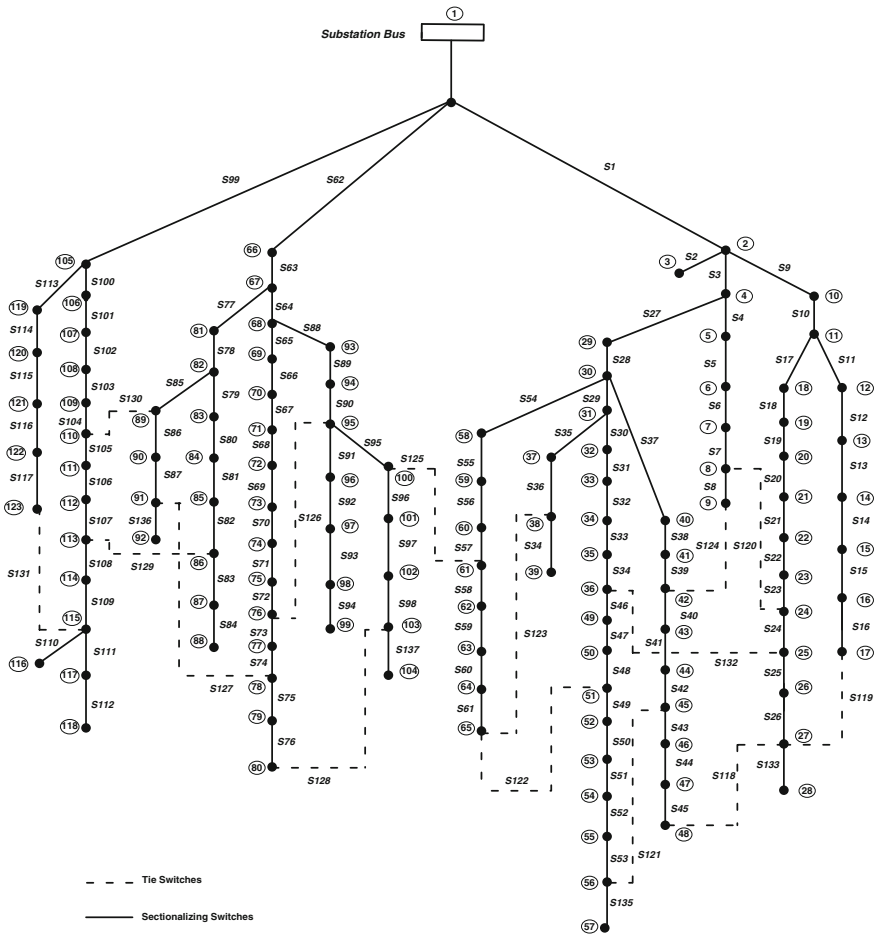

Fig. 5 118 buses distribution system

2. The linearized network model used in this paper is appropriate to use for reliability studies as it is very fast and reliable.
3. The optimal open/close status of the sectionalizing and tie-switches are identified using an intelligent binary particle swarm optimization based search method (BPSO).
4. The probabilistic reliability assessment is conducted using a method based on high probability order approximation.
5. Numerous case studies are demonstrated on a small 33 bus radial distribution system and 118 buses large-scale distribution system, which have both been used as benchmark systems while solving the optimal distribution feeder reconfiguration problem.

6. Distributed generators are constantly used in several of nowadays distribution systems. The effect of distribution generation on distribution system reliability is considered in one case study (Fig. 5).

A.1 10 Appendix

See Tables 6 and 7.

Table 6 Line data of the 33 bus distribution system

From	To	R (Ohms)	X (Ohms)
1	2	0.0922	0.0477
2	3	0.4930	0.2511
3	4	0.3660	0.1864
4	5	0.3811	0.1941
5	6	0.8190	0.7070
6	7	0.1872	0.6188
7	8	1.7114	1.2351
8	9	1.0300	0.7400
9	10	1.0400	0.7400
10	11	0.1966	0.0650
11	12	0.3744	0.1238
12	13	1.4680	1.1550
13	14	0.5416	0.7129
14	15	0.5910	0.5260
15	16	0.7463	0.5450
16	17	1.2890	1.7210
17	18	0.7320	0.5740
2	19	0.1640	0.1565
19	20	1.5042	1.3554
20	21	0.4095	0.4784
21	22	0.7089	0.9373
3	23	0.4512	0.3083
23	24	0.8980	0.7091
24	25	0.8960	0.7011
6	26	0.2030	0.1034
26	27	0.2842	0.1447
27	28	1.0590	0.9337
28	29	0.8042	0.7006
29	30	0.5075	0.2585
30	31	0.9744	0.9630
31	32	0.3105	0.3619
32	33	0.3410	0.5302

Table 7 Load data of the 33 bus distribution system

Node no.	PL (kW)	QL (kVar)
1	0	0
2	100	60
3	90	40
4	120	80
5	60	30
6	60	20
7	200	100
8	200	100
9	60	20
10	60	20
11	45	30
12	60	35
13	60	35
14	120	80
15	60	10
16	60	20
17	60	20
18	90	40
19	90	40
20	90	40
21	90	40
22	90	40
23	90	50
24	420	200
25	420	200
26	60	25
27	60	25
28	60	20
29	120	70
30	200	600
31	150	70
32	210	100
33	60	40

References

1. Amanulla, B., Chakrabarti, S., Singh, S.: Reconfiguration of power distribution systems considering reliability and power loss. IEEE Trans. Power Del. **27**(2), 918–926 (2012)
2. Baran, M., Wu, F.: Network reconfiguration in distribution systems for loss reduction and load balancing. IEEE Trans. Power Del. **4**(2), 1401–1407 (1989)
3. Billinton, R., Allan, R.: Reliability Evaluation of Power Systems, 2nd edn. Plenum, New York (1996)

4. Billinton, R., Kumar, S.: Effect of higher-level independent generator outages in composite-system adequacy evaluation. IEEE Proc. **134**(1), 17–26 (1987)
5. Brown, R.: Electric Power Distribution Reliability. Marcel Dekker Inc., New York City (2002)
6. Chakrabarti, S., Ledwich, G., Ghosh, A.: Reliability driven reconfiguration of rural power distribution systems. In: Proceedings of 3rd International Conference on Power Systems, pp.1–6, (2009)
7. Chen, Q., McCalley, J.: Identifying high risk N-k contingencies for online security assessment. IEEE Trans. Power Syst. **20**(2), 823–834 (2005)
8. Chiang, H., Jean-Jumeau, R.: Optimal network reconfigurations in distribution systems. II. Solution algorithms and numerical results. IEEE Trans. Power Del. **5**(3), 1568–1574 (1990)
9. Civanlar, S., Grainger, J., Yin, H., Lee, S.: Distribution feeder reconfiguration for loss reduction. IEEE Trans. Power Del. **3**(3), 1217–1223 (1988)
10. Diestel, R.: Graph Theory. Elec. Ed. Springer, New York (2000)
11. Falaghi, H., Haghifam, M., Singh, C.: Ant colony optimization based method for placement of sectionalizing switches in distribution networks using a fuzzy multi–objective approach. IEEE Trans. Power Del. **24**(1), 268–276 (2009)
12. Goel, L., Billinton, R.: Determination of reliability worth for distribution system planning. IEEE Trans. Power Del. **9**(3), 1577–1583 (1994)
13. Graph Matrices.: Available online at: http://www.compalg.inf.elte.hu/tony/Oktatas/TDK/FINAL/Chap,.PDF. IEEE Standard for Interconnecting Distributed Resources with Electric Power systems, IEEE Std., 1547–2003, pp. 1–16 (2010)
14. Kennedy, J., Eberhart, R.: Particle swarm optimization. IEEE International Conference on Neural Networks, pp. 1942–1948 (1995)
15. Kennedy, J., Eberhart, R. (1997). A discrete binary version of the particle swarm algorithm. IEEE International Conference on Computational Cybernetics and Simulation, pp. 4104–4108
16. Merlin, A., Back, H.: Search for minimum loss operating spanning tree configuration in an urban power distribution system. In: Proceedings of 5th Power Systems Computing Conference Cambridge, U.K., pp. 1–18, (1975)
17. Mitra, J., Singh, C.: Incorporating the DC load flow model in the decomposition-simulation method of multi-area reliability evaluation. IEEE Trans. on Power Syst. **11**(3), 1245–1254 (1996)
18. Mitra, J.: Application of computational Intelligence in optimal expansion of distribution systems. In: Proceedings of IEEE PES General Meeting, pp. 1–8, (2008)
19. Moradi, V., Firuzabad, M.: Optimal switch placement in distribution systems using trinary particle swarm optimization algorithm. IEEE Trans. Power Del. **23**(1), 271–279 (2008)
20. Overbye, T., Cheng X., Yan S.: A comparison of AC and DC power flow models for LMP calculations. In: Proceedings 37th Annual Hawaii International Conference on Systems Science, pp. 1–9 (2004)
21. Rao, R., Ravindra, K., Satish, K., Narasimham, S.: Power loss minimization in distribution system using network reconfiguration in the presence of distributed generation. IEEE Trans. Power Syst., 1–9 (2012)
22. Shirmohammadi, D., Hong, H.: Reconfiguration of electric distribution networks for resistive line losses reduction. IEEE Trans. Power Del. **4**(2), 671–679 (1989)
23. Skoonpong, A., Sirisumrannukul, S.: Network reconfiguration for reliability worth enhancement in distribution systems by simulated annealing. Proceedings of ECTI-CON, (2008)
24. Vallem, M., Mitra, J.: Siting and sizing of distributed generation for optimal microgrid architecture. In Proceedings of 37th the North American Power Symposium, pp. 611–616 (2005)
25. Ye Bin, Xiu-li, W., Be Zhao-hong, Xi-fan, W.: Distribution network reconfiguration for reliability worth enhancement. IEEE Conf. (1990)
26. Zhang, D., Fu, Z., Zhang, L.: An improved TS algorithm for loss minimum reconfiguration in large-scale distribution systems. Elect. Power Syst. Res. **77**, 685–694 (2007)
27. Zhu, J.: Optimization of Power System Operation. Wiley-IEEE Press (2009)

Machine Learning Aided Efficient Tools for Risk Evaluation and Operational Planning of Multiple Contingencies

Venkat Krishnan

Abstract In power system reliability assessment, the system security limits and adequacy indices depend on the set of contingencies analyzed. Consequently the final solution strategies for short term operational and long term investment planning studies also depend on the set of contingencies considered for planning. Generally, planning is done for the most critical contingency, with the assumption that the solution strategy for the most constraining contingency will also perform well on the contingencies that have lower severity. But this is not always true. In reality, under highly stressed and uncertain nature of power system conditions, the operational rules for the most constraining contingency may not be effective for all other contingencies. In fact some contingencies, which are generally less severe, may have more pronounced ill-effect during certain other operating conditions. Therefore, it is important to perform a comprehensive contingency analysis of many contingencies under several operating conditions (a computationally burdensome task), screen the most important ones among them that may violate the probabilistic reliability criteria, and devise effective solution strategies. Thus, the focus of this chapter is to devise a computationally efficient operational planning strategy against voltage stability phenomena for many critical contingencies. The chapter accomplishes this with the help of a hybrid approach that combines the strength of model-based analytical indicators and data driven techniques to design two important aspects of planning for multiple contingencies, namely: *risk based contingency ranking* and *contingency grouping*. Utilizing realistic probability distributions of operating conditions together with machine learning techniques makes the risk assessment process of multiple contingencies credible and computationally tractable. In order to group the contingencies efficiently for devising a common solution strategy, the chapter introduces a novel graphical index, termed as *progressive entropy* that captures the degree of overlap among post-contingency performances of various contingencies. The objective of the proposed contingency grouping method is to strike a balance between producing simple and accurate operational

V. Krishnan (✉)
Department of Electrical and Computer Engineering, Iowa State University,
Ames, IA 50014, USA
e-mail: vkrish@iastate.edu

A.T. Azar and S. Vaidyanathan (eds.), *Chaos Modeling and Control Systems Design*,
Studies in Computational Intelligence 581, DOI 10.1007/978-3-319-13132-0_12

guidelines for multiple contingencies, while reducing the operational complexity in terms of the total number of guidelines that operators handle.

Keywords Power system operational planning · Contingency risk · Decision trees · Clustering · Progressive entropy

1 Introduction

In power system operational planning studies, system operators use operating guidelines in terms of key system attributes and their corresponding thresholds to assess post-contingency system security of current operating condition [11, 15]. In this context, there is particularly a great interest in using decision trees for their ability to give explicit rules to system operators in terms of critical pre-contingency system attributes [4, 6, 10, 18, 19, 25]. These operating rules help in guiding operators in energy control centers, during conditions for which contingencies may result in violation of reliability criteria. So effectively these operating rules help operators map the pre-contingency scenarios to post-contingency consequences, thereby in a predictive fashion delineating secure operating regions from insecure operating regions in the space of pre-contingency parameters accessible in control centers such as flows, generation levels, load levels etc. Therefore the proximity to a security boundary can be easily monitored, and when an alarm is encountered the operator must take appropriate control action to maneuver into a more secure operating condition. This gives the operators a very simple and easy way to monitor and handle the power system operation, which otherwise is tedious for such a huge non-linear dynamic system.

Generally such decision trees are derived separately for each stability problem (i.e. transient stability, system overload, or voltage stability) based on the database of post-contingency responses over a wide variety of operating conditions [8, 14]. The performance of the tree in predicting post contingency performance is generally measured in terms of classification accuracy for any new operating condition and error rates associated with the classification, namely false alarms (false positives) and hard risks (false negatives).

In such reliability assessment studies, the system security limits depend on the set of contingencies analyzed. Consequently the final solution strategy also depends on the set of contingencies considered in the planning study. Therefore, it is important to perform a thorough contingency analysis of many contingencies, screen the most important ones that may violate reliability criteria, and devise effective solution strategies. In this chapter, the following are the central topics that will be discussed: (1) how do we choose the most important set of contingencies that requires planning in a computationally tractable manner?, (2) how do we create operational planning solutions for multiple contingencies with reduced operational complexity faced by system operators? The operational planning problem considered to demonstrate the developed methodologies in this chapter is voltage instability.

2 Motivation, Related Work, and Objectives

(1) *Risk-based contingency ranking*: Let us begin to answer the first question raised in the introduction section, i.e. how do we choose the most important set of contingencies that requires planning in a computationally tractable manner?

In order to reduce the computational burden of contingency analysis, contingency ranking methods are typically used in the power system reliability assessment. They help in fast screening of the most critical set of contingencies for thorough analysis and planning. While there are many deterministic ranking methods that considers the severity of contingencies [3, 9, 17]; under the current highly stochastic nature of the power system, a contingency ranking method which does not consider the probability of contingencies would lead to misleading operational solutions against real time conditions. For instance, there could be a contingency which has a very severe impact on the system performance, but is highly unlikely to occur. In that case such contingencies may be discounted in the overall planning process, or could be considered separately as a special case. Otherwise this one contingency which is very rare, if considered with all the other contingencies in the planning process, may give forth to very expensive solution strategy under normal operating situations. On the other hand, a contingency which may have a moderate severity on the system performance, but is highly probable, may not be neglected in the planning study. So the first part of this chapter develops a *risk based contingency ranking process* that would help in screening the top contingencies, which could lead to voltage collapse. The risk index of a contingency is estimated as the product its severity over various operating conditions and its probability of occurrence.

Most of the prominent risk based contingency ranking methods proposed in the open literature [12, 24] has a common idea in estimating the risk, i.e. of performing contingency simulations over a wide range of operating conditions, and compute a severity function based upon the post-contingency response database. Then in conjunction with the probability of the contingency, risk is estimated. The same procedure is followed for every other contingency in the selected list, and finally ranked. But the methods developed so far have not considered the actual probabilistic distribution of the operating conditions from which the sampling is done, which may be multivariate and non-parametric in reality. The studies so far have also not addressed the huge computational cost incurred in estimating the risk of multiple contingencies.

So in this chapter, a risk-based contingency ranking method is proposed that estimates contingency risk for many contingencies over a wide range of operating conditions sampled from multivariate non-parametric probability distribution. The proposed method is efficient compared to the existing methods in the following way, i.e. it has the *ability to get realistic risk indices for multiple contingencies at a very highly reduced computational cost*. The risk indices are realistic because of considering the realistic nature of probability distribution of operating parameters.

At the same time, even after accounting for the multivariate nature of operating condition distribution, the risk estimation process is faster as the computation of risk estimation is performed using linear sensitivity information and machine learning methods.

(2) *Contingency grouping for devising operational plans*: Now, let us begin to answer the second question raised in the introduction section, i.e. how do we create operational planning solutions for multiple contingencies with reduced operational complexity faced by system operators?

Typically either a global decision tree or separate trees for all the contingencies are constructed for performing security assessment. Separate tree for a contingency can be constructed using the post-contingency simulation results of that particular contingency as the training database. Usually, the separate decision tree for a contingency gives the best performance; with the disadvantage of burdening the system operators, who will have to deal with complex situation of interpreting and applying too many rules. On the other hand, a global decision tree for many contingencies could be derived from a training database that is formed by combining the post-contingency simulation results of all the contingencies. But such a global decision tree can never outperform the separate trees for every contingency [20]. Moreover, there is also the danger of reducing the operating rule's performance under the most constraining and likely contingency, when we combine all the contingencies' training databases together. One could also form a global decision tree by using only the training database of the most constraining contingency, with the assumption that the operational rule in this case will also perform well on the other contingencies that have lower severity. But this may not be always true, under the current highly uncertain nature of power system.

Considering all the above pros. and cons., this chapter proposes a concept of contingency grouping-based decision trees that designs a decision process striking a balance between producing simple and well performing trees, as well as reducing the number of trees required for multiple contingencies.

The idea of grouping components based on specific performance criteria or geographical proximity is already prevalent in the power system. Typically it is done to reduce computational cost in system reliability studies, in pattern recognition or knowledge discovery studies, and also to obtain valuable guidance in the decision making process. For instance, generators are grouped based on their slow-coherency performance which gives valuable information for controlled islanding to prevent blackout [23]. Generators are grouped based on angle gap criteria for fast contingency screening [16]. Unsupervised learning methods are used to group contingencies based on their effect on bus voltages [7], which is to be used by Neural Networks to predict post-contingency bus voltages under many contingencies. Such grouping concepts are also used for designing defense systems, such as UFLS schemes [21]. This chapter proposes a contingency grouping method based on a newly developed graphical index, *progressive entropy*, in order to obtain efficient decision trees for multiple contingencies. This grouping index is developed

specifically for decision trees considering the technicalities involved in the tree induction process from a training set.

The remaining parts of this chapter are organized as follows. Section 3 presents the proposed method for risk assessment of contingencies, and Sect. 4 presents the concept of contingency grouping and operational planning framework for multiple contingencies. Section 5 presents the numerical simulation results by illustration the developed concepts on French Extra High Voltage (EHV) system for a voltage stability study. Section 6 presents conclusions and future research directions of the work presented in this chapter.

3 Risk Based Contingency Ranking

This section explains the proposed risk based contingency ranking method, beginning with a mathematical definition of contingency risk for voltage collapse in Sect. 3.1. Section 3.2 explains how linear sensitivities computed for multiple stress directions and machine learning methods will be used in conjunction to render the risk estimation methodology faster and realistic.

3.1 Voltage Collapse Risk of a Contingency: Definition

A simple expression for computing risk of a contingency over many probable operating conditions is shown in Eq. (1).

$$\text{Risk}(\text{C}_i) = \text{P}(\text{C}_i) \sum_j \text{P}(\text{X}_j|\text{C}_i) \times \text{Sev}(\text{X}_j|\text{C}_i)) \tag{1}$$

where,

- $P(C_i)$ is the probability of the ith contingency C_i. Assuming that this probability is determined only by the failure rate of the component that causes that contingency, it will be the same for all operating conditions.
- X_j is the jth possible operating condition, and $P(X_j|C_i)$ is the probability of the operating condition given the contingency.
- $Sev(X_{j,}|C_i)$ quantifies the severity of the jth possible operating condition in terms of voltage stability criteria, when subjected to ith contingency.
- $\Sigma P(X_j|C_i)$ $Sev(X_{j,}|C_i)$ quantifies the severity of a contingency considering its influence over all the sampled operating conditions, X_j.

Typically, Poisson distribution is used to describe the occurrence of an event in a particular time interval. So given an occurrence rate λ of a contingency in a certain time interval, the probability of that contingency happening at least once in that time interval is given by Eq. (2).

$$\mathrm{P}(C_i) = \sum_{x=1}^{\infty} P(x) = 1 - P(x=0) = 1 - e^{-\lambda_i} \tag{2}$$

where,

- λ is the mean number of events during a given unit of time
- x is the number of occurrence

The term $P(X_j|C_i)$ in Eq. (1) can be substituted by the probability of performance index subject to a contingency, $P(PI|C_i)$ [24]. So for a voltage instability problem, probability distributions of performance indices such as maximum loadability ($P(L_m|C_i)$) or voltage stability margin ($P(M|C_i)$) can be used. Voltage stability margin (M) is defined as,

$$M = L_m - \textit{System base load} \tag{3}$$

So, for voltage instability problem Eq. (1) becomes,

$$\mathrm{Risk}(\mathrm{C}_i) = \mathrm{P}(\mathrm{C}_i) \sum_j \mathrm{P}(M_j|\mathrm{C}_i) \times \mathrm{Sev}(M_j, \mathrm{C}_i)) \tag{4}$$

The severity function for an operating condition in Eq. (4) is defined by discrete or continuous function. Typically, if post-contingency margin is non-positive for a particular operating condition, then a voltage collapse will occur. So irrespective of the magnitude of non-positive stability margin, the consequence of voltage collapse is assumed to be very severe and generally unacceptable under any condition. So the severity function of an operating condition for voltage collapse is defined as discrete function in Eq. (5).

$$\mathrm{Sev}(\mathrm{M}_j|\mathrm{C}_i)) = \begin{cases} 1, & \textit{if} \quad M_j \leq 0 \\ 0 & \textit{if} \quad M_j > 0 \end{cases} \tag{5}$$

Since the discrete severity function is like an indicator function for collapse, I ($M \leq 0$), the severity function for a particular contingency becomes a probability term, which is referred to as the probability of collapse subject to contingency C_i. It is expressed as,

$$\begin{aligned} \sum_j \mathrm{P}(M_j|\mathrm{C}_i) \times \mathrm{Sev}(M_j|\mathrm{C}_i)) &= \sum_j \mathrm{P}(M_j|\mathrm{C}_i) \times \mathrm{I}(M_j \leq 0|\mathrm{C}_i)) \\ &= P(M \leq 0|\mathrm{C}_i), \vee X_j\textit{'s} \end{aligned} \tag{6}$$

Therefore, for the given discrete severity function, risk in Eq. (4) is rewritten as,

$$\mathrm{Risk}(\mathrm{C}_i) = \mathrm{P}(\mathrm{C}_i) * \mathrm{P}(M \leq 0) \tag{7}$$

So, to estimate risk of a contingency over a wide variety of operating conditions, we must estimate probability of collapse, i.e. $P(M \leq 0)$ in Eq. (7). This is the bottleneck in contingency risk estimation methods. Typically it is done by contingency simulations over various operating conditions produced by Monte Carlo sampling, as in the case of the work by Hsiao et al. [12] that samples many operating conditions in the multivariate parameter space defined by border transactions and system loading conditions. But this is very time consuming, especially if it is to be repeated for several contingencies for ranking purposes. Wan et al. [24] in their effort to estimate risk of an operating condition with respect to voltage collapse proposed utilizing linear sensitivity measures to estimate the maximum system loadability, which could drastically reduce the computational burden for estimating probability of collapse term. But it assumes the loading conditions to follow a multivariate normal distribution, which is usually not the case in reality. Furthermore, it computes linear sensitivities for only one stress direction (load increase direction), while in reality the multivariate loading distribution will have many stress directions.

This chapter proposes a contingency risk estimation method that considers various stress directions in multivariate load distribution, while utilizing the ability of linear sensitivity measures to reduce the computational burden. Latin Hypercube Sampling (LHS) method is used to sample various stress directions in the multivariate load parameter state space, and a machine-learning based method is used to account for the influence of non-parametric nature of multivariate load distribution on risk estimates.

3.2 Contingency Risk Estimation Based on Machine-Learning

Let us consider the uncertainty in operating conditions is represented by system loading conditions. The probabilistic nature of system loading conditions is expressed in terms of real power of individual loads, x_i, that forms a 'n' dimensional operational parameter state space $X = [x_1 \ldots x_n]^T$.

By performing a continuation power flow (CPF) study on an operating condition along a particular stress direction, the maximum loadability (μ_{Lm}) and the margin sensitivities (S_y^p) with respect to real and reactive power injections are obtained. The voltage stability margin (performance measure) is then computed as,

$$M = Lm - \sum_{i=1}^{n} x_i \tag{8}$$

where $\sum_{i=1}^{n} x_i$ is the total system load X_{Total} for that operating condition.

It is to be noted here that all the operating conditions sampled from multivariate distribution will not fall in the same stress direction. Hence before using Eq. (8) to estimate the post-contingency performance, we need to compute the maximum loadability for each of the operating condition by performing CPF along its load stress direction. This is very time consuming, and not affordable. Hence the computational burden is reduced by effectively using the linear sensitivity information (S_y^p) obtained as a by-product of the CPF study done for a particular stress direction. The sensitivity information gives the sensitivity of the voltage stability margin with respect to varying parameters such as real and reactive power injections, along the corresponding stress direction. Equation (9) estimates loadability for a new operating condition based on the μ_{Lm} and S_y^p estimated for the mean operating condition.

$$L_m = \mu_{Lm} + S_y^{pT} \cdot (P - \mu_p) \tag{9}$$

where P is the parameter vector that defines operating condition state space. For each scenario, the parameter vector provides individual real power and reactive power load at every nodes, as given by Eq. (10). μ_p is the mean parameter vector associated with the mean operating condition for which sensitivity information has been found out.

$$P = [X \quad X \quad *r_{ap}]^T \tag{10}$$

where r_{qp} is a diagonal matrix with Q/P ratio at every load node, and $X *r_{qp}$ is the reactive power load at every node with a constant power factor. Therefore, from (8) and (9) we have voltage stability margin for any new operating condition as,

$$M = \mu_{Lm} + S_y^{pT} \cdot (P - \mu_p) - \sum_{i=1}^{n} x_i \tag{11}$$

However, here is a catch. The estimated sensitivities are valid only for a particular stress direction, and hence Eq. (11) will give realistic estimates only for those operating conditions that have similar stress direction as the condition on which CPF was done and sensitivities were computed. Therefore the fact that operating conditions can be grouped into many clusters based on the proximity of their stress directions is utilized here to reduce the computation and make effective use of linear sensitivities to estimate voltage stability margin. This is achieved through machine learning technique, as explained below.

3.2.1 Machine Learning to Advance Performance Measure Estimation

Figure 1 presents the machine learning based risk index estimation method where linear sensitivities computed for few operating conditions are used to estimate the post-contingency performance measure under many other randomly sampled

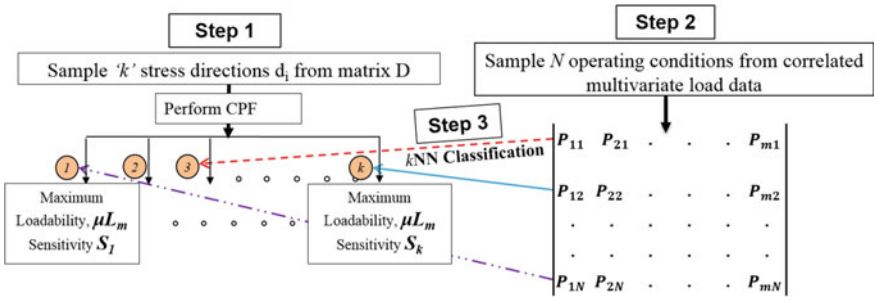

Fig. 1 Mapping operating conditions to stress directions using *k*NN: contingency severity estimation for non-parametric distribution

operating conditions. A particular computed sensitivity is associated with a particular new operating condition based on its intrinsic load stress factors (i.e. individual loads' proportions with respect to total system load) using *k*NN classification (*k* nearest neighbor). The steps are as follows:

1. So the first task is to sample *k* representative stress directions from the historical data, for which the maximum loadability, μ_{Lm} and linear sensitivities, S_k are computed from *k* CPFs. Next section sheds light on the sampling procedure of *k* stress directions.
2. Several operating conditions are sampled (a big number, say *N*), where each one is mapped to a particular stress direction among the sampled *k* directions using *k*NN classification method. Hence the sensitivity and loadability values corresponding to the mapped stress direction are used to estimate the post-contingency performance measure for the operating condition.
3. Likewise, every operating condition is grouped to a particular stress direction, and accordingly its post-contingency voltage stability margin is estimated using Eq. (11).
4. Finally, the probability of collapse under a contingency C_i is computed using the estimated voltage stability margins for all the sampled operating conditions, as shown by Eq. (12).

$$P(M \leq 0)_{C_i} = \frac{\sum_{j=1}^{N} I(M_j \leq 0)_{C_i}}{N} \tag{12}$$

Finally, according to Eq. (7), the product of probability of contingency and severity of contingency (probability of collapse) will give the risk of contingency. This is repeated for every selected contingency, their risks are computed and eventually ranked for screening and subsequent operational planning.

3.2.2 Sampling Multiple Stress Directions Using Latin Hypercube Method

In a realistic system, the loads can undergo stresses in many directions, and along each direction the voltage stability margin and its sensitivities under a contingency varies. Therefore, in order to get realistic assessment of contingency severity, previous section proposed methods that account for the various possible stress directions. The variability in stress directions is captured from the historical distribution of loading conditions, which is multivariate in nature with interdependencies among various individual loads. Typically studies assume this multivariate distribution to be normal, thereby rendering computational part easier using standard techniques. But in reality, hardly do we find normally distributed loads, and many times the distribution does not even fit any standard parametric distributions, thereby making computation challenging. Hence, this issue is addressed to demonstrate how it is important to consider realistic distributions for obtaining credible estimations of severity.

Using the historical load data, a stress factor matrix is formed as shown in Fig. 2, which captures the multivariate load distribution. The required number of stress directions is sampled by sampling random vectors from this multivariate distribution of load stress factors.

If the load distribution is multivariate normal, there are standard sampling techniques to sample normal random vectors [5]. Nevertheless, Latin Hypercube Sampling (LHS) works well for all kinds of distributions, i.e. whether standard or empirical distributions. For sampling k stress directions, LHS is employed to sample k random vectors of stress factors. LHS of multivariate distribution is performed by dividing every variable into k equiprobable intervals, and sampling once from each interval of the variable. Then these samples are paired randomly to form k random vectors from the multivariate distribution. The pairing in LHS is done in such a way so that the rank correlation [27] among the variables are preserved, and hence the dependence structure of the multivariate distribution is captured.

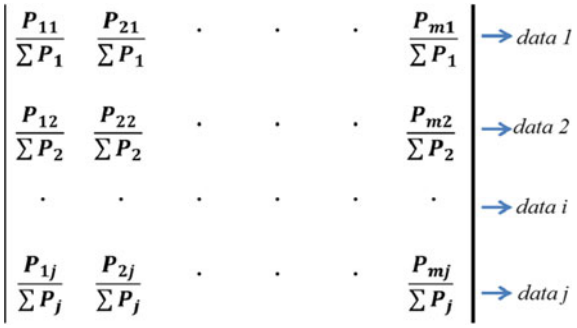

Fig. 2 Stress direction defined by stress factor matrix

4 Contingency Grouping

This section explains the proposed progressive entropy based contingency grouping concept. This is developed to derive a smaller set of rules with good performance for all the screened contingencies. Section 4.1 introduces the new concept, namely progressive entropy and Sect. 4.2 discusses its application to group contingencies.

4.1 Progressive Entropy

Entropy, an information theoretic measure for quantifying information content in a distribution, is also usually used to quantify information content in a database [13, 22]. It is defined as given in [13],

$$Entropy(S) = \sum_{i=1}^{c} -p_i \log_2 p_i \tag{13}$$

where,

- S is training data sampled according to probability distribution,
- c is the number of classes, and
- p_i is the proportion of S classified as class i.

According to (13), the more the non-homogeneity or impurity in class attribute of a database, the more is the entropy. This database variability measure plays an important role in decision tree induction process. Decision tree induction process involves selecting the best attribute at every level, which can effectively partition the data into respective classes. At every level of the tree, the attributes are ranked for their ability to divide the database into homogenous classes by a measure known as information gain [26], which is derived from entropy measure. The information gained from an attribute of the training data is the amount of reduction in database entropy that is possible when branching the tree at certain value of that attribute, i.e. leads to division of training data into homogeneous class values. The higher the information gain for an attribute, better is the attribute for decision tree development.

Therefore, in order to develop common decision trees for a group of contingencies, in this chapter, a new index called progressive entropy is proposed. Figure 3 shows a typical manner in which the post-contingency performance measure for a particular contingency is progressing along the operating parameter state space, i.e. system load in this case. This in effect is also the class boundary progression of training database, which is obtained by sampling these post-contingency system responses. The figure also shows the entropy measure that is derived from incremental databases as we progress along the various values of load attribute. Hence the name *progressive entropy* is coined for this index, which can be used to assess the manner in which the database entropy measure behaves over an

attribute's range under the influence of various contingencies. The idea is, if the entropy measure of post-contingency databases of different contingencies behave similarly over the state space of important attributes, then the information gain which is the principle measure to induce a decision tree also behaves similarly over that range of the attribute. Hence the more similar the progressive entropy curves are for certain contingencies, the higher is the possibility to derive a common decision tree for those contingencies. This is the driving principle behind the newly proposed operational planning method for multiple contingencies based on progressive entropy, which groups many contingencies for deriving a common decision tree.

The progressive entropy curve is computed as follows:

Step 1: Sample many operating conditions from the multivariate parameter distribution

Step 2: Perform simulations, ascertain the post-contingency performance measures, and label them, i.e. acceptable or unacceptable. The computational cost involved at this step can be tremendously saved by employing linear sensitivities of performance measure and machine learning method, as explained in Sect. 3.2.

Step 3: Stack the performance measure variability along a system variable distribution, as shown in Fig. 3.

Step 4: Compute the entropy for every subsets of database S_j as we progress along the distribution of the parameter, as shown in (14); and plot the progressive entropy along the variable, as shown in Fig. 3.

$$\begin{aligned} Progressive\,Entropy &= Entropy(S_j), j = 1, 2, \ldots N \\ &= \sum_{i=1}^{c_j} -p_{ij} \log_2 p_{ij} \end{aligned} \tag{14}$$

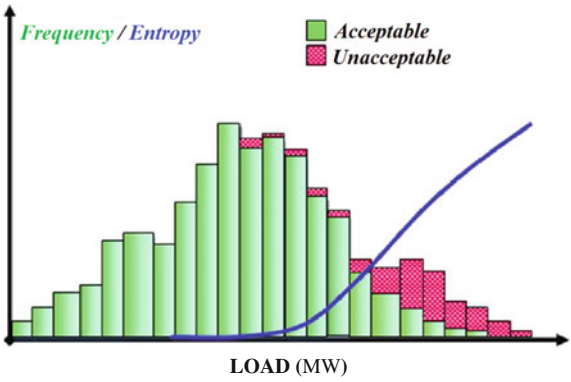

Fig. 3 Performance measure progression and progressive entropy

where,

- S_j is the progressive database, made up of sub-set operating conditions, x_j's, taken in the direction towards unacceptable domain from acceptable domain. For variables such as total system load the unacceptable operating conditions gradually proliferate in ascending direction, and for variables such as reactive reserve the unacceptable operating conditions gradually proliferate in descending direction.
- N is the total number of operating conditions and consequently the total number of progressive databases,
- c_j is the number of classes in the database S_j, and
- p_{ij} is the proportion of S_j classified as class i.

Since the progressive entropy curves capture the similarities among various contingency's influence on operating conditions, they capture the degree of overlap among the class boundary regions of various contingency's training database. Therefore the more similar is the progression of class boundary regions of two contingencies, the more is the possibility to produce a common decision tree for them with good accuracy.

4.2 Contingency Grouping and Training Database Generation

This section explains the proposed contingency grouping method using progressive entropy curves. Figure 4 shows the typical progressive entropy curves for 4 different contingencies C_1, C_2, C_3 and C_4, with C_1 imposing the highest risk. Risk imposed by a contingency is defined as the product of its probability and the measure of its severity, which is a function of its consequence over many operating conditions, as defined in Sect. 3.1. The visualization of these curves in Fig. 4 shows the progressive influence of contingencies over operating conditions. Visual measures to ascertain the degree of closeness among these curves, i.e. whether intertwined or closely enveloping, will aid in recommending contingency groups. These visual measures may also be corroborated with curve-matching techniques such as Hausdorff Distance and Fréchet Distance [2] measures that mathematically computes the similarity between two curves.

For instance, in Fig. 4 the progressive entropy curves for C_1 and C_2 along load variable closely intertwine, indicating they have similar influence on the operating conditions along the load attribute values. So they can be grouped together as Group1 to generate a common decision tree and operating rule. We propose two ways of generating a training database for the common tree.

1. **High Risk Database**: The training database is generated from post-contingency responses of sampled operating conditions under high risk contingency in the group.

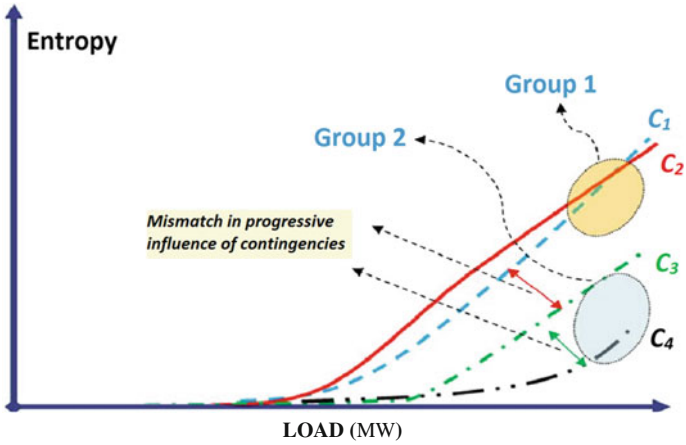

Fig. 4 Contingency grouping based on progressive entropy

2. **Proportional Risk Database**: The training database is generated from post-contingency responses of sampled operating conditions under each contingency in the group, in proportion to their risk.

On further analysis of Fig. 4, it is observed that Group1 contingencies envelope C_3 and C_4. But they are not as close as C_1 and C_2, implying that the progressive influence of the Group1 contingencies over the operating conditions is more severe than the contingencies C_3 and C_4. Therefore in this case, a common rule for all the four contingencies may perform poorly. Similarly, C_3 envelopes C_4, and the operator may choose to group C_3 and C_4 together as Group 2, considering the fact that they both are of lower severity. In cases, where visual measures do not prove conclusive, analytical curve-matching measures may be useful.

Once the contingency groups have been formed, two training databases, namely high risk and proportional risk databases, could be generated for each group and their corresponding rules are obtained. Each group's final common rule is selected based on rule's performance validation over all the contingencies in the group using an independent testing data set.

5 Case Study

The proposed contingency severity estimation and grouping methods are applied in deriving operational rules for multiple contingencies in SEO region (*Système Eléctrique Ouest*, West France, Brittany) of the French EHV system, which is a voltage security-limited region during winter. This region contains 5,331 buses with 432 generators supplying about 83.8 GW.

Table 1 Contingency severity estimates

Contingency	Severity	
	Proposed method	PSS
C2	0.1682	0.1702
C6	0.7713	0.7446
C7	0.1600	0.1466

5.1 Risk Based Contingency Ranking

Seven contingencies (*C1 to C7*) in and around the SEO region are selected for this study. Contingencies *C1* is a nuclear unit outage within SEO region. Contingencies *C2,* C*3* and *C7* are bus bar faults. Contingencies *C4*, *C5*, and *C6* are critical generator outages outside SEO region, in the western belt of French network, with *C4* and *C5* being N − 1 outages, and *C6* being N − 2 outage. These contingencies are usually considered to have severe influence on voltage stability of SEO network during winter under heavy transactions.

The variable part of load within the SEO region of French network is the sampling parameter, which is continuous and multivariate in nature. The various individual loads are mutually correlated, and they do not make up a multivariate normal or any standard distribution. The distribution is multivariate non-parametric. The goal of this study is to estimate the voltage collapse risks of the contingencies, for which two different methods are used:

1. *Proposed method*: Consider the realistic non-parametric multivariate distribution which is mutually correlated, and use linear sensitivities along k stress directions in conjunction with kNN classification.
2. *PSS*: Full-fledged power system simulation for every operating condition sampled (heavy computation).

5.1.1 Numerical Results

Table 1 shows the results for three contingencies, *C2*, *C6* and *C7*, when multiple stress directions are considered for estimating their severity (which is the probability of collapse, i.e. $P(M < 0)$). Fifteen different stress directions ($k = 15$) were sampled from the multivariate state space using LHS. The PSS method involves performing Quasi-steady state (QSS) simulations using ASTRE software.[1] This was done by sampling 975 (N) operating conditions from the non-parametric multivariate load distribution. The sampling was done using LHS method such that it also captured the inter-dependencies or mutual-correlation among various

[1] ASSESS, TROPIC, METRIX software website: http://www.rte-france.com/htm/an/activites/assess.jsp.

Table 2 Risk based contingency ranking

Rank	Contingency	Severity	Probability	Risk
1	C2	0.1682	0.07596	0.01277
2	C5	0.04698	0.2010	0.00944
3	C4	0.04698	0.1928	0.00905
4	C1	0.04698	0.1077	0.00505
5	C6	0.00220	0.7713	0.00170
6	C7	0.00557	0.16	0.00089
7	C3	0.00557	0.0831	0.00046

individual loads. Then the various base cases formed are subject to three contingencies using ASTRE simulation and the post-contingency performances are analyzed. The ASTRE QSS simulation is run for 1,500 s with 10 s step size, and the contingency is applied at 900 s. Scenarios are characterized to be voltage unstable if any of SEO EHV bus voltage falls below 0.8 p.u or the simulation does not converge. Thus, the probability of collapse, and hence the severity is estimated using PSS.

The probability of collapse values estimated by PSS method is 0.1702, 0.7446, and 0.1466 for the three contingencies *C2*, *C6* and *C7* respectively. From Table 1, it is seen that the estimated results from the proposed method closely corroborates with the PSS results, thereby emphasizing that it is essential to take into account the original historical load distribution's characteristics to obtain reliable results.

Table 2 shows probability of all the seven contingencies considered for the study, their estimated severities using the proposed method, and the resultant voltage collapse risk estimates (calculated as per Eq. (7)). Based on their risk, these contingencies are ranked.

Figure 5 shows that the contingencies with high severity measure necessarily doesn't pose high risk. Hence a risk based contingency ranking that also accounts for the probability of contingency occurance will be suitable in identifying the top contingencies accurately. The top contingencies can be screened using a specific cut off value of risk (say, average risk), and can be considered for operational planning study, which will be discussed in the next section.

5.1.2 Computational Benefit

The proposed contingency risk estimation method saves a huge amount of computational requirement. This is because it uses linear sensitivities computed for multiple stress directions, in conjunction with machine learning methods to estimate contingency severity. Table 3 shows the details of computational requirements for seven contingencies involved in this study. The severity estimation for seven contingencies, with fifteen stress directions sampled for the study, required $15 \times 7 = 105$ CPF simulations and linear sensitivity computations to estimate severity of every contingency over 975 different operating conditions (OC), as

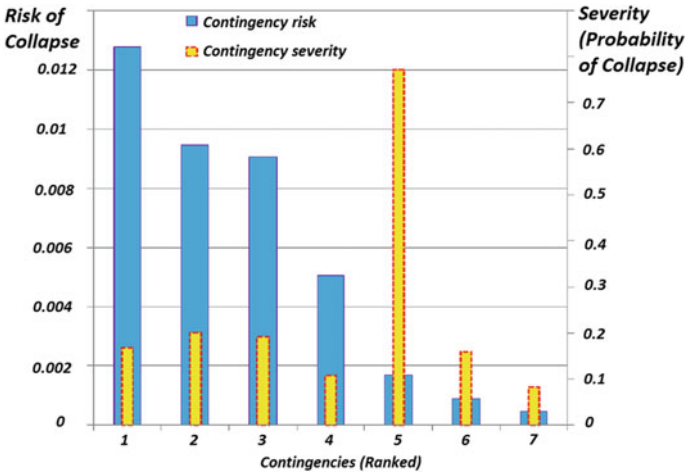

Fig. 5 Contingency severity and risk

Table 3 Computational benefit of proposed contingency risk estimation method

Case	OCs	Total simulations	Maximum speed up
Uncertainty: loads			
PSS	975	6,825	65
Proposed method	975	105	
Uncertainty: loads and SVCs			
PSS (estimation)	3,900	27,300	260
Proposed method (estimation)	3,900	105	

shown in Table 3. The conventional PSS method would require a huge computation of about 975 × 7 = 6,825 CPF computations to compute the stability margin or 6,825 ASTRE dynamic simulations to compute dynamic performance. So the computational requirement of proposed method doesn't depend on the number of operating conditions sampled, but only on the number of stress directions sampled. If a very few stress directions has the ability to effectively characterize the entire load state space, then the computational cost to estimate contingency severity is highly reduced, as shown in Table 3. The number of stress directions sampled could be increased further for increased accuracy, and still the computational requirement would be very less compared to the full-fledged conventional contingency simulations.

The proposed method's ability to reduce computational cost drastically for contingency ranking is even strongly demonstrated when we consider another sampling parameter, such as a discrete parameter like SVC unavailability or generator group unavailability etc., in the stage of Monte Carlo sampling of basecases. Table 3 shows the estimated computational requirements for severity estimation

using conventional PSS and proposed methods, when the operational state space is comprised of both loading conditions and two Static Var Compensators (SVCs) unavailabilities. There could be four combinations of two SVC states, i.e. both unavailable (00), one of them unavailable (01 and 10) and both available (11). So systematically combining these 4 states with the 975 sampled loading conditions, we could obtain 3,900 base operating conditions. So the conventional contingency severity estimation method will have to perform 3,900 × 7 = 27,300 simulations for 7 contingencies. But the computational requirements of the proposed method based on linear sensitivities and machine learning is still proportional only to the number of stress directions characterizing the load state space. This is because the influence of discrete parameter, i.e. SVC unavailability states is accounted using the linear sensitivities, i.e. the sensitivity of stability margin with respect to reactive power injection at the SVC buses [14].

So the proposed contingency severity and risk estimation method enables reducing the computational requirements tremendously in ranking multiple contingencies with respect to voltage collapse risk.

5.2 Contingency Grouping and Operational Planning

This study considers five of the seven critical contingencies in and around the SEO region investigated in the previous section, namely C1, C2, C3, C5 and C7. The contingency C4 is similar in nature and location to C5, and hence it is left out; and contingency C6 is a low probability high severity event that is combination of C4 and C5. The study assesses the impact of these contingencies on voltage stability of SEO region, and develops operational rules using decision trees.

5.2.1 Decision Tree Process—Training Database

The training database for decision trees for a particular contingency is formed by contingency analysis of operating conditions, which are obtained by Monte Carlo sampling of parameters. The sampling parameters include variable part of total SEO load, SVC unavailability and generator group unavailability in Brittany area. From the 2006-07 historical data of the total SEO load, the loading conditions from winter season (Dec 06–Feb 07) are randomly sampled, keeping the power factor of loads constant, to form many operating conditions. There are two SVCs in SEO region, at Plaine-Haute and Poteau-Rouge. Their unavailabilities are sampled such that they both are available in 1/4th, both are unavailable in 1/4th and at least one of them is available in half of the total sampled operating conditions respectively. The unavailability of three main production units, that include nuclear groups at Civaux, Blayais, and St-Laurent, are sampled such that each of these unavailabilities is represented in 1/4th of the total operating conditions. ASSESS (refer *footnote 1*) is used to specify the above mentioned sampling laws for each of these sampling

parameters, and generate base case operating conditions from their combinations for contingency simulations. The convergence of these base cases to initial stable solutions is verified using TROPIC (refer *footnote 1*).

To obtain the post-contingency responses of a particular contingency, ASTRE [22] quasi-steady state simulation is performed for these sampled operating conditions, wherein the contingency is applied at 900 s and the simulation is terminated at 1,500 s. The statistical analysis software SAS is used to process the post-contingency responses, and label each simulation as acceptable or unacceptable based on magnitude of EHV bus voltage in SEO region and the convergence status of simulation at termination. Finally each instance in the training database is formed using EHV node voltages, SVC outputs and generator group reactive reserves within SEO region sampled at 890 s of every simulation, including its respective post-contingency performance label, which is the target attribute for the decision tree. The decision trees are derived and tested using WEKA software.

So far, this section described the process of creating a training database by sampling various parameters and deriving operational rule using decision tree for a single contingency simulation. The next section describes the proposed process for multiple contingencies, wherein it illustrates how various contingencies considered in this study are grouped based on the progressive entropy curves, and how the training databases are generated to obtain a common decision tree for each group.

5.2.2 Progressive Entropy Based Contingency Grouping

The post-contingency responses from simulations are used to compute the progressive entropy curves as explained in Sect. 4.1. Figure 6 shows the progressive entropy curves for all the selected contingencies for this study along the Brittany total load attribute. Considering the closeness and nature of progression of these curves along the operating conditions under each contingency, the possible contingency groups are shown in Table 4, with indication of high risk contingency within each group.

The Hausdorff distance between the curves corresponding to *C3* and *C2* is 0.1912, while between the curve *C3* and the rest (*C7*, *C5*, *C1*) are 0.5745, 0.6789 and 0.8094 respectively. Also, the Hausdorff distance between the curve *C2* and the rest (*C7*, *C5*, *C1*) respectively are 0.3833, 0.4877, and 0.6182. This corroborates grouping the contingencies *C2* and *C3* together as group 1, and not including the rest. On the other hand, the Hausdorff distance between the curves *C1* and *C5* is 0.1305, and between the curves *C7* and *C1* is 0.1044 respectively, and therefore this measure of curve similarity corroborates grouping of these three contingencies together as group 2.

This grouping promises reduction in the number of operational rules from five to two. Training databases based on high risk and proportional risk criteria are formed for each group, as explained in Sect. 4.2. The best common decision rule for all the contingencies within each group is finally selected by rule validation process using independent test data.

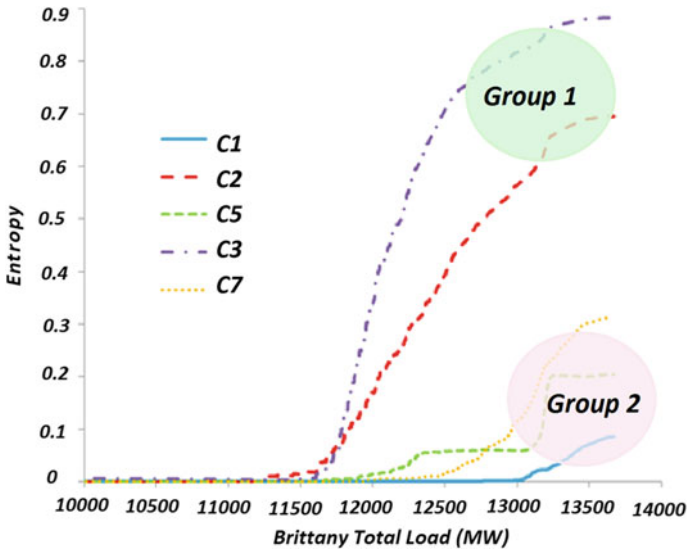

Fig. 6 Progressive entropy based contingency grouping for French network

Table 4 Contingency group & training database recommendations

Group	Contingencies	High risk
1	*C2* and *C3*	*C2*
2	*C7, C5,* and *C1*	*C5*

Figure 7 shows the progressive entropy curves of these contingencies on another influential system attribute, namely Chinon generator group reactive reserve. These curves were obtained from simulation results. The progressive entropy curves for this system attribute corroborates the contingency grouping indicated by the Brittany load attribute in Fig. 6, thereby recommending similar grouping of contingencies. Similar validation of grouping was done using two other system attributes, namely Cordemais bus voltage and total SEO region reactive reserve. This validation and verification of contingency grouping based on all such attributes is significant because these attributes such as system load, reactive reserve in an area, line flows, and generator group reactive reserve are very influential attributes that govern the post-contingency voltage stability performance of the system, and are good candidates for constructing operational rules using decision trees. Therefore a consensus among all these attributes bolsters the grouping conclusions.

The progressive entropy curves can also be estimated using linear sensitivities (as mentioned in Sect. 4.1) of voltage stability margin, a well-known voltage stability performance index [1], with respect to real and reactive power injections at every nodes (as discussed in Sect. 3.2.1). Figure 8 shows comparison of progressive entropy curves obtained by simulation and linear sensitivity based estimation for contingency *C2* along the load variable, which is the sampling parameter. In this

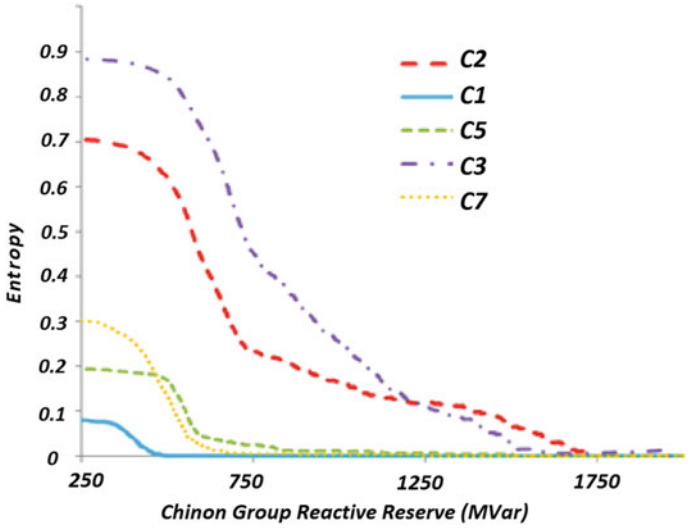

Fig. 7 Progressive entropy curves on Chinon generator group reactive reserve

case, Fig. 8 shows the ability of linear sensitivity based estimation to compute the progressive entropy curve with good approximation, which will ensure achieving computational benefit in computing these curves.

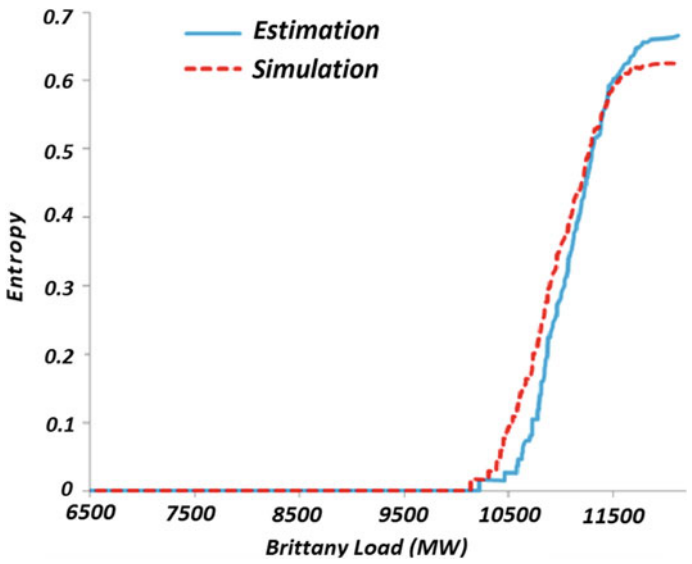

Fig. 8 Estimated versus simulated progressive entropy for contingency *C2*

5.2.3 Operating Rules Validation

The following results present the performances of various operating rules derived from a variety of training databases. The idea is to verify if the training databases recommended by the progressive entropy based contingency grouping performs well when compared with other alternatives or not. The training and test databases are independently formed using the sampling strategy mentioned in Sect. 5.2.1. Every training database is of same size containing about 8,000 operating conditions. Independent test databases are formed for every contingency separately, containing about 4,000 instances. The classification accuracy is defined as the percentage of test instances correctly classified by the tree. False alarm (FA) rate is defined as the proportion of total number of false positives among all unacceptable classifications in the test database, and hard risk (HR) rate is defined as the proportion of total number of false negatives among all acceptable classifications in the test database.

Table 5 presents the performance results of separate decision tree for every contingency, derived based on training database containing its respective post-contingency responses. Rule for each contingency is tested against its respective independent test set. It can be seen that the classification accuracies for every contingency from separate decision trees are very high. But in this case, the system operators will have to deal with five separate rules for five critical contingencies, thereby rendering the whole security assessment process under highly stressed system conditions very strenuous and operationally complicated.

Table 6 shows the performance result of rule from a common decision tree for all contingencies. The common tree is from the training database containing only the *C2* contingency responses, which has the highest risk. This common tree is tested against each contingency's test data, and a marked reduction in performance is observed for other contingencies. For contingency *C3*, hard risks are more, while

Table 5 Separate decision tree for every contingency

S no	Contingency	Accuracy	FA	HR
1	*C2*	94.9783	0.034	0.122
2	*C3*	95.2081	0.039	0.068
3	*C5*	99.3467	0.001	0.203
4	*C1*	99.3723	0.002	0.308
5	*C7*	98.1378	0.008	0.19

Table 6 One common rule based on *C2* contingency responses—high risk

S No	Contingency	Accuracy	FA	HR
1	*C2*	94.9783	0.034	0.122
2	*C5*	82.5067	0.174	0.203
3	*C1*	82.2067	0.18	0
4	*C3*	87.7057	0.011	0.388
5	*C7*	87.2793	0.135	0

for all other contingencies false alarms have increased tremendously. So a common rule based on worst case contingency alone will not be suitable for all the other contingencies.

Table 7 shows the results for a common tree formed by generating a proportional risk training database containing post-contingency responses of all the five contingencies. The rule doesn't perform well for the most constraining contingency *C2*, apart from its poor performance for other contingencies too.

Table 8 shows the results for operating rule performance when contingency *C2* is grouped with other contingencies. Common operating rule is derived for each group from its *proportional risk* database. It is seen that the recommended grouping of *C2* and *C3* contingencies has the best performance, where the rule's performance for *C2* is on par with the highest performance obtained in Table 5 and the rule's performance for *C3* betters the performances in Tables 6 and 7. However, given the fact that the *C3* contingency has lower probability and risk index, the reduction in common rule's performance for *C3* contingency in Table 8 compared to the performance in Table 5 can be traded off considering the prospect of reducing the number of rules. The rule could be further improved by increasing the representation of post-contingency responses of *C3* contingency in the training database.

Figure 9 shows the top five attributes of decision tree under three cases:

- Case-1: Separate tree for contingency *C2* (Table 5).
- Case-2: Separate tree for contingency *C3* (Table 5).
- Case-3: Common tree contingency *C2* and *C3* (Table 8).

The commonality of these top rule attributes in the SEO region of the French grid among each case justifies the grouping of these two contingencies together for security assessment.

Table 9 shows the rule validation results for other contingencies, constituting the Group-2 recommendation made in the Sect. 5.2.2. Along the columns are different

Table 7 One common rule based on all contingency responses—proportional risk

S no	Contingency	Accuracy	FA	HR
1	*C2*	90.6	0.003	0.5
2	*C5*	91.331	0.078	0.375
3	*C1*	90.82	0.09	0.273
4	*C3*	84.85	0	0.532
5	*C7*	96.36	0.026	0.2

Table 8 *C2* contingency grouped with other contingencies

Contingency	Accuracy	
Contingency 1 and 2	*C2*	Contingency 2
C2 and *C3 (Group 1)*	94.86	89.09
C2 and *C5*	92.66	87.07
C2 and *C1*	92.63	86.06

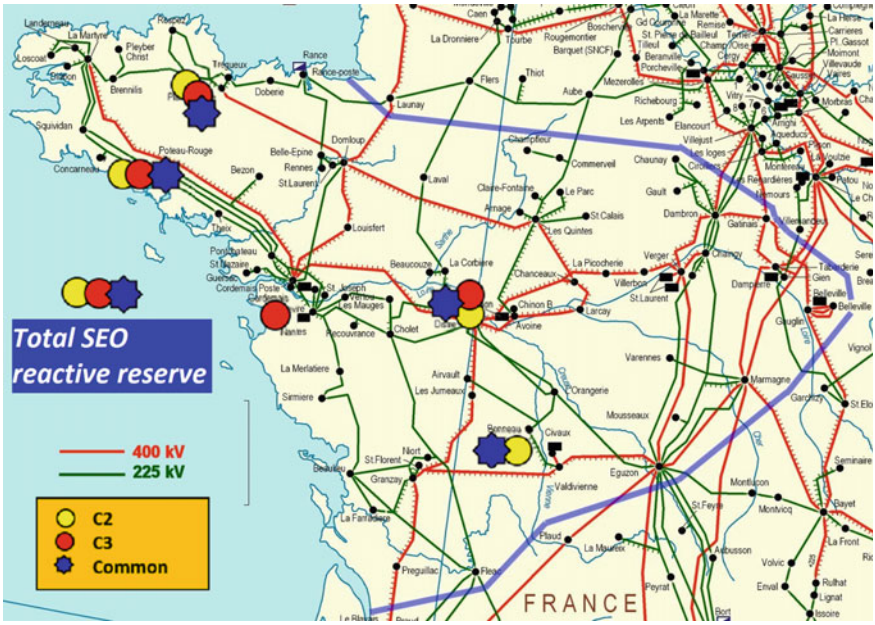

Fig. 9 Top five operating rule attributes for group-1 contingencies

Table 9 Group-2 rule performances from various training databases

Contingency	Training			
	C5	*C7*	*C5* and *C7*	*C5, C7* and *C1*
C5	99.35	92.86	97.67	97.1691
C7	93.93	98.14	94.6	95.1515
C1	96.52	95.44	97.47	98.1169

candidate training databases, starting from a database made of *C5* contingency responses only, then *C7* contingency responses only, then *C5* and *C7* responses together according to proportional risk criteria, and finally *C5*, *C7* and *C1* responses together according to proportional risk criteria.

Among these possible databases, the proposed grouping scheme recommended the first and fourth options. The decision on best operating rule is taken based on the rule's performance on various contingencies within the group, weighed according to the risk levels of each contingency. It can be observed that first database produces a tree that performs best for high risk contingency *C5*, while fourth option produces tree that ensures good performance across all the contingencies, while also performing well for high risk contingency.

It is seen that for both the groups, the proportional risk database based decision trees provide good results for all the contingencies in that group. The performance

can be further enhanced by appropriate feedback process to enrich the training database or meta-learning methods.

Overall, the proposed grouping concept promises:

1. Reduction in operating rules for multiple contingencies.
2. A common rule for each group, which is better than overfitting a global common rule for all the contingencies.
3. Possible computation reduction for generating training databases for multiple contingencies, as lesser number of trees required.

6 Conclusions

In this chapter, a process for performing power system security assessment of multiple contingencies has been described. The system operators require security guidelines to perform operational assessment, which are usually derived from decision trees. In order to do it for multiple contingencies, advancement of two important aspects of planning framework has been proposed and demonstrated in this chapter on French EHV network.

1. ***Risk based contingency ranking***: This chapter proposed a contingency risk estimation method under uncertainties for voltage collapse. The developed method takes into account the realistic nature of multivariate load parameter distribution (i.e. mutual-correlation and non-parametric), which defines the uncertainty in the operating conditions. The LHS method is used to sample various stress directions in the multivariate load parameter state space, which are used to compute the required linear sensitivities of performance measure with respect to changing operating conditions. Then machine learning technique (*k*NN classification) is utilized to produce contingency severity estimation under wide variety of operating conditions at a much reduced computation.
2. ***Contingency grouping and planning***: A novel contingency grouping method is proposed based on newly devised metric called progressive entropy, which is a graphical metric that helps in finding similarities among contingencies based on their consequences on the operating conditions, unlike the conventional methods that match contingencies based on proximity in the grid. This grouping index considering the overlap of class boundary progression of various contingencies is developed specifically for decision trees, considering the technicalities involved in the attribute selection of tree induction process.

The developed concepts were demonstrated on the French network. Seven critical contingencies were selected, and their voltage collapse severity and risks were estimated. The estimates proved to be accurate when compared with results from full-fledged contingency simulations under wide variety of operating conditions, and also proved to be computational very efficient. Then from these seven contingencies, five of them were screened for operational planning using decision

trees. The contingency grouping method guided in obtaining lesser number of operating rules that performed well for all the contingencies in the respective groups. This thereby promises system operators the benefit of dealing with lesser number of rules to efficiently perform the power system security assessment, and undertake timely preventive measures for critical contingencies.

The future directions of research include:

- *Contingency assessment under increased uncertainty*: The computational benefit of the proposed machine learning based contingency risk estimation method is even more pronounced when the dimension of sampling state space is further increased to account for more uncertainties in operating conditions, such as including unavailability of generators, SVCs, and variable generation (wind and solar) output.
- *Application to other stability problems*: The operational planning strategy for multiple contingencies can also be applied to other stability problems, provided the respective performance measure's trajectory sensitivities can be obtained.
- *Advancing visualization of contingency impacts*: The progressive entropy based contingency grouping method provides a visual capture of the impact of multiple contingencies on a range of operating conditions. Therefore, frequently updating the curve and broadcasting them in the control centers will enhance visual aid to the operators.

References

1. Ajjarapu, V.: Computational Techniques for voltage stability assessment and control. Springer, New York (2006)
2. Alt, H., Godau, M.: Computing the Fréchet distance between two polygonal curves. Int. J. Comput. Geom. Appl. **5**, 75–91 (1995)
3. Amjady, N., Esmaili, M.: Application of a new sensitivity analysis framework for voltage contingency ranking. IEEE Trans. Power Syst. **20**, 973–983 (2005)
4. Cholley, P., Lebrevelec, C., Vitet, S., de Pasquale, M.: Constructing operating rules to avoid voltage collapse: a statistical approach. In: Proceedings of International Conference on Power System Technology, POWERCON '98, vol 2: 14 (1998)
5. Devroye, L.: Non-Uniform Random Variate Generation. Springer, Newyork (1986)
6. Diao, R., Sun, K., Vittal, V., O'Keefe, R.J., Richardson, M.R., Bhatt, N., Stradford, D., Sarawgi, S.K.: Decision tree-based online voltage security assessment using PMU measurements. IEEE Trans. Power Syst. **24**, 832–839 (2009)
7. Fischer, D., Szabados, B., Poehlman, S.: Automatic contingency grouping using partial least squares and feed forward neural network technologies applied to the static security assessment problem. In: Large Engineering Systems Conference on Power Engineering, pp. 84–89 (2003)
8. Genc, I., Diao, R., Vittal, V., Kolluri, S., Mandal, S.: Decision tree-based preventive and corrective control applications for dynamic security enhancement in power systems. IEEE Trans. Power Syst. (2010)
9. Greene, S., Dobson, I., Alvarado, F.L.: Sensitivity of the loading margin to voltage collapse with respect to arbitrary parameters. In: IEEE PES Winter Meeting, Baltimore (1996)

10. Hatziargyriou, N.D., Contaxis, G.C., Sideris, N.C.: A decision tree method for on-line steady state security assessment. IEEE Trans. Power Syst. **9**, 1052–1061 (1994)
11. Henry, S., Pompee, J., Devatine, L., Bulot, M., Bell, K.: New trends for the assessment of power system security under uncertainty. IEEE PES Power Syst. Conf. Expos. **3**, 1380–1385 (2004)
12. Hsiao, T.Y., Hsieh, C.A., Lu, C.N.: A risk-based contingency selection method for SPS applications. IEEE Trans. Power Syst. **21**, 1009–1010 (2006)
13. Krishnan, V., McCalley, J. D., Henry, S., Issad, S.: High information content database generation for data mining based power system operational planning studies. In: IEEE PES General Meeting (2010)
14. Krishnan, V., McCalley, J.D., Henry, S., Issad, S.: Efficient database generation for decision tree based power system security assessment. IEEE Trans. Power Syst. **26**, 2319–2327 (2011)
15. Lebrevelec, C., Schlumberger, Y., de Pasquale, M.: An application of a risk based methodology for defining security rules against voltage collapse. IEEE Power Eng. Soc. Summer Meet. **1**, 185–190 (1999)
16. Lee, B., Kwon, S., Lee, J., et al.: Fast contingency screening for online transient stability monitoring and assessment of the KEPCO system. IEE Proc. Gener., Trans. Distrib. **150**, 399–404 (2003)
17. Pandit, M., Srivastava, L., Sharma, J.: Fast voltage contingency selection using fuzzy Parallel self-organizing hierarchical neural network. IEEE Trans. Power Syst. **18**(2), 657–664 (2003)
18. Rovnyak, S., Kretsinger, S., Thorp, J., Brown, D.: Decision trees for real-time transient stability prediction. IEEE Trans. Power Syst. **9**, 1417–1426 (1994)
19. Schlumberger, Y., Pompee, J., de Pasquale, M.: Updating operating rules against voltage collapse using new probabilistic techniques. IEEE/PES Trans. Distrib. Conf. Exhib.: Asia Pac. **2**: 1139–1144 (2002)
20. Senroy, N., Heydt, G.T., Vittal, V.: Decision tree assisted controlled islanding. IEEE Trans. Power Syst. **21**, 1790–1797 (2006)
21. Sigrist, L., Egido, I., Sánchez-Úbeda, E.F., Rouco, L.: Representative operating and contingency scenarios for the design of UFLS schemes. IEEE Trans. Power Syst. **25**, 906–913 (2010)
22. Unger, E.A., Harn, L., Kumar, V.: Entropy as a measure of database information. In: Proceedings of the Sixth Annual Computer Security Applications Conference pp. 80–87 (1990)
23. Vittal, V., Kliemann, W., Ni, Y.X., Chapman, D.G., Silk, A.D., Sobajic, D.J.: Determination of generator groupings for an islanding scheme in the Manitoba hydro system using the method of normal forms. IEEE Trans. Power Syst. **13**, 1345–1351 (1998)
24. Wan, H., McCalley, J.D., Vittal, V.: Risk based voltage security assessment. IEEE Trans. Power Syst. **15**, 1247–1254 (2000)
25. Wehenkel, L., Pavella, M., Euxibie, E., Heilbronn, B.: Decision tree based transient stability method a case study. IEEE Trans. Power Syst. **9**, 459–469 (1994)
26. Witten, I.H., Frank, E.: Data Mining: Practical Machine Learning Tools and Techniques with Java Implementations. Morgan Kaufmann Publishers, San Fransisco, CA (2000)
27. Wyss, W.G., Jorgensen, K.H.: A User's Guide to LHS: Sandia's Latin Hypercube Sampling Software. Sandia Natl. Laboratories R. SAND98-0210, Albuquerque, NM (1998)

Goal Directed Synthesis of Serial Manipulators Based on Task Descriptions

Sarosh Patel, Tarek Sobh and Ausif Mahmood

Abstract Computing the optimal geometric structure of manipulators is one of the most intricate problems in contemporary robot kinematics. Robotic manipulators are designed and built to perform certain predetermined tasks. There is a very close relationship between the structure of the manipulator and its kinematic performance. It is therefore important to incorporate such task requirements during the design and synthesis of the robotic manipulators. Such task requirements and performance constraints can be specified in terms of the required end-effector positions, orientations and velocities along the task trajectory. In this work, we present a comprehensive method to develop the optimal geometric structure (DH parameters) of a non-redundant six degree of freedom serial manipulator from task descriptions. This methodology is devised to investigate possible manipulator configurations that can satisfy the task performance requirements under imposed joint constraints. Out of all the possible structures, the structures that can reach all the task points with the required orientations selected. Next, these candidate structures are then tested to see if they can attain end-effector velocities in arbitrary directions within the user defined joint constraints, so that they can deliver the best kinematic performance. Finally, the synthesized structures are tested to see if they perform the task under the operating constraints. In this work, we also present a novel approach for computing the inverse kinematics using Particle Swarm Optimization (PSO).

Keywords Global optimization · Manipulator synthesis · Simulated annealing · Task-based design

S. Patel (✉) · T. Sobh · A. Mahmood
University of Bridgeport, Bridgeport, CT, USA
e-mail: saroshp@bridgeport.edu

T. Sobh
e-mail: sobh@bridgeport.edu

A. Mahmood
e-mail: mahmood@bridgeport.edu

A.T. Azar and S. Vaidyanathan (eds.), *Chaos Modeling and Control Systems Design*,
Studies in Computational Intelligence 581, DOI 10.1007/978-3-319-13132-0_13

1 Introduction

The goal of robotics is to automate and delegate real-world tasks to robotic manipulators. Today robots are being applied to wide range of tasks; from the very traditional material handling tasks to the very sophisticated tele-robotic surgery.

Robotic manipulators are designed and built to perform certain predetermined tasks. Ideally speaking, one should easily be able to design a manipulator based on its application. The rapid growth in manufacturing technologies has increased the need for design and development of optimal machinery [1]. No longer is the emphasis on machinery that works but on machinery that works faster, consumes less power, and is more functional.

Even though general-purpose manipulators are commonplace they do not guarantee optimal task performance. Task optimized manipulators are more effective and efficient than general purpose manipulators. There is a great need for task optimized industrial manipulators that can perform a certain set of jobs with the best efficiency, in the shortest time, and with the least operating cost and power requirements. The availability of computing power allows us to design and evaluate multiple structures based on user defined criteria and select the best design.

What is the best manipulator configuration for soldering electronic components? What should be the ideal manipulator structure for a painting job? What is optimal manipulator configuration for a material handling job? Computing the optimal geometric structure of manipulators is one of the most intricate problems in contemporary robot kinematics [32].

Robotics researchers over the years have tried to find answers to these questions. But in this case plenty is the problem; there is no unique solution or definite answer to these questions. Instead, in most cases there can be infinite answers to any of the above questions. Equations describing the kinematic behavior of serial manipulators are highly nonlinear with no closed solutions. And the configuration search space is infinitely large. The difficulty in most cases lies not in finding a solution, but finding the 'best' solution out of the numerous possible solutions, or in other words, an optimal solution. Another big challenge in solving this problem is the number of parameters involved and the high non-linearity of the inverse kinematic equations [16]. There is a very close relationship between the structure of the manipulator and its kinematic performance [15, 16]. Researchers have over the years tried to develop a framework to reverse engineer optimal manipulator geometries based on task requirements [21].

Every robotic manipulator can only perform certain set of a set of tasks, and some more efficiently than others. Deciding the best manipulator structure for a required job at the design stage is done mainly on the basis of experience and intuition. The rigorous analysis of a few widely used manipulator structures and a collection of a few ad hoc analytical tools can be of some help [4, 23]. However, the need for a comprehensive framework to reverse engineer manipulator structures from task descriptions that can guarantee optimal task performance under a set of operating constraints is still lacking [21].

The aim of this work is to develop a goal directed design methodology that can serve as a simple and easy tool for kinematic synthesis of robotic manipulators based on task descriptions. The proposed methodology allows a user to enter the task point descriptions and joint constraints, and generates the optimal manipulator structure for the specified task. In this work we also present a novel approach for calculating the inverse kinematic solutions based on the Particle Swarm Optimization (PSO) algorithm. This approach helps in finding all the inverse solutions that lie within the constrained joint space with one run of the algorithm.

2 Existing Approaches

The research area of robotic manipulator design can be broadly classified into general purpose designs and task specific designs. Even though general purpose manipulators are commonplace, they do not guarantee optimal task execution. Because industrial robotic manipulators perform a given set of tasks repeatedly, task-specific or task-optimized manipulator designs are preferred for industrial applications.

The existing approaches for design and synthesis of serial manipulators can be broadly classified into the following three types:

2.1 Geometric Approach

Serial robotic manipulators are open-loop kinematic chains consisting of interconnected joints and links. There is a great body of research dealing with the mobility issues of closed loop kinematic chains. The principles of closed loop mechanical chains can be applied to design highly dexterous serial manipulators by assuming the distance between the base of the manipulator and the task point as a fixed and imaginary link in the closed mechanical chain.

Grashof [8] proposed a simple rule to judge the mobility of links in four-link closed kinematic chains. This rule was further extended and developed into Grashof's criterion by Paul [27]. Robotic researchers have applied Grashof's criterion to design manipulators with high dexterity at the given task points. Where dexterity refers to the ability of the manipulator to attain any orientation about a given point [37]. In [17, 25], authors proposed a method for the optimal design of three-link planar manipulators using Grashof's criterion. In [25] a simple algorithm for the optimal design of three link planar manipulators with full manipulator dexterity at the given task region or trajectory is proposed. The Grashof's criterion has also been extended by researchers to explain the behavior of longer kinematic chains. Ting introduced the five-link Grashof criterion [34] and later extended it to N-link chains [35, 36]. The main advantage of this method is its independence from the necessity to calculate the inverse kinematic solutions to judge its performance.

2.2 Parametric Optimization Approach

Parametric optimization is a classical way of solving an optimization problem One or more criteria that quantify the performance properties of the manipulator, sometimes with associated weighting factors, are maximized or minimized to arrive at a set of optimal design parameters. Parametric optimization has been one of the widely adopted approaches for the synthesis of serial manipulators. Condition number was used by Angeles and Rojas to obtain optimal dimensions for a three-DoF manipulator and three-DoF spherical wrist [2]. Craig and Salisbury used the condition number of the Jacobian as design criterion to optimize the dimensions of the fingers of the Stanford articulated hand [28].

In [32], optimal kinematic synthesis of the manipulator structure was based on the Yoshikawa manipulability ellipsoid at a given set of task points is presents. An objective cost function incorporating the Yoshikawa manipulability index was optimized using the *steepest-descent* algorithm over the manipulator's task trajectory to derive the optimal geometric structure. This work was implemented as a procedural package in Mathematica®[1] (version 4.1) and used the Robotica[2] version 3.60 (a robotics toolkit for Mathematica®). This work was further extended in [30, 31] to simulate the dynamic behavior of such an optimized manipulator.

Kucuk and Bingul [15, 16], implement a multi-variable optimization. The manipulator workspace was optimized based on a combination of local and global indices: Structural length index, manipulability measure, condition number, and global conditioning index.

These parametric optimization methods are task independent and hence do not guarantee the non-existence of a better manipulator for a specific task [22]. Another limitation of this approach is that it has a very limited scope due to the inherent limitations and general shortcomings of the performance metrics. A comprehensive survey of manipulator performance parameters and their limitations can be found in [26].

2.3 Task-Based Design Approach

Task-based design of manipulators uses the prior knowledge of application of the manipulator to design the best possible structure that can guarantee task completion. Task specifications can either be kinematic or dynamic. The ultimate goal of task-based design model is to be able to generate both the manipulator kinematic and dynamic parameters, using the task description and operating constraints [13]. This task-based design approach has seen considerable interest from researchers dealing

[1] [© 2002] Wolfram Research Inc.

[2] [© 1993] Board of Trustees, University of Illinois.

with re-configurable modular manipulators that can be easily re-configured depending on the task at hand.

Paredis and Kholsa [22], use the task requirements to find the optimal structure of a manipulator. They developed a numerical approach for determining the optimal structure of a six degree of freedom non-redundant manipulator. Their proposed method involves generating the DH parameters by minimizing an objective function using numerical optimization. This method does not check for non-singular positions at task points and the ability of the manipulator to generate effective velocities.

In [1], Al-Dios et al., developed a method for optimizing the link lengths, masses and trajectory parameters of a serial manipulator with known DH table using direct non-gradient search optimization. This work was focused to optimize the task time and joint torques for a specific manipulator task.

In [12, 13], authors propose the concept of Progressive Design as a frame work for the general design of manipulators and reconfigurable modulator manipulator systems, using task descriptions. The framework consists of three modules: kinematic design, planning and kinematic control. The kinematic design module encapsulates the task specifications, manipulator specifications and dexterity measure. In [12, 13], authors apply the proposed framework to develop an optimal manipulator for Space Shuttle tile changing operation, using dexterity as the optimizing criterion.

Dash et al. [6], propose a two stage methodology for structure and parameter optimization of reconfigurable parallel manipulator systems. They propose a '*TaskToRobot Map*' database that maps task description to a suitable manipulator configuration depending on the degrees of freedom required for a given task.

The manipulator configuration search space for all possible manipulator configurations is prohibitively large for evaluating all possible solutions, even if unacceptable solutions are eliminated early in the evaluation process. Two of the most applied approaches to search the configuration space are Random line search and Generic algorithms.

Authors in [5, 9, 11] recommend the use of Genetic Algorithms (GA) for designing the structure of self-organizing and modular robotic systems. In [29], authors Shiakolas et al. use evolutionary optimization approaches to optimize the design of a SCARA manipulator.

3 Problem Statement

The task descriptions can be given in terms of the task points p that the manipulator is supposed to reach with a specified orientation. Let P be the set of m task points that define the manipulator's performance requirements.

$$P = \{p_1, p_2, \ldots, p_m\} \in TS \tag{1}$$

All these points belong to the six-dimensional Task Space (*TS*) that defines both the position and orientation of the manipulator's end-effector. Each point in the Task Space (*TS*) can be given as:

$$p_i = \{x, y, z, \varphi, \theta, \psi\} \forall i = 1, 2, \ldots, m \in TS \tag{2}$$

where x, y, z are the real-world coordinates, and φ, θ, ψ are the roll, pitch and yaw angles about the standard Z, Y and X-axis. Figure 1 shows an example of a manipulator doing multiple tasks that require specific positioning and orientation of the manipulator at different points in the workspace.

In this work, we use the standard DH (Denavit-Hartenberg) notation to represent the manipulator structures [7]. The standard DH notation uses four parameters to define each link in the serial manipulator:

1. Link length (a)
2. Link twist (α)
3. Link offset (d)
4. Joint angle (θ)

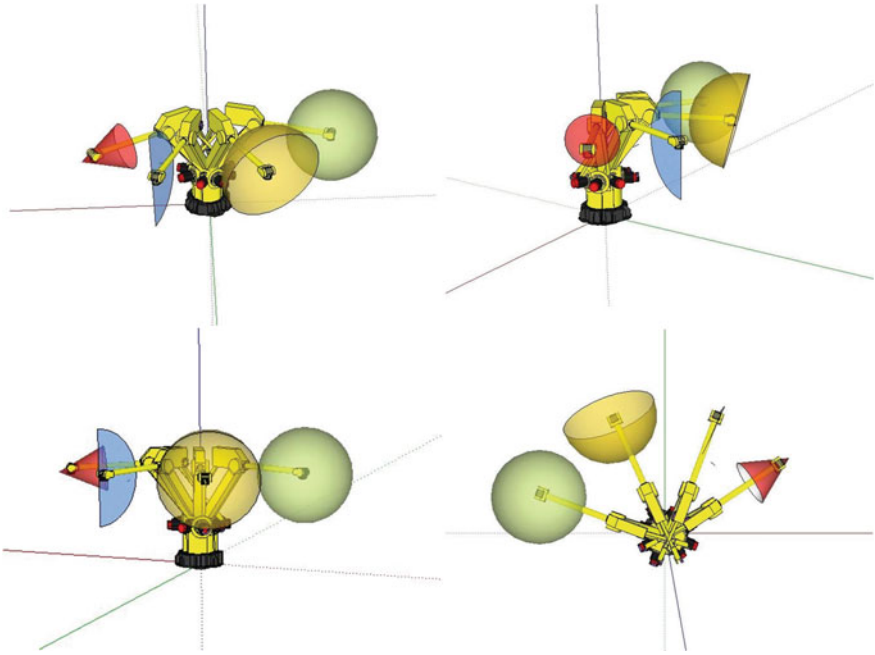

Fig. 1 Manipulator with different orientations at a set of task points

Depending on whether the link is revolute or prismatic, the joint angle (θ) or the link offset (d) is variable while the other three parameters remain constant for any given link. Therefore, each link will have three design parameters that describe it. In the case of a revolute link the design parameters are $\{a, \alpha, d\}$, and in the case of a prismatic link the design parameters are $\{a, \alpha, \theta\}$. A n degree serial manipulator configuration set (DH) can be given as:

$$DH = \{a_0, \alpha_0, \theta_0 \text{ or } d_0, a_1, \alpha_1, \theta_1 \text{ or } d_1, \ldots, a_{n-1}, \alpha_{n-1}, \theta_{n-1} \text{ or } d_{n-1}\} \quad (3)$$

Therefore, an n-link serial manipulator will have $3n$ design parameters. Every set of manipulator configuration parameters can be said to be a point in the Configuration Space (C). Each set of values of the DH vector represents a unique manipulator configuration and a distinct point in the $3n$ dimensional Configuration Space (C).

$$DH = \{a_0, \alpha_0, \theta_0 \text{ or } d_0, a_1, \alpha_1, \theta_1 \text{ or } d_1 \ldots, a_{n-1}, \alpha_{n-1}, \theta_{n-1} \text{ or } d_{n-1}\} \in C \quad (4)$$

Similarly, for an n degree of freedom manipulator, the joint vector q can be a said to be a point in the n dimensional Joint Space (Q), such that:

$$q = [q_1, q_2, \ldots, q_n] \in Q \quad (5)$$

Each joint vector q represents unique manipulator posture and a distinct point in the n dimensional Joint Space (Q). The Joint Space assumes there are no joint limitations (fully revolute ideal joints). But in practice the joints are not fully revolute and are bounded by lower and upper bounds. The values of the joint angles are range bound by user defined joint limits (upper and lower bounds). Hence, we define Q_c as the Constrained Joint Space, such that the joint displacements always satisfy the constraints:

$$q_{i,\min} \leq q_i \leq q_{i,\max} (q_i \in Q_c) \text{ and } Q_c \subset Q \quad (6)$$

Similarly, the manipulator's Reachable Workspace (WS) is defined as the set of points in the world coordinate system that the manipulator's end-effector can reach when no joint constraints are imposed. The manipulator's forward kinematic equations form a mapping $f(C) : Q \rightarrow WS$ between these three spaces: the Configuration Space (C), the Joint Space (Q) and the Workspace (WS).

When the manipulator's joint motion is restricted between joint limits the manipulator can only reach a part of the Reachable Workspace, known as the Constrained Reachable Workspace (CWS), such that $CWS \subset WS$. Constrained Reachable Workspace is defined as the set of points in the real coordinate system that the manipulator's end-effector can reach when joint constraints are imposed. This is given by the forward mapping: $f(C) : Q_c \rightarrow CWS$ and $Q_c \subset Q$.

Figure 2 shows the Reachable Workspace (WS) and Constrained Reachable Workspace (CWS) for a simple planar two-link manipulator as an illustrative example.

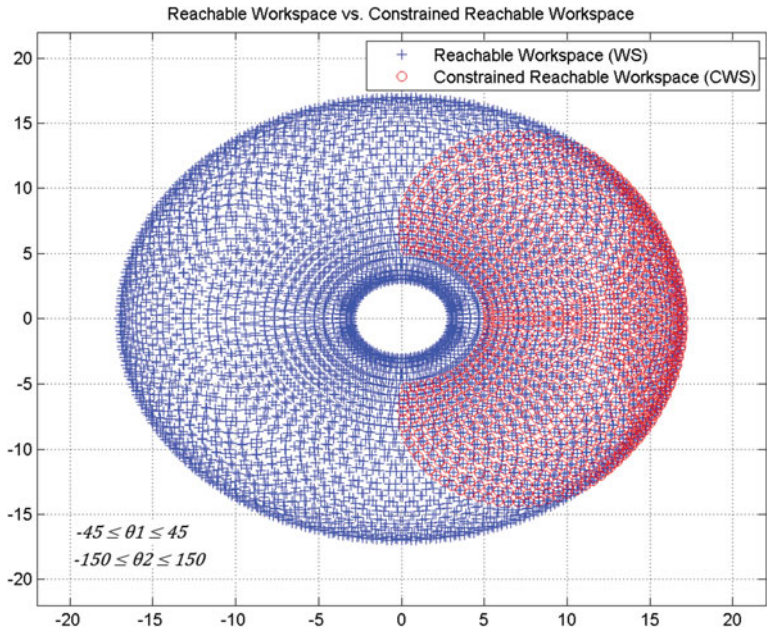

Fig. 2 Reachable workspace (WS) compared with constrained reachable workspace (CWS)

When a given manipulator of configuration set DH, with joint vector q can reach a specific task point p, the mapping can be represented as:

$$f(DH, q) = p \tag{7}$$

Therefore, the problem can be stated as: Find a solution set DH in the $3n$ dimensional Configuration Space such that there exists at least one q in the Constrained Joint Space that can reach the required position and orientation of the end-effector. i.e.

$$\text{Find all } DH \text{ such that } \forall p \in TS; \exists q \in Q_c | f(DH, q) = p$$

Even though this might seem to be a necessary and sufficient condition required for designing a manipulator, simulations and experience will suggest that this solution set might include a few manipulators that are able to reach the one or more of the task points only in singular positions. Such manipulators, if constructed, will not be able to attain good end-effector velocities in one or more directions due to their singular postures at the task point(s). Such manipulators will have very limited mobility at the required task point(s). Infinite forces have to be applied in order to generate motion along one or more directions at singularities. Therefore such manipulator configurations should be removed from the solution set. The test for

singularity is the determinant of the Jacobian matrix, which for a square Jacobian also happens to be the Yoshikawa manipulability index [38].

The Jacobian mapping from joint velocities to end-effector velocities for a manipulator is given as:

$$\xi = J(DH, q)\dot{q} \tag{8}$$

where $\xi = \left[\dot{x}\ \dot{y}\ \dot{z}\ \dot{\phi}\ \dot{\theta}\ \dot{\psi}\right]$ is the end-effector velocity vector.

The Jacobian matrix is posture dependent matrix. It is also important to evaluate the Jacobian of the manipulator because the Jacobian matrix maps joint velocities to end-effector velocities, according to the mapping $J(DH, q) : \dot{q} \rightarrow \xi$. Hence, it is important to check if the Jacobian of manipulator at a given task point is well conditioned, and not in a singular posture. A manipulator with well-conditioned Jacobian at the task points will easily be able to transform joint velocities into end-effector velocities in any required direction, however the opposite cannot be said to be true on the basis of just the Jacobian determinant.

$$\xi = J_1\dot{q}_1 + J_2\dot{q}_2 + \cdots + J_n\dot{q}_n \tag{9}$$

Therefore, we modify the problem statement as follows:
Find all DH such that $\forall p \in TS; \exists q \in Q_c | f(DH, q) = p$ *and* $det(J(q)) \neq 0$

4 Solution Methodology

In this section we define two functions for evaluating the reachability and kinematic performance of the manipulator. To solve the problem we make the following assumptions:

1. The robot base is fixed and located at the origin O.
2. The task points are specified with respect to the manipulator's base frame.
3. The joint limitations are known to the designer.
4. If a joint is prismatic, the joint angle (θ) can assume values in the interval [−180, 180].
5. If a joint is revolute, the joint twist angle (α) can assume values [−180, 180].
6. The last three axes of the six degree of freedom manipulator intersect at a point to form a spherical wrist.
7. To limit the number of inverse kinematic solutions only non-redundant configurations are considered.

Let the task points be represented as $p = [x, y, z, \phi, \theta, \psi]$. The position of the operating point (OP) on the end-effector is given by $p_P = [x, y, z]$ and its orientation by $p_0 = [\phi, \theta, \psi]$.

$$p_i = [p_P \; p_0] \in TS \quad \forall i = 1, 2, 3 \ldots, m \tag{10}$$

In cases where multiple orientations are required at the same point the vector p_P remains same while the orientation vector p_O will assume different values.

The first criterion that needs to be satisfied is that all the points in the Task Space should be a part of the manipulator's Constrained Reachable Workspace. We define the Constrained Reachable Workspace as the set of points that the manipulator is able to reach under constrained joint limitations Q_c, while the normal reachable workspace (*WS*) is the set of points that the manipulator can reach with no joint limits, such that $CWS \subset WS$. Hence, given a set of task points P, the first objective is to find all possible manipulator configurations such that all task points in P are a part of the manipulator's Constrained Reachable Workspace (*CWS*).

$$\textit{Find all DH such that} \; \forall p \in TS; p \in CWS$$

The Constrained Reachable Workspace (*CWS*) of the manipulator is given by the forward kinematic mapping $f(C) : Q_c \rightarrow CWS$. With the help of the standard DH notation parameters, the forward kinematic relationship is given as:

$$f(DH, q) = p \tag{11}$$

Due to the highly non-linear nature of the kinematic equations describing this forward kinematic mapping from the Joint Space to the Task Space, multiple manipulator postures or points in the Joint Space can lead to the same point in the Task Space. In such cases, point(s) in the Task Space will have more than one inverse kinematic solution.

$$q = f^{-1}(DH, p) \tag{12}$$

The inverse kinematic equations often have no unique solution. Depending on the manipulator's structure (*DH*) and location of the task points (p), the number of solutions might range from zero to infinite. And, even in the case where there are multiple known solutions to the above equations, it is still possible that none of them lie within the Constrained Joint Space (Q_c).

$$q = f^{-1}(DH, p) | q \in Q_c \tag{13}$$

In this work we use Particle Swarm Optimization based inverse kinematic approach for finding the inverse kinematic solutions within the constrained joint space. This numerical approach finds all possible inverse kinematic solutions within the specified joint constraints. This is discusses in detail in the following section.

To determine if the structure manipulator is able to reach a given task point with required orientation we construct a reachability function. The reachability function determines if the manipulator can reach and orient the end-effector at the task point within the set joint limitations.

$$reachability(DH) = \max\left[\min\left(\frac{(q_{i,\max} - q_i)(q_i - q_{i,\min})}{(0.5(q_{i,\max} - q_{i,\min}))^2}\right)_{i=1}^{n}\right]_{j=1}^{g} \tag{14}$$

where g is the number of inverse kinematic solutions.

When the joint angle displacements required to reach a task point are within the joint constraints the reachability function is bounded with in zero and unity. And, if the maipulator reaches the task point with at least one joint angle at it maximum displacement, the reachability function will have value of zero. The reachability function will have a maximum value of unity if the manipulator reaches the task point with all joint displacement being mid-range of their joint limits. A reachability value of unity is the ideal case and is only possible with one task point. If the one of the bounds is violated by any given joint out of the n manipulator joints the function will have a negative value. The reachablility function value for different locations of the task point is shown in Table 1.

Since we take a minimum of all the n joints, the reachability indicates the worst joint performance. This reachability function can help in the design of optimal manipulator structures by checking if they can reach the task point with proper joint displacements. To find the best reachable configurations the reachability function needs to be maximized.

Next, to select the best manipulator out of this set of manipulator configurations based their kinematic performance and manipulability. For this we write an objective function that can be maximized or minimized to obtain the optimal manipulator configuration.

$$f(DH)_{velocity} = \max\left[\det\left(J\left(q^1\right)\right), \det\left(J\left(q^2\right)\right), \ldots, \det(J(q^g))\right] \tag{15}$$

where g is the number of inverse kinematic solutions.

This objective function should be maximized to find the optimal manipulator structure that has the best conditioned Jacobian a task points. Such a manipulator will be able to easily transform joint velocities into needed end-effector velocities.

We extend the above formulation for reachability and kinematic performance to include all m points that define the Task Space, as a summation of the function values at the individual task points.

Table 1 Reachability function values

Location of the task point 'p'	Reachability function value
When p is inside the workspace and at least one solution is within joint constraints	[0, 1]
When p is inside the workspace and the best solution has at least one of the joint angles at its extreme position	0
When p is inside the workspace and the best solution is one with all joints displacements mid-range	1

$$reachability(DH) = \sum_{\forall p \in TS} \left(\max \left[\min \left(\frac{(q_{i,\max} - q_i)(q_i - q_{i,\min})}{(0.5(q_{i,\max} - q_{i,\min}))^2} \right)_{i=1}^{n} \right]_{j=1}^{g} \right) \quad (16)$$

$$f(DH)_{velocity} = \sum_{\forall p \in TS} \left(\max \left[\det\left(J\left(q^1\right)\right), \det\left(J\left(q^2\right)\right) \ldots, \det(J(q^g)) \right] \right) \quad (17)$$

To convert these functions into general optimization problems, such that minimizing them will yield optimal solutions we add a negative sign. The functions then become:

$$reachability(DH) = -\sum_{\forall p \in TS} \left(\max \left[\min \left(\frac{(q_{i,\max} - q_i)(q_i - q_{i,\min})}{(0.5(q_{i,\max} - q_{i,\min}))^2} \right)_{i=1}^{n} \right]_{j=1}^{g} \right) \quad (18)$$

$$f(DH)_{velocity} = -\sum_{\forall p \in TS} \left(\max \left[\det\left(J\left(q^1\right)\right), \det\left(J\left(q^2\right)\right) \ldots, \det(J(q^g)) \right] \right) \quad (19)$$

When multiple task points constitute a task goal these functions will have many local minima. This should be kept in mind while selecting a proper optimization algorithm. Using local minimization routines to find optimal solutions will yield acceptable solutions but not global solutions. Only global minimization routines will be able to deliver an optimal solution for the problem. The choice of the global minimization algorithm to be used depends on the number of iterations required, number for function evaluations and the speed of convergence.

4.1 Methodology Flowchart

The presented mathematical formulation and methodology can be represented in the form of a flow chart shown in Fig. 3. Random configurations are generated and tested for the existence of the inverse solutions within the joint limits range. In case a solution exists within the joint constraints, we further test the configurations for good manipulability and other additional performance criteria. Every reachable configuration is saved so that it can be used for further analysis and testing. Some of these configurations can also be used as initial starting points to optimization search algorithms. The final stop criteria can be set in terms of either the number of iterations, number of functional evaluations, or desired objective function value limit or a time limit.

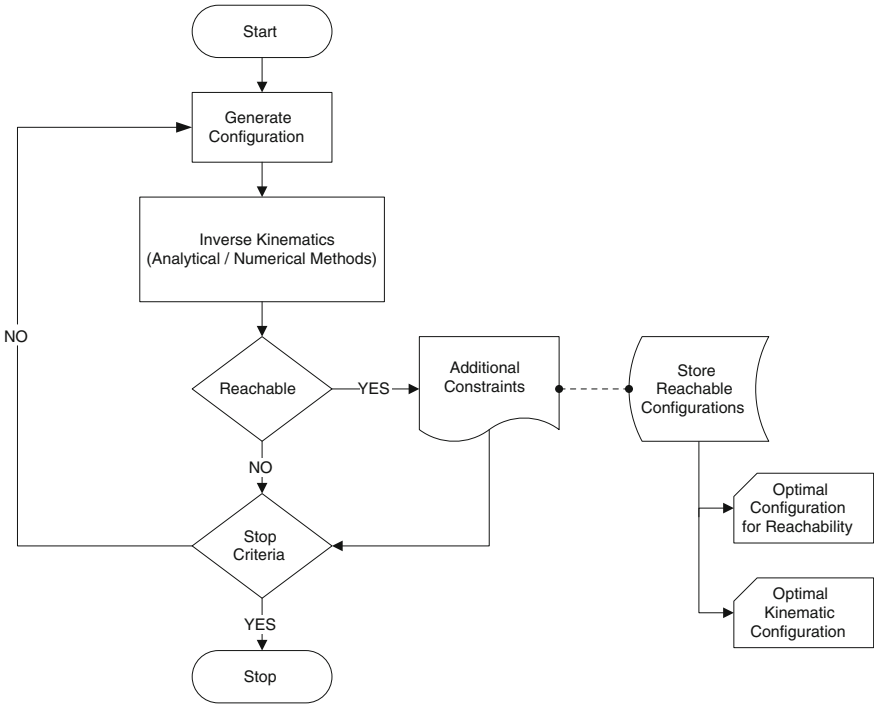

Fig. 3 Proposed methodology flowchart

4.2 Simulated Annealing

There are many approaches to solve a given global optimization problem. The choice of the algorithms greatly depends on factors such as the dimensionality of the problem, the nature of the variables (discrete or continuous), availability of a function derivative. A good global optimization method for a given problem can only be found by matching the features of the problem to the algorithm characteristics and its problem handling capabilities.

In this case, the objective or cost function—which is the reachability function—does not have a direct analytical expression, and is computationally expensive to calculate as it depends on the inverse kinematic solutions. It is also important to note here that this problem does not have a formulation for a function derivative or any function gradient data. The objective function will have multiple local and global minima points where the function value attains the desirable value. The search space is also very exhaustive. Keeping in mind the above factors we chose to implement the problem using Simulated Annealing algorithm. The simulated annealing method is a heuristic algorithm.

Simulated annealing was developed in the 1980s by Scott Kirkpatrick [14] based on a statistical algorithm developed much earlier by Metropolis [20], to improve designs of Integrated Circuit (IC) chips by emulating the actual process of annealing.

Simulated Annealing (SA) is a generic probabilistic meta-heuristic algorithm for finding the global minimum of a cost function that has many local minima. The SA algorithm uses random generated inputs based on a probabilistic model. Only under certain conditions is a change in the objective function due to a new random input accepted. The acceptance condition for a new input is given as follows:

$$\Delta f_{obj} \leq 0 \tag{20}$$

$$\exp\left(-\frac{\Delta f_{obj}}{T}\right) > random[0,1) \tag{21}$$

where Δf_{obj} is the change in the objective function and T is the temperature of the algorithm.

Beginning with a high temperature the algorithm with every iterative step gradually lowers the temperature simulating the annealing process. And, after every fixed number of iterations, known as the annealing period, the temperature is back raised again. Higher temperatures mean greater randomization of the input variables. Therefore, a slow annealing method that lowers the temperature gradually will explore the search space to a greater extent that a fast annealing method that lowers the temperature quickly. At lower temperatures the search space is exploited while at high temperature the algorithm explores the search space.

The algorithm stops when there is no change in the objective function for a certain number of consecutive inputs. SA algorithm remembers the best inputs throughout its run. SA works well with high dimensionality problems even when the search space is extensive.

The Simulated Annealing Method first generates random manipulator configurations that are then tested for reachability using the inverse solutions found by the Particle Swarm Optimization. The PSO based inverse kinematic module only searches for solutions within the user specified joint constraints. All the configurations that are found to be reachable are then further tested based on additional criteria. We keep re-annealing, by raising the temperature of the simulated annealing algorithm when the temperature of the algorithm reaches a minimum. The best reachability table is updated every time a better configuration is found.

4.3 Inverse Kinematics Using Particle Swarm Optimization

The Particle Swarm Algorithm (PSA) was designed to simulate the social behavior of organisms that behave in groups, commonly referred to as Swarm Intelligence. PSA mimics the population behavior followed by groups of animals such as a flock

of birds or a school of fish. PSA over the years has developed from a social behavior simulator to a global optimization algorithm. It was first proposed as a method for global optimization by Kennedy in [10]. Particle Swarm Optimization (PSO) belongs to the family of algorithms commonly referred to as Swarm Intelligence algorithms. The PSO method optimizes iteratively, by having particles learn from each other's position and move accordingly in the search space. With the help of a set of control parameters the algorithm maintains a good balance between the exploration and exploitation of the search space, by controlling the swarm population accordingly.

PSO is a meta-heuristic algorithm that can be used for problems with large search spaces. PSO is very easy to implement and it does not require large computational capabilities. PSO also does not require the objective function to have a gradient or to be differential. It determines the global minima points through cooperation and competition among the individuals of the population or agent particles [24]. PSO can solve complex problems faster than traditional algorithms due to its inherent characteristic of learning from the swarm population.

A very good survey of different applications of PSO to global optimization problems and its variants can be found in paper [24]. The inertia weight of the particles is one of the important factors that determines the how fast the PSO algorithm converges, and therefore has been a topic of interest and research. In [3], authors investigate different inertia weight strategies for PSO when applied to different problems to see which inertia update strategies work the best.

The PSO algorithm has attracted researchers from various backgrounds who have tried to improve its features by applying it to a wide range of problems. In [18, 19, 39] authors propose the use of dynamic multi-swarm methodologies for certain optimization problems.

Though PSO is originally meant to find a global minimum within the search space, it can be adapted to find multiple global minima, as required in this case. In this work the PSO has been used to find the inverse kinematic solutions for six degree of freedom manipulators. One main advantage of using PSO is that the search space can be limited to constrained joint space. Therefore, all solutions found will automatically lie within the constrained joint space, as opposed to the previous approach where all the solutions have to be found and then solutions that are outside the joint limits had to be rejected.

4.3.1 Example of a Two DoF Planar Manipulator

A two degree of freedom planar manipulator has a maximum of two inverse solutions for all points except when the arm is fully extended. These two are commonly referred to as 'elbow up' and 'elbow down' postures. Figure 4 below shows the two postures for a given point in the reachable workspace.

Consider a simple two-link planar manipulator, with link lengths $l_1 = l_2 = 1$ and the desired point $P(x, y) = (1, 1)$. We construct a simple error function in terms of the two joint angles, as follows:

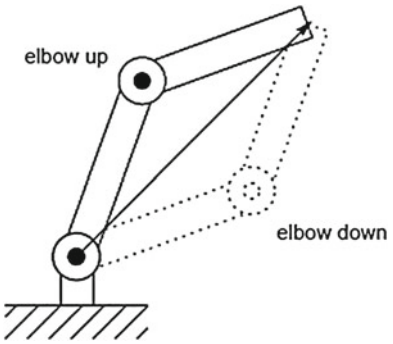

Fig. 4 Inverse kinematic solutions of a two link arm [33]

$$err = |x - l_1 \cos\theta_1 - l_2 \cos(\theta_1 + \theta_2)| + |y - l_1 \cos\theta_1 - l_2 \cos(\theta_1 + \theta_2)| \quad (22)$$

The plot for the error function over the range of θ_1 and θ_2 is shown in Fig. 5. The two minima points are the required inverse kinematic solutions. Figure 6 below shows the contour plot of the error function and the location of the two solutions.

The error function for such a simple manipulator can easily be visualized in a three dimensional plot, but this cannot be done for higher order manipulators that require more than three dimensions. This position error function is given as an input to the PSO algorithm. The different stages of the swarm optimization are shown below in Fig. 7.

The swarm particles/agents can be seen as red dots on the function surface. The swarm particles finally converge at the two minima points in the final plot.

To identify the two global solutions after a specified number of iterations of the PSO algorithm, the following steps are implemented:

(1) Sort the particles in ascending order of the error function value.
(2) Eliminate particles that have an error function value greater than a specified threshold.
(3) Group particles that lie with a specified radius.

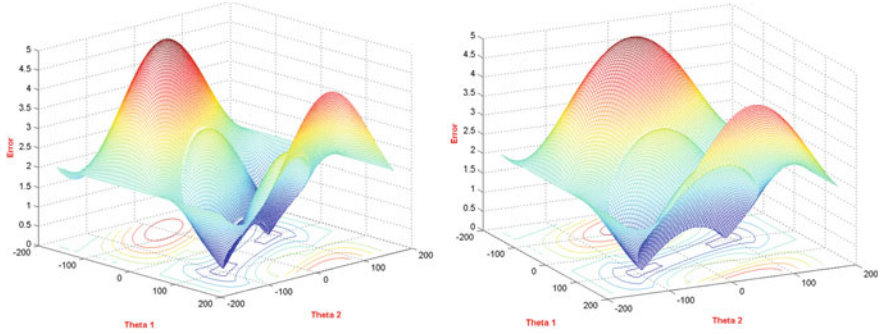

Fig. 5 Position error plot and contour

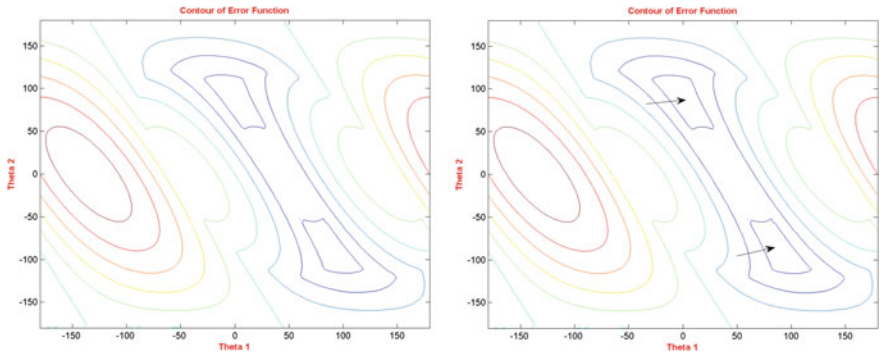

Fig. 6 Position error contour showing the solution points

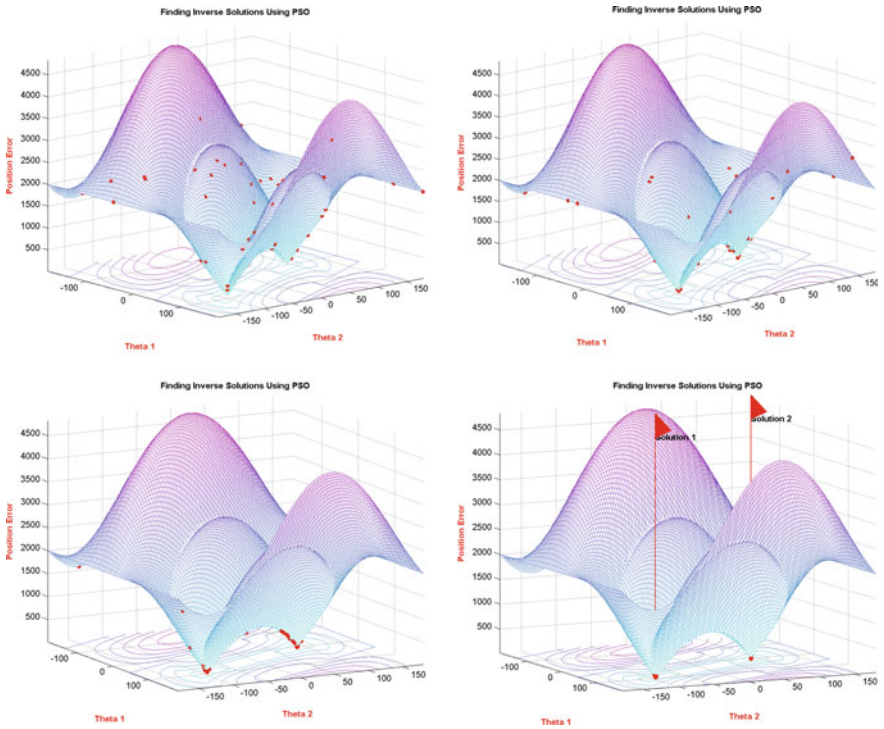

Fig. 7 Stages of the PSO while finding the inverse kinematic solutions

The number of PSO iterations, the threshold, and the grouping radius have to be carefully selected so that all possible solutions can be identified. Fewer iterations will not allow enough time for all the particles to reach the multiple minima points. Choosing a higher threshold can give false solutions that are at a distance from the

goal, while using a very low threshold can eliminate real solutions too. Furthermore, having a large grouping radius can lead to two or more solutions being grouped together.

4.3.2 Six Degree-of-Freedom Example

Next we apply the same PSO bases methodology to compute the inverse kinematic solutions of the six link manipulator with a spherical. When PSO is applied directly to compute all six joint angles for a given reachable point, the PSO has a hard time converging on the solutions due to the high dimensionality of the problem. To do this we approach the problem using the *Greedy Optimization* philosophy, according to which, the global optimum to a large problem consists of the global optimum to each of its sub-problems. Due to the presence of the spherical wrist we can decouple the positioning and the orienting equations as two sub-problems. Finding the global solutions to these two sub-problems will automatically solve the larger inverse kinematics problem.

In this work we have implemented the inverse kinematic solution algorithm in two stages. The first run of the PSO finds all possible joint angles for the first three joints such that the manipulator is able to reach the desired point. Next, for each of the set of solutions for the first three joints the PSO is run to find the possible set of joint angles for the wrist joints such that the desired end-effector orientation can be achieved. This approach also saves precious computation time as there is no need to find the wrist solutions if the arm cannot reach the desired position. Hence, the wrist angles are only calculated if the arm is able to position itself at the desired point. For the class of manipulators with six degrees of freedom and a spherical wrist, below is the algorithm to find the inverse kinematic solutions.

Let P be the target point in the task space such that P can be decoupled into positioning and orienting terms as:

$$P = [p_P \; p_o] = [x, y, z, \emptyset, \theta, \psi] \tag{23}$$

The angles $\emptyset, \theta, \psi$ are such that successive transformations about the respective axes by these angles should lead to the required end-effector orientation, such that:

$$R_6^0 = R(\phi, \theta, \psi) = R_{z,\phi} R_{y,\theta} R_{x,\psi} \tag{24}$$

This final end-effector orientation matrix can also be represented in terms of the normal, sliding and approach vectors as follows:

$$R_6^0 = R(\phi, \theta, \psi) = [n \; s \; a] \tag{25}$$

The following algorithm is used to find the inverse kinematic solution for a given point. First, the wrist center (c) is found by using the approach vector (a):

$$c = p_P - d_6 a \tag{26}$$

Next, we solve the forward kinematic equations for positioning the wrist center (c) at the desired point, using PSO. This yields sets of first three joint angles q_1, q_2, q_3 that can place the wrist center at the desired point. To solve the position of the manipulator using PSO we set up a position error function (*err*):

$$err = \sum |p_P - f(q_1, q_2, q_3)| \tag{27}$$

The multiple minima points of this position error function are the possible sets of the first three joint angles:

$$[q_1, q_2, q_3] = pso(err) \tag{28}$$

Next, for each set of possible q_1, q_2, q_3 we need to find q_4, q_5, q_6 such that the desired orientation is possible. To do this we first calculate the desired orientation due to the last three joints.

$$R_6^3 = \left(R_3^0\right)^T R_6^0 \tag{29}$$

Using Particle Swarm Optimization we solve R_6^3 to get the last three joint angles:

$$[q_4, q_5, q_6] = pso\left(R_6^3 - f(R)\right) \tag{30}$$

The PSO algorithm is configured to search for solutions only within the joint limits; this eliminates the need to check for solutions lying outside the joint limits.

4.3.3 Puma560 Inverse Kinematics

In this section the above algorithm is applied to a PUMA 560 robotic arm to find its inverse kinematic solutions. For most points in the reachable workspace the PUMA 560 arm has four solutions for the inverse position kinematics (unless they violate the joint constraints) as shown in Fig. 8.

The upper bound (UB) and lower bound (LB) for the six revolute joints for a Puma560 manipulator arm in degrees are as follows:

$$\begin{aligned} \text{LB} &= [-160, -45, -225, -110, -100, -266] \\ \text{UB} &= [160, 225, 45, 170, 100, 266] \end{aligned}$$

Below are the example test runs of the PSO-based inverse kinematics method.

a. **Home position**—Here we find the inverse kinematic solutions for the PUMA 560's home position which is given by the point P. The orientation angles are all

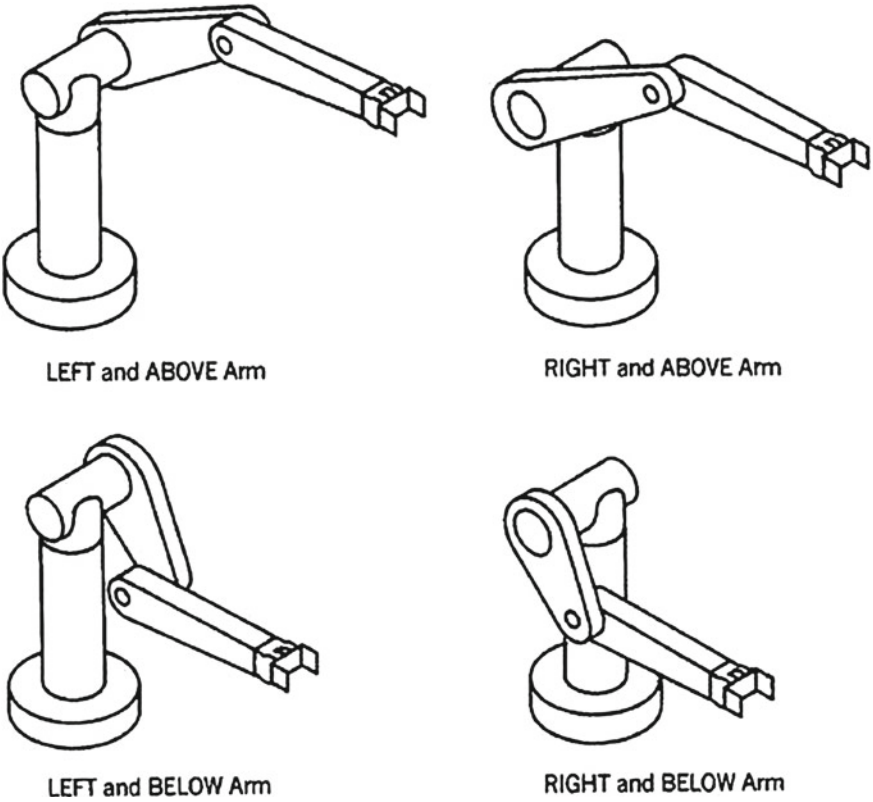

Fig. 8 Four solutions of the inverse position kinematics for the PUMA arm [33]

zero in this case. Figure 9 shows the four inverse position solutions that lead to the same point. Figure 10 shows the end-effector orientation. As seen in Fig. 10 all the normal, sliding, and approach axes of the end-effector perfectly coincide for all four solutions.

$$\mathrm{P} = [\mathrm{x},\ \mathrm{y},\ \mathrm{z}, \emptyset, \theta, \psi] = [0.4521, -0.1500, 0.4318, 0, 0, 0]$$

b. **Top position**—In this example another point P is chosen with arbitrary orientation angles. Figure 11 shows the four inverse position solutions that lead to the same point. Figure 12 shows the end-effector orientation. Again, all the orientation axes of the end-effector perfectly coincide for all four solutions .

$$\mathrm{P} = [\mathrm{x},\ \mathrm{y},\ \mathrm{z}, \emptyset, \theta, \psi] = [0.4521, -0.1500, 0.4318, 0, 0, 0]$$

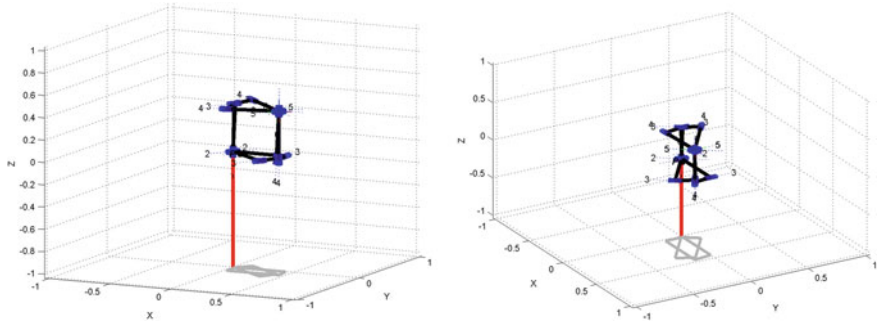

Fig. 9 Inverse position kinematics solutions

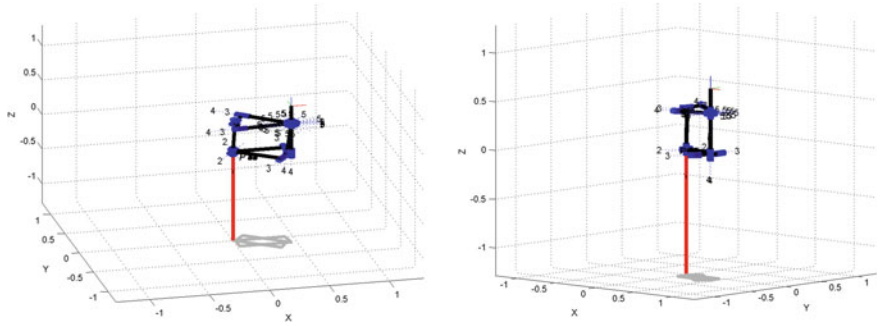

Fig. 10 Inverse position and orientation solutions

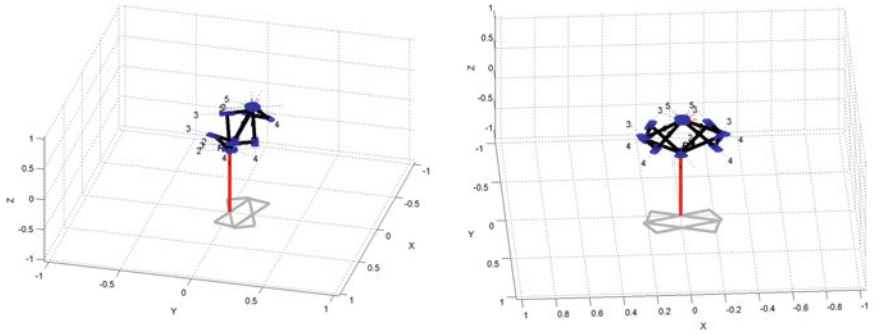

Fig. 11 Inverse position kinematics solutions

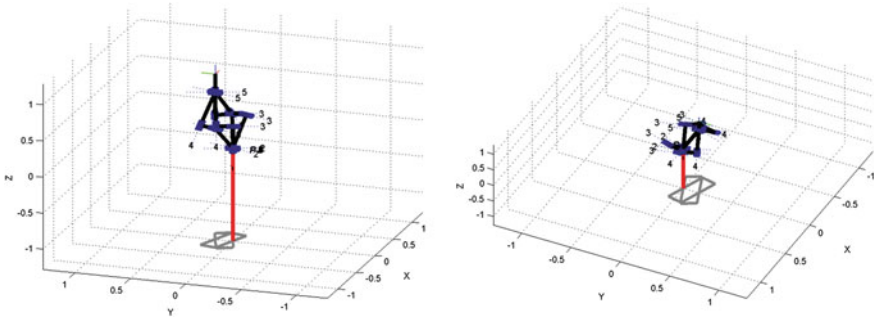

Fig. 12 Inverse position and orientation solutions

5 Experimental Results

In this section we test the proposed methodology to design manipulators based on task point descriptions. The task goals differ in the number of task points and also in the orientation required at these task points. For a prismatic link the joint limit is constrained between zero and unity. The joint limit constraints for the revolute joints are set as follows:

$$\text{Lower Bound} = [-160,\ -45,\ -225,\ -110,\ -100,\ -266]$$
$$\text{Upper Bound} = [160, 225, 45, 170, 100, 266]$$

5.1 Spherical Goal

In this task the manipulator is required to have the ability to reach a task point from all possible approaches or angles. This task involves approaching a point from six different angles separated by 90°, such that they represent the three diagonals of a sphere perpendicular to each other. The task points for a sphere goal are given below.

```
Sphere goal = [
                0 0.75 0 0 0 0;
                0 0.75 0 -3.142 0 -3.142;
                0 0.75 0 0  1.565 0;
                0 0.75 0 0  -1.565 0;
                0 0.75 0 -1.372 1.541 -3.142;
                0 0.75 0 1.784 -1.571 -0.213
            ];
```

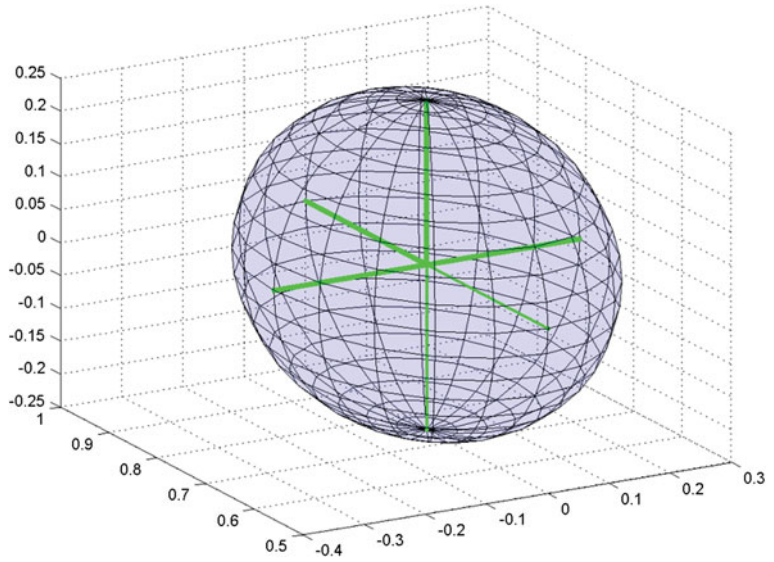

Fig. 13 Task description for the spherical goal

The task visualization is shown in Fig. 13.

Based on the evaluations of all possible configurations, the best configuration that has the maximum overall reachability value for this set of points of the sphere is an RRR-RRR manipulator. This configuration has a reachability value of −0.5441.

The DH parameters of the manipulator are:

```
robot (6 axis, RRRRRR, stdDH)

+---+-----------+-----------+-----------+-----------+
| j |     theta |         d |         a |     alpha |
+---+-----------+-----------+-----------+-----------+
|  1|         q1|     0.9979|     0.8345|     -2.375|
|  2|         q2|     0.7467|     0.9979|      3.101|
|  3|         q3|     0.0025|     0.9978|      2.269|
|  4|         q4|          0|          0|     -1.571|
|  5|         q5|          0|          0|      1.571|
|  6|         q6|       0.25|          0|          0|
+---+-----------+-----------+-----------+-----------+
```

Figure 14 shows superimposed manipulator positions at the required task points.

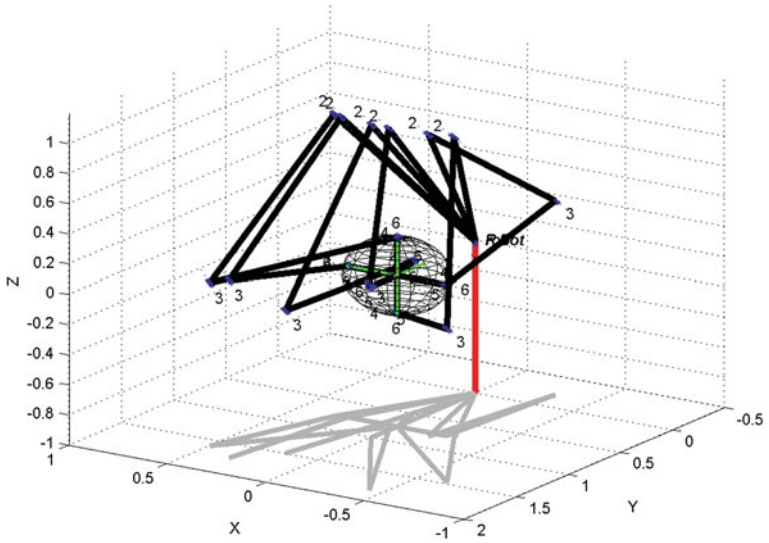

Fig. 14 Designed manipulator reaching all the task points of the spherical goal

For this goal the best kinematic performance structure was found to be:

```
robot (6 axis, RRRRRR, stdDH)

+---+-----------+-----------+-----------+-----------+
| j |     theta |         d |         a |     alpha |
+---+-----------+-----------+-----------+-----------+
|  1|         q1|     0.9956|     0.6492|     -2.342|
|  2|         q2|     0.9973|     0.9956|      3.057|
|  3|         q3|   0.005252|     0.9954|      2.167|
|  4|         q4|          0|          0|     -1.571|
|  5|         q5|          0|          0|      1.571|
|  6|         q6|       0.25|          0|          0|
+---+-----------+-----------+-----------+-----------+
```

5.2 Circular Ring Goal

In this task the manipulator is required to reach eight points on the circumference of a circle with the same orientation at all the task points. The task points for the ring goal are given below.

```
Ring Goal = [
   0.7000   0.5000      0        -3.142 0 -3.142
   0.6414   0.6414      0        -3.142 0 -3.142
   0.5000   0.7000      0        -3.142 0 -3.142
   0.3586   0.6414      0        -3.142 0 -3.142
   0.3000   0.5000      0        -3.142 0 -3.142
   0.3586   0.3586      0        -3.142 0 -3.142
   0.5000   0.3000      0        -3.142 0 -3.142
   0.6414   0.3586      0        -3.142 0 -3.142
];
```

The task visualization is shown in Fig. 15.

Based on the evaluations of all possible configurations, the best configuration that has the maximum overall reachability value for this set of points of the ring task is an RRR-RRR manipulator. This configuration has a reachability value of −0.833

The DH parameters of the manipulator are:

```
robot (6 axis, RRRRRR, stdDH)
```

j	theta	d	a	alpha
1	q1	0.049	0.6576	0.7544
2	q2	0.817	0.908	3.02
3	q3	0.9482	0.6897	1.264
4	q4	0	0	-1.571
5	q5	0	0	1.571
6	q6	0.25	0	0

Figure 16 shows superimposed manipulator positions at the required task points.

For this goal the best kinematic performance structure was found to be:

```
robot (6 axis, RRRRRR, stdDH)
```

j	theta	d	a	alpha
1	q1	0.04902	0.6576	0.7545
2	q2	0.8169	0.908	3.02
3	q3	0.9482	0.6897	1.264
4	q4	0	0	-1.571
5	q5	0	0	1.571
6	q6	0.25	0	0

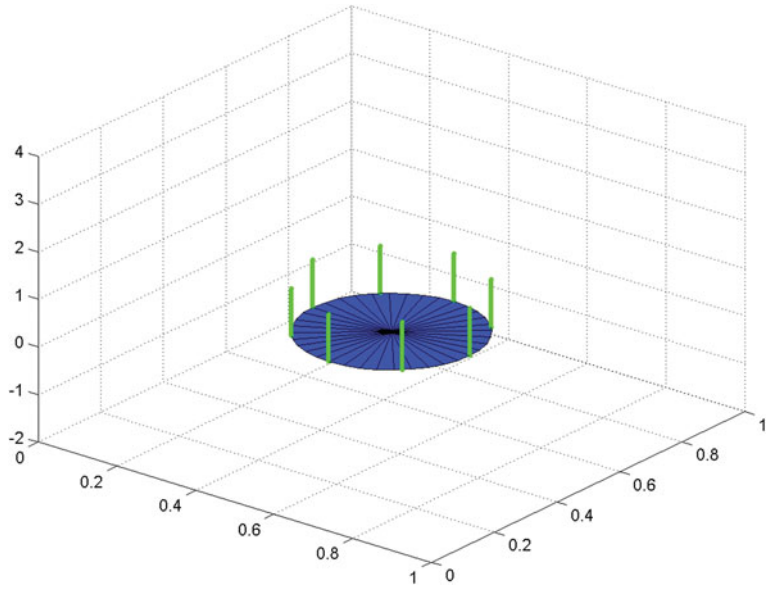

Fig. 15 Task description for the ring goal

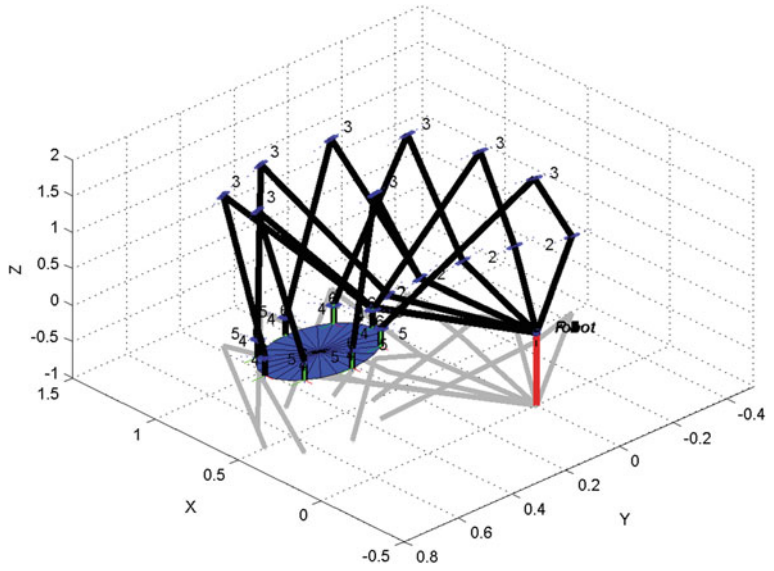

Fig. 16 Designed manipulator reaching all the task points of the ring goal

5.3 Horizontal Plane Goal

This task comprises of nine points that lie in a horizontal plane, the manipulator is supposed to reach all of the task points with the same orientation. This task is similar to the task manipulators execute in the packaging/soldering application. The task points for the horizontal plane goal are given below.

```
Horizontal Plane Goal = [
                        0.9  -0.5  0 -3.142 0 -3.142;
                        0.9   0    0 -3.142 0 -3.142;
                        0.9   0.5  0 -3.142 0 -3.142;
                        0.7  -0.5  0 -3.142 0 -3.142;
                        0.7   0    0 -3.142 0 -3.142;
                        0.7   0.5  0 -3.142 0 -3.142;
                        0.5  -0.5  0 -3.142 0 -3.142;
                        0.5   0    0 -3.142 0 -3.142;
                        0.5   0.5  0 -3.142 0 -3.142;
                    ];
```

The task visualization is shown in Fig. 17.

Based on the evaluations of all possible configurations, the best configuration that has the maximum overall reachability value for this set of points of the horizontal goal is an RRR-RRR manipulator. This configuration has a reachability value of −0.68127.

The DH parameters of the manipulator are:

```
robot (6 axis, RRRRRR, stdDH)

+---+-----------+-----------+-----------+-----------+
| j |     theta |         d |         a |     alpha |
+---+-----------+-----------+-----------+-----------+
|  1|         q1|     0.2472|     0.6404|      0.104|
|  2|         q2|     0.0019|     0.6147|      1.404|
|  3|         q3|     0.3707|     0.3709|     -1.135|
|  4|         q4|          0|          0|     -1.571|
|  5|         q5|          0|          0|      1.571|
|  6|         q6|       0.25|          0|          0|
+---+-----------+-----------+-----------+-----------+
```

Figure 18 shows superimposed manipulator positions at the required task points.

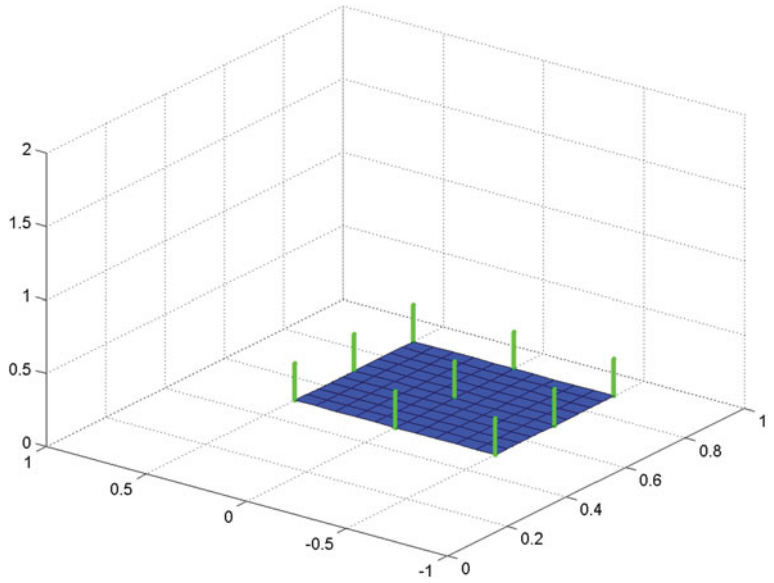

Fig. 17 Task requirements for the horizontal plane goal

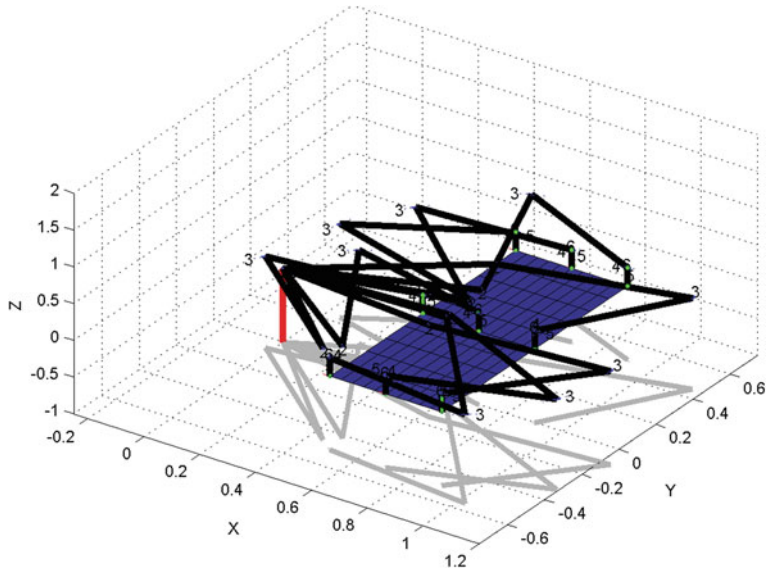

Fig. 18 Designed manipulator reaching all the task points of the horizontal goal

For this goal the best kinematic performance structure was found to be:

robot (6 axis, RRRRRR, stdDH)

j	theta	d	a	alpha
1	q1	0.1855	0.9	2.619
2	q2	0.07636	0.3638	-1.332
3	q3	0.5625	0.3354	-2.649
4	q4	0	0	-1.571
5	q5	0	0	1.571
6	q6	0.25	0	0

6 Discussion

In all the task experiments the initial seed to the algorithm was a set of random values such that the resultant configuration did not constitute an existing structure and did not reach even a single task point. The methodology then iteratively found a set of reachable configurations from which task suitable configurations are selected.

The optimal manipulator structures for the best reachability, and kinematic performance are not always the same. They can be two different manipulators. A manipulator structure having a very good reachability value for a set task may not actually be the most efficient manipulator. Therefore, selecting the right manipulator will involve a certain intelligent trade off with respect to these parameters.

As expected for most of the tasks, the best manipulator structure found happened to be a RRR/RRR manipulator. This supports the fact that most industrial manipulators are RRR robots with spherical wrists as they provide better reachability at the task points and also the ability to orient the end-effector arbitrarily in the workspace.

The manipulator structures that were generated by the methodology for each of the tasks are not ones that would intuitively come to mind for those tasks. Using this task based tool to design manipulators can help the designer in evaluating new and different configurations.

In some cases a few structures failed to reach all the task points with the necessary orientation required for task completion. For example no RPP/RRR configuration could be found that could successfully complete the sphere goal task within the set joint constraints.

7 Conclusion

In this work we have presented a general methodology for task-based prototyping of serial robotic manipulators. This framework can be used to generate specialized goal oriented manipulator structures based on the task descriptions. The framework allows for practical joint constraints to be imposed during the design stage of the manipulator. This methodology incorporates the necessary criteria for the design of a manipulator, such as reachability, orientation and non-singularity. However the sufficient condition can be specified by the user, by incorporating additional constraints. In this work we have used a novel approach based on particle swarm optimization to calculate the inverse kinematic solutions. This work can be viewed as part of a broader program to develop a general framework for the reverse prototyping of robotic manipulators based on task descriptions and operating constraints.

References

1. Al-Dois, H., Jha, A.K., Mishra, R.B.: Task-based design optimization of serial robot manipulators. Eng. Optim. **45**(6), 647–658 (2012)
2. Angeles, J., Rojas, A.: Manipulator inverse kinematics via condition-number minimization and continuation. Int. J. Robot. Autom. **2**(2), 61–69 (1987)
3. Bansal, J.C., Singh, P.K., Saraswat, M., Verma, A., Jadon, S.S., Abraham, A.: Inertia weight strategies in particle swarm optimization. In: Proceedings of the Third World Congress on Nature and Biologically Inspired Computing (NaBIC), pp. 633–640 (2011)
4. Bohigas, O., Manubens, M., Ros, L.: A complete method for workspace boundary determination on general structure manipulators. IEEE Trans. Rob. **28**(5), 993–1006 (2012)
5. Chung, W.K., Jeongheon, H., Youm, Y., Kim, S.H.: Task based design of modular robot manipulator using efficient genetic algorithm. In Proceedings of 1997 IEEE International Conference on Robotics and Automation, pp. 507–512 (1997)
6. Dash, A.K., Chen, I.M., Yeo, S.H., Yang, G.: Task-oriented configuration design for reconfigurable parallel manipulator systems. Int. J. Comput. Integr. Manuf. **18**(7), 615–634 (2005)
7. Denavit, J., Hartenberg, R.S.: A kinematic notation for lower-pair mechanisms based on matrices. Trans. ASME J. Appl. Mech. **22**, 215–221 (1955)
8. Grashof, F.: Thertische Mshinenlehre. Leipzig, pp. 113–183 (1883)
9. Izumi, K., Tamura, H., Watanabe, K.: Task-oriented optimal configuration structure in a three-dimensional self-organizing robot by genetic algorithms. In: Proceedings of IEEE International Conference on Systems, Man, and Cybernetics (SMC'99), pp. 740–745 (1999)
10. Kennedy, J., Eberhart, R.: Particle swarm optimization. In: Proceedings of IEEE International Conference on Neural Networks, pp. 1942–1948 (1995)
11. Kim, J., Khosla, P.K.: A multi-population genetic algorithm and its application to design of manipulators. In: Proceedings of IEEE/RSJ International Conference on Intelligent Robots and Systems, pp. 279–286 (1992)
12. Kim, J., Khosla, P.K.: Design of space shuttle tile servicing robot: an application of task based kinematic design. In: Proceedings of IEEE International Conference on Robotics and Automation, pp. 867–874 (1993a)

13. Kim, J., Khosla, P.K.: A formulation for task based design of robot manipulators. In: Proceedings of IEEE/RSJ International Conference on Intelligent Robots and Systems, pp. 2310–2317 (1993b)
14. Kirkpatrick, S., Gelatt Jr, C.D., Vecchi, M.P.: Optimization by simulated annealing. Science **220**(4598), 671–680 (1983)
15. Kucuk, S., Bingul, Z.: Robot workspace optimization based on a novel local and global performance indices. In: Proceedings of IEEE International Symposium on Industrial Electronics, pp. 1593–1598 (2005)
16. Kucuk, S., Bingul, Z.: Comparative study of performance indices for fundamental robot manipulators. Robot. Auton. Syst. **54**(7), 567–573 (2006)
17. Li, R., Dai, J.S.: Orientation angle workspaces of planar serial three-link manipulators. Sci. China Ser. E: Technol. Sci. **52**(4), 975–985 (2009)
18. Liang, J.J., Suganthan, P.N.: Dynamic multi-swarm particle swarm optimizer. In: Proceedings of the 2005 IEEE Swarm Intelligence Symposium (SIS 2005), pp. 124–129 (2005a)
19. Liang, J.J., Suganthan, P.N.: Dynamic multi-swarm particle swarm optimizer with local search. In: Proceedings of the 2005 IEEE Congress on Evolutionary Computation, pp. 522–528 (2005b)
20. Metropolis, N., Rosenbluth, A.W., Rosenbluth, M.N., Teller, A.H., Teller, E.: Equation of state calculations by fast computing machines. J. Chem. Phys. **21**(6), 1087–1092 (1953)
21. Oetomo, D., Daney, D., Merlet, J.P.: Design strategy of serial manipulators with certified constraint satisfaction. IEEE Trans. Rob. **25**(1), 1–11 (2009)
22. Paredis, C.J.J., Khosla, P.K.: Kinematic design of serial link manipulators from task specifications. Int. J. Robot. Res. **12**(3), 274–287 (1993)
23. Park, F.C., Brockett, R.W.: Kinematic dexterity of robotic mechanisms. Int. J. Robot. Res. **13** (1), 1–15 (1994)
24. Parsopoulos, K.E., Vrahatis, M.N.: Recent approaches to global optimization problems through particle swarm optimization. Nat. Comput. **1**(2–3), 235–306 (2002)
25. Patel, S., Sobh, T.: Optimal design of three-link planar manipulators using Grashof's criterion. In: Sobh, T., Xiong, X. (eds.) Prototyping of Robotic Systems: Applications of Design and Implementation, pp. 70–84. IGI Global, Hershey (2012)
26. Patel, S., Sobh, T.: Manipulator performance measures—a comprehensive literature survey. J. Intell. Robot. Syst. 1–24 (2014). doi:10.1007/s10846-014-0024-y
27. Paul, B.: A reassessment of Grashof's criterio. Trans. ASME J. Mech. Design **101**(3), 515–518 (1979)
28. Salisbury, J.K., Craig, J.J.: Articulated hands: force control and kinematic issues. Int. J. Robot. Res. **1**(1), 4–17 (1982)
29. Shiakolas, P.S., Koladiya, D., Kebrle, J.: Optimum robot design based on task specifications using evolutionary techniques and kinematic, dynamic, and structural constraints. Inverse Probl. Eng. **10**(4), 359–375 (2002)
30. Sobh, T., Wang, B., Patel, S.: A mobile wireless and web based analysis tool for robot design and dynamic control simulation from task points description. J. Internet Technol. **4**(3), 153–162 (2003a)
31. Sobh, T., Wang, B., Patel, S.: Web enabled robot design and dynamic control simulation software solutions from task points description. In: Proceedings of the 29th Annual Conference of the IEEE Industrial Electronics Society (IECON'03), pp. 1221–1227 (2003b)
32. Sobh, T.M., Toundykov, D.Y.: Optimizing the tasks at hand (robotic manipulators). IEEE Robot. Autom. Mag. **11**(2), 78–85 (2004)
33. Spong, M.W., Vidyasagar, M.: Robot Dynamics and Control. Wiley, New York (1989)
34. Ting, K.-L.: Five-bar Grashof criteria. J. Mech. Transmissions Autom. Design **108**(4), 533–537 (1986)
35. Ting, K.-L.: Mobility criteria of single-loop N-bar linkages. J. Mech. Transmissions Autom. Design **111**(4), 504–507 (1989)
36. Ting, K.-L., Liu, Y.-W.: Rotatability laws for N-bar kinematic chains and their proof. J. Mech. Des. **113**(1), 32–39 (1991)

37. Vijaykumar, R., Waldron, K.J., Tsai, M.: Geometric optimization of serial chain manipulator structures for working volume and dexterity. Int. J. Robot. Res. **5**(2), 91–103 (1986)
38. Yoshikawa, T.: Manipulability of robotic mechanisms. Int. J. Robot. Res. **4**(2), 3–9 (1985)
39. Zhao, S.Z., Liang, J.J., Suganthan, P.N., Tasgetiren, M.F.: Dynamic multi-swarm particle swarm optimizer with local search for Large Scale Global Optimization. In: Proceedings of (IEEE World Congress on Computational Intelligence) IEEE Congress on Evolutionary Computation (CEC 2008), pp. 3845–3852 (2008)

Intelligent Tracking Control System for Fast Image Scanning of Atomic Force Microscopes

Sajal K. Das, Hemanshu R. Pota and Ian R. Petersen

Abstract Atomic force microscope (AFM) is a type of scanning probe microscopy technique which is used to measure the characteristics of various specimens at an atomic level through surface imaging. In the imaging process of the AFM the sample is placed on a positioning unit termed as nanopositioner. The performance of the AFM for fast image scanning is limited to the one percent of the first resonance frequency of its positioning unit. Many imaging applications require a faster response and high quality imaging than what can be achieved using the currently available commercial AFMs. The need for high speed imaging is the reduction of the computational time to capture an image. The time require to capture an image of a reference grating sample for an 8 μm × 8 μm area and 256 number of scan lines at the scanning rate of 1 Hz and 125 Hz are 170s and 2 s. This shows the importance of the increase of scan frequency in terms of operation time. The tracking performance of the nanopositioner of the AFM for high speed imaging is limited due to the vibration of the nanopositioner, cross coupling effect between the axes of the nanopositioner and nonlinear effects in the form of hysteresis and creep. In this chapter we have proposed an intelligent multi-variable tracking controller to compensate the effect of vibration, cross coupling and nonlinearities in the form of hysteresis and creep in AFM for fast image scanning. Experimental results in time and frequency domain are presented to show the effectiveness of the proposed controller.

Keywords Piezoelectric tube scanner · Atomic force microscope · Negative-imaginary systems · Passive systems · Resonant controller · Vibration control

S.K. Das (✉) · H.R. Pota · I.R. Petersen
School of Engineering and Information Technology (SEIT), The University of New South Wales, Canberra 2600, ACT, Australia
e-mail: das.k.sajal@gmail.com

H.R. Pota
e-mail: h.pota@adfa.edu.au

I.R. Petersen
e-mail: i.r.petersen@gmail.com

A.T. Azar and S. Vaidyanathan (eds.), *Chaos Modeling and Control Systems Design*, Studies in Computational Intelligence 581, DOI 10.1007/978-3-319-13132-0_14

1 Introduction

Nanotechnology is the branch of science which deals with the manipulation of matters on an extremely atomic level. Nanotechnology as defined by size is naturally very broad, including fields of science as diverse as surface science, organic chemistry, molecular biology, semiconductor physics, and microfabrication. The viewing of surface texture at the atomic level with extremely high resolution was a great challenge until the introduction of the scanning tunneling microscope (STM) [12–15]. The STM was developed by Gerd Binning and his colleagues in 1981 at the IBM Zurich Research Laboratory in Switzerland [12, 13]. The STM was the first SPM technique capable of directly obtaining three-dimensional (3-D) images of solid surfaces. The discovery of the STM has brought Nobel Prize to Binning and Rohrer in Physics in 1986. The STM is only used to measure the topography of surfaces which are electrically conductive to some degree. This limits the use of the STM for the surfaces which are non-conductive in nature. The invention of the AFM has opened a new era to the field of nanotechnology to study non-conductive sample surfaces. The AFM is used to measure the topography of any engineering surface, whether it is electrically conductive or insulating. The invention of the AFM has also led to the invention of the family of scanning probe microscopy techniques (SPMs). These include scanning electrostatic force microscopy (SEFM) [61], scanning force acoustic microscopy (SFAM) (or atomic force acoustic microscopy (AFAM)) [3, 53], magnetic force microscopy (MFM) [58, 31], scanning near field optical microscopy (SNOM) [8, 7], scanning thermal microscopy (SThM) [40, 63], scanning electromechanical microscopy (SEcM) [33], scanning Kelvin probe microscopy (SKPM) [24, 43], scanning chemical potential microscopy (SCPM) [64], scanning ion conductance microscopy (SICM) [30, 49] and scanning capacitance microscopy (SCM) [37, 41]. The reason for calling them as SPM is because of using probe in these devices for investigation and manipulation of matters. The commercial use of the SPM was started in 1987 with the STM and 1989 with the AFM by Digital Instruments Inc. The basic stage for the development of the SPM systems is as follows:

1. 1981—*Scanning tunneling microscope*. G. Binning ang H. Rohrer. Atomic resolution images of conducting surfaces.
2. 1982—*Scanning near-field optical microscope*. D.W. Pohl. Resolution of 50 nm in optical images
3. 1984—*Scanning capacitive microscope*. J.R. Matey, J. Blanc. 500 nm (lateral resolution) images of capacitance variation.
4. 1985—*Scanning thermal microscope*. C.C. Williams, H.K. Wickramasinghe. Resolution of 50 nm in thermal images.
5. 1986—*Atomic force microscope*. G. Binning, C.F. Quate, Ch. Gerber. Atomic resolution on non-conducting (and conducting) samples.
6. 1987—*Magnetic force microscope*. Y. Martin, H.K. Wickramasinghe. Resolution of 100 nm in magnetic images.

7. 1988—*Inverse photoemission microscope*. J.H. Coombs, J.K. Gimzewski, B. Reihl, J.K. Sass, R.R. Schlittler. Detection of luminescence spectra on nanometer scales.
8. 1989—*Near-field acoustic microscope*. K. Takata, T. Hasegawa, S. Hosaka, S. Hosoki, T. Komoda. Low frequency acoustic measurements with the resolution of 10 nm.
9. 1990—*Scanning chemical potential microscope*. C.C. Williams, H.K. Wickramasinghe. Atomic scale images of chemical potential variation.
10. 1991—*Kelvin probe force microscope*. N. Nonnenmacher, M. P. O'Boyle, H K. Wickramasinghe. Measurements of surface potential with 10 nm resolution.
11. 1994—*Apertureless near-field optical microscope*. F. Zenhausern, M.P. O'Boyle, H.K. Wickranmasinghe. Optical microscopy with 1 nm resolution.

2 Operating Principle of the AFM

Atomic force microscope (AFM) is a very high-resolution type of scanning probe microscope with demonstrated resolution on the order of fractions of a nanometer. Despite of the great success of the STM it was obvious that STM has a fundamental disadvantage. The STM can investigate only the conductive or semi-conductive samples. This disadvantage was overcome due to the invention of the AFM. Like the STM, the AFM relies on a scanning technique to produce very high resolution 3-D images of sample surfaces. The AFM is based upon the principle of sensing the forces between a sharp tip and the surface to be investigated. The forces can be attractive or repulsive depending on the operating modes. When tip to sample distance is large the interactive force is attractive and when the tip to sample distance is small the interactive force is repulsive. The forces are measured by measuring the motion of a very small cantilever beam. During the operation of the AFM the sample is scanned instead of the tip (unlike the STM) because the AFM measures the relative displacement between the cantilever surface and the reference surface.

A schematic of the AFM is presented in Fig. 1. The basic components include a micro-cantilever with a sharp tip mounted on a micromachined cantilever, a positioning unit, a laser source, and a laser photodetector. In the imaging process of the AFM, a sample is placed on a positioning unit. There are different types of positioning units used in the AFM such as piezoelectric tube scanner, serial-kinematic scanner, flexure based scanners. The use of the positioning unit depends on the application of the AFM. A detail discussion on the various types of the positioning unit used in the AFM is discussed later. The displacement of the positioning unit during the imaging is measured by sensor. In most of the cases capacitive sensors are used to measure the displacement of the scanner.

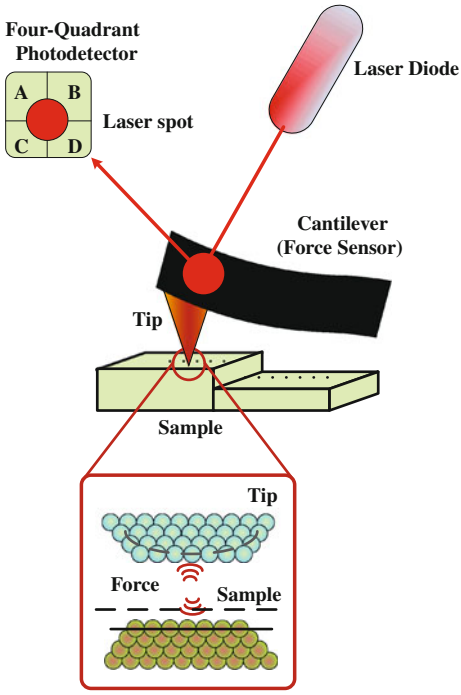

Fig. 1 Block diagram of the AFM working principle

When the sample is placed on the positioning unit, a cantilever beam with a sharp tip is brought in the close proximity of the sample. Various types of cantilevers are used in the AFM. The cantilever used in the AFM should meet the following criteria: (1) low normal spring constant (stiffness); (2) high resonant frequency; (3) high cantilever quality factor Q; (4) high lateral spring constant (stiffness); (5) short cantilever length; (6) incorporation of components (such as mirror) for deflection sensing; and (7) a sharp protruding tip. The cantilever used in the AFM system also has different shape. But in most of the cases a tip is attached with the cantilever.

In order to achieve the large imaging bandwidth the cantilever should have a high resonant frequency. The Young's modulus and the density are the material parameters that determine the resonant frequency, aside from the geometry. This makes the cantilever the least sensitive part of the system. In order to register a measurable deflection with small forces it is also required that the cantilever should have low spring constant. The combined requirement of having high resonance frequency and low spring constant is meet by reducing the mass of the cantilever. The tip used with the cantilever should have radius much smaller than the radii of the corrugations in the sample in order for these to be measured accurately. The cantilever is typically silicon or silicon nitride with a tip radius of curvature on the order of nanometers. Silicon nitride cantilevers are less expensive. They are very rugged and well suited to

imaging in almost all environments. They are especially compatible with organic and biological materials.

The most common methods to detect cantilever deflections are the optical lever method, the interferometric method, and the electronic tunneling method. The optical lever method is the most used one, since it is the most simple to implement. It consists in focusing a laser beam on the back side of the cantilever and in detecting the reflected beam by means of a position sensor, that is usually a quartered photodiode. Both cantilever deflection and torsion signals may be collected.

When the sample is placed on the positioning unit of the AFM, the cantilever is placed in the close contact of the sample. In this process an electric field is applied across the positioning unit of the AFM. This induces a displacement of the positioning unit. The displacement of the positioning unit is measured using sensor such as capacitive sensor. A laser beam is transmitted to and reflected from the cantilever for measuring the cantilever orientation. The reflected laser beam is detected with a position-sensitive detector consisting of two closely spaced photodiodes whose output signal is collected by a differential amplifier. In most of the cases the photo detector has four quadrants. A photodiode is a type of photodetector capable of converting light into either current or voltage, depending upon the mode of operation. The output of the photodetector is provided to a computer for processing of the data for providing a topographical image of the surface with atomic resolution. Currently used position-sensitive detectors are four-sectional that allows measuring not only longitudinal but torsion bending too.

3 Operating Modes of the AFM

The operating mode of the AFM can be classified into different types depending on the different measurement parameters used in sensing the interactive forces. Three basic fundamental operating modes of the AFM are: (1) contact mode; (2) non-contact mode; and (3) tapping mode.

3.1 Contact Mode

In contact mode the tip of the cantilever is placed in contact with the sample. This mode is the most common mode used in the AFM. The force acting on this mode is repulsive force in the order of 10^{-9}. The force is set by pusing the cantilever against the sample surface. In this mode the deflection of the cantilever is first sensed and than compared to some desired value of the deflection. Repulsion force F acting upon the tip is related to the cantilever deflection value x under Hooke's law: $F = -kx$, where k is cantilever spring constant. The spring constant value for

different cantilevers usually vary from 0.01 to several N/m. The deflection of the cantilever is converted into electrical signal DFL. The DFL signal is used to characterized the interaction force between the tip and the surface.

During contact mode when the atoms are gradually brought together, they first weakly attract each other. This attraction increases until the atoms are so close together that their electron clouds begin to repel each other electrostatically. This electrostatic repulsion progressively weakens the attractive force as the interatomic separation continues to decrease. The force goes to zero when the distance between the atoms reaches a couple of Angstroms, about the length of a chemical bond. When the total Van der Waals force becomes positive (repulsive), the atoms are in contact.

The slope of the Van der Waals curve is very steep in the repulsive or contact regime. As a result, the repulsive Van der Waals force balances almost any force that attempts to push the atoms closer together. In AFM this means that when the cantilever pushes the tip against the sample, the cantilever bends rather than forcing the tip atoms closer to the sample atoms. Two other forces are generally present during contact AFM operation: a capillary force exerted by the thin water layer often present in an ambient environment, and the force exerted by the cantilever itself. The capillary force arises when water surrounds the tip, applying a strong attractive force (about 10^{-8} N) that holds the tip in contact with the surface. The magnitude of the capillary force depends upon the tip-to-sample separation. The force exerted by the cantilever is like the force of a compressed spring. The magnitude and sign (repulsive or attractive) of the cantilever force depends upon the deflection of the cantilever and upon its spring constant.

As long as the tip is in contact with the sample, the capillary force should be constant because the distance between the tip and the sample is virtually incompressible. It is assumed that the water layer is reasonably homogeneous. The variable force in contact AFM is the force exerted by the cantilever. The total force that the tip exerts on the sample is the sum of the capillary plus cantilever forces, and must be balanced by the repulsive Van der Waals force for contact AFM. The magnitude of the total force exerted on the sample varies from 10^{-8} to the more typical operating range of $10^{-7}$to 10^{-6}. Most AFMs detect the position of the cantilever with optical techniques. In the most common scheme, a laser beam bounces off the back of the cantilever onto a position-sensitive photodetector (PSPD). As the cantilever bends, the position of the laser beam on the detector shifts. The PSPD itself can measure displacements of light as small as 10 Å. The ratio of the path length between the cantilever and the detector to the length of the cantilever itself produces a mechanical amplification. As a result, the system can detect sub-Angstrom vertical movement of the cantilever tip.

If the deflection of the cantilever is not matched with the predefined value of the deflection a voltage across the positioning unit of the AFM is applied to raise or lower the sample relative to the cantilever to restore the desired value of deflection. The voltage that the feedback amplifier applies to the positioning unit is a measure of the height of features on the sample surface. The predefined value of the cantilever deflection depends on operating modes. Two types of modes are used in

contact mode atomic force microscopy, (a) constant force mode; and (b) constant height mode. In constant force mode the force between the tip and sample remains fixed. This means that the deflection of the cantilever remains fixed. By maintaining a constant cantilever deflection (using the feedback loops) the force between the probe and the sample remains constant and an image of the surface is obtained. In this mode vertical deflection, i.e. the control voltage applied to Z electrode is measured. The vertical deflection is used to plot the surface topography. The advantage of the constant force mode is that this method allows to measure the surface topography with high resolution. Constant force mode is good for rough samples, used in friction analysis.

Constant force mode also has some disadvantages. The scanning speed of the AFM in constant force mode is restricted by the response time of feedback system. The soft samples such as polymers and biological samples can be destroyed due to interaction between the sharp probe and sample. The local flexure of the soft sample surfaces may be varied. The existence of the substantial capillary forces between the probe and the sample can decrease the resolution as well.

During scanning at constant height mode the distance between the tip of the cantilever and sample remains fixed. The cantilever base moves at a constant height from the sample surface. In constant-height mode, the spatial variation of the cantilever deflection can be used directly to generate the topographic data set because the height of the scanner is fixed as it scans. The main advantage of the constant height mode is high scanning speeds. The scanning speed at constant height mode is restricted only by resonant frequency of the cantilever. Constant height mode also has some disadvantages. In constant height mode the samples are required to be sufficiently smooth. The soft sample can be destroyed because the tip is in direct contact with the surface of the sample.

The operation of the contact mode atomic force microscopy is described in Fig. 2 by force versus distance curve. The line in Fig. 2 indicates the position of the cantilever. The flat line indicates that the cantilever is away from the sample. When

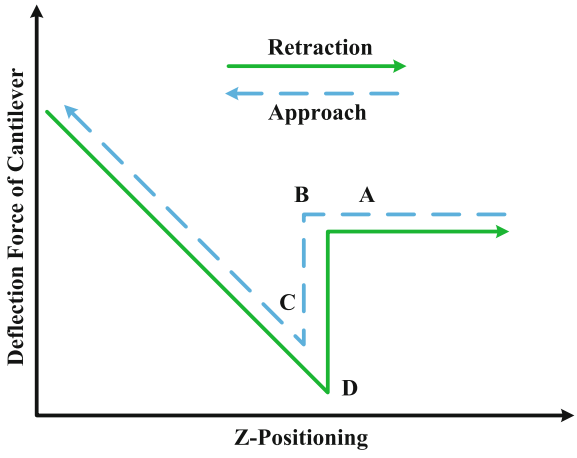

Fig. 2 Force versus distance curve in contact mode of the AFM imaging

cantilever approaches to the sample an attractive force is generated as shown in the point A. The point B indicates that the cantilever touches the sample surface. At point C the tip of the cantilever approaches further to the sample. At this point a repulsive force is generated to deflect the cantilever away from the sample. Again during the retraction period of the sample an attractive force is generated as shown by point D.

3.2 Non-contact Mode

In non-contact mode the probe does not contact the sample surface, but oscillates above the adsorbed fluid layer on the surface during scanning. This mode belongs to a family of modes which refers to the use of an oscillating cantilever. The non-contact mode is used in situations where tip contact might alter the sample in subtle ways. In this mode the tip hovers 50–150 Å above the sample surface. Normally the cantilever used in the non-contact mode has higher stiffness and high spring constant in the order of 10–100 Nm^{-1}. This is to avoid sticking to the sample surface. The forces between the tip and sample are quite low, on the order of pN (10^{-12} N). In this mode the cantilever is usually vibrated at its resonant frequency. The amplitude of the oscillation is kept less than 10 nm. Attractive Van der Waals force is acted between the tip and sample. This attractive force is substantially weaker than the forces used by contact mode. That is why the tip is given a small oscillation so that the AC detection methods can be used to detect the small forces between the tip and the sample. This is done by measuring the change in amplitude, phase, or frequency of the oscillating cantilever in response to force gradients from the sample. The detection scheme is based on measuring changes to the resonant frequency or amplitude of the cantilever due to its interaction with the sample.

The imaging resolution using non-contact mode depends of the distance between tip-sample. The tip-sample distance could be reduced further to achieve AFM images with high resolution. This can also be achieved in ultra-high vacuum (UHV) environment instead of in ambient condition. One of the limitation of operating AFM in ambient condition is that the tip-sample must be set at a larger distance to avoid tip from being trapped in the ambient water layer on the sample surface. Non-contact mode of the AFM is classified into two catagories, namely amplitude modulation (AM) and and frequency modulation (FM). In amplitude modulation mode an external signal with constant amplitude and phase is applied to the piezo actuator of the cantilever to excite and vibrate the cantilever. In this mode the amplitude of the cantilever is affected by the repulsive force acting on the tip during the operation. In frequency modulation mode the cantilever is always excited to vibrate at its resonance frequency. The advantage of the non-contact mode is that in this mode a very low force is exerted on the sample about 10^{-12} N. This extends the lifetime of the probe. The non-contact mode usually results in lower resolution; contaminant layer on surface can interfere with oscillation; usually need ultra high vacuum (UHV) to have best imaging.

3.3 Tapping Mode

The tapping mode is also called as semi-contact mode. This is an important mode in the AFM imaging. This is because this method allows for a high resolution imaging of sample surfaces that are easily damaged, loosely hold to their substrate, or difficult to image by other AFM techniques. In this mode the cantilever is oscillated at its resonant frequency. Tapping mode overcomes problems associated with friction, adhesion and other difficulties. This is done by alternatively placing the tip in contact with the surface to provide high resolution. Then the tip is lifted off surface to avoid dragging the tip across the sample. The oscillation of the cantilever in tapping mode is done using a piezoelectric crystal at the base of the cantilever. When the piezoelectric crystal comes into motion the cantilever oscillates. The amplitude of the oscillation of the cantilever is nearly in the order of 20 nm.

Selection of the optimal oscillation frequency is software-assisted and the force on the sample is automatically set and maintained at the lowest possible level. When the tip passes over a bump in the surface, the cantilever has less room to oscillate and the amplitude of oscillation decreases. Conversely, when the tip passes over a depression, the cantilever has more room to oscillate and the amplitude increases. The oscillation amplitude of the tip is measured by the detector and input to the controller electronics. The digital feedback loop then adjusts the tip-sample separation to maintain a constant amplitude and force on the sample.

During scanning, the vertically oscillating tip alternately contacts the surface and lifts off, generally at a frequency of 50,000–500,000 cycles per second. As the oscillating cantilever begins to intermittently contact the surface, the cantilever oscillation is necessarily reduced due to energy loss caused by the tip contacting the surface. The reduction in oscillation amplitude is used to identify and measure surface features.

Tapping mode inherently prevents the tip from sticking to the surface and causing damage during scanning. Unlike contact and non-contact modes, when the tip contacts the surface, it has sufficient oscillation amplitude to overcome the tip-sample adhesion forces. Also, the surface material is not pulled sideways by shear forces since the applied force is always vertical. Another advantage of the tapping mode technique is its large, linear operating range. This makes the vertical feedback system highly stable, allowing routine reproducible sample measurements.

Tapping mode operation in fluid has the same advantages as in the air or vacuum. However imaging in a fluid medium tends to damp the cantilever's normal resonant frequency. In this case, the entire fluid cell can be oscillated to drive the cantilever into oscillation. This is different from the tapping or non-contact operation in air or vacuum where the cantilever itself is oscillating. When an appropriate frequency is selected (usually in the range of 5,000–40,000 cycles per second), the amplitude of the cantilever will decrease when the tip begins to tap the sample, similar to Tapping Mode operation in air. Alternatively, the very soft cantilevers can be used to get the good results in fluid. The spring constant is typically 0.1 N/m compared to the tapping mode in air where the cantilever may be in the range of 1–100 N/m.

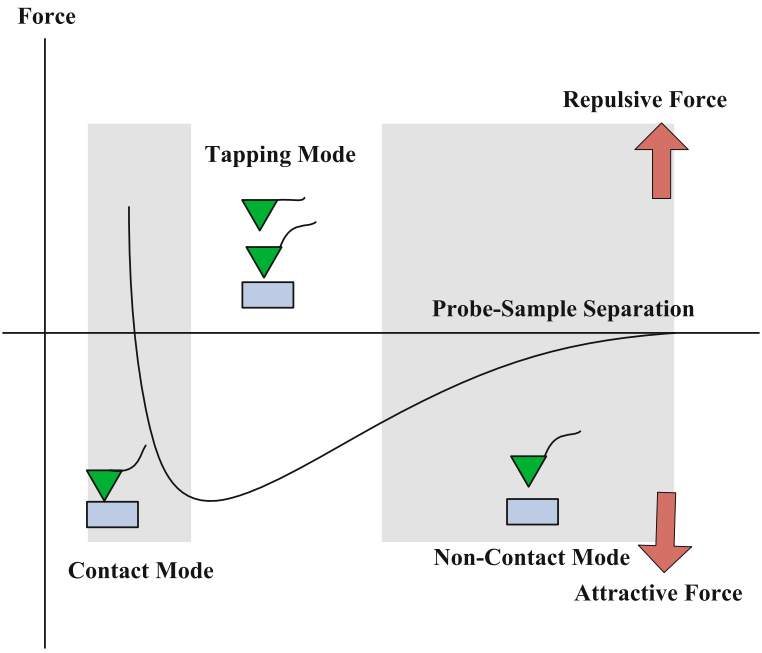

Fig. 3 Plot of force as a function of probe-sample separation

The description of three modes of the AFM in terms of force versus probe-sample distance is shown in Fig. 3. The dominant force acted at the short probe-sample distance in the AFM is the Van der Waals force. Long-range interactions such as capillary, electrostatic, magnetic are significant further away from the surface. During contact with the sample, the probe predominately experiences repulsive Van der Waals forces (contact mode). This leads to the tip deflection described previously. As the tip moves further away from the surface attractive Van der Waals forces are dominant (non-contact mode).

4 Piezoelectric Tube Scanner

Piezoelectric tube scanner (PTS) is an important feature of the AFM. The PTS is used as the positioning unit in the AFM. In most of the cases the PTS is usually fabricated from lead zirconium titanate, (PZT) by pressing together a powder, then sintering the material. The PTS is designed to achieve fine mechanical displacement in the x, y and z axis. Earlier before the invention of the PTS, the three dimensional positioning of the AFM was achieved by tripod scanner. But due to lateral bending, it causes cross coupling and low mechanical resonance which limit the scanning speed of the AFM. Later using the piezoelectricity technology, PTSs were made. The PTS works based on the theory of piezoelectric effect. About 100 years before

than the time of the invention of the STM, Curie brothers, Pierre Curie and Jacques Curie (1880) discovered the piezoelectric effect in the materials.

Piezoelectric materials are ceramics that change dimensions in response to an applied voltage and conversely, they develop an electrical potential in response to mechanical pressure. Piezoelectric materials are polycrystalline solids. Each of the crystals in a piezoelectric material has its own electric dipole moment. These dipole moments are responsible to move the piezo in response to an applied voltage. The dipole moments within the scanner are randomly aligned after sintering. The ability of the scanner to move depends on the align of the dipole. If the dipole moments are not aligned, the scanner has almost no ability to move. The align of the dipole moment is done by using a process called poling.

The process of poling in the scanner is done at 200 °C to free the dipoles. At this moment a direct current voltage source is applied. It takes few hours to align the dipoles. After the aligning process the scanner is cooled to freeze the dipoles into their aligned state. Then electrodes are attached to the outside of the tube, segmenting it electrically into vertical quarters, for $+x$, $+y$, $-x$, and $-y$ travel. The electrode in the z direction of the scanner is attached in the center of the scanner. A typical illustration of a PTS is presented in Fig. 4.

The PTS given in Fig. 4 shows that the PTS is typically consists of a cylindrical tube made of radially poled piezoelectric materials. The PTS is fixed at one end and free at other end. The PTS is segmented into four equal size electrodes. The electrodes are marked as +X, −X, +Y in the figure. Another electrode is not marked in the picture because the electrode is at the opposite end of the figure. The top part of the electrode is unsegmented. Usually a sample holder is placed on the top of the scanner to hold the sample.

Alternating voltages are applied to the $+x$ and $-x$ electrodes of the scanner. The application of this voltage induces strain into the tube which causes it to bend back and forth in the lateral, i.e. the x direction. Similar method is used to apply voltage in the y direction of the scanner. The expansion and contraction of the PTS depends on the polarity of the applied voltage with respect to the polling direction of the material. The PTS expands when the polarity of the applied voltage coincides with the polling direction. The PTS contracts when the the polarity of the applied voltage opposite with the polling direction. Voltages applied to the z electrode cause the scanner to extend or contract vertically. The displacement of the scanner is measured by using sensors. In most of the cases capacitive sensors are used to measure the displacement of the scanner. The reason for using capacitive sensors is their high speed response.

The maximum scan size of the PTS depends on many factors. This includes the length of the scanner tube, the diameter of the tube, its wall thickness, and the strain coefficients of the particular piezoelectric ceramic from which it is fabricated. Typically the PTS can scan from tens of angstroms to over 100 μ in the lateral and longitudinal direction. In the vertical direction it can scan from the sub-angstrom range to about 10 μ. One of the PTS used in this thesis is illustrated in Fig. 5. In this thesis we have used three scanners. We started our experiments with one scanner first. Then after the damage of first scanner we have used a second scanner and ordered a new scanner. Few works of this thesis is done using new scanner as well.

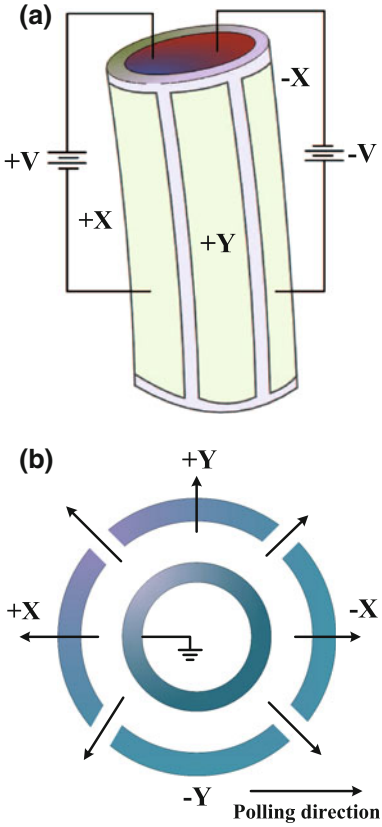

Fig. 4 A typical illustration of a piezoelectric tube scanner. **a** Side view and **b** top view

Fig. 5 A typical piezoelectric tube scanner

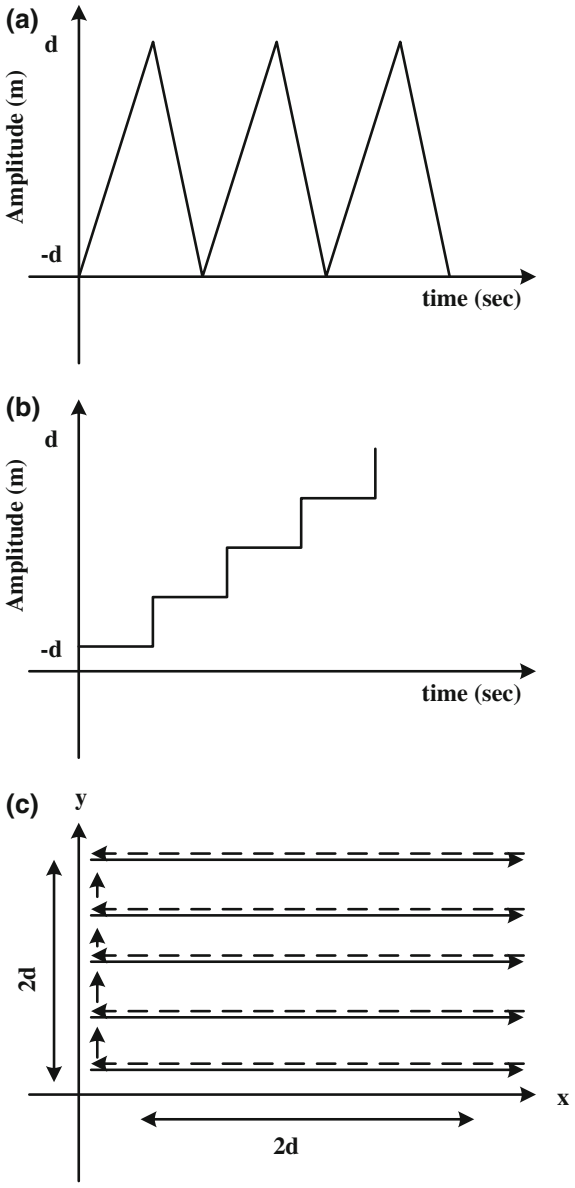

Fig. 6 Raster scanning method in AFM imaging. **a** Triangular signal uses in the *x*-axis, **b** staircase signal uses in the *y*-axis and **c** raster scanning method

In most of the cases the scanning operation in the AFM is performed by using raster scanning pattern. The raster scanning is performed by moving the PTS in forward and backward direction along the *x*-axis and moving the PTS in a small step in *y*-axis. This is done by applying triangular signal in the *x*-axis and staircase signal in the *y*-axis as shown in Fig. 6a, b. When the triangular signal is applied to *x*-axis and a staircase signal is applied to *y*-axis a raster scanning pattern is generated as shown in Fig. 6c.

5 Limiting Factors for High Speed Nanopositioning of the PTS

The imaging performance of the AFM often depends on the accurate positioning performance of the PTS. In order to achieve high quality images of the sample, accurate positioning of the PTS is required. The precision positioning of the PTS depends on the perfect tracking of the reference signals used in the AFM imaging. The high speed imaging performance of the AFM is limited due to some inherent properties of the PTS such as hysteresis, creep and induced vibration. In the following section these issues are further discussed.

5.1 Hysteresis

The term "hysteresis" is derived from an ancient Greek word "hustereia" meaning "deficiency" or "lagging behind". It was Sir James Alfred Ewing who describes the behavior of magnetic materials around 1890. Hysteresis is the dependence of a system which not only depends on its current environment but also on its past environment. This dependence arises because the system can be in more than one internal state. It is the lag in response exhibited by a body in reacting to changes in the forces.

Hysteresis can be represented graphically as a relation in the u–y plane. Figure 7 shows an example of an hysteresis relation along with a sample path. The loop

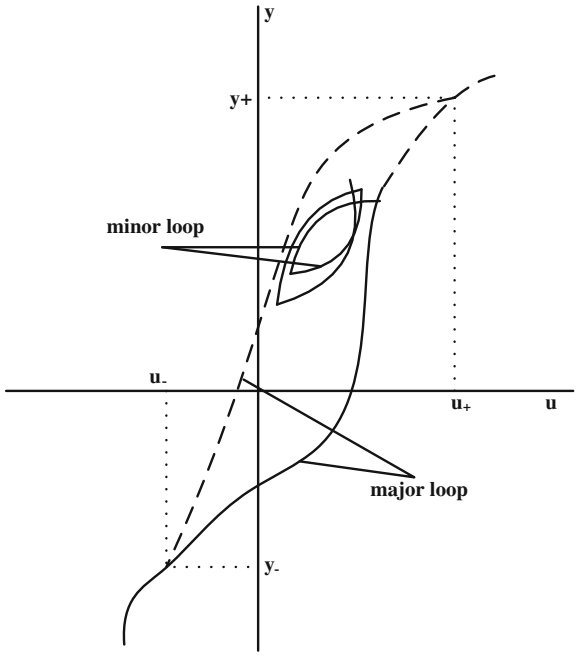

Fig. 7 Hysteresis terminology

which bounds the region where $y(t)$ is multi-valued is called major loop. The domain of input values u corresponding to this region is $[u_-, u_+]$; the range of outputs $[y_-, y_+]$. Each new segment of the output path in the u–y plane is called a branch. Successive branches which cross inside the major loop form minor loops.

Hysteresis arises in diverse applications such as magnetic hysteresis is a typical example. Hysteresis occurs in ferromagnetic materials and ferroelectric materials, as well as in the deformation of some materials (such as rubber bands and shape-memory alloys) in response to a varying force. The PTS is also fabricated from piezoelectric materials which are ferromagnetic in nature. The ferromagnetic nature of the PTS introduces hysteresis in the PTS. In most of the cases the PTS in the AFM is driven by a voltage source. This voltage source is responsible to introduce hysteresis in the PTS (Figs. 8 and 9).

The amount of the effect of the hysteresis in the PTS depends on the magnitude and frequency of the applied voltage signal. The effect of hysteresis increases with the increase of the magnitude and frequency of the applied voltage signal. Due to

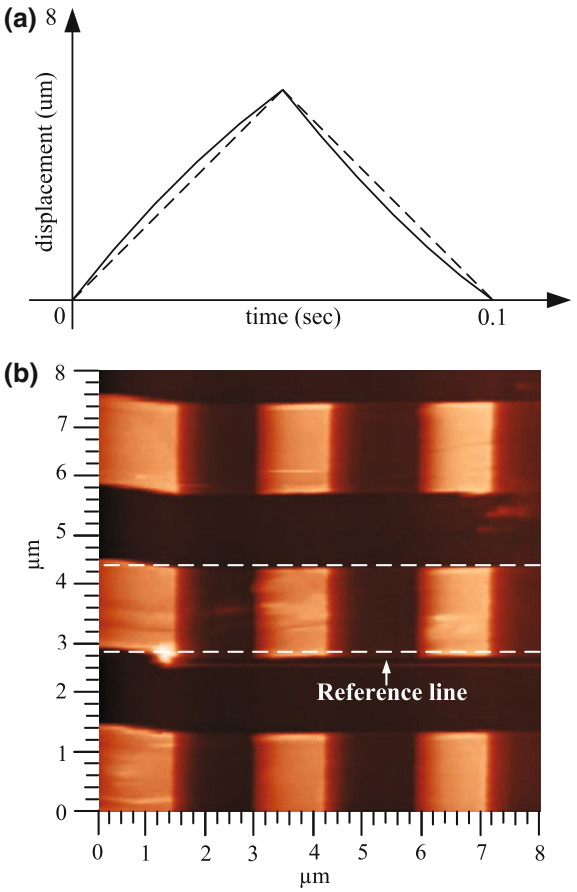

Fig. 8 Effect of hysteresis in imaging. **a** Measured scanners's displacements (*solid line*) for a 10 Hz triangular signal input (*dashed line*), **b** the resulting image of a calibration grating sample

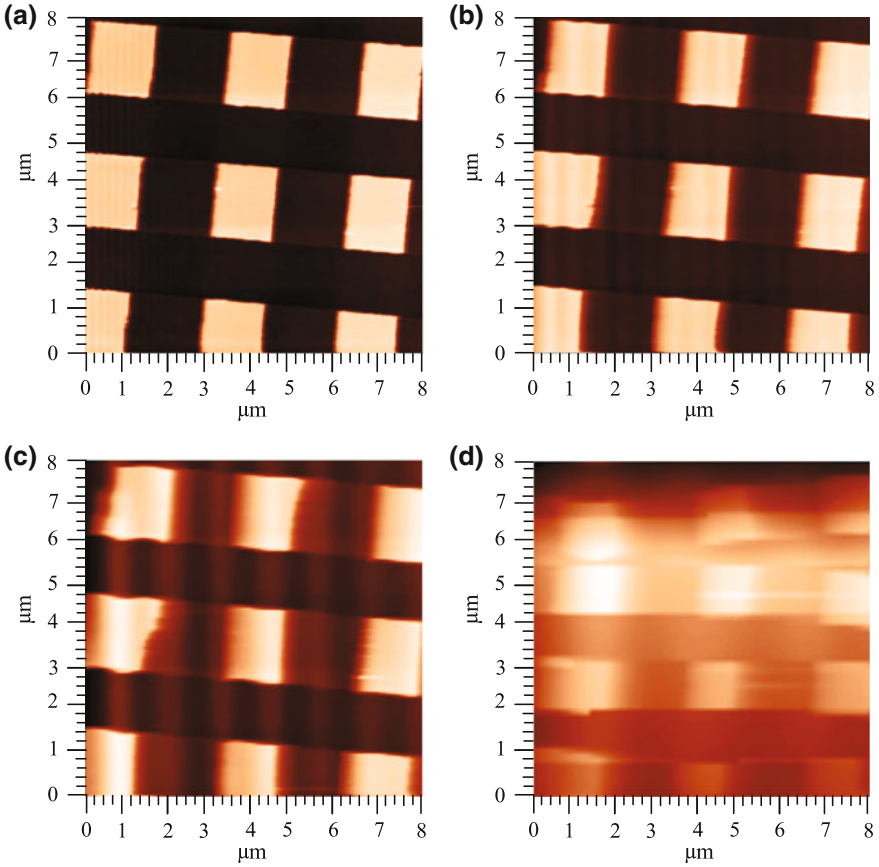

Fig. 9 Open-loop scanned images **a** 15.62 Hz **b** 31.25 Hz **c** 62.5 Hz **d** 125 Hz

the hysteresis effect distortion occurs in the scanned images of the AFM. As the fast axis of the PTS is driven by triangular signal, a deviation of 15 % can occur due to the hysteresis. This effect can be minimized by allowing scan only for low range. This limits the scanner ability for long range scan.

A number of researches available in the literature to model the hysteresis. The most commonly presented hysteresis models can be summarised as follows: Electromechanical models [1], Preisach models [35], Prandtl-Ishlinskii (PI) models [2], Bouc-Wem models [34], Rate-dependent or rate-independent hysteresis models [5]. The compensation of the effect of hysteresis is important because this effect tends to deviate the PTS from accurate nanopositioning. One way to compensate for hysteresis is to model it as a nonlinear function and then eliminate it by cascading its inverse with piezoelectric tube actuator. Though it is useful for open-loop but it requires accurate modeling of the system to compensate hysteresis as it may change with the parameter variation. Current and charge sources can also be used to reduce

the hysteresis instead of voltage source. One of the disadvantages of using the charge source is that, it leads to drift and saturation problem which greatly reduce the range of piezoactuators.

Feedback control technique has also been applied to reduce the hysteresis. Integral or proportional integral (PI) controllers are used in most AFM systems because of their simplicity and ease of implementation. Another advantage of the use of the integral or PI controllers is that these controllers apply high gain at low frequency. This high gain of the integral controller results in reduction of the effect of hysteresis.

5.2 Creep

Piezoelectric creep effect is another major constrain for high speed nanopositioning of the PTS. The creep effect is mainly prominent at slow scanning rate. The creep effect distorts the generated images from the AFM. When a voltage signal is applied across the PTS to move the piezo in three direction, the piezo continuous to displace even after the removal of the induced voltage. This generates the creep effect in the PTS. The creep effect can be minimized by allowing sufficient amount of time.

5.3 Induced Vibration

The X axis of the PTS is actuated by using a triangular signal. The triangular signal contains all odd harmonics of its fundamental frequency. When the PTS is actuated using triangular signal, the odd harmonics of the triangular signal excite the mechanical resonant mode of the PTS. This hampers the tracking accuracy of the PTS. The effect of the induced vibration in AFM imaging is presented in Fig. 25. The comparison shows that the generated images are more distorted at high frequencies as compared to the low scanning speeds.

6 Background

Different approaches [4, 10, 50, 51, 54, 55] to improve the tracking accuracy of nanopositioners can be categorized into two groups, (a) open-loop and (b) closed-loop control. The open-loop control techniques [16] are of interest as they are capable of providing a bandwidth close to the first resonance mode of scanners. The performance of the open-loop control technique depends on accurate system modelling. Two types of nanopositioners are used in SPM systems (a) scan-by-sample and (b) scan-by-head. The dynamics of scan-by-sample scanners change due to the

load change and the dynamics of scan-by-head nanopositioners change due to environmental factors such as outside temperature and humidity.

Feedback-linearized inverse feed-forward methods [36] are designed for reducing vibration in a scanner. The inversion technique can provide a closed-loop bandwidth near or greater than the resonance frequency if the resonance frequency of the PTS remains fixed. The resonance frequency of the scanner does not remain fixed but rather changes with the changing loads on the scanner. A high gain inversion-based feedback controller can make the closed-loop system unstable if the resonance frequency of the scanner changes.

Feedback controllers can provide robustness against the changes in the dynamics of the plant [10, 17–22, 50, 51, 54]. Most commercial SPM systems use integral or proportional integral (PI) controllers because of their simplicity and ease of implementation. One of the drawbacks of using integral controllers in nanopositioning applications is the loss of performance with the changes in plant dynamics. The bandwidth of integral controllers for nanopositioners is limited to $2\omega\xi$, where ω and ξ are the first resonance frequency and damping constant of nanopositioners [26].

Negative imaginary (NI) controllers [46] such as resonant controllers [22], positive position feedback (PPF) controllers [39], integral resonant controllers (IRCs) [29] are designed to improve the tracking performance of integral controllers for nanopositioners. By definition NI systems are stable systems with an equal number of inputs and outputs. A transfer function $G(s)$ is said to be NI if $j[G(j\omega) - G^*(j\omega)] \geq 0$ for all $\omega \in (0, \infty)$ [45]. For a SISO NI system $G(s)$, this is equivalent to the phase condition $\angle G(j\omega) \in [-\pi, 0]$ for all $\omega \in (0, \infty)$ [46]. The positive feedback interconnection between two NI systems $M_1(s)$ and $M_2(s)$ is stable if $|M_1(0)||M_2(0)| < 1$ and one of the system is strictly NI. A transfer function $G(s)$ is said to be strictly negative-imaginary if $j[G(j\omega) - G^*(j\omega)] > 0$ for all $\omega \in (0, \infty)$ [45].

The improvement in performance of nanopostioners using integral controllers is achieved by providing additional damping to the resonant modes of nanopositioners. The motivation to use NI damping controllers to improve the tracking performance of integral controllers is their robustness against the changes in plant dynamics [29]. The IRCs and PPF controllers are low pass controllers. The closed-loop system between scanners and the IRCs and PPF controllers may result in low gain and phase margin due to the low pass nature of the controllers. The resonant controllers are known for providing excellent damping of resonant modes of scanners with large gain and phase margin due to their high pass nature [47]. The high pass nature of resonant controllers may result in high frequency sensor noise which limits the use of the resonant controllers for PTSs.

Passive damping controller such as velocity feedback controllers [6] are also designed to damp the first resonant mode of the scanner. A linear system $P(s)$ is said to be passive if $\mathrm{Re}[P(j\omega)] \geq 0$ for all $\omega > (0, \infty)$ [45]. If a square transfer function matrix $P(s)$ is passive then it follows that $P(j\omega) + P^*(j\omega) \geq 0$, for all $\omega \in \mathbb{R}$ such that $s = j\omega$ is not a pole of $P(s)$ [46] where $P^*(j\omega)$ is the complex conjugate transpose of the matrix $P(j\omega)$. If $P(s)$ is a single-input single-output (SISO) passive transfer function, then, this is equivalent to the phase condition $\angle P(j\omega) \in [-\pi/2, \pi/2]$ for all $\omega > (0, \infty)$. The motivations to design passive damping

controllers for piezo scanners are their band pass nature and robustness against the changes in plant dynamics. The bandpass nature of the passive damping controller for piezo scanner results in large gain and phase margin.

Passive and NI systems are of interest because of their many practical applications, e.g., lightly damped flexible structures with collocated velocity sensors and force actuators [6, 46] and collocated position sensors and force actuators. The term collocated refers to the fact that the sensors and the actuators have the same location and same direction [48]. A guarantee of the closed-loop stability between systems with collocated velocity sensors and force actuators and passive controllers can be established using the passivity theorem [6].

However, in practice the transfer function matrix between the force actuators and position sensors of piezo scanners is neither NI nor passive [45]. Possible reasons for the PTS system not being NI or passive are delays in the sensor or actuator electronics or the collocation of the sensors and actuators may not be perfect. The electronic systems to which a PTS is connected can also add additional phase lag to the system. Therefore the finite-gain stability between the NI and passive damping controllers and piezo scanner can not be established by using NI and passivity theorem alone. A survey of control issues relating to damping based controllers for nanopositioners can be found in [23].

Some previous approaches to the design of damping controllers for piezoelectric tube scanners are based on a single-input single-output (SISO) approach [10, 11]. The axes of the PTSs are considered as independent decoupled single-input single-output systems. In practice, the axes of the nanopositioners are not independent SISO systems. There exists a strong cross coupling effect [25] between the lateral and longitudinal axes of the piezo scanner. Therefore, the design of the SISO controller for piezo scanners cannot guarantee the closed-loop stability.

Model based controllers such as H_∞ [52, 56, 57, 59, 60] controllers are designed for improving the damping and tracking performance of the scanner based on a SISO approach. The design methodology proposed in [52, 56, 59, 60] ignores the effect of cross coupling in the piezoelectric tube scanner.

The cross coupling [25] between the axes of the nanopositioner introduces a significant amount of error for high speed precision positioning. Due to the cross coupling effects the signal applied to one of the axes of the nanopositioner results in a displacement in both axes of the nanopositioner which affects the accuracy of the piezo scanners and if the magnitude of the cross coupling effect is high then the resulting images generated from AFMs are tilted as shown in Fig. 10.

New types of non-raster scanning methods such as spiral scanning [32], cycloid scanning [65], and Lissajous scanning [62] are proposed as alternatives to raster scanning for fast image scanning. The positioning accuracy for spiral scanning, cycloid scanning, and Lissajous scanning is limited due to the presence of cross coupling effects between the axes of scanners.

Design of multi-variable controllers for piezo scanner is of interest because of their ability to consider both the bandwidth and the cross coupling effect in the design process. A SISO damping based controller [29] achieves a bandwidth near to the first resonance frequency of the scanner with no guarantee of the reduction of

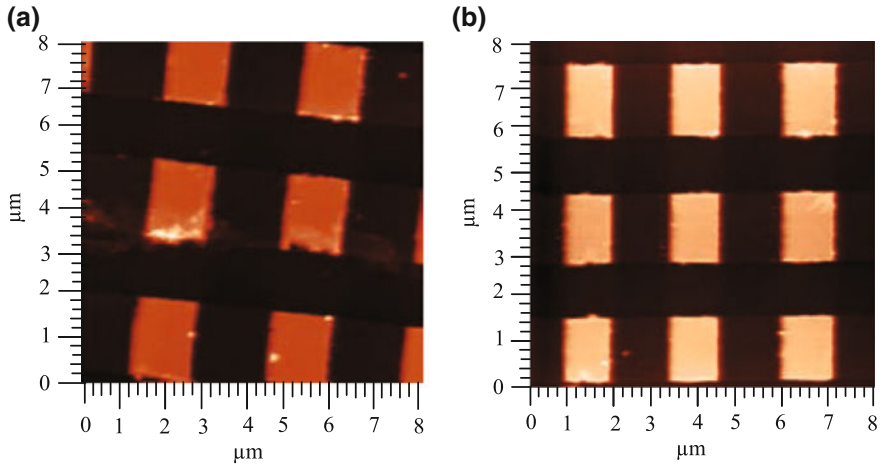

Fig. 10 Effect of cross coupling in surface imaging **a** scanned image with more cross coupling effect and **b** scanned image with less cross coupling effect

cross coupling effects between the axes of scanners. The SISO controller design has no provision to attenuate the cross coupling effects, while a MIMO controller gives a direct way to consider both the bandwidth and cross coupling effects between the axes of scanners.

A MIMO integral resonant controller is implemented [9] to speed up the performance of the AFM by considering the cross coupling effects in the lateral and longitudinal axis of the PTS as symmetric. The MIMO integral resonant controller (IRC) [9] was designed only to achieve maximum bandwidth. The design methodology of IRC [9] does not guarantee the reduction of the cross coupling effect between the axes of the PTS. Also, the IRC controller does not result in zero steady state error which in turn limit the ability of the IRCs to reduce the effect of nonlinearities in the form of hysteresis.

Minimizing the effect of hysteresis is one of the another challenge in designing tracking controller for atomic force microscopes. The tracking performance of PTS is largely affected due to the effect of hysteresis. A deviation of 15 % can occur between the forward and backward movements of the applied signal due to the effects of hysteresis [29, 39]. Integral controllers are designed because of their ability to compensate the effect of hysteresis. The high gain of the integral controller forces the system to track. This reduces the effect of hysteresis at low frequencies. Although the use of integral controller reduces the effect of hysteresis, however, a great challenge with the integral controller is their low closed-loop bandwidth. Current and charge sources [28] can be possible solution instead of voltage sources to reduce the effect of hysteresis in the PTSs. A fivefold reduction in the effects of hysteresis can be achieved using a charge source instead of a voltage source [10, 11]. However, the use of charge sources to drive piezo scanners introduces saturation problems.

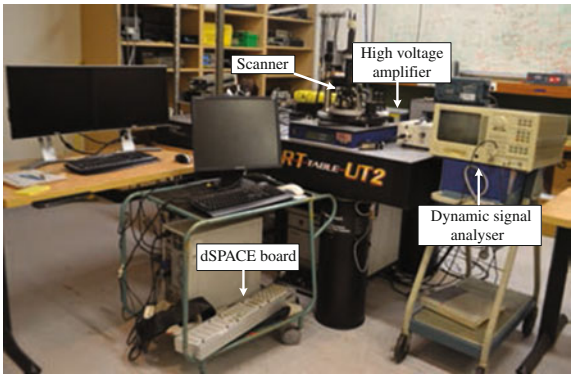

Fig. 11 Experimental setup used in the present work

7 Experimental Setup

The experimental setup consists of (i) an NT-MDT Ntegra scanning probe microscope which is configured to operate as an AFM, (ii) a piezoelectric tube scanner (PTS) which works as a nanopositioner in this paper, (iii) a dynamic signal analyzer (DSA) to measure the frequency response of the PTS at various frequencies of sinusoid signals, (iv) a high voltage amplifier (HVA) with a gain of 15 to apply voltage to the PTS, (v) a signal access module (SAM) to allow direct access to the electrodes of the scanner, and (vi) a dSPACE board for implementing the controller on the nanopositioner as shown in Fig. 11. The experiments are performed at the University of New South Wales, Canberra, Australia.

8 System Identification

The controller design in this paper is based on the input-output data, i.e. the transfer function between the input and output only. The present work uses an experimental approach [27, 28, 39] to obtain a transfer function for the MIMO PTS lateral and longitudinal positioning system.

The transfer function of the MIMO PTS positioning system can be described by the following equation:

$$G(s) = [D_x, D_y]^T \left[\frac{1}{V_x}, \frac{1}{V_y}\right] \tag{1}$$

where $D_x(s)$ and $D_y(s)$ is the Laplace transform of the output voltage from the X and Y sensor attached with the PTS and $V_x(s)$ and $D_y(s)$ is the Laplace transform of the input voltage to the HVA for driving X and Y-axis of the piezo.

The above transfer function matrix in (1) has a state space realization of the following form:

$$\begin{aligned} \dot{x}(t) &= Ax(t) + Bu(t) \\ y(t) &= Cx(t) + Du(t) \end{aligned} \tag{2}$$

where u is the vector of the inputs to the HVA and y is the vector of the outputs from sensors.

Swept sine inputs of 100 mV rms were applied to the HVA to drive the piezoelectric scanner along the X and Y-axes from the dual channel DSA and the corresponding capacitive sensor responses were recorded. The following values of the A, B, C and D matrices of the above state space model are obtained by using the subspace based system identification method [42]:

$$A = \begin{bmatrix} -427.6 & -5583.6 & -1521.1 & 840.01 & -874.82 & 1074 \\ 4963.2 & -423.76 & -1040.6 & -1245.1 & -1828.2 & 1693.9 \\ 959.85 & 1010.9 & -690.68 & 5435.9 & 474.96 & 1528 \\ -587.17 & 1161.8 & -4395.2 & -508.85 & -2304.2 & -2166.5 \\ -102.38 & 609.98 & 458.09 & 1351.9 & -946.65 & 149.69 \\ 251.11 & -708.42 & 71.644 & 1020.2 & -8.7797 & -1686.1 \end{bmatrix},$$

$$B = \begin{bmatrix} 1.6893 & 12.168 \\ 12.022 & 10.622 \\ -0.42926 & 2.964 \\ 8.0813 & -10.904 \\ -17.019 & 1.1707 \\ 0.58665 & 18.898 \end{bmatrix},$$

$$C = \begin{bmatrix} 9.0521 & 16.8150 & -27.5329 & 20.7708 & 35.2925 & 2.4245 \\ 25.6510 & 19.0371 & 30.2869 & -16.1956 & 6.4775 & -58.5076 \end{bmatrix},$$

$$D = \begin{bmatrix} 0 & 0 \\ 0 & 0 \end{bmatrix}.$$

The MIMO system identification process is done to capture first resonant mode of the PTS with low order model and the matching between the MIMO measured data and the identified model is given in Fig. 12. The MIMO identified model captures the first resonant mode of the measured MIMO data. The phase responses of the MIMO identified model is matched with the phases of the MIMO measured data at low frequencies whereas at high frequencies there is a slight difference between the phases of the measured data and the identified model.

The order of the identified model can be separated as follows: The first four orders of the identified model are used to capture the first resonant mode of the scanner in the X- and Y-axis and the rest of the orders of the identified model are representing all other dynamics of the system including delays.

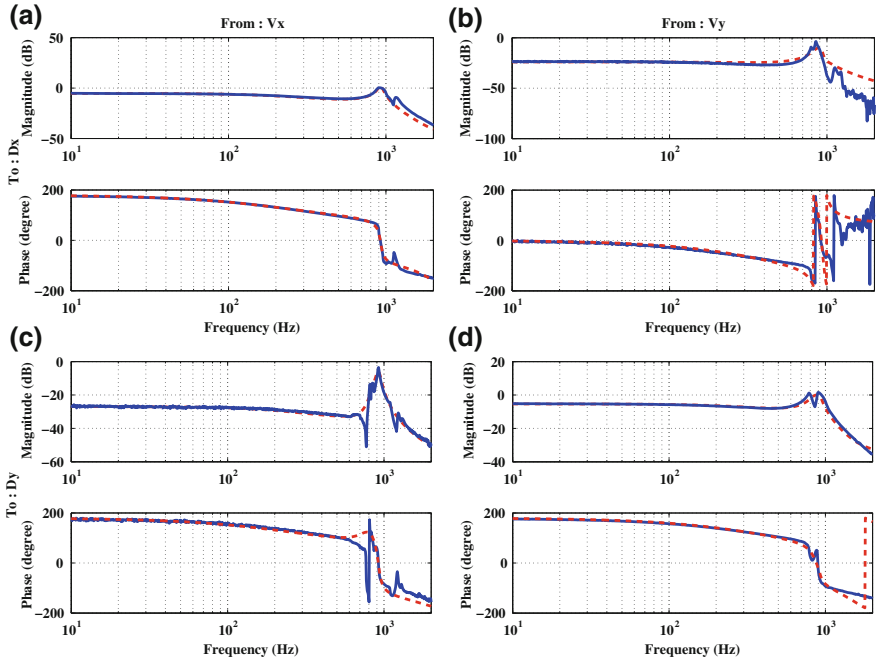

Fig. 12 Open-loop frequency response relating the inputs $[V_x, V_y]^T$ and the outputs $[D_x, D_y]^T$. The *solid line* (–) represents the measured frequency response and the *dashed line* (- -) represents the identified model frequency response. **a** Magnitude frequency response from Vx to Dx, **b** magnitude frequency response from Vy to Dx, **c** magnitude frequency response from Vx to Dy, and **d** magnitude frequency response from Vy to Dx

9 Controller Design

As previously discussed, the PTS suffers from the problem of low mechanical resonance frequency, the first step of this work is to suppress the first resonant mode of the PTS. In order to damp the first resonant mode of the PTS, a MIMO passive damping controller is designed. This type controller is of interest because of its ability to avoid closed-loop instability due to the spill over effect of PTS at high frequencies [6]. The block diagram of the closed-loop system for damping the first resonant mode by using passive damping controller is given in Fig. 13 where $G(s)$ is the plant transfer function matrix, $H_{FB}(s)$ is the transfer function matrix of the passive damping controller, u_1, u_2 are reference signals and y_1, y_2 are sensor output signals. The transfer function matrix of the MIMO passive damping controller is as follows:

$$H_{FB}(s) = -\frac{k_v s}{s^2 + 2\xi_v \omega_v s + \omega_v^2} \beta_{m\times m} \tag{3}$$

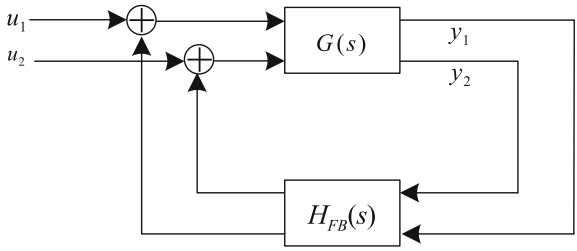

Fig. 13 Block diagram of the closed-loop system for first resonant mode damping of the PTS

where $k_v > 0$ is the gain of the controller, $\xi_v > 0$ and $\omega_v > 0$ are the damping constant and the frequency at which resonant mode needs to be damped. $\beta_{m\times m}$ is a matrix of order $m \times m$. Here, m is the number of inputs and the number of outputs of the system. For the PTS $\beta_{m\times m}$ is a 2×2 matrix.

The piezoelectric tube scanner used in this paper is a system with "mixed" negative-imaginary and small-gain properties Patra and Lanzon [44]. A system having "mixed" negative-imaginary and small-gain properties shows NI property [45] for some frequency range and small-gain property Patra and Lanzon [44] for other frequency range. The small-gain theorem states that, the feedback interconnection of two linear stable time invariant systems is stable if the product of the gains of the systems at each frequency is strictly less than one [38]. The design of the damping controller to damp the first resonant mode of the scanner in this paper is based on the mixed negative-imaginary and small-gain approach Patra and Lanzon [44].

The results of the "mixed" negative-imaginary and small-gain approach Patra and Lanzon [44] show that, the positive feedback interconnection as given in Fig. 13 between two strictly proper, causal and linear time invariant systems $G(s)$ and $H_{FB}(s)$ with mixed negative-imaginary and finite-gain properties bounded by gains k_1 and k_2, respectively is stable if the following conditions are satisfied:

(1) $\lim_{\omega\to\infty} G(j\omega)H_{FB}(j\omega) = 0$.
(2) The systems $G(s)$ and $H_{FB}(s)$ are bounded by gains k_1 and k_2, respectively such that, $k_1 > |G(0)|$, $k_2 > |H_{FB}(0)|$, and $k_1k_2 < 1$.
(3) In the intervals, $\omega \in [\omega_i, \omega_{i+1}]$, for $i = 1, 2, \ldots$, where $G(j\omega)$ does not have the NI property, both $G(j\omega)$ and $H_{FB}(j\omega)$ must be bounded by gains k_1 and k_2, i.e. $|G(j\omega)| < k_1$ and $|H_{FB}(j\omega)| < k_2$ for all $\omega \in [\omega_i, \omega_{i+1}]$, for $i = 1, 2, \ldots$.
(4) In the intervals, $\omega \in [\omega_p, \omega_{p+1}]$, for $p = 1, 2, \ldots$, where $G(j\omega)$ has the NI property and bounded by the gain k_1, $H_{FB}(j\omega)$ must either have NI property or be bounded by the gain k_2 or both.

In order to translate the mixed negative-imaginary and small-gain approach into a suitable design process for the piezoelectric tube scanner and the damping controller the following steps are carried out:

(i) Find the frequencies at which the system $G(s)$ has the NI property.
(ii) Select a gain k_1 such that at the frequencies where $G(s)$ does not have the NI property bounded by the gain k_1.
(iii) Make the gain k_1 as low as possible such that, $G(s)$ has either the NI property or has a finite-gain bounded by the gain k_1 or both at each frequency in order to achieve a large gain of the controller.
(iv) Find the frequencies at which $G(s)$ has only the NI property, only the finite-gain property bounded by the gain k_1 and both.
(v) Select the controller $H_{FB}(s)$ parameters and find the frequencies at which $H_{FB}(s)$ has the NI property.
(vi) Increase the gain of the controller $H_{FB}(s)$ to be as large as possible and select the gain k_2 for $H_{FB}(s)$ such that, (a) $k_1k_2 < 1$, (b) $H_{FB}(s)$ has only the NI property at the frequencies where $G(s)$ has only the NI property, (c) $H_{FB}(s)$ has only the finite-gain property bounded by the gain k_2 at the frequencies where $G(s)$ has only the finite-gain property bounded by the gain k_1, and (d) $H_{FB}(s)$ has either the NI or finite-gain properties bounded by k_2 at the frequencies where $G(s)$ has both the NI and finite-gain properties bounded by the gain k_1.

The values of the $H_{FB}(s)$ parameters obtained in the designed process is as follows: $\omega_v = 925.8021\,\text{Hz},\ \xi_v = 0.56,\ k_v = 7000$, and $\beta_{m\times m} = \begin{bmatrix} 0.66 & 0.005 \\ 0.005 & 0.66 \end{bmatrix}$.

9.1 Stability Analysis of the Interconnected System

The MIMO damping controller design is based on the maximum singular value of the plant $G(s)$ and the controller $H_{FB}(s)$. The maximum singular value plot of $G(s)$ and $H_{FB}(s)$ for positive frequencies are shown in Figs. 14 and 15, respectively. Selecting $k_1 = 1.37(> \bar{\sigma}(G(0)) = 0.5519)$ and $k_2 = 0.725(> \bar{\sigma}(H_{FB}(0)) = 0.0)$ respectively, the mixed properties between $G(s)$ and $H_{FB}(s)$ is shown in Fig. 16. One could also select different bounds so that, $k_1 > \bar{\sigma}(G(0))$ and $k_2 > \bar{\sigma}(H_{FB}(0))$ and the condition $k_1k_2 < 1$ is satisfied.

$G(s)$ has only the small-gain properties between 0 and 5817 rad/s and between 1.0638×10^4 rad/s and ∞. $G(s)$ has both small-gain and the negative-imaginary properties between $5,817$ rad/s and 1.0638×10^4 rad/s. $H_{FB}(s)$ has both negative-imaginary and small-gain properties between 0 to 5,817 rad/s and after that $H_{FB}(s)$ does not show the negative-imaginary properties. It can be seen that, at each frequency when $G(s)$ has the NI property, $H_{FB}(s)$ also has the NI property; and when $G(s)$ has the finite-gain property bounded by gain k_1, $H_{FB}(s)$ has the finite-gain property bounded by gain k_2 and $k_1k_2 < 1$. Hence, the closed-loop system corresponding to interconnection between $G(s)$ and $H_{FB}(s)$ is stable. Therefore, the conditions of Theorem 1 "mixed" negative-imaginary and small-gain approach Patra and Lanzon [44] are satisfied.

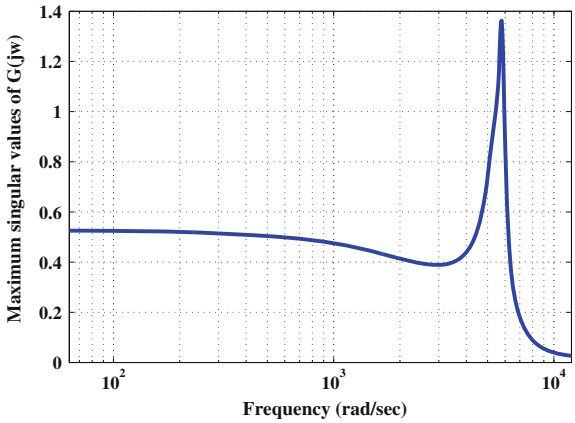

Fig. 14 Maximum singular value $(\bar{\sigma}(G(j\omega)))$ plot of $G(s)$

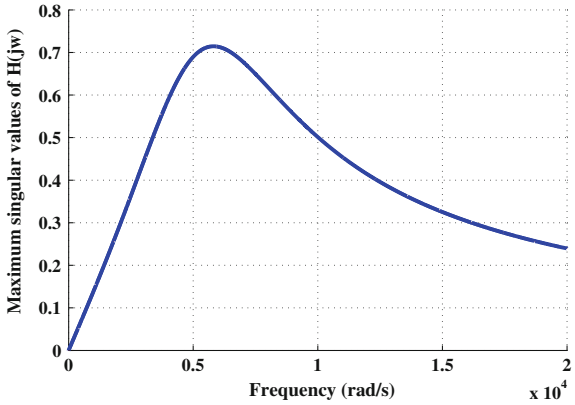

Fig. 15 Maximum singular value $(\bar{\sigma}(H(j\omega)))$ plot of $H_{FB}(s)$

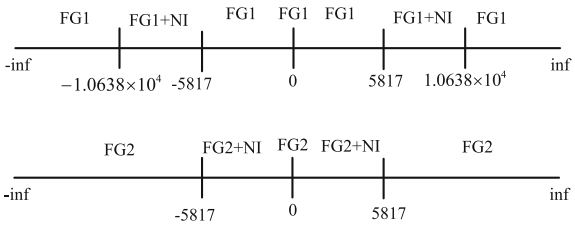

Fig. 16 Frequency intervals (*NI* negative imaginary, *FG1* finite-gain for system G, *FG2* finite-gain for system H_{FB})

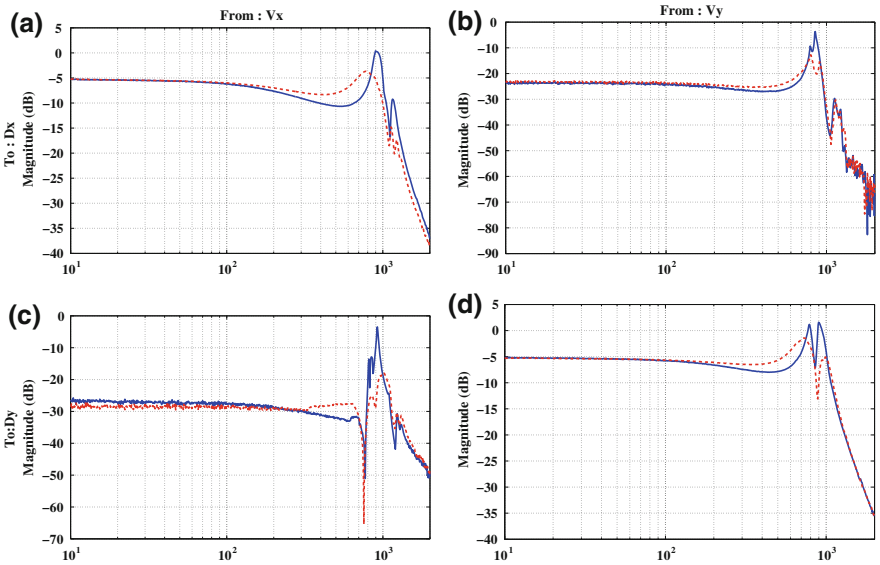

Fig. 17 Comparison of the magnitude frequency response relating the inputs $[V_x, V_y]^T$ and the outputs $[D_x, D_y]^T$. The *solid line* (–) represents the measured open-loop frequency response and the *dashed line* (- -) represents the measured closed-loop frequency response. **a** Magnitude frequency response from V_x to D_x, **b** magnitude frequency response from Vy to Dx, **c** magnitude frequency response from Vx to Dy, and **d** magnitude frequency response from Vy to Dx

The performance of the damping controller is examined by implementing the damping controller on an NT-MDT scan by sample piezoelectric tube scanner. The comparisons of the open- and closed-loop frequency responses by implementing the MIMO damping controller given in Fig. 17 show that the MIMO damping controller is able to provide 3.5 damping of the first resonant mode in the diagonal axes of the PTS.

9.2 Design of a Controller for Damping, Tracking and Cross Coupling Attenuation

The damping controller $H_{FB}(s)$ applied in the feedback path is able to provide a 3.5 damping of the first resonant mode in the diagonal axes of the PTS. Due to the low gain at low frequencies $H_{FB}(s)$ does not able to track the reference signal. In order to track the reference signal a high gain integral controller $C_{FF}(s) = \frac{k_i}{s}\alpha_{m\times m}$, where k_i is the gain of the integral controller and $\alpha_{m\times m}$ is matrix of order $m \times m$ is added in the feed-forward path of the closed-loop system as shown in Fig. 18.

The values of the parameters of the integral controller for the scheme shown in Fig. 18 is obtained to follow a reference transfer function. The values of the

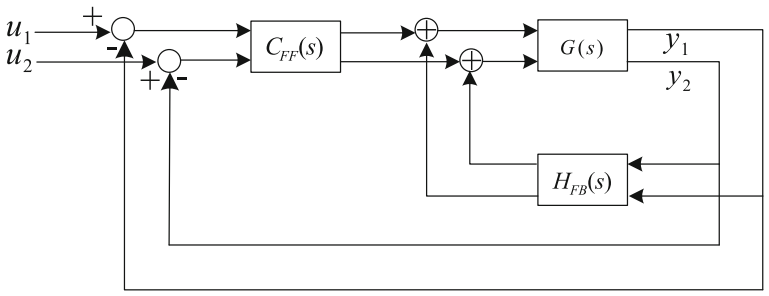

Fig. 18 Block diagram of the closed-loop system for resonant mode damping and tracking improvement

controller parameters are selected by minimizing H_2 norm of the difference between the reference and the actual closed-loop transfer function. The desired or the reference closed-loop transfer function is selected according to the aim of the design process, e.g., to achieve a desired bandwidth with small-cross coupling effects between the axes of the PTS. The desired closed-loop bandwidth is chosen from the observation of the system frequency response. The PTS used in this paper has its first resonant frequency at 918.3 Hz and after the first resonance frequency system rolls-off. It is expected the maximum bandwidth that can be achieved in the design is about 918.3 Hz. A closed-loop bandwidth higher than 918.3 Hz would require a high control input signals at high frequencies which in turn will increase the chances of adding high frequency noise signals.

The transfer function of the desired closed-loop system is chosen as

$$T(s) = \frac{1}{\tau s + 1}\begin{bmatrix} 1 & 0 \\ 0 & 1 \end{bmatrix} \tag{4}$$

where τ is selected to achieve desired bandwidth. In the present work τ is selected as $\frac{1}{918.3\,\mathrm{Hz}}$. The off-diagonal terms of $T(s)$ is zero which indicates that the aim of this MIMO controller design is to make the axes of the PTS independent. The transfer function of the actual closed-loop system of Fig. 18 is

$$T_{cl}(s) = \frac{G(s)C_{FF}(s)}{1 + G(s)(C_{FF}(s) - H_{FB}(s))}$$

The H_2 norm of the error transfer function between the desired $T(s)$ and the actual $T_{cl}(s)$ closed-loop transfer function is $\|E(s)\|_2 = \|T(s) - T_{cl}(s)\|_2$. A finite value of $\|E(s)\|_2$ guarantees the stability of the closed-loop system [19, 38]. The optimization was carried out by using simulated annealing algorithm. The optimization process took 5–8 min to obtain the values of the controller parameters. In the optimization process the initial values of the controller parameters are important for the convergence of the optimization.

In order to select the initial value of the parameters of the integral controller a single-input single-output (SISO) controller designed is performed first by considering each axis of the PTS as independent axis. The design of the SISO integral controller is done by using a root locus method. The initial values of the gain k_i and $\alpha_{m\times m}$ of the integral controller in the optimization process is selected $-1{,}000$ and $\begin{bmatrix} 1 & 0 \\ 0 & 1 \end{bmatrix}$. The maximum and minimum values of the controller parameters are also selected from the SISO design. The maximum value of the gain k_i and $\alpha_{m\times m}$ are selected as -800 and $\begin{bmatrix} 1.5 & 0.5 \\ 0.5 & 1.5 \end{bmatrix}$ and the minimum value of the gain k_i and $\alpha_{m\times m}$ are selected as $-1{,}800$ and $\begin{bmatrix} 0.5 & -0.1 \\ -0.1 & 0.5 \end{bmatrix}$. The convergence time of the optimization process depends on the difference between the minimum and maximum values of the parameters. The integral controller parameters achieved from the optimization process is $k_i = -1388.3$, $\alpha = \begin{bmatrix} 0.86 & 0.075 \\ -0.0587 & 1.15 \end{bmatrix}$.

At this point, it is straight forward to mention that the values of the controller parameters obtained in the optimization process are not for the global minimums of the objective function $\|E(s)\|_2$. A comparison of the open- and closed-loop magnitude frequency responses (MFRs) in the X and Y-axes of the PTS by implementing MIMO controller of the scheme of Fig. 18 is given in Fig. 19. The comparisons of the MFRs show that the closed-loop bandwidth achieved by the scheme of Fig. 18 is only 150 and 220 Hz in the X- and Y-axis of the scanner. The damping achieved by the proposed controller is 20 dB in the both axes of the PTS whereas the damping achieved by the integral controller is only 5 dB.

The MIMO integral controller was added with the MIMO damping controller as shown in Fig. 18 to improve the closed-loop tracking performance at low frequencies. However, due to the low gain of the integral controller at high frequencies, the resultant closed-loop system of Fig. 18 is only able to achieve a bandwidth of 150 and 220 Hz in the X- and Y-axis of the scanner which is still not high enough for the high speed nano-positioning of the PTS. Now, in order to increase the gain of the integral controller at high frequencies a high pass NI damping controller namely the resonant controller $H_{FB}(s)$ is added with the integral controller as shown in Fig. 20. The resonant controller is a high pass controller and adds gain where gain is lower due to the integral controller which in turns increase the bandwidth of the closed-loop system, whereas the other damping controllers such as the integral resonant controller or PPF controller are low pass in nature. The transfer function matrix of the resonant controller $H_{FF}(s)$ used in this paper has the following form:

$$H_{FF}(s) = \frac{s^2 + 2\xi_{\text{ff}}\omega_{\text{ff}}s}{s^2 + 2\xi_{\text{ff}}\omega_{\text{ff}}s + \omega_{\text{ff}}^2}\Omega_{m\times m} \tag{5}$$

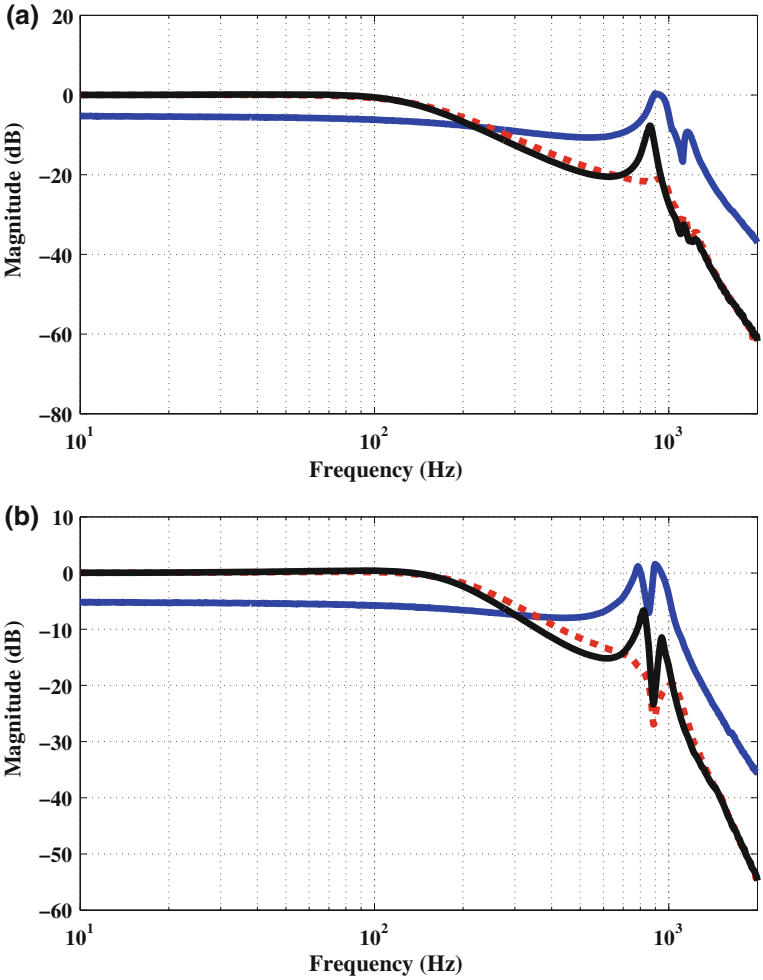

Fig. 19 Comparisons of the open- (the *blue solid line*) and closed-loop magnitude frequency responses obtained by using the MIMO integral controller (the black solid line) and the MIMO integral controller with MIMO damping controller (the *red dashed line*) in the X-axis (**a**) and Y-axis (**b**) of the scanner

where ξ_{ff} is the damping constant, ω_{ff} is the resonance frequency, and $\Omega_{m\times m}$ is a matrix of order $m \times m$. The resonant controller has a zero at the origin in its transfer function which means that the gain of the resonant controller at low frequencies is low. The value of ω_{ff} indicates the frequency where the gain of the resonant controller is maximum. Since the resonant controller is used only to increase the

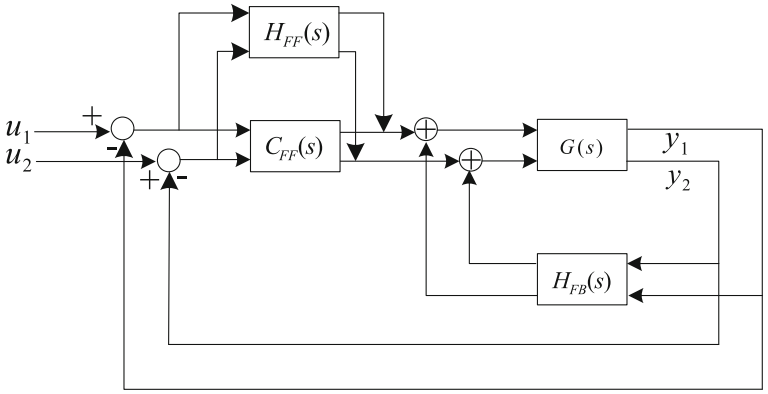

Fig. 20 Block diagram of the closed-loop system for resonant mode damping, tracking and bandwidth improvement

bandwidth, the damping constant ξ_{ff} should be high. A low value of damping constant ξ_{ff} introduces a notch and undesirable phase shift in the closed-loop.

The transfer function of the actual closed-loop system of Fig. 20 is

$$T_{close}(s) = \frac{G(s)(C_{FF}(s) + H_{FF}(s))}{1 + G(s)(C_{FF}(s) + H_{FF}(s) - H_{FB}(s))}$$

The values of the parameters of the integral controller and the resonant controller for the scheme of Fig. 20 are also obtained by minimizing H_2 norm of the difference between the desired $T(s)$ and the actual $T_{close}(s)$ closed-loop transfer functions. In a similar way discussed above, an optimization process by using simulated annealing algorithm is carried out to minimize $\|E(s)_{close}\|_2 = \|T(s) - T_{close}(s)\|_2$. The values of the integral controller and the resonant controller parameters obtained from the optimization process are as follows: $k_i = -1403.6$, $\alpha = \begin{bmatrix} 0.9 & 0.097 \\ -0.097 & 1.1 \end{bmatrix}$, $\xi_{ff} = 0.7$, $\omega_{ff} = 7,800$, $\Omega_{m\times m} = \begin{bmatrix} 1.8 & 0.1 \\ 0.005 & 1.15 \end{bmatrix}$.

In order to measure the performance of the proposed controller, a comparison of the magnitude frequency responses in the open- and closed-loop by implementing the proposed MIMO controller of Fig. 20 is given in Fig. 21. The closed-loop bandwidth increased in the X- and Y-axis are 850 and 775 Hz which is nearly equal to the desired aim of the design process. The amount of damping obtained in the closed-loop for the X- and Y-axis is about 4.5 dB which in turns also reduces the vibration of the scanner. The amount of reduction of cross coupling effects in the intermediate frequency region is higher as compared to low frequency region due to the low gain of the integral controller. However, the magnitude of the cross coupling effects at 10 Hz is less than −45 dB in the both axes which means that both axes can be treated as a independent SISO system.

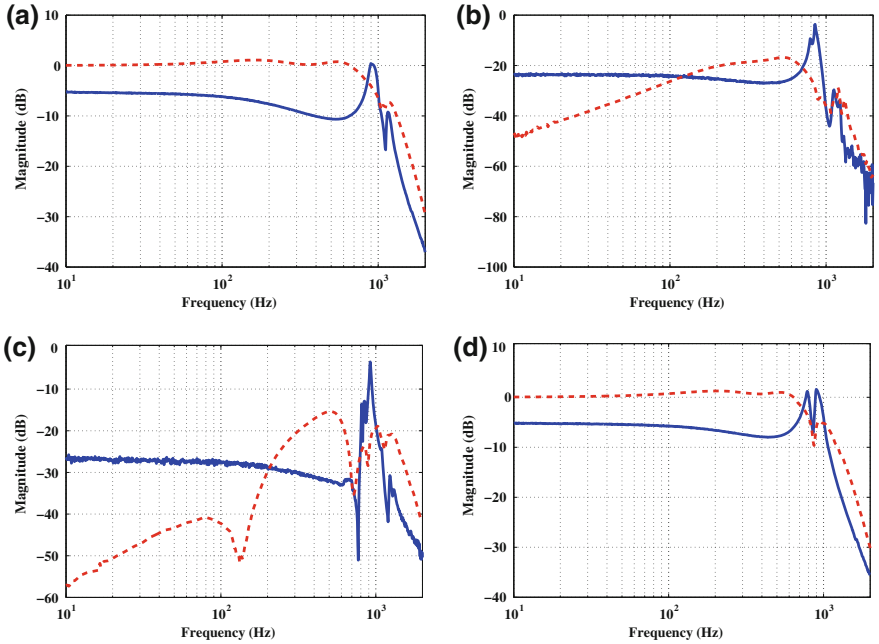

Fig. 21 Comparisons of the Open- and closed-loop magnitude frequency responses (MFRs) relating the inputs $[V_x, V_y]^T$ and the outputs $[D_x, D_y]^T$. The *solid line* (–) represents the measured open-loop MFR and the *dashed line* (- -) represents the measured closed-loop MFR by using the scheme shown in Fig. 20. **a** Magnitude frequency response from Vx to Dx, **b** magnitude frequency response from Vy to Dx, **c** magnitude frequency response from Vx to Dy, and **d** magnitude frequency response from Vy to Dx

9.3 Robustness of the Proposed Controller

The resonance frequency of the piezoelectric tube scanner changes with changing loads. The maximum resonance frequency occurs when there is no load on the scanner. Controllers design for high speed nano-positioning must be able to maintain the closed-loop stability against the changes in resonance frequency which are due to the load change on the scanner. In order to show the performance of the proposed controller in terms of load change on the scanner, a comparison of the open- and closed-loop magnitude frequency responses (MFRs) are given in Fig. 22. The closed-loop MFRs are taken by using the SISO and MIMO double resonant controller in the X-axis of the scanner. As the load on the scanner increases, the resonance frequency of the scanner in the X-axis starts moving towards left, i.e. the resonance frequency of the system decreases. In all cases the closed-loop system remains stable and provides a bandwidth near to the resonance frequency.

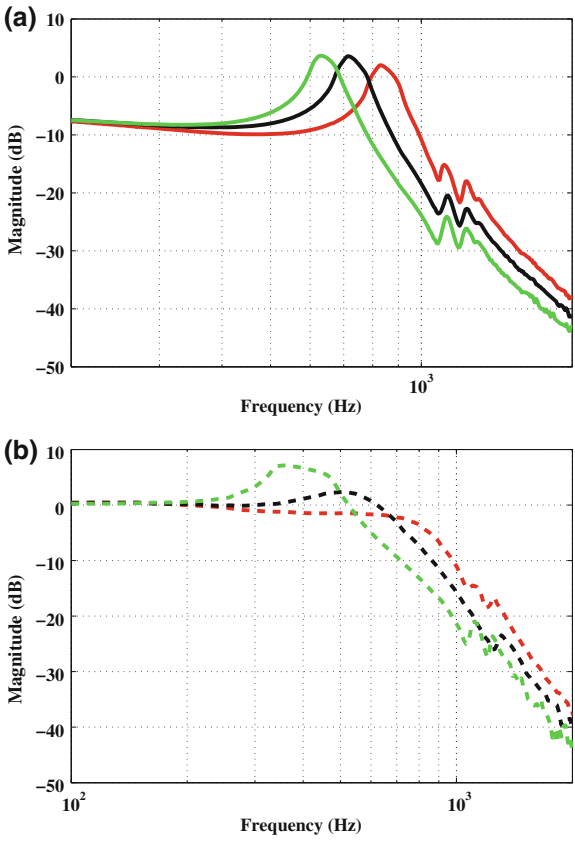

Fig. 22 Open-loop **a** and closed-loop **b** magnitude frequency responses (MFRs) of $G_{xx}(s)$ for different loads on the scanner. The same color in **a** and **b** represents the corresponding open- and closed-loop MFR

10 Image Scanning Results

After improving the lateral positioning of the PTS, investigation is done to evaluate the overall performance of the proposed controller for imaging capability. The experimental images presented in Figs. 23 and 24 show a comparison of the scanned images between the images obtained by implementing the built-in AFM PI controller and the proposed controller of Fig. 20, respectively. The current settings of the AFM used in this paper has no access to measure the gain of the built-in PI controller of the AFM. The software automatically select the gains of the PI controller during the imaging process.

The reference signals applied to the X and Y directions of the piezoelectric tube scanner are generated from the AFM software. The sample used for each imaging is a TGQ1 grating reference sample and the images are taken at scanning rates of 15.62, 31.25, 62.5, and 125 Hz. The structure of the sample is composed of number of squares. From the comparisons of the scanned images it can be observed that the blocks in the scanned images by means of the AFM PI controller are stretched to

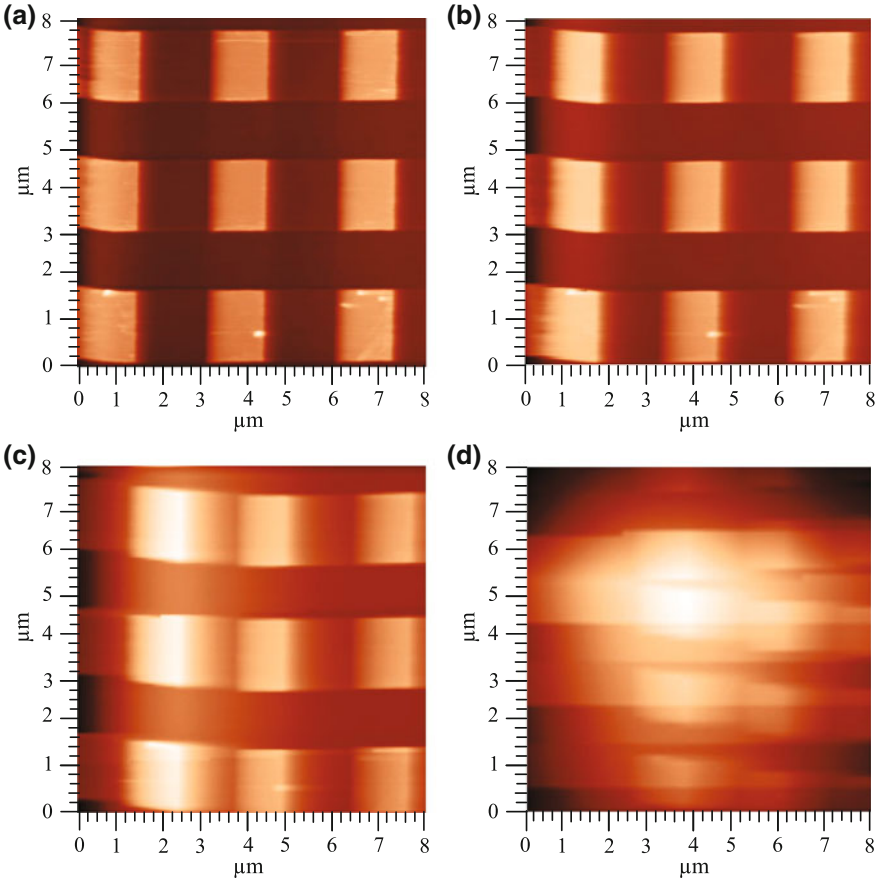

Fig. 23 Scanned images obtained by using the built-in PI controller of the AFM at **a** 15.62, **b** 31.25, **c** 62.5, and **d** 125

the left at low scanning rates. The proposed controller is able to show more uniform blocks at the low scanning frequencies. The scanned images obtained by using of the AFM PI controller are gradually blurred at higher scanning speed. Smother and sharper images are achieved at higher scanning speeds by using the designed controller.

Experimental images shown in Fig. 25 are obtained in open-loop. Note that, the scanned images obtained in open-loop are rotated which are due to the cross coupling effects between the axes of the scanner, whereas the scanned images obtained by using the proposed controller have less rotation. Although, the scanned images obtained by using built-in PI controller of the AFM have less rotation as compared to open-loop scanned images, however, the scanned images obtained by using built-in PI controller of the AFM have distortion at high frequencies which in turn limit the use of built-in PI controller of the AFM.

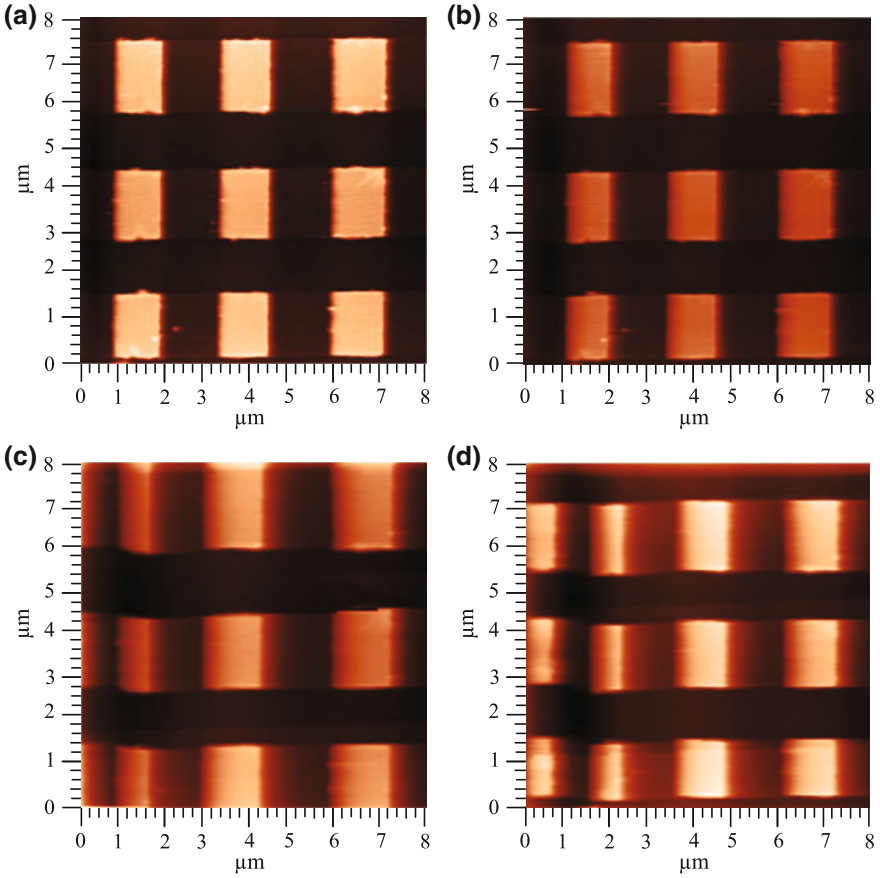

Fig. 24 Scanned images obtained by using the proposed controller at **a** 15.62, **b** 31.25, **c** 62.5, and **d** 125

The comparisons of the tracking performances between the open- and closed-loop for 8 µm × 8 µm area scanning given in Figs. 26 and 27, respectively show that, the proposed controller has a good command over tracking the reference signal at low frequencies whereas the open-loop system is not able to track the reference signal. Although the tracking error increases using the proposed controller at high scanning rate, however, the high closed-loop bandwidth of the proposed controller enables faster scanning as compared to the built-in PI controller of the AFM.

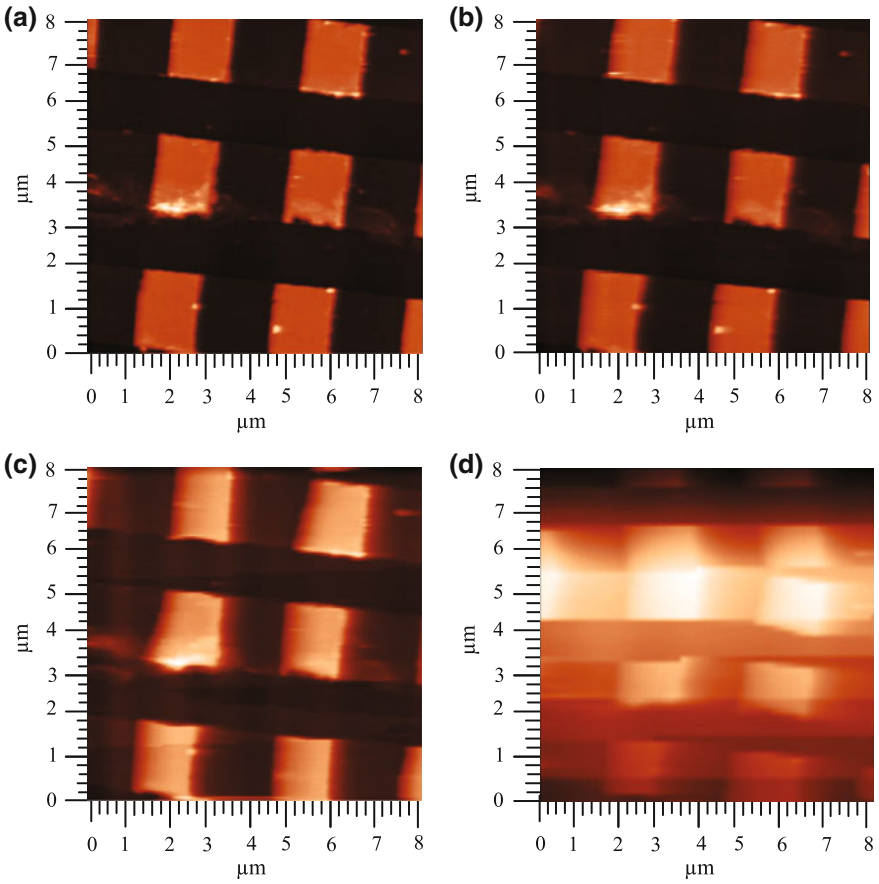

Fig. 25 Open-loop scanned images at **a** 15.62 Hz **b** 31.25 Hz **c** 62.5 Hz and **d** 125 Hz

11 Future Research Directions

This Chapter presents the design of a passive damping controller with a negative-imaginary controller for damping, tracking and cross coupling reduction of a nanopositioner to improve the high speed nanopositioning performance of an AFM. The design of the controller in this Chapter is presented for the X and Y-axis only. The future aim of this work is to incorporate the effect of Z-axis in the controller design.

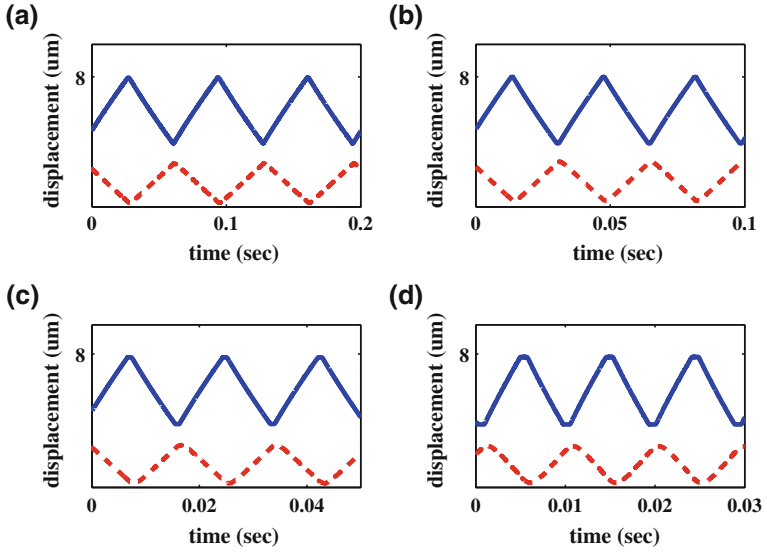

Fig. 26 Open-loop tracking performance at **a** 15.62 Hz, **b** 31.25 Hz, **c** 62.5 Hz and **d** 125 Hz. The *solid line* (–) represents the input signal and the *dashed line* (- -) represents the output signal

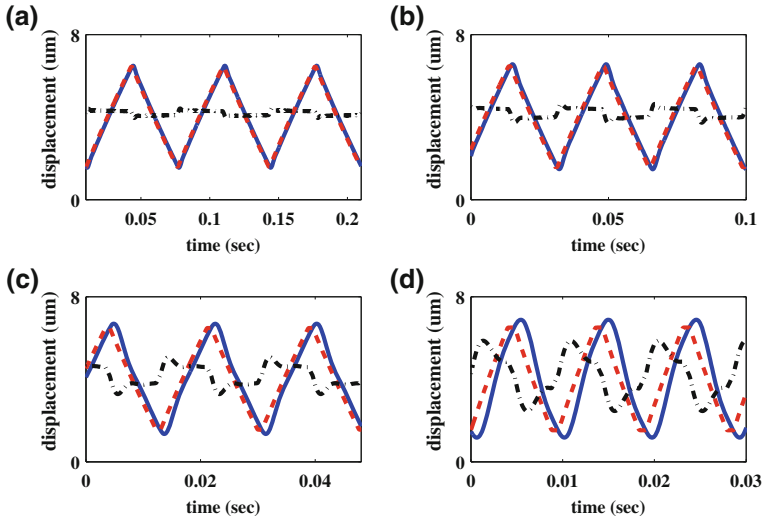

Fig. 27 Closed-loop tracking performance at **a** 15.62 Hz, **b** 31.25 Hz, **c** 62.5 Hz and **d** 125 Hz. The *solid line* (–) represents the input signal, the *dashed* (- -) *line* represents the output signal and the *dashed dot* (-.) *line* represents the error signal between the input and output signal

12 Conclusion

In this Chapter, both SISO and MIMO controllers along with an integral controller are implemented to improve the high speed nanopositioning performance of a PTS by damping the first resonant mode of the PTS, reducing the cross coupling effect between the axes of the PTS, and increasing the bandwidth. Compared to a standard integral controller the proposed controller is able to achieve five times higher bandwidth than the integral controller. The controller design presented in this paper is able to achieve a closed-loop bandwidth near to first resonance frequency of the scanner with a reduction of cross coupling effects. Comparisons of the experimental images presented in the paper obtained by using SISO and MIMO controller show that, the MIMO controller provides substantial improvement in image quality at high scanning rates as compared to the SISO controller.

References

1. Adriaens, H., De Koning, W., Banning, R.: Modeling piezoelectric actuators. IEEE/ASME Trans. Mechatron **5**(4), 331–341 (2000)
2. Al Janaideh, M., Rakheja, S., Su, C.Y.: An analytical generalized Prandtl-Ishlinskii model inversion for hysteresis compensation in micropositioning control. IEEE/ASME Trans. Mechatron. **16**(4), 734–744 (2011)
3. Amelio, S., Goldade, A.V., Rabe, U., Scherer, V., Bhushan, B.: Measurments of mechanical propoerties of ultra-thin diamond-like carbon coatings using atomic force acoustic microscopy. Thin Solid Films **392**, 75–84 (2001)
4. Ando T, Uchihashi T, Kodera N, Yamamoto D, Taniguchi M, Miyagi A, Yamashita H.: High-speed Atomic Force Microscopy for Nano-visualization of Biomolecular Processes. Wiley-VCH Verlag GmbH & Co. KGaA. pp. 277–296 (2009)
5. Ang WT, Garmon F, Khosla P, Riviere C.: Modeling rate-dependent hysteresis in piezoelectric actuators. In: Proceedings. 2003 IEEE/RSJ International Conference on Intelligent Robots and Systems, 2003 (IROS 2003), vol. 2, pp. 1975–1980 (2003)
6. Balas, M.J.: Direct velocity feedback control of large space structures. J. Guidance Control **2** (3), 252–253 (1979)
7. Barbara, P.F., Adams, D.M., O'Connor, D.B.: Characterization of organic thin film materials with near-field scanning optical microscopy. Annu. Rev. Mater. Sci. **29**, 433–469 (1999)
8. Betzig, E., Finn, P.L., Weiner, J.S.: Combined shear force and near-field scanning optical microscopy. Appl. Phys. Lett. **60**(20), 2484–2486 (1992)
9. Bhikkaji B, Yong YK, Mahmood IA, Moheimani SR.: Multivariable Control Designs for Piezoelectric Tubes. In: Proceedings of the 18th IFAC World Congress. August 28–September 2, vol. 18. Milano, Italy (2011)
10. Bhikkaji, B., Moheimani, S.O.: Integral Resonant Control of a Piezoelectric Tube Actuator for Fast Nanoscale Positioning. IEEE/ASME Trans. Mech. **13**(5), 530–537 (2008)
11. Bhikkaji, B., Ratnam, M., Fleming, A.J., Moheimani, S.O.R.: High-Performance Control of Piezoelectric Tube Scanners. IEEE Trans. Control Sys. Tech. **15**(5), 853–866 (2007)
12. Binnig, G., Rohrer, H.: American Physical Society; Scanning tunneling microscopy from birth to adolescence. Rev. Mod. Phys. **59**, 615–625 (1987)
13. Binnig, G., Smith, D.P.E.: Single-tube three-dimensional scanner for scanning tunneling microscopy. Rev. Sci. Instrum. **57**(8), 1688–1689 (1986)

14. Binnig, G., Quate, C.F., Gerber, C.: American Physical Society; Atomic Force Microscope. Phys. Rev. Lett. **56**, 930–933 (1986)
15. Binnig, G., Quate, C.F., Gerber, C.: American Physical Society; Atomic Force Microscope 2D and 3D. Phys. Rev. Lett. **56**, 930–933 (1986)
16. Croft D, Shedd G, Devasia S.: Creep, hysteresis, and vibration compensation for piezoactuators: atomic force microscopy application. In: Proceedings of American Control Conference, pp. 2123–2128 (2000)
17. Das SK, Pota HR, Petersen IR. Damping controller design for nanopositioners: a mixed passivity, negative-imaginary and small-gain approach. IEEE/ASME Trans. Mechatronics (2014, In Press)
18. Das SK, Pota HR, Petersen IR.: Multi-variable Double Resonant Controller for Fast Image Scanning of Atomic Force Microscope, Asian Control Conference, Washington, 23–26 June 2013, pp. 1–6. Istanbul (2013b)
19. Das SK, Pota HR, Petersen IR.: Multi-variable Resonant Controller for Fast Atomic Force Microscopy. In: Proceedings of Australian Control Conference. pp. 448–453. Sydney, Australia (2012b)
20. Das SK, Pota HR, Petersen IR.: Resonant control of atomic force microscope scanner: A "mixed" negative-imaginary and small-gain approach. In: American Control Conference, Washington, June 17–19, 2013, pp. 5476–5481. Washington DC, USA (2013a)
21. Das SK, Pota HR, Petersen IR.: Resonant controller design for a piezoelectric tube scanner: a mixed negative-imaginary and small-gain approach. IEEE Trans. Control Syst. Technol. (2013c, In Press)
22. Das SK, Pota HR, Petersen IR.: Resonant Controller for Fast Atomic Force Microscopy. In: Proceedings of Conference on Decision and Control. pp. 2471–2476. Maui, Hawaii (2012a)
23. Devasia, S., Eleftheriou, E., Moheimani, S.: A Survey of Control Issues in Nanopositioning. IEEE Trans. Control Sys. Tech. **15**(5), 802–823 (2007)
24. DeVecchio, D., Bhushan, B.: Use of a nanoscale Kelvin probe for detecting wear precursors. Rev. Sci. Instrum. **69**(10), 3618–3624 (1998)
25. El Rifai OM, Youcef-Toumi K.: Coupling in piezoelectric tube scanners used in scanning probe microscopes. In: Proceedings of American Control Conference the 2001, vol. 4, pp. 3251–3255 (2001)
26. Fleming, A.J.: Nanopositioning system with force feedback for high-performance tracking and vibration control. IEEE/ASME Trans. Mechatron. **15**(3), 433–447 (2010)
27. Fleming AJ, Leang KK.: Evaluation of charge drives for scanning probe microscope positioning stages. In: Proceedings of American Control Conference, pp. 2028–2033 (2008)
28. Fleming, A.J., Moheimani, S.O.R.: Precision current and charge amplifiers for driving highly capacitive piezoelectric loads. Electron. Lett. **39**(3), 282–284 (2003)
29. Fleming, A.J., Aphale, S.S., Moheimani, S.O.R.: A New Method for Robust Damping and Tracking Control of Scanning Probe Microscope Positioning Stages. IEEE Trans. Nanotechnology **9**(4), 438–448 (2010)
30. Hansma, P., Drake, B., Marti, O., Gould, S., Prater, C.: The scanning ion-conductance microscope. Science **243**(4891), 641–643 (1989)
31. Hartmann, U.: Magnetic force microscopy. Annu. Rev. Mater. Sci. **29**, 53–87 (1999)
32. Hung, S.K.: Spiral Scanning Method for Atomic Force Microscopy. J. Nanosci. Nanotechnol. **10**, 4511–4516 (2010)
33. Husser, O.E., Craston, D.H., Bard, A.J.: Scanning eletromechanical microscopy-high resolution deposition and etching materials. J. Electrochem. Soc. **136**, 3222–3229 (1989)
34. Ikhouane, F., Manosa, V., Rodellar, J.: Dynamic properties of the hysteretic Bouc-Wen model. Syst. Control Lett. **56**(3), 197–205 (2007)
35. Kuhnen, K., Krejci, P.: Compensation of complex hysteresis and creep effects in piezoelectrically actuated systems—a new Preisach modeling approach. IEEE Trans. Autom. Control **54**(3), 537–550 (2009)

36. Leang, K.K., Devasia, S.: Feedback-Linearized Inverse Feedforward for Creep, Hysteresis, and Vibration Compensation in AFM Piezoactuators. IEEE Trans. Control Syst. Technol. **15** (5), 927–935 (2007)
37. Lee, D.T., Pelz, J.P., Bhushan, B.: Instrumentation for direct, low frequency scanning capacitance microscopy, and analysis of position dependent stray capacitance. Rev. Sci. Instrum. **73**, 3523–3533 (2002)
38. Green M, Limebeer DJN.: Linear Robust Control. Prentice-Hall, NJ (1995)
39. Mahmood, I.A., Moheimani, S.O.R.: Making a commercial atomic force microscope more accurate and faster using positive position feedback control. Rev. of Sci. Instrum. **80**(6), 063705(1)–063705(8) (2009)
40. Majumdar, A.: Scanning thermal microscopy. Annu. Rev. Mater. Sci. **29**, 505–585 (1999)
41. Matey, J., Blanc, J.: Scanning capacitance microscopy. Annu. Rev. Mater. Sci. **57**, 1437–1444 (1999)
42. McKelvey, T., Akay, H., Ljung, L.: Subspace-based identification of infinite-dimensional multivariable systems from frequency-response data. Automatica **32**(6), 885–902 (1996)
43. Melitz, W., Shen, J., Kummel, A.C., Lee, S.: Kelvin probe force microscopy and its application. Surf. Sci. Rep. **66**(1), 1–27 (2011)
44. Patra, S., Lanzon, A.: Stability Analysis of Interconnected Systems With "Mixed" Negative-Imaginary and Small-Gain Properties. IEEE Trans. Autom. Control **56**(6), 1395–1400 (2011)
45. Petersen IR.: Negative imaginary systems theory in the robust control of highly resonant flexible structures. In: Australian Control Conference. Melbourne, Australia. pp. 1–6 (2011)
46. Petersen, I., Lanzon, A.: Feedback Control of Negative-Imaginary Systems. IEEE Control Sys. Mag. **30**(5), 54–72 (2010)
47. Pota H, Moheimani SR, Smith M.: Resonant controllers for flexible structures. In: Proceedings Conference of Decision and Control, vol. 1. pp. 631–636 (1999)
48. Pota, H., Reza Moheimani, S., Smith, M.: Resonant controller for smart structures. Smart Mater. Struct. **11**, 1–8 (2002)
49. Prater, C., Hansma, P., Tortonese, M., Quate, C.: Improved scanning ion-conductance microscope using microfabricated probes. Rev. Sci. Instrum. **62**(11), 2634–2638 (1991)
50. Ratnam M, Bhikkaji B, Fleming A, Moheimani S. PPF Control of a Piezoelectric Tube Scanner. In: 44th IEEE Conference on Decision and Control and European Control Conference, pp. 1168–1173 (2005)
51. Rost, M.J., vanBaarle, G.J.C., Katan, A.J., vanSpengen, W.M., Schakel, P., vanLoo, W.A., Oosterkamp, T.H., Frenken, J.W.M.: John Wiley and Sons Asia Pte Ltd; Video-rate scanning probe control challenges: setting the stage for a microscopy revolution. Asian J. Control **11**(2), 110–129 (2009)
52. Salapaka, S., Sebastian, A., Cleveland, J.P., Salapaka, M.V.: High bandwidth nano-positioner: A robust control approach. Rev. Sci. Instrum. **73**(9), 3232–3241 (2002)
53. Scherer, V., Arnold, W., Bhushan, B.: John Wiley & Sons, Ltd.; Lateral force microscopy using acoustic friction force microscopy. Surf. Interface Anal. **27**(5–6), 578–587 (1999)
54. Schitter G, Astrom KJ, DeMartini B, Fantner GE, Turner K, Thurner PJ, Hansma PK. Design and modeling of a high-speed scanner for atomic force microscopy. In: Proceedings of American Control Conference (2006)
55. Schitter G, Rost MJ. Scanning probe microscopy at video-rate. Mater. Today **11**(0), 40–48 (2008)
56. Schitter G, Stemmer A, Allgower F. Robust 2 DOF-control of a piezoelectric tube scanner for high speed atomic force microscopy. In: Proceedings of American Control Conference the 2003, vol. 5, pp. 3720–3725 (2003)
57. Schitter, G., Menold, P., Knapp, H.F., Allgöwer, F., Stemmer, A.: High performance feedback for fast scanning atomic force microscopes. Rev. Sci. Instrum. **8**, 72 (2001)
58. Schoenenberger, C., Alvarado, S.: Springer, Understanding magnetic force microscopy. Z. Phys. **80**(3), 373–383 (1990)

59. Sebastian A, Salapaka MV, Cleveland JP.: Robust control approach to atomic force microscopy. In: Proceedings of 42nd IEEE Conference on Decision and Control, vol. 4, pp. 3443–3444 (2003)
60. Sebastian, A., Salapaka, S.M.: Design methodologies for robust nano-positioning. IEEE Trans. on Control Sys. Tech. **13**(6), 868–876 (2005)
61. Stern, J.E., Terris, B., Mamin, H., Rugar, D.: Deposition and imaging of localized charge on insulator surfaces using a force microscope. Appl. Phys. Lett. **53**(26), 2717–2719 (1988)
62. Tuma, T., Lygeros, J., Kartik, V., Sebastian, A., Pantazi, A.: High-speed multiresolution scanning probe microscopy based on Lissajous scan trajectories. Nanotechnology **23**(18), 185501 (2012)
63. Williams, C., Wickramasinghe, H.: Scanning thermal profiler. Appl. Phys. Lett. **49**(23), 1587–1589 (1986)
64. Williams, C.C., Wickramasinghe, H.K.: Microscopy of chemical-potential variations on an atomic scale. Nature **344**, 317–319 (1990)
65. Yong YK, Moheimani SOR, Petersen IR. 2010. High-speed cycloid-scan atomic force microscopy. Nanotechnology 21(36)

Fault Diagnosis Algorithms by Combining Structural Graphs and PCA Approaches for Chemical Processes

Rafika El Harabi, Rahma Smaili and Mohamed Naceur Abdelkrim

Abstract This work presents a diagnosis algorithm that combines structural causal graphical model and nonlinear dynamic Principal Component Analysis (PCA) for nonlinear systems with coupled energies incorporate the chemical kinetics of an equilibrated reaction, heat and mass transport phenomena. Therein, a coupled Bond Graph (BG) model, as an integrated decision tool, is used for modeling purpose. A Signed Directed Graph (SDG) is then deduced. A fault detection step is later carried out by generating initial responses through causal paths between exogenous and measured variables. After that, the localization of the actual fault is performed based on a nonlinear PCA (NLPCA) and back/forward propagations on the SDG. Simulation results on a pilot reactor show that the physic-chemical defects such as matter leakage, thermal insulation, or appearance of secondary reaction or temperature runaway when a very exothermic reaction occurs, can be detected and isolated.

Keywords Structural graphs · PCA · Fault diagnosis · Chemical process

1 Introduction

The increasing diversity of products manufactured by chemical process industries has made it more and more common for these industries to use reactors, conduits and storage vessels in which hazardous substances are handled at elevated

R. El Harabi · R. Smaili (✉) · M.N. Abdelkrim
MACS, National Engineering School of Gabès, University of Gabès, 6029 Gabès, Tunisia
e-mail: rahma.smaili@gmail.com

R. El Harabi
e-mail: rafikaharabi@yahoo.fr

M.N. Abdelkrim
e-mail: naceur.abdelkrim@enig.rnu.tn

A.T. Azar and S. Vaidyanathan (eds.), *Chaos Modeling and Control Systems Design*,
Studies in Computational Intelligence 581, DOI 10.1007/978-3-319-13132-0_15

temperatures and/or pressures. In fact, accidents in such units caused either by material failure (such as crack in the storage vessels), operational mistakes (such as raising the pressures temperature/flow-rate beyond critical limits) and secondary events appear in chemical reactions (undesired secondary reactions, hazard event of thermal runaway…etc) can have serious-often catastrophic-consequences (see [1, 2, 5, 27] for wide overview). Fault Detection and Isolation (FDI) of chemical reactors is then a difficult task and their modelling is often complex and therefore less developed in the literature. It is this fact that has motivated our research in this paper.

The graphical modelling such as the bond graph tool becomes further significant in this case, because it is appropriate for multiphysics modelling of complex systems, as it is given in [6, 28] through node and arcs which represent a power transfer (effort-flow) within a system and the interaction of different phenomena (chemical, thermal and fluidic). Indeed, the multiport elements represent energy dissipation (R-element), storage (C-element), inertia (I-element), balance and continuity equations (0- and 1-junctions) or inter-domain coupling (TF transformer and GY gyrator elements). However, this tool can be used for residual generation and monitorability analysis of systems [22, 23]. Analytical Redundancy Relations (ARRs) are derived from the set of over-determined equations obtained from the structural system model. Hence, the ARR derivation from bond graphs incurs high computational costs for equation derivation and structural equivalence checking, and this method cannot be applied when unknown variables cannot be eliminated because of the presence of algebraic loops and nonlinear non-invertible constraints [24]. Although, some times component signs for monitoring and diagnosis should be determined. Unlike bond graph methodology, a signed directed graph becomes more adequate for this situation.

In this context, a SDG model captures both the information flow and the direction of effect (increase and decrease). Iri et al. [7] were the first to introduce SDG for modeling chemical processes. Recently, Maurya et al. [13] have proposed algorithms for the systematic development of SDGs and digraphs for various types of systems and gave methodologies for SDG analysis to predict initial and steady-state responses of system variables for deviations in exogenous variables from their nominal value for fault diagnosis. In fact, nodes in the SDG assume values of (0), (+) and (−) representing the nominal steady-state value, higher and lower than steady-state values, respectively. Directed arcs point from a cause node to its effect node. Arc signs associated with each directed arc can take values of (+) or (−) representing whether the cause and effect change in the same direction or opposite direction, respectively. Based upon the procedure for SDG-based analysis, this graph has been combined with many approaches like the Qualitative Trend Analysis (QTA) [14] to improve the isolability of faults, moreover, Vedam et al. have combined the PCA and the signed directed graph [29], where a fault detection is performed using PCA and a SDG model is involved to isolate the root causes.

After all in our previous works [25, 26], case studies show that SDG-based initial response analysis helps in fault diagnosis, for nonlinear systems, considerably.

The results can be further narrowed down by using steady-state measurements. It's shown also, that almost no quantitative information is required to develop the SDG model; the diagnosis resolution and performance are quite good. The reliability of SDG-based analysis and fault diagnosis results is yet dependent upon the correctness of the mathematical model from which the SDG or the qualitative equations are developed. Initial or steady-state responses obtained from forward/back propagations can generate spurious solutions that can not indicate (identify) the actual fault.

Two causal graphical tools (BG and SDG) discussed above have more advantages than the PCA detailed in the next section. A more comprehensive comparison of causal graphical methods (qualitative and quantitative) for diagnosis is presented in [19].

In this paper, we keep our focus on methods that exploit the causal structure implied by the bond graph and signed directed graph models. Moreover, to overcome the problems cited above, we shall propose a combined nonlinear dynamic PCA and graphical approaches (BG, SDG) based fault diagnosis algorithm to update FDI systems to track process changes for industrial chemical processes when the secondary events (secondary reaction, hazard event of thermal runaway… etc) appear in a chemical reaction. This extension improves the fault detection and isolation stages based on ARRs [19]. Based on the behavioral, structural and causal properties of an integrated coupled bond graph models, a signed directed graph is hence deduced. Fault detection is later performed using initial responses of all measured variables. Whenever an abnormality is indicated, a nonlinear dynamic PCA (obtained by using a neuronal network with five layers and three hidden layers) and back/forward propagations through paths from exogenous variables to system variables on SDG models are combined so as to identify fault roots through contribution plots.

The rest of the paper is organized as follows. Section 2 presents a PCA theory and its interest for fault diagnosis. After that, Sect. 3 provides the integrated design scheme combining graphical and nonlinear PCA approaches for FDI system. The efficiency of the proposed methods is then applied to monitor the pilot reactor equipped with a mono-fluid heating/cooling system in Sect. 4, the main results are also discussed therein. Section 5 presents concluding remarks and future scope of works.

2 Nonlinear Principal Component Analysis

In this section, we focused on a NLPCA method which is assumed as an extension of linear PCA [11, 21]. The aim of NLPCA is to extract both linear and nonlinear relationships between process variables.

Let us consider $x(k) = [x_1, \ldots, x_n]^T \in \mathbb{R}^n$ the vector formed with n observed variables at time instant k. The data matrix X, with m samples $x(k)$, is then:

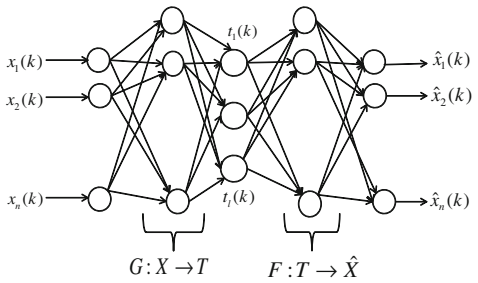

Fig. 1 Network architecture

$$X = \begin{bmatrix} x_1(1) & x_2(1) & \cdots & x_n(1) \\ x_1(2) & x_2(2) & \cdots & x_n(2) \\ \vdots & \vdots & & \vdots \\ x_1(m) & x_2(m) & \cdots & x_n(m) \end{bmatrix} \tag{1}$$

By analogy to PCA, the data matrix X and the principal components matrix T are determined as follows:

$$X = \hat{X} + E = F(T) + E \, and \, T = G(X) \tag{2}$$

where $\hat{X}$ is the estimated of X, F and G are nonlinear vector functions which are selected to minimize the prediction error E. To extract the nonlinear principal components, an auto-associative neural network [9] is used in the present paper. This method is based on a neuronal network with five layers and three hidden layers. The first hidden layer represents the nonlinear function G and the last one is the function F (see Fig. 1), the bottleneck layer is the nonlinear principal component t_i. The extraction of these components can be carried out of sequential or parallel way. Training of each network is complete when E, the sum of squared errors between the inputs and outputs of the network given in Eq. (3), is minimized:

$$E(k) = \sum_{i=1}^{n} (x_i(k) - \hat{x}_i(k))^2 \tag{3}$$

2.1 Fault Diagnosis Using a PCA

Fault detection using a PCA is based on two detection index: the *SPE* (squared prediction error) and the Hotelling's T^2 [11]. Whenever the detection index exceeds its confidence limit [8], the presence of an abnormality is indicated. Process diagnosis using PCA model is done by identifying the measured variable with

significant contributions to the residual [15]. The contribution of process variable j to the *SPE*-statistic at time period k is defined as:

$$cont_j^{SPE}(k) = (e_j(k))^2 = (x_j(k) - \hat{x}_j(k))^2 \tag{4}$$

In the case of T^2-statistic, the contribution of process variable x_j for a normalized principal component $\left(\frac{t_i}{\sigma_i}\right)^2$ (σ_i is a singular value equal to $\sqrt{\lambda_i}$) is:

$$cont_{i,j} = \frac{t_i}{\lambda_i} p_{i,j} x_j \tag{5}$$

where $p_{i,j}$ is the jth element of the eigenvector P_i corresponding to the eigenvalue λ_i. Thus, the total contribution to the T^2-statistic of a variable x_j is as follows:

$$Cont_j = \sum_{i=1}^{l} cont_{i,j} \tag{6}$$

Consequently, a process variable is identified as a fault when it has the higher contribution plot.

2.2 Dynamic PCA

The PCA discussed previously assume implicitly that the observations at one time instant are statistically independent to observations at past time instances. For typical industrial processes, this suggests that a method taking into account the serial correlations in the data is needed in order to implement a process monitoring method with fast sampling times. Alternatively, PCA can be used to take into account the serial correlations by augmenting each observation vector with the previous s observations [10] and stacking the data matrix in the following manner:

$$\begin{aligned} X(s) &= [X(k)\ X(k-1)\ \cdots\ X(k-s)] \\ &= \begin{bmatrix} x^T(k) & x^T(k-1) & \cdots & x^T(k-s) \\ x^T(k-1) & x^T(k-2) & \cdots & x^T(k-s-1) \\ \vdots & \vdots & \ddots & \vdots \\ x^T(k+s-n) & x^T(k+s-n-1) & \cdots & x^T(k-n) \end{bmatrix} \end{aligned} \tag{7}$$

The procedure for selecting s is discussed in detail in [10].

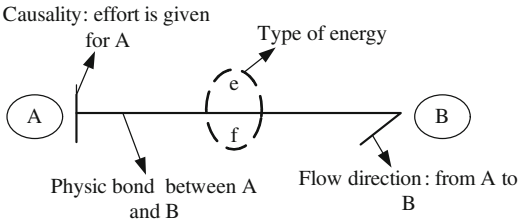

Fig. 2 Bond graph representation

3 Causal Graphical Approaches for FDI

3.1 Bond Graph Methodology

Bond graph language allows to deal with the enormous amount of equations describing the process behavior and to display explicitly the power exchange between the process components starting from the instrumentation architecture Dauphin-Tanguy [3]. The exchanged power between two variables *A* and *B* (Fig. 2) is represented by a bond (half arrow) and it is the product of two generic power variables named effort *e* and flow *f*. The causal stroke indicates the direction in which the effort signal is directed [18]. In a bond graph, two sources (S_e and S_f), three generalized passive elements (*I*, *C*, and *R*) and four constraints (0, 1, *TF*, and *GY*) are used to model any energetic processes.

3.1.1 Coupled Bond Graph

Industrial processes are very nonlinear, principally due to the interaction of different phenomena (chemical, thermal and fluidic). Therefore, the bond graph models the interaction of phenomena by a multiport element, indeed, the multiport elements represent energy dissipation (**R-element**) (electrical, mechanical or thermal friction), storage (**C-element**) (as compliance for instance or volume), inertia (**I-element**) (electrical inductance and mechanical inertia), balance and continuity equations (the **0- and 1-junctions**) or inter-domain coupling (the **TF transformer** and **GY gyrator elements**). Finally to reproduce the architecture of the global system to be modelled, bond graph elements (R, C, I,..) are interconnected by a "0" junctions when they have a common effort and by "1" junction if their flow is the same. In addition to matter transformation phenomena, chemical and electrochemical processes involve additional complexity in the modelling task, since the mass that flows through the process carries the internal energy which is stored in it, and which is thus transported from one location to another in a non-dissipative fashion. Power variables are thus in vectorial form [17]:

$$E = [\, e_h \quad e_t \quad e_c \,]^T \tag{8}$$

$$F = [\, f_h \quad f_t \quad f \,]^T \tag{9}$$

where e_h, e_t and e_c are, respectively, the hydraulic, thermal and chemical effort. f_h, f_t and f_c are, respectively, the corresponding flows.

3.1.2 Bond Graph for FDI System

The causal properties of the BG model is used to determine the origin and consequences of faults, they also generate analytical redundancy relations (ARRs) based on energy conservation equations from junctions 0 and 1. There are essentially two parts in a monitored system using BG: a bond graph model and an information system. The bond graph model consists of the process and the set of actuators. The sensors and the control system form the information system. A system S may be described by a set of constraints F (which represents the system model), a set of variables Z and a set of parameters q; $S = S(F, Z, \theta)$. The constraints, F, can be seen as any relation which links the system variables and the parameters. It has to include information about the structure, the behavior, the measurement and the control system. The set of constraints, F, map to a set of variables, Z: known (K) contains the control variables u, the variables whose values are measured by the sensors, Y_m; and the supervision parameter (such as set points) and is associated with the characteristics of R, C, and I elements. Unknown (X) are the power variables (flow and effort) that label the bonds. The constraints and variables are deduced directly from the bond graph model [17].

3.1.3 Generation of Fault Indicators

Finding the ARRs can be done by eliminating the unknown variables which are systematically obtained from the model BG thanks to causal properties and through causal paths.

- **Algorithms for generation the ARRs**:
  (1) the Bond Graph model should be converted in preferred derivative causality (by reversing the causality of detectors);
  (2) write the equations of the model;
  (3) for all constitutive equations of the junction 0 and 1 containing at least one detector: Eliminate the unknown variables by covering causal paths in the bond graph and for sensors whose causality is reversed an ARR is deducted;
  (4) An ARR is obtained from each controller by comparing the measured output with the output predicted by the control algorithm;

(5) repeat steps (3) and (4): if the ARRs obtained are strictly different from those already obtained then keep them, otherwise continue until all equations junctions and those regulators are considered.

- **Fault signature matrix**:
The structure of the residuals forms a binary matrix S_{ji} which expresses discrepancy in which component j (sensors, actuators, controllers and physical devices) can change the value of which residual, i.

$$S_{ji} = \begin{cases} 1 & \text{if the ith residual contains the jth component;} \\ 0 & \text{otherwise.} \end{cases} \tag{10}$$

The matrix S_{ji} is called the fault signature matrix that provides the logic for the process fault isolation after the monitoring application has detected a fault. Each component has a corresponding signature and its fault is isolable if its signature is unique, i.e. different from the signatures of all other components.

3.2 Signed Directed Graph

A signed directed graph is a representation of the process causal information, in which the process variables (and parameters) are represented as graph nodes and causal relations are showed by directed arcs [13]. Nodes in the SDG assume values of (0), (+) and (−) representing the nominal steady-state value, higher and lower than steady-state values, respectively. Directed arcs point from a cause node to its effect node. Arc signs associated with each directed arc can take values of (+) or (−) representing whether the cause and effect change in the same direction or opposite direction, respectively.

Definition 1 (*exogenous variables*) Exogenous variables are the variables (denoted by $\forall e_i \varepsilon E$) that are not affected by any other variable. They represent disturbance and fault variables and can change independently. Thus, there are no arcs incident on them [13].

Definition 2 (*System variables*) These variables (denoted by $\forall x_j \varepsilon X$) get affected by exogenous variables and affect each other. So, they have both input and output arcs associated with them. These are often called state variables also [13].

SDGs for the processes modeling can be derived from expert or operator knowledge of the process or from known model equations that define the behavior of the system. In this section, only algorithms for development the signed digraph models from analytic system models.

3.2.1 Build the SDG Model

- Algorithm for systems described by DE: In systems described by differential equations, explicit causality is from right to left [20]. To develop the SDG, for every differential equation, the variable on the left-hand side is matched with that equation and directed arcs are drawn from all the variables on the right-hand side to the system variable on the left-hand side in that equation. The arc sign $(e_l \rightarrow x_i)$ is given by $[\frac{\partial f_i}{\partial e_l}]$.
  Example: Consider the DE system given below

$$\begin{cases} \frac{dx_1}{dt} = x_1 - x_2 + 2e_1 \\ \frac{dx_2}{dt} = -x_1 - 4e_1 \end{cases} \tag{11}$$

  The SDG for the DE in Eq. (11) is given in Fig. 3.
- Algorithm for AE systems: A bi-partite graph between the equations and the system variables is drawn and a perfect matching is performed. A perfect matching between the equations and the dependent variables is a complete matching in which each equation is matched with a variable and no variable or equation is left unmatched. The arc sign $\text{sign}(e_l \rightarrow x_j)$ is given by $-(\frac{\partial f_i}{\partial e_l} / \frac{\partial f_i}{\partial x_j})$.
  Example: Consider the AE system given by Eq. (12)

$$\begin{cases} 2x_1 - e_1 - e_2 = 0 \\ x_1 - 2x_2 + x_3 - 2e_1 = 0 \\ 2x_2 + 4x_3 - 3e_1 + e_2 = 0 \end{cases} \tag{12}$$

  The SDG for Eq. (12) is shown in Fig. 4.
- Algorithm for DAE systems: The previous two algorithms (DE and AE) are combined to develop the algorithm for DAE systems.
  Example: Consider the DAE system given by Eq. (13)

$$\begin{cases} \frac{dx_1}{dt} = x_1 - x_2 + 2e_1 \\ \frac{dx_2}{dt} = -x_1 - 4e_1 \\ 2x_2 + 4x_3 - 3e_1 + e_2 = 0 \end{cases} \tag{13}$$

  The corresponding SDG for Eq. (13) is represented in Fig. 5.

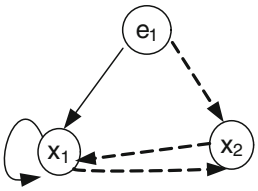

Fig. 3 SDG for the DE system

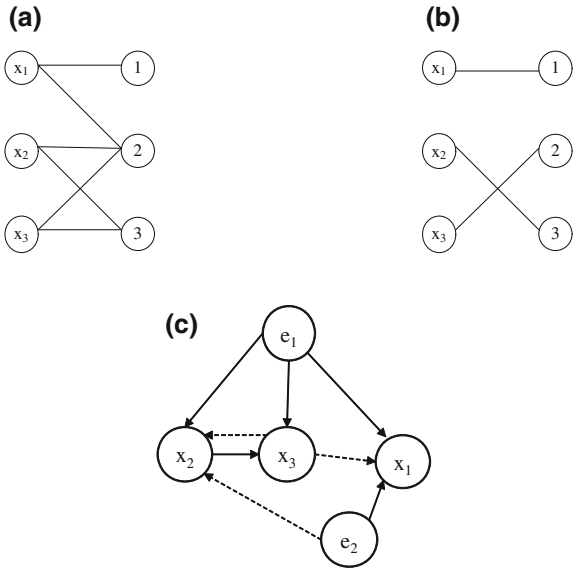

Fig. 4 **a** Bi-partite graph, **b** Perfect matching, **c** SDG

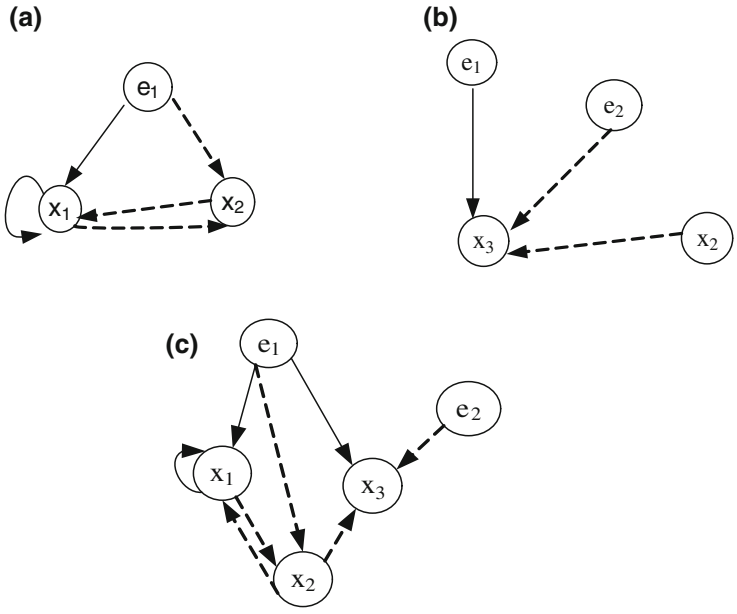

Fig. 5 SDG for the **a** DE, **b** AE, **c** DAE

3.2.2 Procedures for SDG Analysis

Definition 3 (*Initial response*) The initial response of a system variable is its first nonzero response [13].

Definition 4 (*Steady-state response*) The ultimate response of a dynamic system is governed by the AE system [13].

The SDG developed using algorithms presented in the previous section is analyzed to predict the initial response and/or steady-state response of the system for deviations in exogenous variables from their nominal value.

- For DE systems, initial response of a system variable x_j due to changes in an exogenous variable e_l can be predicted by propagation through all the shortest path(s) from e_l to x_j in the SDG.
- For AE systems, if it has only one perfect matching, the response of an AE system is predicted by propagation through paths in a SDG. If not, this response is incomplete but, there is an exception: in the SDG should exist negative cycles.
- For DAE system, by considering the arc length for the arcs corresponding to the DE is 1 and to the AE is 0, the initial response, with only one perfect matching, is obtained by propagation through shortest paths from e_l to x_j.

3.2.3 FDI Based on Signed Directed Graph

Algorithm 1 (*initial response*) This algorithm is applied for system equations and it consists on: the generation of SDG model, then determination of measured node deviations for a given fault (these deviations called initial response). Finally, comparing the simulation results with the prediction of initial response. Fault diagnosis for single faults using measurements simulation and initial response is performed separately. The possible faults are identified as the faults that are predicted by both analysis.

Algorithm 2 (*steady-state response*) [12] is applied when the system is in its steady-state (corresponding algebraic equations). Steps of this algorithm are given below:

1. Chose a system variable x_i and push it on to the stack S (initially S was empty). Go to Step 2.
2. For a chosen x_i, use back-propagation to infer the signs of the predecessor nodes.
3. If the predecessor node x_j or e_l has not been explored in any other parts of the search tree, go to Step 4. Else, go to Step 5.

4. If this node is an exogenous variable (e_l), it could be a possible fault. To verify this, perform forward-propagation to predict the sign of measured nodes. If there are no violations, it is concluded that e_l, with its sign, is a candidate fault, else it is not. In either case, go to Step 5. If the predecessor node is a system variable (x_j), it must be further explored. Push x_j on to the stack S and go to Step 2.
5. If there are no unexamined predecessor nodes, the search is complete and stop. Else select and explore another predecessor node from P(x_i). Go to Step 3.

4 New Algorithm for Multi-energy Systems

The proposed generalized algorithm combines graphical approaches [quantitative (BG) and qualitative (SDG)] and nonlinear dynamic PCA so as to improve the robustness of the isolation from residuals generated by a model based diagnosis system. This algorithm involves three steps: modelling, fault detection and isolation steps (see Fig. 6). The overall flow of the FDI algorithm is summarized as follows:

- Modelling step: The bond graph methodology is a suitable tool for modelling nonlinear processes with coupled phenomena. A signed directed graph model is then generated directly from this coupled bond graph, using causal and structural properties of these graphs (see BG-SDG analog Table 1), consequently, the graphical model is obtained.
- Fault detection is an important step because it indicates the state (normal or abnormal situation). Abnormal situations are detected when initial responses of all measured variables due to deviation in exogenous variables on the SDG model are determined. Thus, the given non-zero sign of a measured variable, a fault is detected.
- Fault isolation: whenever a fault is detected, contribution plots of process variables are determined using a nonlinear PCA, the variable with a higher contribution is the faulty variable. It is selected (with its sign) and if it is a measured node in the SDG, a backward-propagation from this variable to the fault node is performed. If it was an exogenous variable then it constitutes a candidate fault.

Note that, when the contribution of process variables to SPE-statistic is used, sign of the selected variable is taken from initial response table.

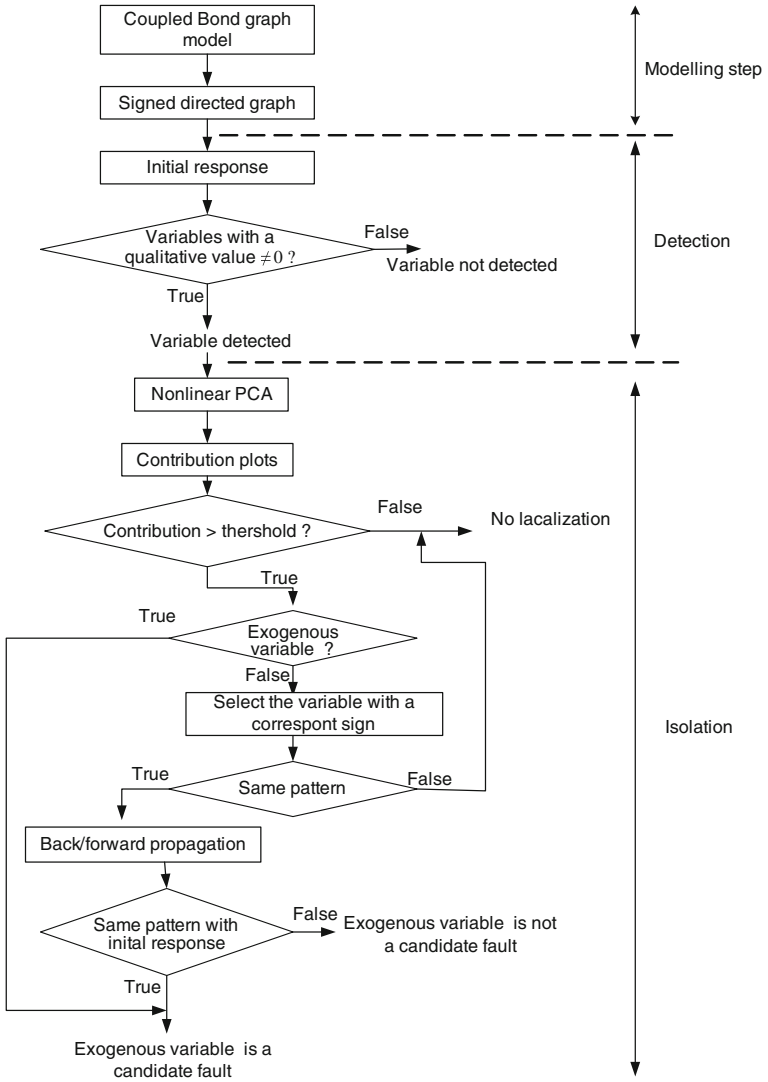

Fig. 6 Proposed algorithm

5 Case Study and Discussion of Results

A case study is developed to test the effectiveness of the proposed scheme on a simulation model built in the Matlab/Simulink environment and Symbols 2003 software. The pilot unit that we have considered here is a continuous stirred tank reactor (CSTR) equipped with coolant jacket developed in [19]. The following exothermic reaction scheme is considered:

Table 1 BG-SDG analog

	BG element	Gain	SDG element
L_0	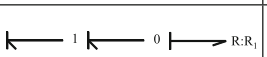	$\frac{-R_1}{I_1 s}$	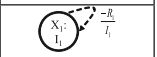
	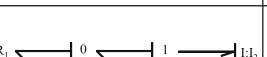	$\frac{-R_1}{I_2 s}$	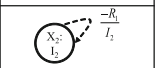
	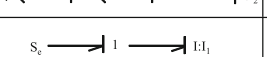	1	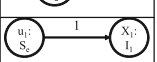
	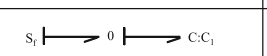	1	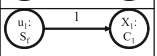
L_1	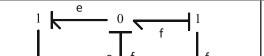	$\frac{R_1}{I_2 s}$	
	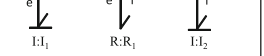	$\frac{R_1}{I_1 s}$	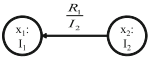
	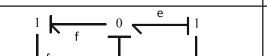	$\frac{-1}{C_1 s}$	
	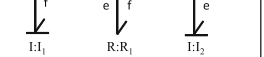	$\frac{1}{I_1 s}$	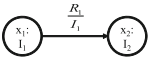
		$\frac{1}{C_1 s}$	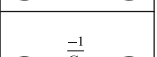
	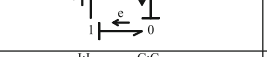	$\frac{1}{I_2 s}$	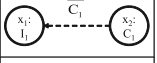
	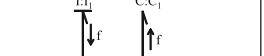	$\frac{-R_1}{I_1 s}$	
	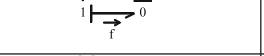	$\frac{R_1}{I_2 s}$	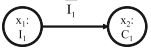

$$v_A A + v_B B \rightleftharpoons v_C C + v_D D \tag{14}$$

where v_i (for $i = A, B, C, D$) are the stoichiometric coefficients. A simple sketch of the process is shown in Fig. 7 and more details on the system description can be

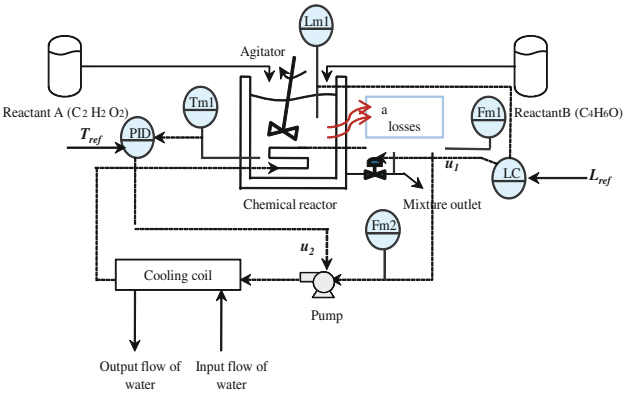

Fig. 7 Scheme of the CSTR

found in [4, 19]. The CSTR is highly nonlinear with its state variables, volume of the water inside the tank and total enthalpy, being nonlinear functions of the input flows. The tank's thermodynamic properties and the output flow also have nonlinear characteristics. Moreover, inside the closed-loop, time varying reference signals causes plant's dynamics to change rapidly. The relevant parameters of the reactor and jacket models are summarized in Table 2. In the previous researches [4, 19], because of modular and functional aspect of the bond graph, a pseudo bond graph model of the system developed from the energy and mass balances has been presented as subsystems modeled separately.

Thus to design a nonlinear FDI scheme, the SDG model must be constructed with the information obtained from coupled bond graph models in integral causality based on BG-SDG analog (see Table 1), as shown in Fig. 8. The positive (→) and negative (→) arcs indicate positive and negative influence.

The faults that may occur in the chemical process can be broadly divided into four groups; namely: physical faults (matter leakage in the tank reactor, blockage of the valve, thermal insulation and appearance of secondary reaction), actuator faults (pump defect), sensor faults (temperature and level sensors) and controller faults. These faults are listed in Table 3. In fact, nodes in the SDG assume values of (0), (+) and (−) representing the nominal steady-state value, higher and lower than steady-state values, respectively.

The initial responses are predicted by cause-effect propagation through the shortest paths on the SDG from local exogenous variables to relevant system variables. Hence, Table 3 shows the effect of the fault witch is propagated from the root node (fault node) to the nodes representing system variables in the SDG.

To perform comparison between these initial responses and simulation results, all faults are tested. In fact, two separate process faults are treated here. They are leakage of the mixture from the reactor vessel and appearance of secondary product. The rate of leakage in the tank $[R(+)]$ can be fast in a time window from 75 to 100 min. From Fig. 9, one can see that the measured variables (h, T, m_C, m_b) are

Table 2 Simulation parameters

Variable description	Tag	Value
Concentration of acid	C_A	4.313 mol L^{-1}
Concentration of alcohol	C_B	12.49 mol L^{-1}
Mass of acid	m_A	1.2 kg
Mass of alcohol	m_B	2.7 kg
Factor Arrhenius	k_0	4.1410^{13} $L_{min}^{-1}mol^{-1}$
Activation energy	E	76,534.704 J mol^{-1}
Inlet temperature	T_A, T_B	275 K
Heat of the reaction	H	1170 cal
Reaction rate	J	$2.513e^{-6}$ mol s^{-1}
Density of the mixture	ρ	1,000 g L^{-1}
Heat capacity of mixture	C_p	4.2 J g^{-1} K^{-1}
Heat transfer coefficient × area	$S.A$	12.10^5 J min^{-1} K^{-1}
Heat capacity of coolant	C_{p_w}	4,200 J kg^{-1} K^{-1}
Inlet jacket temperature	T_J	250 K
Coolant temperature	T_C	–
Chemical potential	μ	–
Thermal transfer	T_L	–
Level	h	–
Surrounding temperature	T_0	–

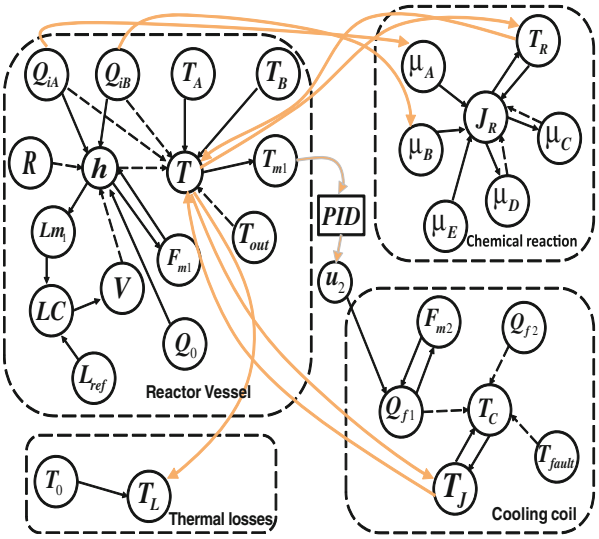

Fig. 8 SDG of a CSTR

Table 3 Faults description

Fault	Description	Symbol	Type
1	Inlet flow A	$Q_{iA}(+)$	Actuator
2	Inlet flow B	$Q_{iB}(+)$	Actuator
3	Chemical fault	$\mu_E(+)$	Process
4	Flow	$F_{m1}(+)$	Sensor
5	Flow	$F_{m2}(+)$	Sensor
6	Level	$L_{m1}(+)$	Sensor
7	Level	$L_{m2}(+)$	Sensor
8	Pump	$Q_{f1}(-)$	Actuator
9	Leakage	$R(+)$	Process
10	Cooling coil	$T_{fault}(+)$	Process
11	Temperature control	$PID(+)$	Controller
12	Level control	$LC(+)$	Controller
13	Reaction rate	$J_R(+)$	Sensor

sensitive to fault 9. By comparing the initial response in Table 4, $R(+)$ can be detected.

It is assumed now for example that the cooling system is never failing and that the exits of the regulators and the sensors are always correctly measured. A sudden appearance of secondary product E occurs from 70 min. The reaction dynamics are modified and the reaction scheme becomes:

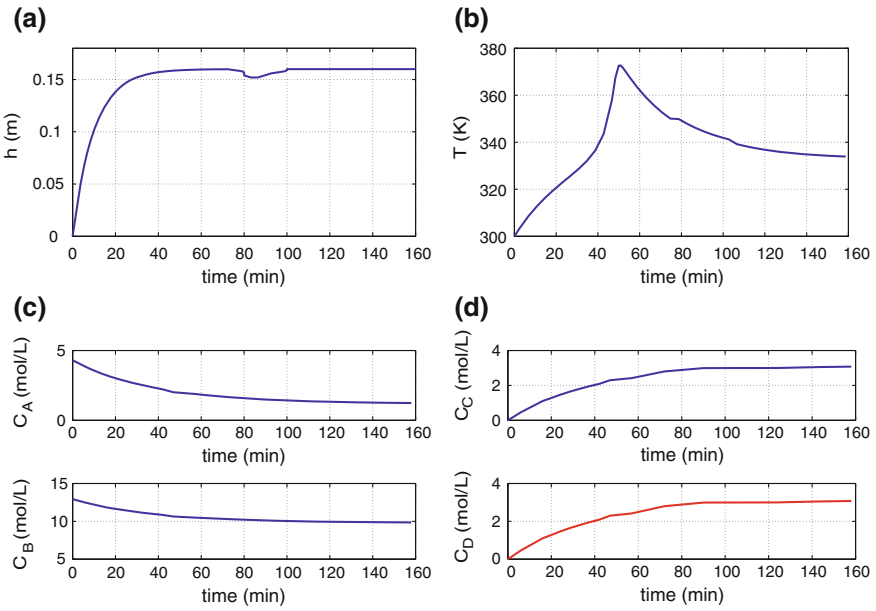

Fig. 9 Variables responses in faulty case (leakage)

Table 4 Initial response

Fault no.	Measured variables					
	h	T	μ_A	μ_B	μ_C	μ_D
1	+	−	+	0	+	+
2	+	−	0	+	+	+
3	0	+	0	0	+	+
4	+	−	0	0	−	−
5	0	+	0	0	−	−
6	−	+	0	0	+	+
7	0	−	0	0	−	−
8	0	+	0	0	+	+
9	−	+	0	0	+	+
10	0	+	0	0	+	+
11	0	−	0	0	−	−
12	−	+	0	0	+	+
13	0	+	0	0	+	+

$$v_A A + v_B B \rightleftharpoons v_C C + v_D D + v_E E \tag{15}$$

An exothermal chemical reaction requires an extensive knowledge of their thermodynamic characteristics, not only under normal operation conditions, but also in the case of deviations. Indeed, to stop the evolution of the secondary reaction and to eliminate these effects in real-time, it is necessary to add a reagent able to eliminate the undesirable products. As can be seen in Fig. 10, the chemical fault $\mu_E(+)$ affects (T, m_C and m_D) variables and generates a same qualitative signature $[0 \quad + \quad 0 \quad 0 \quad + \quad +]$. Thus, fault 3 is detected.

After a fault has been detected, the dynamic nonlinear PCA is then used. The case study has six measured variables (h, T, μ_A, μ_B, μ_C and μ_D), therefore, the vector $x(k)$ is $x(k) = [h \quad T \quad \mu_A \quad \mu_B \quad \mu_C \quad \mu_D]^T$. Here, only $m = 50$ samples are used. By using the eigenvalues analysis of the covariance matrix method and a Cumulative Percentage of Total Variation $C(l)$, the number l of principal components retained is 2 (Fig. 11). In Fig. 11a, we can see that from $l = 2$ the eigenvalues is lower than 1. Indeed, as shown in Fig. 11b, the Percentage $c(l)$ can explain 99.5 % from $l = 2$. To select the time-lagged s, we have applied the algorithm presented in [10] which allows in this case study to get $s = 1$.

When a leakage $R(+)$ is occurred, the contribution of process variables to *SPE*-statistic, as shown in Fig. 12, indicates that only the second variable (T) has the highest contribution with a positive sign (according to the initial response table). This variable is selected and as T is a measured variable in SDG model, backward propagation from this variable give $R(+)$, $T_A(+)$ and $T_B(+)$. But only the forward propagation from $R(+)$ allows the same pattern of measured variables found in the initial response table (we assumed that others exogenous variables (Q_{iA} and Q_{iB}) are in faulty-free case). Thus a leakage $R(+)$ is a root cause.

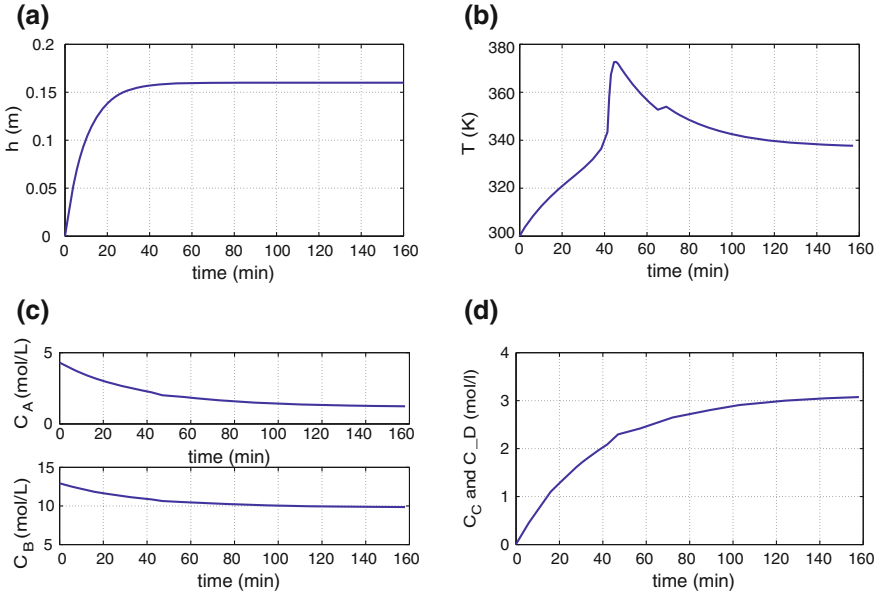

Fig. 10 Variables responses in faulty case (chemical fault)

Furthermore, we note that the contribution of process variables to *SPE*-statistic (Fig. 13) indicate that only the temperature variable T has the highest contribution with a positive sign in the occurrence of chemical fault ($\mu_E(+)$). This variable is selected and as T is a measured variable in the SDG model, therefore, the backward propagation from this variable is performed. By exploiting causal paths between variables of the SDG, the predecessor variables of T are μ_E and Q_{iA}, Q_{iB} and R. But only the forward propagation from $\mu_E(+)$ allows the same pattern of measured variables found in the initial response table (we assumed that others exogenous variables (T_A and T_B) are in faulty free case). Thus an undesirable product $\mu_E(+)$ is as a root cause. Consequently, $R(+)$ and $\mu_E(+)$ are isolated as candidate faults.

The above simulation results further demonstrate the merits of the proposed FDI algorithm. The result of a fault isolation is consistent when process and chemical faults are occurred so as the candidate fault is identified exactly.

Comparison of Causal graphical and PCA methods:

The signed directed graph (SDG) is a qualitative model-based diagnosis method. The qualitative model is created from causal or inferential analysis. Therefore, a detailed mathematical model is not necessary. The nodes of a SDG are process variables, measurements, inputs, and faults. To use a SDG for fault diagnosis, high and low thresholds are defined for variables. In fact, if a detailed model of the process is available then one can easily construct a SDG from the model. The causality concept in bond graph (BG) model is helpful in this regard. The procedure for the construction of a SDG from a bond graph model is similar to construction of temporal causal graphs from bond graph models as detailed in [16].

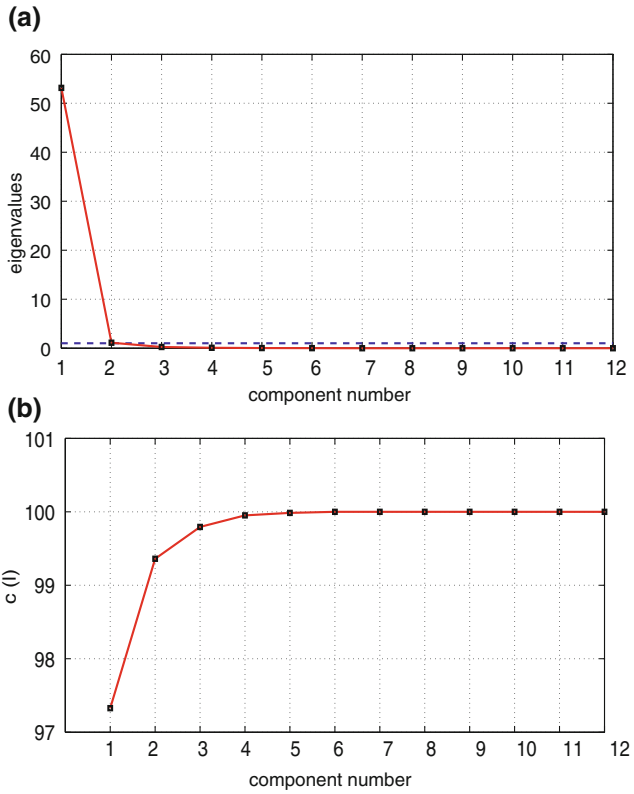

Fig. 11 Principal component retained

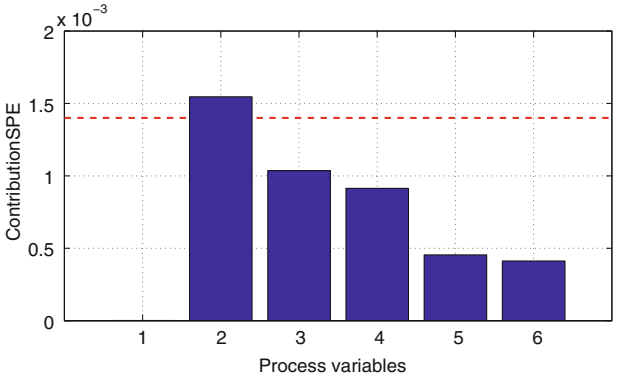

Fig. 12 SPE in the case of leakage

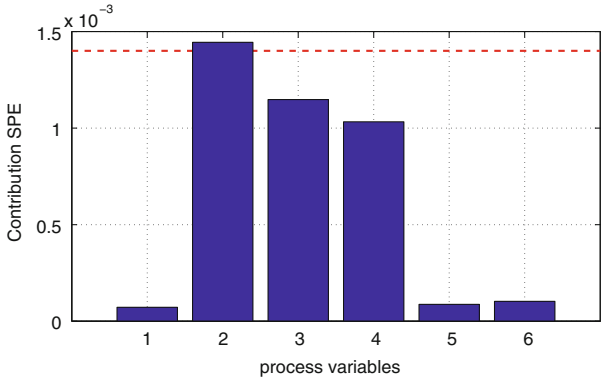

Fig. 13 SPE in the case of chemical fault

The SDG model can be used in different ways for diagnosis. The forward propagation method assumes one or more faults in variables (nodes) in the SDG and propagates the fault effects to adjacent nodes. The qualitative states of the measured variables are then recorded in a knowledge base which stores the symptoms seen in the measured variables for each fault case. The backward propagation method traverses from symptoms (qualitative states of measurements) to qualitative states of physical variables and needs conflict resolutions when ambiguities arise during the propagation process. The approach developed in this article has the potential to be a unified approach for carrying out various activities involved in process supervision by using a common modeling tool. Some process faults may not be isolated with the given sensor architecture. In such situations, more than one fault candidates are hypothesized. In fact, such Principal Component Analysis is often able to isolate the actual fault although the fault is structurally not isolating. Thus, the analysis of the transient's setup due to fault occurrence gives useful information about the nature of the fault. A SDG can be derived from the bond graph model through a set of transformations. The SDG approach uses ACP to improve the fault isolation capability especially when some faults cannot be isolated structurally.

Note that the development of a combining graphical and PCA-based multiple fault diagnosis algorithm is introduced here in order to be used later. The proposed method is an extension of the single fault case. It consists, essentially after a construction of the signed directed graph model directly from the bond graph, on:

- According to the obtained SDG model, determine the initial response of all measured variables due to the deviation of exogenous variables as in single fault diagnosis case;
- For an abnormal situation, arrange the root nodes in lists that explain the same symptom;

- For each symptom, get lists which contain combinations of the root nodes;
- Contributions plots of PCA is used to fix the number N of faults that can affect the system. Hence, the correspond list is identified. For instance, if a contribution plots of two variables exceeds its confidence limit then N is set equal to 2;
- The combination of greater than N fault origins occurring simultaneously should be deleted. For the others combinations, forward propagation from these exogenous variables for all measured variables is performed to obtain their deviations (signs), if this symptom is the same that found previously then this list (eventually combination) is considered as the root causes.

6 Conclusion

In this paper, the new FDI generalized algorithm for nonlinear processes with coupled energies in presence of chemical and thermodynamic phenomena has been addressed. Indeed, we investigated an automated framework for the interpretation of causal graphical approaches (coupled BG and SDG) using a nonlinear dynamic PCA to perform process monitoring in normal situations as well as in the presence of failures without any need of numerical calculations.

An advantage of this approach is the automation of SDG-based fault diagnosis where the situation ambiguities to determine the faulty variables is replaced by automated interpretation of the contribution plots using NPCA.

The proposed algorithm further reduced the number of spurious solutions of the SDG-based fault diagnosis, in which a faulty variable is selected by NPCA and the use of back/forward propagation on the SDG. The effectiveness of this combination is has been validated to a chemical reactor coupled with a complex heat exchanger taking into account chemical faults such as occurrence of secondary reaction.

In our future works, we will consider multiple fault diagnosis issues. Extension to nonlinear uncertain processes will be also envisaged.

References

1. Chiang, L.H., Braatz, R.D., Russell, E.L.: Fault Detection and Diagnosis in Industrial Systems. Springer, London (2001)
2. Colbert, D.: Toxic Relief: Restore Health and Energy Through Fasting and Detoxification. Charisma Media, Lake Mary (2011)
3. Dauphin-Tanguy, G.: Les Bond Graphs. Hermès Science, Paris (2000)
4. El Harabi, R., Ould-Bouamama, B., Gayed, M.K.B., Abdelkrim, M.N.: Pseudo bond graph for fault detection and isolation of an industrial chemical reactor part I: bond graph modeling. In:

Proceedings of the 2010 Spring Simulation Multiconference, p. 220. Society for Computer Simulation International (2010)
5. Gilles, E.D.: Network theory for chemical processes. Chem. Eng. Technol. **21**(2), 121–132 (1998)
6. Heny, C., Simanca, D., Delgado, M.: Pseudo-bond graph model and simulation of a continuous stirred tank reactor. J. Franklin Inst. **337**(1), 21–42 (2000)
7. Iri, M., Aoki, K., O'Shima, E., Matsuyama, H.: An algorithm for diagnosis of system failures in the chemical process. Comput. Chem. Eng. **3**(1), 489–493 (1979)
8. Jackson, J.E., Mudholkar, G.S.: Control procedures for residuals associated with principal component analysis. Technometrics **21**(3), 341–349 (1979)
9. Kramer, M.A.: Nonlinear principal component analysis using autoassociative neural networks. AIChE J. **37**(2), 233–243 (1991)
10. Ku, W., Storer, R.H., Georgakis, C.: Disturbance detection and isolation by dynamic principal component analysis. Chemometr. Intell. Lab. Syst. **30**(1), 179–196 (1995)
11. MacGregor, J., Kourti, T., Nomikos, P.: Analysis, monitoring and fault diagnosis of industrial processes using multivariate statistical projection methods. In: Proceedings of 13th IFAC World Congress, San Francisco, USA (1996)
12. Maurya, M., Rengaswamy, R., Venkatasubramanian, V.: A signed directed graph-based systematic framework for steady-state malfunction diagnosis inside control loops. Chem. Eng. Sci. **61**(6), 1790–1810 (2006)
13. Maurya, M.R., Rengaswamy, R., Venkatasubramanian, V.: A systematic framework for the development and analysis of signed digraphs for chemical processes. 1. Algorithms and analysis. Ind. Eng. Chem. Res. **42**(20), 4789–4810 (2003)
14. Maurya, M.R., Rengaswamy, R., Venkatasubramanian, V.: A signed directed graph and qualitative trend analysis-based framework for incipient fault diagnosis. Chem. Eng. Res. Des. **85**(10), 1407–1422 (2007)
15. Miller, P., Swanson, R.E., Heckler, C.E.: Contribution plots: a missing link in multivariate quality control. Appl. Math. Comput. Sci. **8**, 775–792 (1998)
16. Mosterman, P.J., Biswas, G.: Diagnosis of continuous valued systems in transient operating regions. IEEE Trans. Syst. Man Cybern. Part A Syst. Hum. **29**(6), 554–565 (1999)
17. Ould Bouamama, B.: Modélisation et supervision des systèmes en Génie des procédés–approche Bond Graphs. PhD thesis, Laboratoire d'Automatique et Informatique Industrielle de Lille USTL, France (2002)
18. Ould Bouamama, B.: Applications de la méthode bond graph à la modélisation des systèmes énergétiques. Article publié dans les techniques d'ingénieurs (2005)
19. Ould-Bouamama, B., El Harabi, R., Abdelkrim, M.N., Ben Gayed, M.: Bond graphs for the diagnosis of chemical processes. Comput. Chem. Eng. **36**, 301–324 (2012)
20. Oyeleye, O., Kramer, M.: Qualitative simulation of chemical process systems: steady-state analysis. AIChE J. **34**(9), 1441–1454 (1988)
21. Raich, A., Cinar, A.: Statistical process monitoring and disturbance diagnosis in multivariable continuous processes. AIChE J. **42**(4), 995–1009 (1996)
22. Samantaray, A., Ghoshal, S.: Bicausal bond graphs for supervision: From fault detection and isolation to fault accommodation. J. Franklin Inst. **345**(1), 1–28 (2008)
23. Samantaray, A.K., Bouamama, B.O.: Model-Based Process Supervision. Springer, London (2008)
24. Samantaray, A.K., Medjaher, K., Ould Bouamama, B., Staroswiecki, M., Dauphin-Tanguy, G.: Diagnostic bond graphs for online fault detection and isolation. Simul. Model. Pract. Theory **14**(3), 237–262 (2006)
25. Smaili, R., El Harabi, R., Abdelkrim, M.N.: Fdi based on causal graphical approaches for nonlinear processes. In: 10th International Multi-conference on Systems, Signals and Devices (SSD), 2013, pp. 1–6. IEEE (2013a)
26. Smaili, R., Harabi, R.E., Abdelkrim, M.N.: Model-based process diagnosis: bond graph and signed directed graph tools. In: International Conference on Control, Decision and Information Technologies (CoDIT), 2013, pp. 782–787. IEEE (2013b)

27. Stoessel, F.: Thermal Safety of Chemical Processes: Risk Assessment and Process Design. Wiley, Weinheim (2008)
28. Thoma, J., Bouamama, B.O.: Modelling and Simulation in Thermal and Chemical Engineering: A Bond Graph Approach. Springer, Berlin (2000)
29. Vedam, H., Venkatasubramanian, V.: PCA-SDG based process monitoring and fault diagnosis. Control Eng. Pract. **7**(7), 903–917 (1999)